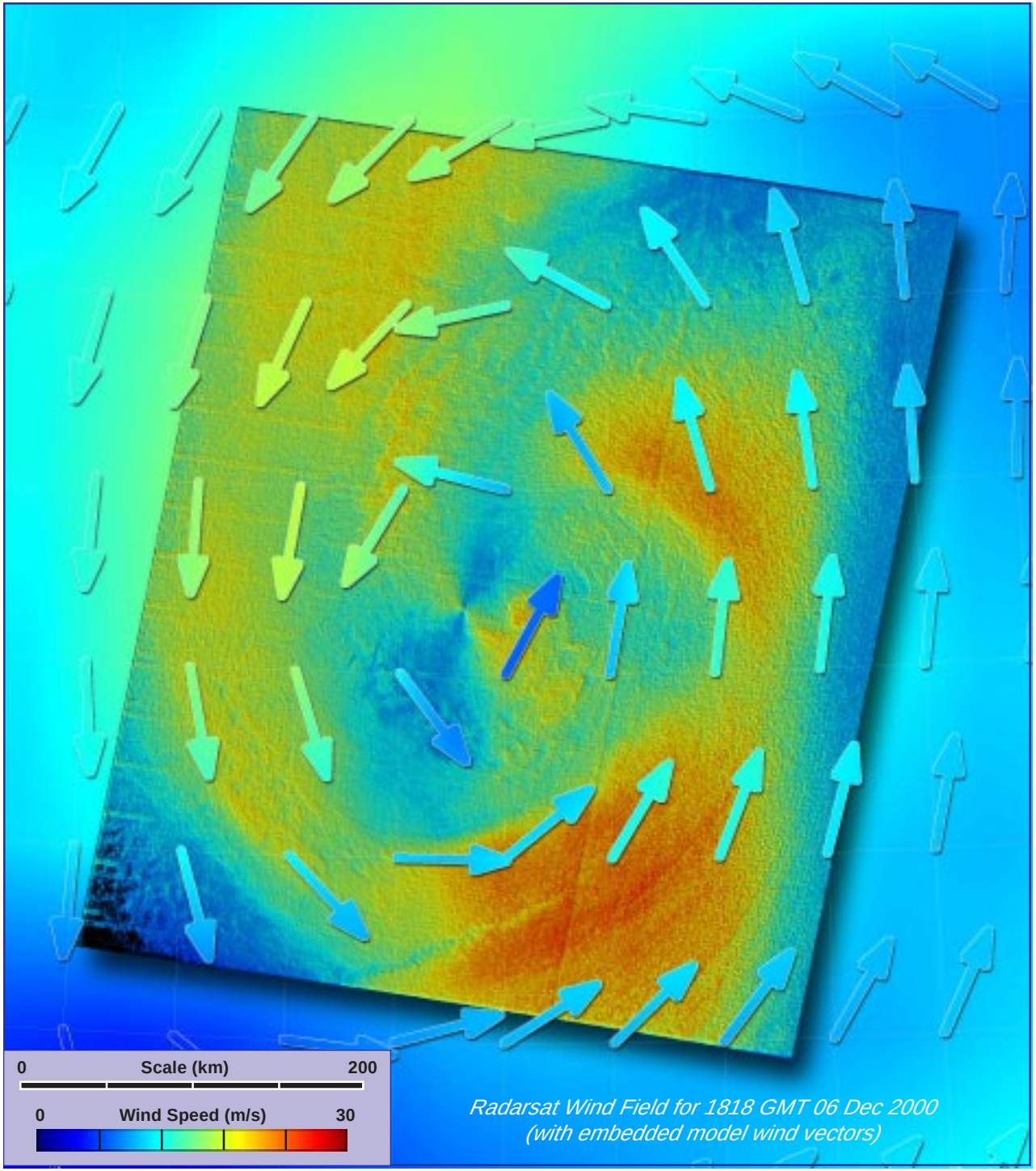

Radarsat Wind Field for 1818 GMT 06 Dec 2000
(with embedded model wind vectors)

High Resolution Wind Monitoring with Wide Swath SAR: A User's Guide

Bob Beal
SSARGASSO Associates

George Young
Pennsylvania State University

Frank Monaldo
Don Thompson
Nathaniel (Pete) Winstead
The Johns Hopkins University
Applied Physics Laboratory

Carven Scott
Anchorage Weather Forecast Office

May 2004

High Resolution Wind Monitoring with Wide Swath SAR: A User's Guide

Bob Beal
rcbeal@aol.com
SSARGASSO Associates
12222 Carroll Mill Road
Ellicott City, MD 21042

George Young
young@ems.psu.edu
Pennsylvania State University
503 Walker Building
University Park, PA 16802

Frank Monaldo
f.monaldo@jhuapl.edu
Don Thompson
d.thompson@jhuapl.edu
Nathaniel (Pete) Winstead
n.winstead@jhuapl.edu
The Johns Hopkins University
Applied Physics Laboratory
11100 Johns Hopkins Road
Laurel, MD 20723

Carven Scott
carven.scott@noaa.gov
Anchorage Weather Forecast Office
6930 Sand Lake Road
Anchorage, AK 99502

Table of Contents

Foreword

High resolution SAR-derived wind fields over the ocean offer the potential for a new and unique perspective of the spatially evolving wind field, especially within storms and along coasts. SAR wind fields often show a spatial variability neither modeled nor measured by any other technique. But the SAR wind estimates are not error-free, and themselves contain systematic, random, and sometimes nonlinear errors not yet fully characterized. Nevertheless, as this Guide testifies, even our present limited understanding of the complete error structure is sufficient to demonstrate the unique power of this new tool.

The history, current status, and future prospect of scientific SAR constitute a tale of a continuing quest for wider swath, higher resolution, lower noise, better calibration, more accurate algorithms, and quicker delivery of targeted products to specific user communities: in the case of this work, the operational meteorological community. In addition to the technical and scientific problems, difficult political issues must be addressed: a viable SAR global meteorological network must contain a guarantee of reliable and inexpensive access to a coordinated data base from the array of internationally sponsored SARs, both currently operating and in the planning stage.

More than a quarter century has elapsed since the U.S. Seasat, carrying the first civilian SAR launched solely for scientific purposes, provided the first exciting and provocative high resolution radar images of the ocean from space. The Seasat SAR (L-band, ~20 cm Bragg interaction wavelength, 100 km swath) operated for only about 100 days from 4 July to 10 October 1978 before it failed, but the spatial patterns in its ocean surface images revealed a rich variety of physical processes that was, for the most part, quite unexpected in the scientific community. Even the first crude optically processed (with lenses instead of computers) images clearly showed ocean and atmospheric internal wave patterns, tropical storm cells, Gulf Stream signatures, spatially evolving wind generated waves, and many other phenomena of potential interest to both oceanographers and meteorologists. The Seasat SAR, however, was for the most part uncalibrated, and image processing usually took hours, sometimes months.

In the wake of this short burst of activity in the late 1970's, no other civilian free-flying (non-Shuttle) scientific SAR was launched for more than a decade. Then, in 1991, after several years of design and preparation, both the European and Japanese Space Agencies launched SARs: ERS-1 and JERS-1, operating at C-band (~5 cm Bragg interaction, 100 km swath) and L-band (~20 cm Bragg interaction, 75 km swath), respectively. ERS-1 provided the main source of high quality oceanographic SAR imagery during the first half of the 1990's. The JERS-1 SAR unfortunately was seriously handicapped by excessive ambiguities (ghosts) in its imagery originating from a faulty antenna, greatly reducing its value as a calibrated scientific instrument. The ERS-1 SAR and its identical successor on ERS-2 in 1995 provided for the first time carefully calibrated and stable instruments from which quantitative radar backscatter, in combination with an appropriate geophysical algorithm, including an estimate of the local wind direction, could yield accurate values of the surface wind magnitude on sub-kilometer scales, a feat not possible with any other sensor, nor indeed even easily modeled.

In 1995, another major step in the evolution of SAR was taken with the launch of the Canadian Radarsat-1. Radarsat-1 contained the first "ScanSAR", a sophisticated improvement over all previous conventional SARs that allowed much wider swaths (>400 km) by coherently combining the returns of several antenna beams. Unfortunately the Radarsat-1 ScanSAR had an offsetting liability: an engineering oversight allowed a nonlinear (scene-dependent) instrument transfer function, thus precluding the possibility of accurate calibration in high winds. Nevertheless, Radarsat-1, with its 400 to 500 km swath width and international accessibility, has provided a vast and compelling inventory of high resolution wind patterns over the ocean.

In the latter half of 2002 and early 2003, wide swath imagery from the European Envisat "Advanced SAR" (ASAR) began to emerge. From the early evidence (see following section), most of the engineering problems associated with the Radarsat-1 ScanSAR have been largely overcome in the Envisat wide swath ScanSAR modes. With respect to Radarsat-1, the Envisat ScanSAR antenna beam corrections are more precise, the radar system dynamic range is wider and more linear, and more attention has been given to the absolute calibration of its wide swath modes. As a consequence, the performance of the ScanSAR itself appears finally to be only a minor source of error in the determination of wind speed. Other error sources resulting from uncertainties in 1) the backscatter-to-wind-speed relationship (especially at winds higher than ~15 m/s) and 2) the initial wind direction estimate are now dominant. As more data from Envisat and future SARs such as Radarsat-2 and the Japanese ALOS are collected, the first error will gradually be reduced to acceptable levels. But the second error, under some circumstances, for example in the vicinity of fronts and within small-scale vorticies, can produce wind magnitude errors of a factor of two. Reduction of these kinds of errors clearly will require some kind of blending of information both from high resolution forecast models and from features within the SAR imagery itself.

Clearly substantial progress has been made, especially in the past decade, toward achieving well-calibrated scientifically viable 400 to 500 km wide swath SARs. The next step, towards *operational* viability, will require a concerted international effort to coordinate multiple ScanSAR satellites, effectively achieving swath widths of 1200 to 1500 km. Such effective swath widths would for the first time allow twice-daily coverage of most of the world's oceans.

It is easy to be optimistic about the future. Government reluctance to freely disseminate high resolution SAR imagery is an outdated legacy arising from its historical value in military intelligence gathering. But high resolution (sub-km) wind fields are at least two orders of magnitude removed from any useful intelligence mode. SAR wind field products should be treated like any other satellite wind field products. For example, QuikSCAT winds are now delivered to the

public several times daily through the web site of the U.S. National Data Buoy Office. It takes little imagination to envision one additional link to a concurrent (but much higher resolution) SAR wind field from any of three wide swath SARs planned to be operating by 2005.

Merely coordinating a suite of international wide swath SARs and achieving rapid and accurate wind field production, however, will still not be sufficient to insure operational viability. The critical link that must be forged lies within the operational forecast offices themselves. The SAR wind products need to be delivered in a sufficiently convenient format to the forecaster, who is already overwhelmed with data inputs from a large variety of sources of varying credibility, that they will blend smoothly into his routine. Ultimately, the SAR wind fields must simplify the task of the forecaster, not complicate it. For this to be accomplished, continuing collaboration with the weather forecast offices will be an essential component of this final transition phase.

The Guide is composed of three parts. Section I (SAR as a High Resolution Scatterometer) outlines the physical and empirical basis for deriving quantitative high resolution wind fields from SAR, illustrates the form of some major errors and uncertainties unique to the instrument, and concludes with an example of how multiple wide swath SARs can work together to effectively double (or triple) the coverage of any single one.

Section II (Meteorological Phenomena in High Resolution SAR Wind Imagery) contains a description of and tutorial on the classes of meteorological phenomena commonly found in SAR wind imagery. Eleven distinct classes are identified: island and mountain wakes, point wakes, mountain lee waves, simple gap flows, hybrid gap flows (including both reverse gap flow and gap flow/synoptic interaction), synoptic fronts, synoptic lows, mesoscale lows along fronts, mesoscale lows associated with cold air outbreaks, convection, and coastal barrier jets. Examples from each of the 11 classes are drawn from the comprehensive Radarsat-1 wind field inventory of Section III.

Section III (Inventory of Radarsat SAR Wind Fields), the core of this Guide, contains a selected set of 60 Radarsat wide-swath (~430 km) SAR-estimated wind fields accompanied with narrative, analysis, and interpretation, presented in the context of concurrent U.S. Navy forecast/nowcast Global Atmospheric Prediction System (NOGAPS) model fields. All 60 passes were acquired over the Gulf of Alaska and Bering Sea between 31 October 1999 and 14 November 2001. This set of 60 has been chosen from the more than 10,000 available to demonstrate the unprecedented and unique potential of wide swath SAR to reveal the intricate details of surface wind patterns over the ocean.

These three major sections are followed by a brief example (Appendix A) illustrating the potential value of SAR in an actual operational scenario.

This three-year project contains the efforts of several of my colleagues at the Applied Physics Laboratory, and the end product has benefitted greatly from the many conversations and discussions we have had over that period. I am especially indebted to my good friend and colleague of 25 years, Frank Monaldo, who provided me with the necessary IDL (Interactive Data Language) software and Radarsat wind speed files necessary to create the imagery of Section III. I would also particularly like to acknowledge George Young of Penn State University for his outstanding and, I think, quite unique theoretical narrative and analysis to be found in Section II, as well as his meticulous reviews of my own contributions. It must have been a labor of love, George, because there certainly was little financial incentive.

Finally, the outstanding landform elevation maps that are precision overlaid on all the SAR wind images have their genesis in the work of Ray Sterner of the Applied Physics Laboratory, who has assembled an extensive landform inventory from various global elevation data bases. The landform maps are especially valuable in the context of high resolution SAR wind fields, since local topography often controls the spatial patterns revealed by SAR.

The nearly concurrent Radarsat and Envisat overpasses on 07 January 2003 described towards the end of Section I were partly planned, partly serendipitous. The planning portion included the combined efforts of both Karen Friedman in the NOAA/NESDIS Office of Research and Applications group in Camp Springs, Maryland for the Radarsat acquisition, and the ESA planning group in Frascatti, Italy for the Envisat acquisition. I am most grateful for the cooperation and assistance of both groups.

It is my hope that this Guide will more firmly establish the future role of wide swath SAR in both theoretical and operational meteorology over the ocean, and in so doing help promote and encourage the future international cooperation and institutional commitment necessary to move this unique instrument from merely an interesting research application towards a vital operational tool.

This project was supported and monitored by the Office of Research and Applications of the National Oceanic and Atmospheric Administration (NOAA) under Grant No. NA06EC0243. The Program Officer was William G. Pichel (William.G.Pichel@noaa.gov).

The views, opinions, and findings contained herein are solely those of the authors and should not be construed as an official National Oceanic and Atmospheric Administration or U.S. Government position, policy, or decision.

Bob Beal
Principal Investigator

Section I

SAR as a High Resolution Scatterometer

Bob Beal, Don Thompson, Frank Monaldo

1.1 The Basis of SAR Wind Field Estimates: Accuracy and Error Structure

As the surface wind over the ocean increases, the radar backscatter from the wind-driven short (cm scale) waves increases, interacting with the incident energy of the radar through a Bragg-like resonance. For most radar frequencies of a fixed polarization, with off-nadir angles between about 20 and 55 degrees, for wind speeds between about 3 and 30 m/s, and for an arbitrary (but fixed) angle between the radar look direction and the surface wind direction, the intensity of the radar backscatter is a monotonically increasing function of surface wind speed. Under certain conditions, and with certain assumptions, this monotonic relationship, valid for SAR down to sub-kilometer scales (but not necessarily down to a pixel, because of Doppler effects from the moving ocean), can be inverted to deduce surface wind speed from the intensity of the radar backscatter.

The limits of this monotonic relationship, however, are still not completely understood, even after several decades of study. For example, significant distortions in the relationship can result from surface currents, contaminants, atmospheric stability changes at the air-sea boundary layer, and foam and breaking waves generated by high winds working on a fresh young sea. Nevertheless, driven by years of deep ocean data from the ERS-1 and ERS-2 scatterometers, the empirical backscatter-to-wind-speed relationship for vertically polarized C-band (5.3 GHz), radar return (referred to as CMOD) has now been extensively researched and refined (e.g., Freilich and Dunbar 1993; Stoffelen and Anderson 1993), and is most recently described in Hersbach (2003) as CMOD5.

Although CMOD5 may be empirically superior to its predecessor CMOD4, all the SAR wind fields contained in this Guide have been derived from a modification of CMOD4. The modification (Thompson and Beal 2000; Thompson et al. 2001) is necessary to account for the inconvenience that the Radarsat-1 SAR operates with horizontal polarization, and therefore lacks the decade-long data base generated by the ERS-1 and ERS-2 scatterometers.

The backscatter-to-wind-speed relationship for SAR is unique only if the wind direction is known a priori, or can be reasonably estimated. This is not a trivial requirement, and if not done with care, can lead to large errors in the wind speed estimate, even if the SAR is perfectly calibrated. Figure 1-1 illustrates how this is possible.

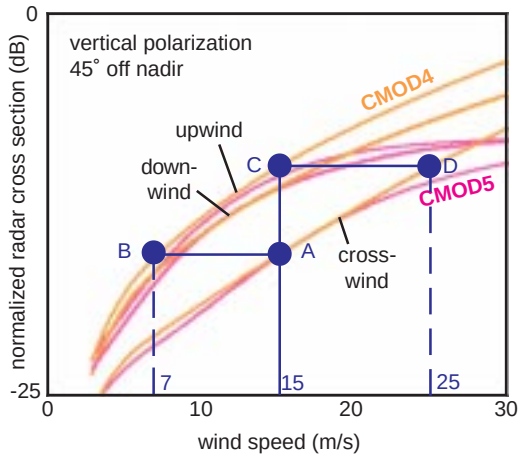

Figure 1-1. Relationship between radar backscatter and surface wind speed for C-band vertical polarization at 45˚ off nadir angle. Upwind, downwind, and crosswind relationships are shown for both CMOD4 and CMOD5 algorithms.

Point A in the figure shows a case where a 15 m/s wind with direction normal to the SAR look direction will produce the same backscatter as a 7 m/s wind travelling toward the SAR (point B). Conversely, the same 15 m/s wind travelling toward the SAR (point C) will produce the same backscatter as a 25 m/s wind travelling normal to the SAR. These values result from the CMOD4 algorithm; similar but even greater differences in the high wind region result from CMOD5, which exhibits saturation at lower wind speeds.

For this Guide, the initial wind direction estimates are taken from the closest available NOGAPS model forecast, interpolated down to a SAR pixel. The accuracy of the resulting wind speed estimates is suggested by the scatter in figure 1-2 (Monaldo et al. 2001), which shows Radarsat-vs-buoy wind comparisons obtained mostly in the NW Atlantic during the winter of 99-00. For Radarsat off-nadir angles from 25˚ to 45˚ the standard deviation of the differences was 1.76 m/s for buoy wind speeds up to 21 m/s.

However, as figure 1-1 shows, NOGAPS model wind direction errors can create significant errors in the SAR backscatter-to-wind-speed transformation,

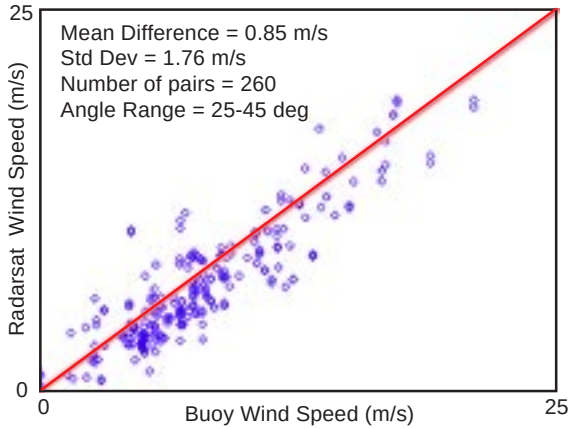

Figure 1-2. Radarsat vs buoy wind speeds using NOGAPS wind directions (from Monaldo et al. 2001)

and therefore can create significant scatter. To estimate how significant, figure 1-3 (from Monaldo et al. 2003) shows a similar comparison of Radarsat wind speed versus QuickSCAT wind speed, using (the presumably more accurate) QuikSCAT wind directions rather than NOGAPS model directions to derive the SAR wind speeds. By incorporating the more accurate wind directions, the resulting rms differences are reduced from 1.76 m/s down to only 1.24 m/s.

In spite of the evident tendency toward a slight positive SAR bias at high winds (to be discussed in more detail below), the low residual scatter of figure 1-3 makes a good case for the viability of SAR winds.

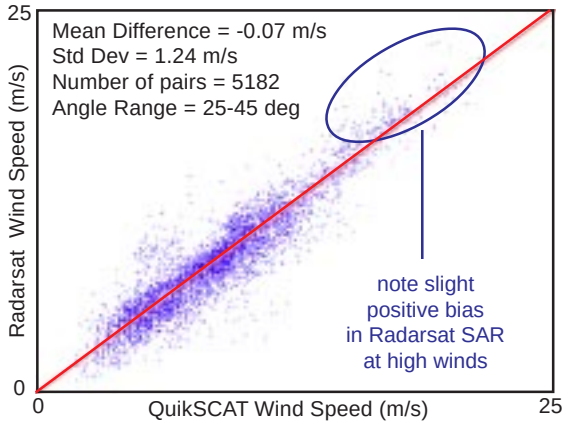

Figure 1-3. Radarsat vs QuikSCAT wind speeds using QuikSCAT wind directions (from Monaldo et al. 2003)

A few caveats are in order, however. Concurrent scatterometer winds are usually not available; indeed, in the absence of either scatterometer or buoy information, there are generally only two ways to estimate the local wind direction prior to applying the SAR wind algorithm. The estimate must come either from some forecast model or from an analysis of spatial features within the SAR image itself. Neither method alone is completely satisfactory. Probably some optimum blending of the best model with a sophisticated analysis of the relevant SAR features (i.e., those likely aligned with the local wind direction) will eventually produce the best results.

Meanwhile, for all SAR wind fields shown in this Guide, the local wind direction was taken (as in Monaldo et al. 2001) from the nearest NOGAPS (one degree grid) model field, usually within +/- 6 hrs of overpass time. Sometimes, especially during rapid change, this strategy is clearly inadequate, as some of the following examples will illustrate. Nevertheless, in most cases, the unique spatial resolution possible with SAR allows the observation of phenomena not otherwise possible.

Figures 1-4 and 1-5 illustrate the results of applying the CMOD4 algorithm, modified for horizontal polarization, to a SAR backscatter field. This SAR image of a polar low contains the full range of local

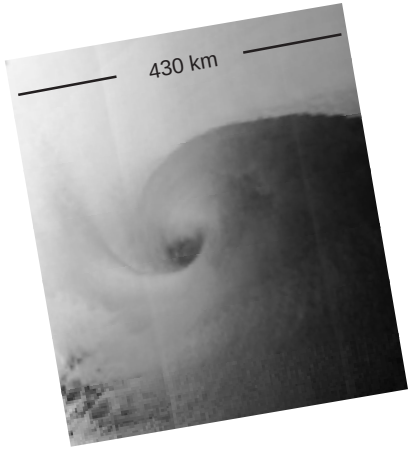

Figure 1-4. Polar low imaged by 430 km wide swath mode of Radarsat SAR, before application of wind algorithm, 0602 GMT 05 Feb 1998.

wind directions (Sikora et al. 2000; Friedman et al. 2001). The conversion of SAR backscatter to SAR winds demands an accurate knowledge of the local wind direction Although a competent meteorologist could probably overlay a wind direction grid more accurate than the NOGAPS model, such a process is not so easy to automate. Figure 1-5 shows not only the resulting SAR wind magnitude, but also the embedded NOGAPS wind vectors, both identically color coded. Note that the SAR-estimated winds exceed those of the model in most of the upper half of the storm. In this case, the positive bias is likely induced by a Radarsat non-linearity unique to its wide ScanSAR mode, as will be discussed below.

A montage of the 60 Radarsat wind estimates included in Section III is shown in figure 1-6. Each of these frames was selected from the several thousand available because it revealed some unique aspect of the wind field not normally observed with conventional scatterometers. The ScanSAR frames (typical dimension 430 km across-track by 500 km along-track) are concentrated in the Gulf of Alaska and Bering Sea. Many of the frames transect coastal areas, and reveal the complexity of topographical influences on the surface wind that are presently impossible to capture in

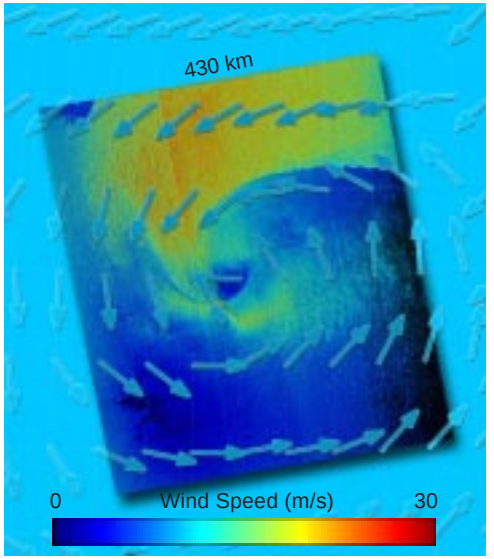

Figure 1-5. Polar low of 05 Feb 1998 after application of wind algorithm, embedded in NOGAPS model wind field (arrows).

such detail by any other method, either via instrument or computer model.

For example, figures 1-7 and 1-8 from 24 Dec 1999 show Radarsat sub-km detail of Kármán vortices created downwind of the Pogromni volcanic peak in the central Aleutians. Figures 1-9 and 1-10 are simulated QuikSCAT images of the same region, where the spatial resolution of the SAR has been degraded to 15 km. None of the detail is visible at the degraded resolution. Of course, the increased resolution of the SAR does not come without a price: the assumed model directions, shown by the embedded arrows, cannot possibly be correct in all sectors of the vortices. So the wind algorithm will fail to capture the true wind, except when the local wind aligns with the larger scale wind field. In other sectors, the error will be comparable to those discussed above in the context of figure 1-1. These direction errors are usually subtle and difficult to detect. Occasionally, however, they are revealed by a characteristic “hourglass” pattern that results when the model misplaces a center of circulation. In such cases, when the actual wind is fairly unidirectional, the wind algorithm acts erroneously and

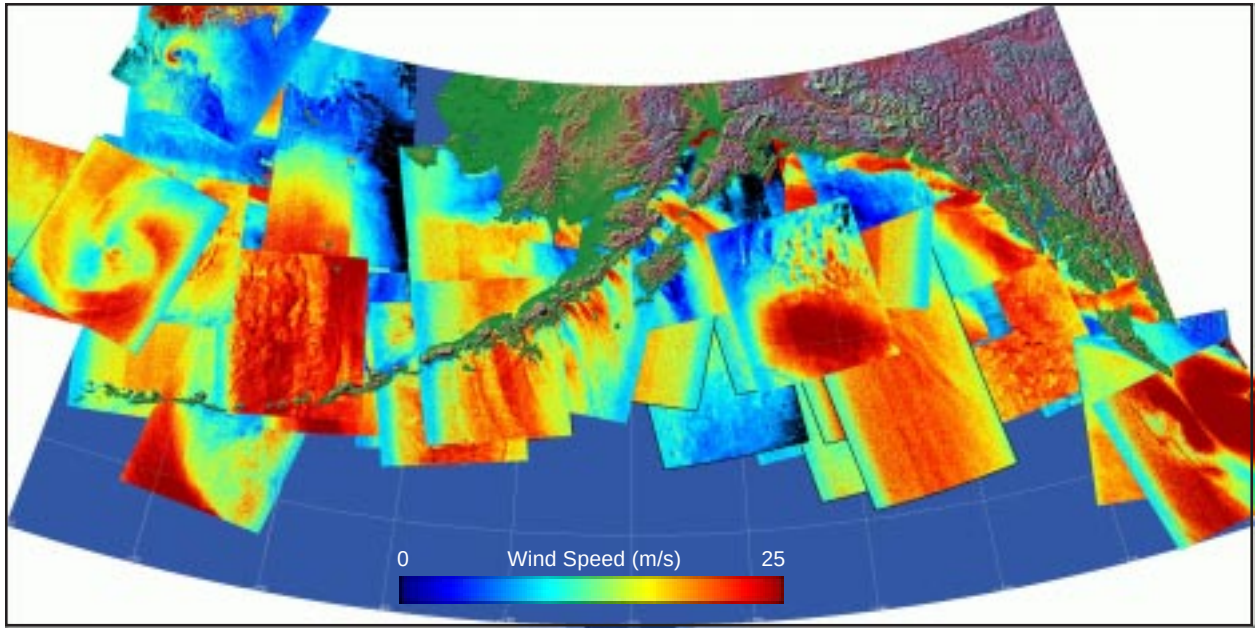

Figure 1-6. Spatial distribution of selected subset of 60 Radarsat frames located in the Gulf of Alaska and Bering Sea acquired between 31 Oct 1999 and 14 Nov 2001. Each of the frames is narrated in Section III.

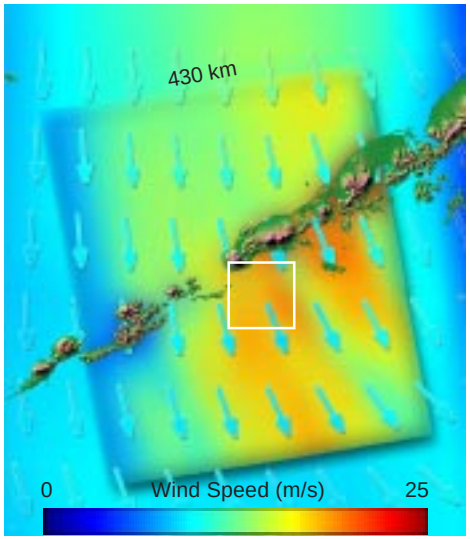

Figure 1-9. Radarsat SAR-derived wind field of 24 Dec 1999 with resolution degraded to 15 km, simulating typical scatterometer resolution, such as QuikSCAT.

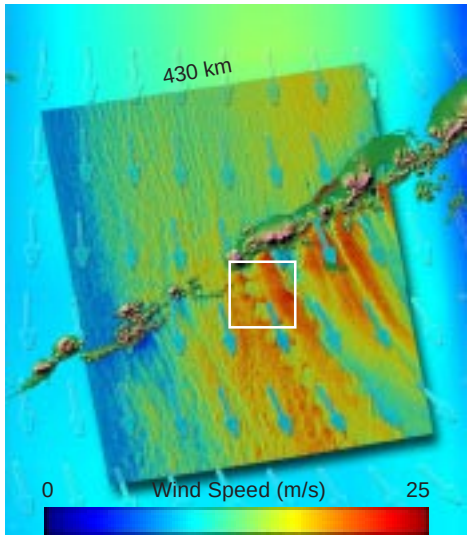

Figure 1-7. Radarsat SAR-derived wind field of 24 Dec 1999, showing detail of Kármán vortices created in the wake of the Pogromni volcanic peak (altitude 2000 m). Spatial resolution ~300 m.

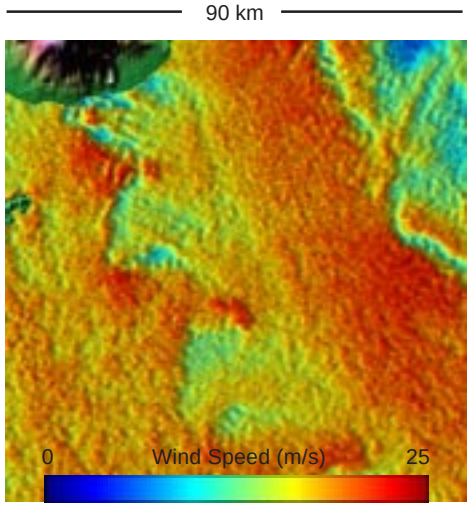

Figure 1-8. Magnified view of white square above, showing Kármán vorticies created downwind of Pogromni Volcano. Spatial resolution ~300 m.

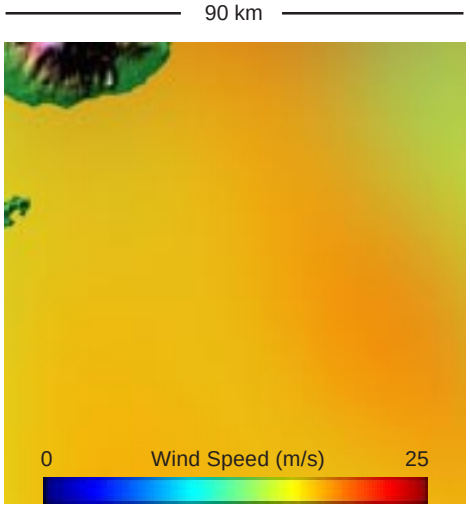

Figure 1-10. Magnified view of white square above, showing no sign of Kármán vorticies downwind of Pogromni Volcano. Spatial resolution degraded to 15 km, comparable to that of QuikSCAT.

effectively creates an image of the transfer function of the algorithm itself. Two such examples are shown in figures 1-11a and 1-12a, and their resulting wind profiles along the scan lines AB in figures 1-11b and 1-12b. In figure 1-11, the estimated SAR wind is erroneously enhanced because the assumed wind direction is nearly normal to the SAR look direction, when it is in fact nearly in line with it. In figure 1-12, the complimentary case is shown, with a corresponding suppression of the SAR-estimated wind speed. These are both extreme cases, and only rarely seen. However, they serve as a useful reminder that every SAR wind field will exhibit at least some of this class of error unless the assumed wind direction is perfect down to the sub-kilometer scale. Of course, this is never the case.

There is another significant error source associated with Radarsat wide swath imagery, evidently becoming more significant at winds above about 15 m/s. Figure 1-3 may give a hint of the error in the form of the positively biased SAR data cloud in the upper right. Although this error is difficult to characterize with a limited data set, it appears to have the following characteristics: it is a strong, noncontinuous function of the SAR off-nadir angle, with a distinct discontinuity at one off-nadir angle; it is a strong function of wind speed over a large range of off-nadir angles, producing negative bias at low off-nadir angles and positive bias at medium to high off-nadir angles. The effect is illustrated in figure 1-13 along with its associated scan shown in figure 1-14. This effect is evidently caused by an oversight in the instrument design, where the automatic gain control for the entire swath is controlled by the energy received in the nearest-to-nadir beam of the ScanSAR mode. It is not a fundamental error, but nevertheless distorts the vast majority of Radarsat high wind images. It is certainly evident in most of the set of 60 SAR wind fields contained in Section III.

Figure 1-15 shows a comparison between a histogram of the entire set of 300 m pixels extracted from the 60 Radarsat frames and the collocated NOGAPS interpolated values on the same scale. In addition, the several-year average distribution of January wind

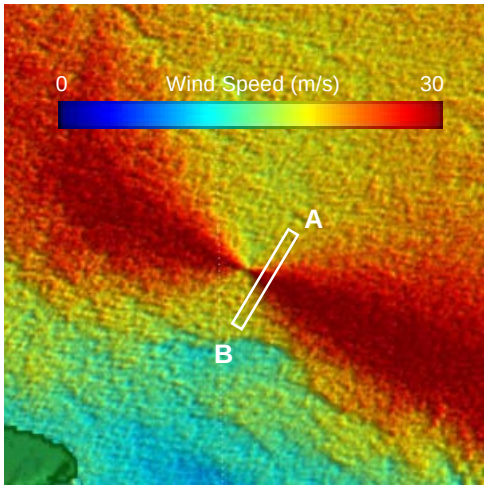

Figure 1-11a. The “hourglass” shaped feature resulting from mispositioning of a cyclonic center prior to a backscatter-to-wind transformation (1555 GMT 12 Oct 2001).

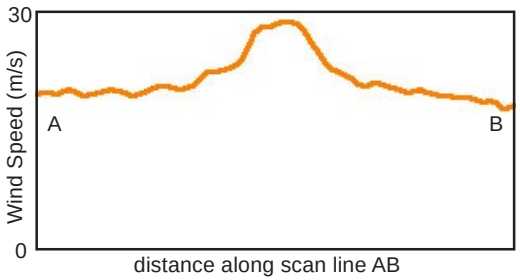

Figure 1-11b. SAR-estimated wind speed along the scan line AB (1555 GMT 12 Oct 2001). Mispositioning of a cyclonic center results in a false wind peak.

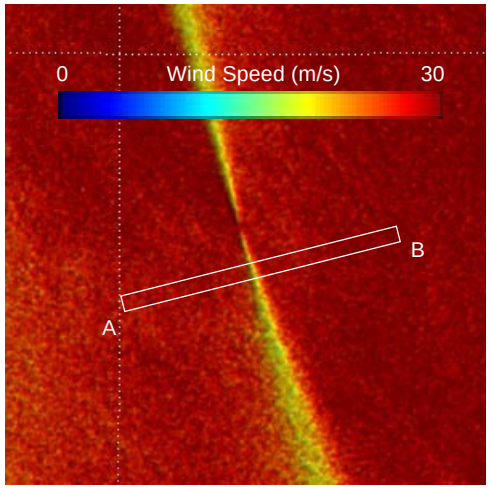

Figure 1-12a. The complimentary case to Figure 1-11a, resulting from mispositioning of a cyclonic center prior to a backscatter-to-wind transformation (0230 GMT 10 Jan 2001).

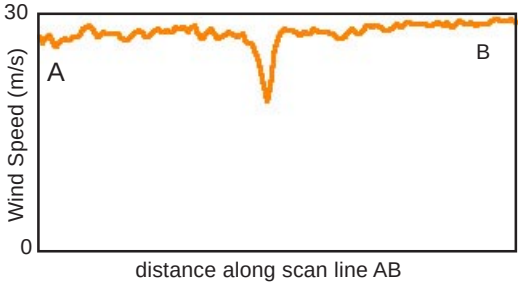

Figure 1-12b. SAR-estimated wind speed along the scan line AB (0230 GMT 10 Jan 2001). Mispositioning of a cyclonic center results in a false wind dip.

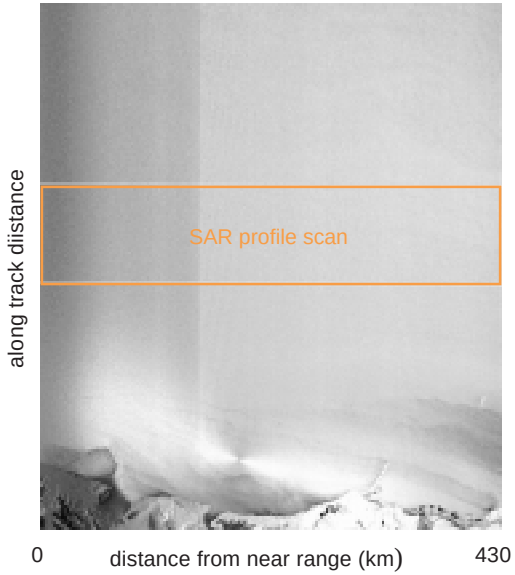

Figure 1-13. Radarsat wind field in a high wind region just off the southeast Alaska coast (1555 GMT 12 Oct 2001) illustrating two separate sources of error. Satellite velocity vector is toward the top and SAR is right-looking.

speeds recorded by NOAA buoy 46035, a 12 m discus buoy located in the Bering Sea (see figure 1-16) is shown overlaid on the other two. Whereas the buoy and model agree quite well on the whole, the Radarsat SAR wind fields are distinctly biased high. One effect of the bias is the false implication that gale force is reached over about a third of the total area sampled, when in actuality (according to NOGAPS, and at least indirectly confirmed by buoy 46035), gale force is reached over much less than 10% of the area. Gale force winds are quite rare, even during the North Pacific winter.

In spite of these quite significant biases, the Radarsat SAR has yielded valuable insight into the high resolution structure of the wind field, especially in the near-shore regions which are inaccessible to conventional lower resolution scatterometers.

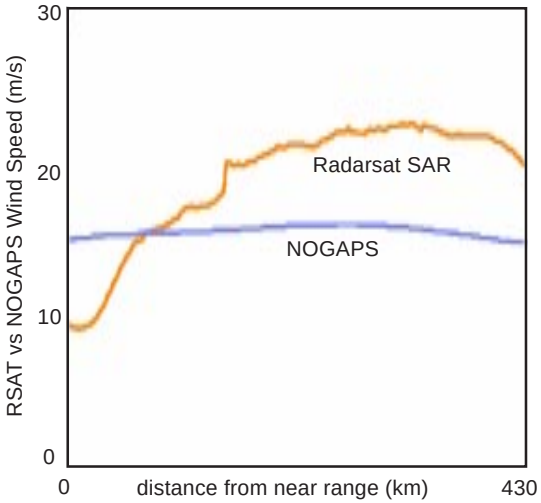

Figure 1-14. Averaged cross-track trend of Radarsat vs NOGAPS for 13 nearly homogeneous wind fields typified by the 12 Oct 2001 image, and compared with concurrent NOGAPS model winds.

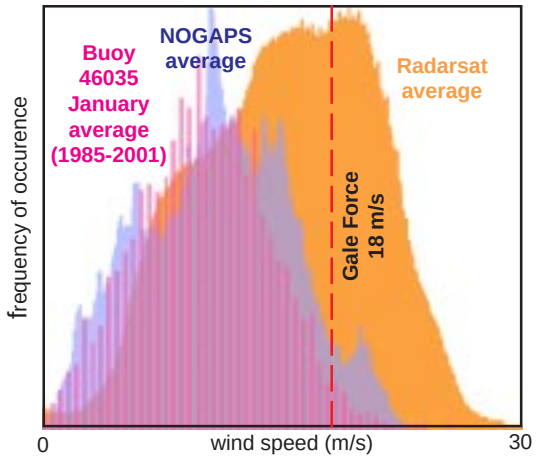

Figure 1-15. Histograms of 60 Radarsat wind estimates, concurrent NOGAPS model estimates, and January average wind speed climate at buoy 46035 (Sep 1985 to Nov 2001).

References

Friedman, K.S., T.D. Sikora, W.G. Pichel, P. Clemente-Colón, and G.Hufford, 2001: Using Spaceborne Synthetic Aperture Radar to Improve Marine Surface Analyses: Weather and Forecasting, Vol. 16 (2), pp. 270-276.

Freilich, M. H. and R. S. Dunbar, 1993: A Preliminary C-band Scatterometer Model Function for the ERS-1 AMI Instrument: Proc. First ERS-1 Symp., Cannes, France, 4-6 Nov 92, ESA SP-359, pp. 79-83.

Hersbach, Hans, 2003: CMOD5: An Improved Geophysical Model Function for ERS C-band Scatterometry: European Centre for Medium Range Weather Forecasting Technical Report #395.

Monaldo, F. M., D. R. Thompson, R. C. Beal, W. G. Pichel, and P. Clemente-Colón, 2001: Comparison of SAR-Derived Wind Speed with Model Predictions and Ocean Buoy Measurements: IEEE Trans. Geosci. Remote Sensing, Vol. 39, pp. 2587-2600.

Monaldo, F. M., D. R. Thompson, W. G. Pichel, and P. Clemente-Colón, 2004: A Systematic Comparison of QuikSCAT and SAR Measured Wind Speeds: IEEE Trans. Geosci. Remote Sensing, Vol. 42, pp. 283-291.

Sikora, T., K.S. Friedman, W.G. Pichel, and P. Clemente-Colón, 2000: Synthetic Aperture Radar as a Tool for Investigating Polar Mesoscale Cyclones: Weather and Forecasting, Vol. 15 (6), pp. 745-758.

Stoffelen, A. C. M. and D. L. T. Anderson, 1993: Wind Retrieval and ERS-1 Radar Backscatter Measurements: Adv. Space Res. ,Vol. 13 **(**5**)**, pp. 53-60.

Thompson, D. R. and R. C. Beal, 2000 :Mapping High Resolution Wind Fields Using Synthetic Aperture Radar: Johns Hopkins APL Technical Digest, Vol. 21, pp. 58-67 (Jan-Mar) .

Thompson, D. R., F. M. Monaldo, W. G. Pichel, and P. Clemente-Colón, 2001: Combined Estimates Improve High-Resolution Coastal Wind Mapping: EOS Trans. AGU, Vol. 82, p. 469 ff.

1.2 Benefits of Envisat and Radarsat Dual Coverage in Gale Force Winds: the 07 January 2003 Storm

During late 2002, after several months of validation activities, the Envisat C-band ASAR began producing imagery in its wide swath modes. The Envisat ASAR is similar to, but somewhat more advanced than, the Canadian Radarsat SAR. Both can operate in wide swath (> 400 km) ScanSAR modes, but while Radarsat is horizontally polarized, Envisat operates in either horizontal or vertical polarization. Neither polarization has clearly demonstrated superiority with respect to wind monitoring. With the advent of Envisat, however, this issue can be seriously addressed with empirical data, since the ASAR can operate in an alternating polarization mode (albeit with a narrower swath), simultaneously collecting imagery of the same region in both polarizations. Presumably, one polarization will yield a more robust monotonic relationship between backscatter and wind speed over larger ranges of wind speeds and off-nadir angles than the other, and with greater asymmetry in the relationship between wind direction and radar look direction. These are key aspects of the algorithm that directly influence the degree of ambiguity in the wind inversion process.

During the first week of January 2003, an unusually deep low pressure system located in the NW Pacific travelled steadily toward the NE, reaching the central Aleutians on 07 January with a broad band of gale force winds in its northern and eastern quadrants. By

1800 GMT, gale force winds formed a continuous arc stretching from the central Bering Sea through the northern Aleutians and down to the southern Gulf of Alaska.

At 1752 GMT a descending Radarsat SAR pass cut through the Bering Sea just east of NOAA buoy 46035, and directly over buoy 46072. Less than 3 hrs later, at 2043 GMT, a descending Envisat ASAR pass cut through the Gulf of Alaska, directly over NOAA buoy 46066. Figure 1-16 shows a spatial snapshot of the rapidly evolving wind field from the MM5 model nowcast of 2100 GMT, with both Radarsat and Envisat SAR passes overlaid, along with the locations of the three buoys and their associated wind vectors at the relevant overpass times.

Gale force winds (i.e., 2 min average of at least 18 m/s) at buoy 46035 in January have a probability of occurrence of only about 3%, according to the National Data Buoy Center records compiled from 1985 to 2001. According to a multiyear data set from the ERS-1 scatterometer, the January wind averages for regions around buoys 46035 and 46072 are ~ 11 m/s, slightly less (~ 9 m/s) around buoy 46066.

Figure 1-17 shows the actual records at each of the three buoys on three different time scales centered around the SAR overpass times. The buoy records reinforce the rarity of this confluence of events. The six-month records confirm that average winds during the day-long passage of the event from buoy 46072 in the southwest through buoys 46035 and 46066 were among the three highest averages recorded during the entire winter at all three buoys. Moreover, the six-day and 24 hr records of figure 1-17 confirm that gale force winds were present: 1) at buoy 46035 for nearly a full day before and after Radarsat overpass time, 2) at buoy 46066 for more than 6 hrs immediately subsequent to Envisat overpass time, and 3) at buoy 46072 from 15 to 19 hrs prior to Radarsat overpass time. To have captured the highest wind portions of this rare event with both the Radarsat and Envisat SARs in their wide swath modes, and to have had all three buoys operating throughout the entire passage of the event is quite phenomenal. Most importantly, it provides an opportunity to examine the performance of both SARs under high wind conditions, and it suggests a future when multiple wide swath SARs might operate in concert to effectively increase their operational coverage.

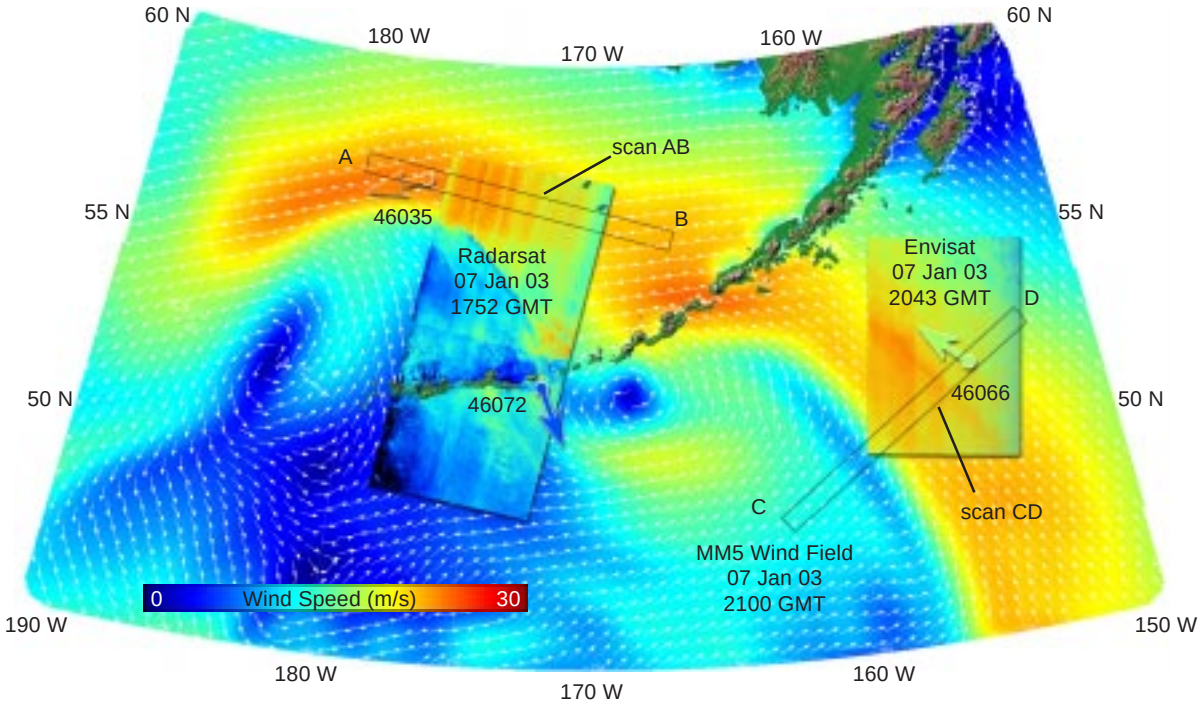

Figure 1-16. Radarsat and Envisat wide swath SAR wind fields over a gale force event in the Bering Sea and Gulf of Alaska on 07 Jan 2003. SAR wind fields and buoys 46035, 46066, and 46072 are shown embedded in nearest concurrent MM5 wind field.

Like Radarsat, Envisat achieves its wide swath by combining the radar returns of several antenna beams in the cross-track direction. The proper combination of these individual beams is necessary to synthesize one single wide beam. Careful calibration and correction for the composite beam is essential to produce an error-free radar backscatter map, which is then used to drive the wind inversion algorithm. Small errors in the creation of the composite backscatter map can yield large errors in the estimated wind speed, especially at the larger off-nadir angles where the radar return is greatly reduced, even approaching the noise level of the radar receiver.

As an experiment, the Envisat SAR composite backscatter map for the 07 January pass was iterated three times by a European Space Agency SAR processor. Each time, processor parameters were varied to attempt to minimize the discontinuities (or “seams”) between the adjacent antenna beams. Figure 1-18 shows the results of the three attempts. The first and second attempts have two clear discontinuities, although they are somewhat reduced in the iteration. By the next (and final) reiteration, the nearest-range (left) discontinuity is practically eliminated and the farthest-range (right) is greatly reduced, but evidently at the expense of slightly raising another at an intermediate (center) range. The effect of these small discontinuities on the resulting SAR wind estimate can lead to significant errors, as figures 1-19 and 1-20 show. Resulting wind speed discontinuities in the initial processed product approach 1.5 m/s along the two major seams,

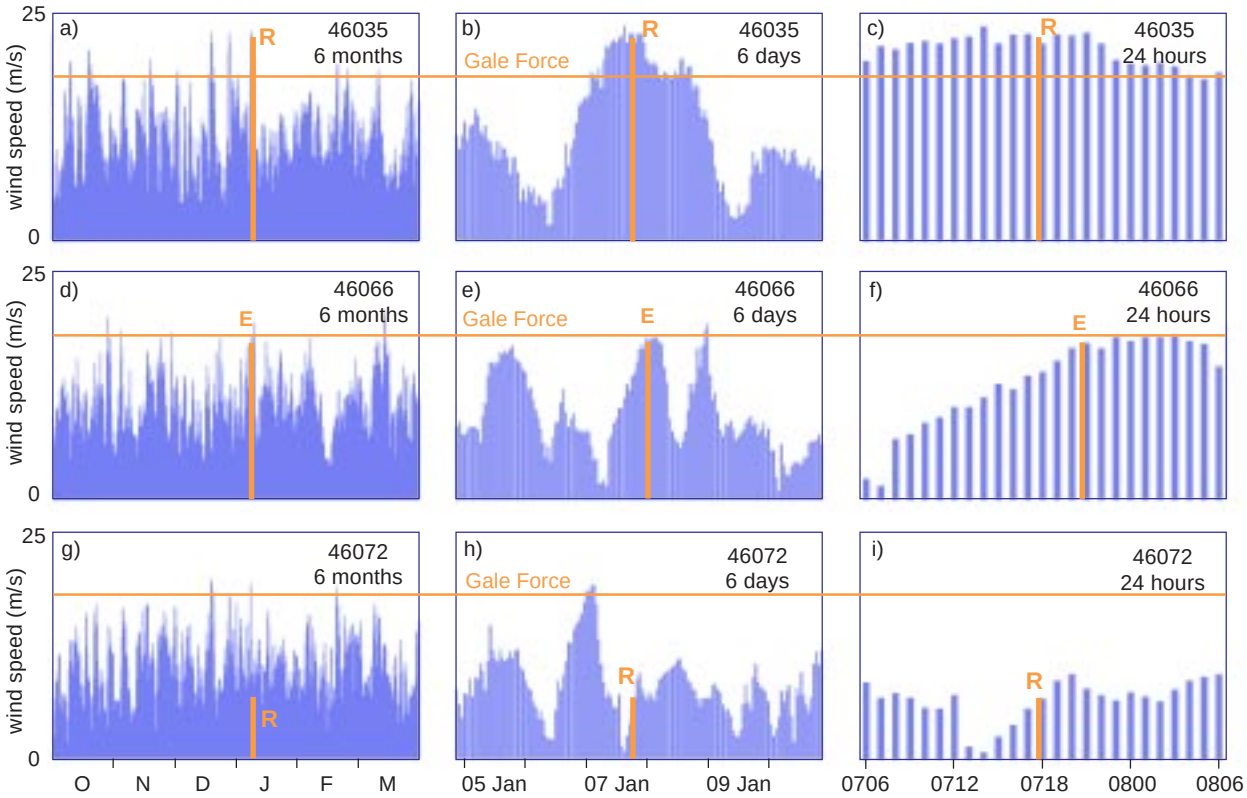

Figure 1-17. Wind speeds at buoys 46035, 46066, and 46072 for the winter of 2002-2003, expanded around the nearly simultaneous overpass times of Radarsat and Envisat on 07 Jan 2003. Note that gale force winds were present at overpass time at 46035, within 2 hrs of overpass time at 46066, and within a day of overpass time at 46072, all from the same high wind event. From panels a) and d), this was one of the three highest wind events of the winter at all three buoys. E (Envisat) and R (Radarsat) mark the winds at times of overpass.

and exceed 0.5 m/s along two minor seams. Two iterations fail to completely eliminate the discontinuities, but evidently reduce the resulting wind errors to less than 1 m/s. Such small errors will not usually be dominant, but can under some circumstances be detectable, since their signature appears as a small discontinuity in the direction of the satellite velocity vector, i.e., along track. This signature is evident in both the Radarsat and Envisat wind images of figure 1-16.

In spite of these subtle discontinuities, which will probably remain even in the most carefully processed ScanSAR image, the performance of both Radarsat and Envisat on 07 January is quite remarkable, and demonstrates their excellent potential to deliver accurate high resolution wind fields, even in gale force events. Figures 1-21 and 1-22 show estimated SAR winds for both instruments along scan lines AB and CD shown in figure 1-16. Also plotted for comparison are both the concurrent NOGAPS model (not the MM5, which

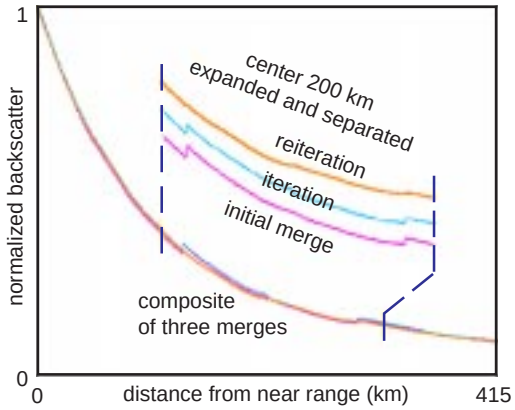

Figure 1-18. Composite merging of multiple ASAR antenna beams from the 07 January 2003 pass showing the problem of imperfect beam correction.

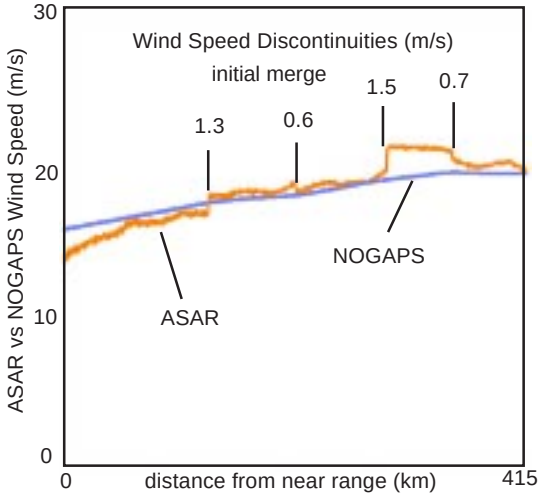

Figure 1-19. Impact of imperfect beam boundary merging (initial merge) on the resulting ASAR-estimated wind speed for 07 Jan 2003.

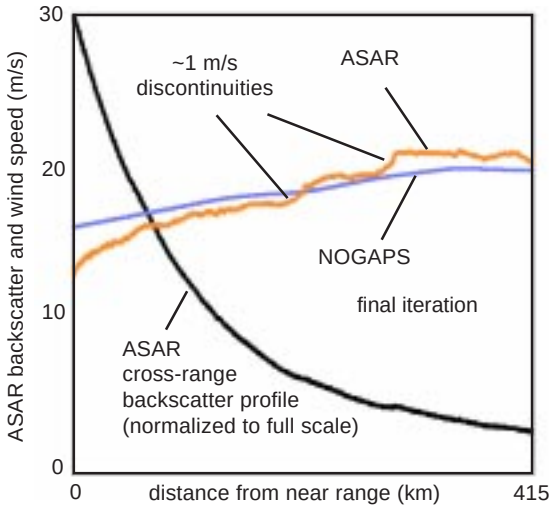

Figure 1-20. Residual ASAR wind speed variations remaining after the final iteration of 07 Jan 2003.

is displayed in figure 1-16) and an hourly time series of the two relevant buoys centered around the overpass times. The agreement among all three sources for both SARs is most remarkable, with mean differences of the order 1 m/s. Residual variations in the SAR wind field, at least for this case where the local wind directions were evidently well modelled, possibly result from ScanSAR antenna discontinuities, as described above.

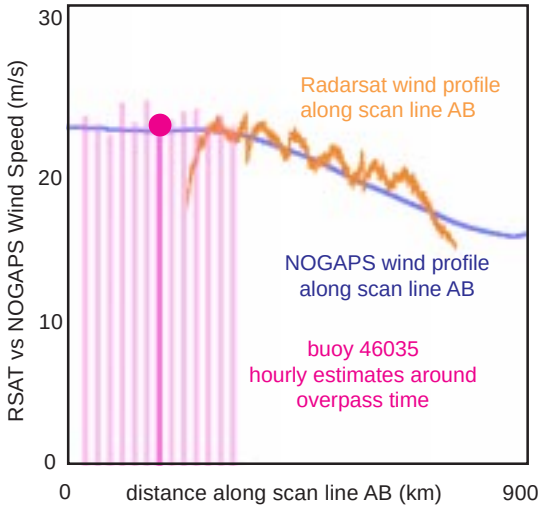

Figure 1-21. Radarsat SAR-estimated wind profile along scan AB compared with nearly concurrent NOGAPS wind profile and nearby hourly time series from buoy 46035.

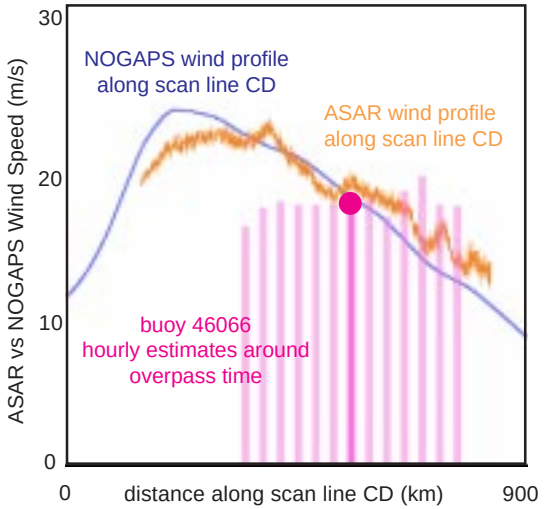

Figure 1-22. Envisat ASAR-estimated wind profile along scan CD compared with nearly concurrent NOGAPS wind profile and nearby hourly time series from buoy 46066.

1.3 Summary

Tremendous strides have been made in SAR technology and science in the past 25 years, from the first relatively crude optically-processed narrow swath images from Seasat in 1978 to the present well-calibrated ScanSAR images from Envisat. When the Envisat ScanSAR wind field products are combined with those of Radarsat-1 or, even better, the Japanese ALOS (scheduled for a 2004 launch), and Radarsat-2 (scheduled for a 2005 launch), there will be the possibility of three simultaneously orbiting and cooperating ScanSARs, with a composite available swath width approaching 1200 km. Figure 1-23 shows the historical evolution of this parameter, and suggests the importance of international cooperation to reap the full benefits of this recent progress. A ScanSAR triad, equipped with near-real-time wind field processing (within ~ 1 hr) and an efficient, interactive, and user-friendly delivery system, would reap immediate substantial benefits in operational weather forecasting.

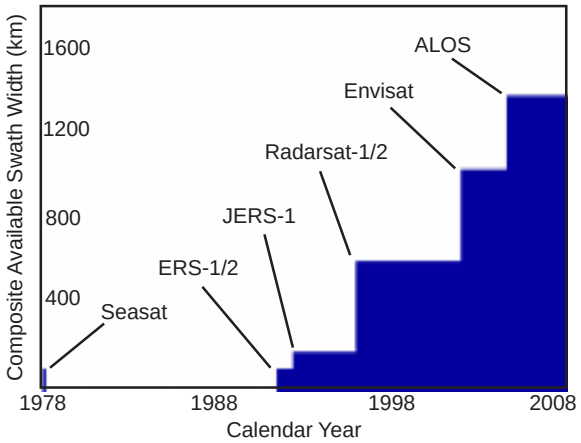

Figure 1-23. Evolution of composite available SAR swath width from various scientific SARs, assuming sucessful operation of Japanese ALOS in 2004 and Canadian Radarsat-2 in 2005.

1.4 Bibliography

(adapted from "The SAR Measurement of Ocean Surface Winds: A White Paper for the 2nd Workshop on Coastal and Marine Applications of SAR", Longyearbyen, Spitsbergen, Norway, 8–12 September 2003, eds: F. Monaldo and V. Kerbaol, in press.)

Alpers, W., and B. Bruemmer, 1994: Atmospheric Boundary Layer Rolls Observed by the Synthetic Aperture Radar aboard the ERS-1 Satellite. J. Geophys. Res: Vol. 99, pp. 12,613-12,621.

Alpers, W., 1995: Measurement of Mesoscale Oceanic and Atmospheric Phenomena by ERS-1 SAR. URSI (International Union of Radio Science): Bulletin No. 275, pp. 14-22.

Alpers. W., M. Gade, C. Melsheimer, M. Bao, L. Masuko, and T. Kobayashi, 1995: The Imaging of Different Ocean and Atmospheric Phenomena by SIR-C/X-SAR. International Geoscience and Remote Sensing Symposium: Florence, Italy, 10-14 July.

Alpers, W., and G. Stilke, 1996: Observation of a Nonlinear Wave Disturbance in the Marine Atmosphere by the Synthetic Aperture Radar aboard the ERS-1 Satellite. J. Geophys. Res: Vol. 101, pp. 6513-6525.

Alpers, W., U. Pahl, and G. Gross, 1998: Katabatic Wind Fields in Coastal Areas studied by ERS-1 Synthetic Aperture Radar Imagery and Numerical Modeling. J. Geophys. Res: Vol. 103, pp. 7875-7886.

Attema, E. P. W., 1986: An experimental campaign for the determination of the radar signature of the ocean at C-band. Proc. Third International Colloquium on Spectral Signatures of Objects in Remote Sensing: Les Arcs, France, ESA, SP-247, pp. 791-799.

Babin, S., D. R. Thompson, 2000: Effects of Atmospheric Boundary Layer Moisture on Friction Velocity with Implications for SAR imagery. IEEE Trans. Geosci. Remote Sensing: Vol. 38, pp. 618-612.

Babin, S. M., T. D. Sikora and N. S. Winstead, 2002: A Case Study of Satellite Synthetic Aperture Radar Signatures of Spatially Evolving Atmospheric Convection over the Western Atlantic Ocean. Boundary Layer Meteorology: Vol. 106, pp. 527-546.

Bauer, E., 1997: Statistical Comparison of Winds from ERS-1 Scatterometer and ECMWF Model in Time and Wavenumber Domain. Proc. Third ERS Symposium on Space at the Service of the Environment: ESTEC, Florence, Italy, pp. 1195-1200.

Beal, R. C., 1980: The Seasat SAR Wind and Ocean Wave Monitoring Capabilities: A Case Study for Pass 1339M. Johns Hopkins Univ. APL Tech. Report: S1R 79U-019, 41 p.

Beal, R. C. and W. G. Pichel, 1998: StormWatch 1997-98 and Beyond: Application of SAR as a High Resolution Scatterometer in Coastal Regions. Proc. 1998 International Geoscience and Remote Sensing Symposium: Seattle, WA., pp. 1379-1381, 6-10 July.

Beal, R. C., 2000: Toward an International StormWatch using Wide-Swath SAR. The Johns Hopkins Univ. Tech. Digest: Vol. 21, pp. 12-20 (Jan).

Boggs, D. H., 1982: Seasat Scatterometer Geophysical Data Record (GDR) Users Handbook. JPL Document D-129: Jet Propulsion Laboratory, California Institute of Technology, Pasadena, CA

Brown, R. A., 1970: A Secondary Flow Model for the Planetary Boundary Layer. J. Atmos. Sci: Vol. 27, pp. 742-757.

Brown, R. A., 1980: Longitudinal Instabilities and Secondary Flows in the Planetary Boundary Layer: A Review. Rev. Geophys: Vol.18, pp. 683-697.

Brown, R. A., 1983: On Satellite Scatterometer Capabilities in Air-Sea Interactions. J. Geophys. Res: Vol. 88, pp. 1663-1673.

Brown, R. A., 1986: On a Satellite Scatterometer as an Anemometer. J. Geophys. Res: Vol. 91, pp. 2221-2232.

Brown, R. A., 2000: Serendipity in the Use of Satellite Scatterometer, SAR, and other Sensor Data. The Johns Hopkins Univ. Tech. Digest: Vol. 21, pp. 100-107.

Campbell, J. W. M. and P. W. Vachon, 1997: Extracting Ocean Wind Vectors from Satellite Imagery. Backscatter: Vol. 8, pp. 16-21.

Chapron, B., F. Collard, H. Johnsen and G. Engen, 2002: ASAR Wave Mode First Geophysical Results. ENVISAT Calibration Review: ESTEC, Noordwijk, The Netherlands, 9-13 September.

Chunchuzov, I., P. W. Vachon, and X. Li, 2000: Analysis and Modeling of Atmospheric Gravity Waves Observed in Radarsat SAR images. Remote Sensing of Environment: Vol. 74, pp. 343-361.

Clemente-Colón, P., 2001: Coastal Oceanography Applications of Spaceborne Synthetic Aperture Ra-dar (SAR) in the Middle Atlantic Bight (MAB). PhD Dissertation: College of Marine Studies, University of Delaware, Newark , 233p.

Du, Y., P. W. Vachon, J. Wolf, 2002: Wind Direction Estimation from SAR Images of the Ocean using Wavelet Analysis. Can. J. Remote Sens: Vol. 28, pp. 498-509.

Elfouhaily, T., D. R. Thompson, D. Vandemark, and B. Chapron, 1999: A New Bistatic Model for Electromagnetic Scattering from Perfectly Conducting Random Surfaces. Waves in Random Media: Vol. 9, pp. 281-294.

Engen, G., K.A. Hoegda and H. Johnsen, 1998: A New Method for Wind Field Retrieval from SAR Data. Proc. CEOS SAR Workshop: ESTEC, WPP-138, pp. 43-51.

Fetterer, F., D. Gineris, and C. C. Wackerman, 1998: Valdating a Scatterometer Wind Algorithm for ERS-1 SAR. IEEE Trans. Geosci. Rem. Sens: Vol. 36, pp. 479–492.

Fichaux, N., T. Rachin, 2002: Combined Extraction of High Spatial Resolution Wind Speed and Direction from SAR Images: A New Approach Using Wavelet Transform. Can. J. Remote Sens: Vol. 28, pp. 510–516.

Freilich, M. H. and R. S. Dunbar, 1999: The Accuracy of the NSCAT-1 Vector Winds: Comparisons with National Data Buoy Center Buoys. J. Geophys. Res: Vol. 104, pp. 11,231–11,246.

Friedman, K. S. and X. Li., 2000: Monitoring Hurricanes over the Ocean with Wide-Swath SAR. The Johns Hopkins Univ. Tech. Digest: Vol. 21, pp. 80-85.

Friedman, K. S., T. D. Sikora, W. G. Pichel, P. Clemente-Colón, and G. Hufford, 2001: Using spaceborne Synthetic Aperture Radar to Improve Marine Surface analyses. Weather Forecasting: Vol. 16, pp. 270-276.

Fu., L. L. and B. Holt, 1982: Seasat Views Oceans and Seas with Synthetic Aperture Radar. JPL Publ. 81-102: Jet Propulsion Laboratory, Pasadena, CA.

Furevik, B. R. and E. Korsbakken, 2000: Comparison of Derived Wind Speed from Synthetic Aperture Radar and Scatterometer during the ERS Tandem Phase. IEEE Trans. Geosci. Rem. Sens: Vol. 38, pp. 1113-1121.

Furevik, B. R. and H. A. Espedal, 2002: Wind Energy Mapping using Synthetic Aperture Radar. Canadian J. of Rem. Sens: Vol. 28, pp. 196-204.

Gerling, T. W., 1986: Structure of the surface wind field from the Seasat SAR. J. Geophys. Res: Vol. 91, pp. 2308-2320.

Hasager, C. B., H. Frank and B. R. Furevik, 2002: On Off-Shore Wind Energy Mapping using Satellite SAR. Canadian J. Rem. Sens: Vol. 28, pp. 80-89.

Hawkins, J. D. and P. G. Black, 1983: Seasat Scatterometer Detection of Gale Force Winds near Tropical Cyclones. J. Geophys. Res: Vol. 88, pp. 1674-1682.

Hersbach, H., 2003: An Improved Geophysical Model Function for ERS C-band Scatterometry. ECMWF Tech. Mem. 395: Reading, U.K.

Horstmann, J., 1997: Investigation of Wind Speed Retrieval with Synthetic Aperture Radar aboard the ERS-1/2 satellites. GKSS Report: 97/E/55.

Horstmann, J., W. Koch, S. Lehner, and W. Rosenthal, 1998: Ocean Wind Fields and their Variability derived from SAR. Earth Observation Quarterly: Vol. 59, pp. 8-12.

Horstmann, J., W. Kock, S. Lehner, and R. Tonboe, 2000: Wind Retrieval over the Ocean using Synthetic Aperture Radar with C-band HH polarization. IEEE Trans. Geosci. Rem. Sens: Vol. 38, pp. 2122-2131.

Horstmann, J., S. Lehner, W. Kock, and R. Tonboe, 2000: Computation of Wind Vectors over the Ocean using Spaceborne Synthetic Aperture Radar. The Johns Hopkins Univ. Tech. Digest: Vol. 21, pp. 100-107.

Johannessen, O. M. and E. Korsbakken, 1998: Determination of Wind Energy from SAR Images for Siting Windmill Locations. Earth Observation Quarterly: pp. 2-4.

Johannessen, O. M., H. Espedal, B. Furevik, D. Akimov and A. Jenkins, 1999: COAST WATCH: Integrating Satellite SAR in an Operational System for Monitoring Coastal Currents, Wind, Surfactants and Oil Spills: Proc. Second International Conference on EuroGOOS, Rome, Italy, pp. 11-13 (March).

Johannessen, J. A., 2000: Coastal Observing Systems: The Role of Synthetic Aperture Radar. The Johns Hopkins Univ. Tech. Dig: Vol. 21, pp. 41-48.

Johannessen, J. A., R. Garello, B. Chapron, R. Romeiser, P. Pavlakis, I. Robinson, N. Connolly, K. Nittis, T. Hamre, S. Uffermann, W. Alpers, H. Espedal, B. R. Furevik, V. Cummins, D. Tarchi, 2001: Marine SAR Analysis and Interpretation System á MARSAIS. Annales de Telecommunications: Vol. 56, pp. 655-660.

Jones, W. L., V. E. Delnore, E. M. Bracalente, 1981: The Study of Mesoscale Ocean Winds. Spaceborne Synthetic Aperture Radar for Oceanography (eds. R. C. Beal, P. S. DeLeonibus, and I. Katz): The Johns Hopkins University Press, Baltimore, MD, pp. 87-94.

Katsaros, K. B., P. W. Vachon, P. G. Black, P. P. Dodge, and E. W. Uhlhorn, 2000: Wind fields from SAR: Could they improve our understanding of storm dynamics? The Johns Hopkins Univ. Tech. Dig: Vol. 21, pp. 86–93.

Kerbaol, V., B. Chapron, and P. Queffeulou, 1998: Analysis of the Wind Field during the “VendéeGlobe” Race: A Kinematic SAR Wind Speed Algorithm. Earth Observation Quarterly: Vol. 59, pp. 16-19.

Kerbaol V., B. Chapron and P. W. Vachon, 1998: Analysis of ERS-1/2 Synthetic Aperture Radar Wave Mode Imagettes. J. Geophys. Res: Vol. 103, pp. 7833-7846.

Korsbakken E., 1996: Quantitative wind field retrieval from ERS SAR images. European Space Agency (ESTEC) Technical Report.

Korsbakken and B. Furevik, 1998: Wind field Retrieval from SAR Compared with Scatterometer Wind Field during ERS Tandem Phase. Earth Observation Quarterly: Vol. 59, pp. 23-26.

Korsbakken E, J. A. Johannessen, and O. M. Johannessen, 1998: Coastal Wind Retrievals from ERS Synthetic Aperture Radar. J. Geophys. Res: Vol. 103, pp. 7857-7874.

Laur, H., P. Bally, P. Meadows, J. Sanchez, B. Schaettler, E. Lopinto, D. Esteban, 2002: Derivation of the Backscattering Coefficient (σ_0) in ESA ERS SAR PRI Productions. ESA Document No. ES-TN-RS-PM-HL09, Vol. 17 (September).

Lehner, S., J. Horstmann, W. Koch, W. Rosenthal,1998: Mesoscale Wind Measurements using Recalibrated ERS SAR images. J. Geophys. Res: Vol. 103, pp. 7847-7856.

Lehner, S., J. Schulz-Stellenfleth, B. Schattler, H. Breit, J. Horstmann, 2000: Wind and Wave Measurements using Complex ERS-2 SAR Wave Mode Data. IEEE Trans. Geosci. Rem. Sens: Vol. 38, pp. 2246-2257.

Li, X., P. Clemente-Colón, W. G. Pichel, and P. W. Vachon, 2000: Atmospheric Vortex Streets on a Radarsat SAR Image. Geophys Res. Lett: Vol. 27, pp. 1655-1658.

Mastenbroek, K., 1998: High-Resolution Wind Fields from ERS SAR. Earth Observation Quarterly: Vol. 59, pp. 20-22.

Meadows, P., H. Laur, J. I. Sanchez, and B. Schattler, 1998: The ERS SAR performance. CEOS SAR Workshop: Noodwijk, The Netherlands, pp. 223-232.

Monaldo, F. M. and R. C. Beal, 1998: Toward Real-Time Processing, Blending, and Dissemination of Operational Wind Products from the Radarsat SAR. Proc. 1998 International Geoscience and Remote Sensing Symposium: Seattle, WA., pp. 959-961, 6-10 July.

Monaldo, F. M., 2000: The Alaska SAR Demonstration and Near Real-Time Synthetic Aperture Radar Winds. The Johns Hopkins Univ. Tech. Digest: Vol. 21, pp. 75-84 (Jan).

Monaldo, F. M., D. R. Thompson, R. C. Beal, W. G. Pichel, and P. Clemente-Colón, 2001: Comparison of SAR-Derived Wind Speed with Model Predictions and Buoy Comparisons. IEEE Trans. Geosci. Rem. Sens: Vol. 39, pp. 2587-2600.

Monaldo, F. M., D. R. Thompson, W. G. Pichel, and P. Clemente-Colón, 2003: A Systematic Comparison of QuikSCAT and SAR Ocean Surface Wind Speeds. IEEE Trans. Geosci. Remote Sensing: Vol. 34 (in press).

Moore, R. K (and others), 1974: Simultaneous Active and Passive Microwave Response of the Earth in the Skylab RADSCAT experiment. Proc. Ninth International Symposium on Remote Sensing of the Environment: Vol. I, University of Michigan, pp. 189-217.

Mourad, P., D. Mourad, D. C. Vandemark, and D. R. Thompson, 2000: Towards Extracting Fine-Scale Wind Fields from Synthetic Aperture Radar Imagery of the Ocean Surface. The Johns Hopkins Univ. Tech. Digest: Vol. 21, pp. 108-115 (Jan).

Mueller, G., B. Bruemmer, and W. Alpers, 1999: Roll Convection within an Arctic Cold Air Outbreak: Interpretation of In Situ Aircraft Measurements and Spaceborne SAR Imagery by a Three-Dimensional Atmospheric model. Monthly Weather Review: Vol. 127, pp. 363-380.

Offiler, D., 1994: The Calibration of ERS-1 Satellite Scatterometer Winds. J. Atmos. Oceanic Tech: Vol. 11, pp. 1002-1017.

Pichel, W. G. and P. Clemente-Colón, 2000: NOAA CoastWatch SAR Applications and Demonstration. The Johns Hopkins Univ. Tech. Digest: Vol. 21, pp. 49-57 (Jan).

Pierson, W. J., 1983: The Measurement of the Synoptic Scale Wind over the Ocean. J. Geophys. Res: Vol. 88, pp. 1683-1708.

Portabella M., A. Stoffelen, and J. A. Johannessen, 2002: Toward an Optimal Inversion Method for Synthetic Aperture Radar Wind Retrieval. J. Geophys. Res: Vol. 107 (C8), pp. 1.1-1.13.

Quilfen, Y. and A. Betamy, 1994: Calibration/Validation of ERS-1 Scatterometer and Precision Products. Proc. 1994 International Geoscience and Remote Sensing Symposium: Pasadena, CA, pp. 945-947, 8-12 August.

Romeiser, R., W. Alpers, and V. Wissmann, 1997: An Improved Composite Model for the Radar Backscattering Cross Section of the Ocean Surface: 1. Theory and Model Validation/Optimization by Scatterometer Data. J. Geophys. Res: Vol. 102, pp. 25,237-25,250.

Sandvik, A. D. and B. R. Furevik, 2002: Case study of a Coastal Jet at Spitzbergen: Comparison of SAR and Model Estimated Wind. Monthly Weather Rev: Vol. 19, pp. 1040-1051.

Scoon A., I. S. Robinson, and P. J. Meadows, 1996: Demonstration of an Improved Calibration Scheme from ERS-1 Imagery using a Scatterometer Wind Model. Int. J. Remote Sensing: Vol. 17, pp. 413-418.

Shimada, T., H. Kawamra, and M. Shimada, 2003: An L-band Geophysical Model Function for SAR Wind Retrieval using JERS-1 SAR. IEEE Trans. Geosci. Remote Sensing: Vol. 41, pp. 518-531.

Sikora, T. D., K. S. Friedman, W. G. Pichel, and P. Clemente-Colón, 2000: Synthetic Aperture Radar as a Tool for Investigating Polar Mesoscale Cyclones. Weather Forecasting: Vol.15, pp. 745-758.

Sikora, T. D., D. R. Thompson, and J. C. Bleidorn, 2000: Testing the Diagnosis of Marine Atmospheric Boundary Layer Structure from Synthetic Aperture Radar. The Johns Hopkins Univ. Tech. Digest: Vol. 21, pp. 94-99.

Stoffelen, A. C. M. and D. L. T. Anderson, 1993: ERS-1 Scatterometer Data Characteristics and Wind Retrieval Skill. Adv. Space Res: Vol. 13, pp. 553-560.

Stoffelen, A. C, M. and D. L. T. Anderson, 1997: Scatterometer Data Interpretation: Estimation and Validation of the Transfer Function CMOD4. J. Geophys. Res: Vol. 102, pp. 5767-5780.

Stoffelen, A. C. M., 1999: A Simple Method for Calibration of a Scatterometer over the Ocean. J. Atmos. Oceanic Technol: Vol. 16, pp. 275-282.

Thompson, D. R., T. M. Elfouhaily, and B. Chapron, 1998: Polarization Ratio for Microwave Backscattering from the Ocean Surface at Low to Moderate Incidence Angles. Proc. 1998 International Geoscience and Remote Sensing Symposium: Seattle, WA., pp. 1671-1676, 6-10 July.

Thompson, D. R. and R. C. Beal, 2000: Mapping High-Resolution Wind Fields using Synthetic Aperture Radar. The Johns Hopkins Univ. Tech. Dig: Vol. 21, pp. 58-67 (Jan).

Thompson, D. R., F. M. Monaldo, R. C. Beal, W. G. Pichel, and P. Clemente-Colón, 2001: The Use of Radarsat SAR Imagery with QuikSCAT Wind Directions for High-Resolution Coastal Wind Mapping. EOS: (October 9).

Unal, C. M. H., P. Snooji, and P. J. F. Swart, 1991: The Polarization-Dependent Relation Between Radar Backscatter from the Ocean Surface and Wind Vectors at Frequencies Between 1 and 18 GHz. IEEE Trans. Geosci. Rem. Sens: Vol. 29, pp. 621-626.

Vachon, P. W., H. E. Krogstad and J. S. Patterson, 1994: Airborne and Spaceborne Synthetic Aperture Radar of Ocean Waves. Atmos. Ocean: Vol. 32, pp. 83-112.

Vachon, P. W. and F. W. Dobson, 1996: Validation of Wind Vector Retrieval from ERS-1 SAR Images Over the Ocean. The Global Atmos. and Ocean: Vol. 5, pp. 177-187.

Vachon, P. W., I Chunchuzov, and F. W. Dobson,1998: Wind Field Structure and Speed from Radarsat SAR Images. Earth Observation Quarterly: Vol. 59, pp. 12-15.

Vachon P. W. and F. W. Dobson, 2000: Wind Retrieval from Radarsat SAR Images: Selection of a Suitable C-band HH Polarization Wind Retrieval Model. Canadian J. Rem. Sens: Vol. 26, pp. 306-313.

Vachon, P. W., P. Adlakha, H. Edek, M. Henschel, B. Ramsay, D. Flett, M. Rey, F. Staples, and S. Thomas, 2000: Canadian Progress toward Marine and Coastal Applications of Synthetic Aperture Radar. The Johns Hopkins Univ. Tech. Digest: Vol. 21, pp. 33-40.

Vandemark, D., P. W. Vachon, B. Chapron, 1998: Assessment of ERS-1 SAR Wind Speed Estimates Using an Airborne Altimeter. Earth Observation Quarterly: Vol. 59, pp. 5-8.

Wackerman, C. C., R, Rufenach, J. Johannessen, and K. Davison, 1996: Wind Vector Retrieval Using ERS-1 Synthetic Aperture Radar Imagery. IEEE Trans. Geosci. Rem. Sens: Vol. 34, pp. 1343-1352.

Wackerman, C. C., 2000: Estimating Wind Vectors from Radarsat Synthetic Aperture Radar Imagery. Tech. Rep. 10032100-1-T, Veridian Int., Ann Arbor, MI.

Wackerman, C., P. Clemente-Colón, W. Pichel, X. Li, 2002: A Two-Scale Model to Predict C-band VV and HH Normalized Radar Cross Section Values over the Ocean. Can. J. Rem. Sens: Vol. 28, pp. 367-384.

Wackerman, C. C., W. G. Pichel, P. Clemente-Colón, 2003: Automated Estimation of Wind Vectors from SAR. Proc. 83rd AMS Annual Meeting: Long Beach, CA, 9-13 February.

Weissman, D. E., D. King, and T. W. Thompson, 1979: Relationship Between Hurricanes Surface Winds and L-band Radar Backscatter from the Sea Surface. J. Applied Meteorol: Vol. 18, pp. 1023-1034.

Weissman, D. E., T. W. Thompson, and R. Legeckis, 1980: Modulation of Sea Surface Radar Cross Section by Surface Stress: Wind Speed and Temperature Affects across the Gulf Stream. J. Geophys. Res: Vol.85, pp. 5032-5042.

Wentz, F. J., L. A. Mattox, and S. Peteherych, 1986: New Algorithms for Microwave Measurements of Ocean Winds: Applications to Seasat and the Special Sensor Microwave Imager. J. Geophys. Res: Vol. 91, pp. 2289-2307.

Winstead, N. S. and P. D. Mourad, 2000: Shallow Great Lake Scale Atmospheric Thermal Circulation Imaged by Synthetic Aperture Radar. Monthly Weather Review: Vol. 128, pp. 3654-3663.

Winstead, N. S. and G. S. Young, 2000: Analysis of Drainage Flow Exit Jets over the Chesapeake Bay. J. Applied Meteorol: Vol. 39, pp. 1269-1281.

Winstead, N. S., 2001: Characteristics of the Wind Speed Distribution over Cold Bay and Leonard Harbor, Alaska. Johns Hopkins APL Tech. Rep: SRO-01-09, Laurel, MD, May.

Winstead, N. S., R. M. Schaaf, and P. D. Mourad, 2001: Synthetic Aperture Radar Observations of the Surface Signatures of Cold-season Bands over the Great Lakes. Weather and Forecasting: Vol.16, pp. 315-328.

Winstead, N. S., T. Sikora, and D. R. Thompson, P. D. Maurad, 2002: Direct Influence of Gravity Waves on Surface-layer Stress during a Cold Air Outbreak as shown by Synthetic Aperture Radar. Monthly Weather Review: Vol. 130, pp. 2764-2776.

Young, G. S., 2000: SAR Signatures of the Marine Atmospheric Boundary Layer: Implications for numerical weather forecasting. The Johns Hopkins Univ. Tech. Digest: Vol. 21, pp. 27-32.

Young, G. S. and T. Sikora, 1998: Distinguishing Boundary Layer Signatures from Mesoscale and Ocean Clutter in SAR imagery. Proc. 1998 International Geoscience and Remote Sensing Symposium: Seattle, WA, pp. 1385-1387, 6-10 July.

Section II

Meteorological Phenomena in High Resolution SAR Wind Imagery

George Young and Nathaniel Winstead

2.0 Introduction

This section discusses the common high-wind phenomena seen on SAR imagery of Alaska's offshore waters. The purpose of this discussion is twofold. First, to provide the meteorologist with the information needed to unambiguously identify each of the phenomena by its signature in a SAR image. Second, to provide sufficient insight into workings of these phenomena for a forecaster to make useful deductions about the weather. For most of these phenomena, the existence of a particular SAR signature allows one to deduce far more than just the surface wind-field at image time.

The remainder of this section is organized into a series of subsections each focusing on a single phenomenon or closely related group of phenomena. Each subsection begins with a description of the salient features of the phenomenon's SAR signature, illustrated with SAR images from Section III. The structure and behavior of the phenomenon is then discussed. The dynamics of the phenomenon are explored with a focus on providing the insight needed to make maximum deductive use of the SAR products in nowcasting and forecasting. References to the literature are included as needed to support the discussion and to provide a source of further information.

2.1 Island and mountain wakes

The flow past islands and isolated peaks often results in low-speed wakes trailing off in the lee of the highest terrain. These wakes are common in the Aleutians and in other Alaskan locations such as the Barren Islands and Augustine Island in the Cook Inlet. The most common form is a linear band of low wind speed known as a "weak wake" (Schär and Smith 1993a, Smith et al. 1997). These linear wakes are called "weak" because of their easily met environmental requirements rather than for any lack of intensity as a phenomenon. Less common because of its more restrictive environmental requirements is a wake type known as the Kármán vortex street. Section III provides a number of good examples of linear wakes in 0458 GMT 12 Dec 2000, 0531 GMT 03 Jan 2000, and 0348 GMT 30 Sep 2000. 1746 GMT 06 Feb 2000 even shows these wakes occurring in the heart of a cyclone, curving with the synoptic scale winds. A clearly defined Kármán vortex street can be seen in 0441 GMT 22 Dec 1999 along with linear wakes from adjacent islands.

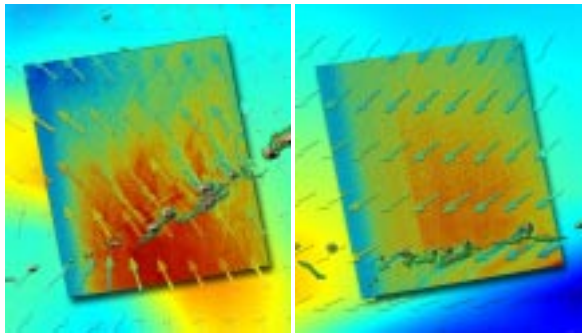

0458 GMT 12 Dec 2000 0531 GMT 03 Jan 2000

Linear wakes are easily detected on SAR imagery as long plumes of markedly lower wind-speed downwind of islands and peaks. This plume is generally narrower than the peak but much longer. Lengths of several hundred kilometers are rather common even for wakes with widths on the order of 10 kilometers. The low-speed plume is often sharply bounded with a near zero-order transition to the higher wind speeds on either side. Kármán vortex streets, in contrast, have a much more complex SAR signature. The vortices shedding off the peak alternate direction of spin from vortex to vortex. Thus the SAR signature of a Kármán vortex street consists of trains of chevrons or spirals of alternating orientation as in 0441 GMT 22 Dec 1999. The pattern is generally as wide or wider than the peak responsible. Thus an island's wake will be wider if it takes the form of a Kármán vortex street than if it takes the linear form. The two forms are roughly equally persistent with Kármán vortex streets often extending hundreds of kilometers and many eddies downwind of their parent island.

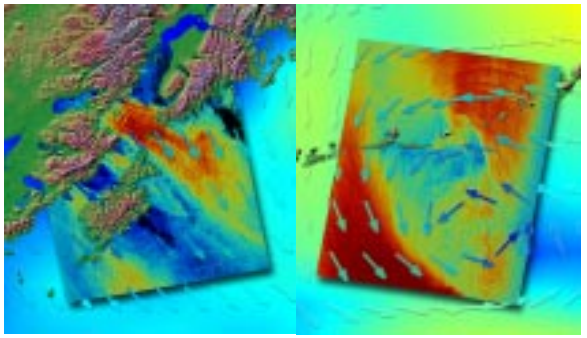

0348 GMT 30 Sep 2000 1746 GMT 06 Feb 2000

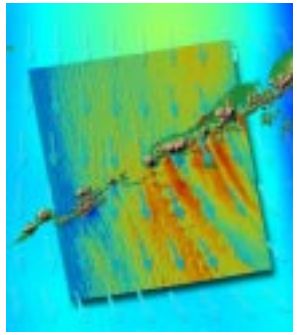

0441 GMT 22 Dec 1999

A linear wake consists of three distinct features: a hydraulic jump on the lee side of a terrain summit, a long plume of low-speed boundary layer air trailing downwind of the hydraulic jump, and a sharp wind-shear line on either side of the low-speed plume. These shear-lines are often called potential vorticity (PV) banners (Schär and Smith 1993a). Figure 2-1a diagrams these features as seen from overhead. For extreme cases, the wind direction may even reverse in the core of the wake, particularly in the immediate lee of the island. There is generally moderate to strong turbulence aloft in the lee of the peak, most intense where the flow over the peak transitions from shallow and supercritical to deeper and subcritical, i.e. at the hydraulic jump. Likewise, there could be turbulence in the strong shear-layer at the top of the low-speed

wake (i.e. near the top of the surface airmass or boundary layer). The formation of a linear island wake via a lee-side hydraulic jump, adapted from figure 2 in Schär and Smith (1993a), is depicted in figure 2-1a. The lower wind speeds in the wake are depicted in yellow as in the SAR imagery. The island is shown in green, the hydraulic jump in light blue, and the shear lines (potential vorticity banners) in dashed blue. Streamlines are shown in black. Kármán vortex streets consist of a series of counter-rotating vertically oriented vortices drifting downwind from an island or peak as shown in figure 2-1b. Thus, the surface wind direction is wildly meandering (±90 degrees). The vortices also result in interwoven areas of fast and slow winds with fairly sharp boundaries as seen in 0441 GMT 22 Dec 1999. The individual vortices drift downwind to be replaced by new ones forming just to the lee of the peak. Given the resulting spatial and temporal variations in both wind speed and direction, the state of the

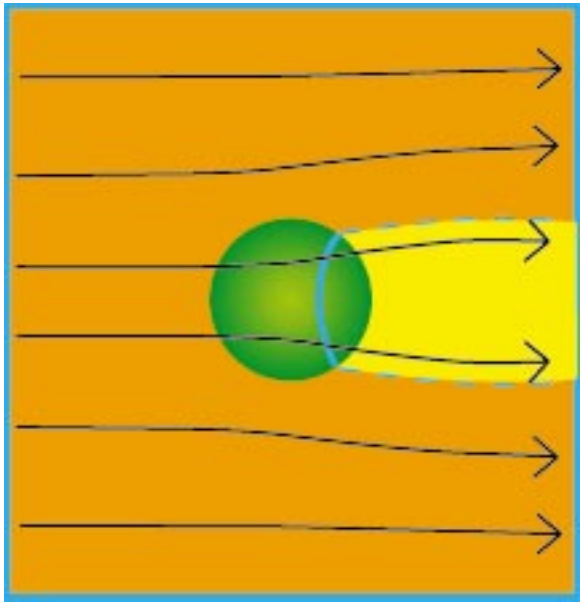

Figure 2-1a. The formation of a linear island wake via a lee-side hydraulic jump, adapted from figure 2 in Schär and Smith (1993a). The lower wind speeds in the wake are depicted in yellow as in the SAR imagery. The island is shown in green, the hydraulic jump in light blue, and the shear lines (potential vorticity banners) in dashed blue. Streamlines are shown in black.

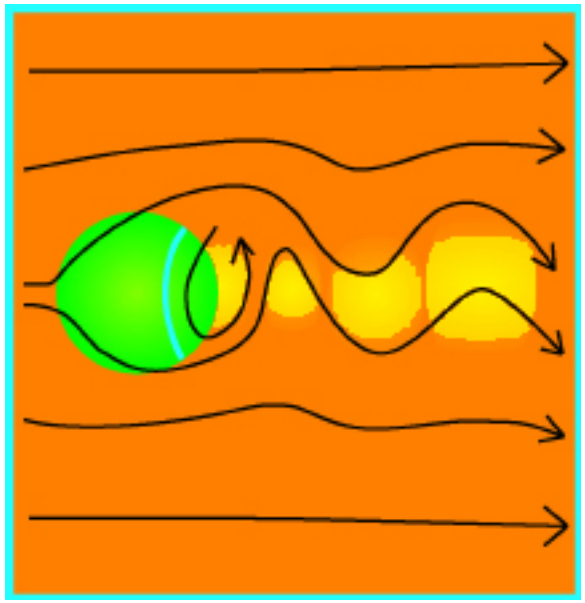

Figure 2-1b. The formation of a Kármán vortex street in the lee of an island, adapted from figure 9a in Schär and Smith (1993b). The island is shown in green, the hydraulic jump in light blue, and the streamlines in black. Slower wind speeds in the vortex cores are depicted in yellow.

wind-driven sea could become quite confused. Both simulations and cloud images suggest that Kármán vortex streets are barotropic, so flow is probably similar throughout the boundary layer or air mass. As with linear wakes, turbulence is expected in the lee of the peak and strong wind shear at the top of the wake. Both types of wakes generally persist for as long as the synoptic conditions support their existence, typically hours to days.

The physical mechanism for creation of linear wakes depends on the existence of a hydraulic jump or, in more smoothly stratified situations, breaking of a vertically propagating mountain lee wave. The turbulence associated with these closely related phenomena consumes kinetic energy, thereby slowing the mean wind and creating the low-speed wake. The literature (e.g., Schär and Smith 1993b) often poses this argument in terms of viscous generation of potential vorticity, casting the wake as the space between two jump-driven PV banners rather than viewing the banners as the edges of the wake. The two arguments are actually equivalent. The existence of the hydraulic jump depends on the flow over the peak becoming supercritical (i.e. faster than the relevant gravity wave phase speed) and then slowing to subcritical on the lee slope. Similarly, breaking mountain lee waves depend on the existence of a critical layer above which the flow becomes subcritical.

Kármán vortex streets are created by more intense manifestations of this same mechanism (Schär and Smith 1993). When the shear-lines (PV banners) become strong enough, perturbations on the two sides of the wake interact making the wake wiggle laterally and then break down into vertically oriented vortices of alternating sign. The shedding period for these vortices goes as $D \cdot F_r / U$ where D is island diameter, U the upstream wind speed, and F_r the Froude number. Most research has been done with shallow water models. Translating these results to the continuously stratified real atmosphere takes some care but suggests that the shedding period is proportional to $D \cdot (g \cdot N \cdot U)^{1/2}$ where N is the Brunt-Visalia frequency. Thus, the time between shedding of successive vortices increases with island size, but decreases with stability and wind speed.

The existence of linear wakes or Kármán vortex streets requires specific conditions and so can tell the meteorologist a lot about the environment in which they are occurring (Smith et al. 1997). Both require a fairly steep-sided obstacle upwind. The wind below summit altitude upwind of that obstacle must be strong enough to surmount the terrain despite the existence of a stable layer at or below the summit. Linear wake formation occurs when the summit is high enough to induce wave breaking. The transition to lee vortices occurs when summit height is twice that required for the initiation of linear wakes. Thus, for a given island, the sequence of transitions from no wake to linear wake to wake vortices occurs with decreasing wind speed and/or increasing stability. Given that SAR provides a wind speed estimate, wake type can be used to estimate airmass stability, at least qualitatively. The vortices begin to shed when the Reynolds number, $R_e = H/C_D \cdot L$

exceeds 20, where H is the depth of the vortex, C_D is lower boundary drag coefficient (0.0015±0.0005), and L is the horizontal scale of the peak. Thus, squat islands are less likely to produce Kármán vortex streets than are more sharply peaked islands.

References

Schär, Christoph, Ronald B. Smith, 1993a: Shallow-Water Flow past Isolated Topography. Part II: Transition to Vortex Shedding. Journal of the Atmospheric Sciences: Vol. 50, No. 10, pp. 1401-1412.

Schär, Christoph, Ronald B. Smith, 1993b: Shallow-Water Flow past Isolated Topography. Part I: Vorticity Production and Wake Formation. Journal of the Atmospheric Sciences: Vol. 50, No. 10, pp. 1373-1400.

Smith, Ronald B., Arthur C. Gleason, Paul A. Gluhosky, Vanda Grubii, 1997: The Wake of St. Vincent. Journal of the Atmospheric Sciences: Vol. 54, No. 5, pp. 606-623.

2.2 Point Wakes

Points along a coast can act either to accelerate (1812 GMT 13 Dec 2000) or decelerate (1502 GMT 10 Mar 2000) boundary-layer flow to their lee. The low-speed form generally involves flow separation from a fairly sharp point as it does here. In contrast, the high-speed form is an expansion fan resulting from supercritical flow remaining attached to the coast after passing a point (Samelson 1992). Such flow attachment is more likely at less acute points, such as that in 1812 GMT 13 Dec 2000.

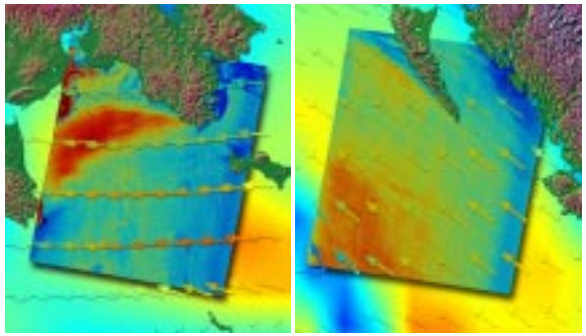

1812 GMT 13 Dec 2000 1502 GMT 10 Mar 2000

Low-speed point wakes are just one-sided versions of the linear island wakes discussed in the previous subsection. They can be recognized as a long region of low wind (up to several hundred kilometers) trailing downwind from the point and extending in to the lee shore. As with linear island wakes, a sharp shearline separates the flow passing point from the low-wind wake along the coast. 1502 GMT 10 Mar 2000 captures all of these features. The SAR signatures of accelerating wakes are markedly different although they too may include a low-speed region along the coast in the lee of the point. The defining feature of an accelerating point wake is the expansion fan, a spreading region of high-speed surface winds expanding downwind from the point. As in 1812 GMT 13 Dec 2000 the fastest winds may occur 100 kilometers or so downwind of the point. Likewise slower wind speeds are often observed inshore of the expansion fan. The offshore edge of the expansion fan is not as abrupt as that of a low-speed wake and angles acutely downwind from the point. Expansion fans either decelerate gradually over hundreds of kilometers due to friction or end abruptly at a hydraulic jump if they encounter obstructing terrain. The remainder of this subsection will focus on accelerating point wakes. Low-speed point wakes can be understood and their behavior anticipated by making reference to the linear island wake discussion in the previous subsection.

The expansion fan of an accelerating point wake is illustrated in planview in figure 2-2. The key features of this phenomenon include spreading streamlines, decreasing boundary layer depth, and accelerating flow. The streamlines spread downwind of the point as the flow remains attached to the coast. Because of this spreading the boundary layer depth decreases leading via the Bernoulli equation to an acceleration of the flow. The decrease in boundary layer depth could cause clearing of low-level clouds on some occasions. The acceleration of the surface flow can result in a low-level jet capped by a shear layer. The wave signatures seen along the offshore edge of the jet in 1812 GMT 13 Dec 2000 may be the result of such shear. If seen, such wave signatures would be highly suggestive of turbulence within both the boundary layer and the capping inversion. Turbulence should also be expected at the hydraulic jump if the expansion fan is observed to slow abruptly at its downwind edge. Modeling suggests that these hydraulic jumps may angle sharply downwind so the coastal terrain must be examined to determine if a hydraulic jump has occurred or a low-speed point wake has developed inshore of the high-speed wake of an upwind point. 1812 GMT 13 Dec 2000 provides a good illustration of this sort of compound point wake as well as demonstrating the importance of the relative angle of downwind coast in deter mining the type of wake formed by a particular point.

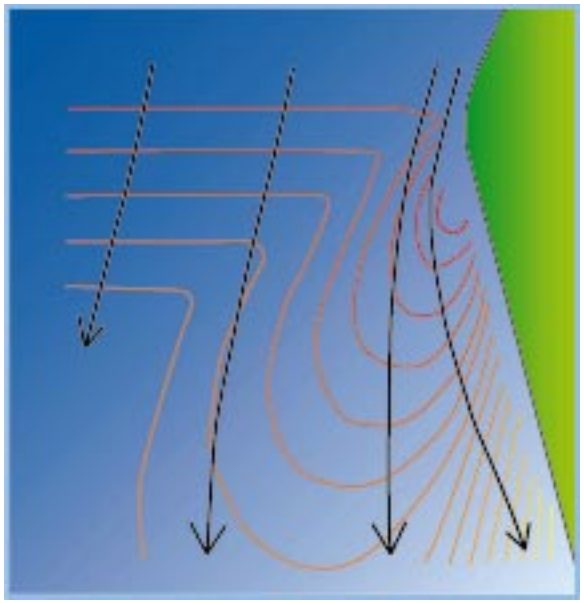

Figure 2-2. A point wake with friction, adapted from figure 4 in Samelson (1992). The coast is shaded green, the marine boundary layer blue with lighter meaning shallower. The contours are of wind speed with red being faster than yellow as in the SAR imagery. Streamlines are shown in black.

The coast immediately downwind of the primary point is angled only 10 or 20 degrees to the mean flow, so the flow is able to remain attached after passing the point thus causing an expansion fan and the associated flow acceleration. Further downstream, the coast bends more sharply to the right and the flow separates from the coast causing the formation of a low-speed wake inshore of the expansion fan. Friction can eventually

cause inshore slowing even without such topographic assistance.

The expansion fan---streamline spreading downstream of a point---occurs when supercritical flow remains attached to the coast. Because the gravity wave speed is slower than the wind speed, the atmospheric response to this surface difluence is to decrease the boundary layer depth, and increase the wind speed as required to conserve the Bernoulli function (Samelson 1992). The flow attachment requirement is most easily met if the pressure gradient is along the coast upwind of the point. If it is along the coast downwind of the point, the flow tends to bend around the point with no interesting mesoscale dynamics. There is some disagreement as to whether the upstream flow must be supercritical or whether the flow need only become supercritical in passing the point (Dorman and Winant 2000). The distinction is difficult to make because it is often unclear which form of the Froude number is most relevant. If most of the static stability is concentrated in the capping inversion, the shallow water form $U/N \cdot h$ is appropriate, where $N=\sqrt{(g \cdot h \cdot D_q/q)}$, U the upstream wind speed, h the depth of the boundary layer, g the gravitational acceleration, q the boundary layer potential temperature, and D_q the potential temperature increase at the capping inversion. It is less clear what Froude number to use if the stability is more uniformly distributed. N is then lapse rate dependent, but what is the appropriate length scale? This question leads to a further complication, the possibility of accelerated flow aloft if the point throws a vertically propagating gravity wave (Burk and Thompson 1996), a topic that will be covered in the next subsection.

From the discussion above it is clear that the necessary conditions for point wakes include terrain, wind, and stability requirements. The nature of the upwind point determines the form of the wake: if the lee shore is at an acute angle to the wind, low-speed wakes are expected; if it is at a shallow angle to the wind, accelerating wakes are favored. The existence of a bight downwind of the point greatly increases the chances of an accelerating wake ending abruptly in a hydraulic jump. While slow-wake formation depends on the criticality of flow over the point (Doyle and Bond 2001), accelerating wake formation depends on the criticality of the boundary layer itself. Thus, strong boundary layer winds favor accelerating wakes. Supercritical flow is also favored by reduced gravity wave speed in capping inversion. Both shallow boundary layers and weaker capping inversions provide this effect although these two conditions may be anti-correlated in many situations. Weaker stability aloft and weaker winds aloft may also favor accelerated wakes. Both low-speed and accelerating wakes should be expected to persist for as long as the requisite synoptic conditions last (hours to days). The positions of the features may, however, evolve as the synoptic conditions (wind speed, direction, and static stability) evolve (Haack et al. 2000).

References

Burk, Stephen D., William T. Thompson, 1996: The Summertime Low-level Jet and Marine Boundary Layer Structure along the California Coast. Monthly Weather Review: Vol. 124, No. 4, pp. 668–686

Dorman, C. E., C. D. Winant, 2000: The Structure and Variability of the Marine Atmosphere around the Santa Barbara Channel. Monthly Weather Review: Vol. 128, No. 2, pp. 261–282.

Doyle, James D., Nicholas A. Bond, 2001: Research Aircraft Observations and Numerical Simulations of a Warm Front Approaching Vancouver Island. Monthly Weather Review: Vol. 129, No. 5, pp. 978–998.

Haack, Tracy, Stephen D. Burk, Clive Dorman, David Rogers, 2001: Supercritical Flow Interaction within the Cape Blanco–Cape Mendocino Orographic Complex. Monthly Weather Review: Vol. 129, No. 4, pp. 688–708.

Samelson, R. M., 1992: Supercritical Marine-Layer Flow along a Smoothly Varying Coastline. Journal of the Atmospheric Sciences: Vol. 49, No. 17, pp. 1571–1584.

2.3 Mountain Lee Waves

There are two basic types of mountain lee wave, horizontally and vertically propagating (Durran and Klenp 1982). While either type can be generated by either isolated peaks or extended ranges, their vertical structure and surface manifestations are very different. Horizontally propagating lee waves are the easiest to detect on SAR imagery (0428 GMT 23 Feb 2001; 0348 GMT 30 Sep 2000). Their SAR signature is similar to that of the shear-driven gravity waves in 1812 GMT 13 Dec 2000, a series of parallel bands of fast

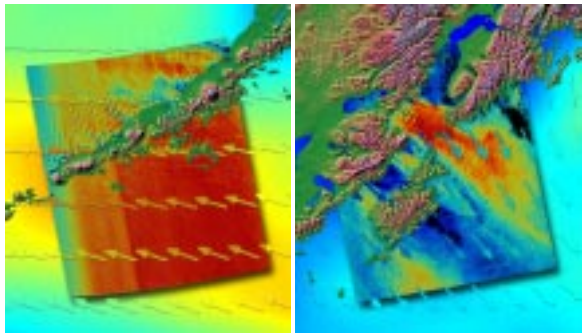

0428 GMT 23 Feb 2001 0348 GMT 30 Sep 2000

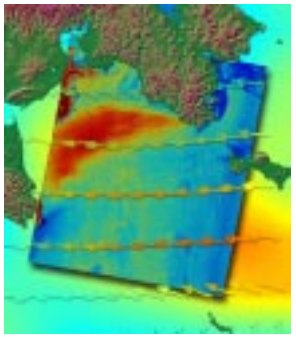

1812 GMT 13 Dec 2000

and slow winds. Unlike the shear-driven waves, however, lee waves trail downwind from a peak or mountain range. The lee wave bands downwind of a range are therefore aligned parallel to the terrain responsible rather than being aligned perpendicular to the shear as would shear-driven waves or parallel to the wind as would horizontal roll vortices (cloud streets). The latter phenomenon is discussed in a later subsection. Horizontally propagating mountain lee waves typically have a band spacing of 3 to 30 kilometers and extend several to many cycles downwind. While phase speed

is canceled by wind speed for horizontally propagating waves, their position may drift in response to changes in wind or stability. For similar reasons, horizontally propagating waves generated by an isolated peak form chevrons of fast and slow wind with their point on lee slopes of the peak (Sharman and Wurtele 1983). Vertically propagating mountain lee waves would have very different SAR signatures as only the first high-speed band in lee of the peak reaches the surface. Such waves may cause strong winds just off the lee shore or the surface manifestation may be entirely onshore and so undetectable by SAR.

Horizontally propagating mountain lee waves consist of a series of vertical oscillations of a statically stable layer that has been perturbed by flowing over a mountain (Durran and Klemp 1982). The wave amplitude decreases both with height and toward the surface. Nonetheless, these waves frequently modulate the surface wind even in conditions where an underlying convective boundary layer exists (Winstead et al. 2001). Figure 2-3 depicts this flow in cross section. Alternating bands of fast and slow wind are encountered at any level within the wave train. The fast winds occur within the oscillating layer and the slow winds under the crests and above the troughs. The high-speed bands on SAR images mark trough touchdown locations. The wave oscillations typically have updrafts and downdrafts of from a few meters per second up to ten times that. Because horizontally propagating mountain lee waves do not tilt with height, the updrafts should be expected just downwind of the fastest surface winds and the downdrafts just downwind of the slowest surface winds. These drafts can cause lenticular clouds in otherwise clear situations and breaks in the overcast (foehn gaps) in cloudy situations. The vertical motion in combination with stable stratification results in large variations in temperature and consequently hydrostatic pressure. Non-hydrostatic pressure perturbations may further complicate the situation for aircraft relying on pressure altimeters. There is also the potential for variation in the air/sea temperature difference with the air being hottest where wind is fastest. Turbulence aloft is likely to be most intense under the wave crests where rotors result in slowing or even reversal of the surface winds.

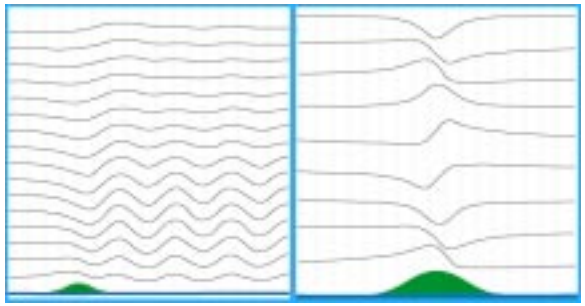

Figure 2-3. Cross sections of flow in a horizontally (left panel) and vertically (right panel) propagating mountain wave, adapted from Durran and Klemp 1982. The streamlines are shown in black, the terrain in green and the sea surface in blue.

While horizontally propagating mountain lee waves typically die out in approximately the mid troposphere, the vertically propagating version may extend up into the stratosphere as depicted in figure 2-3. The surface manifestation of these waves is a strong, often warm, wind on the lee slopes. Surface wind speeds there may exceed that at any level upwind of the mountains (Klemp and Lilly 1978). Updrafts and downdrafts, while at least as strong as those for horizontally propagating lee waves, are often restricted to the area over the lee slopes and peak. The foehn gap, if it exists, will be near the lee slope. For both types of wave, the phenomenon can last for as long as the synoptic situation persists (hours to days).

Mountain lee waves are buoyantly driven oscillations of vertically displaced parcels in a stable layer. Thus, they oscillate as gravity waves with a frequency near N, the Brunt-Väisälä frequency. The wave type (horizontally or vertically propagating) depends on the vertical profile of wind and stability. The controlling parameter is an inverse wavelength (N/U) corrected for shear effects. It is generally called the Scorer parameter (Durran and Klemp 1982). If the Scorer parameter decreases with height, horizontal propagation occurs. Thus, wind speed increasing with height and stability decreasing with height both favor horizontal propagation. The resulting trapped gravity waves have inverse wavelength within the range spanned by the Scorer parameter gradient. In contrast, if the Scorer parameter increases with height, vertical propagation occurs.

Because of this Scorer parameter dependence, mountain waves form only when there is an appropriate combination of terrain, wind, and stability. The key requirement is a peak or range reaching up into a stable layer. A row of peaks can act much like a range (0428 GMT 23 Feb 2001). Stability above peak height affects wave type as described above. Stability below peak height may affect the degree of wind speed perturbation at the surface. Less surface wind variation and thus, weaker SAR signatures should be expected if the boundary layer is deep or unstable (Winstead et al. 2001). The wind requirements for mountain lee wave generation are easily met in Alaska, as the component of flow perpendicular to the crest need only exceed 7 to 15 meters per second. Because of these easily met conditions, mountain lee waves can occur in a broad range of synoptic settings. 0428 GMT 23 Feb 2001 shows large-amplitude waves northwest of the Aleutians in a pre-warm-frontal jet. 0348 GMT 30 Sep 2000 shows similarly intense waves superimposed on gap flow (see the next subsection) and island wakes (see subsection 2.1) in the Kennedy Entrance area.

References

Durran, Dale R., Joseph B. Klemp, 1982: The Effects of Moisture on Trapped Mountain Lee Waves. Journal of the Atmospheric Sciences: Vol. 39, No. 11, pp. 2490-2506.

Klemp, J.B., D.K. Lilly, 1978: Numerical Simulation of Hydrostatic Mountain Waves. Journal of the Atmospheric Sciences: Vol. 35, No. 1, pp. 78-107.

Sharman, R.D., M.G. Wurtele, 1983: Ship Waves and Lee Waves. Journal of the Atmospheric Sciences: Vol. 40, No. 2, pp. 396-427.

Winstead, N. S., T. Sikora, and D. R. Thompson, P. D. Maurad, 2002: Direct Influence of Gravity Waves on Surface-layer Stress during a Cold Air Outbreak as shown by Synthetic Aperture Radar: Monthly Weather Review, Vol. 130, pp. 2764-2776.

2.4 Simple Gap flows

Gap flows occur when synoptic airmass movement is constricted through one or more gaps in a mountain range or island chain. While common anywhere with appropriate terrain (i.e. along every rugged portion of the Alaskan or Siberian coast), gap flows can be particularly spectacular when an air mass moves through the Iliamna Lake passes and on out through the Kennedy Entrance between Apognak Island and the Kenai Peninsula as seen in 0344 GMT 24 Dec 1999, 0344 GMT 31 Oct 2000, 0348 GMT 30 Sep 2000 and 1637 GMT 12 Dec 1999. The latter two SAR images extend far enough southwest to show the strong gap flows downwind of the Alaska Peninsula. While the resulting plumes of high-speed wind typically have moderately sharp lateral edges, these boundaries are sometimes blurred by interaction with flow through adjacent mountain gaps or over the major offshore landmasses. The gap flows in 0344 GMT 24 Dec 1999, 0348 GMT 30 Sep 2000 and 1637 GMT 12 Dec 1999 all exhibit the downwind spreading one would expect with a high-speed expansion fan. In contrast, the offshore portions of 0344 GMT 31 Oct 2000 do not, probably because the effect was counteracted by confluence in the synoptic scale flow. If islands obstruct the gap flow, wakes can occur as described in subsection 2.1. Such wakes are common in the lee of the Barren Islands and Augustine Island as seen in 0344 GMT 24 Dec 1999, 0348 GMT 30 Sep 2000, and 1637 GMT 12 Dec 1999. These wakes can be of aid in judging surface wind direction in situations where the flow curves to avoid more major obstructions such as Apognak Island and the Kenai Peninsula. As seen in 0348 GMT 30 Sep 2000, it is also possible to have quite intense mountain lee waves superimposed on the gap flow. When all three phenomena combine, the resulting wind field can be complex in the extreme.

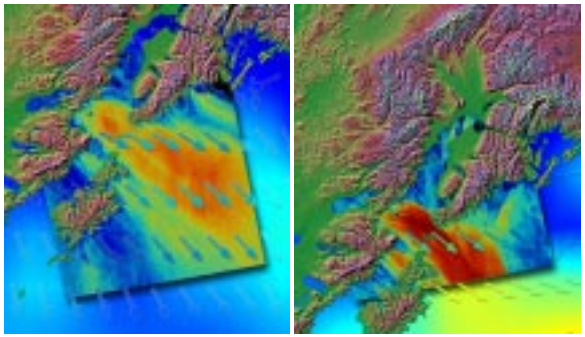

0344 GMT 24 Dec 1999 0344 GMT 31 Oct 2000

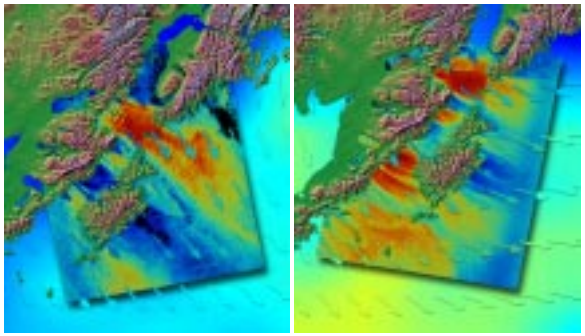

0348 GMT 30 Sep 2000 1637 GMT 12 Dec 1999

Figure 2-4 provides a schematic diagram of the streamlines through the Iliamna Lake gaps and Kennedy Entrance. Typical features of this and other Alaskan gap flows are strong wind in passes upwind of the gap flow (i.e. in the gaps themselves) and strong winds extending hundreds of kilometers downwind of the gaps. Depending on the interplay of synoptic pressure gradients and friction, these flows may not always decelerate until far downstream. In many ways gap flows can be thought of as two accelerating point wakes joined at the core. Thus, they often have fairly sharp lateral boundaries (Mass et al. 1995) and fan out to greater width downstream. Conditions aloft are also reminiscent of those in accelerating point wakes with wind speeds often decreasing between the top of the gap flow and the level of the flanking peaks. The gap flow itself often forms a supercritical expansion fan with the resultant decrease in boundary layer depth (Bond and Maklin 1993, Mass et al. 1995).

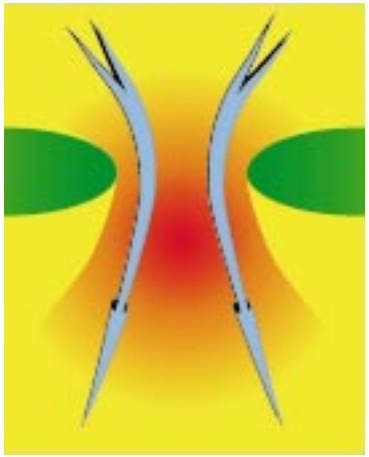

Figure 2-4. Gap flow between two points (green). Wind speed is indicated by shading with red being fastest, as in the SAR imagery. Streamlines are depicted as blue arrows.

Gap flows occur when the Froude number (computed relative to the height of the side walls) is small because, under these conditions, the flow is blocked everywhere but in the gap (Bond and Maklin 1993). In order to force flow through the gap, a synoptic pressure gradient across the barrier is required. Thus, most gap flows are highly ageostrophic with a pressure gradient across the barrier acting to accelerate the flow through the barrier (Mass et al. 1995). Balanced flow is eventually restored approximately one Rossby radius offshore, a few hundred kilometers for the latitude of Alaska (Bond and Macklin 1993). As with point wakes (see subsection 2.2) the Bernoulli effect plays a role in gap flows (Jackson and Steyn 1994). Thus, expansion fan effects can cause the flow to accelerate further upon leaving the gap (Colle and Mass 2000). This flow spreading results from variations in cross-flow pressure gradient caused by doming of cool air in the center of the outflow (Steenburgh et al. 1998). Supercritical flow can also occur within the gaps, possibly in patches rather than continuously (Finnigan et al. 1994).

Gap flow interaction with mountain waves is common in some parts of Alaska (Colman and Dierking 1992). For example the Taku wind of southeast Alaska is a manifestation of an amplified mountain wave. A complicating factor in understanding the Taku is the coincident occurrence of gap flow, although Colman and Dierking were able to demonstrate that these are

distinct phenomena. Conditions that favor mountain waves tend to have the cross-barrier pressure gradients needed for gap flow. Therefore, gap flows will frequently accompany mountain waves if appropriate gaps exist.

The existence of gap flow tells the meteorologist much about the movement of surface airmasses and the stability aloft. The required synoptic-scale pressure gradient across the barrier generally results from cold air damming of one sort or another. For gaps with passes well above sea level the depth of the cold airmass is important. If the stable layer capping the cold airmass reaches down to the floor of the gap, the flow through the gap is greatly reduced, particularly at sea level beyond the gap. This is yet another manifestation of the Froude number effect: the opposition of buoyancy to the flow of stably stratified air over high terrain. Thus, when a stable layer fills the pass, mountain waves result rather than gap flows (Colle and Mass 1998). Downstream terrain can also play a major role in gap flows. If there is a terrain barrier downstream of the gap, the flow will twist so as to pass out through any gaps in that barrier as seen in 0344 GMT 31 Oct 2000. As with most other phenomena resulting from the interaction of a stable atmosphere with terrain, gap flows will persist for as long as the required synoptic conditions prevail (hours to days).

References

Bond, Nicholas A., S. Allen Macklin, 1993: Aircraft Observations of Offshore-directed Flow near Wide Bay, Alaska. Monthly Weather Review: Vol. 121, No. 1, pp. 150–161.

Colle, Brian A., Clifford F. Mass, 1998: Windstorms along the Western Side of the Washington Cascade Mountains. Part I: A High-Resolution Observational and Modeling Study of the 12 February 1995 Event. Monthly Weather Review: Vol. 126, No. 1, pp. 28–52.

Colle, Brian A., Clifford F. Mass, 2000: High-Resolution Observations and Numerical Simulations of Easterly Gap Flow through the Strait of Juan de Fuca on 9–10 December 1995. Monthly Weather Review: Vol. 128, No. 7, pp. 2398–2422.

Colman, Bradley R., Carl F. Dierking, 1992: The Taku Wind of Southeast Alaska: Its Identification and Prediction. Weather and Forecasting: Vol. 7, No. 1, pp. 49–64.

Finnigan, Timothy D., Jason A. Vine, Peter L. Jackson, Susan E. Allen, Gregory A. Lawrence, Douw G. Steyn, 1994: Hydraulic Physical Modeling and Observations of a Severe Gap Wind. Monthly Weather Review: Vol. 122, No. 12, pp. 2677–2687.

Jackson, Peter L., D.G. Steyn, 1994: Gap Winds in a Fjord. Part I: Observations and Numerical Simulation. Monthly Weather Review: Vol. 122, No. 12, pp. 2645–2665.

Mass, Clifford F., Steve Businger, Mark D. Albright, Zena A. Tucker, 1995: A Windstorm in the Lee of a Gap in a Coastal Mountain Barrier. Monthly Weather Review: Vol. 123, No. 2, pp. 315–331.

Steenburgh, W. James, David M. Schultz, Brian A. Colle, 1998: The Structure and Evolution of Gap Outflow over the Gulf of Tehuantepec, Mexico. Monthly Weather Review: Vol. 126, No. 10, pp. 2673–2691.

2.5 Hybrid Gap Flows

Not all gap flows take the classic exit jet form described in subsection 2.4. Gap flows are common enough in Alaska that SAR frequently observes them interacting with other phenomena. Likewise, they can form in a wide range of synoptic settings, not just the classic one of a cold pool inland of a terrain barrier. This subsection explores some of the possible variations.

Reverse gap flow occurs when the cold pool lies offshore as in 1636 GMT 10 Apr 2000 or when a synoptic-scale on-shore flow passes through a gap as in 0340 GMT 11 Feb 2001 and 0353 GMT 19 Jun 2000. Synoptic-scale flow passing through a gap can also lead to outflows that curve with the offshore synoptic flow as in 0347 GMT 04 Jan 2001. Even classic ageostrophic gap flows of the type discussed in subsection 2.4 may turn downstream to merge with the synoptic scale flow as in 0253 GMT 30 Dec 2000. Drainage flows offer yet another complication. It is very hard to determine how much of a gap flow is contributed by drainage as most are forced by the pressure gradient associated with a pool of cold air blocked by terrain. Pure drainage flow occurs when the cold air originates within the terrain while pure gap flow when it originates behind the terrain barrier. For many Alaskan locations, gap flow through passes may be augmented by drainage flow from their side valleys, making pure cases of either hard to come by.

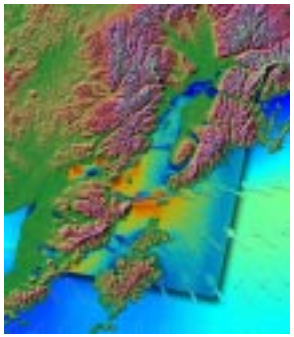

1636 GMT 10 Apr 2000

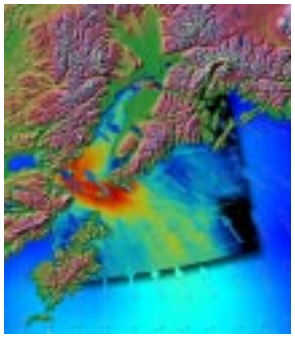

0340 GMT 11 Feb 2001

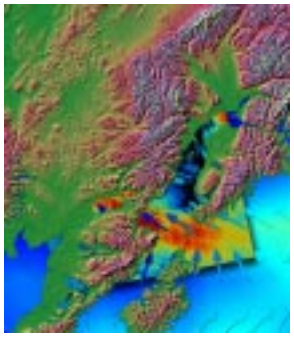

0353 GMT 19 Jun 2000

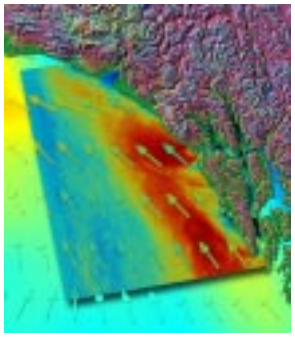

0253 GMT 30 Dec 2000

2.5.1 Reverse Gap Flow

Reverse gap flow in a situation where the pressure gradient is aligned through the gap is just the upstream half of the phenomenon described as classic gap flow in subsection 2.4. 1636 GMT 10 Apr 2000 illustrates the salient features. Confluence into the gap is widespread and can extend 100 or more kilometers upwind of the gap. The flow acquires sharp edges (PV banners) only after passing through the gap as the

terrain provides the only source of PV. Island wakes such as those of the Barren Islands seen in 1636 GMT 10 Apr 2000 can be very useful in distinguishing gap flow from reverse gap flow. 0340 GMT 11 Feb 2001 illustrates a more complex situation with merger of reverse gap flows from the Cook Inlet and the Kennedy Entrance. In some cases (e.g., 0353 GMT 19 Jun 2000) reverse gap flow does have sharp edges upstream of the barrier. The PV source for these shearlines is unclear. The resemblance of these anomalous reverse-flow cases to normal (exiting) gap flow makes determination of the true wind direction via island wakes essential.

Figure 2-4 in subsection 2.4 shows the streamline pattern in a gap flow including the portions upwind of the barrier (i.e. the reverse gap flow). The surface features of this upstream portion of a gap flow include confluence and acceleration. Historically this part of the flow has been less damaging than the downstream expansion fans and so has been little studied. Thus, the discussion that follows is based on a generalization of the hydraulic theory discussed in subsection 2.4. Such arguments suggest that the boundary layer (or cold airmass) should deepen via damming upstream of the barrier and become more shallow where the flow accelerates into the gap. Likewise, hydraulic arguments suggest that there is probably much less flow response above the boundary layer. Therefore shear and turbulence probably occur at the boundary layer top during reverse gap flow. Because reverse gap flow is just the upwind half of classic gap flow, terrain and stability requirements are the same (see subsection 2.4).

The salient features of reverse gap flow (upstream confluence and acceleration) might at first glance seem to require flow upstream of the barrier to be subcritical relative to boundary layer gravity waves. Yet such upstream effects may also be possible in faster flows if the flow remains subcritical with respect to the terrain on either side of the gap. In those circumstances cold air would pile up upwind of terrain causing a mesoscale pressure gradient towards the gap down which the flow could accelerate causing convergence. Mesoscale modeling could test this conjecture.

2.5.2 Gap Flow / Synoptic Interaction

Classic (exiting) gap flows occur when there is a cross-barrier pressure gradient (see subsection 2.4). If this pressure gradient continues offshore as in 0253 GMT 30 Dec 2000, the exit jets encounter offshore flow parallel to the coast, roughly perpendicular to the highly ageostrophic gap flow. This isobaric pattern is favored by the presence of a cyclone off the coast. In this situation, the gap flows bend anticyclonically to merge with the offshore flow as in 0239 GMT 09 Dec 1999. In doing so several gap flows may merge to form a jet along the coast as in 0253 GMT 30 Dec 2000. In contrast, 0347 GMT 04 Jan 2001 shows a non-classic case in which the gap flows appear to be in synoptic-scale balance, turning only as the offshore synoptic scale flow bends around a coastal cyclone. Other interesting features in this image include the sharp island wakes (PV banners) and the waves on them, especially downwind of Kodiak Island. These waves suggest weather conditions were favorable for the formation of Kármán vortex streets but that the island was too wide for the perturbations from the two PV banners to interact. Convection is responsible for the mottling to the south (see subsection 2.10).

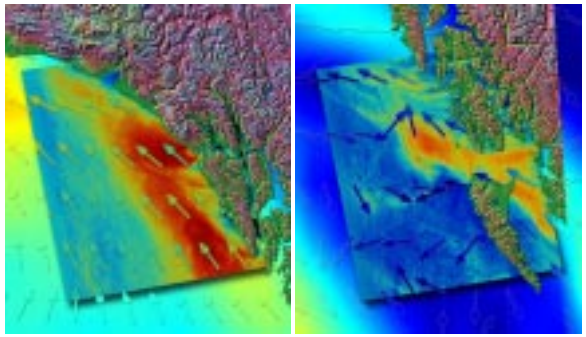

0253 GMT 30 Dec 2000 0239 GMT 09 Dec 1999

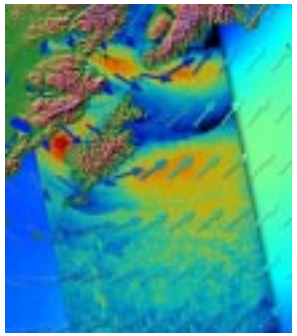

0347 GMT 04 Jan 2001

Figure 2-5 shows the streamlines and downstream evolution of the forces acting on a classic gap flow exit jet in the presence of a strong seaward pressure gradient offshore. The streamlines turn from down gradient at the gap to cross gradient downstream suggesting a transition from accelerating hydraulic flow to steady balanced flow. This flow begins with exit jets from one or more gaps. These jets then curve downstream to match the offshore synoptic flow direction. In the process the exit jets may decelerate over a few hundred kilometers to match the synoptic flow speed

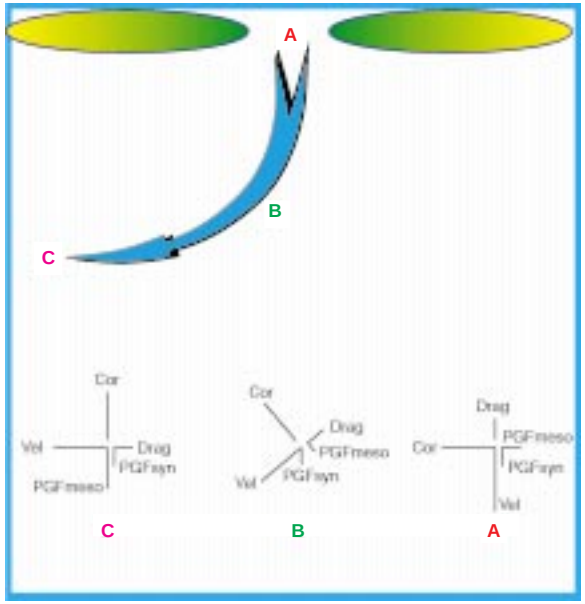

Figure 2-5. Plan view of a turning gap flow with force diagrams for three key points along a streamline (blue arrow). Diagram A shows the forces acting on a parcel in the gap, diagram B the forces acting on the same parcel while it is turning, and diagram C the forces after the parcel has turned parallel to the coast. The forces do not balance at any of these points. The flow is accelerating at point A, turning at point B, and decelerating at point C.

or may form a high-speed barrier jet along the coast. The latter may require a larger supply of cold air (i.e. more mass flux through the gaps) as it would require creation of a cold pool along the coastal barrier. Barrier jets are discussed in subsection 2.11. The features aloft in a turning gap flow are probably similar to the classic gap flows discussed in subsection 2.4.

SAR imagery suggests two mechanisms for gap flow/synoptic interaction. For cases with a cyclone offshore such as 0253 GMT 30 Dec 2000, the gap flow begins in the classic ageostrophic form although the "pull" of the cyclone offshore may be replacing to some extent the "push" of an anticyclone inland of the barrier. Once clear of the gap the Coriolis force gradually turns the flow, eventually achieving a three-way balance between Coriolis, pressure gradient, and friction (i.e. matching the rest of the synoptic scale flow). The resulting pool of cold air along the coastal mountain barrier enhances the offshore-directed pressure gradient and so could lead to a barrier jet as seen in 0253 GMT 30 Dec 2000. In contrast, for situations with balanced synoptic flow aligned with the gap as in 0347 GMT 04 Jan 2001 the gap flow does not result from the classic mechanism of ageostrophic acceleration but rather of air coasting through the gap on its own momentum. The flow in such situations is already in or near synoptic balance upon leaving the gap. Thus, it continues to follow a normal trajectory around the cyclone or anticyclone responsible as seen in 0347 GMT 04 Jan 2001. Thus, merger of gap flows with the offshore synoptic flow requires either that the offshore isobars roughly parallel the coast with lower pressure offshore or that the synoptic scale flow is aligned through the gap. In either situation the phenomenon is expected to last for as long as synoptic conditions persist (i.e. hours to days).

2.6 Synoptic Fronts

Synoptic-scale fronts are often readily apparent on SAR imagery, typically as a sharp change in backscatter intensity. This change can approach a zero order discontinuity as seen in 1819 GMT 16 Feb 2001, 0557 GMT 02 Feb 2000, and 0528 GMT 17 Nov 2000.

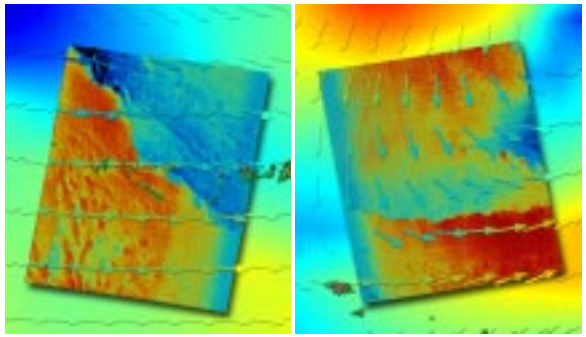

1819 GMT 16 Feb 2001 0557 GMT 02 Feb 2000

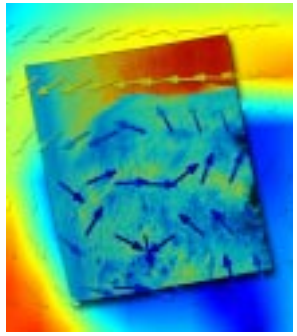

0528 GMT 17 Nov 2000

Some examples (1819 GMT 16 Feb 2001, 0557 GMT 02 Feb 2000) are lobed, suggesting cold fronts with their gravity-current structure (Houze 1993). In contrast, warm or occluded fronts such as 0528 GMT 17 Nov 2000 are often smooth. A thorough synoptic climatology is needed to determine if this characteristic provides a reliable means of frontal typing. Frontal orientation as seen on SAR images can also provide insight into frontal type, particularly when SAR is used synergistically with numerical model analyses. The analysis provides a first guess at the wind and thermal fields allowing more confident interpretation of the SAR image. The SAR image in turn provides more detailed and accurate depiction of frontal location, intensity, and structure than is possible with a large-scale numerical model analysis.

Synoptic-scale fronts often exhibit a very sharp, nearly zero order, discontinuity in wind speed and direction (Miller et al. 1996). SAR backscatter responds to both wind direction and wind speed so fronts are particularly likely to produce detectable signatures. The wind direction dependence can be computed and removed as was done with the images in this document. The current method is incomplete however as it assumes a smooth wind direction field well resolved by a large-scale numerical model analysis or by a remote sensor of equivalent horizontal resolution (e.g. a scatterometer). Because frontal discontinuities in wind direction often occur over horizontal distances of less than a kilometer, they are neither smooth nor well resolved on this scale. Thus, the contribution of the frontal shift in wind direction to the backscatter discontinuity remains largely intact.

The air temperature difference across a front can also contribute to its SAR signature. Given broadly equal sea surface temperatures (not always a good assumption), the atmospheric surface layer will be more stable for warm air than for cold. The resulting stability gradient across fronts leads to a gradient in turbulence intensity, surface stress, roughness, and SAR backscatter with the greatest backscatter under the cold air. Wind speed variations are however greater than the stability induced variations in surface stress, so this is most often a secondary effect particularly at high wind speeds.

Frontal signatures in SAR imagery take on two general forms, lobed and smooth. Lobed fronts such as those in 1819 GMT 16 Feb 2001 and 0557 GMT 02 Feb 2000 closely resemble the fine-scale structure of gravity currents (Houze 1993), suggesting that these are cold fronts. Indeed, both of the examples presented here occurred in synoptic settings suggesting advection of a cold air mass around the west or south side of a synoptic-scale cyclone. These two images present an interesting contrast, with 1819 GMT 16 Feb 2001 having strong winds behind and perpendicular to the front and 0557 GMT 02 Feb 2000 strong winds ahead of and parallel to the front. The latter image may thus be of a cold front in the process of becoming stationary.

Fronts may also exhibit mesoscale wave and cusp patterns as do the warm/occluded front in 0528 GMT 17 Nov 2000 and the cold front east of the low in 0459 GMT 31 Oct 1999. The latter image shows a family of these features with those on the southern part of the front being open waves and further north being more fully wrapped. This phenomenon is discussed in subsection 2.8. Gravity wave signatures similar to those described in subsection 2.3 are also frequently observed in association with fronts. These signatures are typically seen immediately to the cool side of fronts and can occur even in the absence of terrain. 0529 GMT 24 Oct 2000 is a typical example with the gravity waves lying just north of the surface front.

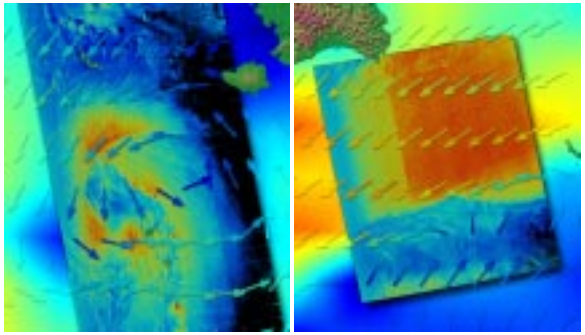

0459 GMT 31 Oct 1999 0529 GMT 24 Oct 2000

The primary surface feature of a synoptic-scale front is the quasi-discontinuity of wind, temperature, and humidity where the frontal surface intersects the ground. As seen in figure 14 of Miller et al. (1996), wind direction is generally the most discontinuous with a near zero-order jump at the front. In contrast temperature falls off exponentially on the cold side of a front, beginning with a precipitous decrease and continuing with a more gradual decline. This pattern results from the frontogenesis process. Shear and stretching act to concentrate gradients of both wind and temperature in frontal zones. As the wind concentrates its own gradient the process becomes increasingly effective, driving the gradients towards a discontinuity. Mixing, both laterally across the surface front and vertically through the overlying frontal inversion, act to limit the intensity of the front itself and spread the gradients into a broader frontal zone. This process is more effective for temperature than for momentum, perhaps because pressure effects act both to accelerate the mean flow and to reduce the turbulent flux of momentum.

Because of this self-organizing nature, fronts are remarkably persistent. The wind pattern in particular may last for days after cessation of the external frontogenetic forcing. Because of the temperature and stability gradients across fronts, surface fluxes generally act to reduce the thermodynamic gradient at a greater rate.

The gravity waves are typically seen to the cool side of fronts in SAR imagery because the frontal inversion provides a ducting layer. Weaker stability above and below the frontal zone traps the gravity waves within the inversion (Uccellini and Koch 1987). Geostrophic adjustment tends to generate gravity waves with lengths of 50 to 500 km, larger than those seen in a typical SAR frontal image. In contrast, shear (thermal wind) across the frontal zone generates gravity waves with scales of a few kilometers, matching the SAR observations. Moreover, the SAR signatures of gravity waves are generally aligned perpendicular to the thermal wind (i.e. nearly perpendicular to the front) as required by this forcing mechanism. Thus, the wave signatures seen in 0529 GMT 24 Oct 2000 are probably the result of shear-generated gravity waves. The signatures are apparent only when the wave duct (i.e. frontal inversion) is close enough to the surface for the wave-induced wind perturbations to affect the surface stress (Winstead et al. 2001). Thus, while the SAR signatures of frontal zone gravity waves are most common near the surface front, the waves themselves may be more widespread.

References

Houze, Robert A., 1993: Cloud Dynamics, Academic Press, San Diego California, 573 pp.

Miller, L. Jay, Margaret A. LeMone, William Blumen, Robert L. Grossman, Nimal Gamage, Robert J. Zamora, 1996: The Low-Level Structure and Evolution of a Dry Arctic Front over the Central United States. Part I: Mesoscale Observations. Monthly Weather Review: Vol. 124, No. 8, pp. 1648-1675.

Uccellini, Louis W., Steven E. Koch, 1987: The Synoptic Setting and Possible Energy Sources for Mesoscale Wave Disturbances. Monthly Weather Review: Vol. 115, No. 3, pp. 721-729.

Winstead, N. S., T. Sikora, and D. R. Thompson, P. D. Maurad, 2002: Direct Influence of Gravity Waves on Surface-layer Stress during a Cold Air Outbreak as shown by Synthetic Aperture Radar: Monthly Weather Review, Vol. 130, pp. 2764-2776.

2.7 Synoptic Lows

Mature extratropical cyclones are often readily apparent in SAR imagery. Younger systems with the warm or occluded front just beginning to wrap around the low appear as a bend in the westward end of the pre warm-frontal jet (i.e. the cold conveyor belt,

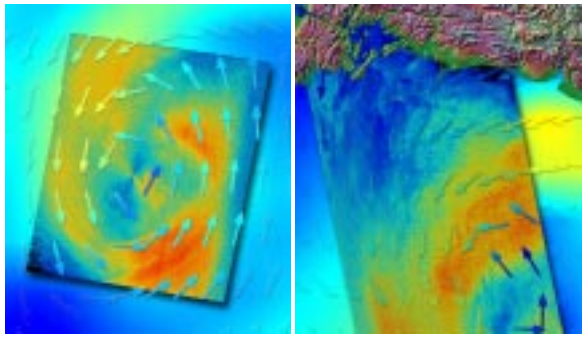

1819 GMT 06 Dec 2000 0318 GMT 05 Jan 2001

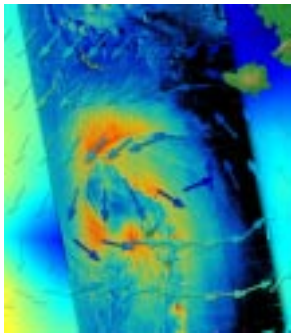

0459 GMT 31 Oct 1999

Carlson 1980) as shown in 0528 GMT 17 Nov 2000 and discussed in subsection 2.6. This section discusses more fully occluded cyclones in which the fronts have wrapped entirely around the storm center. Such storms can show an "eye" as in 1819 GMT 06 Dec 2000, 0318 GMT 05 Jan 2001 and 0459 GMT 31 Oct 1999.

0459 GMT 31 Oct 1999 shows an occluding system with the low center still near the occlusion point. There is a well defined "eye" with surface-level jets wrapping around it. These jets appear to have sharp (approximately zero order) inner edges. In the 0459 GMT 31 Oct 1999 case the jets meet at an angle at a point northeast of the low center. This arrangement suggests that the air moving up the eastern side of the cyclone is warmer than that wrapping around the north and west and is, therefore, riding up over it. This configuration is the classic T-bone frontal pattern with a warm conveyor belt overrunning a cold conveyor belt (Carlson 1980, Neiman and Shapiro 1993). Note that the global model does not position the low correctly in this case.

A more fully occluded system is shown in 1819 GMT 06 Dec 2000. In this system the tip of the occluded front has wrapped back on itself forming a seclusion (Kuo et al. 1992). The model fields capture the wind shift and jet associated with this occluded front as well as those associated with the warm and cold fronts. The triple point of the occlusion lies 20 degrees longitude east of the seclusion in the model fields. The model fields also show that the wind band around the secluded "eye" is an extension of the jet north of the occluded front which is itself an extension of the cold conveyor belt northeast of the warm front. A number of features of this image are less easily explained. Why, for example, are there two wind maxima on opposite sides of the vortex? Likewise, why is there such a sharp inner edge to the wind maximum circling the "eye"? Is the inner edge of the wind maximum sharp just because it is a frontal surface bounding the cold conveyor belt? Could the stability difference across the front matter? Does the SAR sensitivity to wind direction play a roll in highlighting this windshift line? Could vortex Rossby waves and their momentum flux convergence explain these two features? SAR imagery shows new features of vortex structure - but what do they mean and how do we forecast them? Some of this will become clear in the discussion below, but other aspects will require further research.

A land-falling system is shown in 0318 GMT 05 Jan 2001. Again there is a low-wind "eye" with fairly sharply defined inner edge. The "eye-wall" is much sharper in SAR than in the model output, but an "eye" exists in both. The frontal patterns are much less clear in this land-falling storm than they were for open sea systems such as 1819 GMT 06 Dec 2000 and 0459 GMT 31 Oct 1999. Is the "eye" a remnant of the wrapping of once much more prominent fronts?

Figure 2-6a presents a schematic isotherm/streamline analysis for an occluding system with low center still near the occlusion point. Occluding systems exhibit several consistent surface features. A cold front typically trails southwards from just east of the low, with a warm conveyor belt (Carlson 1980) flowing northward ahead of the front. A warm front extends eastward from just north of the low with a cold conveyor belt (Carlson 1980) flowing westward ahead of the front. The occlusion point marks the intersection of these two fronts. The warm conveyor belt overruns the warm front east of the occlusion point, thus lifting away from the surface to cross over the cold conveyor belt. This feature is captured well in 0459 GMT 31 Oct 1999. The occluded front itself is a westward extension of the warm front. This extension results from differential temperature advection as the cold conveyor belt wraps around the low (Kuo et al. 1992, Neiman and Shapiro 1993, Read et al. 1994). Thus, the occluded front is embedded within air that was earlier located within the baroclinic zone ahead of the low center, not air that was previously in proximity to the warm and cold fronts. Models of the occlusion pro-

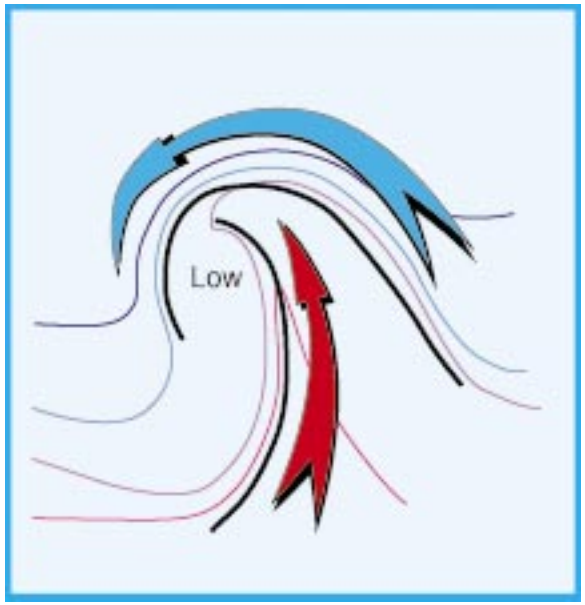

Figure 2-6a. A synoptic scale cyclone just beginning the occlusion process, adapted from figure 21 of Neiman and Shapiro (1993). Isotherms are shown in color (red as warm and blue as cool) and fronts are shown in black. The warm conveyor belt is shown as a red arrow and the cold conveyor belt as a blue arrow.

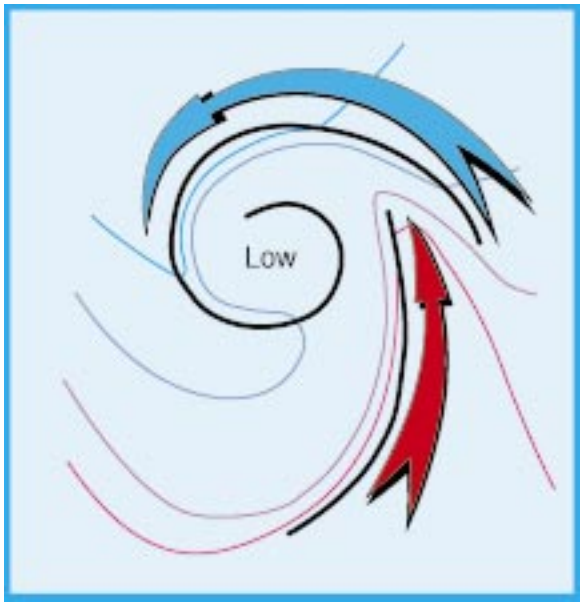

Figure 2-6b. A synoptic scale cyclone completing the seclusion process, adapted from figure 21 of Neiman and Shapiro (1993). Isotherms are shown in color (red as warm and blue as cool) and fronts are shown in black. The warm conveyor belt is shown as a red arrow and the cold conveyor belt as a blue arrow.

cess show that the largest thermal gradient often occurs along the occluded front, not along the warm or cold fronts. The "eye" of an occluding cyclone is bounded by the wrapping cold conveyor belt and the warm conveyor belt.

Figure 2-6b shows the isotherm/streamline analysis for a more fully occluded system. In this systemthe cold conveyor belt has wrapped completely around the low, forming a seclusion (Kuo et al. 1992, Neiman and Shapiro 1993, Read et al. 1994). As the cyclone matures to this stage the occlusion point moves well away from the secluded "eye" as seen in 1819 GMT 06 Dec 2000. Thus, the cold front and warm conveyor belt lie well to the east of the low. The warm front and its adjacent cold conveyor belt continue to play a central roll in the creation and maintenance of the occluded front via the differential temperature advection mechanism described above. SAR imagery reflects a number of features found in the simulations reported by Kuo et al. (1992), Neiman and Shapiro (1993), and Read et al. (1994). The sharp backscatter contrast along the inner part of the occluded front may reflect in part the sharpness of the simulated temperature gradient there as a large change in air/sea temperature difference across the front would greatly affect the air/sea momentum transfer. Likewise, the low backscatter "eye" reflects both the surface layer stability of the secluded pocket of warm air and its low wind speed (Neiman and Shapiro 1993).

Using the SAR depiction of the surface features of an occluding or secluded cyclone, a forecaster can deduce the presence of a number of features aloft. Perhaps the easiest to recognize is the surface layer stability gradients across fronts, with unstable air/sea temperature differences below the cold conveyor belt and behind the cold front being markedly greater than elsewhere. Kuo et al. (1992) suggest that there should also be a trough of warm air aloft (trowal), lying over the surface manifestation of the occluded front. The warm air seclusion also extends aloft (Neiman and Shapiro 1993), reaching perhaps 500 mb and increasing in horizontal dimension with height. In a fully secluded system, this pool of warm air may be completely cut off from the trowal. Thus, a fully secluded cyclone will have a warm core in the lower half of the troposphere, caused by differential advection rather than subsidence or diabatic processes (Kuo et al. 1992).

The physical mechanism for the occlusion process described above differs somewhat from the classic Norwegian model. Instead of the cold front overtaking the warm front, the cold conveyor belt acts to extend the warm front back into the cold airmass (Kuo et al. 1992). As the cold conveyor belt moves westward past the point where the warm and cold fronts meet, it brings with it air colder than that found behind the cold front. This happens via a difference in sign of temperature advection across the wind shift line (i.e. the south edge of the cold conveyor belt). The resulting horizontal gradient in temperature advection extends the warm front westward as an occluded front. The seclusion of relatively warm air at low levels results when the more rapidly moving cold conveyor belt wraps around the low center from front to rear. Thus, the warm air in the seclusion originates in the baroclinic zone ahead of the low. Latent heat release along the bent back (occluded) front is one of the reasons the low migrates back along the occluded front, away from the junction of the warm and cold fronts (Steenburgh and Mass 1996). It is thus also responsible in part for the wrapping of the cold conveyor belt into a circle well back into the cold air.

Occluding cyclones form as a direct consequence of the maturing of a synoptic-scale baroclinic wavecyclone. Thus, their preferred environment is the east or northeast portions of long-wave troughs. The occlusion process is often associated with the partial cutting off of the supporting upper-level short wave. The occlusion process takes one or more days to complete and may be followed by a day or more in which the seclusion vortex breaks off from the occluded front and drifts with the flow (Reed et al. 1994). Terrain can be a complicating factor with alongshore coastal surges and intense winds in landfalling storms, particularly those with bent back occluded fronts. (Steenburgh and Mass 1996)

References

Carlson, Toby N., 1980: Airflow Through Midlatitude Cyclones and the Comma Cloud Pattern. Monthly Weather Review: Vol. 108, No. 10, pp. 1498-1509.

Kuo, Ying-Hwa, Richard J. Reed, Simon Low-Nam, 1992: Thermal Structure and Airflow in a Model Simulation of an Occluded Marine Cyclone. Monthly Weather Review: Vol. 120, No. 10, pp. 2280-2297.

Neiman, Paul J., M.A. Shapiro, 1993: The Life Cycle of an Extratropical Marine Cyclone. Part I: Frontal-Cyclone Evolution and Thermodynamic Air-Sea Interaction. Monthly Weather Review: Vol. 121, No. 8, pp. 2153-2176.

Reed, Richard J., Ying-Hwa Kuo, Simon Low-Nam, 1994: An Adiabatic Simulation of the ERICA IOP 4 Storm: An Example of Quasi-Ideal Frontal Cyclone Development. Monthly Weather Review: Vol. 122, No. 12, pp. 2688-2708.

Steenburgh, W. James, Clifford F. Mass, 1996: Interaction of an Intense Extratropical Cyclone with Coastal Orography. Monthly Weather Review: Vol. 124, No. 7, pp. 1329-1352.

2.8 Mesoscale Lows along Fronts

A variety of mesoscale waves have been observed along surface fronts. Line echo wave patterns (LEWP) have been associated with severe weather along cold fronts (Johns and Doswell 1992), while other waves of similar scale have been observed along occluded fronts (Liu et al. 1997). These waves typically initiate in the form of a wave and cusp in the surface front as seen in 0528 GMT 17 Nov 2000 and 0429 GMT 05 Feb 2000. Subsequent development may be into distinct frontal vortices as in 0506 GMT 08 Feb 2001, possibly associated with frontal breaks as in narrow cold frontal rain bands (Parsons and Hobbs 1983). The spacing of mesoscale frontal waves can range from less than 20 km as seen in 0429 GMT 05 Feb 2000 and 0506 GMT 08 Feb 2001 to around 200 km as seen in 0528 GMT 17 Nov 2000. Frontal vortices can form on warm fronts as in 0528 GMT 17 Nov 2000 and 0429 GMT 05 Feb 2000, on cold fronts as in 0506 GMT 08 Feb 2001, and even along the wrapping fronts of synoptic scale seclu-

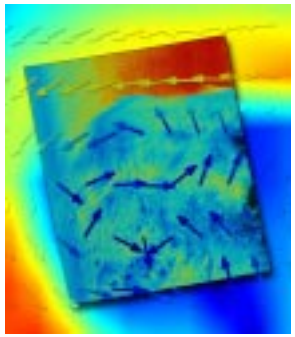

0528 GMT 17 Nov 2000

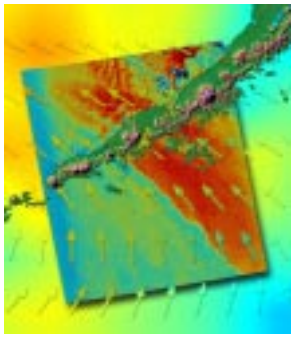

0429 GMT 05 Feb 2000

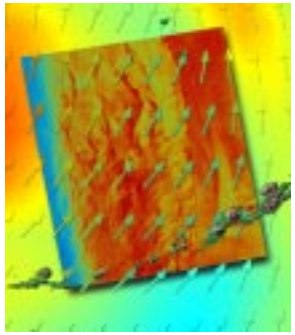

0506 GMT 08 Feb 2001

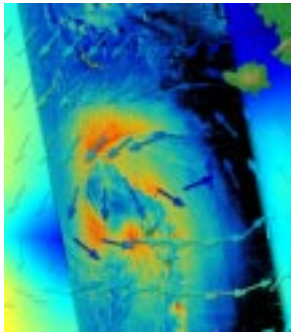

0459 GMT 31 Oct 1999

sions as in 0459 GMT 31 Oct 1999. Because of the small scale of the phenomena depicted, these SAR images often do a better job of capturing the wind field than does the superimposed large-scale analysis.

The SAR signatures of mesoscale frontal waves have many similarities across this broad range of scales. The SAR image of a wave-bearing front usually includes a sharp across-front gradient in backscatter, reflecting in most cases a sharp frontal discontinuity in the along-front wind component as in 0528 GMT 17 Nov 2000, 0429 GMT 05 Feb 2000, and 0506 GMT 08 Feb 2001. The first stage of frontal wave formation is a sinusoidal perturbation of the frontal position. Such waves soon begin to cusp as seen in the westernmost wave in 0528 GMT 17 Nov 2000 and all of the waves in 0429 GMT 05 Feb 2000. As these waves mature they break, weakening the frontal gradient as in the easternmost wave in 0528 GMT 17 Nov 2000. This weakening breaks the front into segments, one tangent to each side of the resulting mesoscale vortex as in 0506 GMT 08 Feb 2001. In some cases (e.g. 0506 GMT 08 Feb 2001), the SAR image shows a backscatter maximum in the mesoscale vortex, suggesting locally enhanced winds.

The life cycle of a mesoscale frontal wave can thus be thought of in three stages (Figure 2-7): the incipient stage in which a frontal instability creates a sinusoidal wave, a growing stage in which the wave forms a cusp, and a breaking stage in which the resulting frontal vortex creates a break in the surface front. The key surface features are the sharp cross-front gradient in wind speed, the perturbation of the frontal shape over mesoscale distances, and the creation of possibly intense vortices on the meso- and sub-mesoscale. The vortex cores in 0506 GMT 08 Feb 2001, for example, are only 1 to 2 km across yet have SAR-estimated winds of 25 m/s. The vertical structure of these frontal vortices is not well understood. Some conjectures can however be made from the dynamics of their formation as described below.

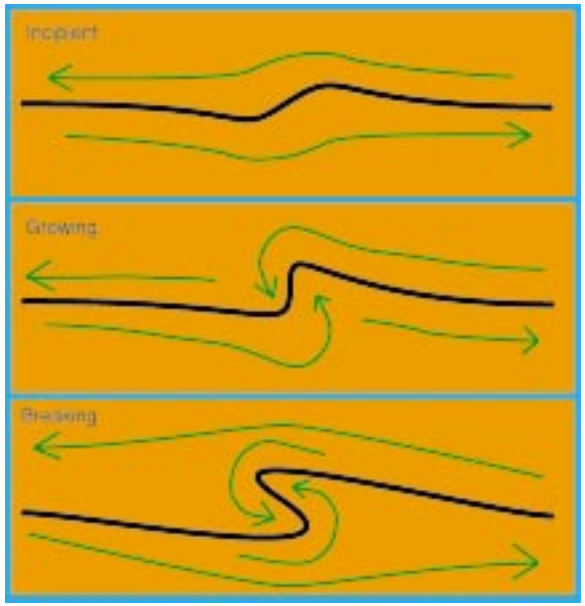

Figure 2-7. The three stages of the life cycle of a mesoscale frontal wave are depicted schematically. The frontal boundary is shown in black and the streamlines in green.

Explanations for frontal wave formation are many and varied although the along-front component of shear is thought to play a role in many cases (Parsons and Hobbs 1983). The variety of environments in which mesoscale frontal waves form and the range of scales at which they occur suggest that more than one of these mechanisms may be at work depending on the circumstances. The details remain sketchy as retrieval of the evolving three-dimensional wind and temperature fields from observations is difficult and modeling of a full synoptic weather system at the required horizontal resolution is computationally intensive. Larger mesoscale waves are probably due to baroclinic instability (Bond and Shapiro 1991) as are their synoptic scale counterparts. If so, these waves would grow in environments with strong thermal wind, i.e. vertical shear across the sloping frontal surface. In such cases the frontal wave may well tilt back over the cold air as it does with synoptic scale baroclinic waves. For smaller mesoscale frontal waves, a form of barotropic instability involving the wrapping up of a vortex sheet (Wakimoto and Wilson 1989) is probably responsible. Vertical stretching by either frontal circulations or the convection it triggers can intensify such vortices (Wakimoto and Wilson 1989) and ensure their vertical orientation. If this stretching is sufficient, waterspout/landspout type phenomena may result (Wakimoto and Wilson 1989, Golden 1974).

As seen above, shear, either horizontally or vertically across the front, plays the central role in formation of frontal waves and vortices. In contrast, terrain is not thought to be required for the triggering or intensification of frontal vortices although it is responsible for several other forms of mesoscale vortices (e.g. section 2.1). Stability requirements have received limited attention in the literature, although they can be expected to be relevant as both baroclinic instability and convective stretching of barotropic vortices are more successful in less stable environments. Low stability also acts to minimize the vortex radius for baroclinic waves by decreasing the Rossby radius of deformation (Bond and Shapiro 1991).

While the life cycle of mesoscale frontal waves is reasonably well understood, their lifespan is a matter of conjecture because most observations over water have been snapshots from aircraft penetrations or airborne weather radar. Dimensional analysis suggests that the development time of an individual frontal wave is at least as great as the distance between crests divided by wind difference across the front. The relevant wind difference would be the thermal wind for larger scale baroclinic vortices and the horizontal shear for smaller scale barotropic vortices. For the examples presented in this section this timescale ranges from 10 minutes to 5 hours. Thus, the full lifespan of a frontal wave/vortex should be on the order of one hour to a day or so. Mesocale waves would continue to reform along the front until the waves mixed out the baroclinic zone (as occurs when synoptic scale lows occlude and die) or until the shear and frontogenesis decrease (for smaller scale lows).

References

Bond, Nicholas A., Melvyn A. Shapiro, 1991: Polar Lows over the Gulf of Alaska in Conditions of Reverse Shear. Monthly Weather Review: Vol. 119, No. 2, pp. 551–572.

Golden, Joseph H., 1974: Scale-Interaction Implications for the Waterspout Life Cycle. II. Journal of Applied Meteorology: Vol. 13, No. 6, pp. 693–709.

Johns, Robert H., Charles A. Doswell III, 1992: Severe Local Storms Forecasting. Weather and Forecasting: Vol. 7, No. 4, pp. 588-612.

Liu, Ching-Hwang, Roger M. Wakimoto, Frank Roux, 1997: Observations of Mesoscale Circulations within Extratropical Cyclones over the North Atlantic Ocean during ERICA. Monthly Weather Review: Vol. 125, No. 3, pp. 341-364.

Parsons, David B., Peter V. Hobbs, 1983: The Mesoscale and Microscale Structure and Organization of Clouds and Precipitation in Midlatitude Cyclones. XI: Comparisons between Observational and Theoretical Aspects of Rainbands. Journal of the Atmospheric Sciences: Vol. 40, No. 10, pp. 2377-2398.

Wakimoto, Roger M., James W. Wilson, 1989: Non-supercell Tornadoes. Monthly Weather Review: Vol. 117, No. 6, pp. 1113–1140.

2.9 Mesoscale Lows within Cold Air Outbreaks

Mesoscale lows can also form within air masses well poleward of the primary synoptic scale fronts. These polar mesoscale cyclones result from at least three mechanisms and are known by several names including polar low, arctic instability low, and comma cloud. One of the most common forms occurs when cold air moves out from the ice edge over relatively warmer water as seen in 0502 GMT 09 Apr 2000 and 1821 GMT 16 Jan 2001. While the overall circulation can be 100 to 200 miles in diameter, the core of intense winds typically spans only a quarter of that distance. Polar mesoscale cyclones can form singly as in 0502 GMT 09 Apr 2000 and 1821 GMT 16 Jan 2001, in unconnected groups, or even in a linked series spaced a diameter or two apart along a distinct wind shear line (Sikora et al. 2000).

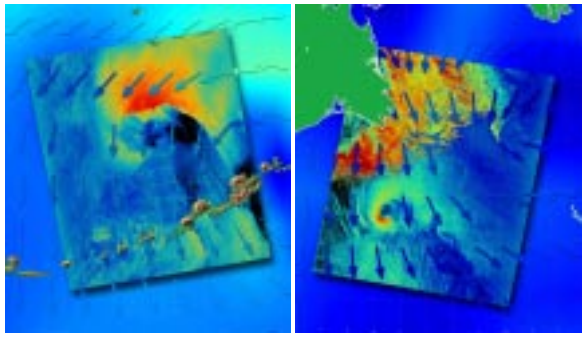

0502 GMT 09 Apr 2000 1821 GMT 16 Jan 2001

The SAR signature of a polar mesoscale cyclone is quite distinctive, consisting of one or more bands of high backscatter spiraling in towards a common center. These bands of higher wind speed often wrap around a calmer eye in the more intense or fully developed cases as in 0502 GMT 09 Apr 2000 and 1821 GMT 16 Jan 2001. The eye may be entirely absent in younger or less well-developed systems. Because the mesoscale cyclone drifts with the flow, the surface wind field is often highly asymmetric with more intense winds on the side where the cyclone's circulation reinforces the synoptic flow and weaker wind on the side where the two are in opposition. Good examples of this asymmetry and its orientation relative to the synoptic scale wind direction can be seen both in 0502 GMT 09 Apr 2000 and 1821 GMT 16 Jan 2001. Both the spiral bands and eye wall often have very sharp wind shear lines on their inner edges wherein wind speed and/or wind direction exhibit a near discontinuity. The overall structure of the surface wind field is thus reminiscent of that in a hurricane as noted by Businger and Baik (1991). The intensity rarely if ever exceeds the hurricane threshold however (Reed 1992). While the spiral bands of a polar mesoscale cyclone also resemble the fronts in the synoptic scale cyclones presented in section 2.7 they are not necessarily baroclinic boundaries between airmasses. Nonetheless both phenomena share a number of features including the tendency for small-scale shear instability along the wind shear line as seen in 1821 GMT 16 Jan 2001, a phenomena discussed in section 2.8.

Because polar mesoscale cyclones are a low-level phenomenon, most of their salient features are captured by the SAR imagery. These surface features include a central eye with low wind speeds with a partial or complete eye wall having winds markedly stronger than synoptic background flow on at least one side. The sharp inner edge of the eye wall often originates with the wrapping of the outer (spiral) wind shear lines around the cyclone center. Moist convection is often a key element in polar mesoscale cyclones and may be organized and enhanced by convergence along the spiral wind shear lines. The overall structure of many polar mesoscale cyclones is essentially barotropic with a warm core in the lower troposphere, so the wind pattern decays aloft with little change in form. Both the circulation and convection may extend into the mid or upper troposphere (Douglas et al. 1991).

While the subject remains controversial, it is becoming apparent that there are at least three types of polar mesoscale cyclones, each corresponding to a particular forcing mechanism and synoptic setting (Businger and Read 1989). The first mechanism is baroclinic instability along a shallow frontal zone paralleling the ice edge. The resulting polar mesoscale cyclones are sometimes said to be of the arctic-front

type (Businger and Read 1989). A second mechanism involves convective feedback, reminiscent of that in a hurricane. Because of the need for convective instability this form often involves strong surface fluxes of heat and moisture and/or the existence of a region of cold air aloft. Thus, this form of polar mesoscale cyclone typically occurs where flow off the ice results in large air-sea temperature differences (Businger and Baik 1991). The favored synoptic setting also includes a cold low aloft (Businger and Baik 1991). The latter feature has led some authors to call this the cold-low type (Businger and Read 1989). The name is somewhat misleading because polar mesoscale cyclones of this type generally develop a warm core in the lower to mid troposphere (Rasmussen 1981). Because of their structure and forcing, these systems are comparable in a dynamical sense to hurricanes (Businger and Baik 1991). The third mechanism involves deep baroclinic instability associated with a shortwave or jet-streak located well poleward of preexisting frontal boundaries (Read and Blier 1986). Surface pressure falls and enhanced convective instability caused by positive vorticity advection aloft are key factors in the subsequent development of a convective comma cloud and a surface circulation (Read and Blier 1986). In some cases differential advection by the surface circulation eventually leads to the development of a baroclinic front along the comma cloud (Read and Blier 1986). Given the complexities of real-world synoptic settings hybrids of all of these types exist (Businger and Read 1989).

Because there are at least three different mechanisms for their formation, polar mesoscale cyclones develop in a variety of synoptic settings. The ice edge is the dominant terrain feature. Surface flow is usually off the ice for the cold-low type and along the ice edge for the arctic-front type (Businger and Read 1989). The thermal wind may oppose the surface flow, resulting in what are called reverse shear storms wherein the cloud comma and associated wind shear line bow into rather than with the synoptic scale low-level flow (Bond and Shapiro 1991). Winds aloft also vary between cyclone types, often featuring a cold-core cyclone for the cold-low type and a jet-streak or shortwave for the comma-cloud type. Because of the role of moist convection in most polar mesoscale cyclones the low to mid troposphere is generally unstable in their vicinity, either because of enhanced surface fluxes (cold-low and arctic-front types) or because of ascending motion aloft (comma-cloud type).

Forecasting polar low initiation presents particular challenges both because of their small scale and because they may form spontaneously in regions devoid of surface or upper air observations. Moreover, they are often obscured in visible and infrared satellite imagery by an overlying cloud deck. Water vapor imagery may allow detection and tracking of the small-scale jet-streaks or shortwaves responsible for comma-cloud type polar mesoscale cyclones. Because of their weaker link to upper-level features, the more spontaneous cold-low and arctic-front type polar mesoscale cyclones are not as likely to show up in water vapor imagery. Likewise, because of their initially shallow depth, these types may not be obvious on infrared imagery during their formative stages, making them difficult to detect during the long winter nights. SAR imagery may be one of the few means of detecting the more spontaneous initiation of cold-low and arctic-front type polar mesoscale lows. The differing mechanisms likewise lead to different storm tracks for the various types of polar mesoscale cyclone. While the arctic-front type and the cold-low type both tend to move with the low-level flow, the comma-cloud type often moves with its parent vorticity maximum tracking the jetstream instead. The expected lifetime is highly variable but is often on the order of a day.

References

Bond, Nicholas A., M.A. Shapiro, 1991: Polar Lows over the Gulf of Alaska in Conditions of Reverse Shear. Monthly Weather Review: Vol. 119, No. 2, pp. 551–572.

Businger, Steven, Jong-Jin Baik, 1991: An Arctic Hurricane over the Bering Sea. Monthly Weather Review: Vol. 119, No. 9, pp. 2293–2322.

Businger, Steven, and Richard J. Read, 1989: Polar lows in “Polar and Arctic Lows”, Paul F. Twitchell, Erik A. Rasmussen, and Kenneth L. Davidson, Editors, Deepak Publishers, pp. 3-46.

Douglas, Michael W., L.S. Fedor, M.A. Shapiro, 1991: Polar Low Structure over the Northern Gulf of Alaska Based on Research Aircraft Observations. Monthly Weather Review: Vol. 119, No. 1, pp. 32–54.

Rasmussen, Erik, 1981: An Investigation of a Polar Low with a Spiral Cloud Structure. Journal of the Atmospheric Sciences: Vol. 38, No. 8, pp. 1785–1792.

Reed, Richard J., 1992: Comments on “An Arctic Hurricane over the Bering Sea”. Monthly Weather Review: Vol. 120, No. 11, pp. 2713–2713.

Reed, Richard J., Warren Blier, 1986: A Case Study of Comma Cloud Development in the Eastern Pacific. Monthly Weather Review: Vol. 114, No. 9, pp. 1681–1695.

Sikora, T. D., K. S. Friedman, W. G. Pichel, and P. Clemente-Colón, 2000: Synthetic Aperture Radar as a Tool for Investigating Polar Mesoscale Cyclones. Weather Forecasting: Vol.15, pp. 745-758.

2.10 Convection

Most forms of convection leave distinctive signatures on SAR imagery. While thunderstorm and squall line signatures are quite common in the mid-latitudes and tropics, this section will focus on the boundary-layer rolls (LeMone 1973) and post-frontal squalls (Cooper et al. 2000) observed over Alaska's offshore waters. A typical example of roll vortices can be seen north of the Aleutians in 0441 GMT 22 Dec 1999 as long parallel lines of higher wind speed. In contrast, the wind squalls of cellular deep convection result in the larger-scale mottled patterns seen in 0252 GMT 29 Jan 2000, 0506 GMT 08 Feb 2001, and 0330 GMT 27 Nov 1999.

The roll signatures in 0441 GMT 22 Dec 1999 are typical, parallel bands of higher wind speed, each band much longer than it is wide. These bands, and the horizontal roll vortices they reflect, are most often aligned within 10 degrees of the surface wind direction as they are in this image. The boundary layer wind is also closely aligned with the surface wind direction, given the degree of vertical mixing associated with boundary-layer rolls. When boundary layer rolls break

down, they do so by becoming more cellular as seen in the western portions of this image. Often the transition can be quite gradual, as seen here, with large areas of intermediate forms.

Deep cellular convection (i.e. precipitating convective cells) produces very characteristic SAR signatures via its downdraft outflow. 0252 GMT 29 Jan 2000 is a fairly typical example with each convective cell producing a roughly circular signature 10 to 50 km across. As in this image, one side of the circle typically has a sharply defined outer edge, usually lined with an arc of higher speed wind. This is the gust front, the leading edge of the downdraft's surface outflow. The remainder of the outflow is bounded by more gradual gradients of wind speed with the side opposite the gust front being the least well defined. The vertical wind shear vector (surface to downdraft source level) is aligned through the high-wind arc of the gust front like the arrow in a bow. In 0252 GMT 29 Jan 2000 the wind and shear are aligned, coming from the southwest, so the gust front signatures point towards the northeast. 0506 GMT 08 Feb 2001 shows similar signatures for convective cells behind a cold front. The contrast between the convective signatures in the western portion of the image and uniform winds in the eastern third suggests a stability gradient. Careful examination of island wakes in the image shows that there is a corresponding wind shift between these two regions, despite the conflicting evidence of the model analysis winds. Further confirmation that the model analysis is in error can be obtained by examining the angle of the gust fronts to the analyzed winds. The misalignment suggests a thermal wind from the west-southwest, and thus warm advection, if the analyzed south-southeast winds are correct. This sign of advection seems unreasonable for a post cold frontal setting. 0330 GMT 27 Nov 1999 further illustrates the variations possible with cellular convective signatures on SAR images. While the cells have the same form as the previous two cases, their gust fronts are pushing into the wind instead of with it, so they're actually "lull fronts". This pattern means the shear opposes the low-level wind.

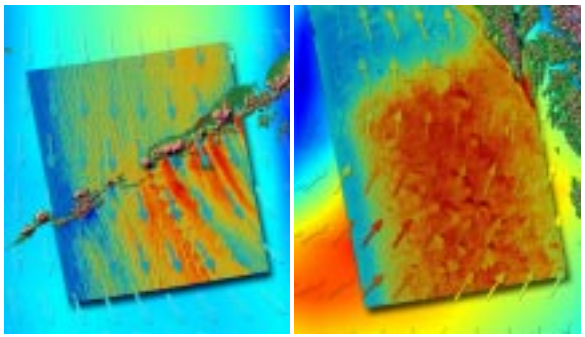

0441 GMT 22 Dec 1999 0252 GMT 29 Jan 2000

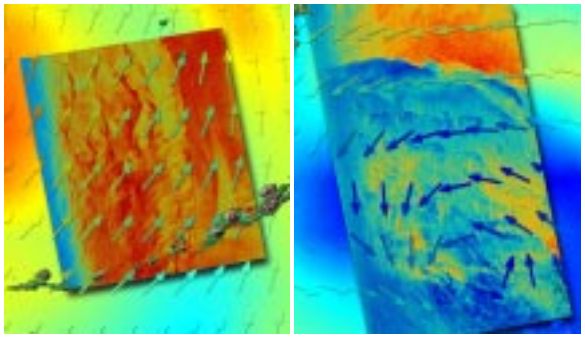

0506 GMT 08 Feb 2001 0330 GMT 27 Nov 1999

Boundary-layer rolls are a form of convection found in high-shear environments (LeMone 1973); indeed they may even draw some of their energy from the shear. In their fully developed state, rolls are two-dimensional so the cross section in figure 2-8 fully illustrates their flow. The roll downdrafts bring fast air to the surface, resulting in higher stress and the high-backscatter streaks seen in the SAR imagery. The air in these downdrafts diverges upon reaching the surface, slowing gradually due to surface drag. The meeting of these outflows causes a line of convergence midway between each pair of adjacent downdrafts, resulting in a pattern of alternating downdraft and updraft bands. The updrafts are fed by air that has been in contact with the sea surface longest and hence contain the lowest wind speeds. Clouds (if any) will be over the updrafts - and hence over the slowest winds.

Deep cellular convection (i.e. precipitating convection with three-dimensional cells) includes snow squalls (Cooper et al. 2000), rain showers, and single-cell thunderstorms. Figure 2-9a depicts the downdraft cross-section common to such storms (Wilson et al. 1984). Figure 2-9b depicts the resulting surface streamlines and isotachs. The surface features responsible for the SAR signature are the outflow from the downdraft and the gust front around the outflow. The up-shear/down-shear asymmetry of these outflows result from the downward transfer of horizontal momentum in the downdraft (Wilson et al. 1984). This wind component is superimposed on the radial outflow from the downdraft, adding to it in the down-shear direction and subtracting from it in the up-shear directions.

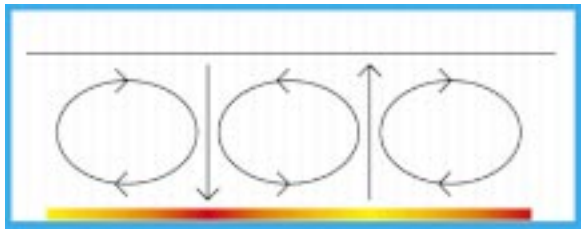

Figure 2-8. A cross section of the flow in group of boundary layer rolls. The synoptic scale wind is blowing into the figure. Thus, the arrows represent the roll-induced flow perpendicular to the mean wind direction. The surface wind speeds are fastest (red) under the roll downdrafts and slowest (yellow) under the roll updrafts. The capping inversion is depicted as a black line along the top of the rolls.

Thus, the momentum transfer results in enhanced convergence at the down-shear gust front and reduced convergence at the up-shear gust front. This difference in gust front sharpness and the asymmetry of the outflow wind pattern are both quite evident in SAR signatures of convection. Detection of such a signature thus allows the forecaster to deduce both the direction of the shear vector and the existence of a penetrative downdraft. The latter implies the existence of convection and, given the scale of these signatures, probably precipitation. Non-precipitating boundary layer convection produces similar downdraft signatures but on a smaller scale (Sikora et al. 1997). The interthermal downdrafts responsible are only 1.5 times as wide (at the surface) as the boundary layer is deep, resulting in signatures a few kilometers across for non-precipitating convection versus a few tens of kilometers across for precipitating convection.

Figure 2-9a. Cross section of flow associated with a sheared convective cloud (blue). Vertical wind shear is from left to right (i.e. the synoptic scale wind is from left to right and increasing with height). Convective downdraft is depicted by blue arrows and convective updraft is depicted by a red arrow.

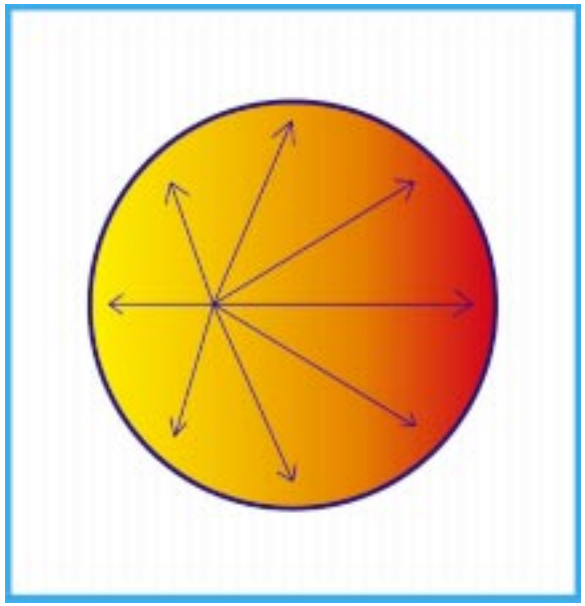

Figure 2-9b. Plan view of surface streamlines (black arrows) and wind speed (red fast, yellow slow) for the same convective squall. Gust front is shown as a solid circle bounding the squall-induced winds.

Instability (Braham and Kristovich 1996) is the key environmental requirement for all of these convective phenomena, with shear playing a more qualitative roll determining the form of convection. Terrain is generally irrelevant unless it is tall enough to disrupt the mean flow. While convection can occur with only an updraft present, SAR signatures as described above require downdrafts and their surface outflows. Thus, there must be buoyant forcing for both updrafts and downdrafts. Braham and Kristovich (1996) document these buoyancy profiles for snow squalls and discuss the concepts of updraft and downdraft convective available potential energy (CAPE). For Alaska's offshore regions, updraft buoyancy is most likely provided by sea surface fluxes of sensible and latent heat, and subsequent latent heat release. The negative buoyancy of the downdrafts results from precipitation loading, sublimation, melting, and evaporation. Radiative effects including infrared cloud-top cooling may be important in less strongly forced environments.

Neither a mean wind nor vertical wind shear is required for convection. The presence of shear does, however, have a strong influence on the pattern of convection. Strong shear confined to the lower third of the boundary layer results in rolls (Cooper et al. 2000). Deeper shear results in asymmetric squalls (Wilson et al. 1984). If there is no shear, circularly symmetric outflows result.

The lifetime of convective cells is roughly one-half to two hours, perhaps longer for rolls. The SAR signature is however more long-lived as it will persist until the wind field of the outflow has recovered to pre-convective conditions. This recovery can take from half an hour to a full day depending on the scale of the outflow with larger storms producing more long-lived outflows. The field of convection can persist much longer than the individual cells, lasting as long as the synoptic situation permits. This could be days in the case of advection of cold air over warmer water.

References

Braham Jr., Roscoe R., David A.R. Kristovich, 1996: On Calculating the Buoyancy of Cores in a Convective Boundary Layer. Journal of the Atmospheric Sciences: Vol. 53, No. 4, pp. 654-664.

Cooper, Kevin A., Mark R. Hjelmfelt, Russell G. Derickson, David A. R. Kristovich, Neil F. Laird, 2000: Numerical Simulation of Transitions in Boundary Layer Convective Structures in a Lake-Effect Snow Event. Monthly Weather Review: Vol. 128, No. 9, pp. 3283-3295.

LeMone, Margaret Anne, 1973: The Structure and Dynamics of Horizontal Roll Vortices in the Planetary Boundary Layer. Journal of the Atmospheric Sciences: Vol. 30, No. 6, pp. 1077-1091.

Sikora, Todd D., George S. Young, Hampton N. Shirer, Rick D. Chapman, 1997: Estimating Convective Atmospheric Boundary Layer Depth from Microwave Radar Imagery of the Sea Surface. Journal of Applied Meteorology: Vol. 36, No. 7, pp. 833-846.

Wilson, James W., Rita D. Roberts, Cathy Kessinger, John McCarthy, 1984: Microburst Wind Structure and Evaluation of Doppler Radar for Airport Wind Shear Detection. Journal of Applied Meteorology: Vol. 23, No. 6, pp. 898-915.

2.11 Coastal Barrier Jets

Shore-parallel low-level jets are a common feature along the southern coast of Alaska and the steep westward facing coasts as far south as Baja California. SAR captures this phenomena as a well defined band of high backscatter along the coast as seen in 0323 GMT 29 Dec 2000, 0328 GMT 15 Jan 2001, 0310 GMT 18 Feb 2000, 0306 GMT 22 Oct 2000, and 0306 GMT 04 Sep 2000. These coastal barrier jets occur in a wide variety of synoptic settings. 0323 GMT 29 Dec 2000 shows a barrier jet formed when a pre-frontal jet made landfall at a sharp angle to the coast. The pre-frontal jet dies out as it approaches the coast, to be replaced by a sharply defined along-coast jet. This barrier jet is not a continuation of the pre-frontal jet, but is instead oriented perpendicular to it. The shore-parallel direction of this coastal flow is easily deduced from the wake orientation of the offshore islands. 0310 GMT

18 Feb 2000 shows the formation of a similar coastal barrier jet in a very different synoptic setting, a synoptic-scale low approaching the coast. Another similar coastal barrier jet can be seen in 0328 GMT 15 Jan 2001, but this time forming near the intersection of the warm and cold conveyor belts of a synoptic-scale cyclone. The cold conveyor belt lies along the coast, enhanced perhaps by the barrier jet effects discussed below.

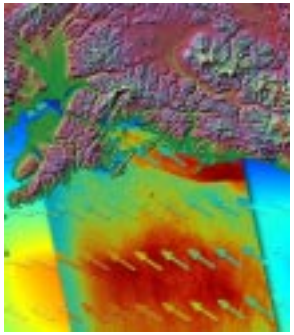

0323 GMT 29 Dec 2000

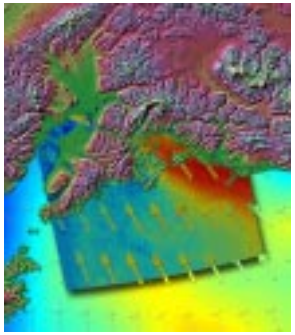

0328 GMT 15 Jan 2001

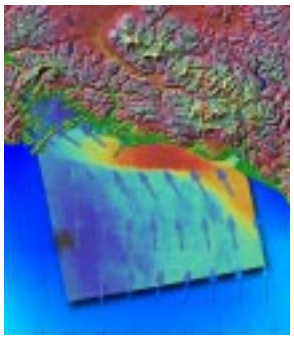

0310 GMT 18 Feb 2000

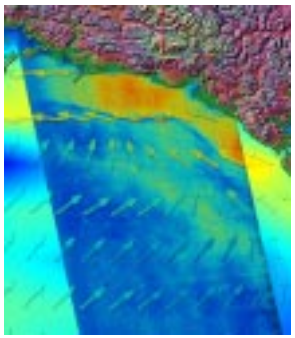

0306 GMT 22 Oct 2000

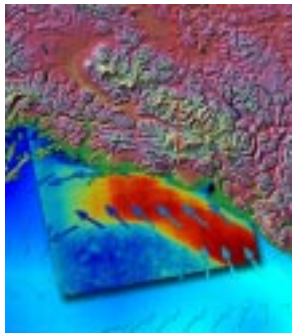

0306 GMT 04 Sep 2000

A coastal barrier jet appears in SAR imagery as a narrow band of strong winds parallel to the coast. The alignment of the wind direction with the coast can be verified using island wakes as seen in 0306 GMT 04 Sep 2000, 0306 GMT 22 Oct 2000 and 0323 GMT 29 Dec 2000. In the Alaskan region this low-level jet is typically 60 to 110 km wide. This value depends in part on the Coriolis parameter so barrier jets are wider off the western coast of the Lower 48. These barrier jets frequently exhibit a sharp offshore boundary as seen in 0306 GMT 04 Sep 2000, 0306 GMT 22 Oct 2000, 0310 GMT 18 Feb 2000, and 0323 GMT 29 Dec 2000. The wind-speed gradient may, however, be much more gradual as in 0328 GMT 15 Jan 2001. The existence of strong shear between the low-level jet and the overlying flow, and the presence of an inversion between the two, allow for the formation of trapped gravity waves as seen in 0306 GMT 04 Sep 2000. Because the shear vector often parallels the low-level flow for these jets, the waves are generally aligned perpendicular to the coast as seen here. Coastal barrier jets can also be reinforced by, or even caused by, turning exit jets as discussed in section 2.5 and seen in 0306 GMT 04 Sep 2000. Sometimes, as in parts of this case, the interaction of exit jets with the coastal barrier jet can give the latter phenomenon a sharp inshore edge.

Because the coastal barrier jet is a low-level phenomenon, its primary surface manifestation is a band of strong shore-parallel winds just offshore. This band extends offshore for about one Rossby radius of deformation (Mass and Albright 1987, Chien et al.1997), often transitioning quite abruptly to slower, more onshore, winds at its outer edge. The band of wind parallel to the shore is often associated with a mesoscale ridge of high pressure along the coastal barrier, contributing a strong offshore component to the local pressure gradient (Chien et al. 1997). This ridge is caused by a sloping inversion, with the low-level cool air being deeper against the slopes of the coastal barrier than it is out to sea (Chien et al. 1997). Shear-driven gravity waves can cause turbulence, possibly intense at times, on this capping inversion.

The key element in the creation of a coastal barrier jet is the production of a strong alongshore pressure gradient by the synoptic scale flow (Mass and Albright 1987). There are at least four synoptic scale mechanisms for creating such an alongshore component to the pressure gradient, hence the wide variety of settings in which coastal barrier jets are observed. Moving either a synoptic-scale low (Mass and Albright 1987) or a synoptic-scale high (Chien et al. 1997) across the coast can result in a purely synoptic-scale alongshore pressure gradient. Interaction of the synoptic-scale flow with the coastal terrain can also lead to a mesoscale pressure gradient along the coast. Offshore flow can cause subsidence warming and, thus, the formation of a mesoscale lee trough (Mass and Albright 1987, Chien et al. 1997, Thompson et al. 1997, and Skamarock et al. 1999). Likewise, onshore flow can be blocked by terrain (Chien et al. 1997), causing cold air to pile up along the coast, resulting in a localized ridge of high pressure (Skamarock et al. 1999). Following formation of an alongshore pressure gradient by any of these mechanisms, the air near the coast accelerates ageostrophically along the coast (Mass and Albright 1987). Coriolis forces act to turn this flow into the coast (Chien et al. 1997). If the resulting Froude number is high, the flow will surmount the coastal barrier and no barrier jet will form (Chien et al. 1997 and Thompson et al. 1997). 0343 GMT 24 Nov 2000 provides a good example of this. The convective signatures offshore demonstrate the lack of stability, and hence the high Froude number. As a result no coastal barrier jet is seen in this image. In contrast, if the offshore air is too stable to surmount the coastal barrier, the cold air in the alongshore flow piles against mountains resulting in a mesoscale pressure gradient pointing offshore. The pile up increases the inversion slope until this offshore directed pressure gradient force balances the Coriolis force of the alongshore wind component and friction balances the alongshore component of the pressure gradient force. The pre-balance stages of this process can behave as a coastally trapped Kelvin wave, that is the mass fields propagate slower

than alongshore wind (Chien et al. 1997, Skamarock et al. 1999). In contrast, the post-balance stages of a barrier jet act as a coastally trapped gravity current with the mass field propagating at about the speed of the alongshore wind (Mass and Albright 1987, Chien et al. 1997, and Thompson et al. 1997). At both stages the enhanced alongshore flow is confined to within one Rossby radius of coast (Mass and Albright 1987). Thus, the width l of a coastal barrier jet can be calculated using the formula l = c/f where c is the gravity wave speed and f is the Coriolis parameter. For a coastally trapped cold air mass (as in a barrier jet) c is $\sqrt{(g \cdot h \cdot Dq/q)}$, where h is the depth of the cold pool and Dq is the increase in potential temperature across the top of the cold pool.

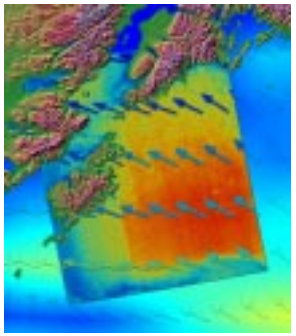

0343 GMT 24 Nov 2000

The combination of steep coastal terrain and offshore stability is the key environmental requirement for formation of a coastal barrier jet. The coastal terrain must be too high for the Coriolis turning of the ageostrophic alongshore flow to surmount given the existing static stability. Moreover, if the alongshore pressure gradient force is to arise from onshore flow of cold air, the mountains must also be too high for that flow to surmount. As described above, there are multiple mechanisms for creation of an alongshore pressure gradient so either onshore or offshore synoptic-scale flow will suffice as will locating either a synoptic-scale high or low along the coast. Little wonder coastal barrier jets are a relatively common occurrence. The resulting mesoscale wind pattern continues for as long as the alongshore pressure gradient persists (typically one or more days). The alongshore flow propagates to the point of lowest coastal pressure, but usually not beyond it (Thompson et al. 1997).

References

Chien, Fang-Ching, Clifford F. Mass, Ying-Hwa Kuo, 1997: Interaction of a Warm-Season Frontal System with the Coastal Mountains of the Western United States. Part I: Prefrontal Onshore Push, Coastal Ridging, and Alongshore Southerlies. Monthly Weather Review: Vol. 125, No. 8, pp. 1705-1729.

Mass, Clifford F., Mark D. Albright, 1987: Coastal Southerlies and Alongshore Surges of the West Coast of North America: Evidence of Mesoscale Topographically Trapped Response to Synoptic Forcing. Monthly Weather Review: Vol. 115, No. 8, pp. 1707-1738.

Skamarock, William C., Richard Rotunno, Joseph B. Klemp, 1999: Models of Coastally Trapped Disturbances. Journal of the Atmospheric Sciences: Vol. 56, No. 19, pp. 3349-3365.

Thompson, William T., Tracy Haack, James D. Doyle, Stephen D. Burk, 1997: A Nonhydrostatic Mesoscale Simulation of the 10-11 June 1994 Coastally Trapped Wind Reversal. Monthly Weather Review: Vol. 125, No. 12, pp. 3211-3230.

Section III

Inventory of Radarsat SAR Wind Fields
Bob Beal and Frank Monaldo

This section contains an inventory of 60 uniformly processed, chronologically ordered Radarsat SAR wind fields. A uniform format and time/space perspective aids the interpretation and permits easy cross-comparison among SAR wind fields from different passes. The left-hand pages present the synoptic situation surrounding each acquisition as deduced from the U.S. Navy Fleet Numerical NOGAPS forecast model perspective. The first four panels (1-4) depict the evolving surface pressure field during the ~36 hrs prior to acquisition. The next four panels (5-8) contain additional potentially relevant parameter fields: surface winds, surface wave height, surface inverse wave age (ratio of the vector wind speed to the vector wave phase velocity), which is a measure of the wave steepness of the dominant wave system, and the air-minus-sea temperature, which is a measure of the Marine Atmospheric Boundary Layer (MABL) stability. These last two parameters, both potentially important to understanding some of the error sources of SAR wind estimates, are derived from other model parameters. The model surface wind field within the highlighted region of the first 8 panels is expanded in a gnomic projection (9), centered on the SAR frame(s), with the corresponding SAR wind field overlaid. The right-hand pages (panels 10 and higher) are devoted to a higher resolution presentation of the SAR wind field estimates, in the context of both model winds and available buoy measurements. Enlargements of some of the more interesting features are included, along with direct model-versus-SAR wind estimates (in most cases), wind histograms (in some cases) and, when available and relevant, concurrent in-situ buoy wind measurements around overpass time from records available on the National Data Buoy Center (NDBC) web site. The NDBC buoys 46001, 46035, and 46066 (which came on-line in June of 2000) are all located in the open ocean, and did not always survive the most extreme storms that passed over them between October 1999 and November 2001. Nevertheless, when they were operating, the buoys often provided vital insights into the SAR/model wind measurement discrepancies.

Section III: Inventory of Radarsat SAR Wind Fields

Table of Contents

1. Surface Pressure (mb) ~ t_0-36h

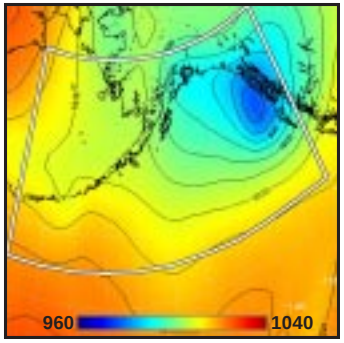

2. Surface Pressure (mb) ~ t_0-24h

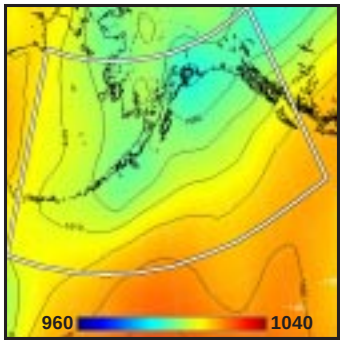

3. Surface Pressure (mb) ~ t_0-12h

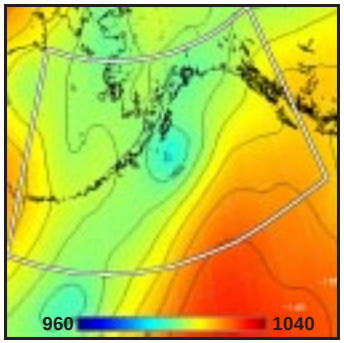

4. Surface Pressure (mb) ~ t_0

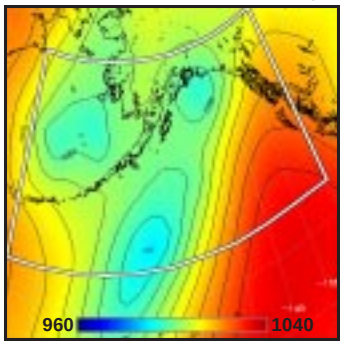

9. Enlarged Surface Wind Field ~ t_0

0000 GMT 31 Oct 1999

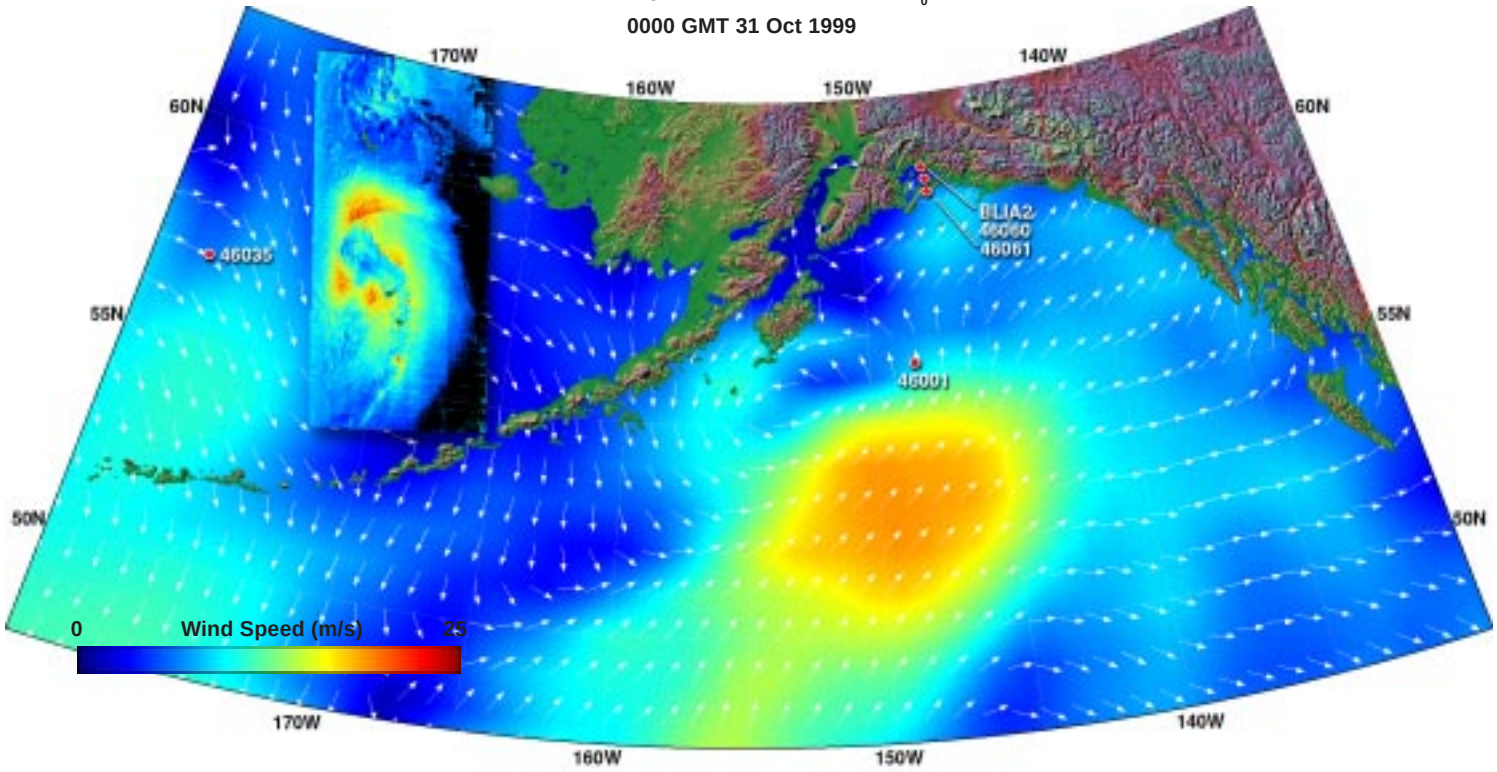

Model (this page): As a primary low pressure system in the Gulf of Alaska weakens into an elongated trough (1-4), a secondary low begins to form in the Bering Sea to the west. Model winds (5, 9) north of the Aleutians show the beginnings of a weak asymmetric circulation under the SAR. Concurrent model waves are low (6) but growing (7). The MABL is extremely unstable (8), especially on the western side of the SAR frame.

SAR (facing page): The SAR winds (10) reveal much greater and more complex variability than the model, including the classic T-bone frontal pattern with a warm conveyor belt overrunning a cold conveyor belt (11) [see section 2.7]. Maximum winds in the northwesterly arm of the storm (10, 11, 12) approach 20 m/s, more than double the model estimates. [ref. sections 2.6: synoptic fronts, 2.7: synoptic lows.]

5. Surface Wind Field (m/s) ~ t_0

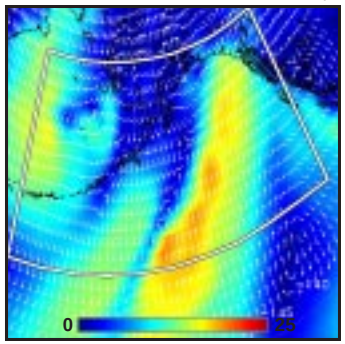

6. Surface Wave Height (m) ~ t_0

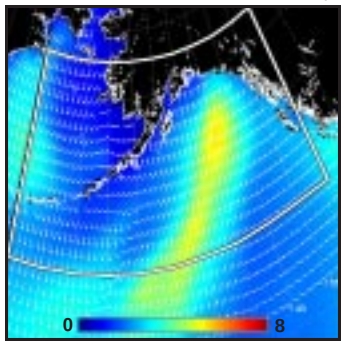

7. Inverse Wave Age (norm) ~ t_0

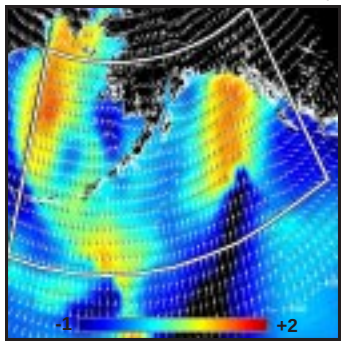

8. Air-Sea Temperature (˚C) ~ t_0

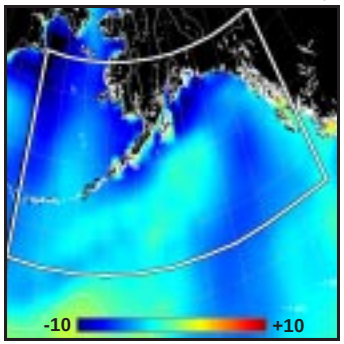

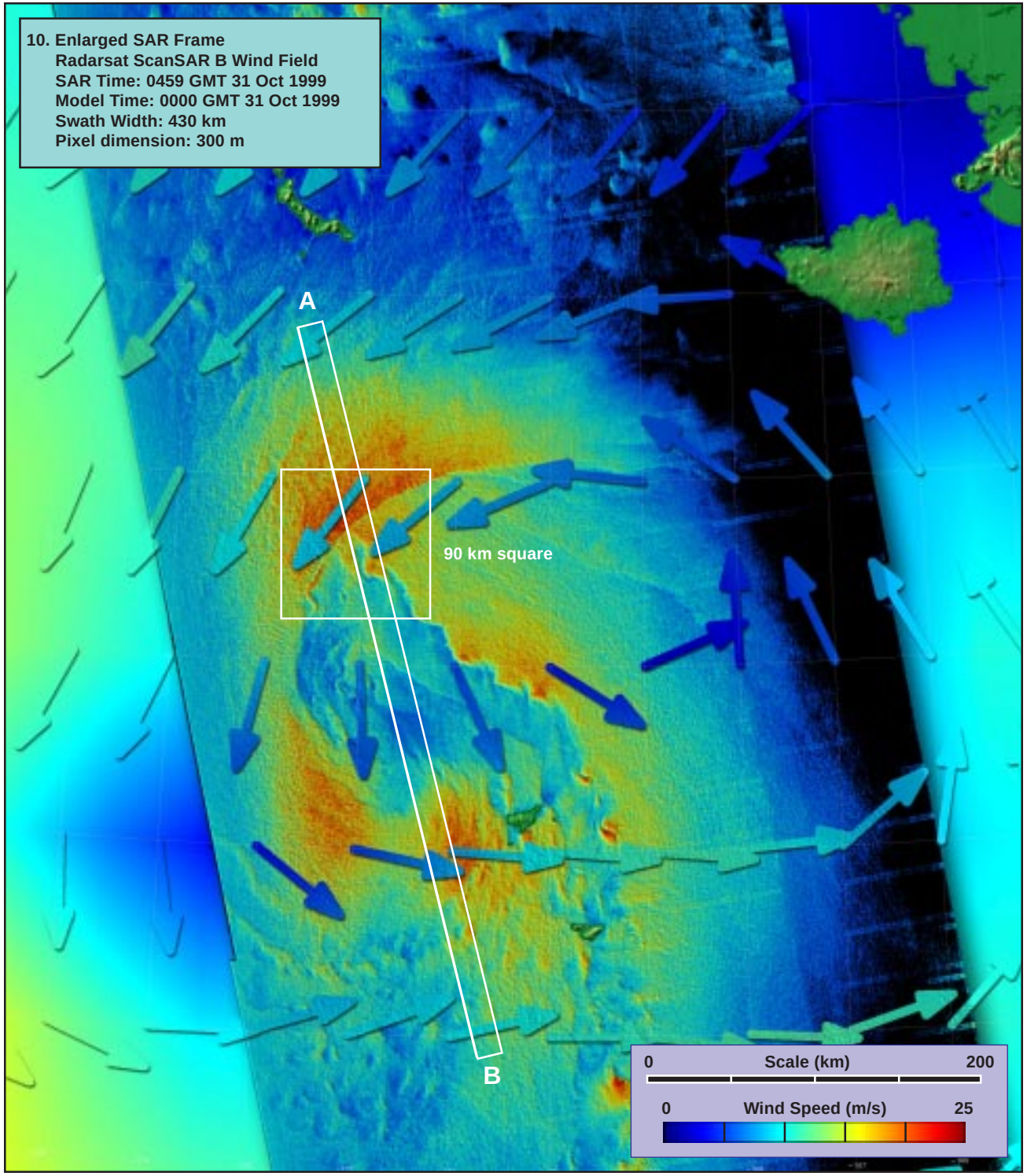

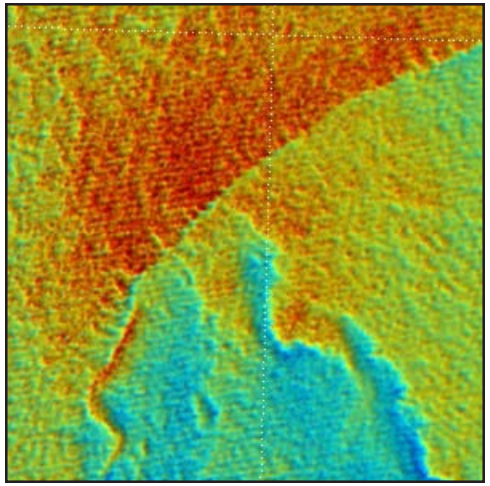

90 km square

11. Enlargement of Frontal Intersection (x 2.5)

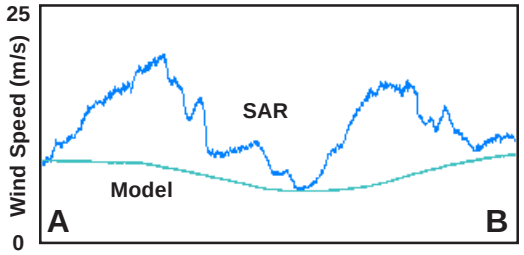

12. Model vs SAR Wind Profile along Line AB

1. Surface Pressure (mb) ~ t_0-36h

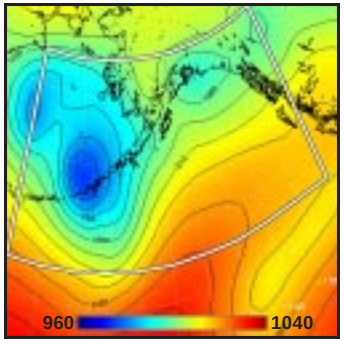

2. Surface Pressure (mb) ~ t_0-24h

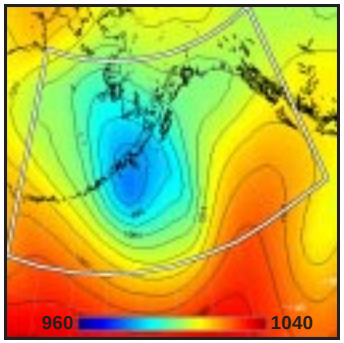

3. Surface Pressure (mb) ~ t_0-12h

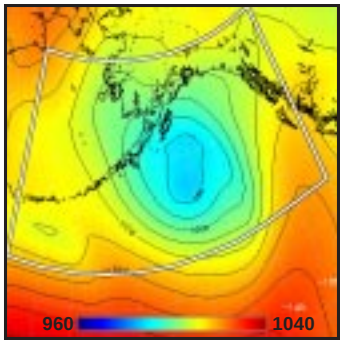

4. Surface Pressure (mb) ~ t_0

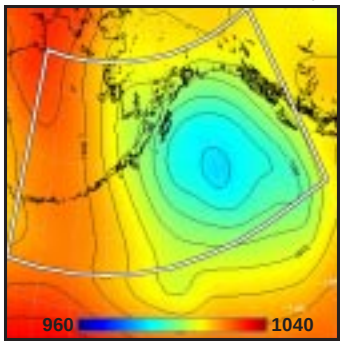

9. Enlarged Surface Wind Field ~ t_0

0000 GMT 27 Nov 1999

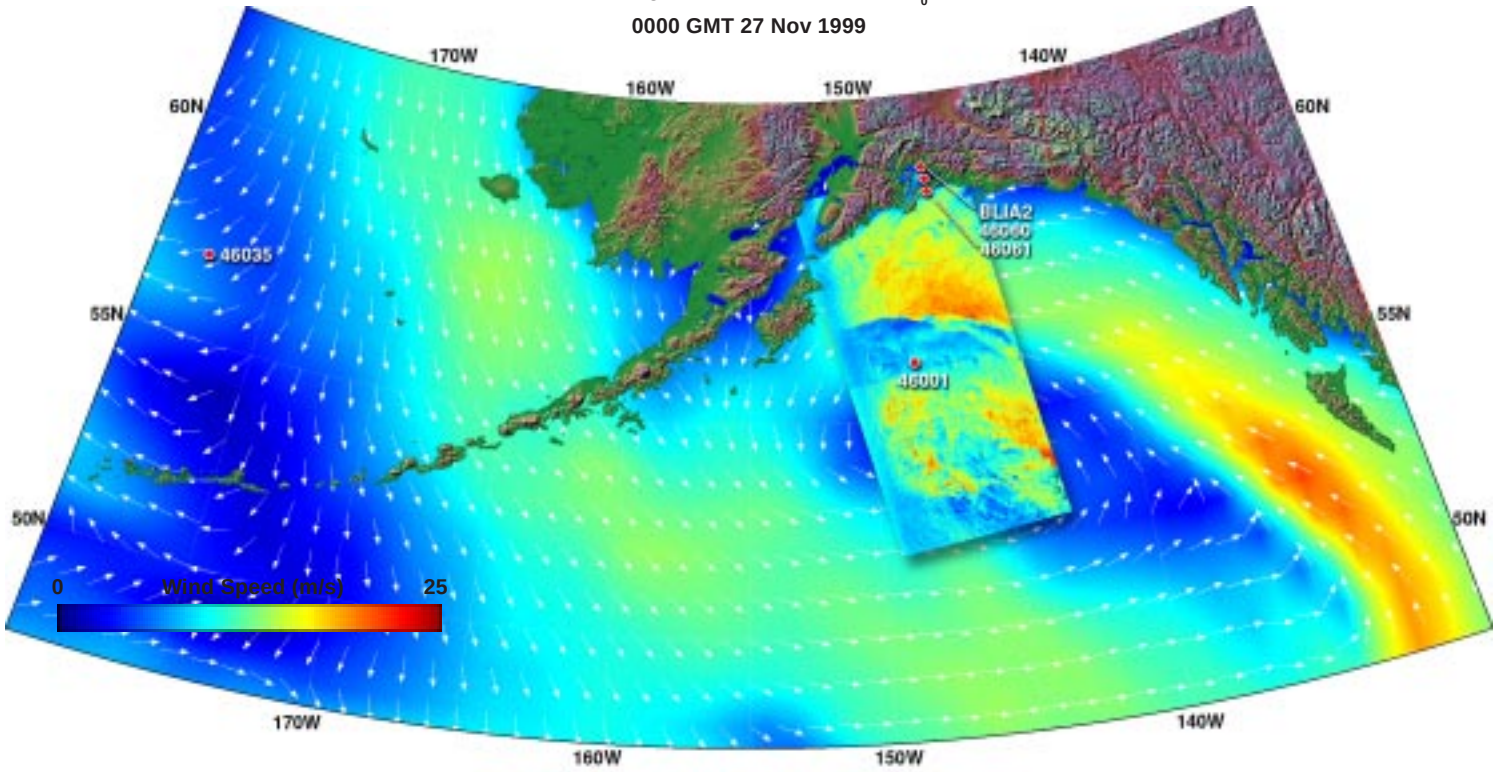

Model (this page): A massive but weakening low pressure system (1-4) drifts to the east, encompassing the entire Gulf of Alaska. Model winds (5, 9) approach 20 m/s in the eastern Gulf of Alaska, but somewhat less within the SAR frame to the north. Concurrent model waves exceed 8 m south of the SAR pass, but only about 5 m and decaying in the north (6, 7). The MABL is neutral to slightly unstable (8) within the SAR pass.

SAR (facing page): The SAR winds (10) reveal a much sharper front, and also show multiple wave and cusp patterns (11) [see section 2.6: Synoptic Fronts], with scale of about 60 km. A broad region of convective cells dominates the center of the SAR pass south of the front. Maximum SAR winds on a few of the stronger cells approach 20 m/s on scales of a few km. This variation is not at all visible in the model, where the estimated winds are less than 10 m/s over a broad region (12). [ref. section 2.10: convection.]

5. Surface Wind Field (m/s) ~ t_0

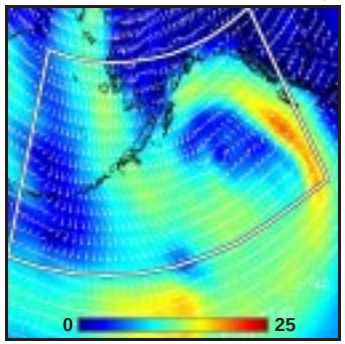

6. Surface Wave Height (m) ~ t_0

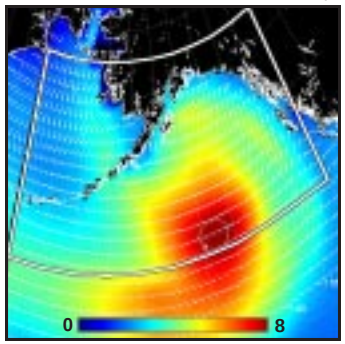

7. Inverse Wave Age (norm) ~ t_0

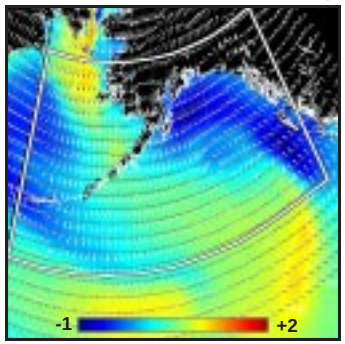

8. Air-Sea Temperature (˚C) ~ t_0

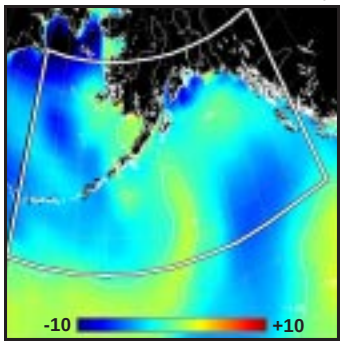

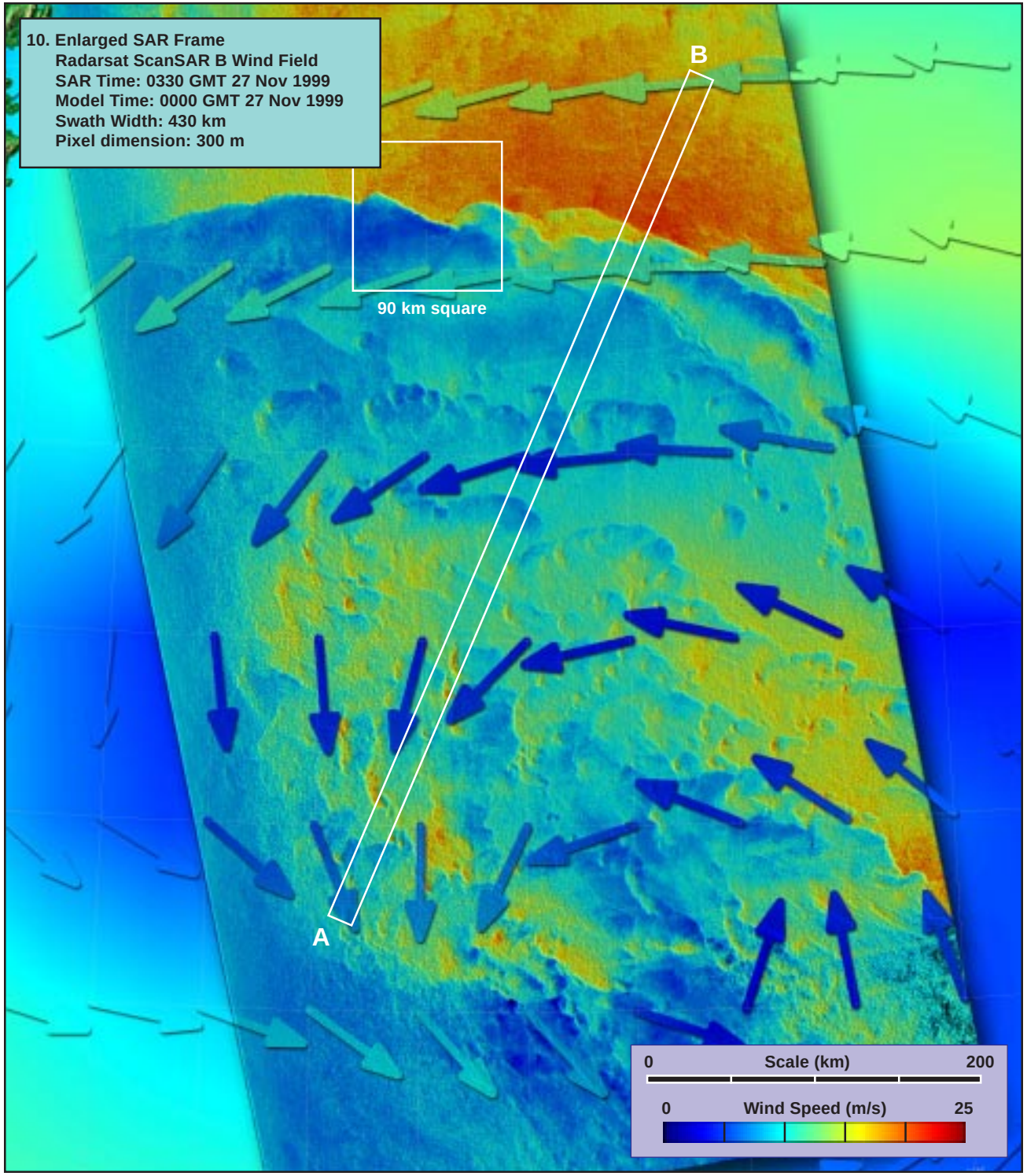

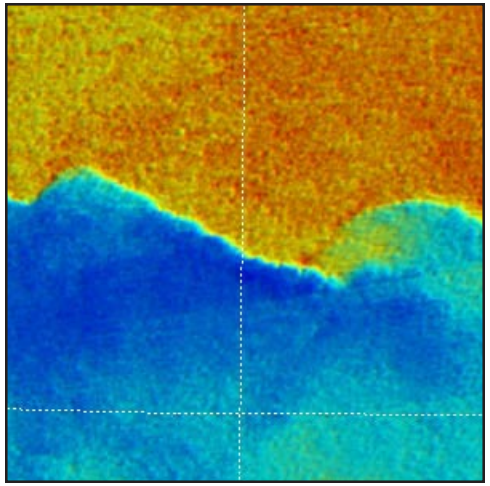

90 km square

11. Enlargement of Frontal Detail (x 2.5)

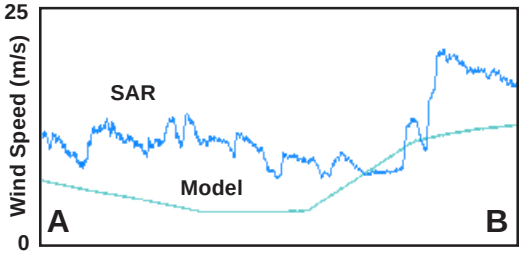

12. Model vs SAR Wind Profile along Line AB

1. Surface Pressure (mb) ~ t_0-36h

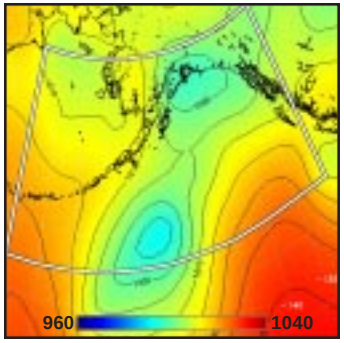

2. Surface Pressure (mb) ~ t_0-24h

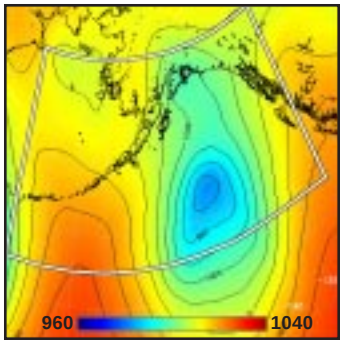

3. Surface Pressure (mb) ~ t_0-12h

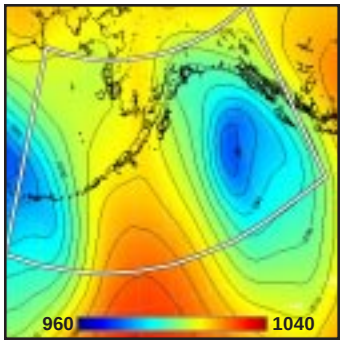

4. Surface Pressure (mb) ~ t_0

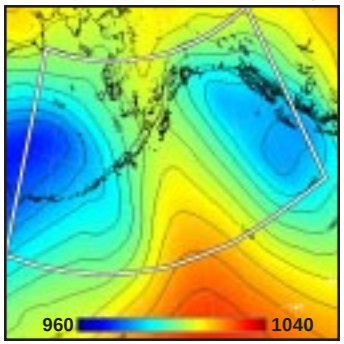

9. Enlarged Surface Wind Field ~ t_0

0000 GMT 09 Dec 1999

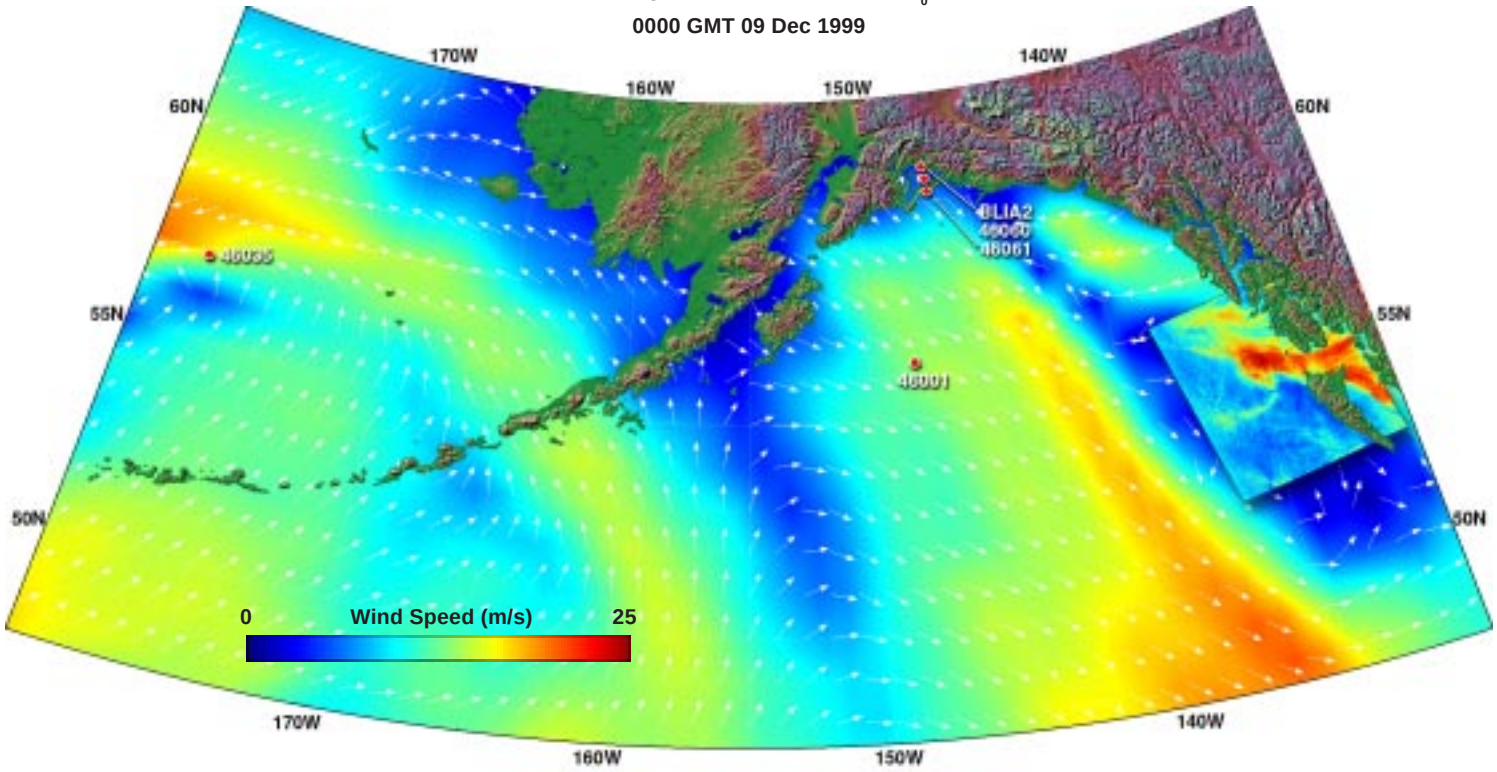

Model (this page): A low pressure system intensifies as it moves to the ENE across the southern Gulf of Alaska (1-4). Model winds near overpass time are strongest to the south and west of the storm center (5, 9), but also show a significant (20 m/s) flow from the southeast, along the coast. Concurrent model waves on the eastern edge exceed 6 m, still actively growing at overpass time (6, 7). The MABL is nearly neutral to slightly stable over the eastern sector of the storm (8).

SAR (facing page): The SAR winds show how the wind is drawn through several inland gaps to finally converge into a single strong jet that exits through the Dixon Entrance just north of the Queen Charlotte Islands (10, 11). Peak SAR winds seaward of the gap by 100 km exceed 20 m/s, while the concurrent model estimates barely reach 5 m/s (12). A family of gravity waves is embedded just upstream of the maximum winds (11). [ref. section 2.5.2: gap flow/synoptic interaction.]

5. Surface Wind Field (m/s) ~ t_0

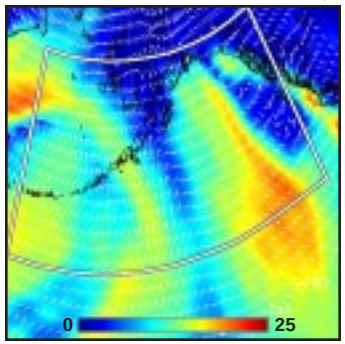

6. Surface Wave Height (m) ~ t_0

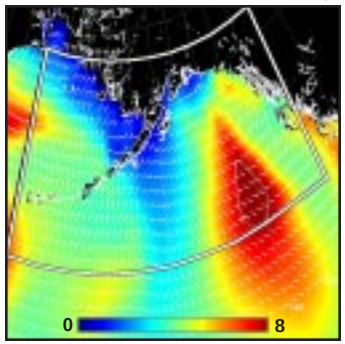

7. Inverse Wave Age (norm) ~ t_0

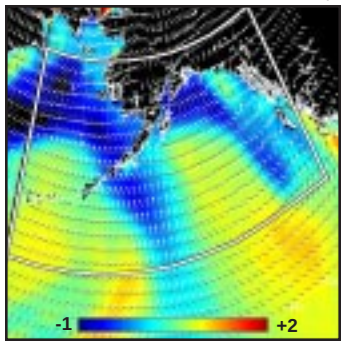

8. Air-Sea Temperature (˚C) ~ t_0

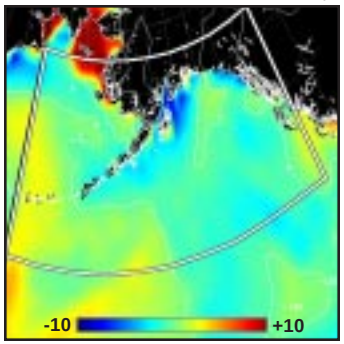

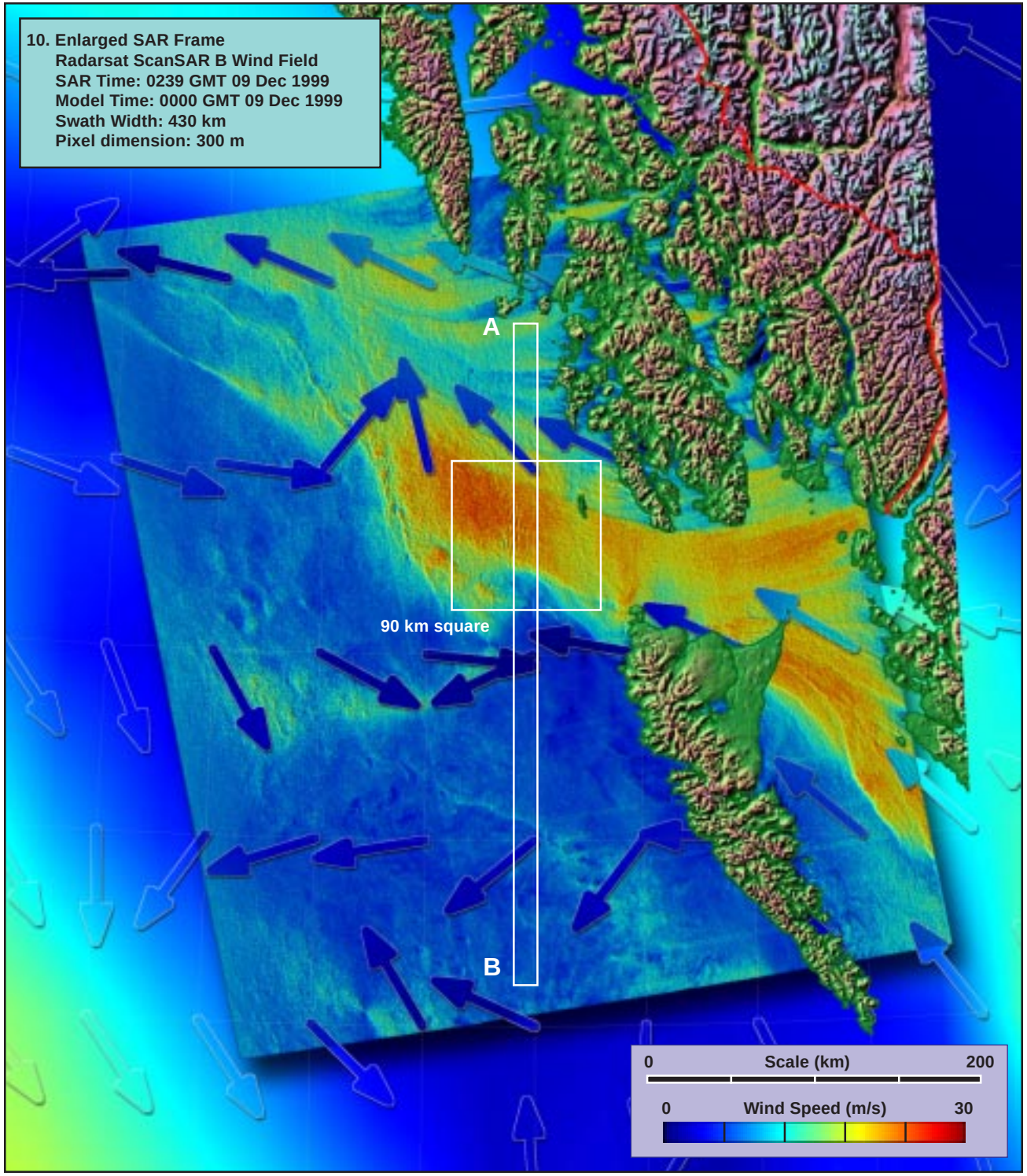

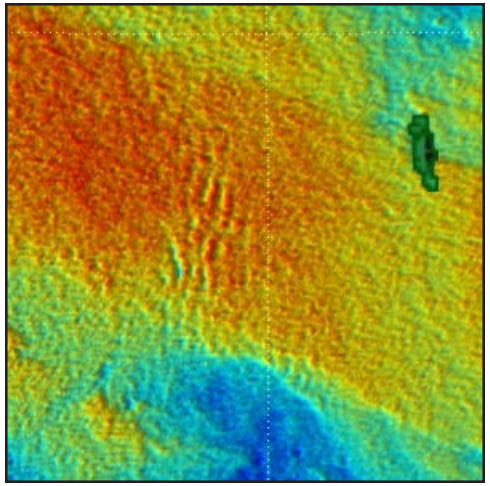

90 km square

11. Enlargement of Jet (x 2.5)

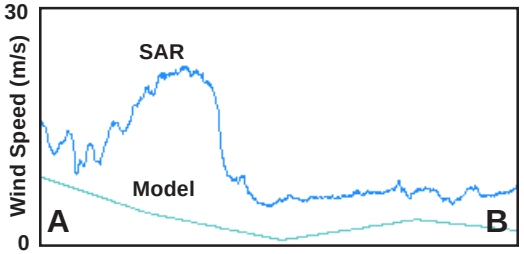

12. Model vs SAR Wind Profile along Line AB

1. Surface Pressure (mb) ~ t_0-36h

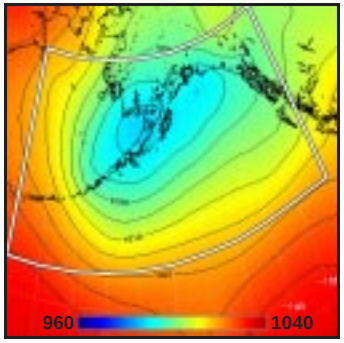

2. Surface Pressure (mb) ~ t_0-24h

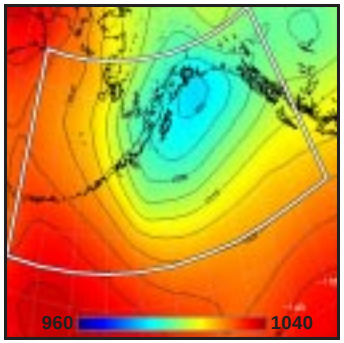

3. Surface Pressure (mb) ~ t_0-12h

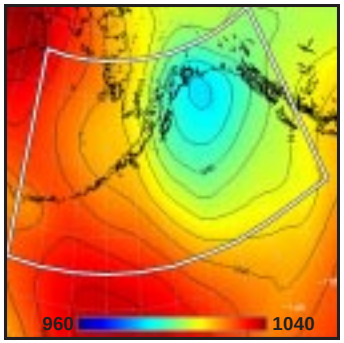

4. Surface Pressure (mb) ~ t_0

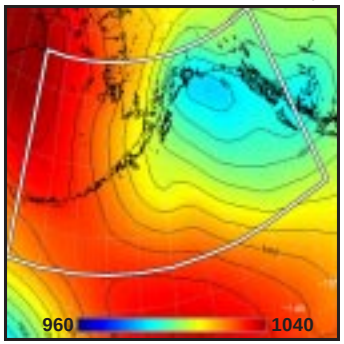

9. Enlarged Surface Wind Field ~ t_0

1200 GMT 12 Dec 1999

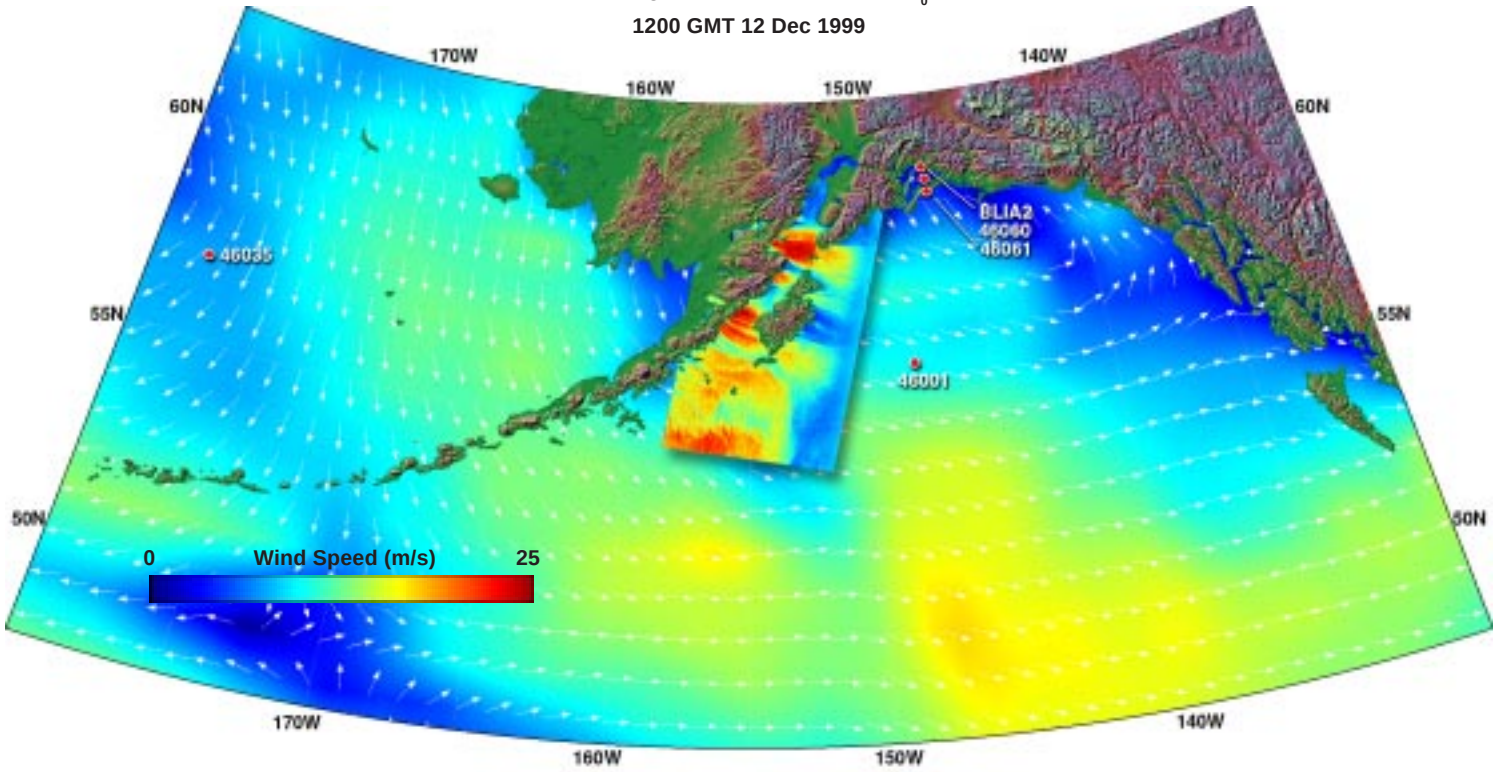

Model (this page): A weakening low pressure system travels up the Aleutian Chain (1-4), producing moderate northwesterly winds in its wake. Model winds (5, 9) are generally below 15 m/s within the SAR pass, and show no spatial structure. Concurrent model waves exceed 6 m well to the southeast of the pass, still growing (6, 7), but within the pass the waves are below 4 m and decaying. The MABL is extremely unstable (8) both upwind and within the SAR frame.

SAR (facing page): The SAR winds (10) show a rich field of topographically induced variability just downstream of the Aleutian peninsula, with maximum winds 20 to 25 m/s extending 50 to 100 km off shore, generally more than double the model estimates (11, 12). [ref. section 2.4: gap flows.]

5. Surface Wind Field (m/s) ~ t_0

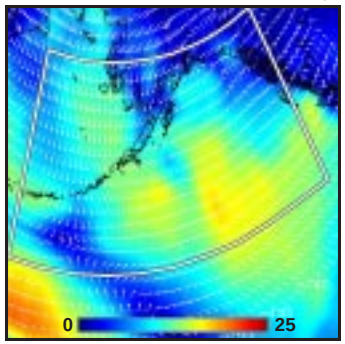

6. Surface Wave Height (m) ~ t_0

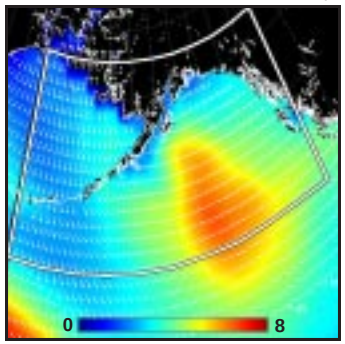

7. Inverse Wave Age (norm) ~ t_0

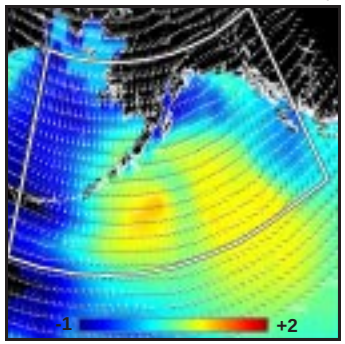

8. Air-Sea Temperature (˚C) ~ t_0

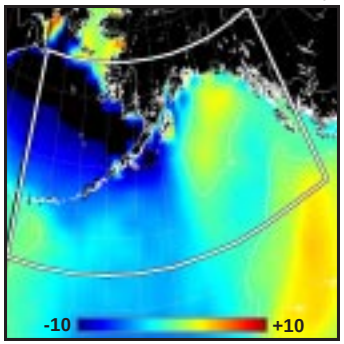

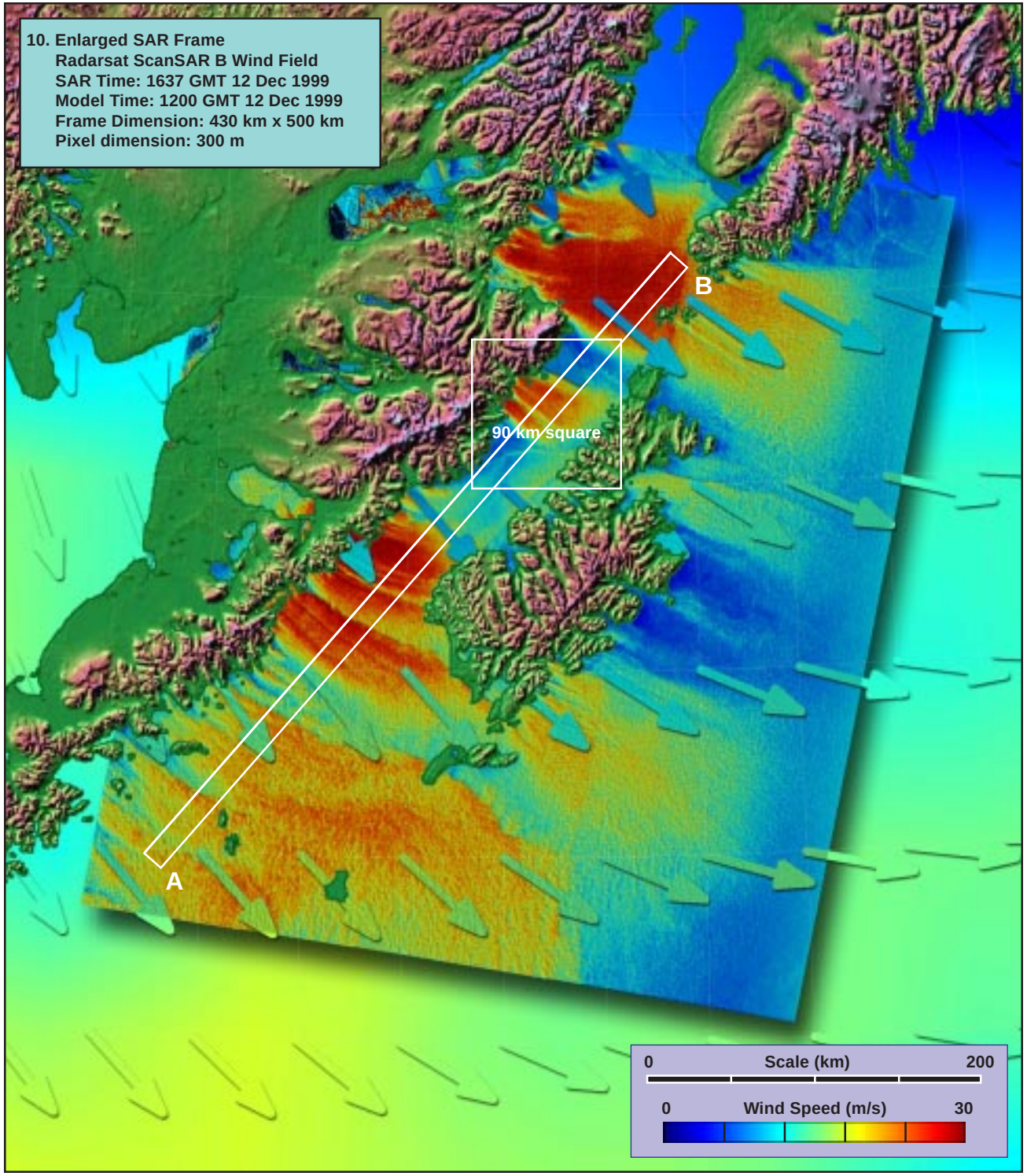

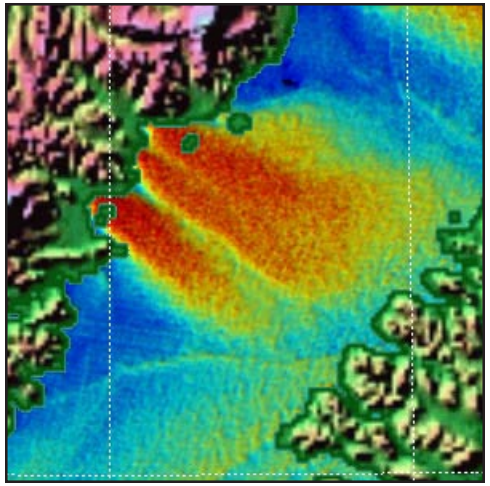

90 km square

11. Enlargement of Shadowing (x 2.5)

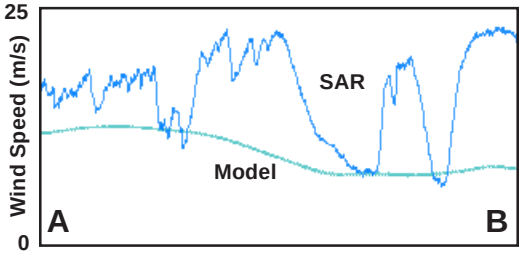

12. Model vs SAR Wind Profile along Line AB

1. Surface Pressure (mb) ~ t_0-36h

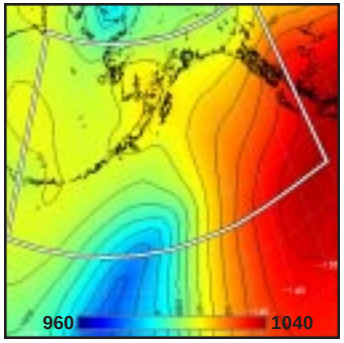

2. Surface Pressure (mb) ~ t_0-24h

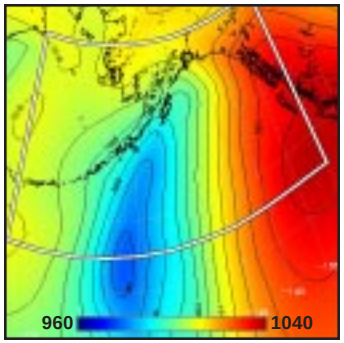

3. Surface Pressure (mb) ~ t_0-12h

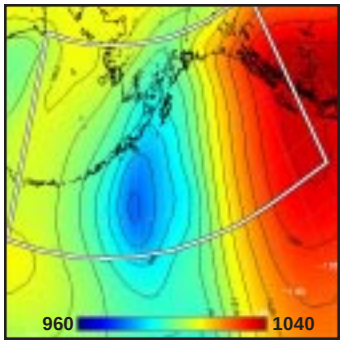

4. Surface Pressure (mb) ~ t_0

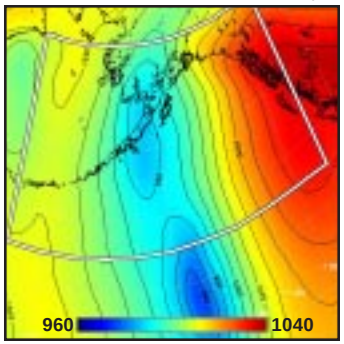

9. Enlarged Surface Wind Field ~ t_0

0000 GMT 22 Dec 1999

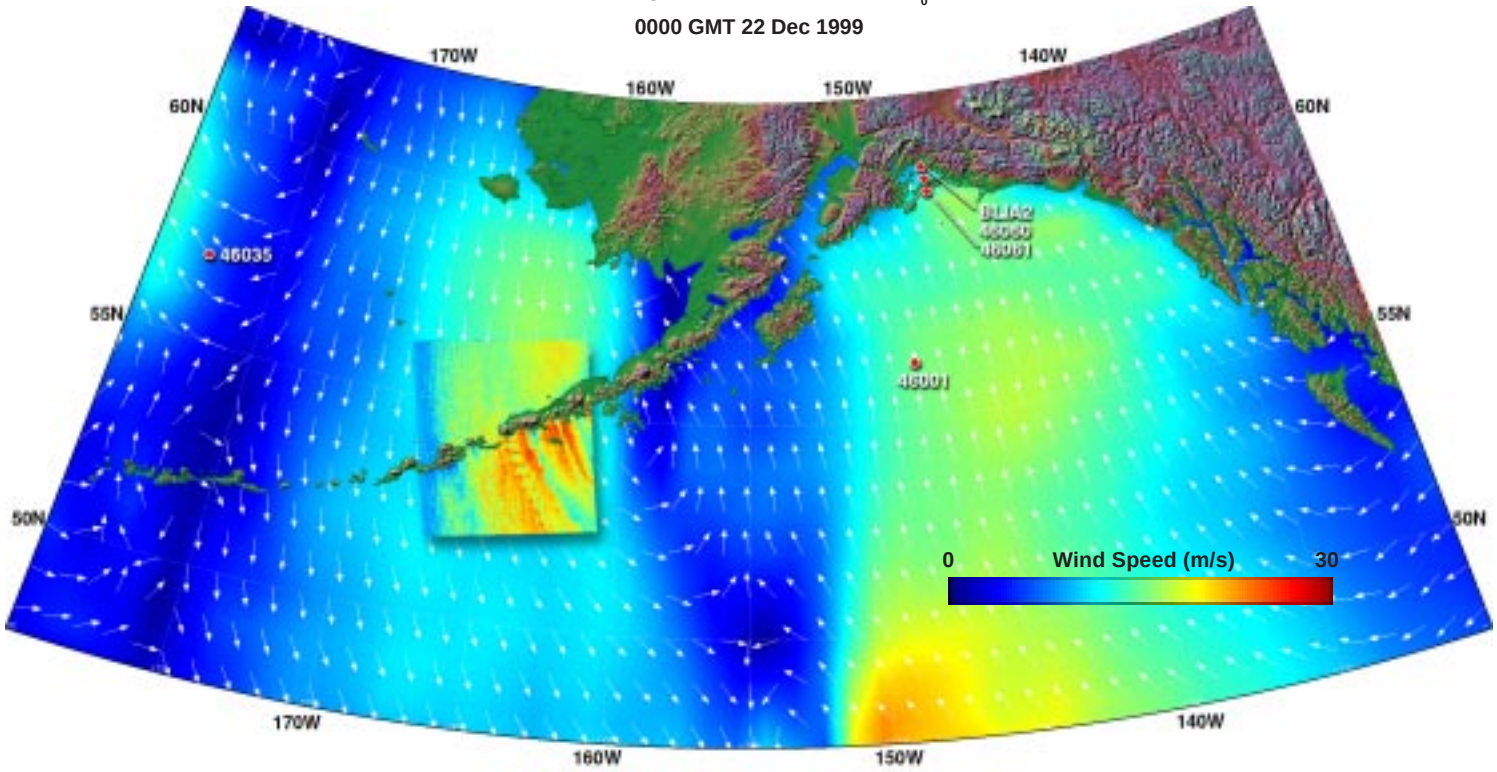

Model (this page): A weakening low pressure system bifurcates (1-4) as the northern component passes over the northern Aleutians, producing a N-S oriented trough. Model winds (5, 9) reach 15 m/s north of the Aleutians, but only about 10 m/s within the SAR frame to the south. Concurrent model waves are low but growing (6, 7). The MABL is extremely unstable (8) both upwind and within the SAR frame.

SAR (facing page): The SAR winds (10) reveal much greater and more complex variability, including a rare example of topographically induced Kármán vortex streets (11). Many of these features exhibit downwind spatial coherence of more than 300 km. There are also nice longitudinal roll vortices upwind of the islands and potential vorticity banners (wake/jets couplets) downwind of the islands. Maximum SAR winds along line AB (crosswind) exceed 25 m/s, while the model estimate (-4 hrs) is less than half that (12). Upwind and downwind histograms (13) quantify the increases in both mean and variance induced by the topographically induced turbulence. [ref. sections 2.1: island and mountain wakes, 2.10: convection.]

5. Surface Wind Field (m/s) ~ t_0

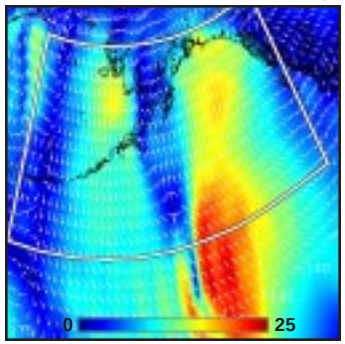

6. Surface Wave Height (m) ~ t_0

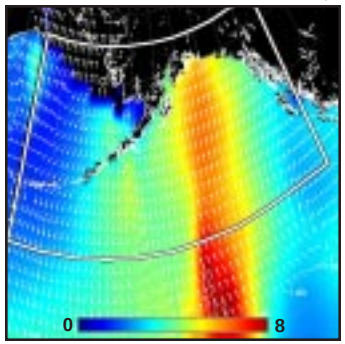

7. Inverse Wave Age (norm) ~ t_0

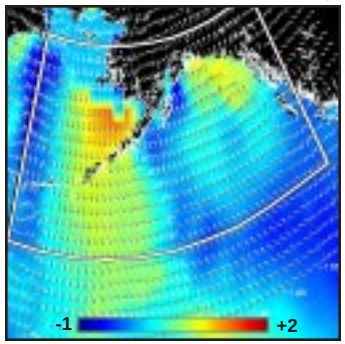

8. Air-Sea Temperature (˚C) ~ t_0

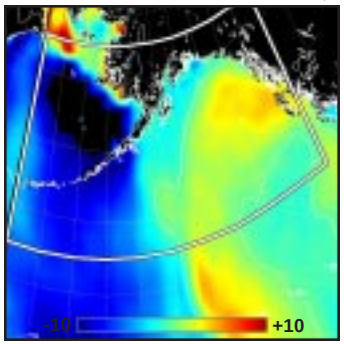

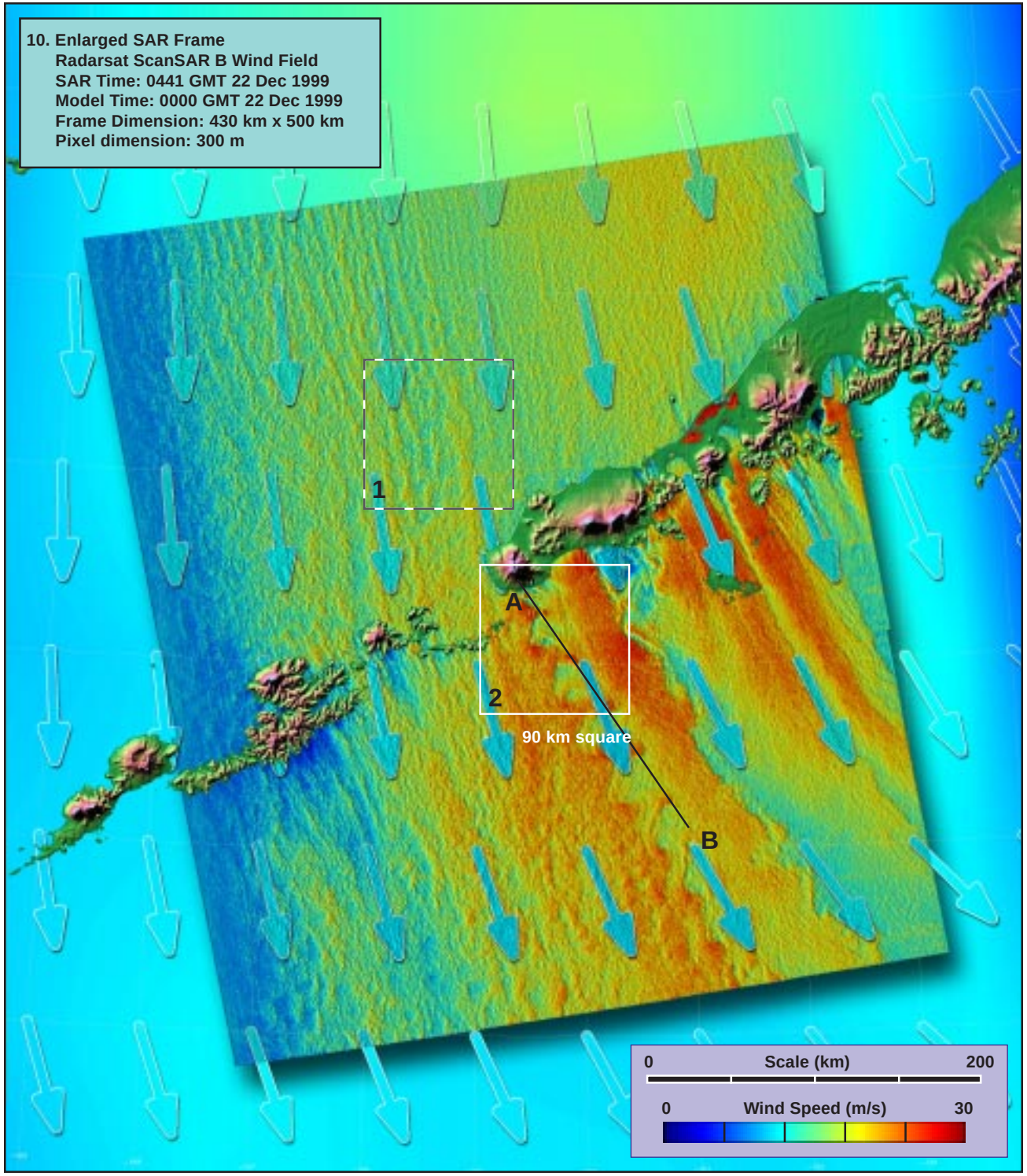

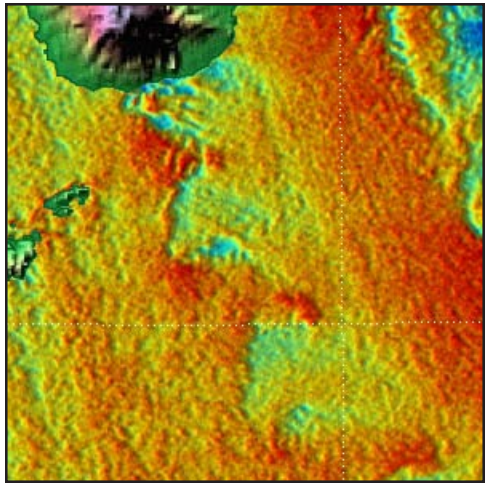

90 km square

11. Enlargement of Vortices Detail (x 2.5)

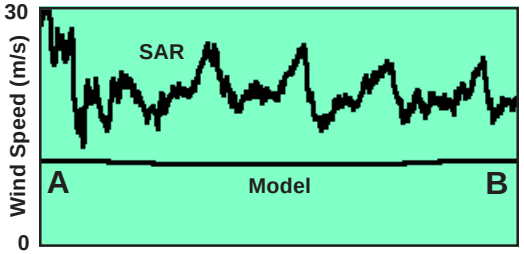

12. Model vs SAR Wind Profile along Line AB

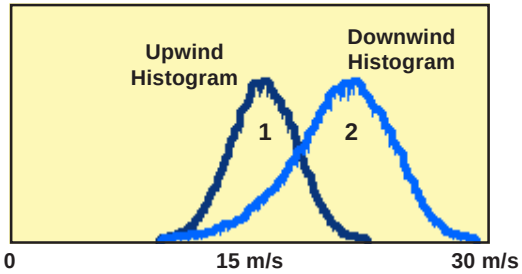

13. Downwind Evolution of Histograms

1. Surface Pressure (mb) ~ t_0-36h

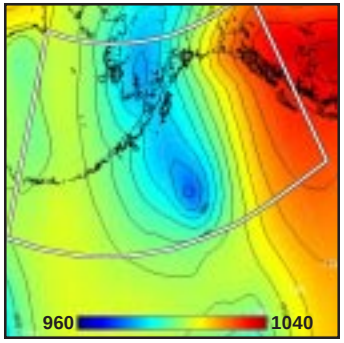

2. Surface Pressure (mb) ~ t_0-24h

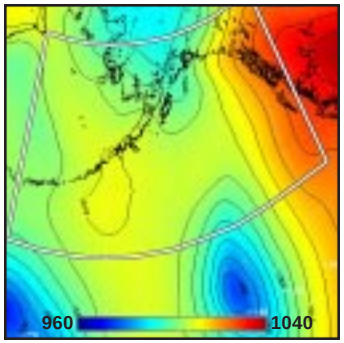

3. Surface Pressure (mb) ~ t_0-12h

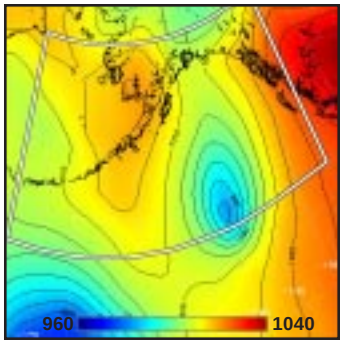

4. Surface Pressure (mb) ~ t_0

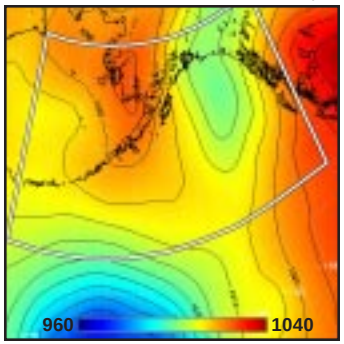

9. Enlarged Surface Wind Field ~ t_0

0000 GMT 24 Dec 1999

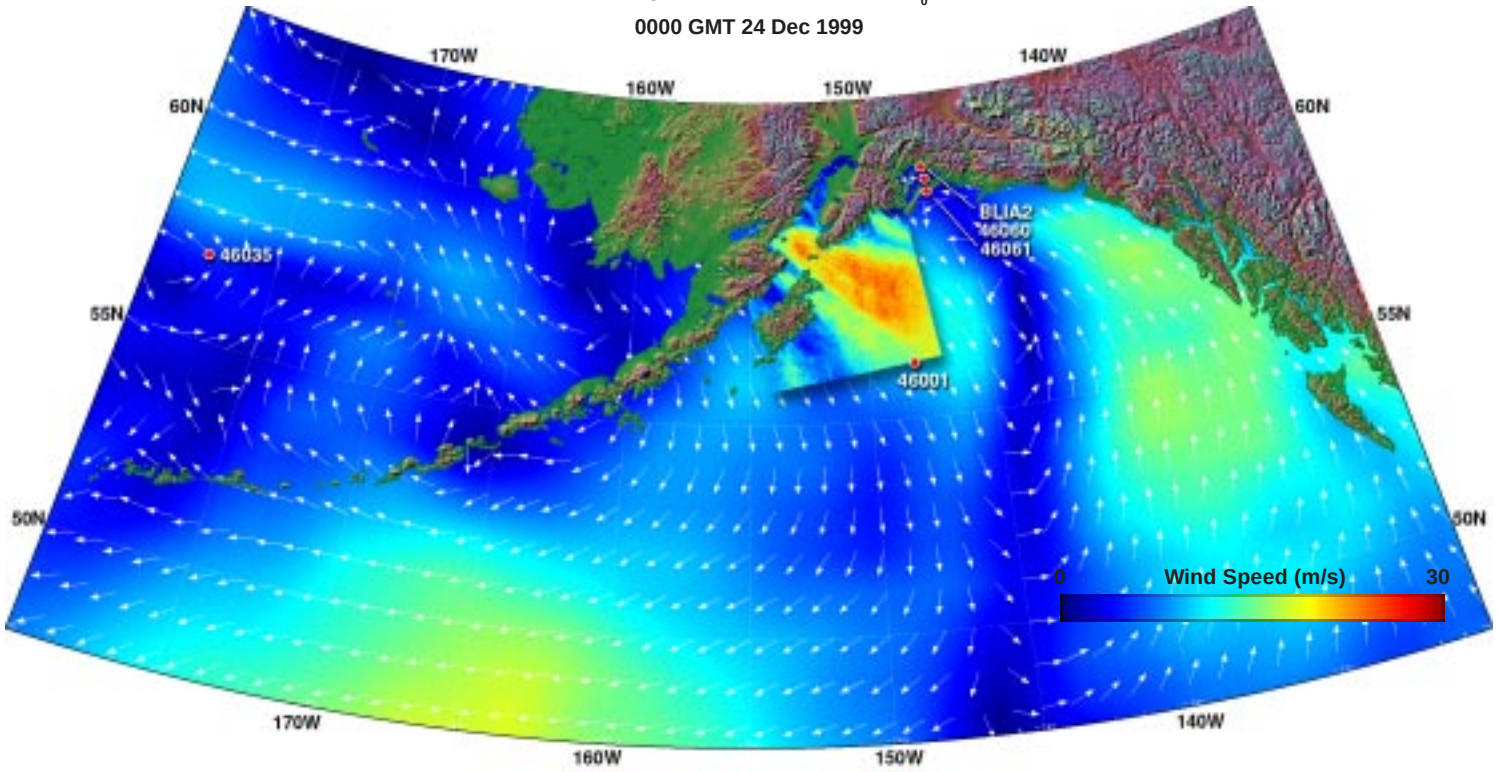

Model (this page): A weakening low becomes a trough as it passes into the Northern Gulf of Alaska (1-4), producing a strong E-W pressure gradient across Cook Inlet. Model winds (5, 9) show a local maximum of 10-15 m/s, but with nearly opposing swell from the south (6). Local wind-waves are growing (7), and the MABL resulting from the northerly wind is extremely unstable (8).

SAR (facing page): The SAR winds (10) reveal greater topographically related variability (11), and higher peaks than the model (12). Some features of the wind field are spatially coherent even 100 km downwind of the islands. Convergence lines, longitudinal roll vortices, and jets exiting from the valleys are all evident. There are also possible signatures of mountain lee waves over the bay. Maximum SAR winds along line AB (crosswind) exceed 20 m/s, while concurrent model winds (-4 hrs) scarcely reach 10 m/s (12). [ref. section 2.4: gap flows.]

5. Surface Wind Field (m/s) ~ t_0

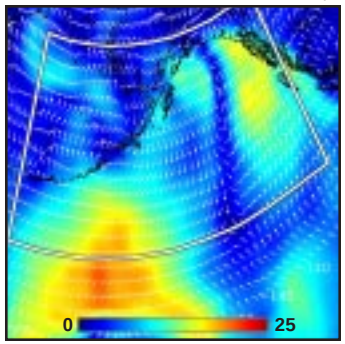

6. Surface Wave Height (m) ~ t_0

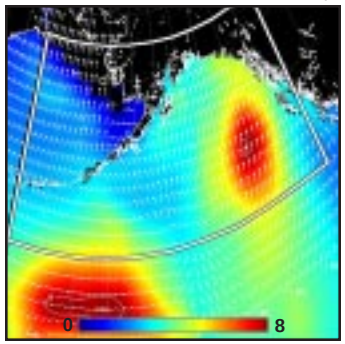

7. Inverse Wave Age (norm) ~ t_0

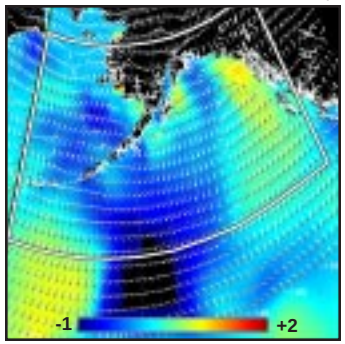

8. Air-Sea Temperature (˚C) ~ t_0

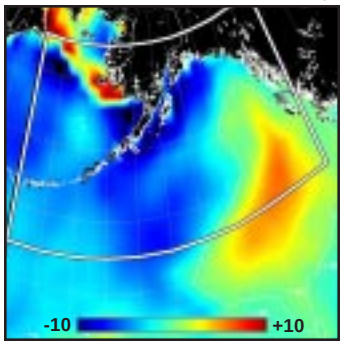

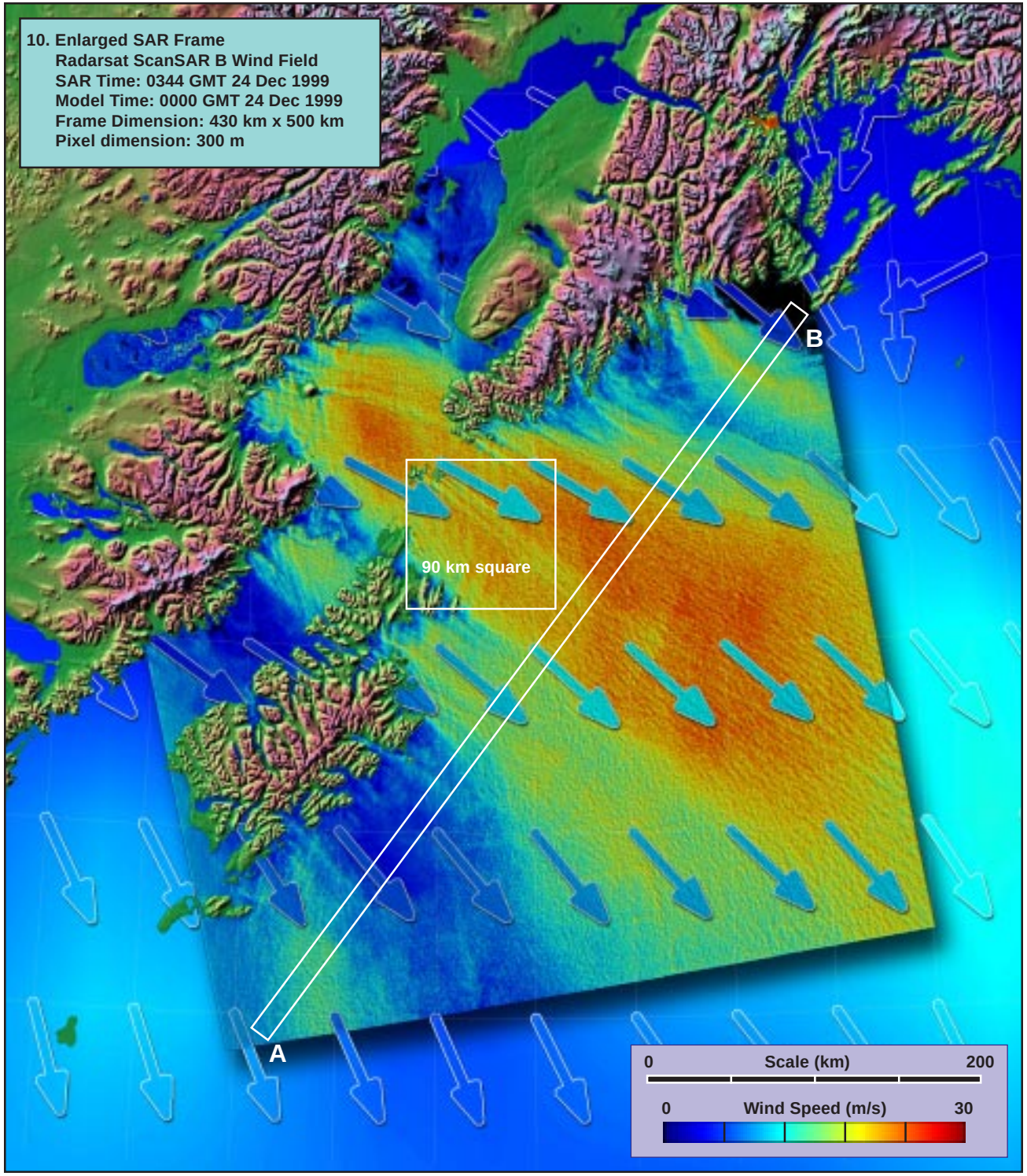

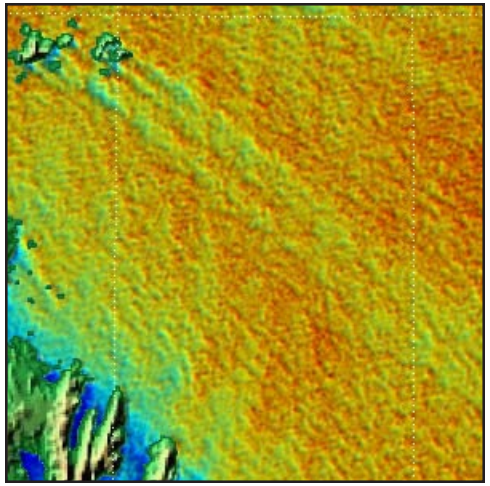

90 km square

11. Enlargement of Island Shadows (x 2.5)

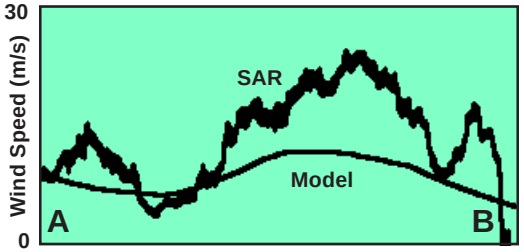

12. Model vs SAR Wind Profile along Line AB

1. Surface Pressure (mb) ~ t_0-36h

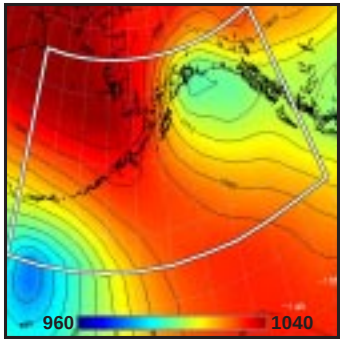

2. Surface Pressure (mb) ~ t_0-24h

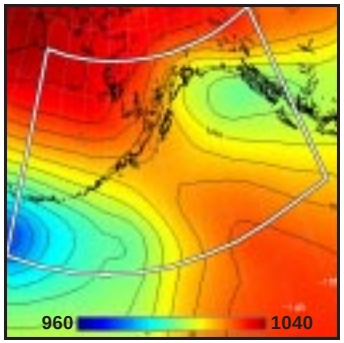

3. Surface Pressure (mb) ~ t_0-12h

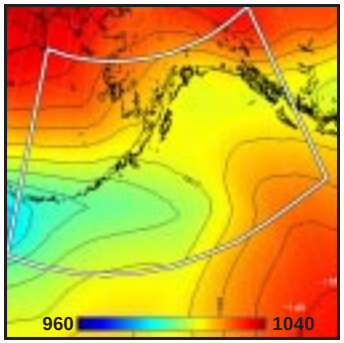

4. Surface Pressure (mb) ~ t_0

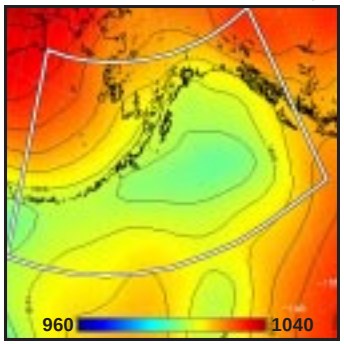

9. Enlarged Surface Wind Field ~ t_0

0600 GMT 03 Jan 2000

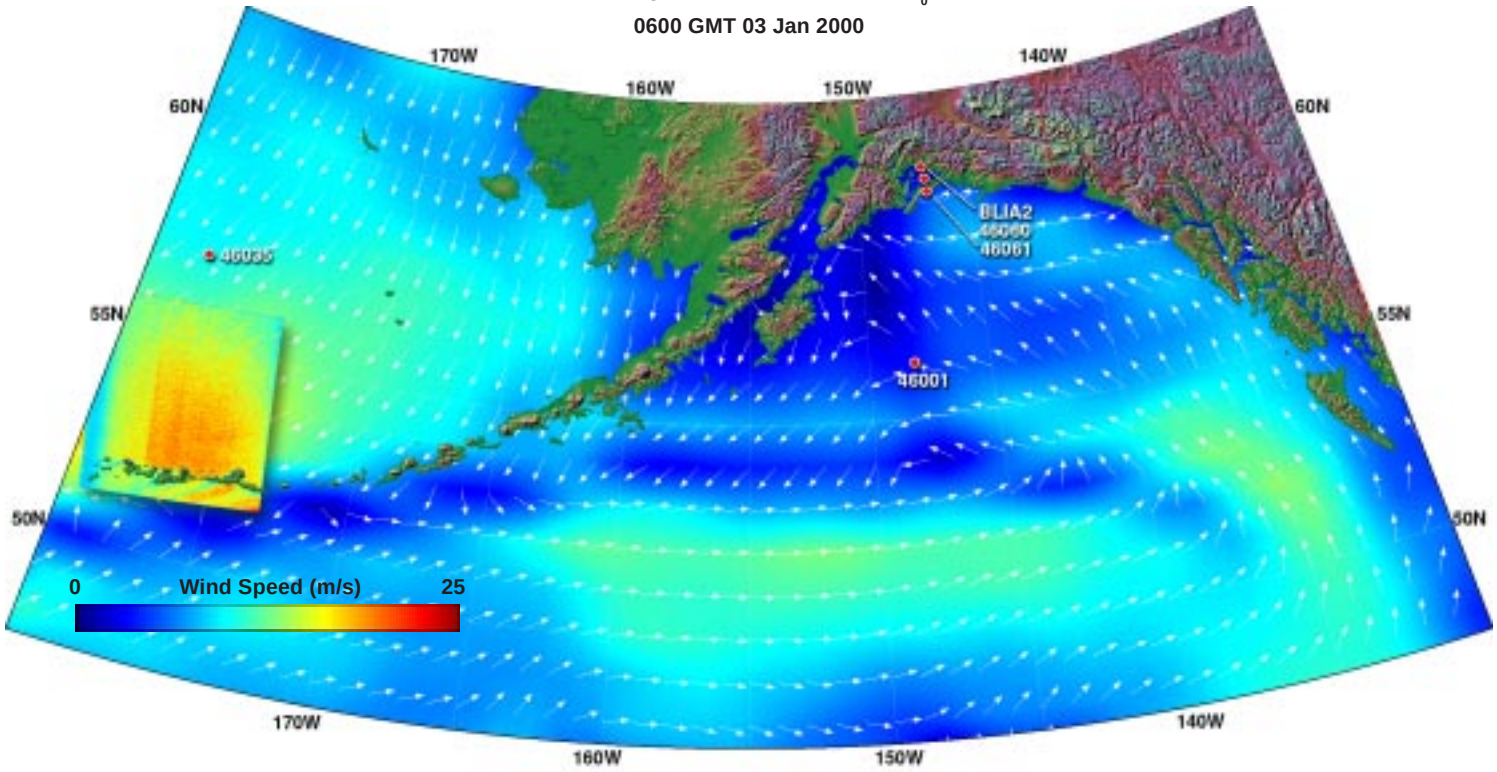

Model (this page): A stationary high pressure system in the Bering Sea combines with a developing trough (1-4) to produce a broad region of northeasterly winds just north of the outermost Aleutians. Model winds (5, 9) reach 20 to 25 m/s just north of the Aleutians, in the southern part of the SAR frame. Concurrent model waves approach 7 to 8 m, actively growing at overpass time (6, 7). The MABL is close to neutral, slightly stable in the south transitioning to slightly unstable in the north (8).

The SAR winds (10) show a generally mottled variability over scales of just a few km, with a tendency to elongation and rows along the local wind direction (11), patterns typical of boundary layer convection in windy conditions as are the terrain-induced variations in wind speed south of the Aleutians. The nonuniform response of the SAR at higher wind speeds is quite clear in this example. [ref. section 2.1: island and mountain wakes.]

5. Surface Wind Field (m/s) ~ t_0

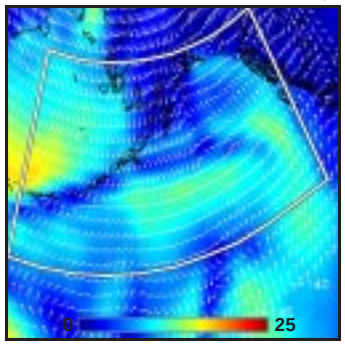

6. Surface Wave Height (m) ~ t_0

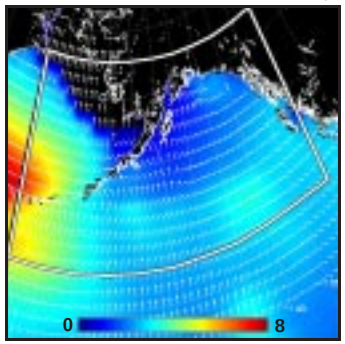

7. Inverse Wave Age (norm) ~ t_0

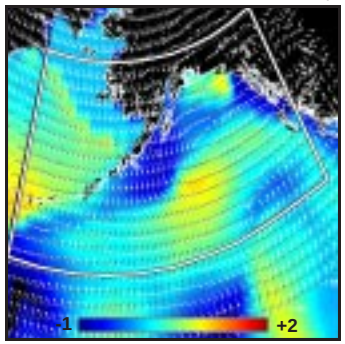

8. Air-Sea Temperature (˚C) ~ t_0

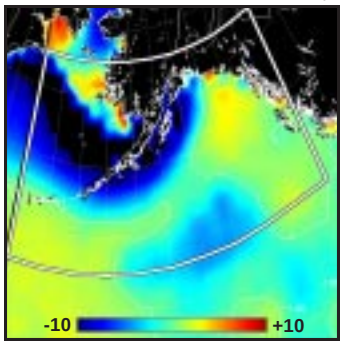

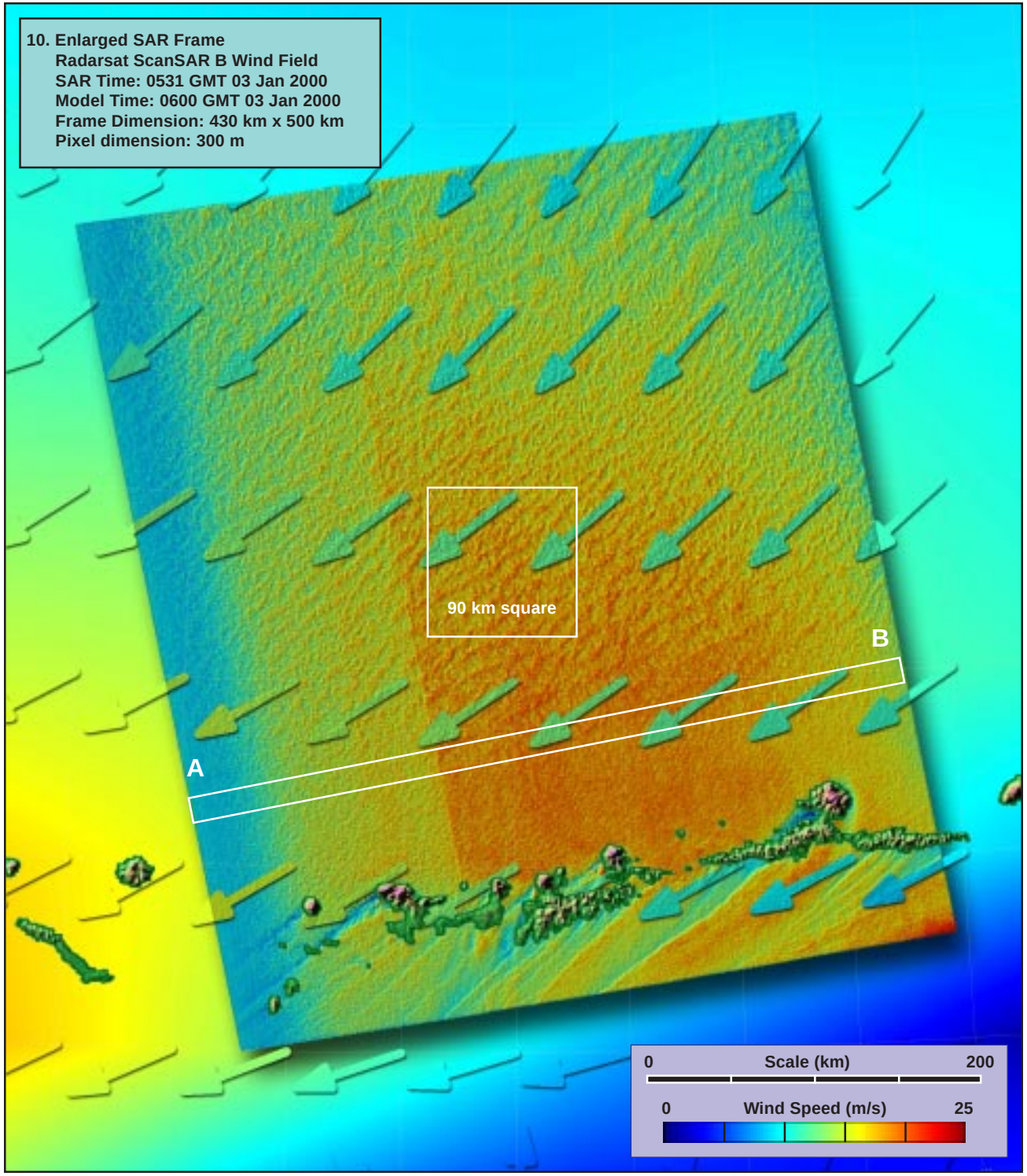

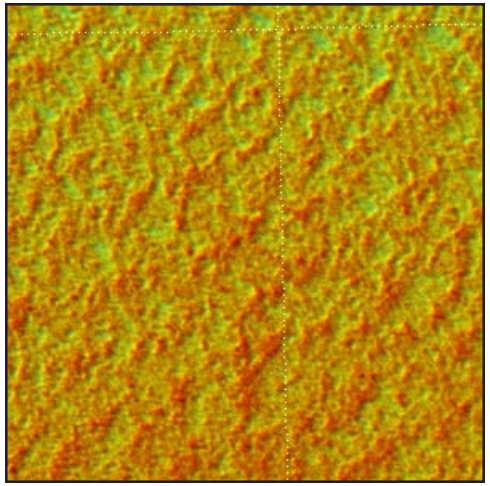

90 km square

11. Enlargement of Instability Patterns (x 2.5)

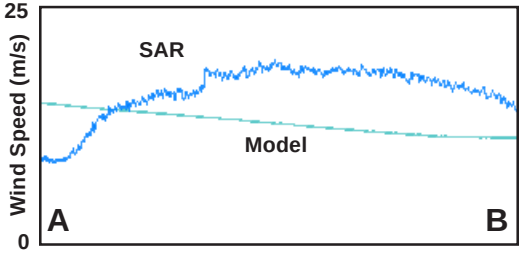

12. Model vs SAR Wind Profile along Line AB

1. Surface Pressure (mb) ~ t_0-36h

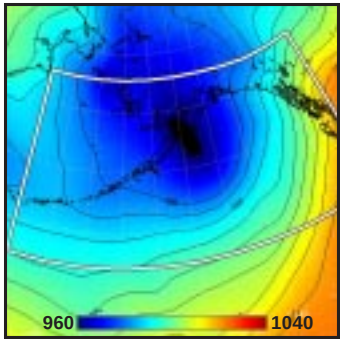

2. Surface Pressure (mb) ~ t_0-24h

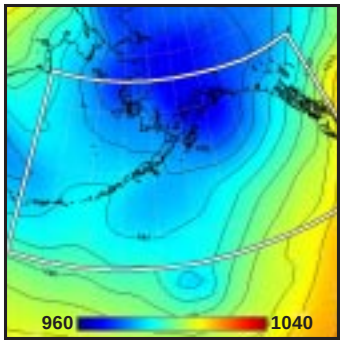

3. Surface Pressure (mb) ~ t_0-12h

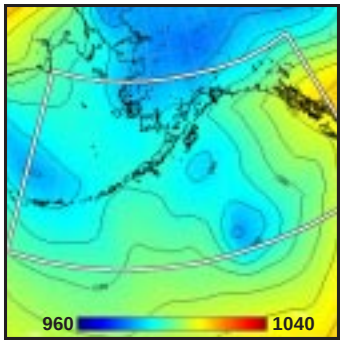

4. Surface Pressure (mb) ~ t_0

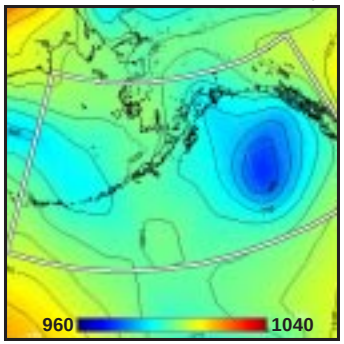

9. Enlarged Surface Wind Field ~ t_0

0000 GMT 29 Jan 2000

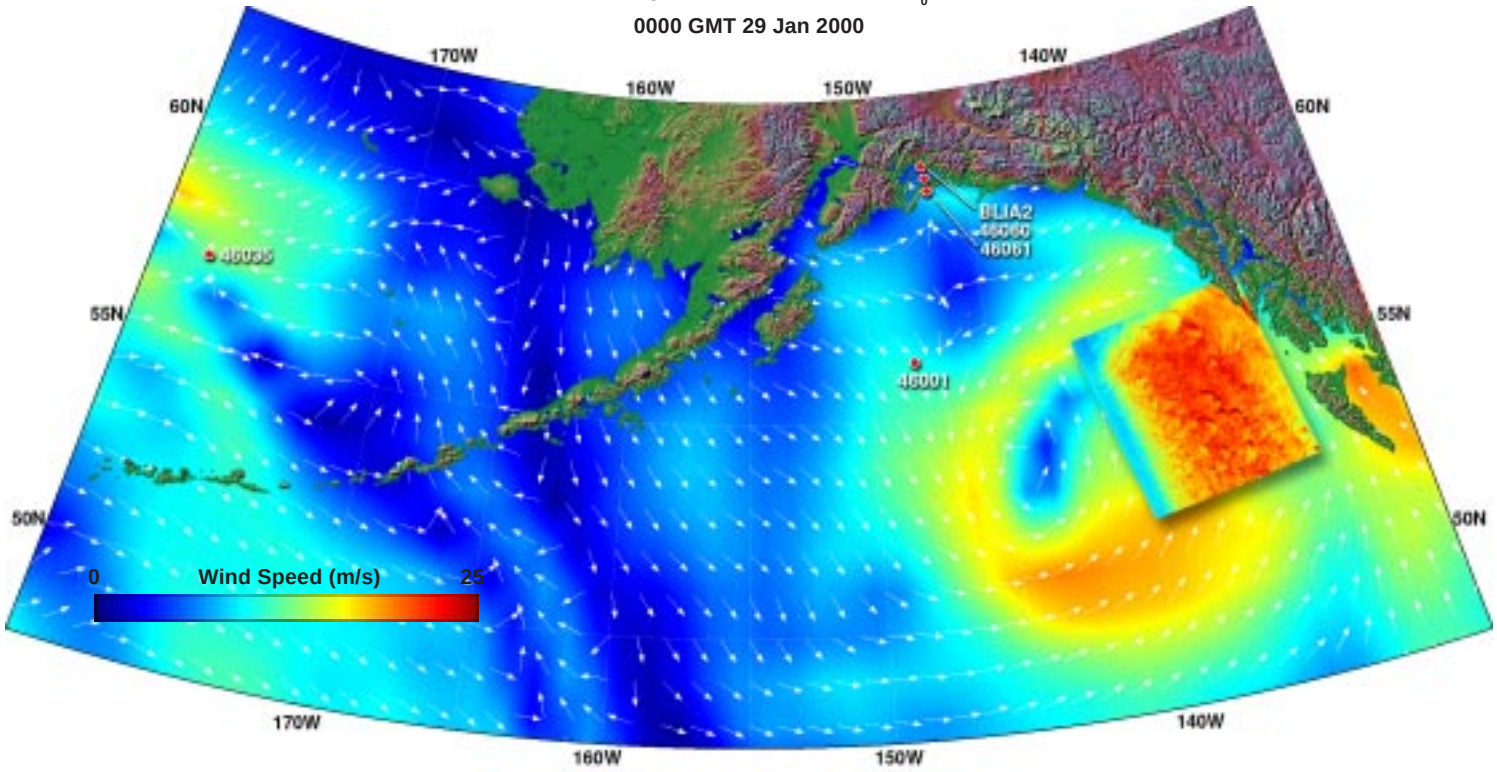

Model (this page): A strengthening low pressure system in the eastern Gulf of Alaska (3, 4) spins off from a weakening larger one to the northwest (1-2). Model winds (5, 9) reach 20 m/s south and east of the well defined center, extending well into the southern half of the SAR frame. Concurrent model waves there are 6 to 7 m, near equilibrium (6, 7). The MABL is stable (8).

SAR (facing page): The SAR winds (10) show a wide region of well-defined gust fronts, the strongest of which contain thin expanding arcs of local winds approaching 25 m/s (11, 12). Typical arc lengths of the expanding fronts are 25 km, with widths of about 5 km. The relatively large scale of these gust fronts suggests deep precipitating convection, a phenomena not dependent on MABL stability. [ref. section 2.10: convection.]

5. Surface Wind Field (m/s) ~ t_0

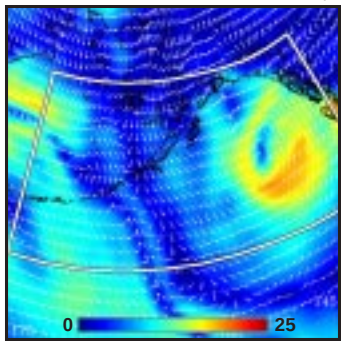

6. Surface Wave Height (m) ~ t_0

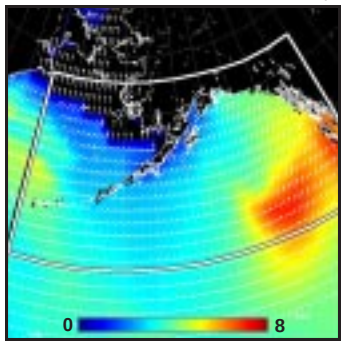

7. Inverse Wave Age (norm) ~ t_0

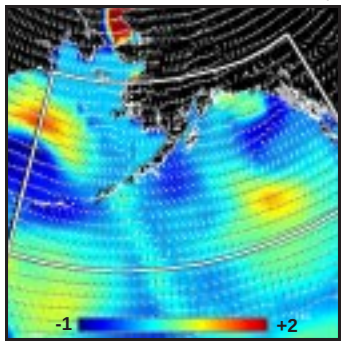

8. Air-Sea Temperature (˚C) ~ t_0

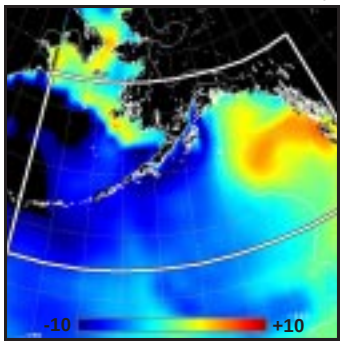

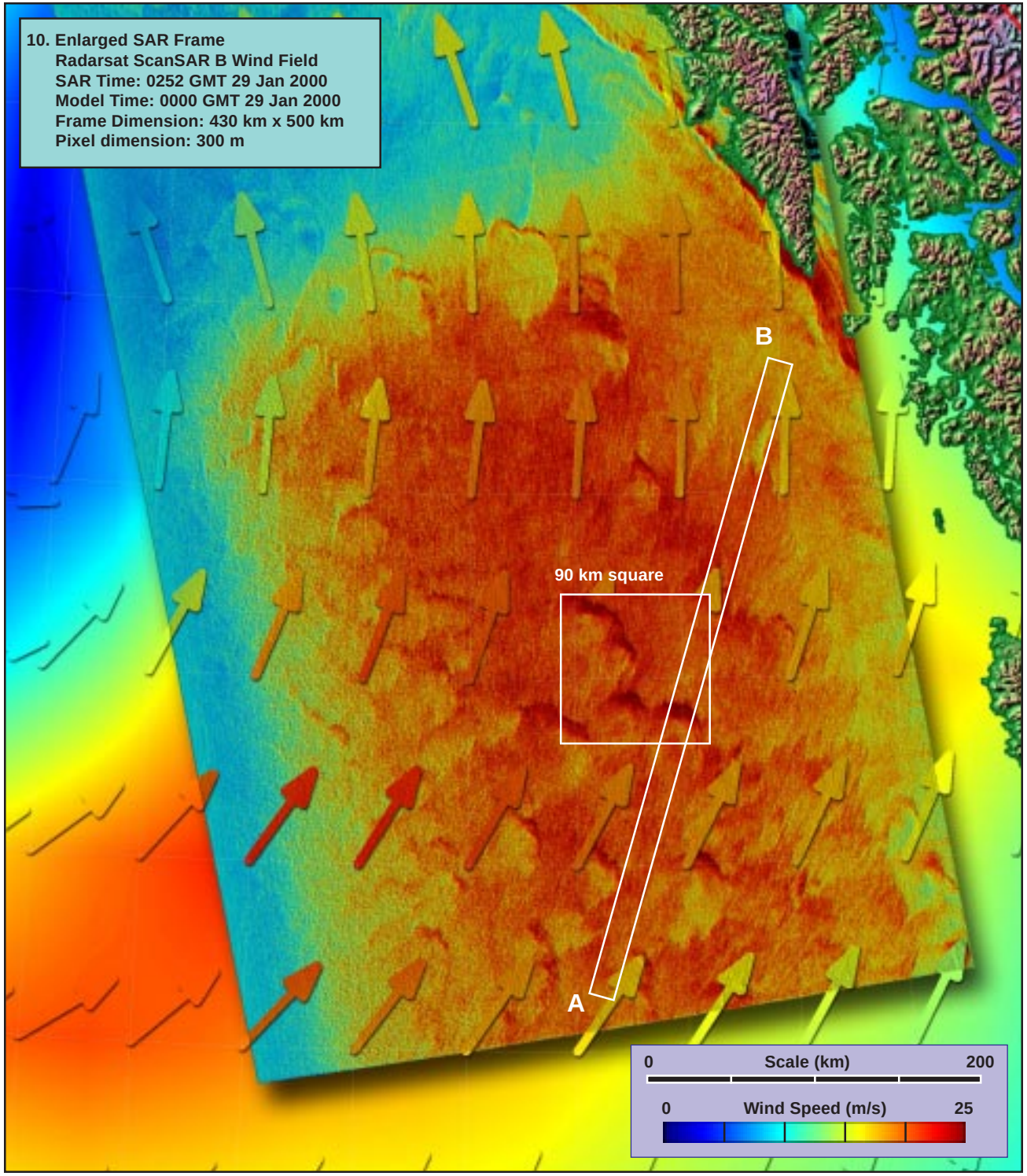

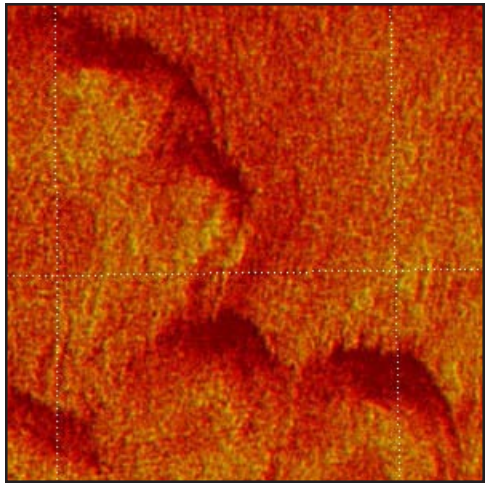

90 km square

11. Enlargement of Gust Front Patterns (x 2.5)

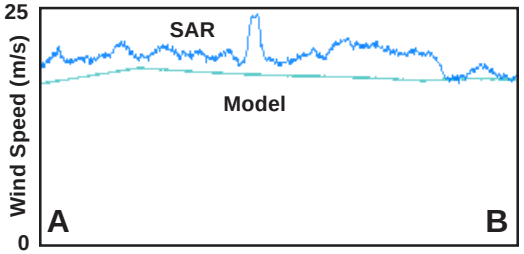

12. Model vs SAR Wind Profile along Line AB

1. Surface Pressure (mb) ~ t_0-36h

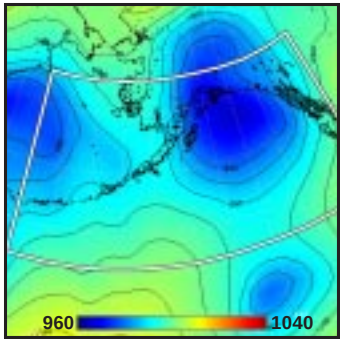

2. Surface Pressure (mb) ~ t_0-24h

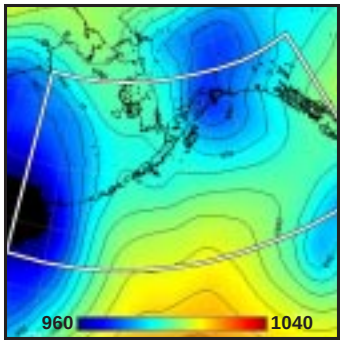

3. Surface Pressure (mb) ~ t_0-12h

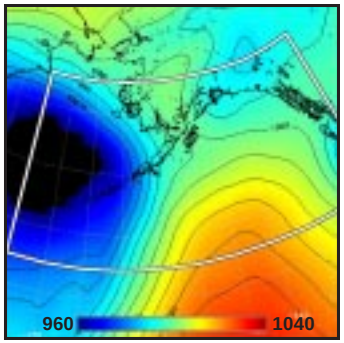

4. Surface Pressure (mb) ~ t_0

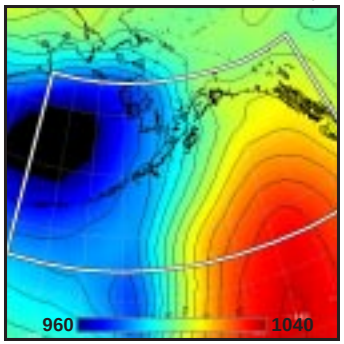

9. Enlarged Surface Wind Field ~ t_0

0000 GMT 02 Feb 2000

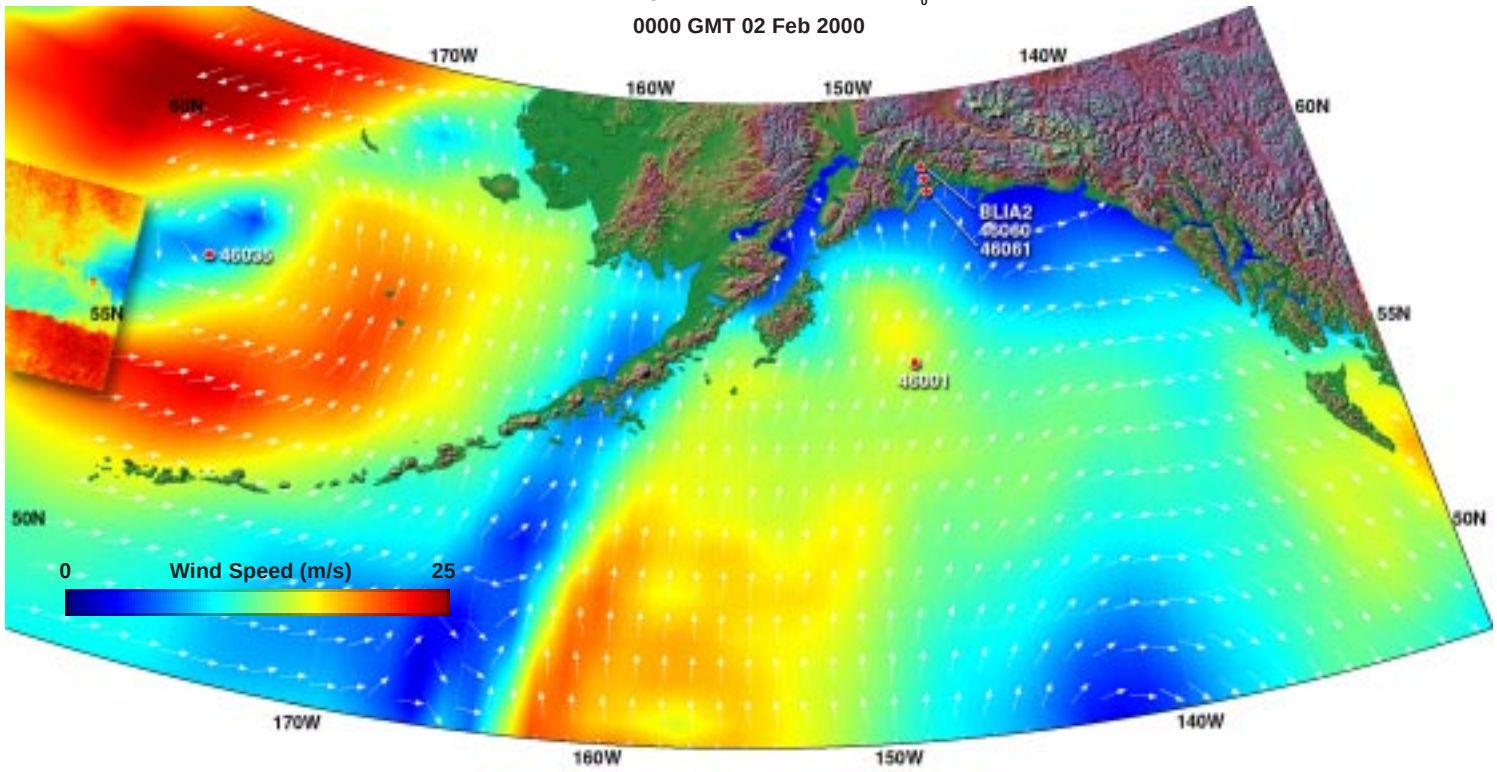

Model (this page): A very deep and well formed low pressure system travels to the north over the western Aleutians (1-4), setting up a large cyclonic circulation encompassing much of the Bering Sea. Model winds (5, 9) approach 30 m/s in the northern sector, 25 m/s in the south. Concurrent model waves are 10 to 12 m immediately to the north and east of the SAR pass, but probably exceed 8 m, and growing, at the northern and southern ends of the SAR frame (6, 7). The MABL is close to neutral or slightly unstable (8).

SAR (facing page): The SAR winds (10) show a smooth north-to-south transition from 20 m/s down to 10 m/s, followed by a sharp step transition back to nearly 25 m/s (11, 12) along the scalloped southern frontal boundary. The model shows a broad minimum with no hint of the sharp transition [ref. section 2.6: synoptic fronts.]

5. Surface Wind Field (m/s) ~ t_0

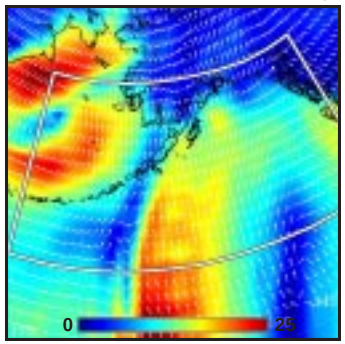

6. Surface Wave Height (m) ~ t_0

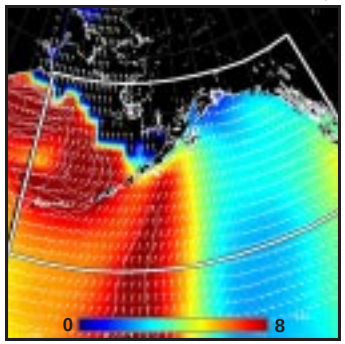

7. Inverse Wave Age (norm) ~ t_0

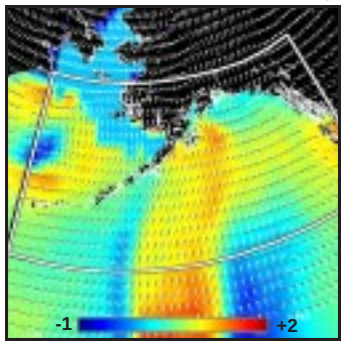

8. Air-Sea Temperature (˚C) ~ t_0

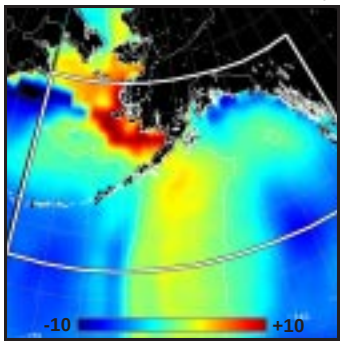

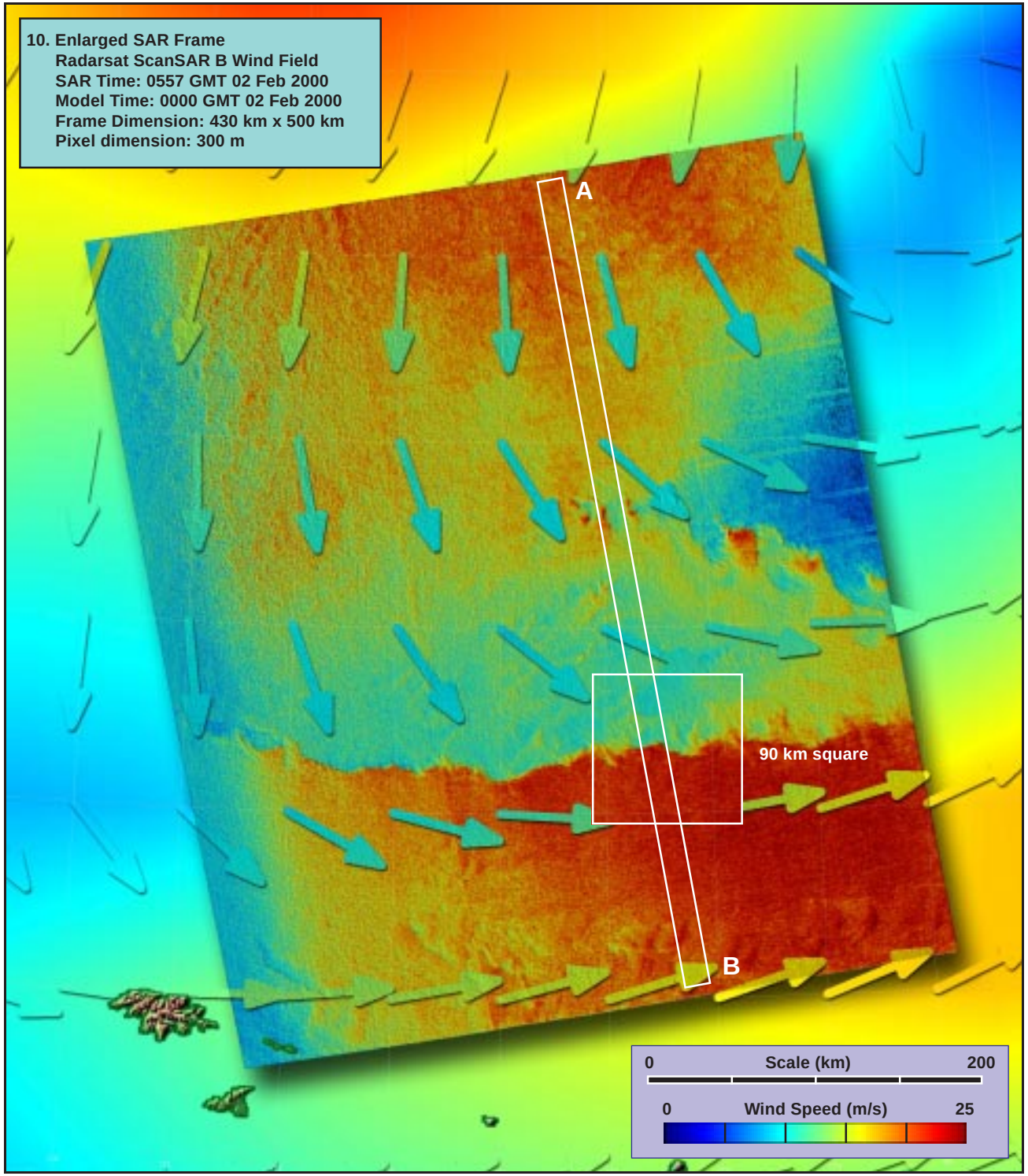

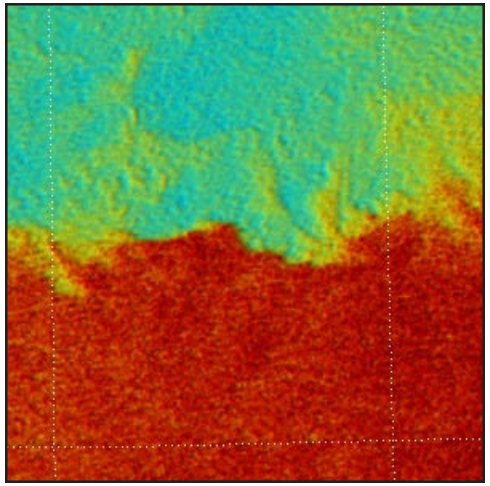

90 km square

11. Enlargement of Frontal Boundary (x 2.5)

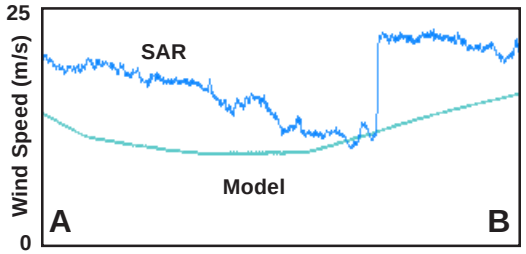

12. Model vs SAR Wind Profile along Line AB

1. Surface Pressure (mb) ~ t_0-36h

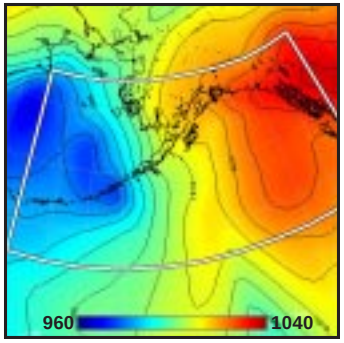

2. Surface Pressure (mb) ~ t_0-24h

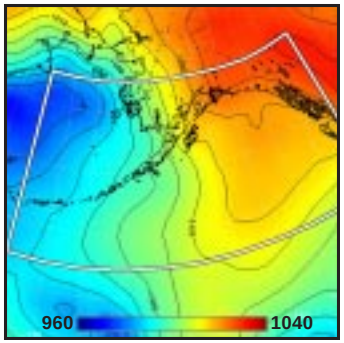

3. Surface Pressure (mb) ~ t_0-12h

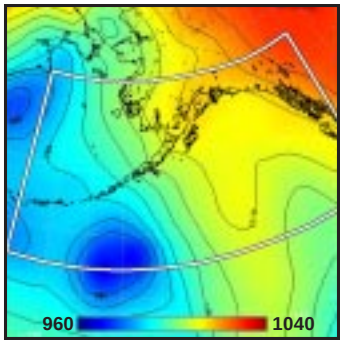

4. Surface Pressure (mb) ~ t_0

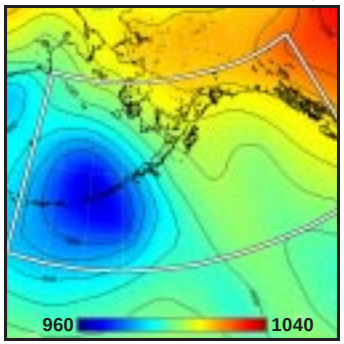

9. Enlarged Surface Wind Field ~ t_0

0600 GMT 05 Feb 2000

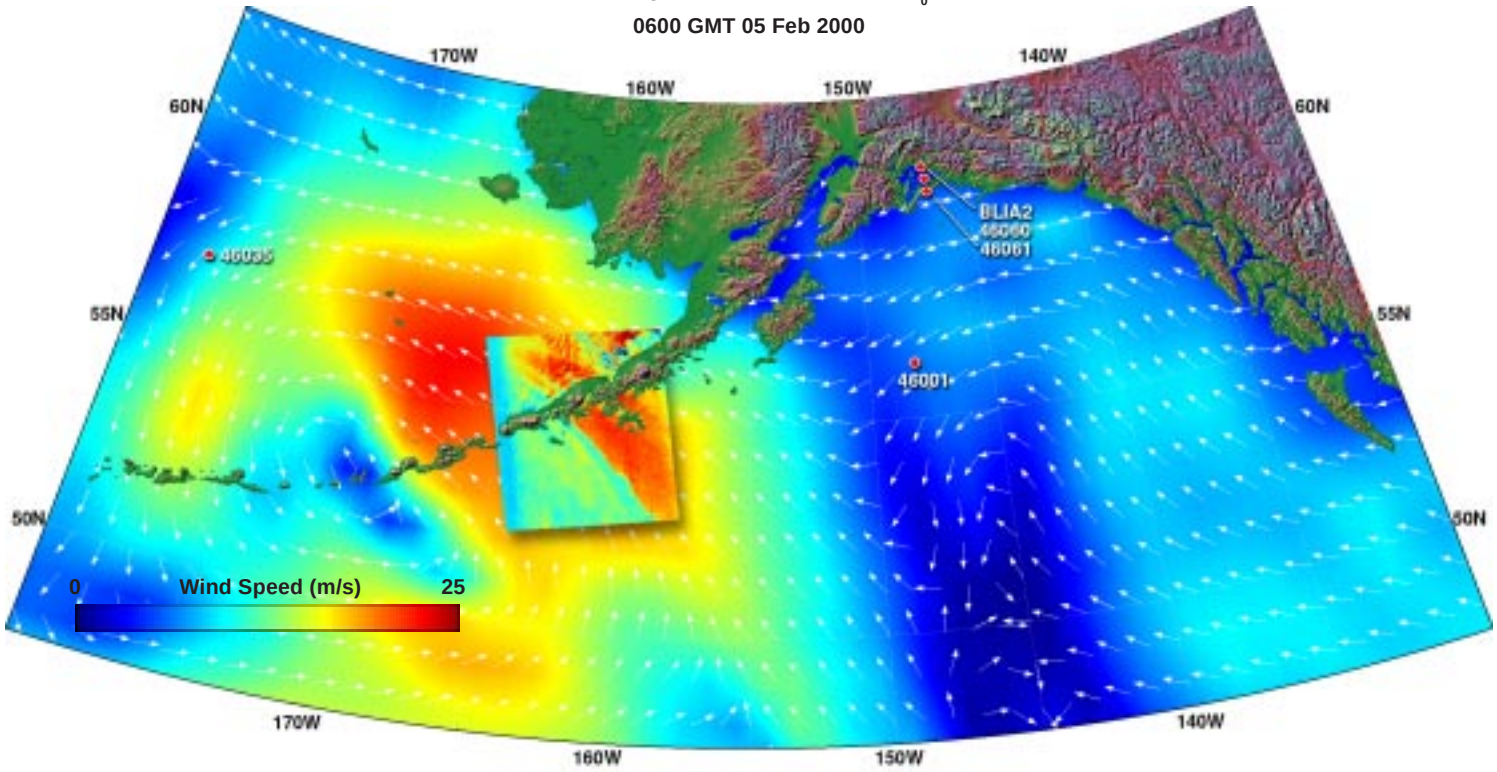

Model (this page): A weak but deepening low pressure system moves north across the Aleutians (2-4) as the trailing portion of a high exiting to the northeast squeezes the isobars along the peninsula. Model winds (5, 9) in the compressed isobar region approach 25 m/s. Concurrent model waves are about 6 m, still growing (6, 7). The MABL is increasingly stable toward the north of the SAR frame (8).

SAR (facing page): The SAR winds (10) show a northeast wall considerably displaced from the model, along with a rich pattern of topographically induced lee waves in the top center of the frame. Topographic shadowing is evident both upwind (11) and downwind of the peninsula. Downwind, it takes the form of a spatial modulation of the lee wave patterns. Again, the SAR boundary is much sharper than that of the model (12). The strong signature in the top right portion of the frame (10) is likely due to ice cover. [ref. section 2.8: mesoscale lows along fronts.]

5. Surface Wind Field (m/s) ~ t_0

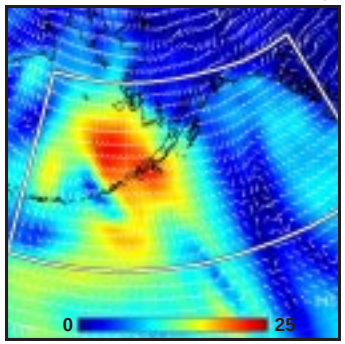

6. Surface Wave Height (m) ~ t_0

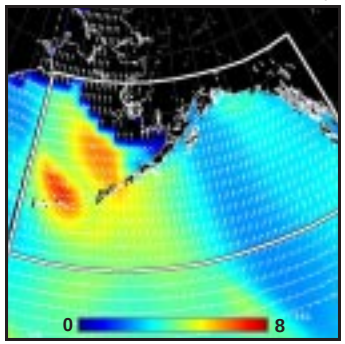

7. Inverse Wave Age (norm) ~ t_0

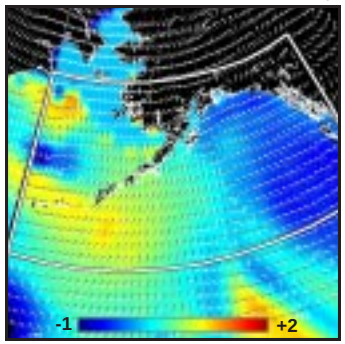

8. Air-Sea Temperature (˚C) ~ t_0

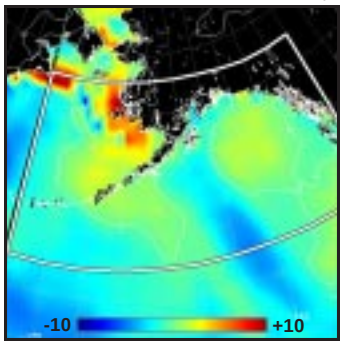

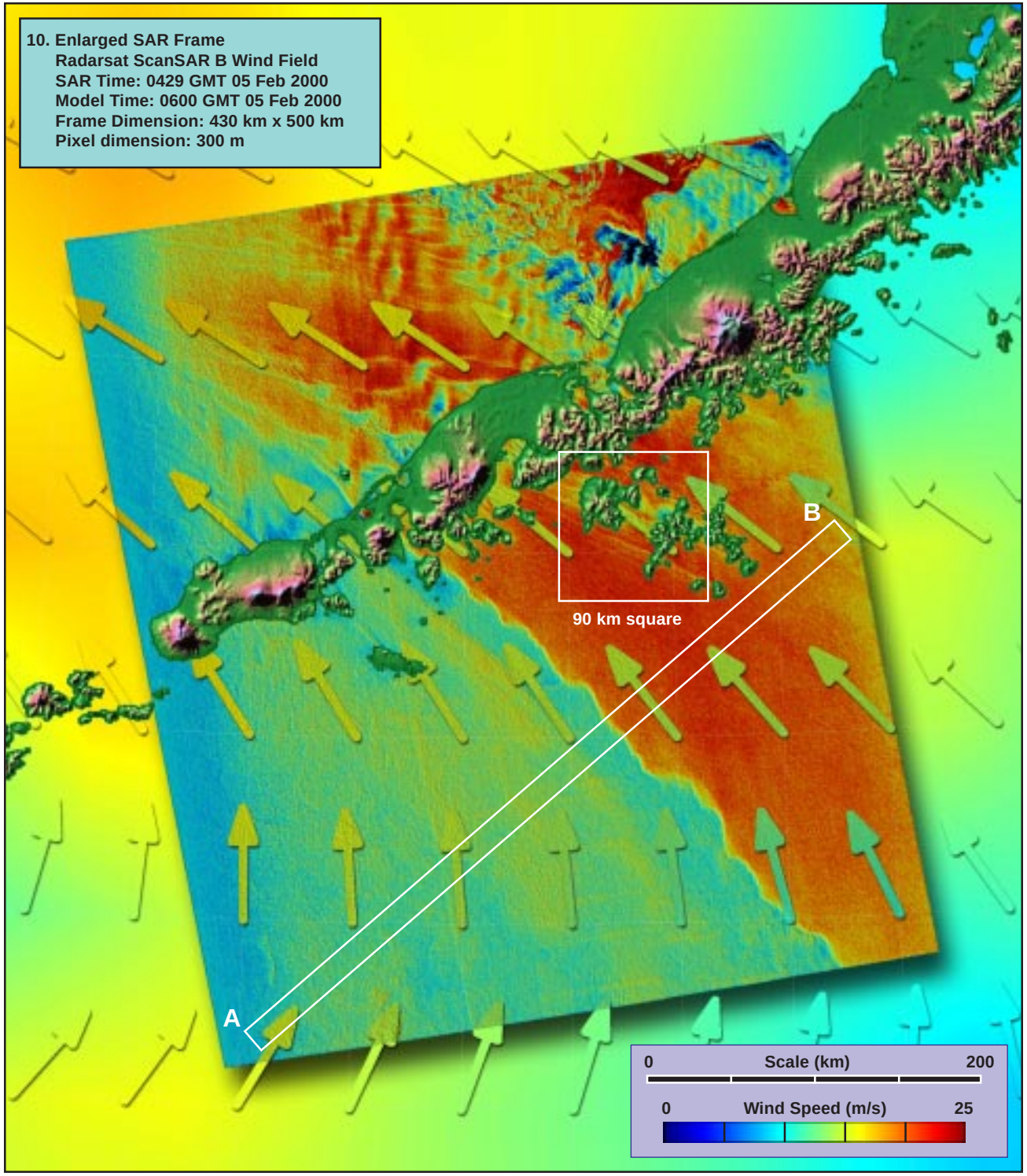

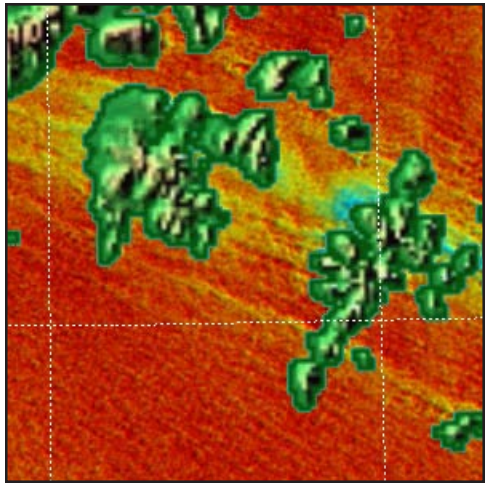

90 km square

11. Enlargement of Island Wakes (x 2.5)

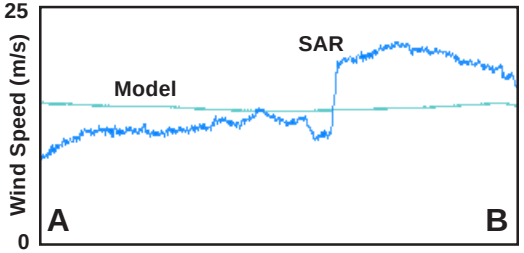

12. Model vs SAR Wind Profile along Line AB

1. Surface Pressure (mb) ~ t_0-36h

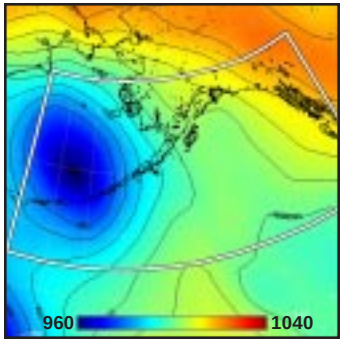

2. Surface Pressure (mb) ~ t_0-24h

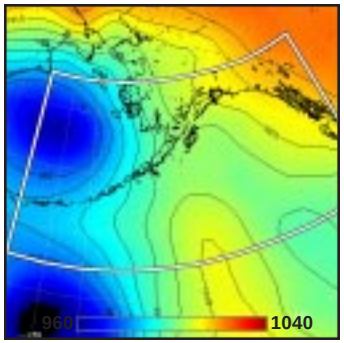

3. Surface Pressure (mb) ~ t_0-12h

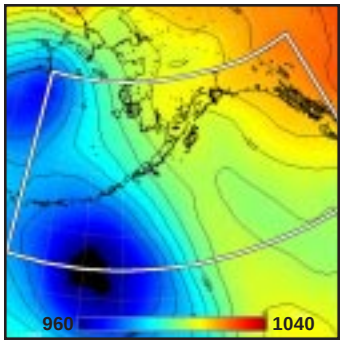

4. Surface Pressure (mb) ~ t_0

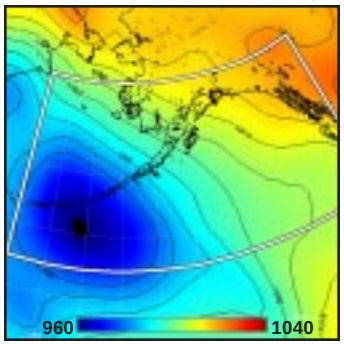

9. Enlarged Surface Wind Field ~ t_0

2400 GMT 06 Feb 2000

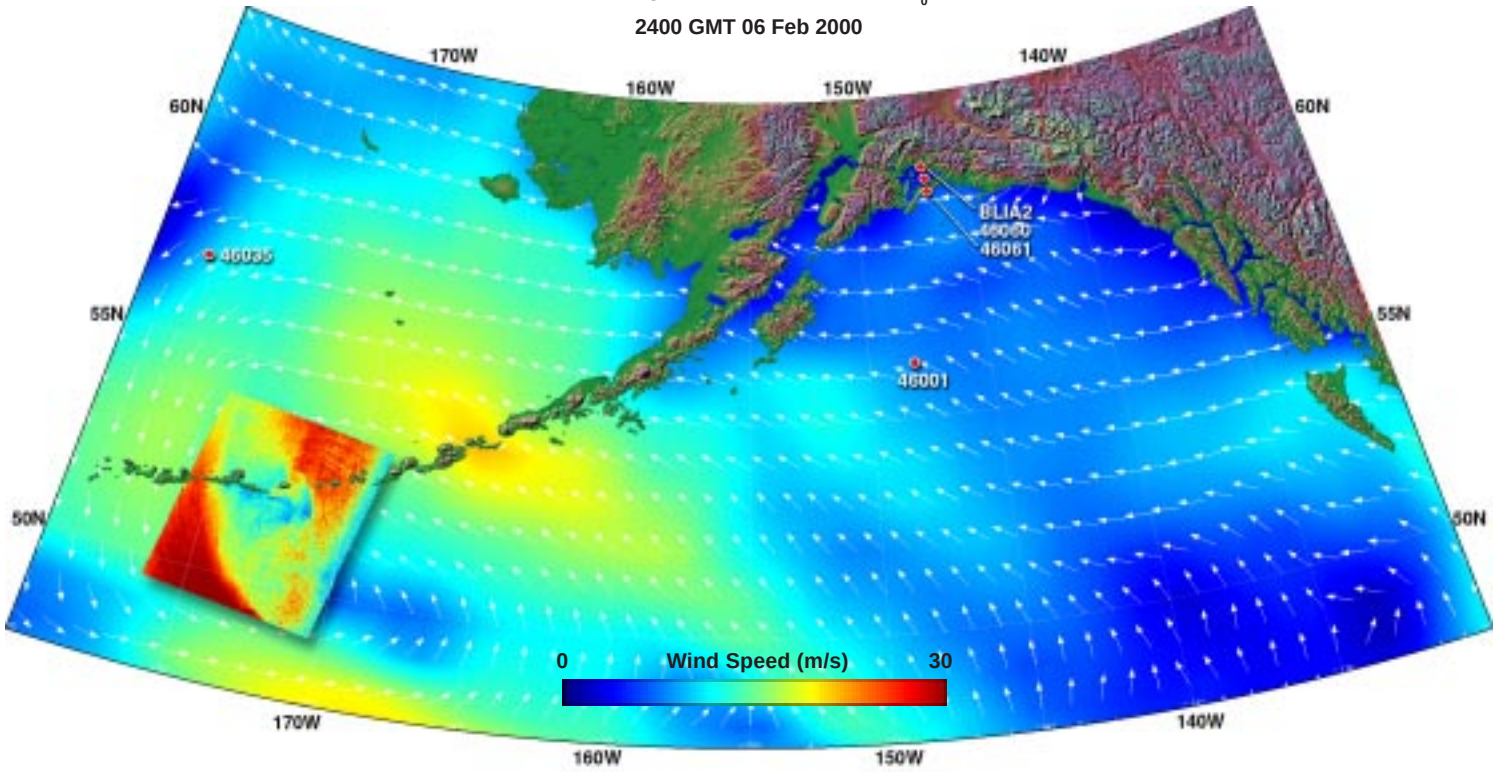

Model (this page): A well developed polar low moves northward toward the southern Aleutians (1-4), producing a distinct cyclonic circulation (5, 9). Peak model winds approach 25 m/s in the SW quadrant, with associated waves exceeding 8 m (6), and well developed (7). The MABL around the storm is slightly unstable (8).

SAR (facing page): The SAR winds (10) reveal the oblong symmetry of the center along with characteristic downwind coherence leeward of the islands (11). There are interesting island wakes. Some of them look like fast/slow couplets, not the expected pattern at all (slow behind islands, fast behind gaps). The SAR captures much more structure in the center (12) than that indicated by the model. [ref. section 2.1: island and mountain wakes.]

5. Surface Wind Field (m/s) ~ t_0

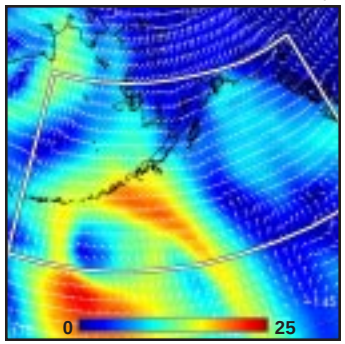

6. Surface Wave Height (m) ~ t_0

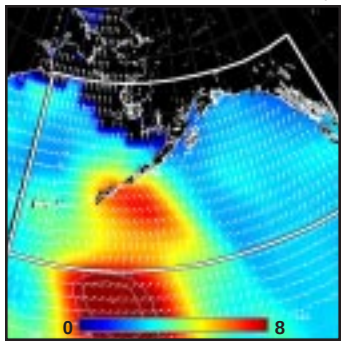

7. Inverse Wave Age (norm) ~ t_0

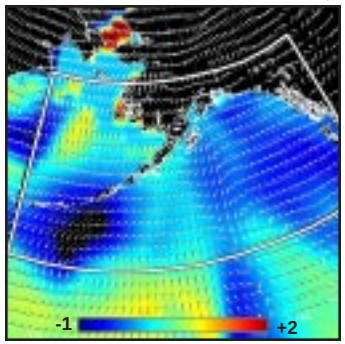

8. Air-Sea Temperature (˚C) ~ t_0

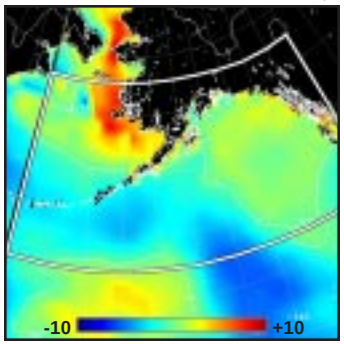

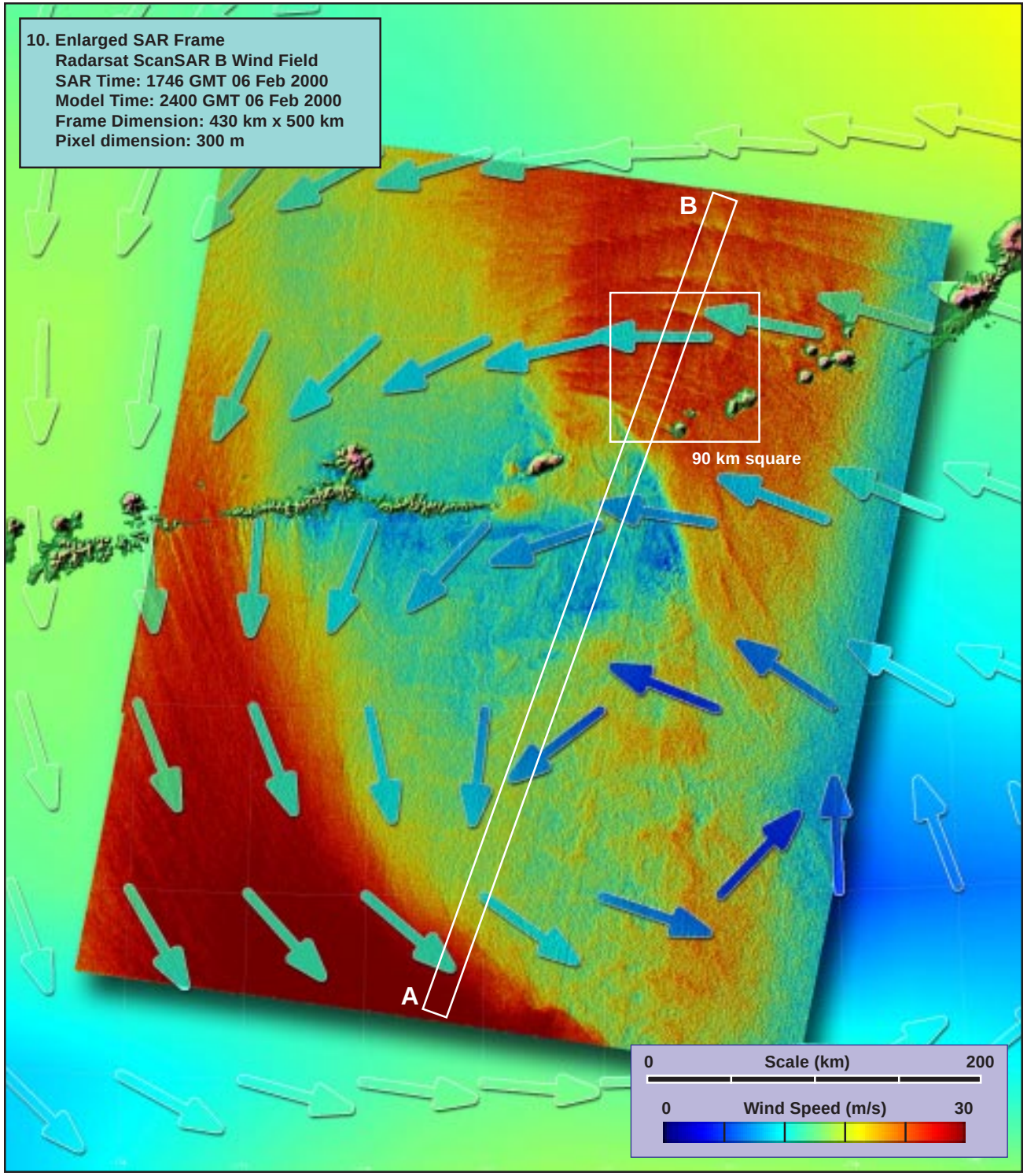

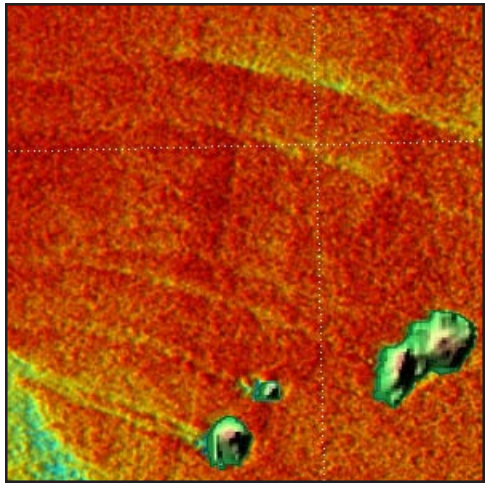

90 km square

11. Enlargement of Island Shadows (x 2.5)

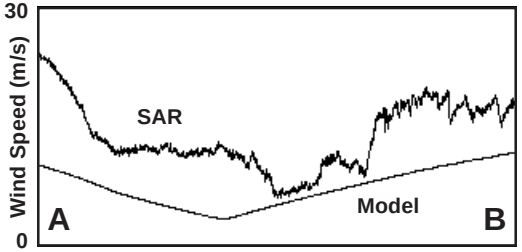

12. Model vs SAR Wind Profile along Line AB

1. Surface Pressure (mb) ~ t_0-36h

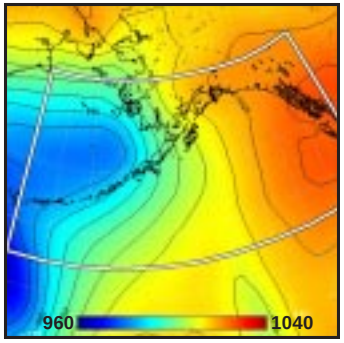

2. Surface Pressure (mb) ~ t_0-24h

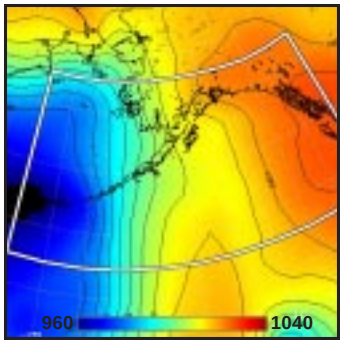

3. Surface Pressure (mb) ~ t_0-12h

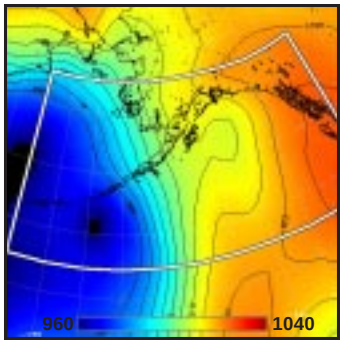

4. Surface Pressure (mb) ~ t_0

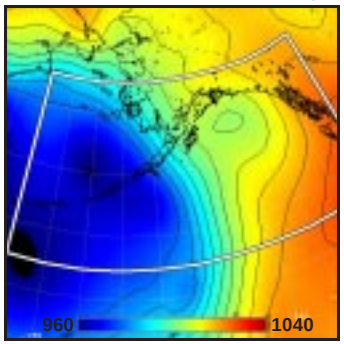

9. Enlarged Surface Wind Field ~ t_0

0600 GMT 18 Feb 2000

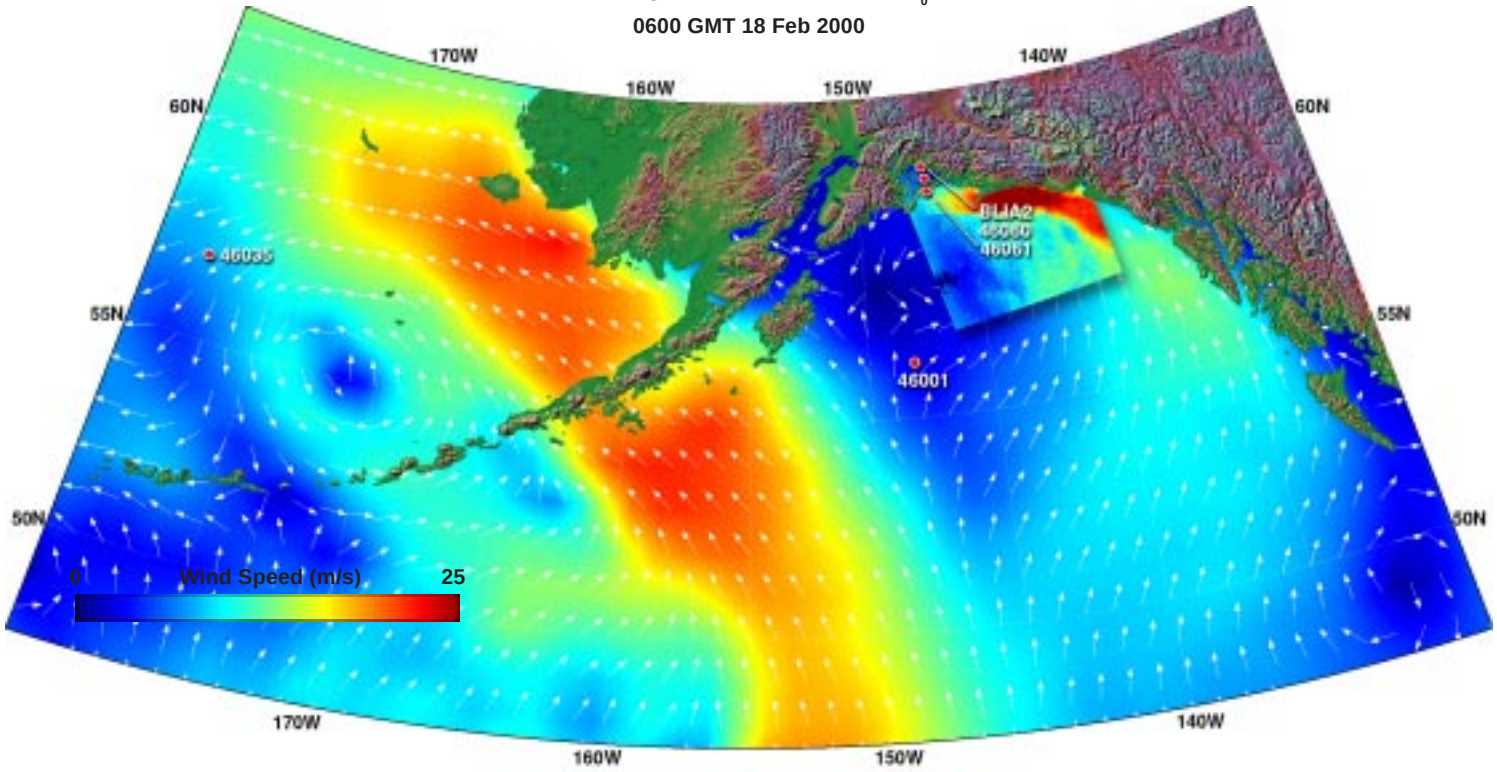

Model (this page): A deep, broad bottomed, nearly stationary low pressure center in the western Aleutians (1-4) produces a narrow arc of high winds and waves to its northeast, and spawns a minor low centered in the northern Gulf of Alaska at overpass time (3,4). Model winds associated with the northeastern sector of the minor low (5, 9) press against the coastal range to form a local wind of 10 to 15 m/s. Concurrent model waves are 3 to 4 m, decaying (6, 7). The MABL along the coast is nearly neutral (8).

SAR (facing page): The SAR winds (10, 11) along the coast show a strong, well-defined barrier jet with maximum winds near 30 m/s, more than three times the model estimate (12). The seaward boundary of the jet, located at least 50 km from shore, exhibits some scalloping (11), and there is some evidence of shear-induced atmospheric gravity waves embedded within the jet. [ref. section 2.11: coastal barrier jets.]

5. Surface Wind Field (m/s) ~ t_0

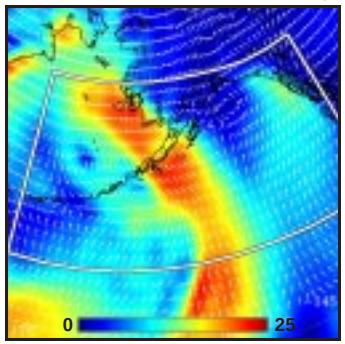

6. Surface Wave Height (m) ~ t_0

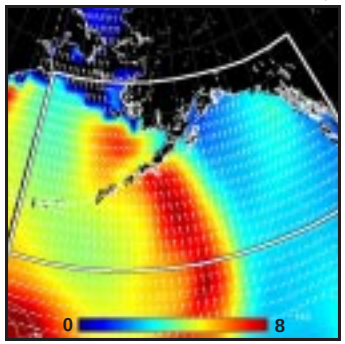

7. Inverse Wave Age (norm) ~ t_0

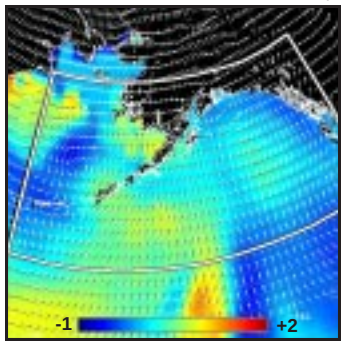

8. Air-Sea Temperature (˚C) ~ t_0

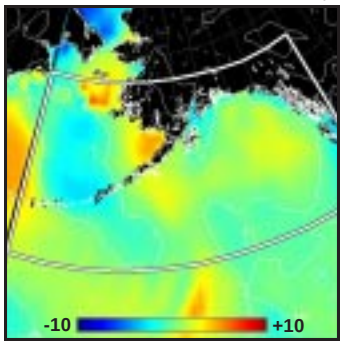

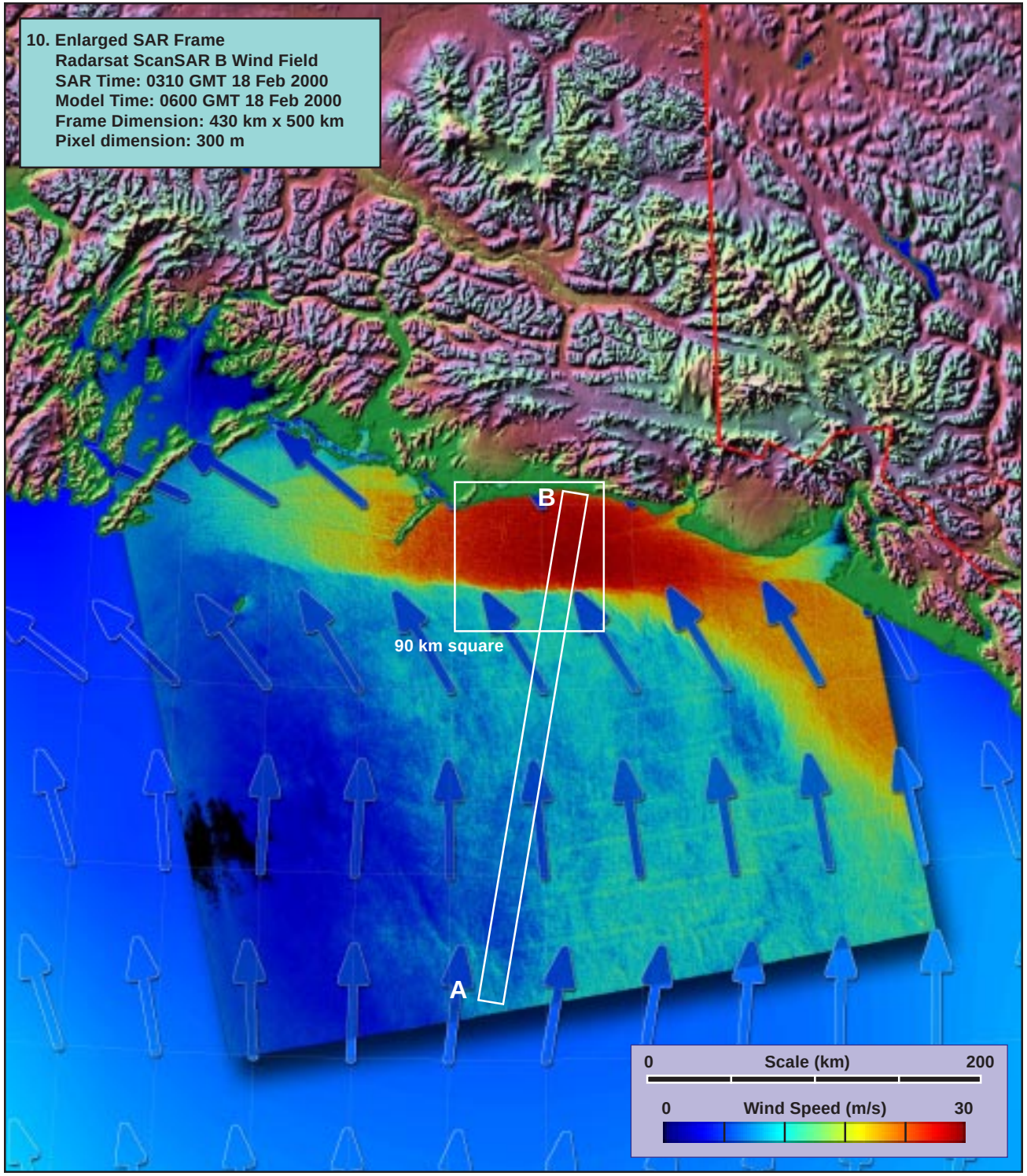

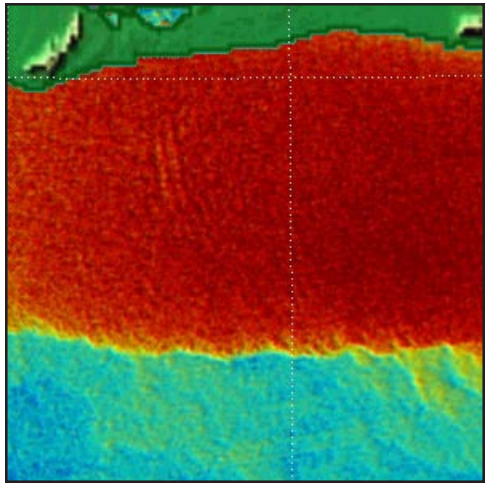

90 km square

11. Enlargement of Frontal Boundary (x 2.5)

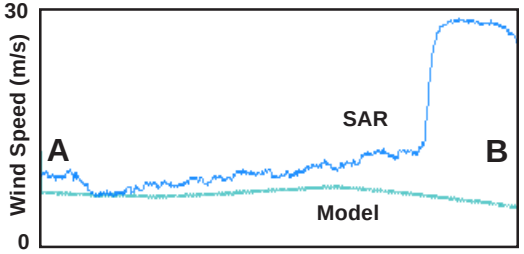

12. Model vs SAR Wind Profile along Line AB

1. Surface Pressure (mb) ~ t_0-36h

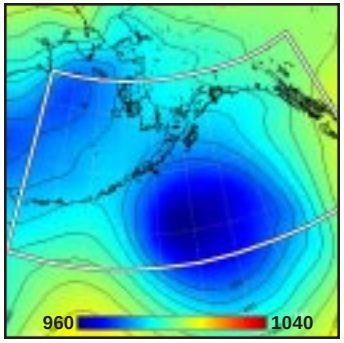

2. Surface Pressure (mb) ~ t_0-24h

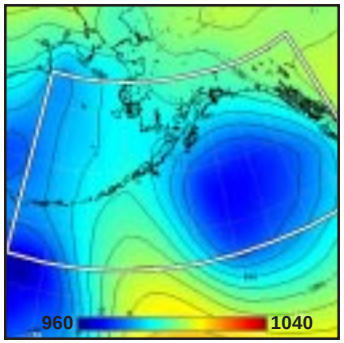

3. Surface Pressure (mb) ~ t_0-12h

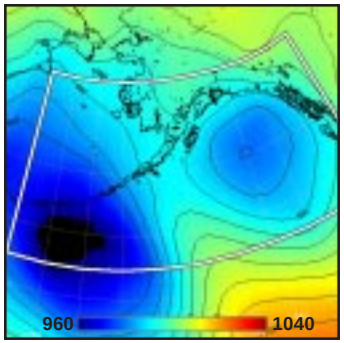

4. Surface Pressure (mb) ~ t_0

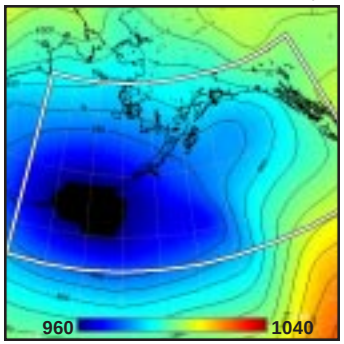

9. Enlarged Surface Wind Field ~ t_0

1200 GMT 02 Mar 2000

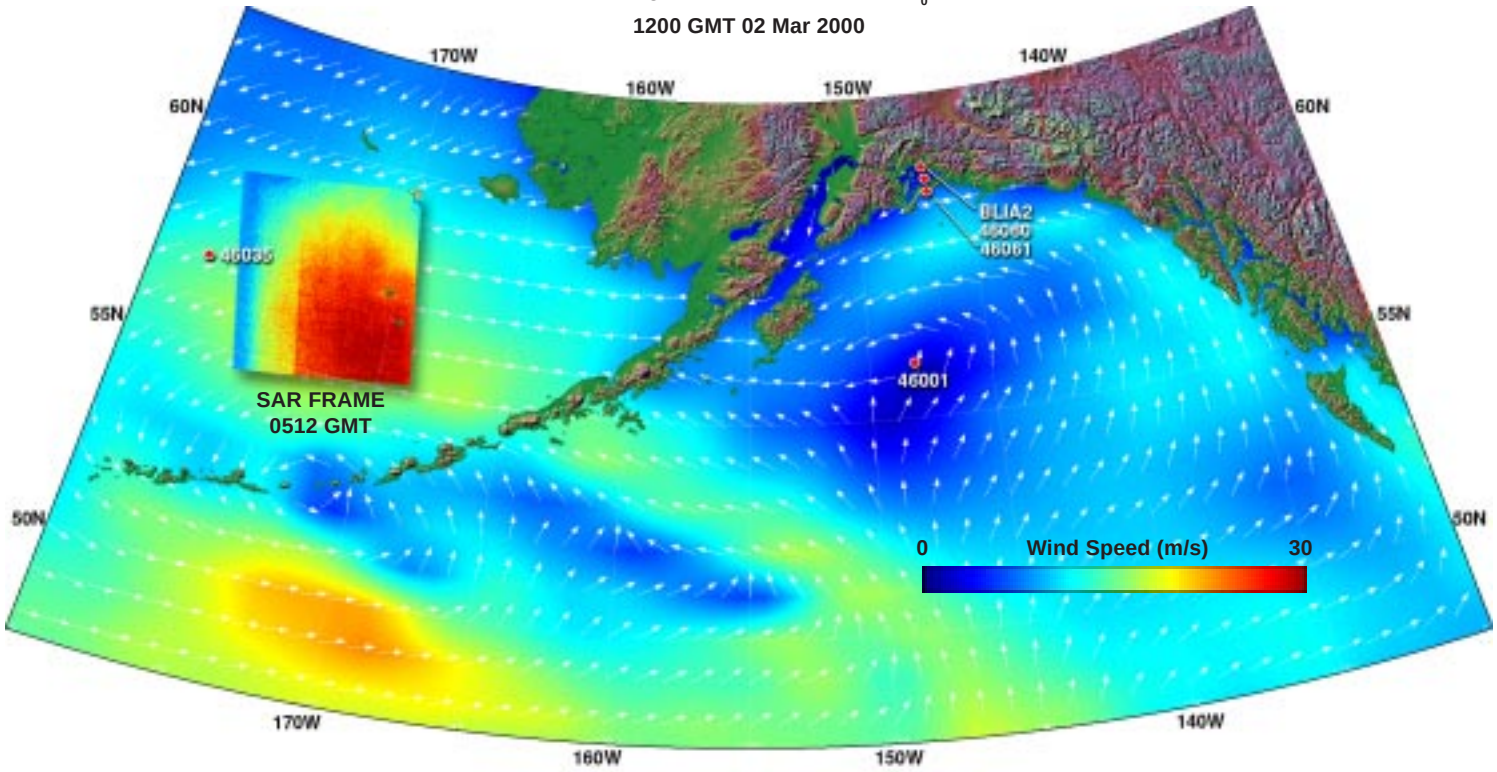

Model (this page): A huge low pressure system moves northward over the southern Aleutians (1-4), producing a wide region of cyclonic circulation (5, 9). Peak model winds approach 25 m/s in its southern region, and ~20 m/s in its northern region (where the SAR acquisition occurs). Associated waves in the north approach 6 m (6), evidently decaying (7), and the MABL there is near neutral (8).

SAR (facing page): The SAR winds (10) are quite high, approaching 30 m/s in the southern portion of the frame, nearly double the model estimate. However, the model and a nearby buoy 46035 agree quite well (11CD and 11EF), casting some doubt on the veracity of the SAR estimates. Furthermore, the set of five cross-scans (11) suggests a pattern of nonlinear behavior in the SAR which varies with both wind speed and cross-track distance (i.e., angle of incidence). The SAR appears biased high in the center at high winds, and low at the near-range (westernmost) angles. This latter effect is quite clear on all SAR frames; the former becomes most evident when the wind exceed 15 m/s over a broad region, as it does here.

5. Surface Wind Field (m/s) ~ t_0

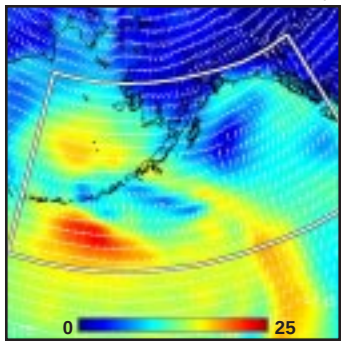

6. Surface Wave Height (m) ~ t_0

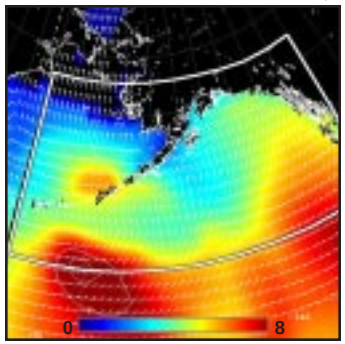

7. Inverse Wave Age (norm) ~ t_0

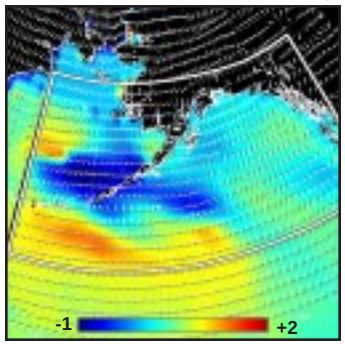

8. Air-Sea Temperature (˚C) ~ t_0

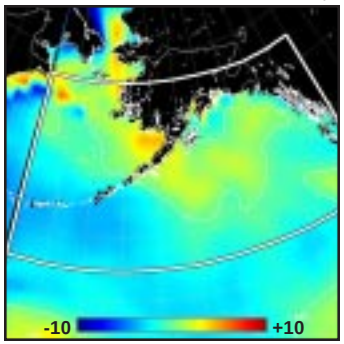

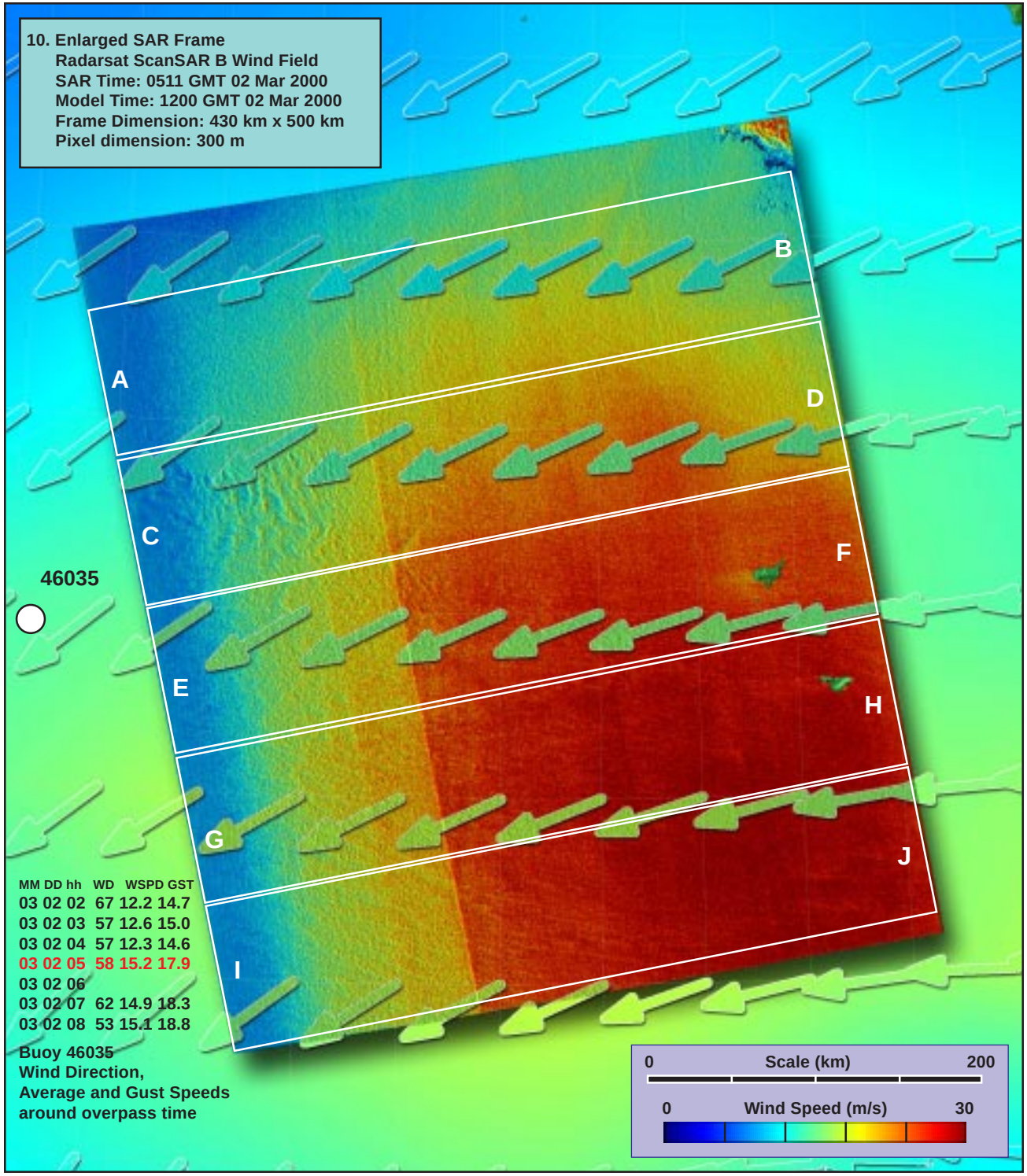

11. Model vs SAR Winds (90 km scan widths)
(vertical scale expanded to 40 m/s for clarity)

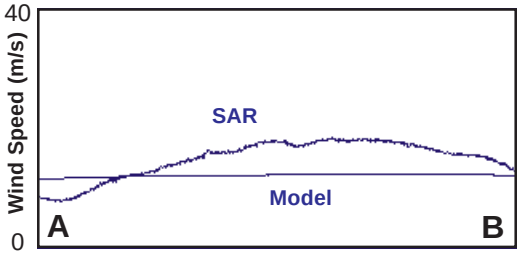

Distance along scan swath AB

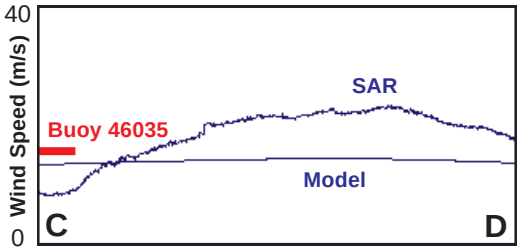

Distance along scan swath CD

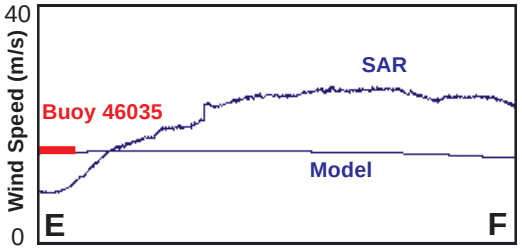

Distance along scan swath EF

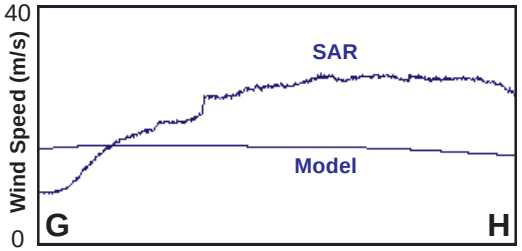

Distance along scan swath GH

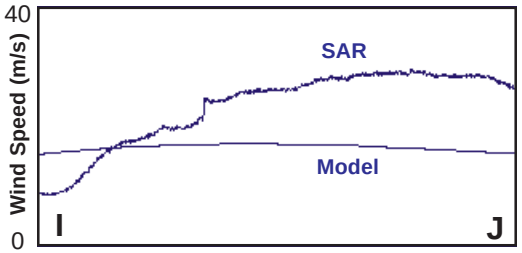

Distance along scan swath IJ

1. Surface Pressure (mb) ~ t_0-36h

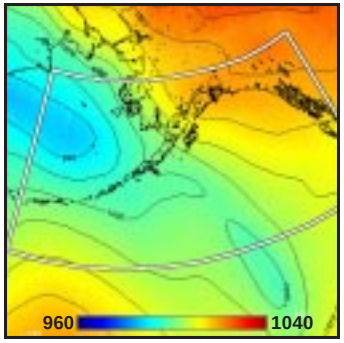

2. Surface Pressure (mb) ~ t_0-24h

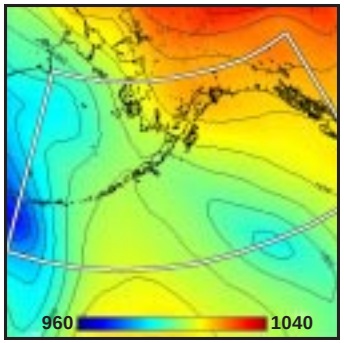

3. Surface Pressure (mb) ~ t_0-12h

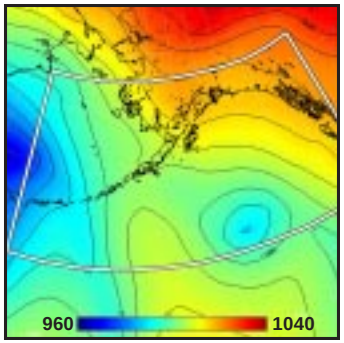

4. Surface Pressure (mb) ~ t_0

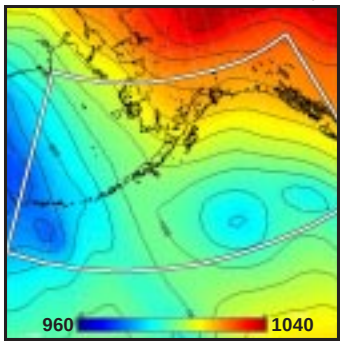

9. Enlarged Surface Wind Field ~ t_0

1800 GMT 10 Mar 2000

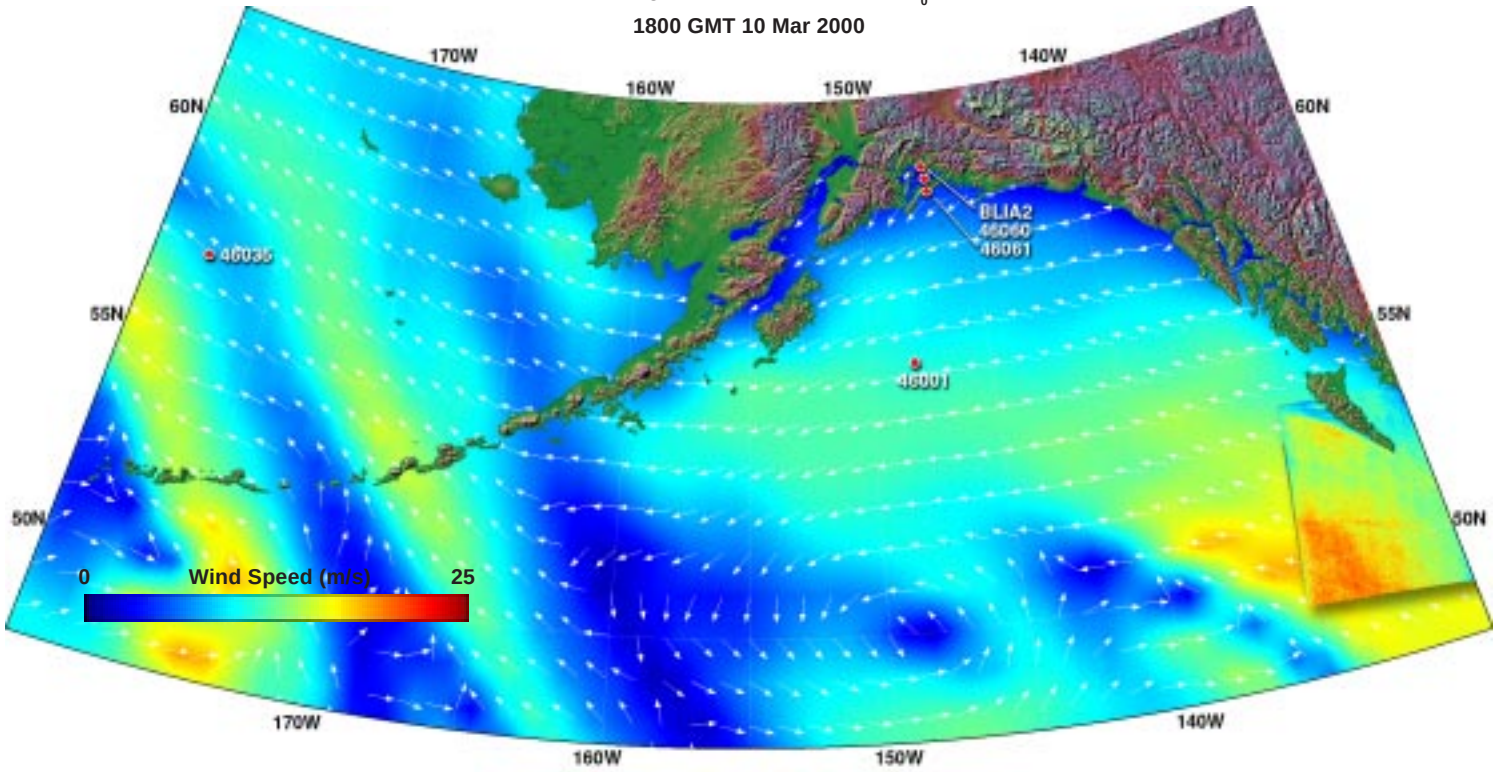

Model (this page): A weak low pressure system in the southern Gulf of Alaska, blocked by a strengthening ridge to the northeast, remains nearly stationary for 24 hrs prior to SAR overpass time (1-4). Model winds in the high gradient region just seaward of the Queen Charlotte Islands reach 15 to 20 m/s (5, 9). Concurrent model waves are 5 to 6 m, actively growing (6, 7). The MABL under the SAR is slightly unstable (8).

SAR (facing page): The SAR winds (10, 11) in the mean are similar to those of the model. The point wake emanating from the southern tip of the Queen Charlotte Islands provides sheltering for several hundred km downwind. Within the sheltered region, the mean wind is reduced by about 10 m/s (12). [ref. section 2.2: point wakes.]

5. Surface Wind Field (m/s) ~ t_0

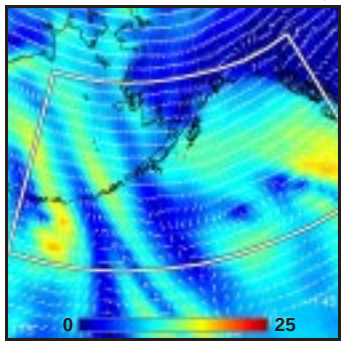

6. Surface Wave Height (m) ~ t_0

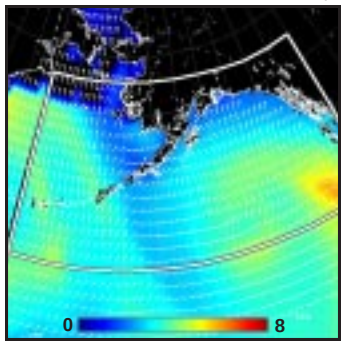

7. Inverse Wave Age (norm) ~ t_0

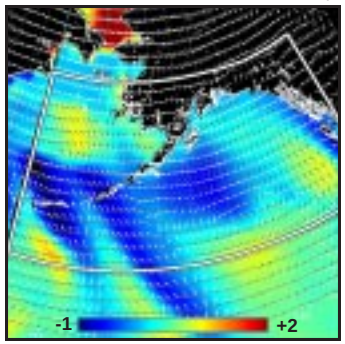

8. Air-Sea Temperature (˚C) ~ t_0

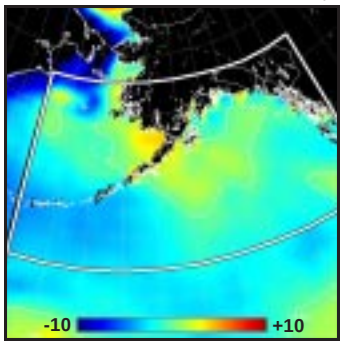

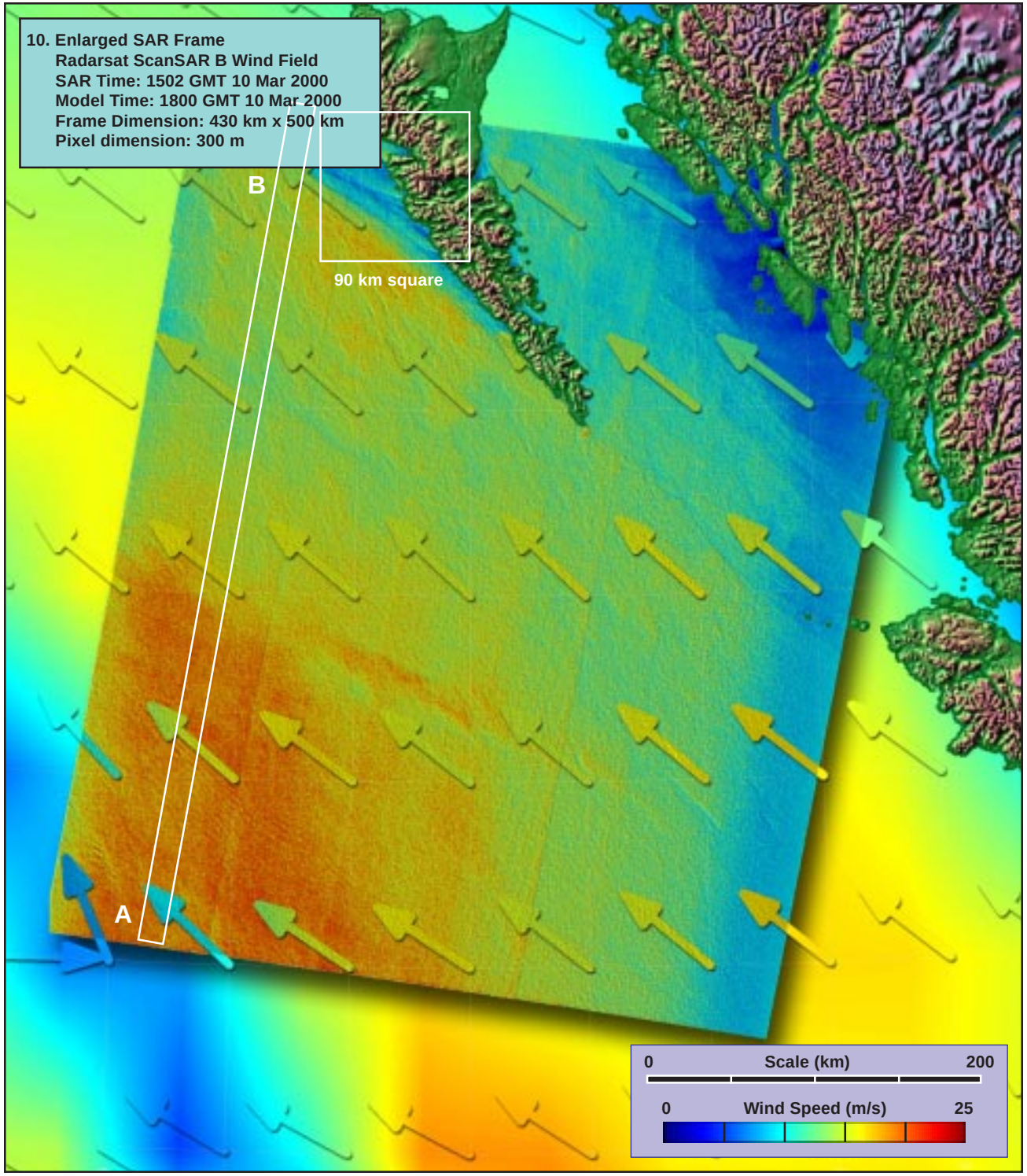

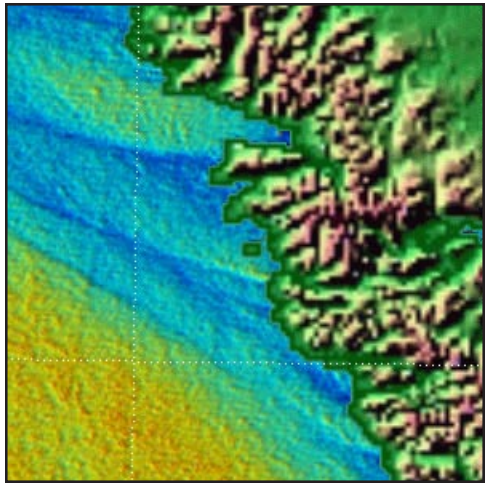

90 km square

11. Enlargement of Point Wake Detail (x 2.5)

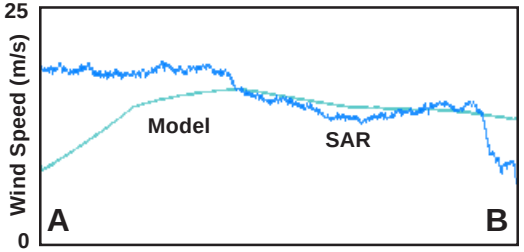

12. Model vs SAR Wind Profile along Line AB

1. Surface Pressure (mb) ~ t_0-36h

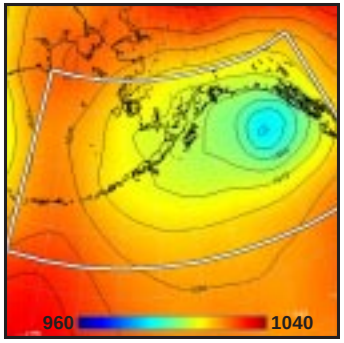

2. Surface Pressure (mb) ~ t_0-24h

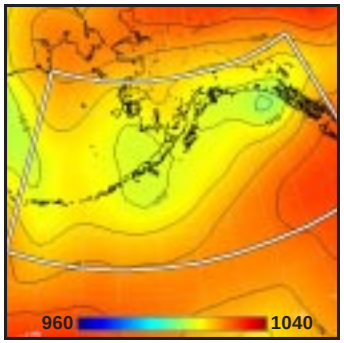

3. Surface Pressure (mb) ~ t_0-12h

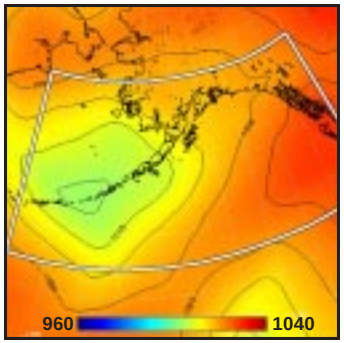

4. Surface Pressure (mb) ~ t_0

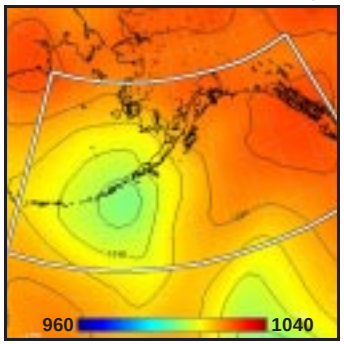

9. Enlarged Surface Wind Field ~ t_0

0600 GMT 09 Apr 2000

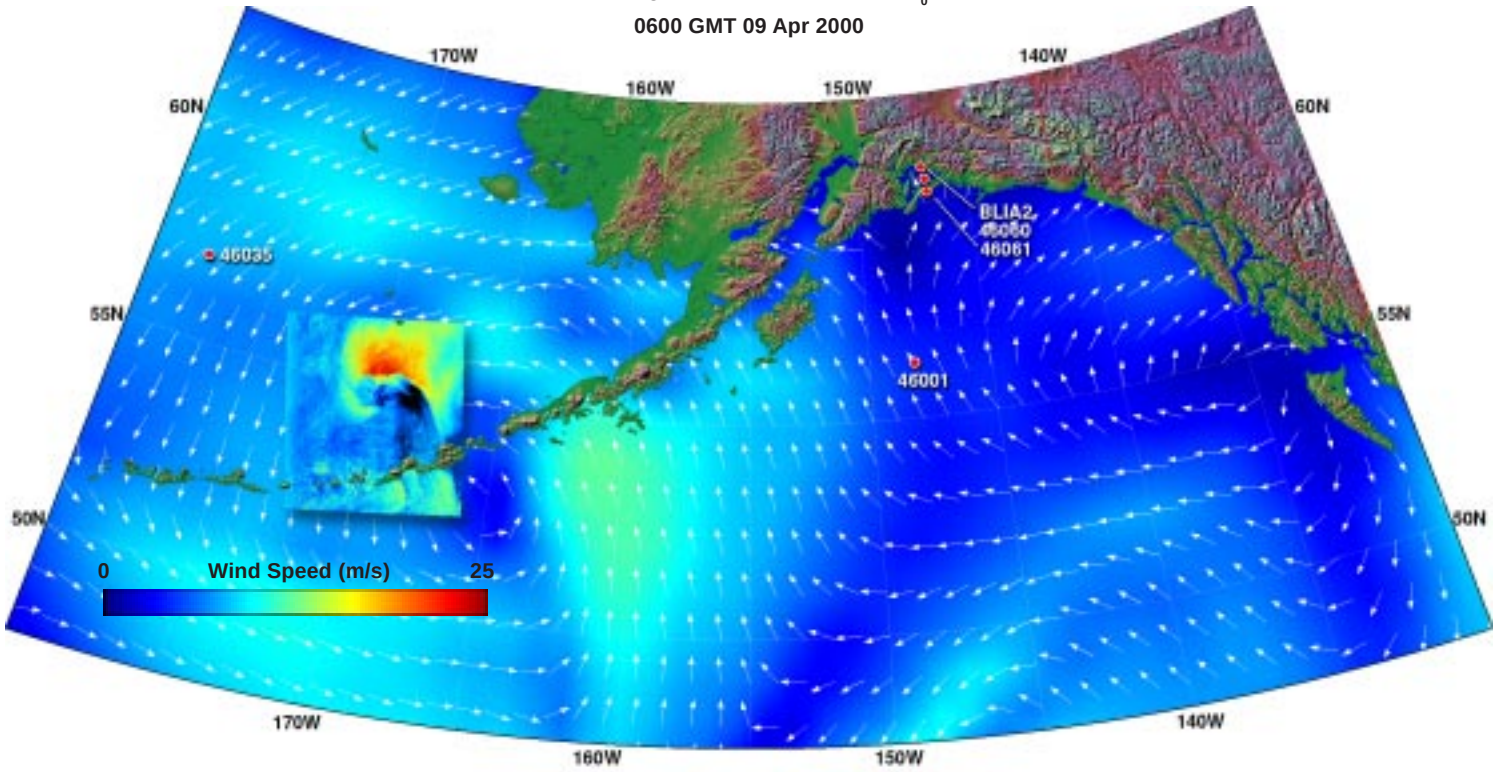

Model (this page): A weak, nearly symmetric low pressure system begins to form along the central Aleutians (1-4). Model winds are nearly circular around the center, with the strongest winds approaching 10 to 12 m/s in the eastern sector (5, 9) . Concurrent model waves are nearly uniform from the west at no more than 3 m (6, 7), and close to equilibrium. The MABL is extremely unstable, especially toward the northern end of the SAR pass (8).

SAR (facing page): The SAR winds (10, 11) capture the complex detail of a mesoscale low, evidently in an early stage of its development. Peak SAR winds just to the north of the developing storm center approach 20 m/s, about double the model estimate, even allowing for some displacement error in the model. The shear front seen by the SAR is extremely sharp, producing wind differentials of up to 20 m/s within a few km. [ref. section 2.9: mesoscale lows associated with cold air outbreaks.]

5. Surface Wind Field (m/s) ~ t_0

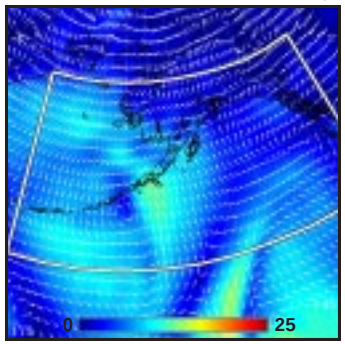

6. Surface Wave Height (m) ~ t_0

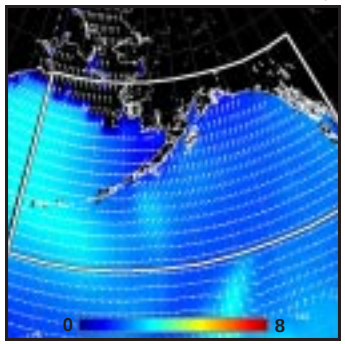

7. Inverse Wave Age (norm) ~ t_0

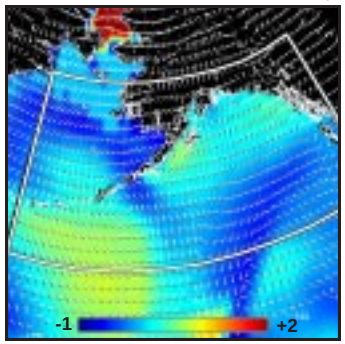

8. Air-Sea Temperature (˚C) ~ t_0

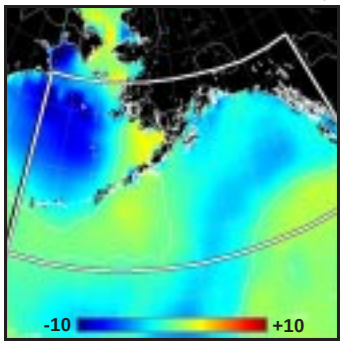

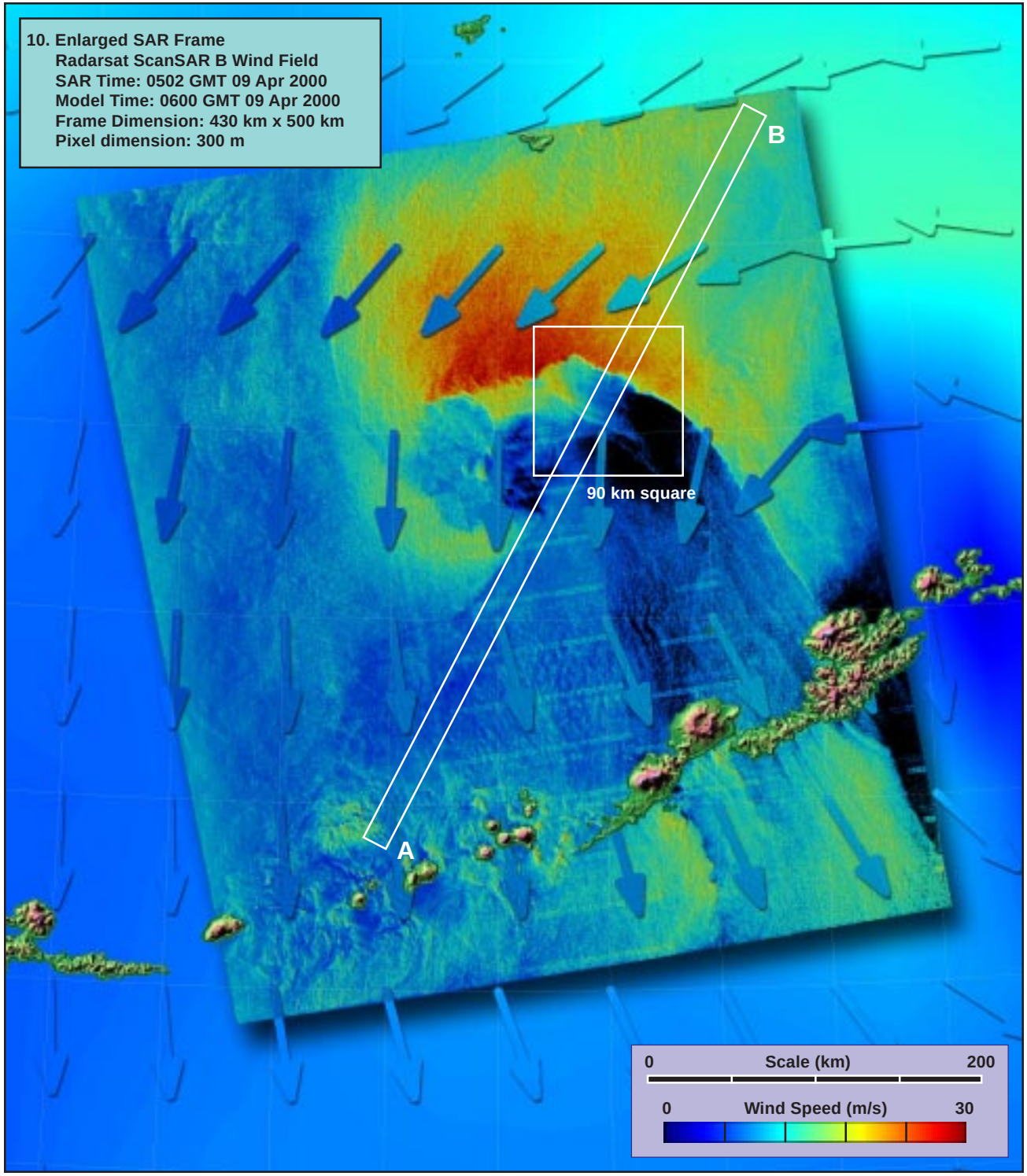

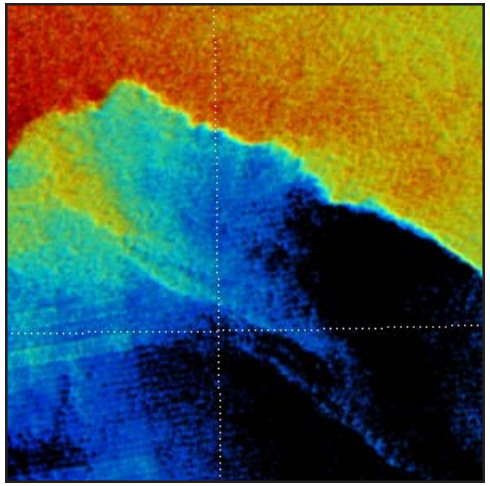

90 km square

11. Enlargement of Storm Front (x 2.5)

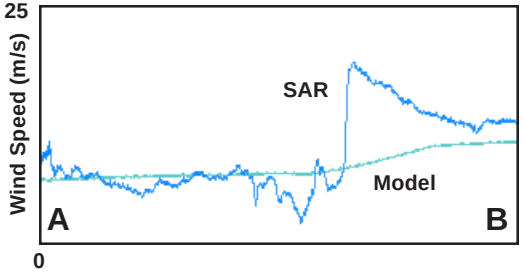

12. Model vs SAR Wind Profile along Line AB

1. Surface Pressure (mb) ~ t_0-36h

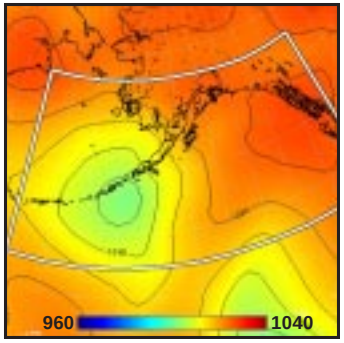

2. Surface Pressure (mb) ~ t_0-24h

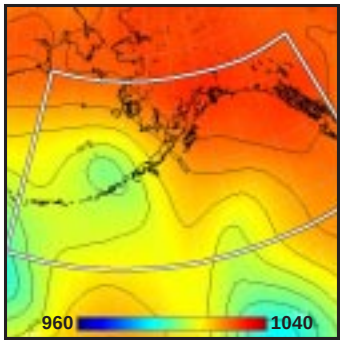

3. Surface Pressure (mb) ~ t_0-12h

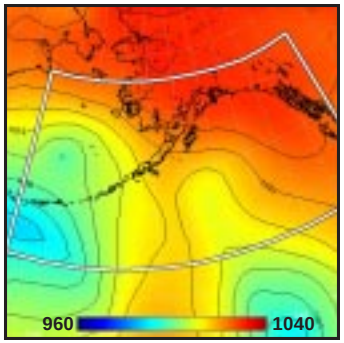

4. Surface Pressure (mb) ~ t_0

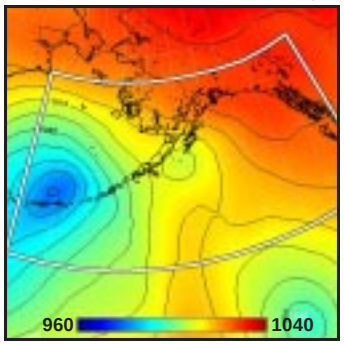

9. Enlarged Surface Wind Field ~ t_0

1800 GMT 10 Apr 2000

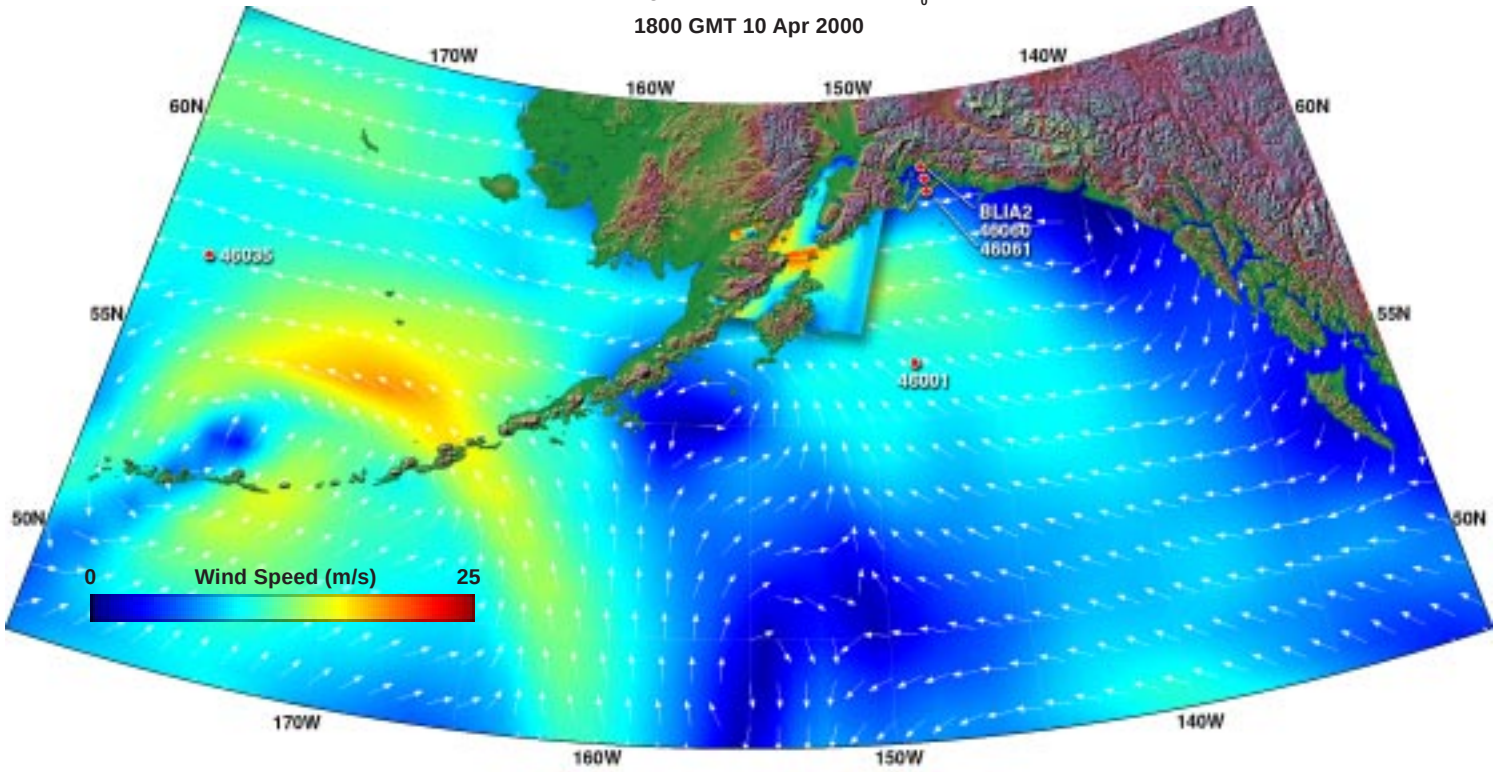

Model (this page): A diminishing low pressure system (1,2) yields to a stronger and deepening one (2-4) in the western Aleutians, the latter producing a concentrated arc of high winds to its northeast (5, 9), and the former producing a residual, more diffuse region of moderate winds in the northern Gulf of Alaska (5, 9). Southeasterly to easterly model winds within this region peaking at about 15 m/s converge on the topographical gap separating Kodiak Island from the Kenai Peninsula. Concurrent model waves are about 3 m, diminishing (6, 7). The MABL is neutral to slightly unstable (8).

SAR (facing page): The SAR winds (10, 11) show the focusing effect of the topographic gap, with peak winds approaching 20 m/s within and downstream of the gap (12), nearly double the model estimate within the gap region of influence. [ref. section 2.5.1: reverse gap flow.]

5. Surface Wind Field (m/s) ~ t_0

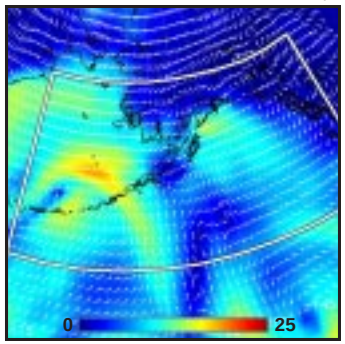

6. Surface Wave Height (m) ~ t_0

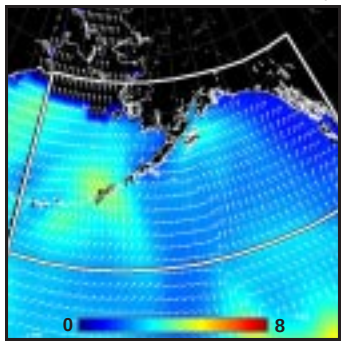

7. Inverse Wave Age (norm) ~ t_0

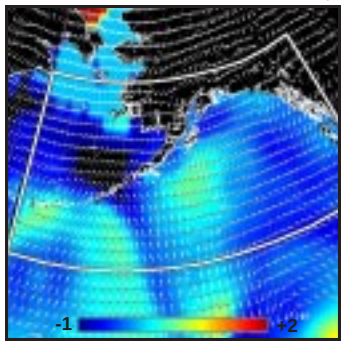

8. Air-Sea Temperature (˚C) ~ t_0

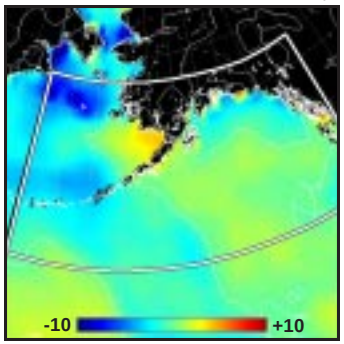

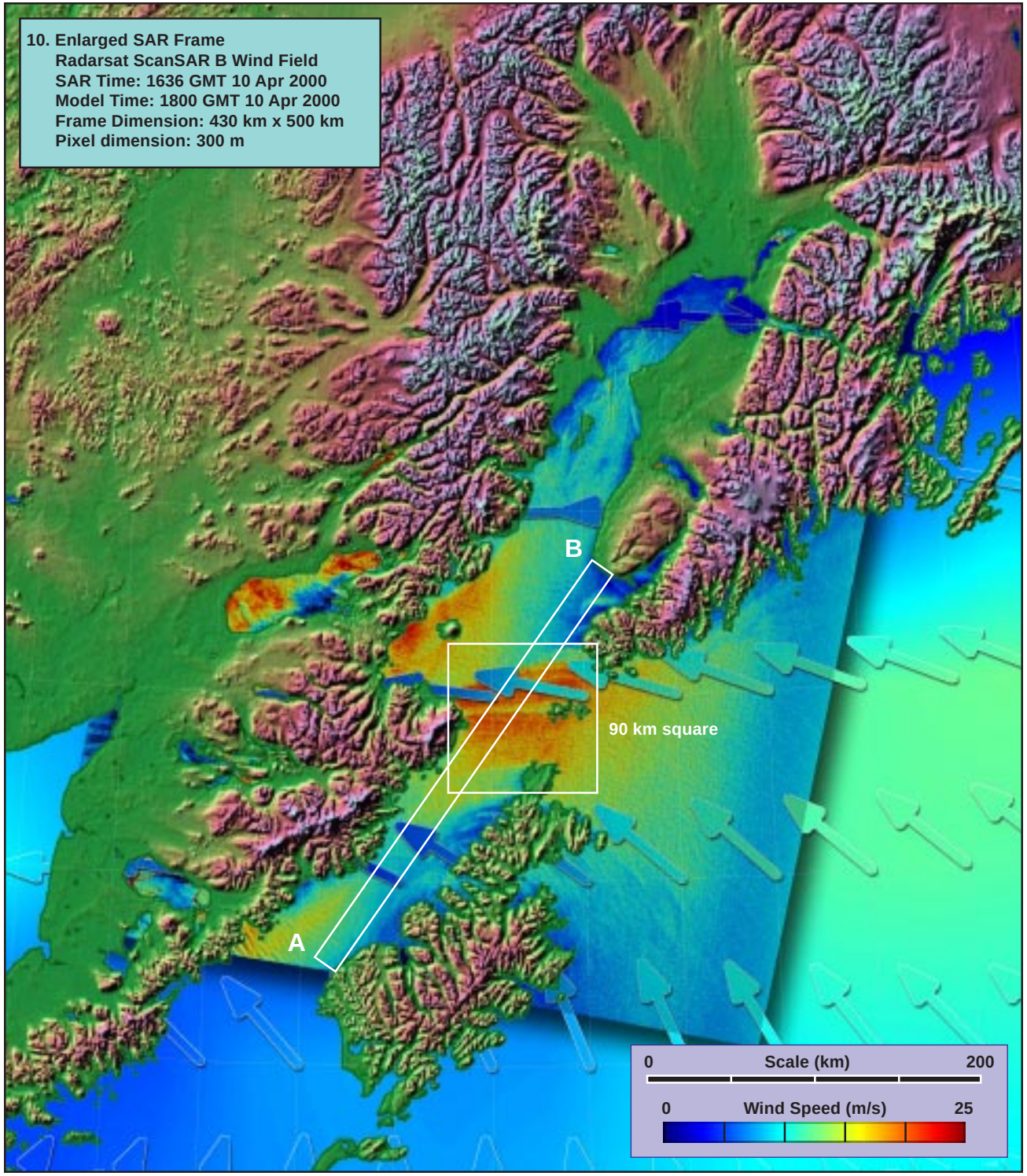

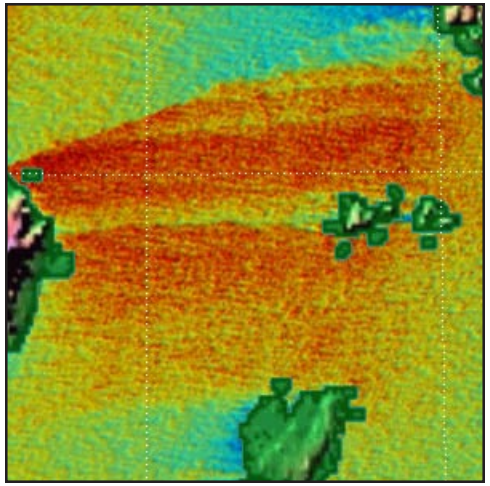

90 km square

11. Enlargement of Island Wakes (x 2.5)

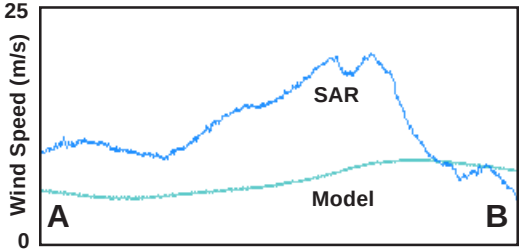

12. Model vs SAR Wind Profile along Line AB

1. Surface Pressure (mb) ~ t_0-36h

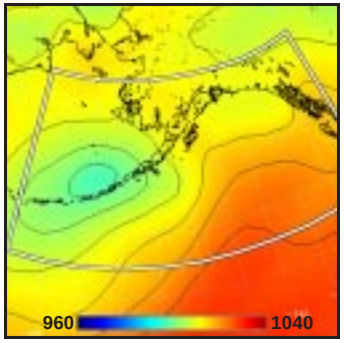

2. Surface Pressure (mb) ~ t_0-24h

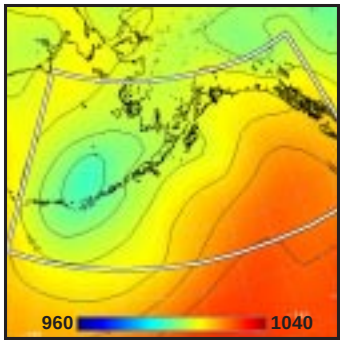

3. Surface Pressure (mb) ~ t_0-12h

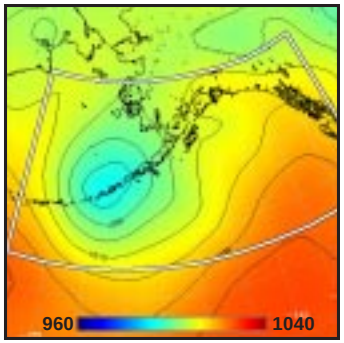

4. Surface Pressure (mb) ~ t_0

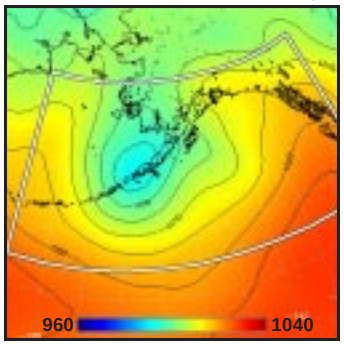

9. Enlarged Surface Wind Field ~ t_0

0600 GMT 19 Jun 2000

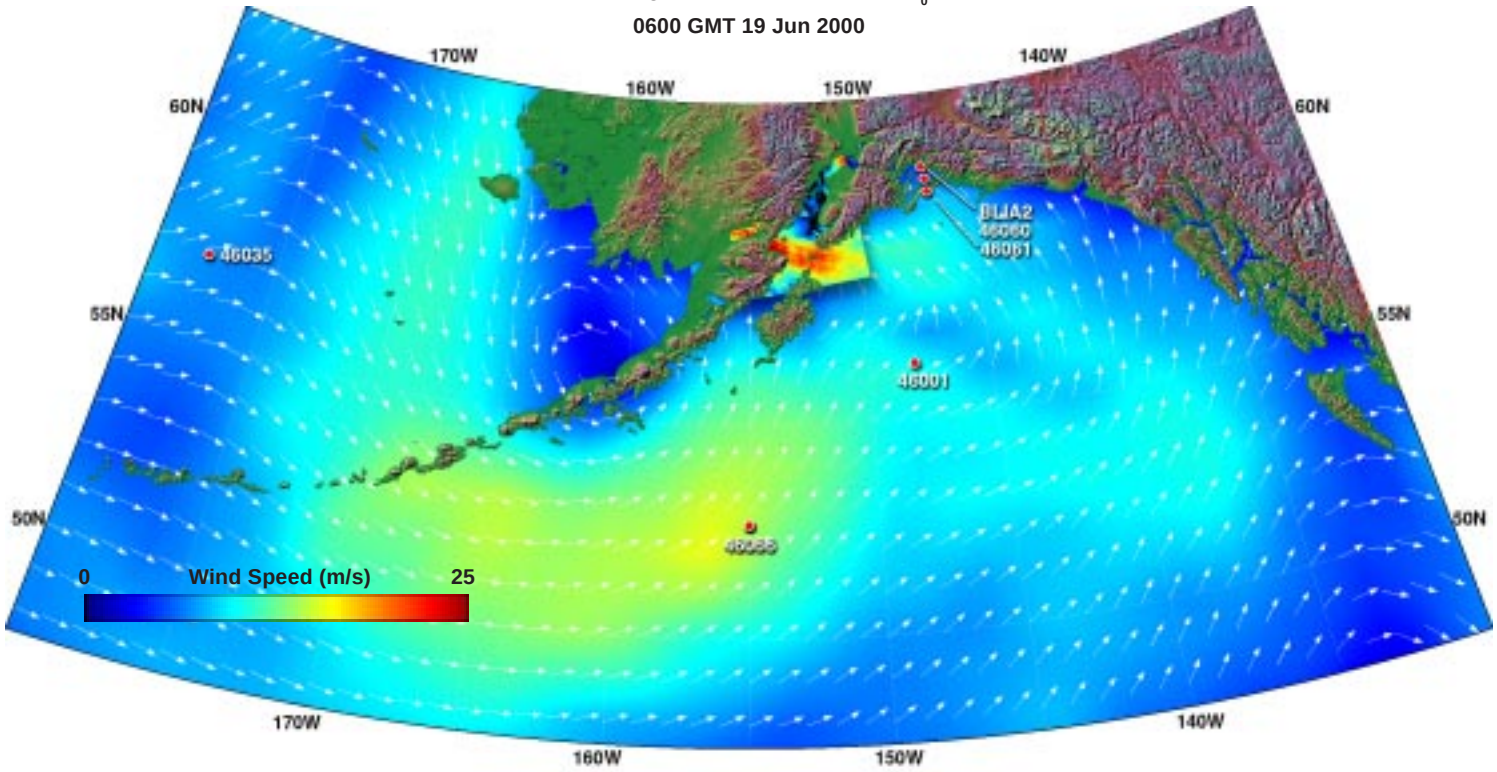

Model (this page): Similar to the 10 April 2000 conditions, a deepening low pressure system in the central Aleutians (1-4) produces a moderate southeasterly wind flow in the eastern Gulf of Alaska. Model winds (5, 9) show a local maximum of 10 to 15 m/s in the topographical gap north of Kodiak Island. Concurrent model waves (6, 7) are nearly crosswind, and close to equilibrium. The MABL is nearly neutral in the vicinity of the gap (8).

SAR (facing page): As in 10 April 2000, the SAR winds (10, 11) exceed those of the model by at least a factor of two within the gap region of influence. In this case, the focusing effect of the gap extends well downwind and across Iliamna Lake to the west. The peak model wind estimates of 5 to 10 m/s are estimated by the SAR at 20 m/s or greater. [ref. section 2.5.1: reverse gap flow.]

5. Surface Wind Field (m/s) ~ t_0

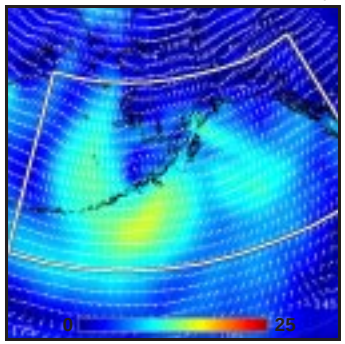

6. Surface Wave Height (m) ~ t_0

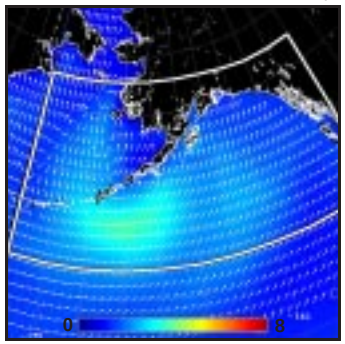

7. Inverse Wave Age (norm) ~ t_0

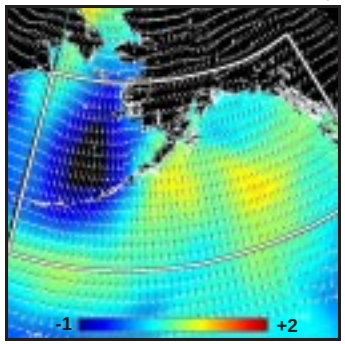

8. Air-Sea Temperature (˚C) ~ t_0

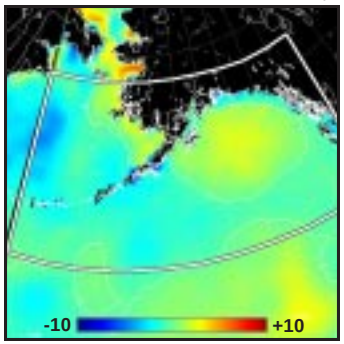

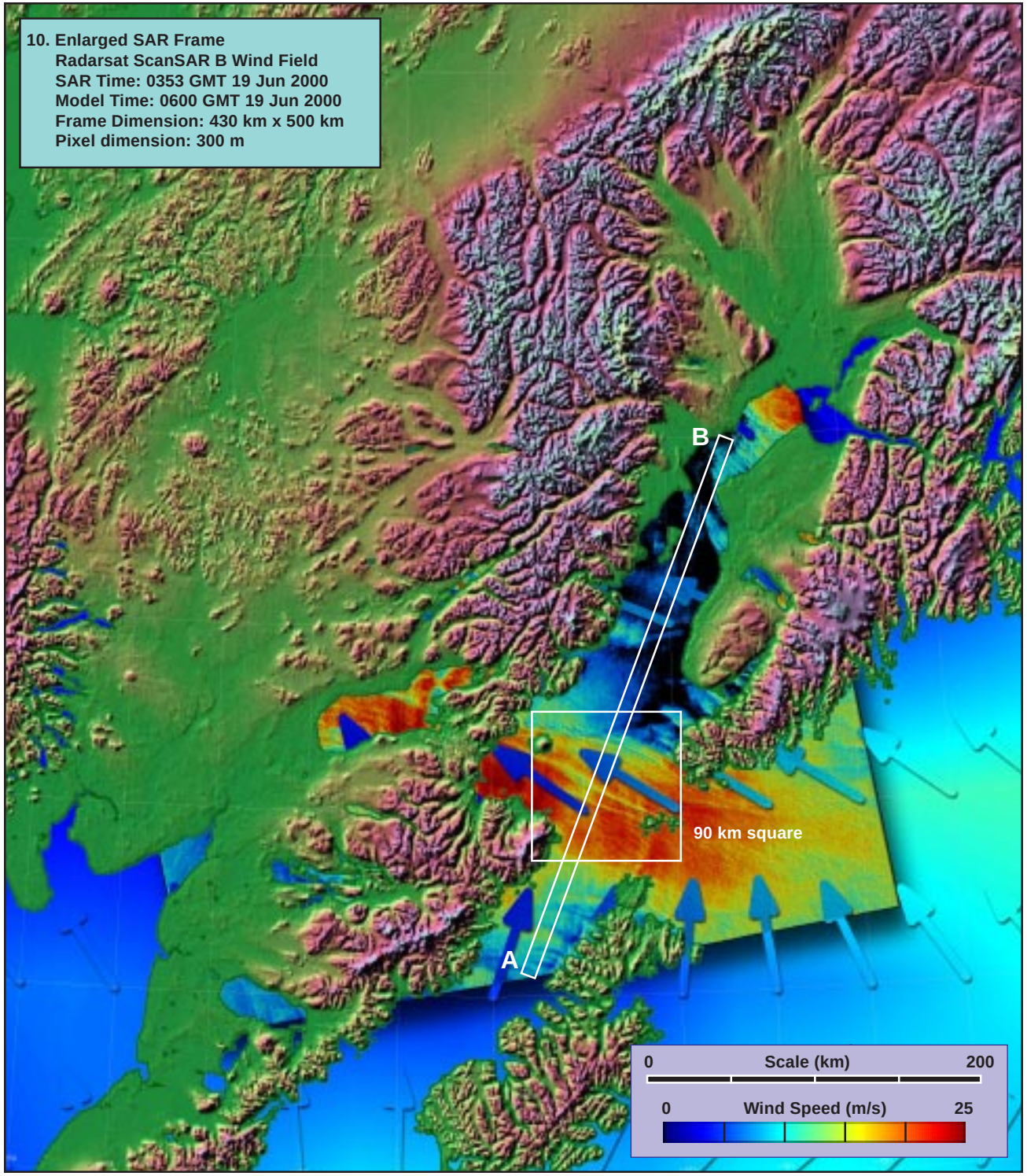

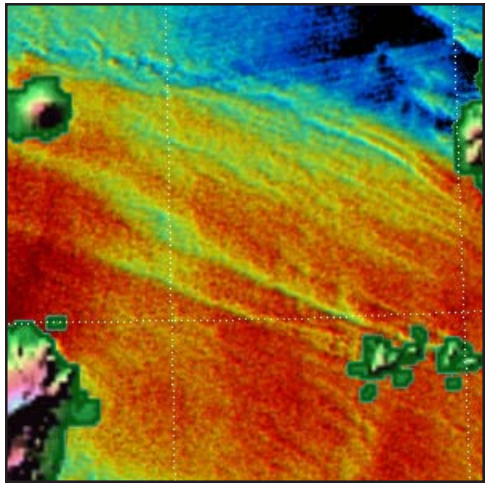

90 km square

11. Enlargement of Island Wakes (x 2.5)

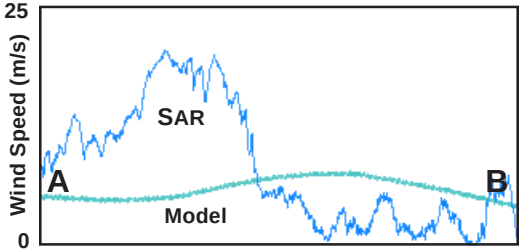

12. Model vs SAR Wind Profile along Line AB

1. Surface Pressure (mb) ~ t_0-36h

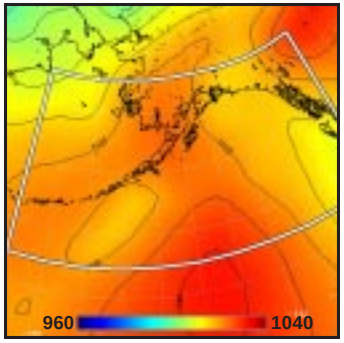

2. Surface Pressure (mb) ~ t_0-24h

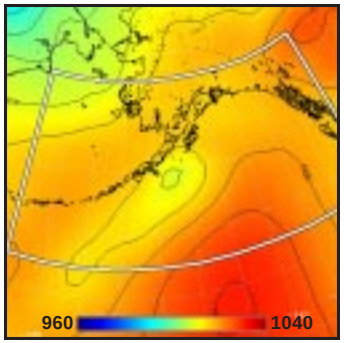

3. Surface Pressure (mb) ~ t_0-12h

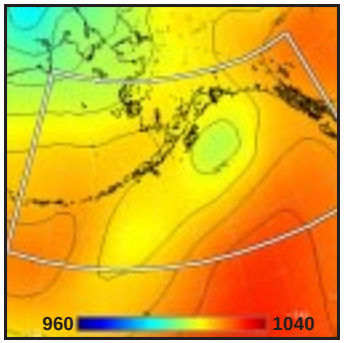

4. Surface Pressure (mb) ~ t_0

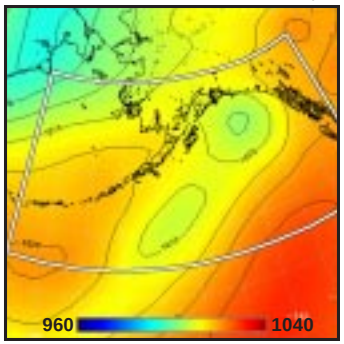

9. Enlarged Surface Wind Field ~ t_0

0600 GMT 04 Sep 2000

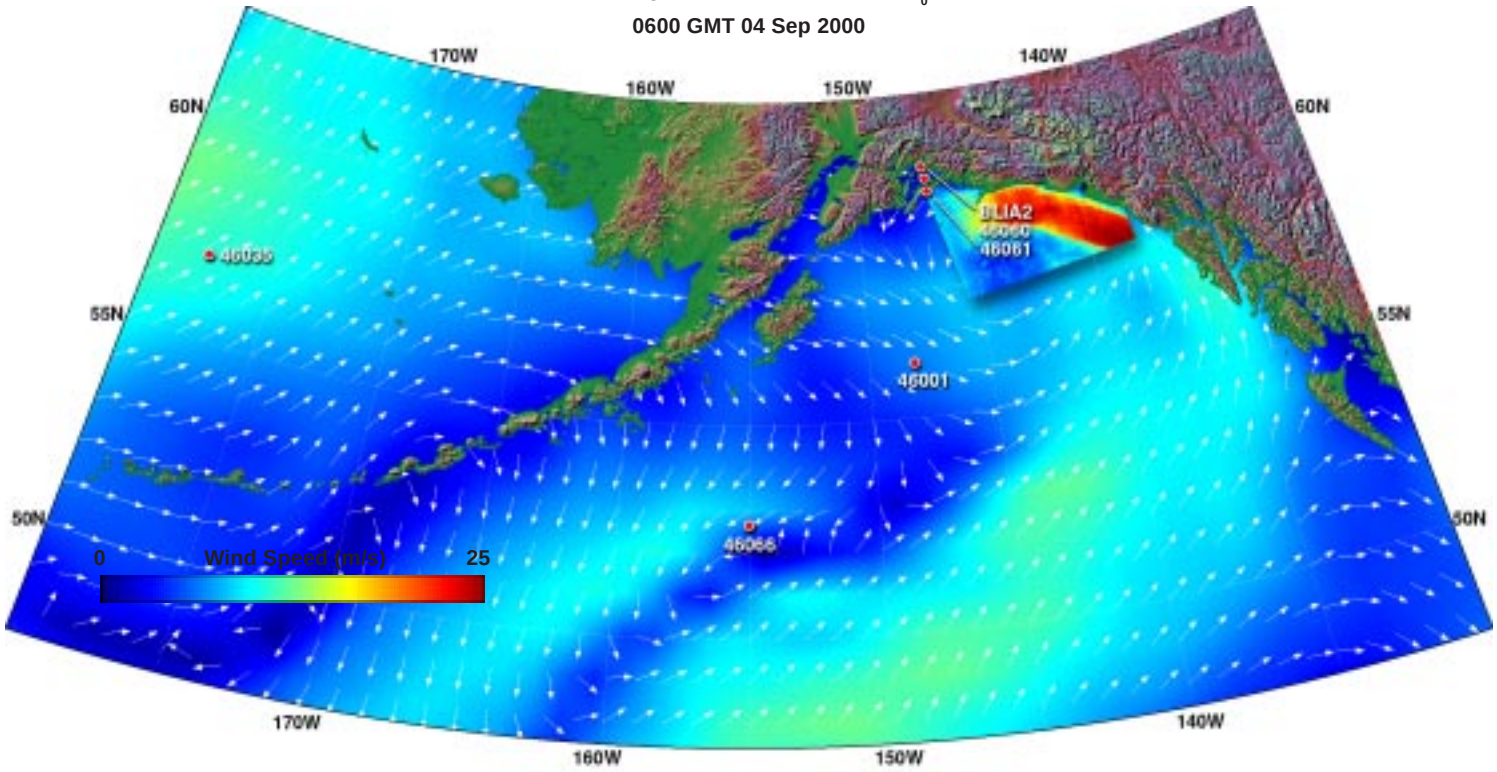

Model (this page): A pair of weak low pressure centers develop along a trough just to the east of the Aleutian Chain (1-4). The stronger and more northerly of the two, located in the northern Gulf of Alaska, induces a broad band of higher winds to its north and east, peaking at 10 to 15 m/s (5, 9). Concurrent model waves (6, 7) peak at about 3 m, actively growing in the south, but still diminishing along the coast, within the SAR pass. The MABL all along the northern Gulf Coast is unstable (8).

SAR (facing page): The strong tangential flow along the coast just to the north of the storm center is revealed by the SAR winds (10, 11) as a barrier jet, with a strong southern frontal boundary, and a wind band within 100 km of the coast peaking at nearly 25 m/s, more than twice the model estimate (12). Within the jet, especially along its southern boundary, trains of shear-induced atmospheric gravity waves appear. [ref. section 2.11: coastal barrier jets.]

5. Surface Wind Field (m/s) ~ t_0

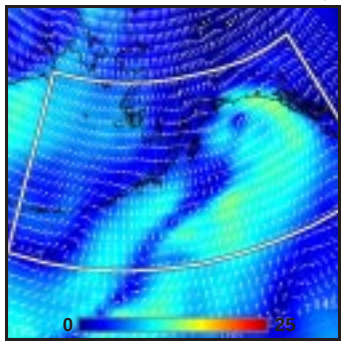

6. Surface Wave Height (m) ~ t_0

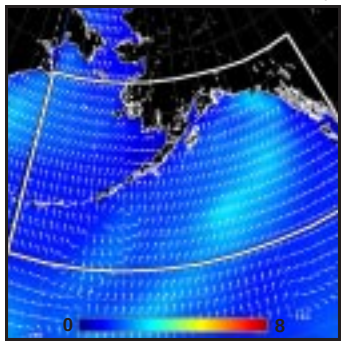

7. Inverse Wave Age (norm) ~ t_0

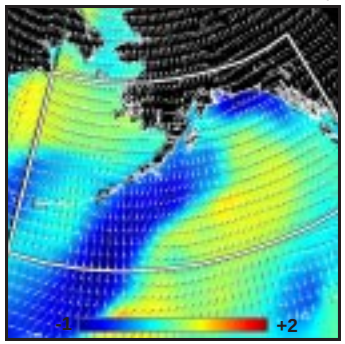

8. Air-Sea Temperature (˚C) ~ t_0

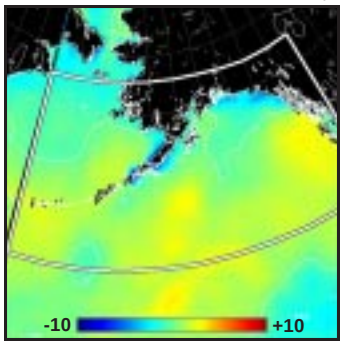

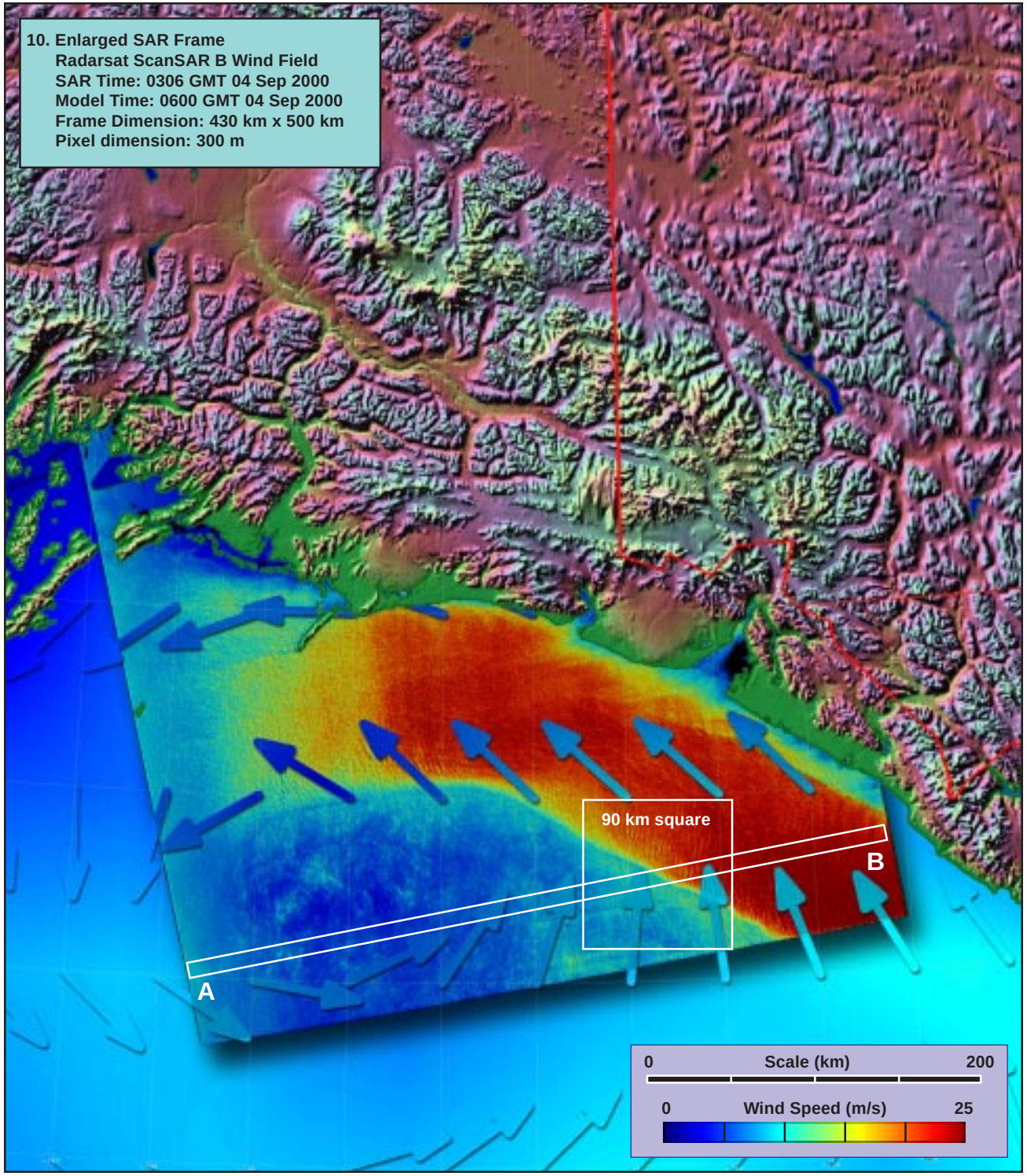

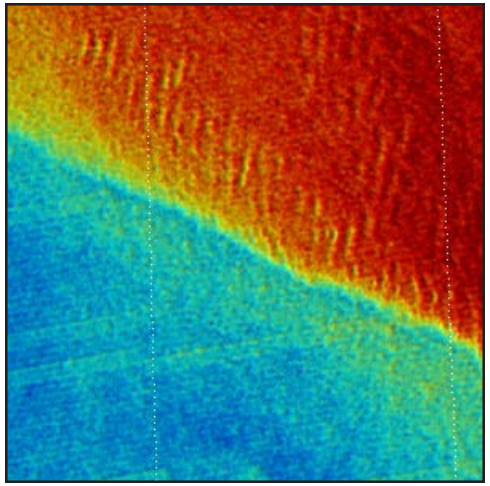

90 km square

11. Enlargement of Frontal Boundary (x 2.5)

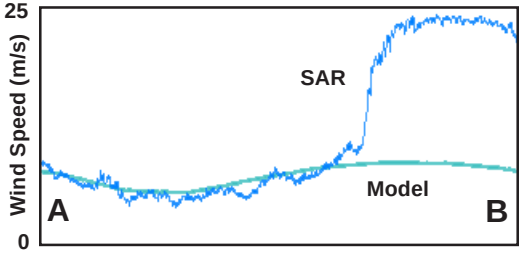

12. Model vs SAR Wind Profile along Line AB

1. Surface Pressure (mb) ~ t_0-36h

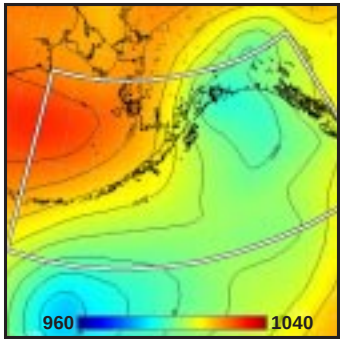

2. Surface Pressure (mb) ~ t_0-24h

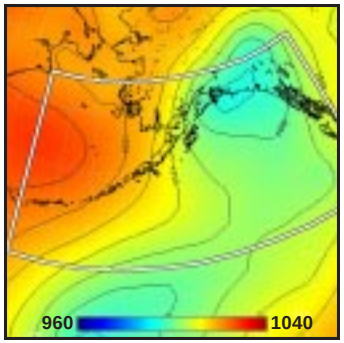

3. Surface Pressure (mb) ~ t_0-12h

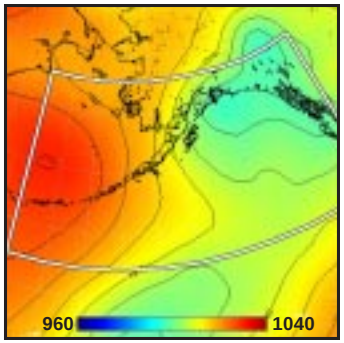

4. Surface Pressure (mb) ~ t_0

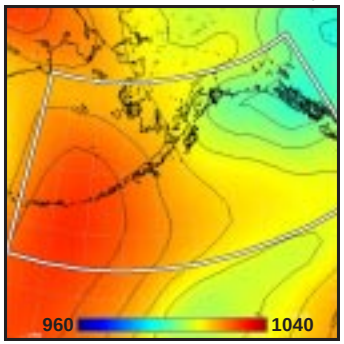

9. Enlarged Surface Wind Field ~ t_0

0600 GMT 30 Sep 2000

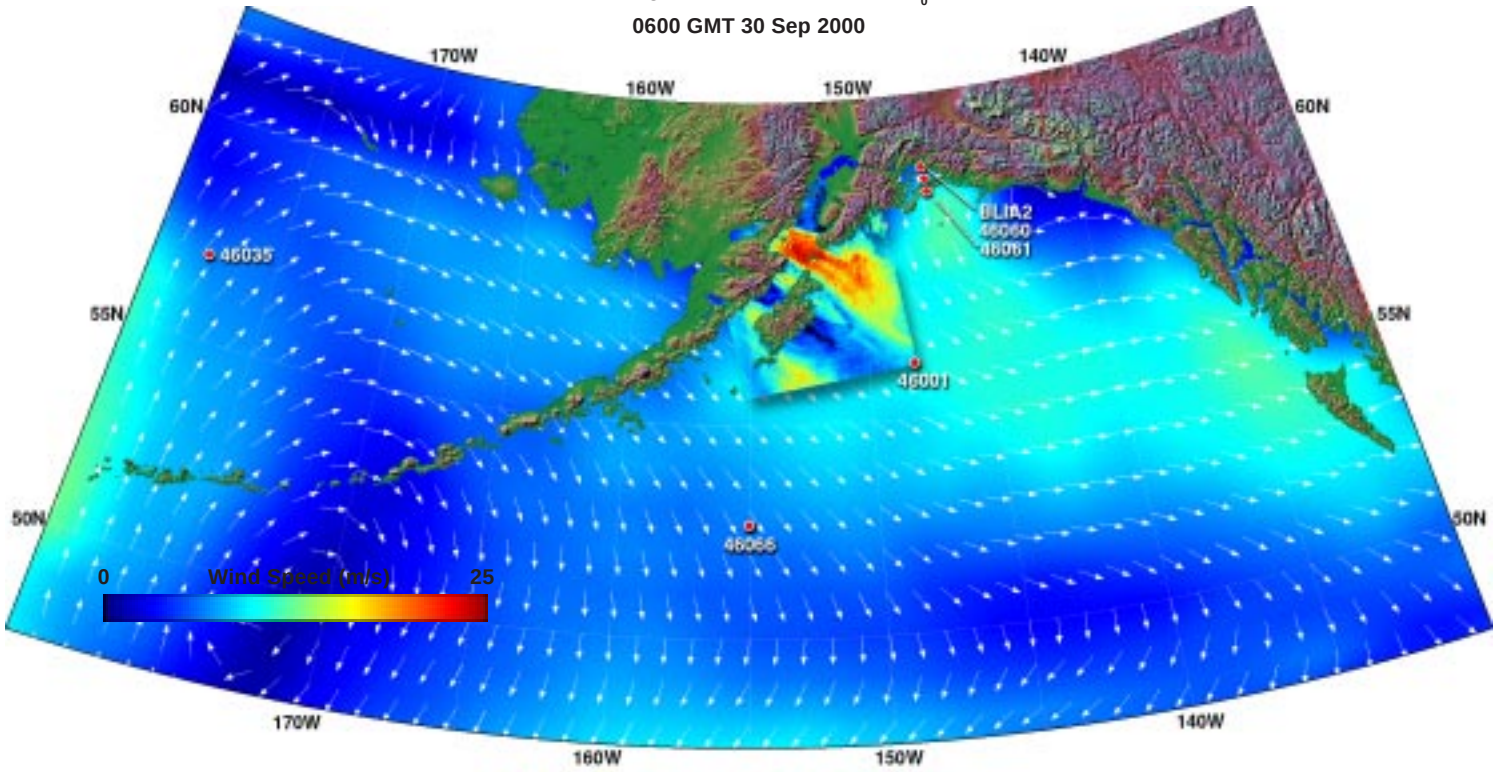

Model (this page): A receding low pressure system in the northern Gulf of Alaska coupled with an advancing high pressure system to its southwest produces a broad region of moderate northwesterly winds (1-4). Model wind estimates in the gap just north of Kodiak Island are 10 to 15 m/s (5, 9). Concurrent model waves are less than 2 m (6), nearly opposing the wind, and rapidly decaying (7). The MABL is unstable in the vicinity of the gap (8).

SAR (facing page): The SAR winds in the gap just north and east of Kodiak Island approach 25 m/s (10, 11, 12), roughly double the model estimates, and are heavily modulated by both mountain lee waves and island and mountain wakes. Some of the island wakes are still visible as much as 150 km downwind. [ref. sections 2.1: island and mountain wakes, 2.3: mountain lee waves, 2.4: gap flows.]

5. Surface Wind Field (m/s) ~ t_0

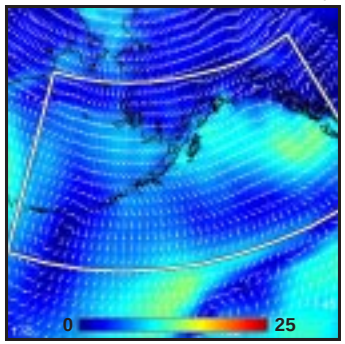

6. Surface Wave Height (m) ~ t_0

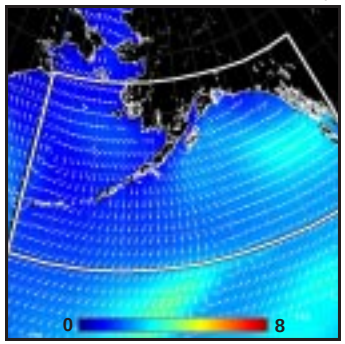

7. Inverse Wave Age (norm) ~ t_0

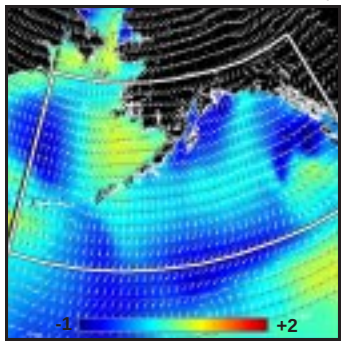

8. Air-Sea Temperature (˚C) ~ t_0

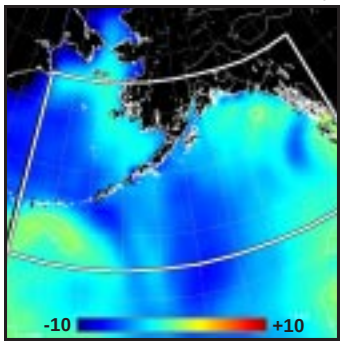

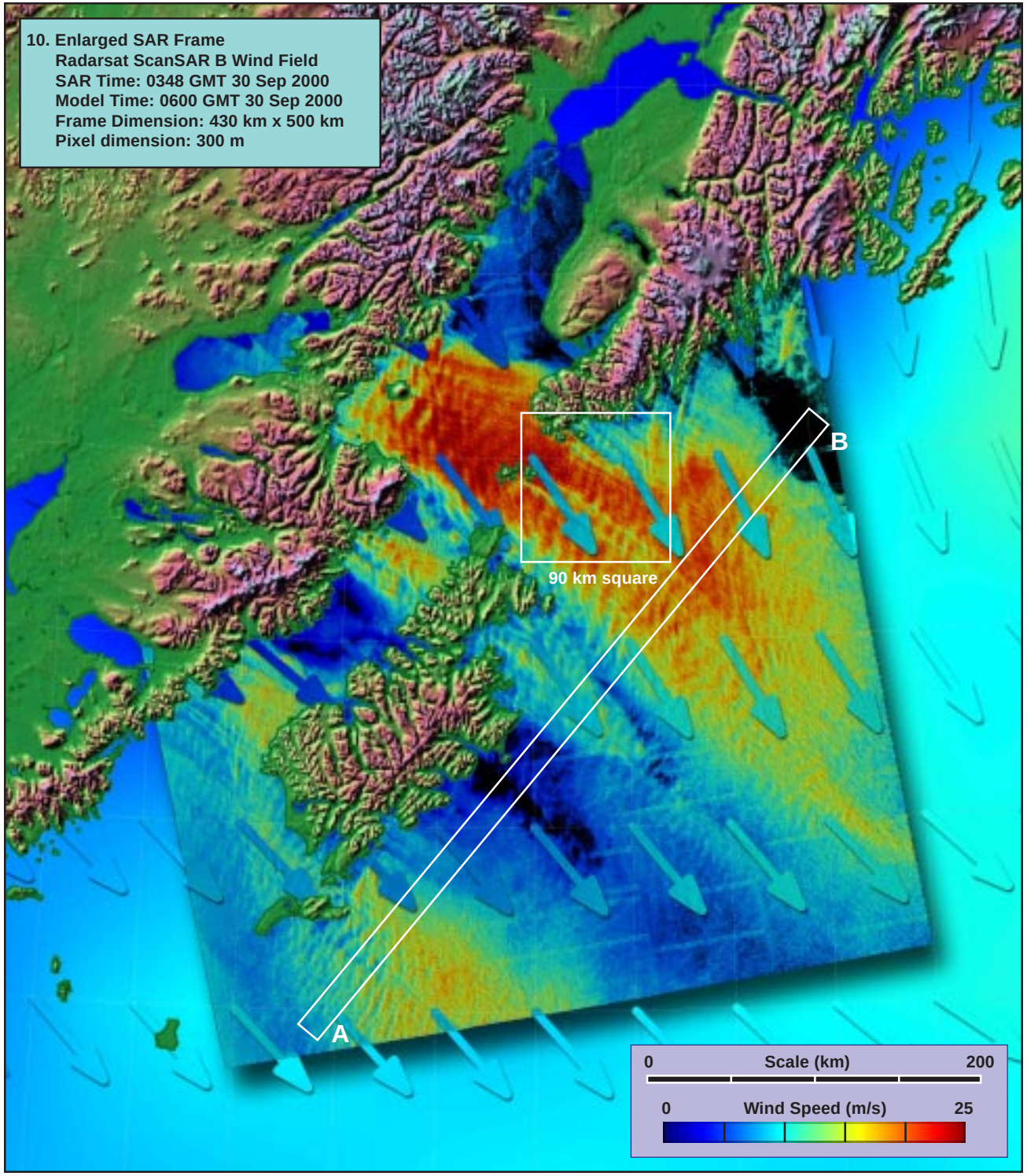

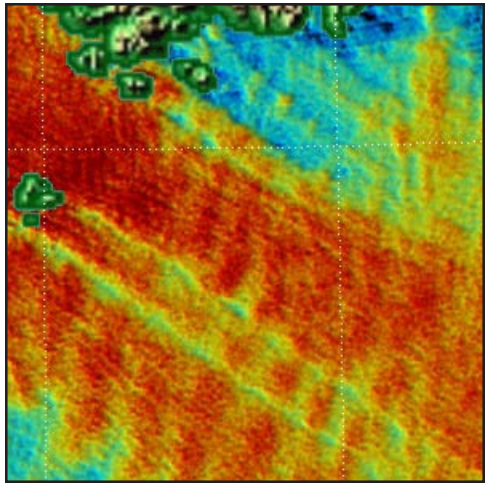

90 km square

11. Enlargement of Island Wakes (x 2.5)

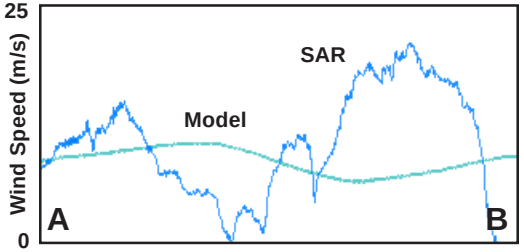

12. Model vs SAR Wind Profile along Line AB

1. Surface Pressure (mb) ~ t_0-36h

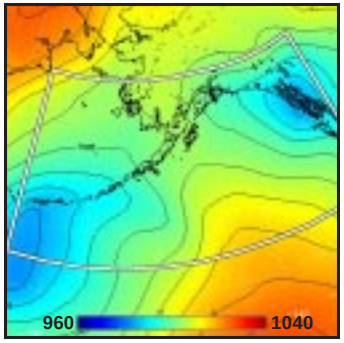

2. Surface Pressure (mb) ~ t_0-24h

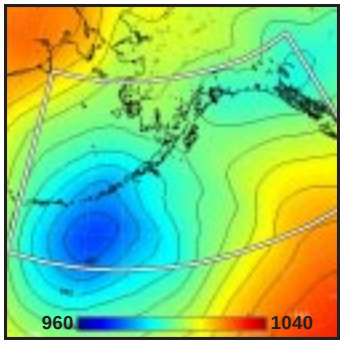

3. Surface Pressure (mb) ~ t_0-12h

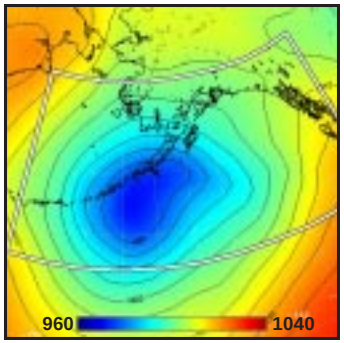

4. Surface Pressure (mb) ~ t_0

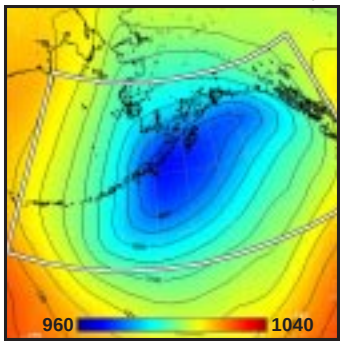

9. Enlarged Surface Wind Field ~ t_0

0600 GMT 22 Oct 2000

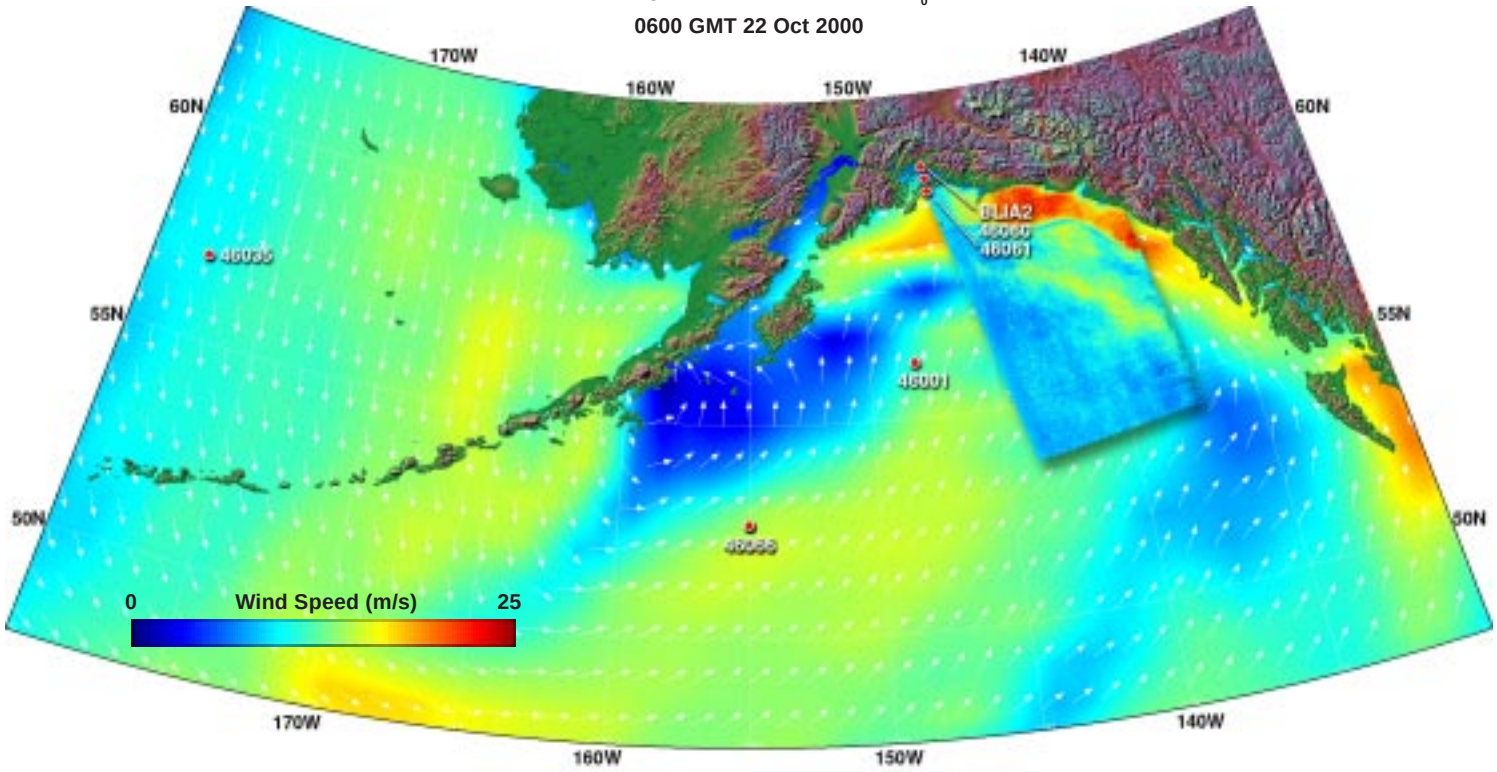

Model (this page): A rapidly deepening low pressure system moves up the Aleutian Chain (1-4), generating a long arc of counterclockwise winds along the southern Alaskan coast. Model winds (5, 9) along the coast reach 20 to 25 m/s, and take the form of a well defined barrier jet. Concurrent model waves are only 2 to 3 m, crosswind from the south, and decaying (6, 7). The MABL is slightly unstable along the coast (8).

SAR (facing page): The SAR winds (10, 11) clearly show a coastal barrier jet. In this case, the SAR and model winds are in reasonable agreement, with maximum winds from both about 20 m/s (12). The SAR, however, indicates two additional features absent from the model: the regular patterns of atmospheric waves especially evident within the region of maximum winds, and the narrow (5 to 10 km wide) band of low (5-10 m/s) winds immediately seaward of the jet boundary. This "low wind band" may be a limitation of the SAR wind algorithm, resulting from an (unmodeled) discontinuity in the wind direction at the jet boundary. [ref. section 2.11: coastal barrier jets.]

5. Surface Wind Field (m/s) ~ t_0

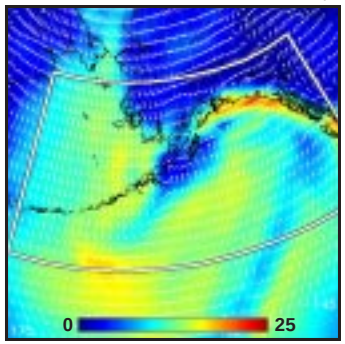

6. Surface Wave Height (m) ~ t_0

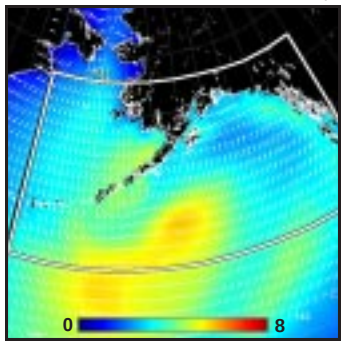

7. Inverse Wave Age (norm) ~ t_0

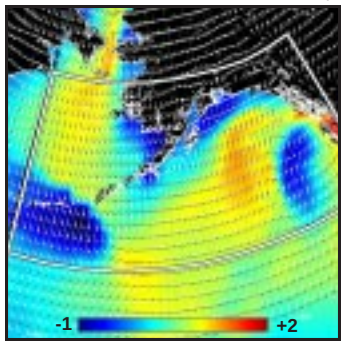

8. Air-Sea Temperature (˚C) ~ t_0

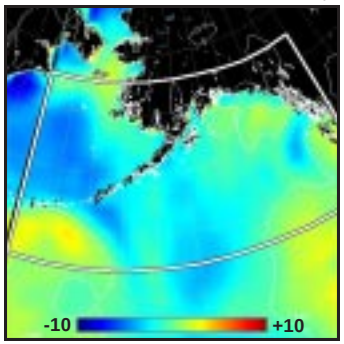

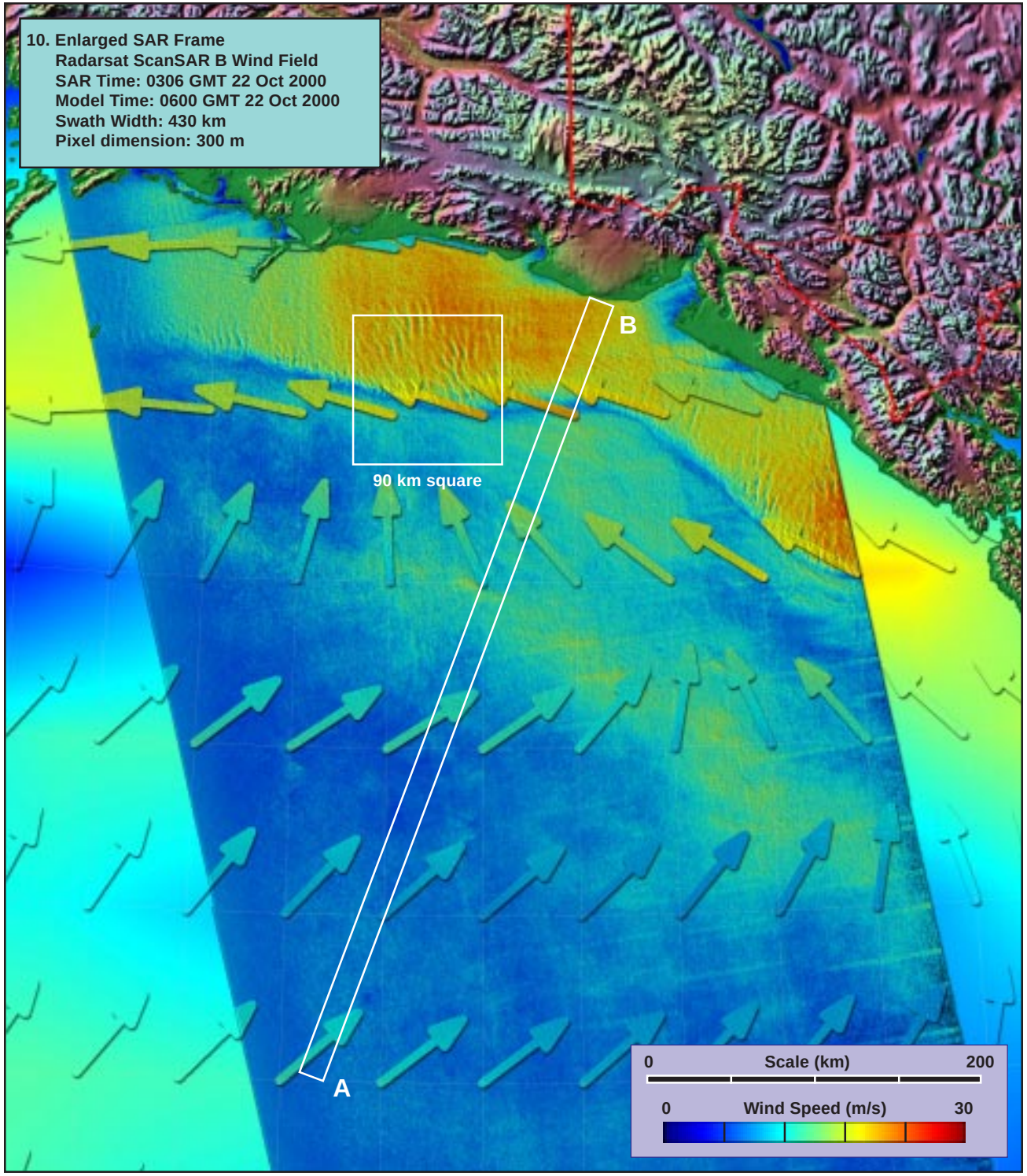

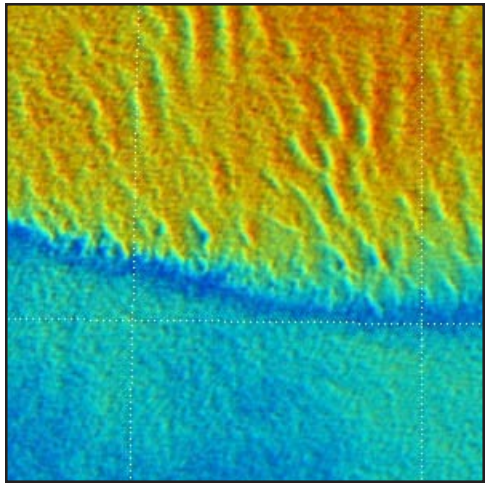

90 km square

11. Enlargement of Gravity Waves (x 2.5)

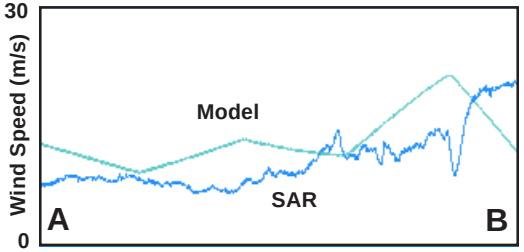

12. Model vs SAR Wind Profile along Line AB

1. Surface Pressure (mb) ~ t_0-36h

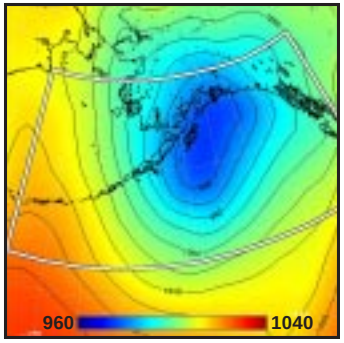

2. Surface Pressure (mb) ~ t_0-24h

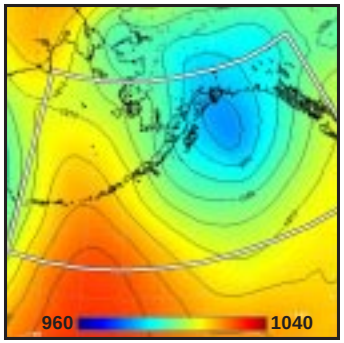

3. Surface Pressure (mb) ~ t_0-12h

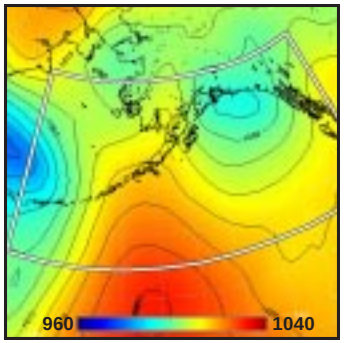

4. Surface Pressure (mb) ~ t_0

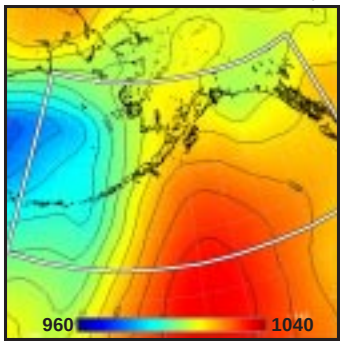

9. Enlarged Surface Wind Field ~ t_0

0600 GMT 24 Oct 2000

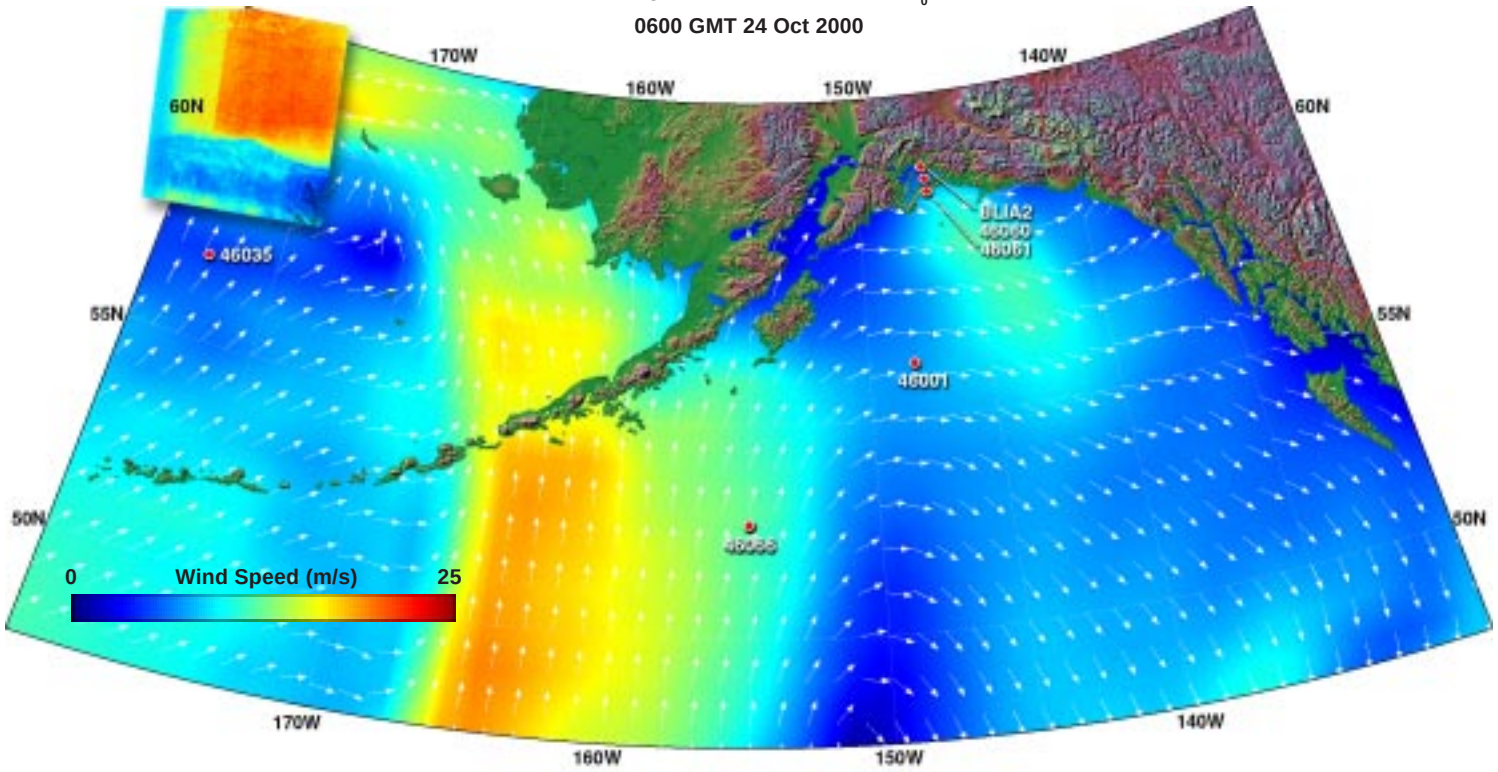

Model (this page): As one low pressure system in the northern Gulf of Alaska diminishes, a second approaches and deepens in the Bering Sea to the west (1-4) . Model winds from this second system form a huge arc extending from well south of the Aleutian Chain north and west through the Bering Sea (5, 9). Model winds in the northernmost portion of the arc approach 20 m/s. Concurrent model waves in the north are 5 to 8 m, actively growing (6, 7). The MABL under the SAR pass is unstable to the west, stable to the east (8).

SAR (facing page): The SAR winds (10, 11) reveal a sharp east-west zone of transition, in remarkable agreement with the model. Peak SAR winds are about 25 m/s, slightly higher than those of the model. A nearly continuous region of atmospheric gravity waves is evident all along the high wind side of the front. [ref. section 2.6: synoptic fronts.] The SAR antenna beam effect is quite evident in the western third of the pass (12). There is a strong suggestion here that the SAR estimates are high by ~5 m/s in the eastern (higher incidence angles) side of the swath, and low by 5 to 10 m/s in the western (lower incidence angles).

5. Surface Wind Field (m/s) ~ t_0

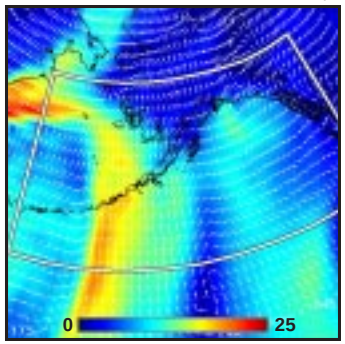

6. Surface Wave Height (m) ~ t_0

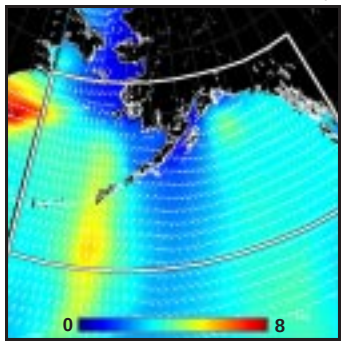

7. Inverse Wave Age (norm) ~ t_0

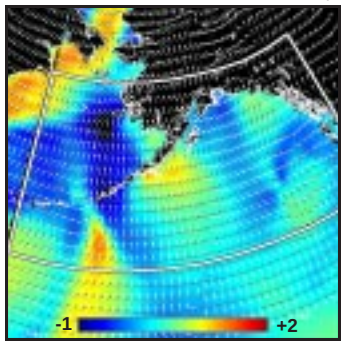

8. Air-Sea Temperature (˚C) ~ t_0

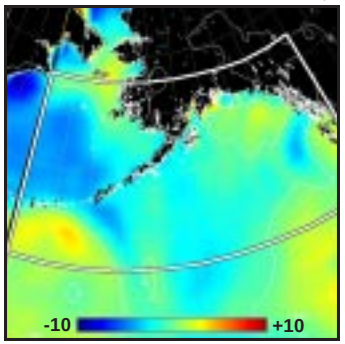

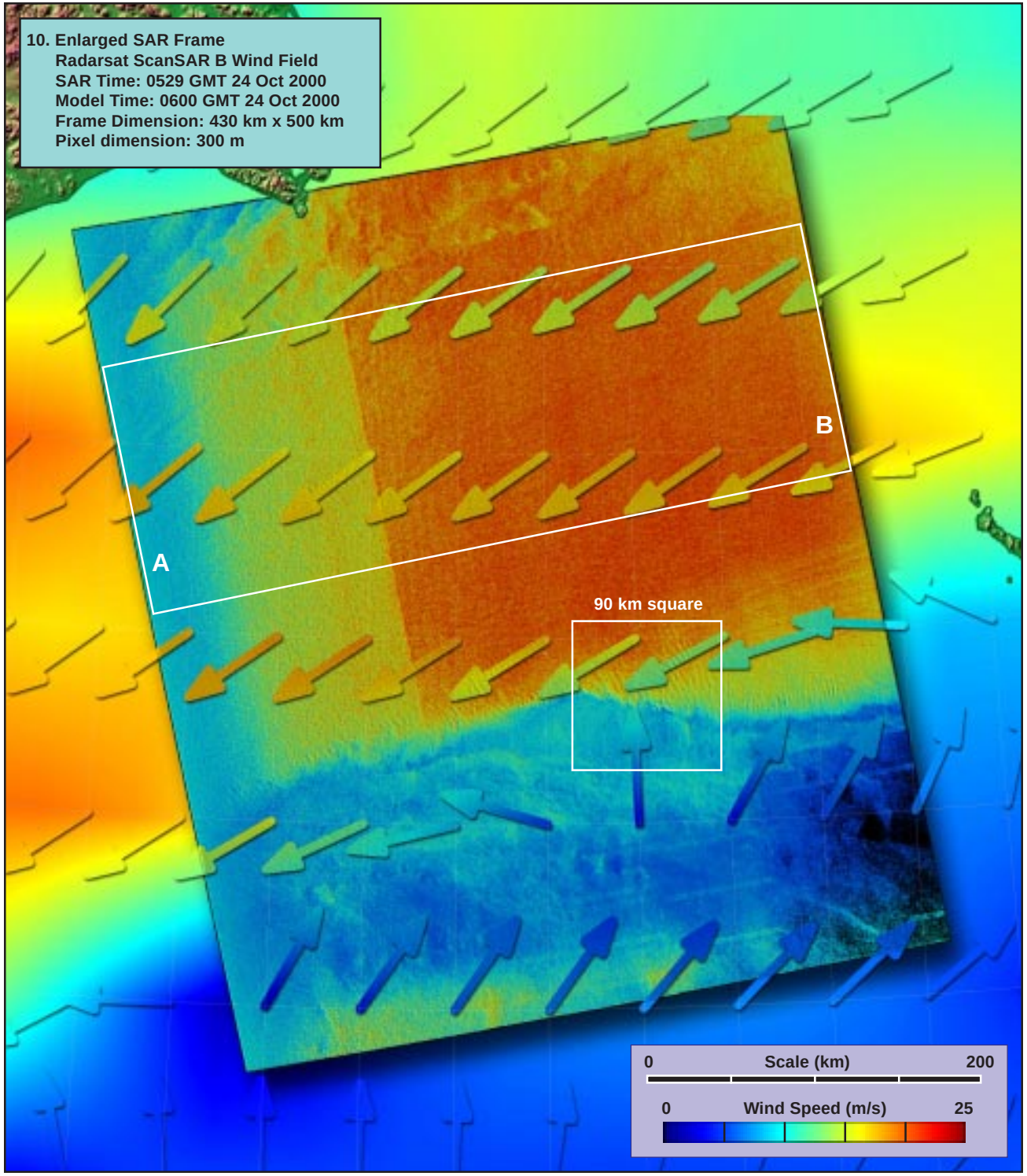

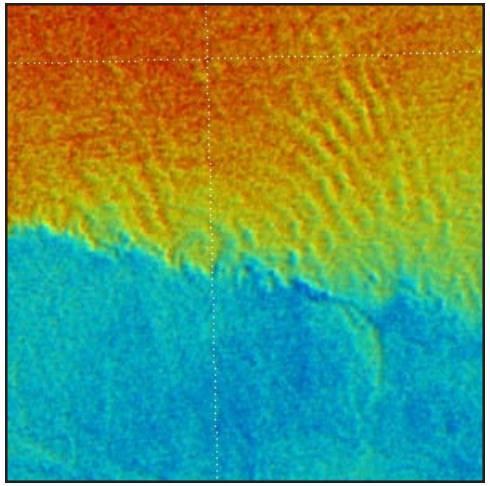

90 km square

11. Enlargement of Gravity Waves (x 2.5)

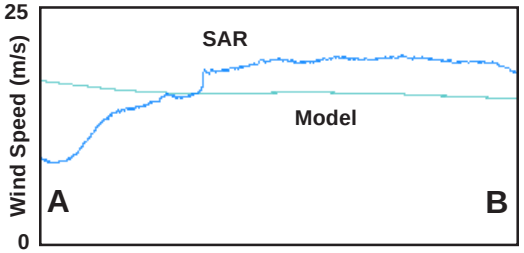

12. Model vs SAR Wind Profile along Line AB

1. Surface Pressure (mb) ~ t_0-36h

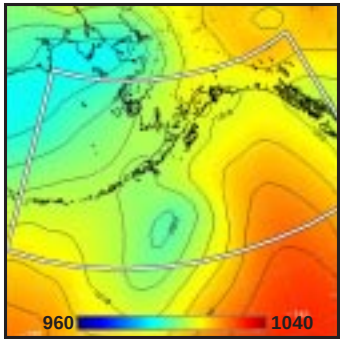

2. Surface Pressure (mb) ~ t_0-24h

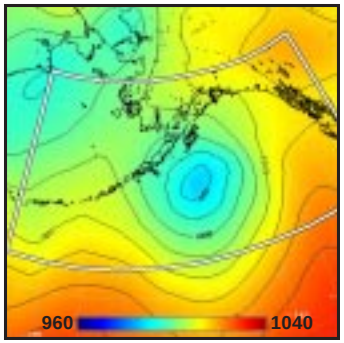

3. Surface Pressure (mb) ~ t_0-12h

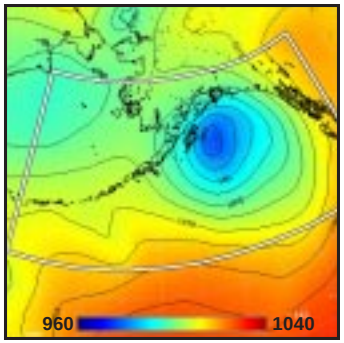

4. Surface Pressure (mb) ~ t_0

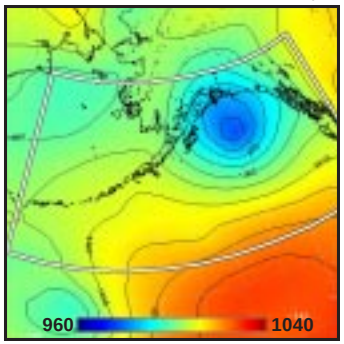

9. Enlarged Surface Wind Field ~ t_0

0600 GMT 31 Oct 2000

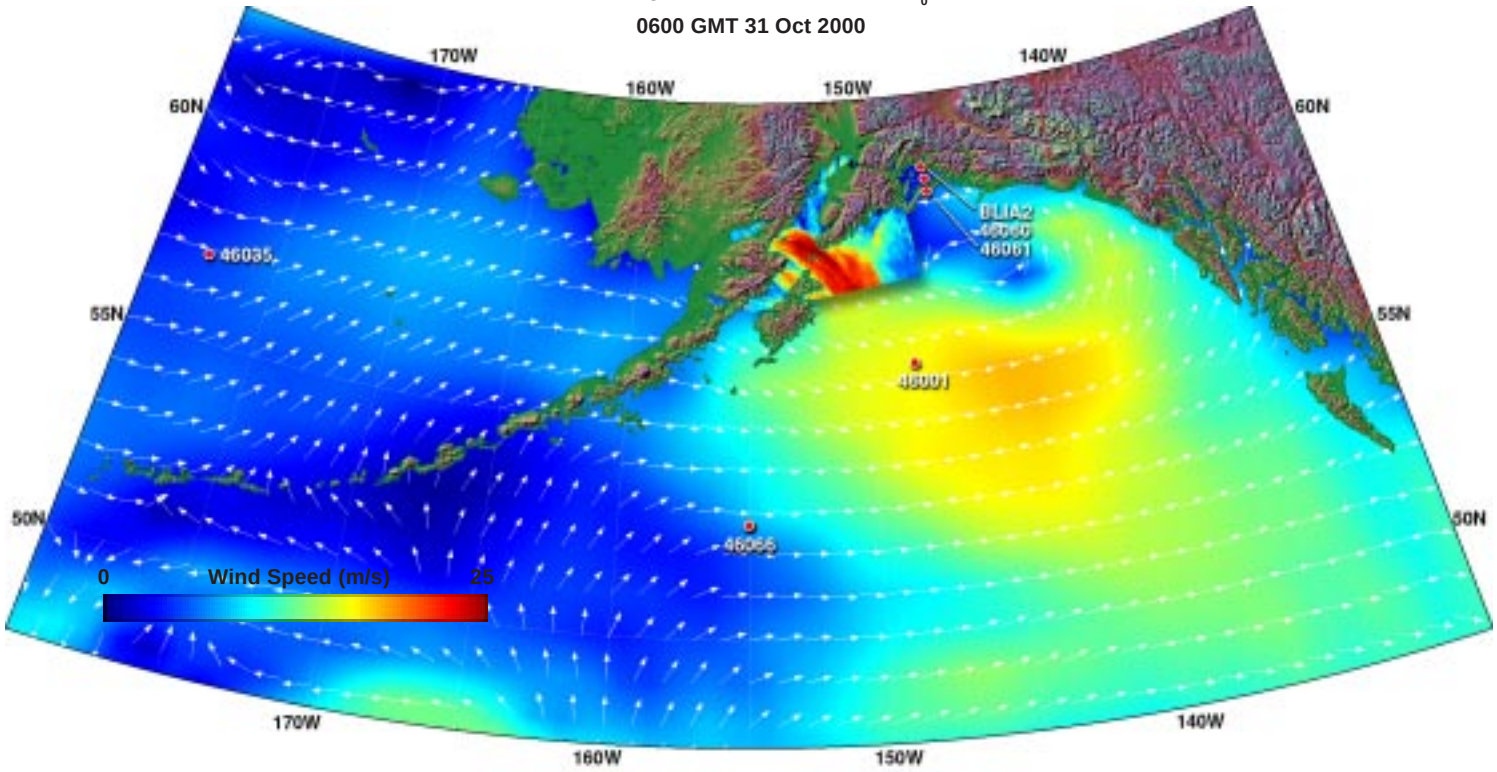

Model (this page): A deep, well-defined low pressure system passes just east of the gap between Kodiak Island and the Kenai Peninsula (1-4), drawing down strong northwesterly winds in its wake. Although model winds well offshore reach 15 m/s, in the gap they are less than half that (5, 9). Concurrent model waves within the gap are only 3 to 4 m, decaying as they are opposed by the local wind (6, 7). The MABL within the gap is unstable (8).

SAR (facing page): The SAR winds within and up to 50 km of both sides of the gap exceed 20 m/s (10). Island and mountain wakes are also evident The upstream enhancement evidently results from gap flow through the broad but narrowing lowlands just east of Iliamna Lake (11). Just upstream of the gap, the SAR wind estimates reach nearly 25 m/s, more than double the model estimates (12). [ref. section 2.4: gap flows.]

5. Surface Wind Field (m/s) ~ t_0

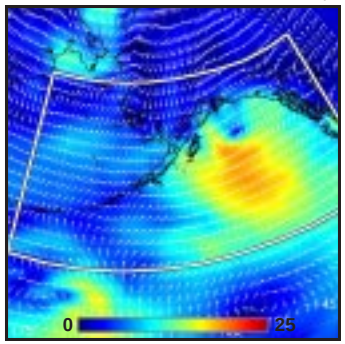

6. Surface Wave Height (m) ~ t_0

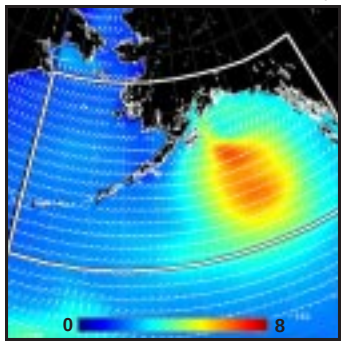

7. Inverse Wave Age (norm) ~ t_0

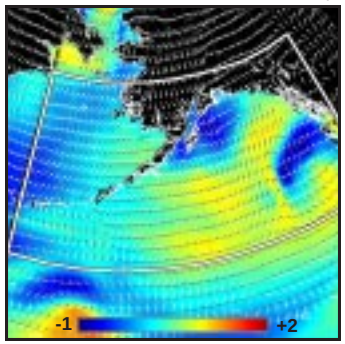

8. Air-Sea Temperature (˚C) ~ t_0

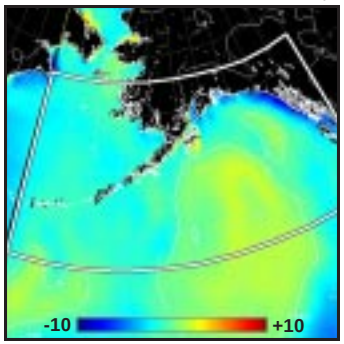

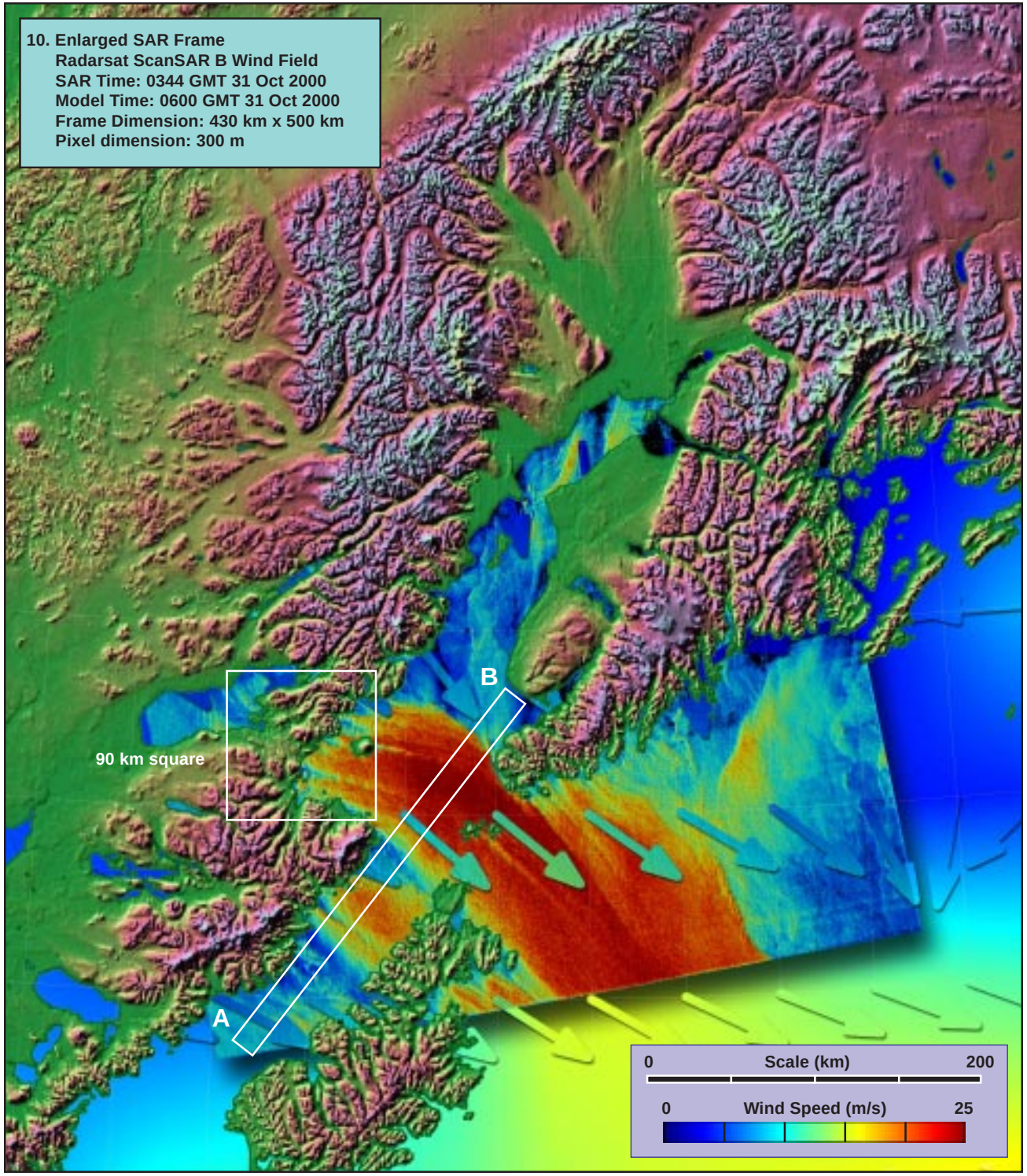

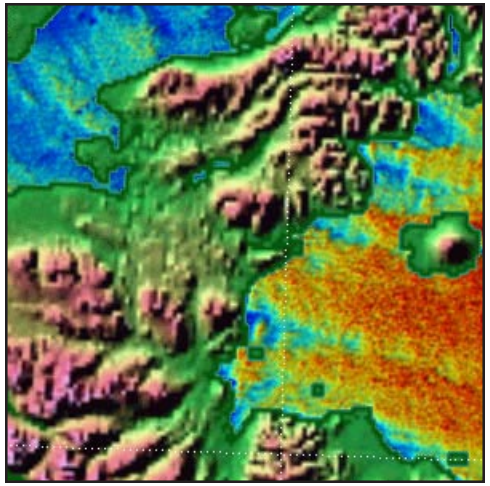

90 km square

11. Enlargement of Lowlands (x 2.5)

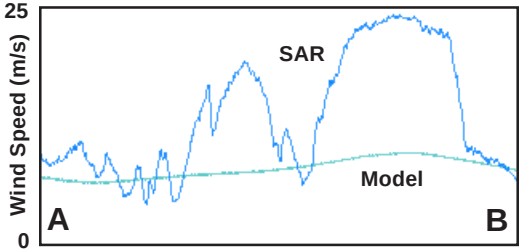

12. Model vs SAR Wind Profile along Line AB

1. Surface Pressure (mb) ~ t_0-36h

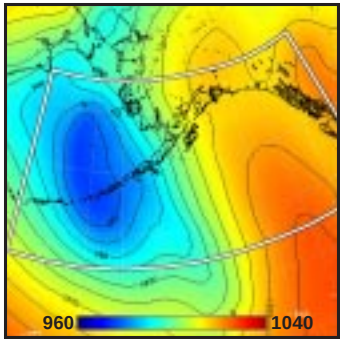

2. Surface Pressure (mb) ~ t_0-24h

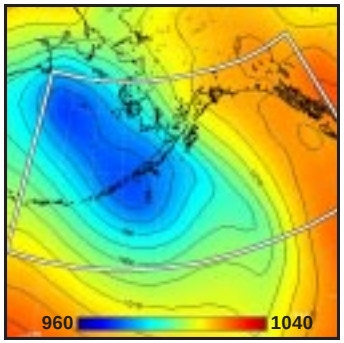

3. Surface Pressure (mb) ~ t_0-12h

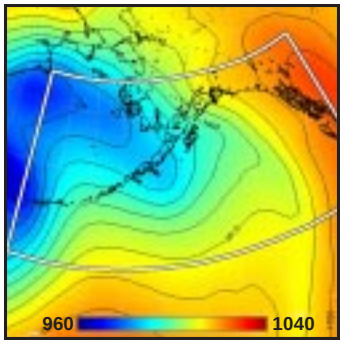

4. Surface Pressure (mb) ~ t_0

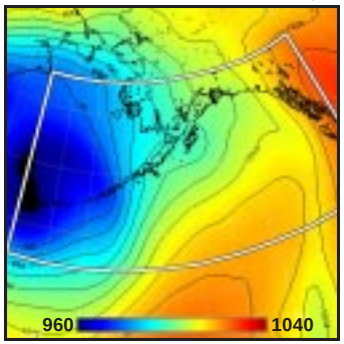

9. Enlarged Surface Wind Field ~ t_0

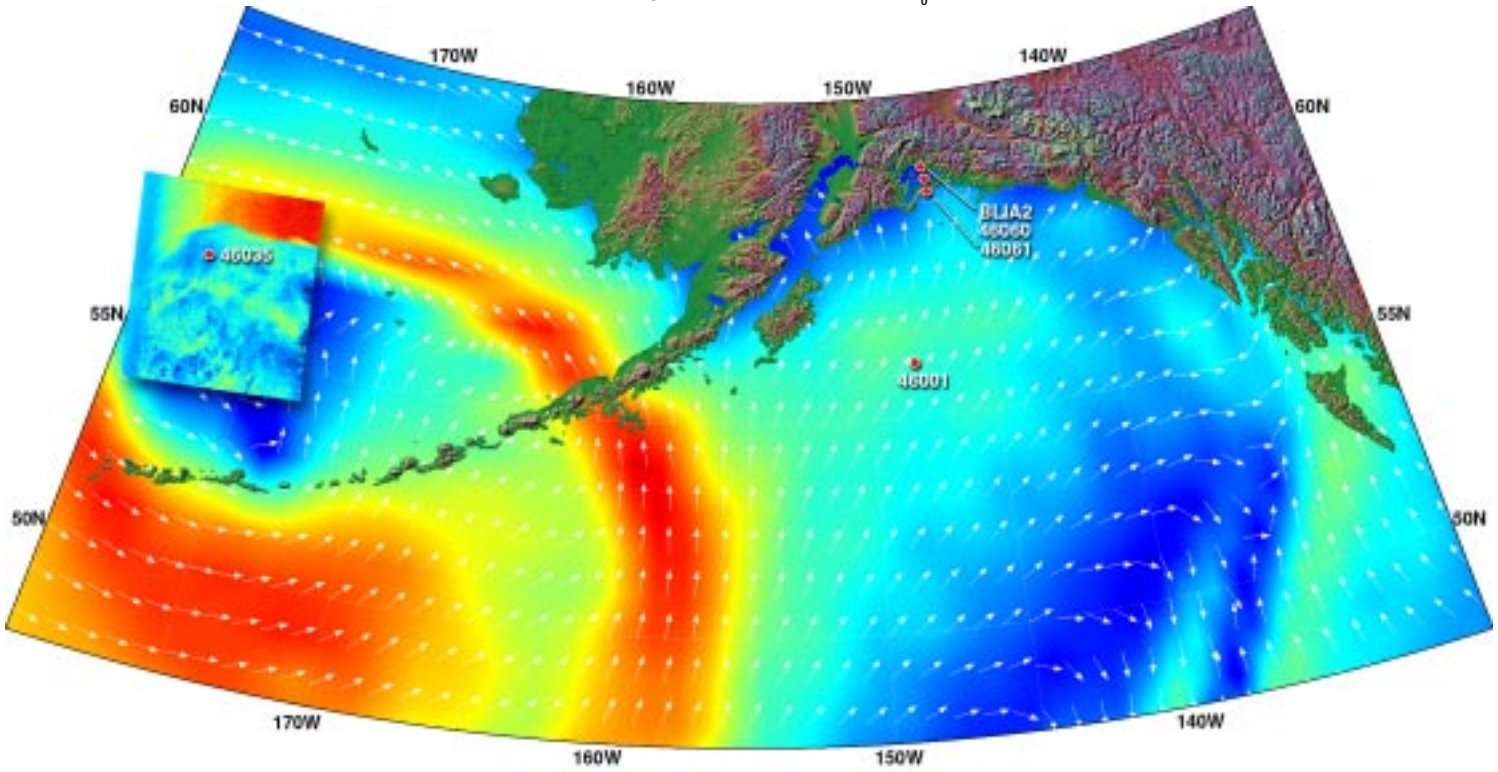

Model (this page): A persistent and deep low pressure system lingers just north of the western Aleutians, producing a nearly complete annulus of high winds (1-4). Within the annulus, model winds are 20 to 25 m/s (5, 9), except at its northernmost reach, where they are only 15 to 20 m/s. Concurrent model waves peak at 10 m south of the Aleutians, but within the SAR pass are only 3 to 4 m, and decaying (6, 7). The MABL within the high wind annulus is stable (8).

SAR (facing page): The SAR winds (10, 11) show an extremely sharp and well defined front, with wind estimates exceeding those of the model in that region by 5 to 10 m/s. There is some evidence of scalloping at the frontal boundary, but no sign of atmospheric gravity waves anywhere. [ref. sections 2.6: synoptic fronts, 2.8: mesoscale lows along fronts.] The SAR antenna beam problem is evident along the top left edge of the frame.

5. Surface Wind Field (m/s) ~ t_0

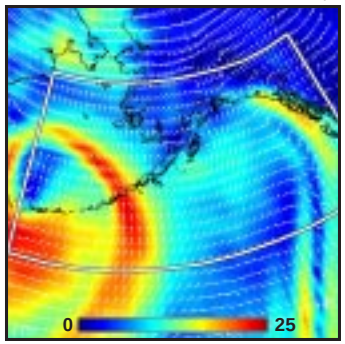

6. Surface Wave Height (m) ~ t_0

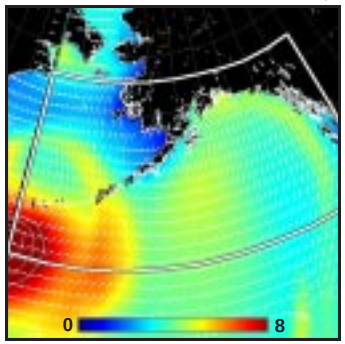

7. Inverse Wave Age (norm) ~ t_0

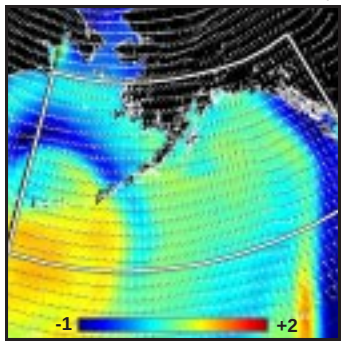

8. Air-Sea Temperature (˚C) ~ t_0

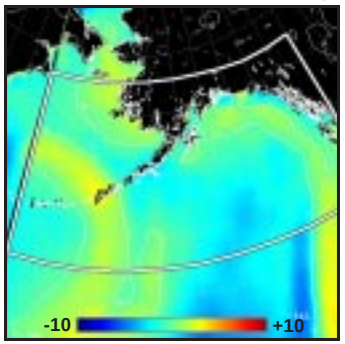

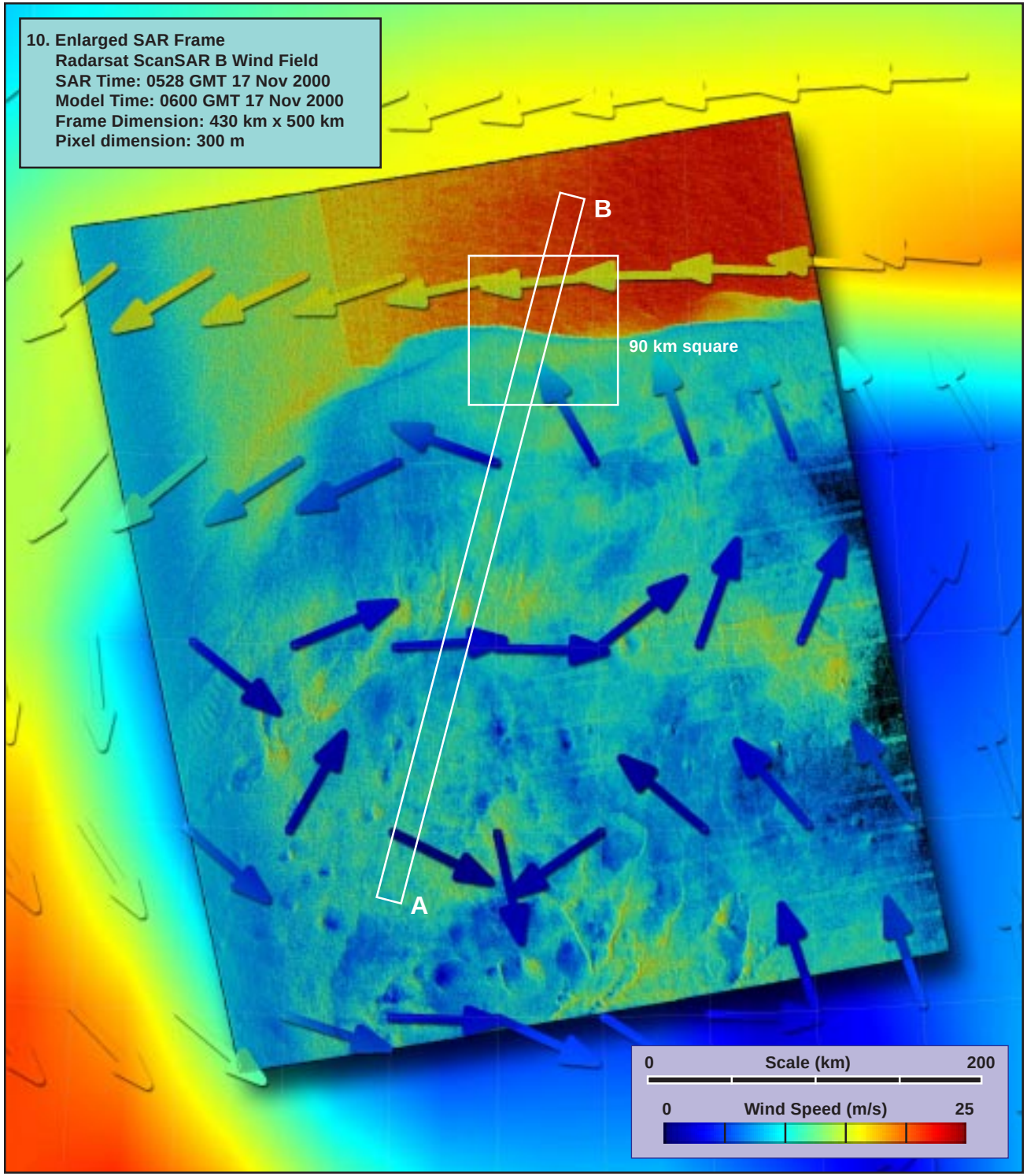

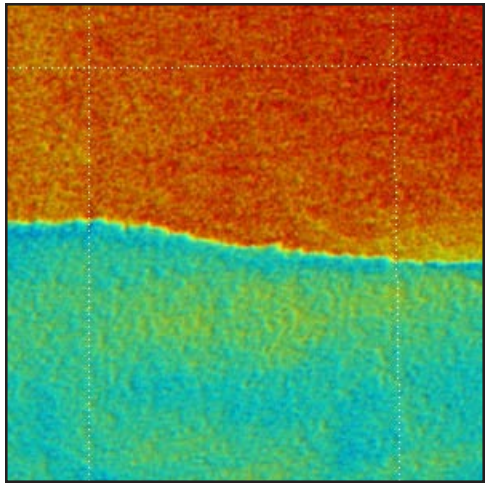

90 km square

11. Enlargement of Frontal Boundary (x 2.5)

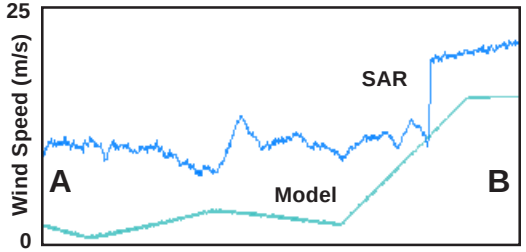

12. Model vs SAR Wind Profile along Line AB

1. Surface Pressure (mb) ~ t_0-36h

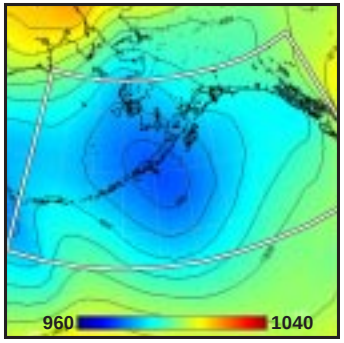

2. Surface Pressure (mb) ~ t_0-24h

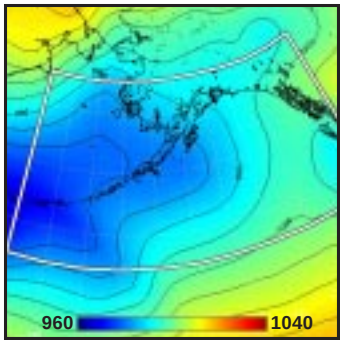

3. Surface Pressure (mb) ~ t_0-12h

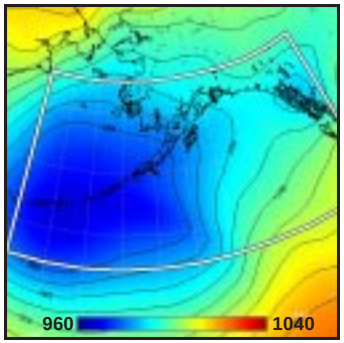

4. Surface Pressure (mb) ~ t_0

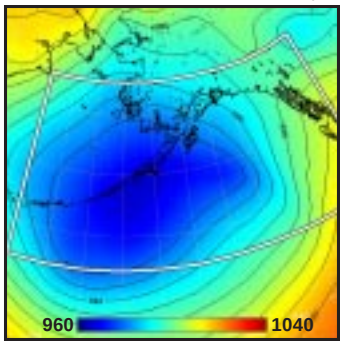

9. Enlarged Surface Wind Field ~ t_0

0600 GMT 24 Nov 2000

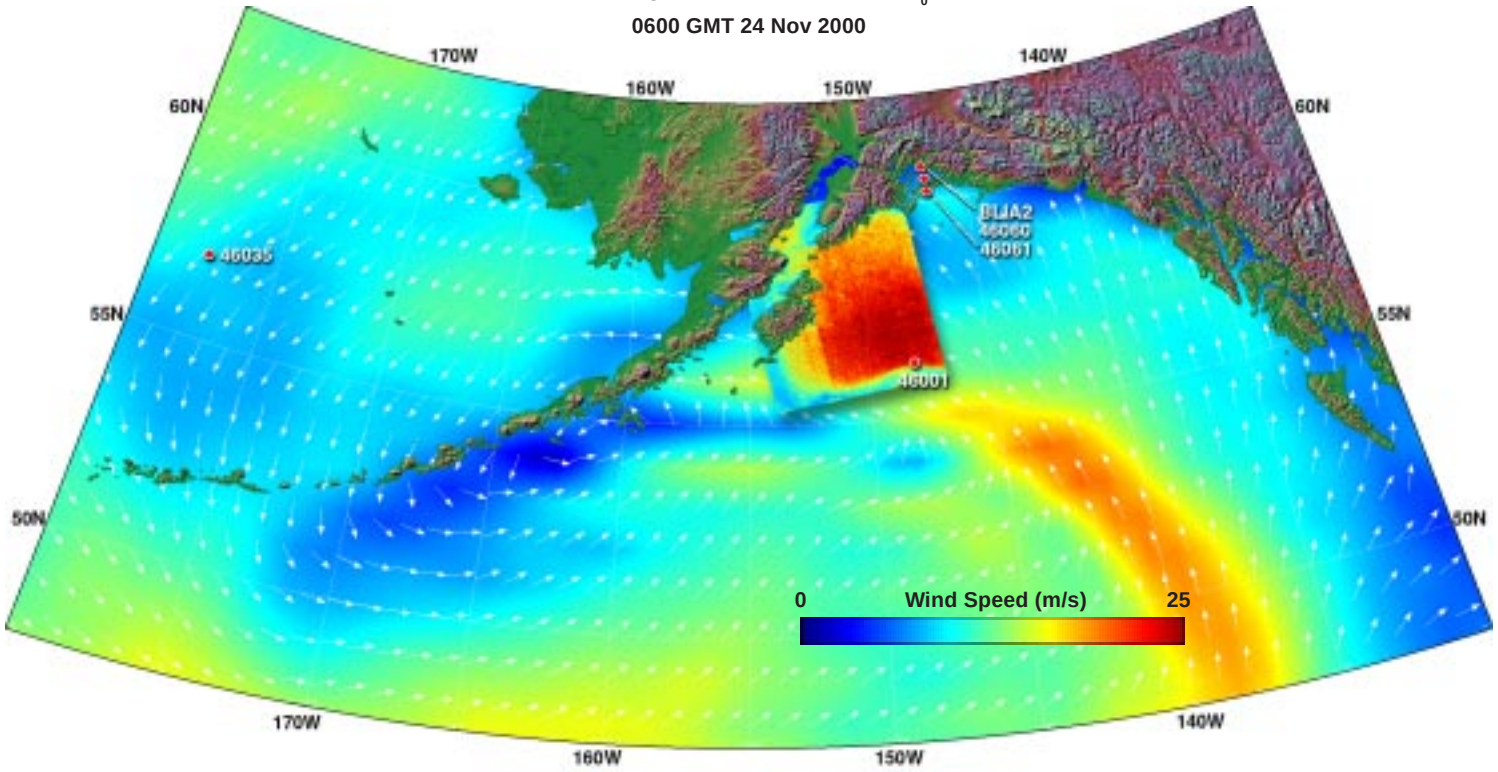

Model (this page): A large broad low pressure system lingers over the central Aleutians (1-4), producing a broad arc of high winds in the central Gulf of Alaska. Model winds (5, 9) peak at 15 to 20 m/s, but taper off toward Kodiak Island, where the SAR pass is located. Concurrent model waves are 2 to 4 m, close to equilibrium (6, 7). The MABL is nearly neutral (8).

SAR (facing page): The SAR winds are once again more than double the model estimates (10), although the SAR antenna beam pattern problem is quite evident in the western portion of the frame (11, 12). Buoy 46001, although located approximately 50 km south of the scan line AB, is nevertheless still well within the high wind region, and records a wind speed between 16 and 17 m/s at overpass time (12). This is about 5 m/s higher than the model estimate, and 7 m/s below the SAR estimate. [ref. section 2.11: coastal barrier jets (absence of).]

5. Surface Wind Field (m/s) ~ t_0

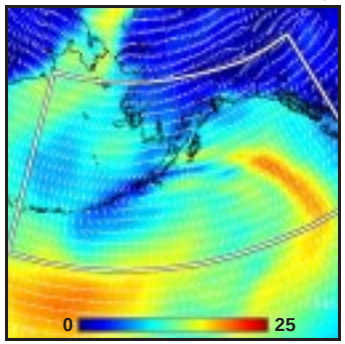

6. Surface Wave Height (m) ~ t_0

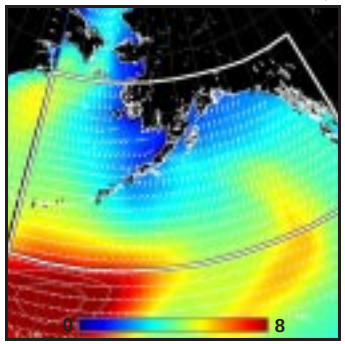

7. Inverse Wave Age (norm) ~ t_0

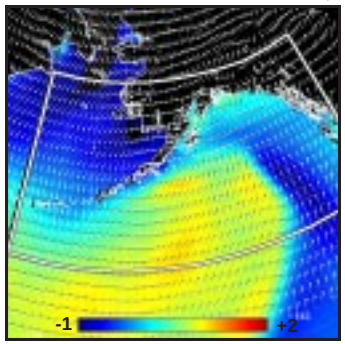

8. Air-Sea Temperature (˚C) ~ t_0

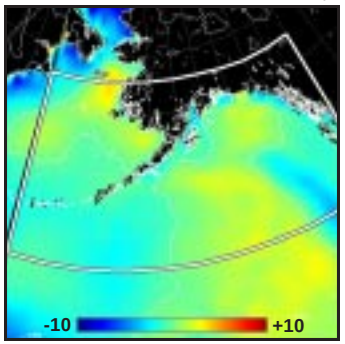

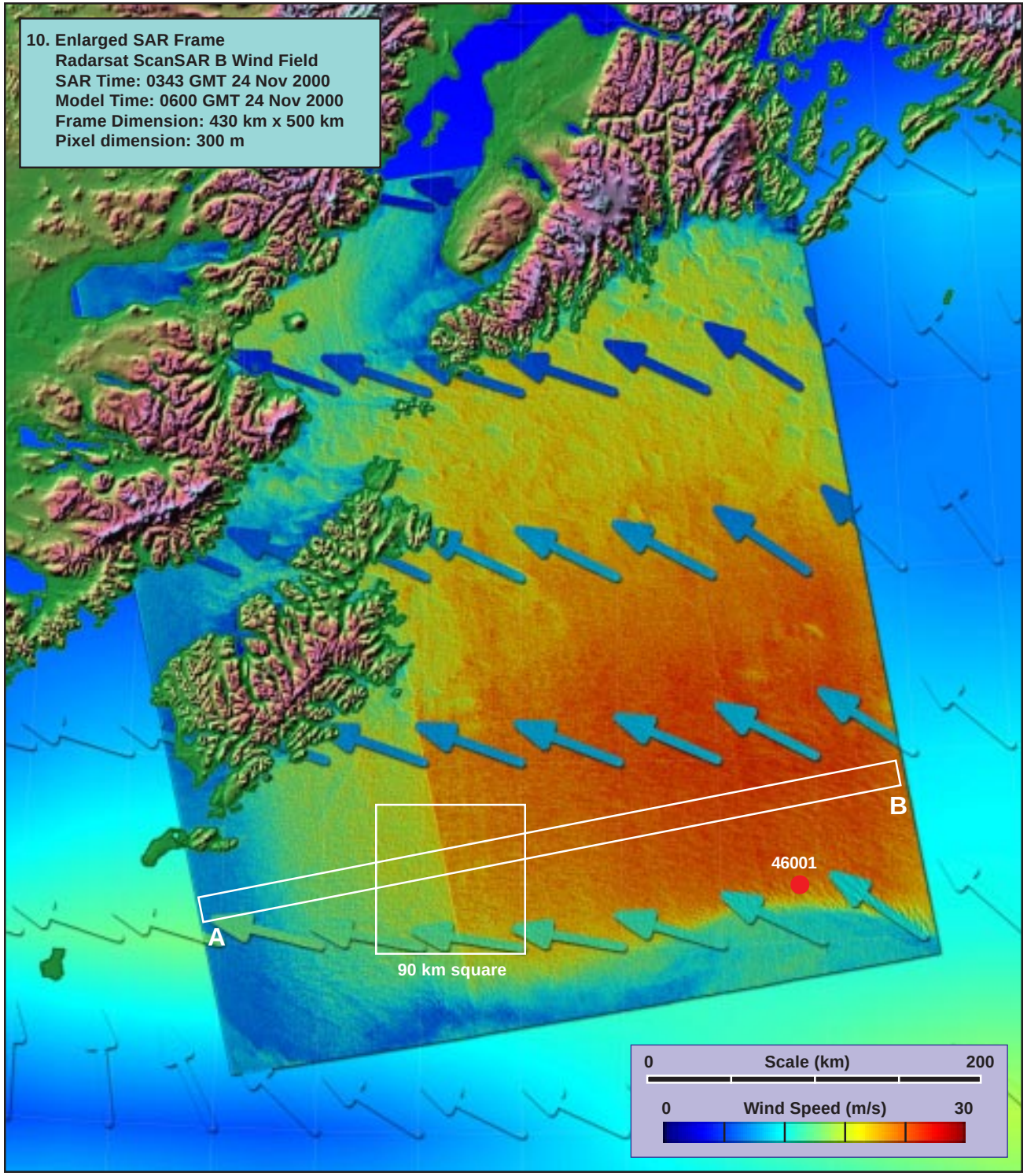

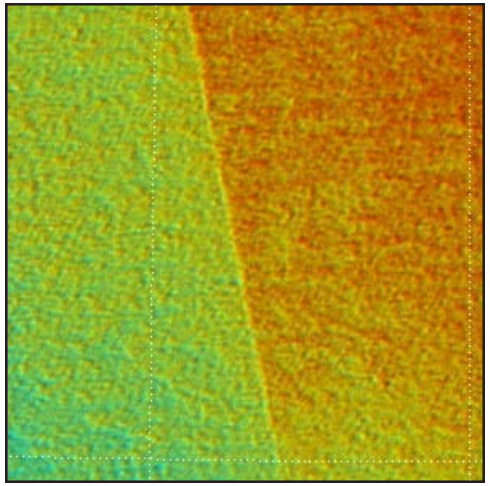

90 km square

11. Enlargement of Step Artifact (x 2.5)

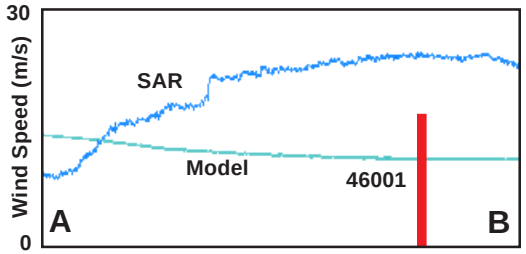

12. Model vs SAR Wind Profile along Line AB

1. Surface Pressure (mb) ~ t_0-36h

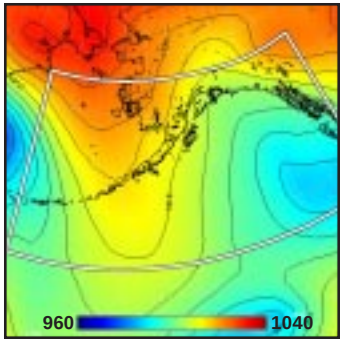

2. Surface Pressure (mb) ~ t_0-24h

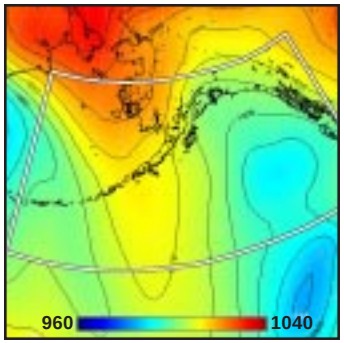

3. Surface Pressure (mb) ~ t_0-12h

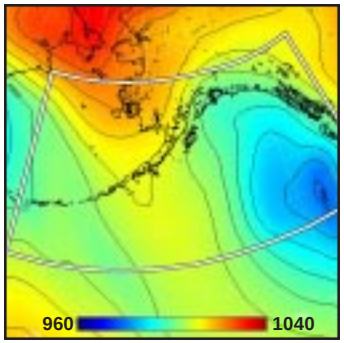

4. Surface Pressure (mb) ~ t_0

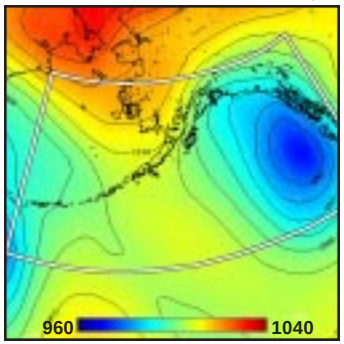

9. Enlarged Surface Wind Field ~ t_0

0600 GMT 01 Dec 2000

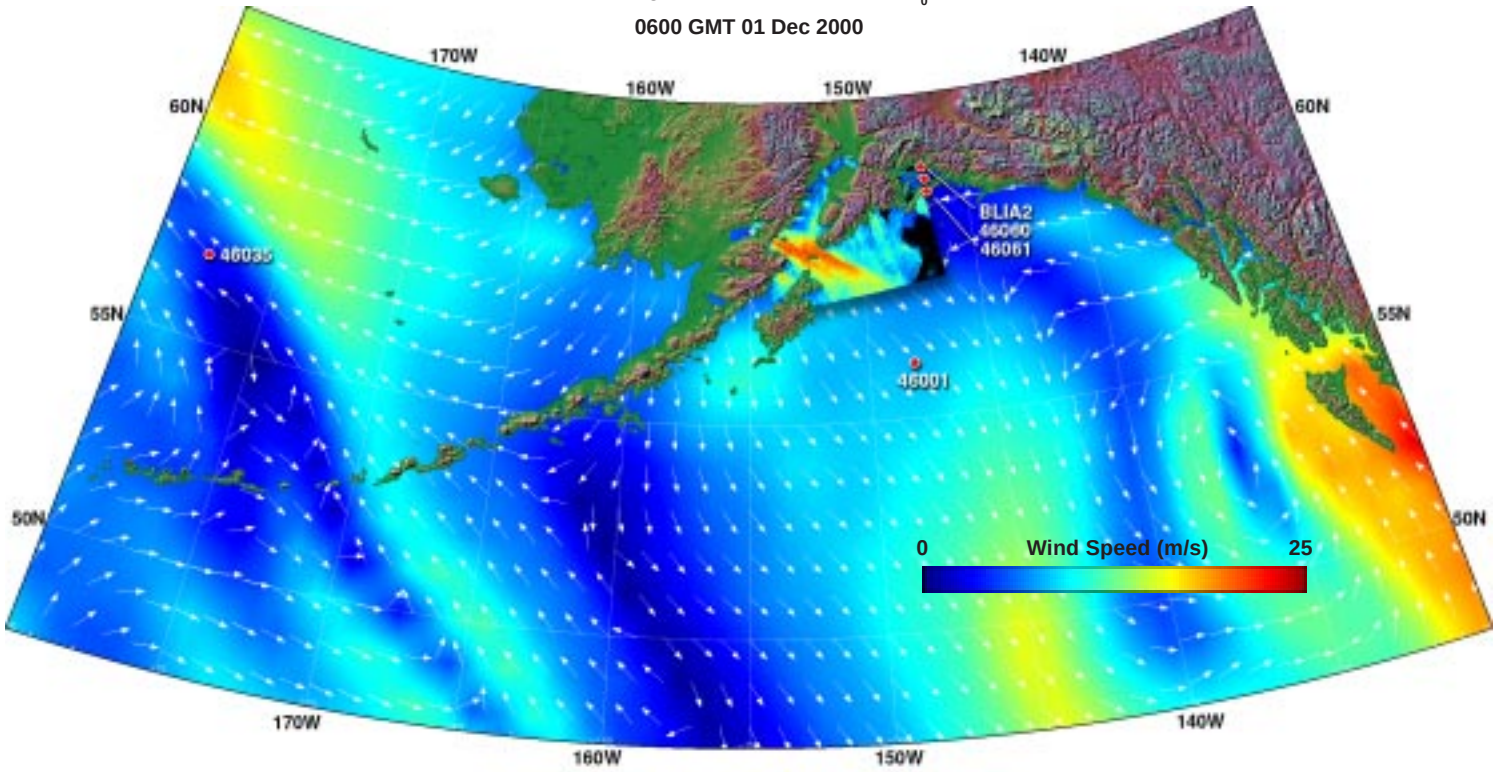

Model (this page): A deepening low pressure system moves slowly northward in the eastern Gulf of Alaska (1-4), combining with a high pressure to the NW to form a pressure gradient, which produces moderate (~5 m/s) NW winds in Cook Inlet (5, 9) with opposing (6) and decaying (7) swell, and a very unstable MABL (8). The string of model wind field minima in the SW is an artifact of the interpolation scheme.

SAR (facing page): The SAR winds again show much more variability (10, 11), with maximum wind estimate in the center of the topographic gap approaching 20 m/s, more than twice the model estimate (12). A convergence of streamlines is evident (11), with the stronger frontal gradient appearing downstream of the convergence. Cross-track strips in the very low wind region (SE corner) are instrument artifacts.

5. Surface Wind Field (m/s) ~ t_0

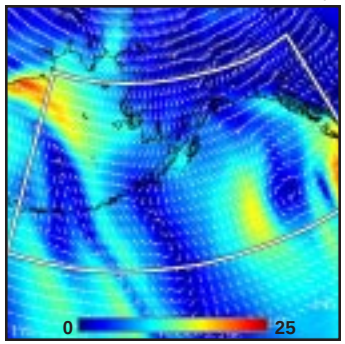

6. Surface Wave Height (m) ~ t_0

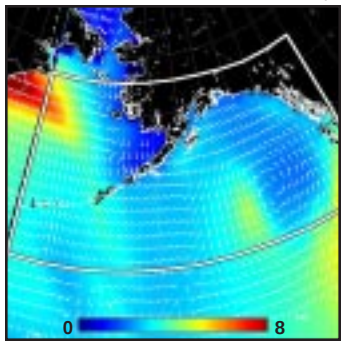

7. Inverse Wave Age (norm) ~ t_0

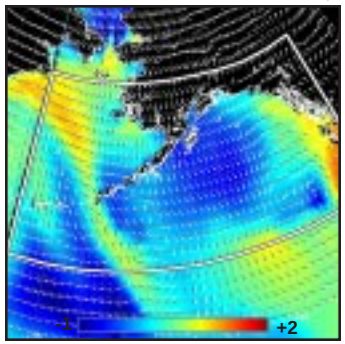

8. Air-Sea Temperature (˚C) ~ t_0

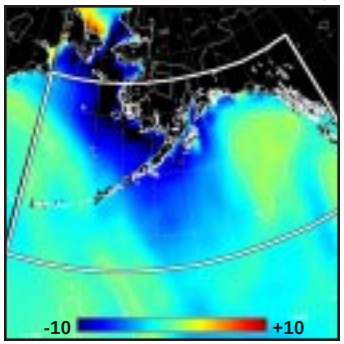

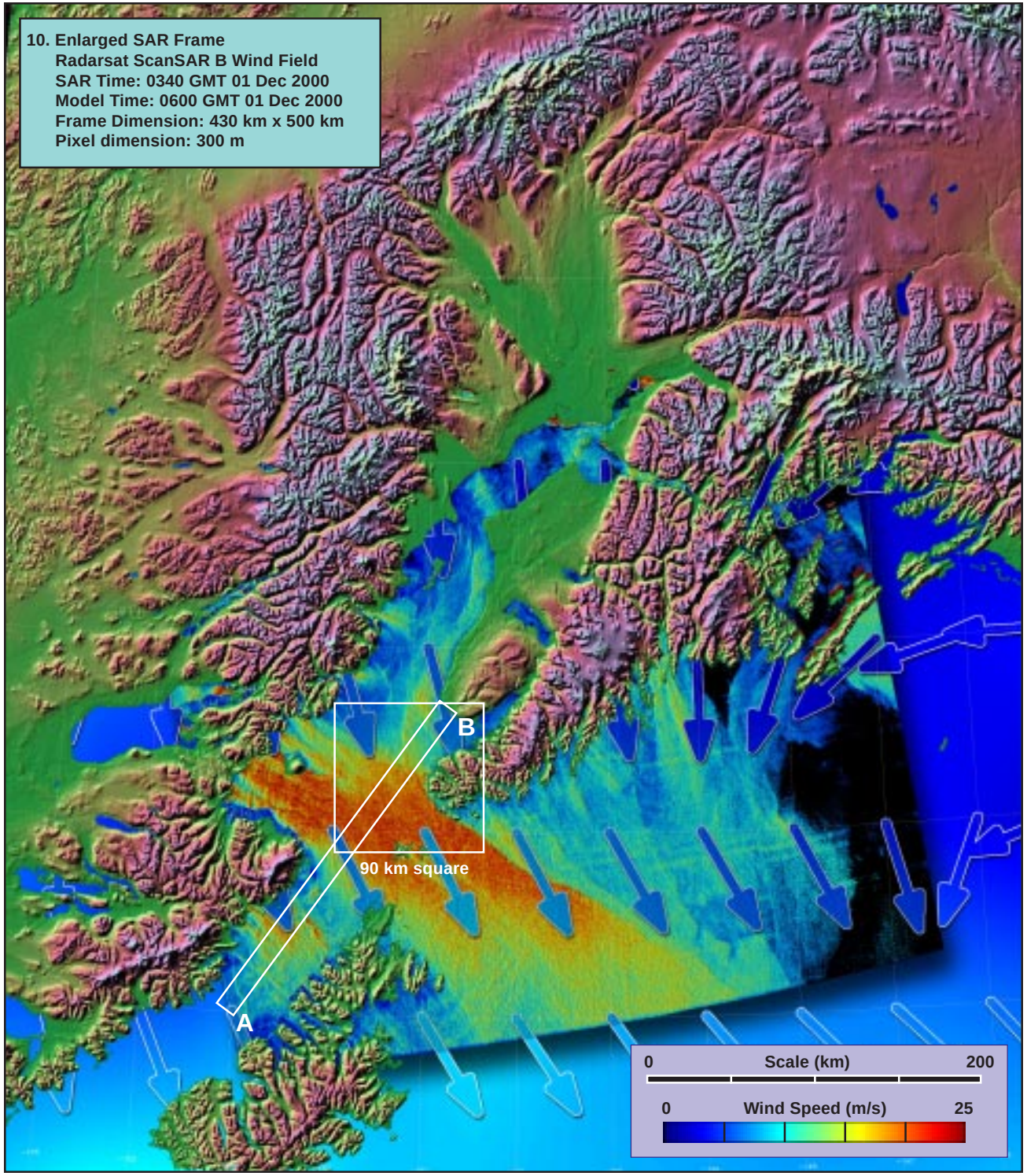

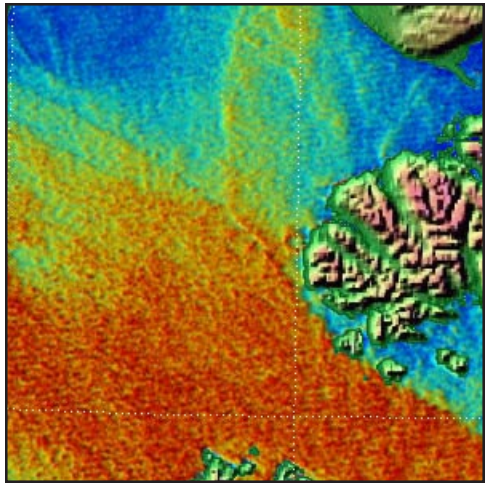

90 km square

11. Convergence of Stream Lines (x 2.5)

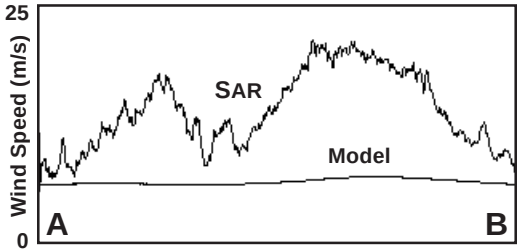

12. Model vs SAR Wind Profile along Line AB

1. Surface Pressure (mb) ~ t_0-36h

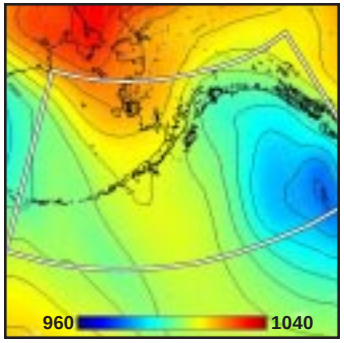

2. Surface Pressure (mb) ~ t_0-24h

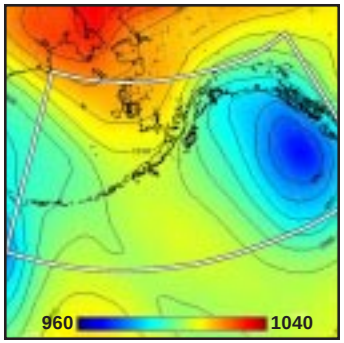

3. Surface Pressure (mb) ~ t_0-12h

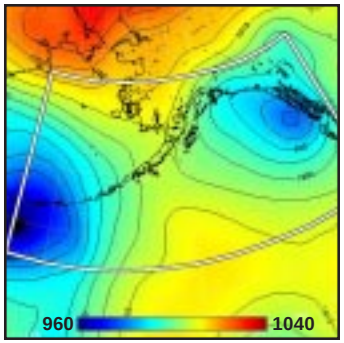

4. Surface Pressure (mb) ~ t_0

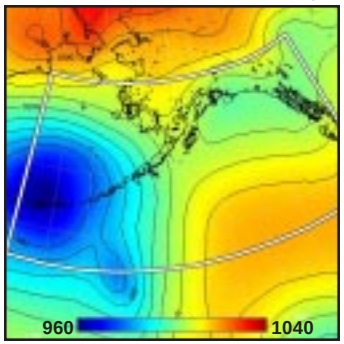

9. Enlarged Surface Wind Field ~ t_0

0000 GMT 02 Dec 2000

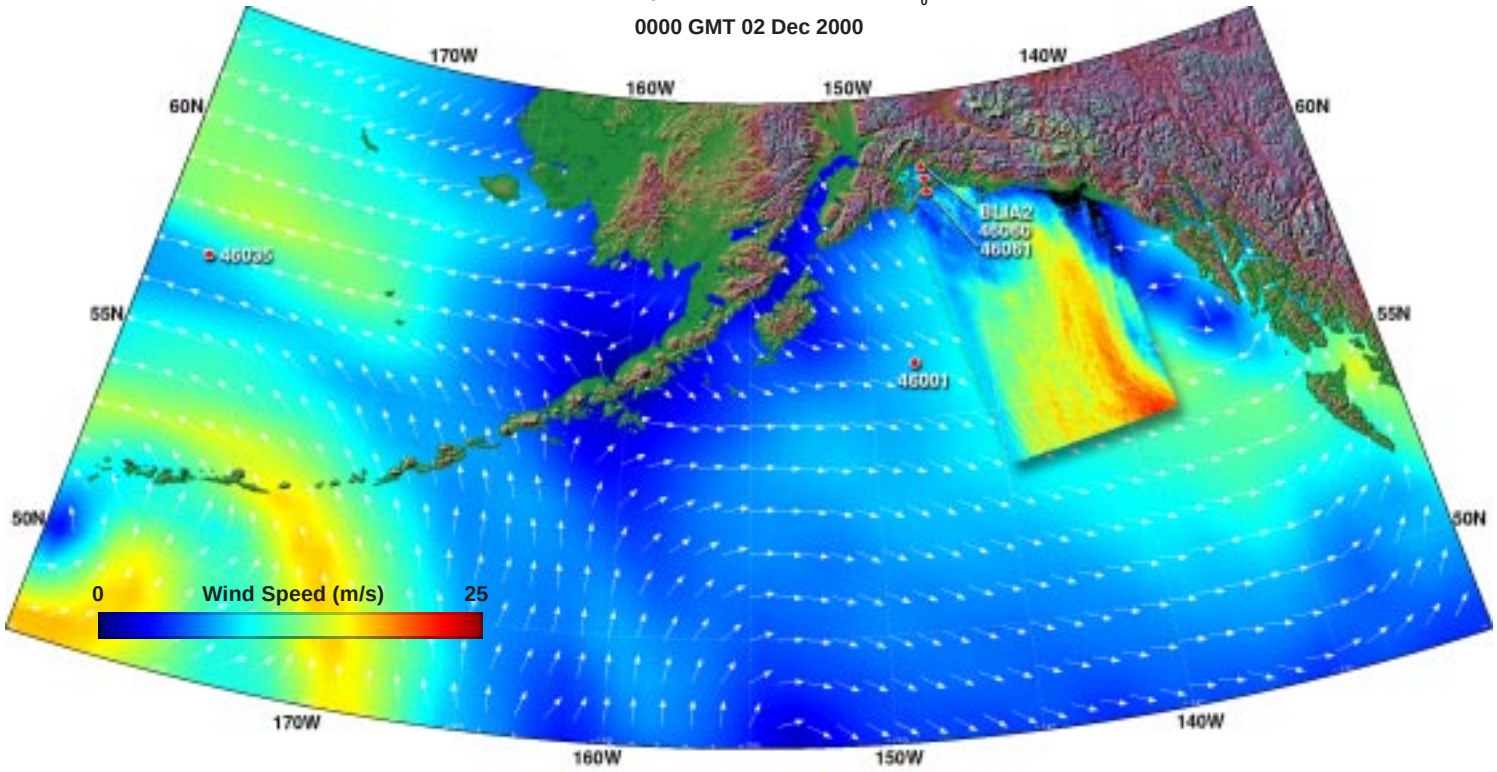

Model (this page): An initially deepening, and then rapidly weakening, low pressure system moves slowly NNE (1-4), setting up a persistent NW to westerly flow in the eastern Gulf of Alaska (5, 9) with nearly colinear (6) but decaying (7) wind waves, and an increasingly unstable MABL to the west and south (8).

SAR (facing page): The SAR winds clearly delineate the position and curvature of a well defined front, possibly associated with flow off the land (10, 11). A scan across the northern third of the frame shows a close agreement between the SAR and model wind estimates in that region (12), with the SAR however indicating a much higher variability and a steeper frontal gradient than the model.

5. Surface Wind Field (m/s) ~ t_0

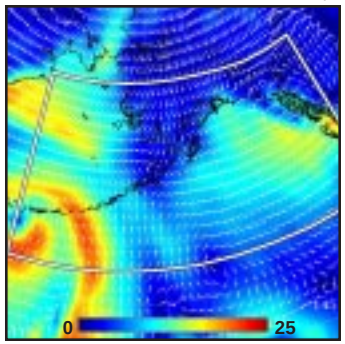

6. Surface Wave Height (m) ~ t_0

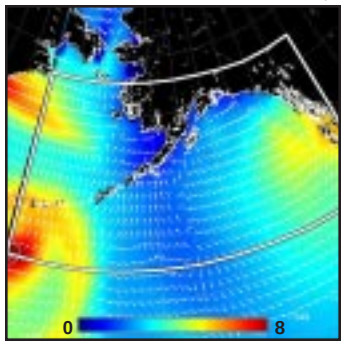

7. Inverse Wave Age (norm) ~ t_0

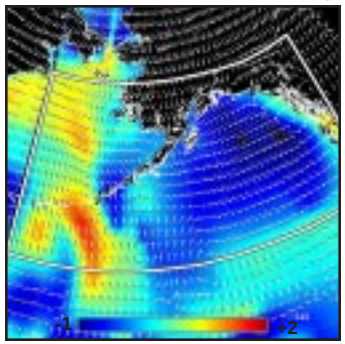

8. Air-Sea Temperature (˚C) ~ t_0

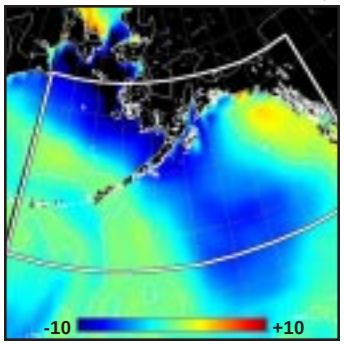

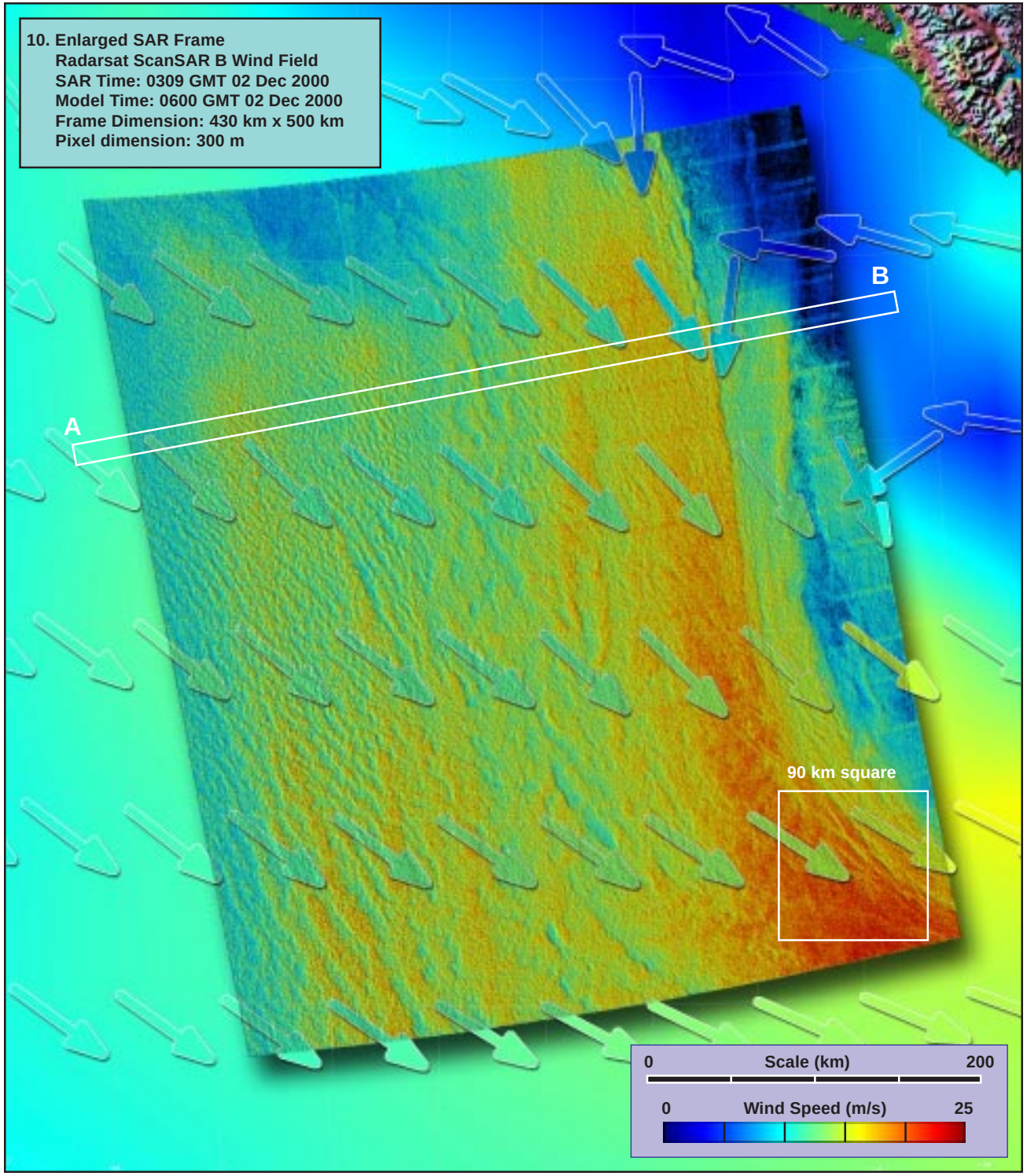

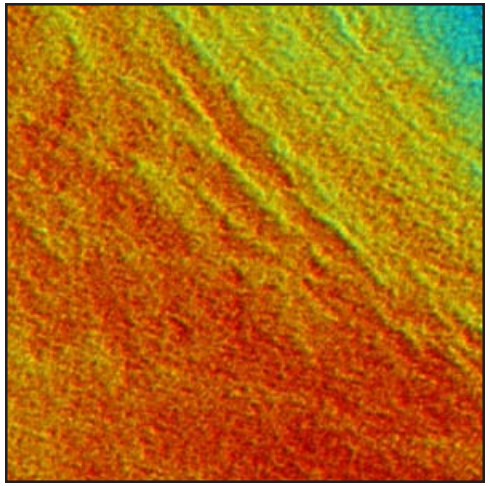

90 km square

11. Enlargement of Frontal Zone (x 2.5)

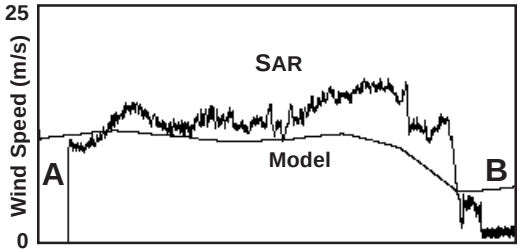

12. Model vs SAR Wind Profile along Line AB

1. Surface Pressure (mb) ~ t_0-36h

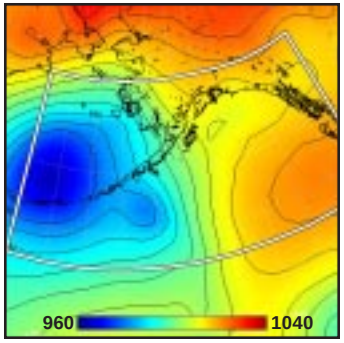

2. Surface Pressure (mb) ~ t_0-24h

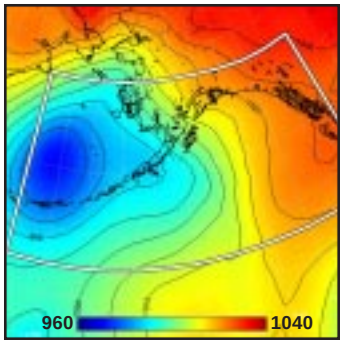

3. Surface Pressure (mb) ~ t_0-12h

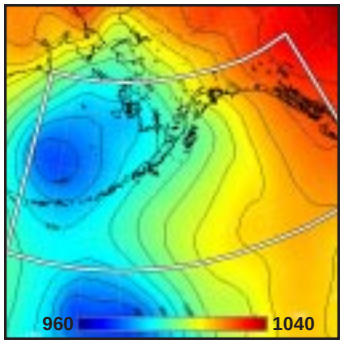

4. Surface Pressure (mb) ~ t_0

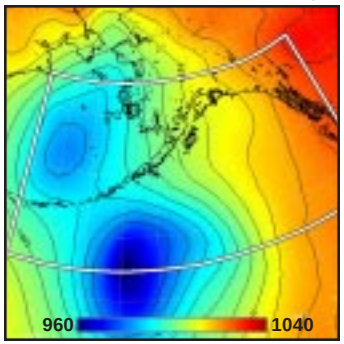

9. Enlarged Surface Wind Field ~ t_0

0006 GMT 04 Dec 2000

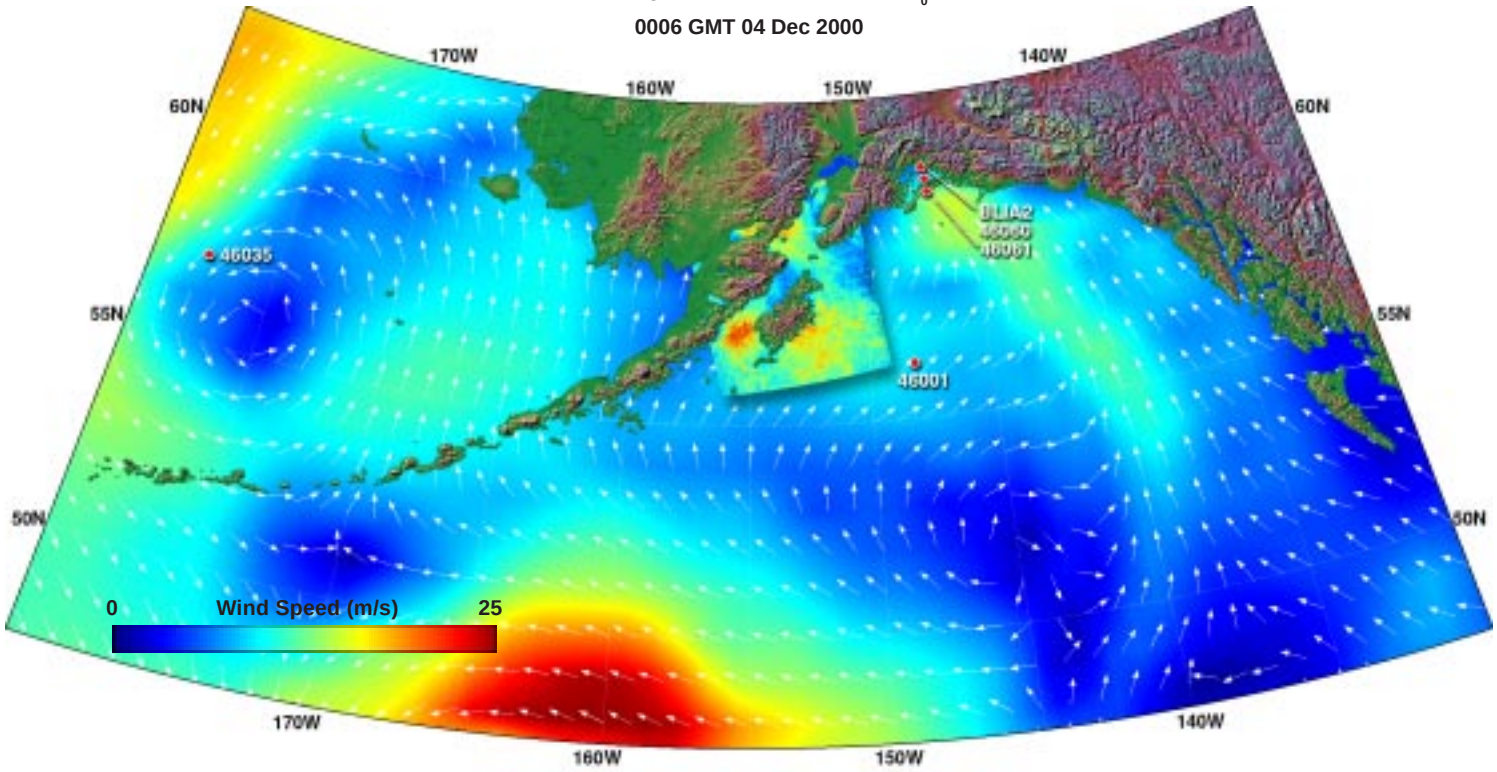

Model (this page): Far to the east of a pair of interacting lows, a weak W-to-E pressure gradient (1-4) induces a light (~5 m/s) wind from the SW around Kodiak Island (5, 9), turning toward the NW at the southern entrance to Cook Inlet. Waves there are generally from the SE (6), stable or decaying in the south, but growing in the north (7). The MABL is mildly unstable, tending to strongly unstable just north of Kodiak Island (8).

SAR (facing page): The SAR winds are generally higher and more variable than the model (10). A scan though Shelikof Strait shows a stronger maximum to the south (11, 12) and a weaker one to the north. The SAR features (e.g., island shadowing) indicate a much sharper turning of the wind toward the NW than does the model, possibly the result of a slight mislocation of the field position within the model.

5. Surface Wind Field (m/s) ~ t_0

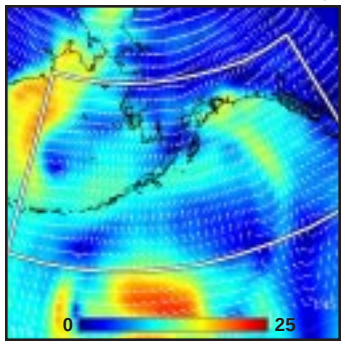

6. Surface Wave Height (m) ~ t_0

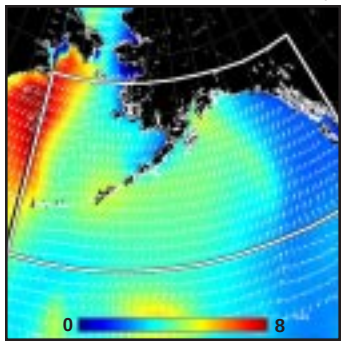

7. Inverse Wave Age (norm) ~ t_0

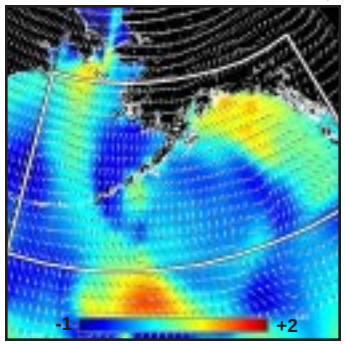

8. Air-Sea Temperature (˚C) ~ t_0

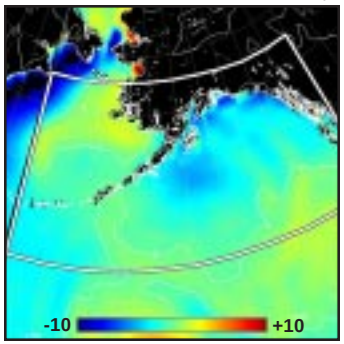

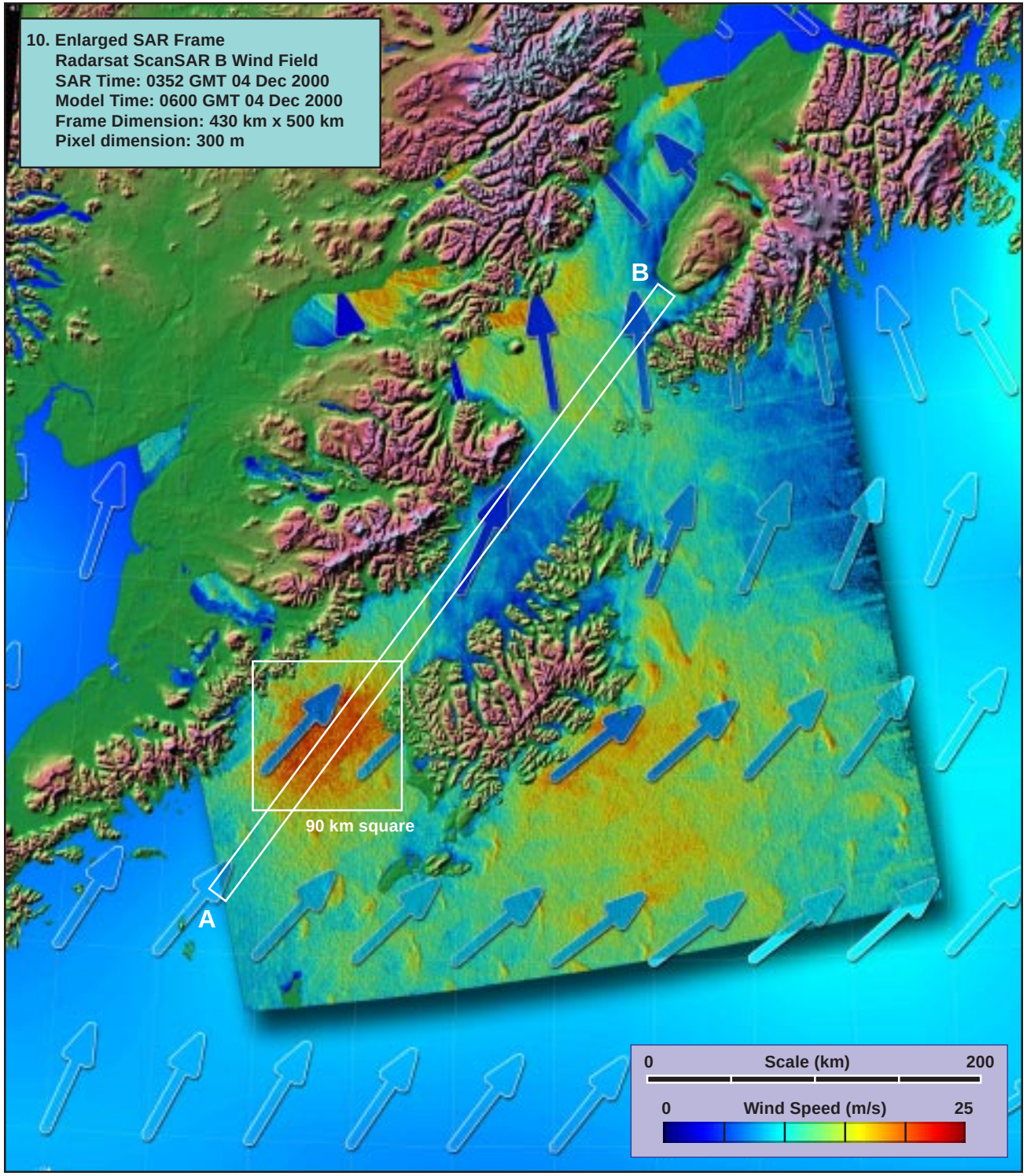

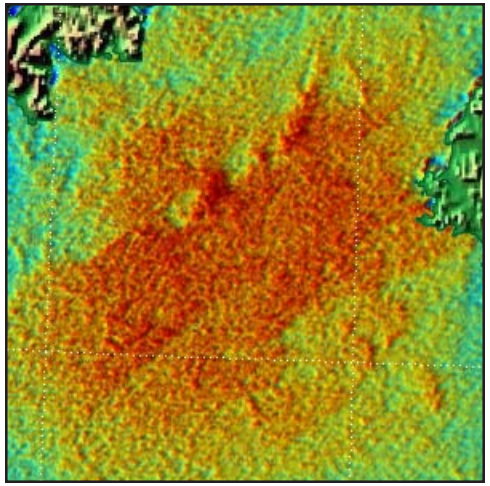

90 km square

11. Enlargement of Rain Cells (?) (x 2.5)

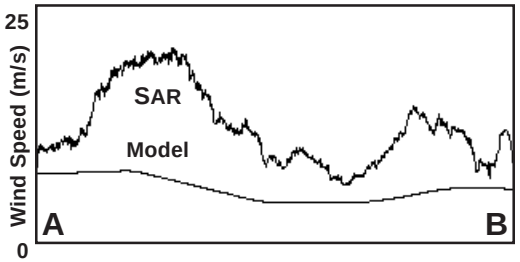

12. Model vs SAR Wind Profile along Line AB

1. Surface Pressure (mb) ~ t_0-36h

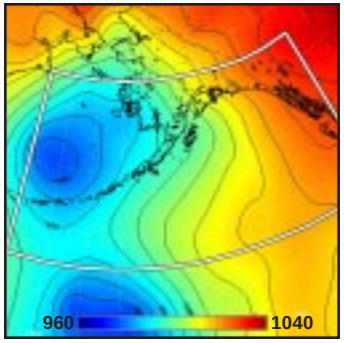

2. Surface Pressure (mb) ~ t_0-24h

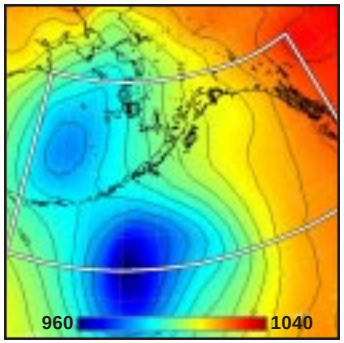

3. Surface Pressure (mb) ~ t_0-12h

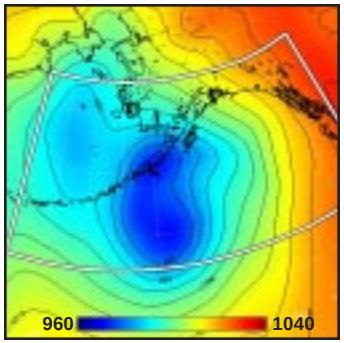

4. Surface Pressure (mb) ~ t_0

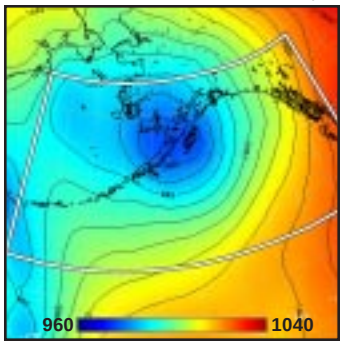

9. Enlarged Surface Wind Field ~ t_0

0600 GMT 05 Dec 2000

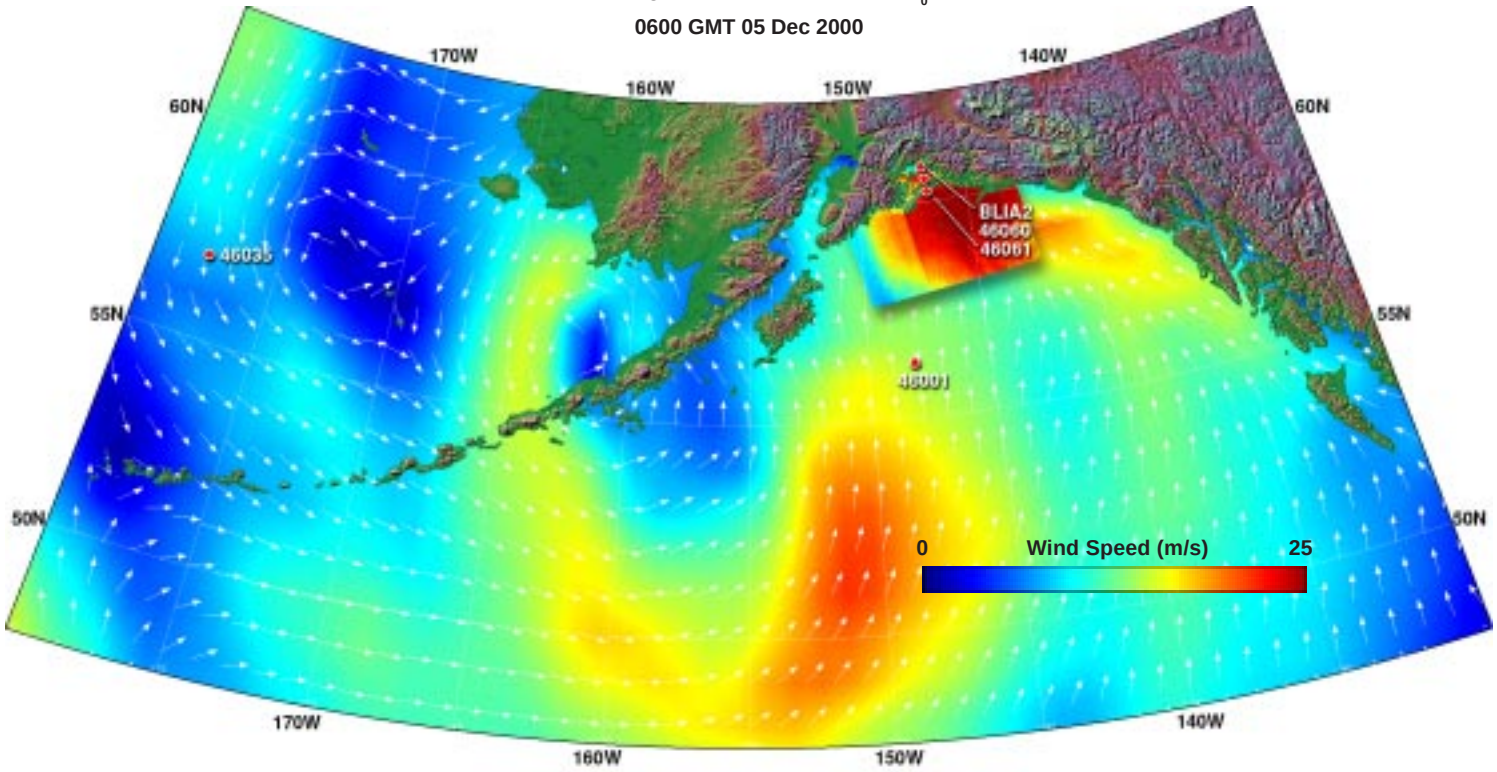

Model (this page): The southern low of the previous day (04 Dec) becomes dominant as it moves NE over the Alaska Peninsula (1-4), producing increasing SE winds (5, 9) and growing waves (6, 7) in the northern Gulf of Alaska. The MABL, although quite stable to the south, is locally unstable in the vicinity of the coast, especially around Prince William Sound (8).

SAR (facing page): The SAR winds, again showing systematic across-track wind biases (see, e.g., 6 March 2000) nevertheless reveal an abrupt wind frontal boundary passing through Prince William Sound (10, 11). A scan through three buoys (12) shows how well the SAR captures the sharp gradient, but also suggests again that the SAR wind estimates are 5 to 10 m/s higher than the two deep water buoys (46060 and 46061) at higher winds (~15 m/s).

5. Surface Wind Field (m/s) ~ t_0

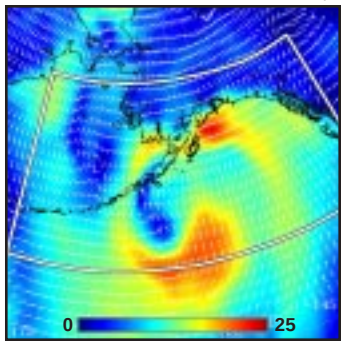

6. Surface Wave Height (m) ~ t_0

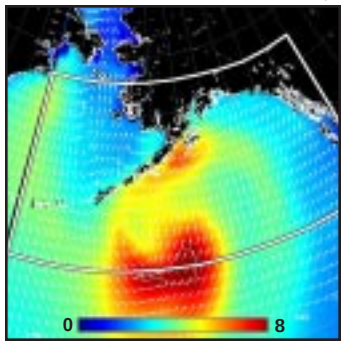

7. Inverse Wave Age (norm) ~ t_0

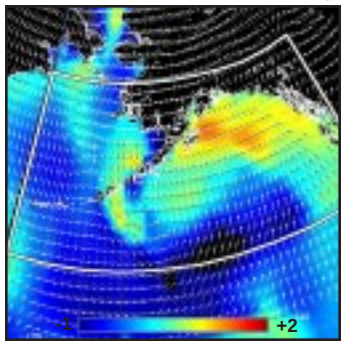

8. Air-Sea Temperature (˚C) ~ t_0

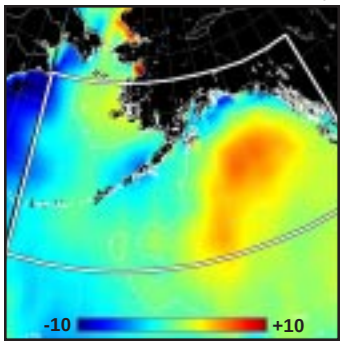

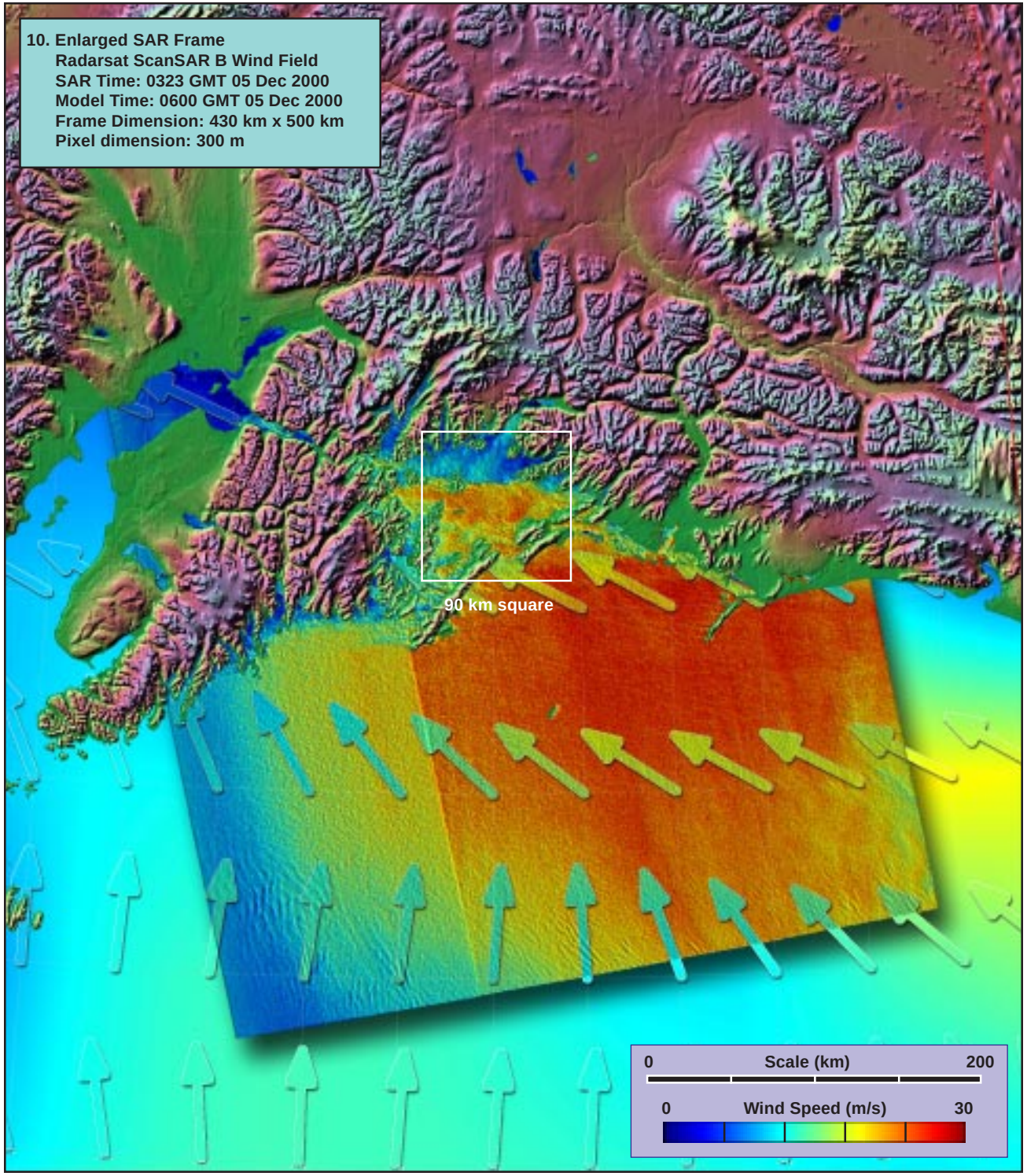

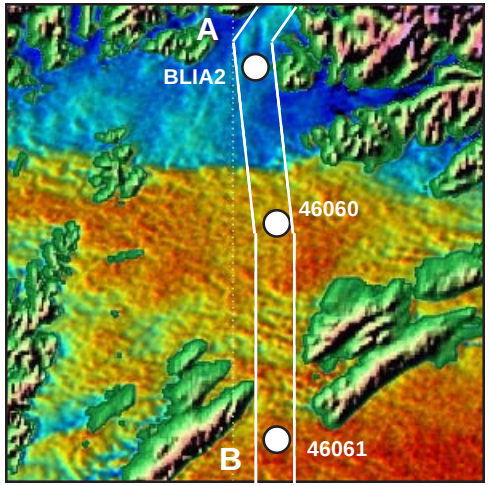

90 km square

11. Prince William Sound (x 2.5)

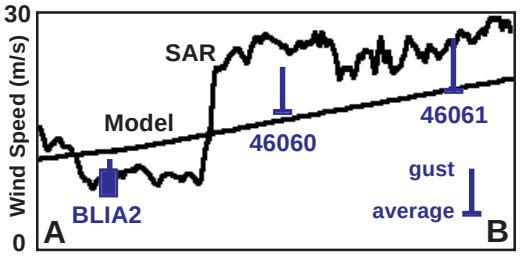

12. Model vs SAR Wind Profile along Line AB

	YY MM DD hh mm	DIR	SPD	GSP
Buoy BLIA2	00 12 05 02	16	8.6	9.4
	00 12 05 03	20	8.6	9.6
	00 12 05 04	47	5.6	7.1
	00 12 05 05	14	7.2	7.6
Buoy 46060	00 12 05 02 50	88	13.2	17.4
	00 12 05 03 00	93	12.9	
	00 12 05 03 10	97	13.2	
	00 12 05 03 20	93	14.2	
	00 12 05 03 30	87	14.7	
	00 12 05 03 40	74	13.9	
	00 12 05 03 50	77	13.8	19.2
Buoy 46061	00 12 05 02 50	84	16.0	20.5
	00 12 05 03 00	81	16.9	
	00 12 05 03 10	82	16.9	
	00 12 05 03 20	87	16.3	
	00 12 05 03 30	91	16.9	
	00 12 05 03 40	90	16.4	
	00 12 05 03 50	92	17.6	22.2

overpass time

1. Surface Pressure (mb) ~ t_0-36h

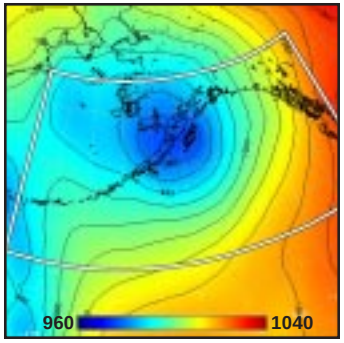

2. Surface Pressure (mb) ~ t_0-24h

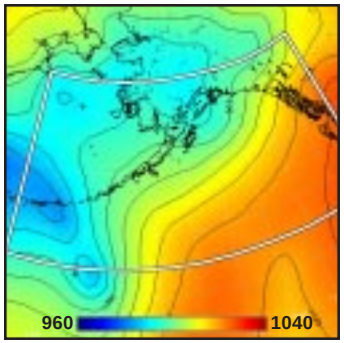

3. Surface Pressure (mb) ~ t_0-12h

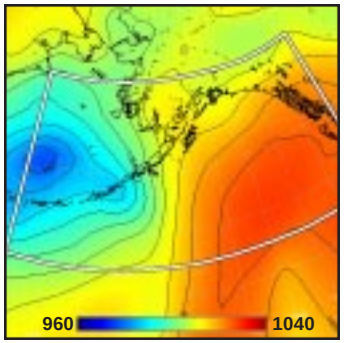

4. Surface Pressure (mb) ~ t_0

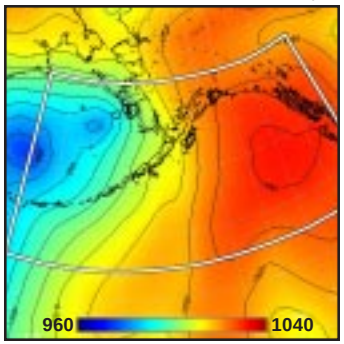

9. Enlarged Surface Wind Field ~ t_0

1800 GMT 06 Dec 2000

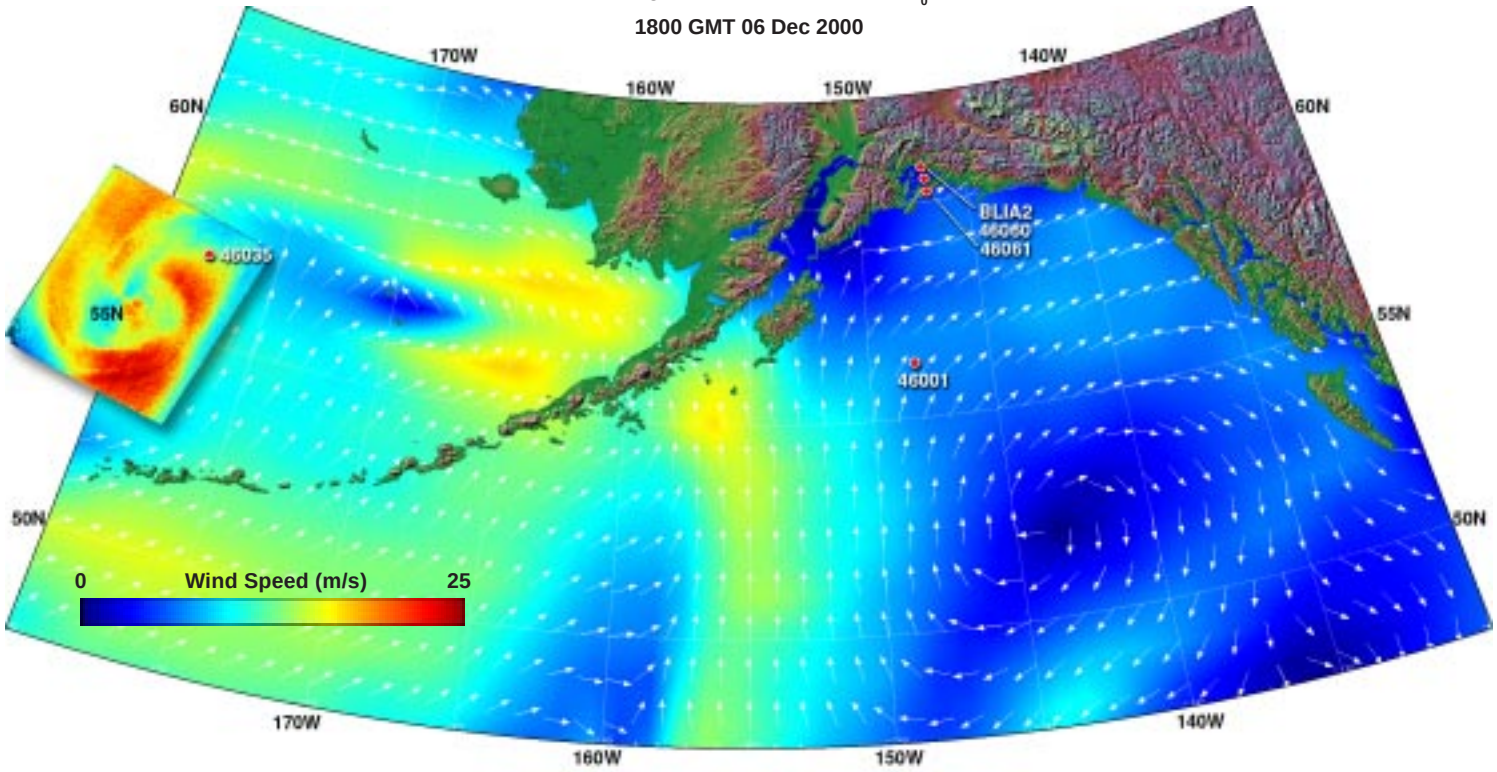

Model (this page): As the low of the previous day (05 Dec) dissipates over central Alaska, another strengthens over the central Bering Sea (1-4), producing a tight, nearly circularly symmetric wind field with a long arm of high winds stretching eastward over the Alaska Peninsula and then southward through the Gulf of Alaska (5, 9). Highest waves are in the western sector of the storm (6), but are more fully developed (steeper) in the eastern sector (7). The MABL is unstable in all sectors (8).

SAR (facing page): Both the SAR and the model beautifully capture the structure of the nearly symmetrical wind field, but the SAR again reveals a more complex morphology (10). A scan just eastward of the center (10, 11, 12) but through buoy 46035 (11, 12, 13) shows peak SAR winds exceeding 25 m/s in the south, and 20 m/s in the north, while the model peaks are less than 15 m/s, actually a little more consistent with buoy 46035. Thus, the SAR wind estimates again appear biased high with respect to both the model and the buoy, even though the morphology revealed by the SAR is doubtless more accurate than from the model. [ref. section 2.7: synoptic lows.]

5. Surface Wind Field (m/s) ~ t_0

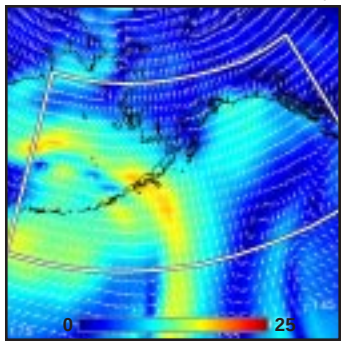

6. Surface Wave Height (m) ~ t_0

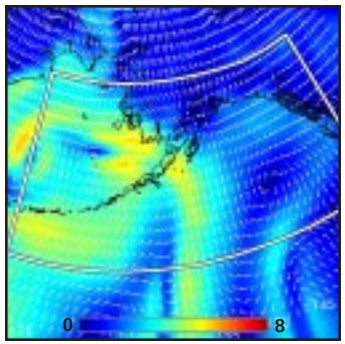

7. Inverse Wave Age (norm) ~ t_0

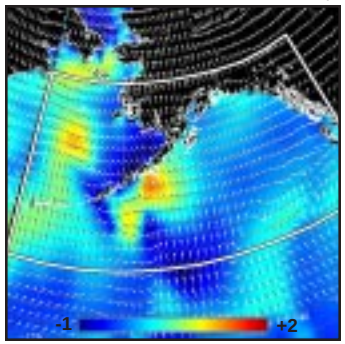

8. Air-Sea Temperature (˚C) ~ t_0

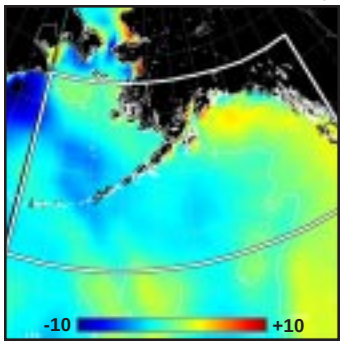

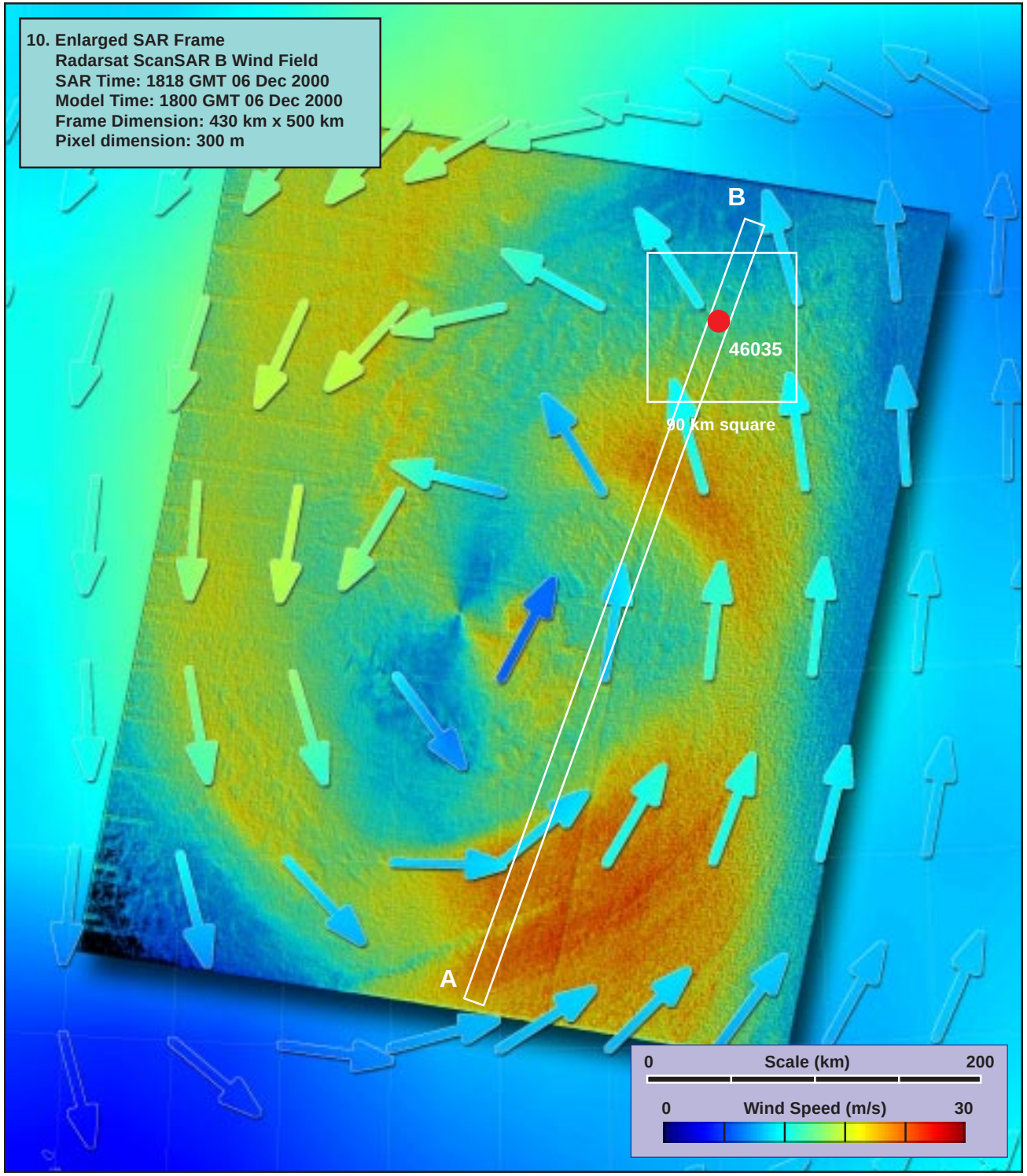

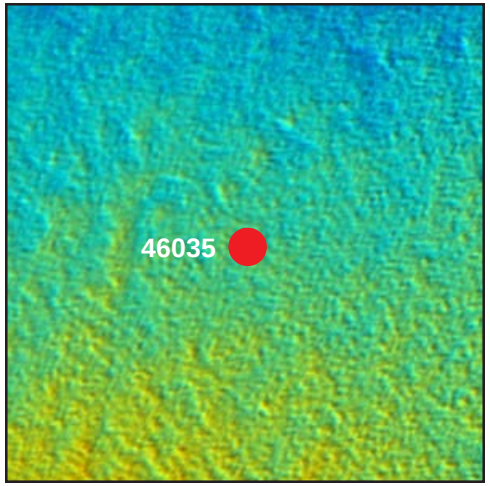

90 km square

11. Vicinity of Buoy 46035 (x 2.5)

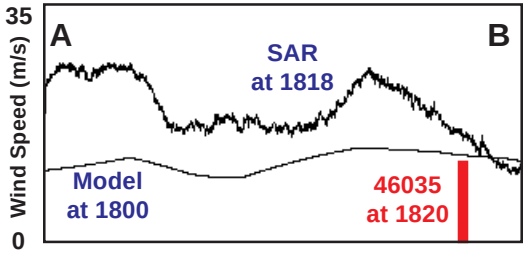

12. Model vs SAR Wind Profile along Line AB

13. Buoy 46035 around overpass time

YY	MM	DD	hh	mm	DIR	SPD	GDR	GSP	
00	12	06	17	50	124	10.6	109	15.0	
00	12	06	18	00	121	11.0			
00	12	06	18	10	123	10.6			
00	12	06	18	20	125	12.1			(overpass time)
00	12	06	18	30	123	11.4			
00	12	06	18	40	123	11.5			
00	12	06	18	50	127	11.3	121	14.7	

YY	MM	DD	hh	DIR	SPD	GSP	
00	12	06	10	58	15.1	18.5	
00	12	06	11	53	15.4	19.7	
00	12	06	12	53	16.3	19.9	(maximum winds)
00	12	06	13	58	15.3	19.3	
00	12	06	14	78	15.2	19.0	
00	12	06	15	83	13.0	16.3	
00	12	06	16	106	10.4	13.7	
00	12	06	17	119	10.8	13.4	
00	12	06	18	125	10.6	12.5	(overpass time)
00	12	06	19	127	11.4	14.1	
00	12	06	20	122	11.4	14.2	

1. Surface Pressure (mb) ~ t_0-36h

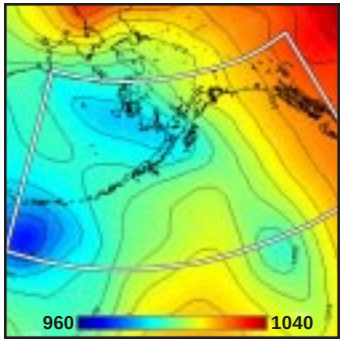

2. Surface Pressure (mb) ~ t_0-24h

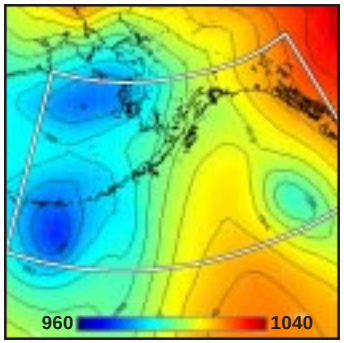

3. Surface Pressure (mb) ~ t_0-12h

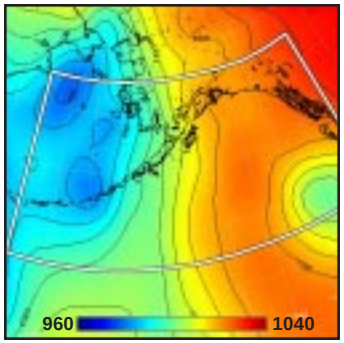

4. Surface Pressure (mb) ~ t_0

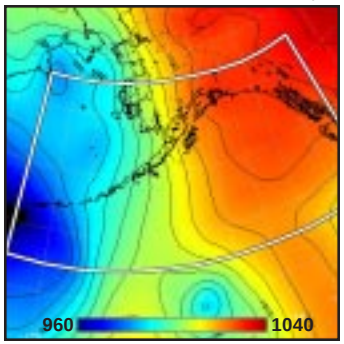

9. Enlarged Surface Wind Field ~ t_0

0600 GMT 12 Dec 2000

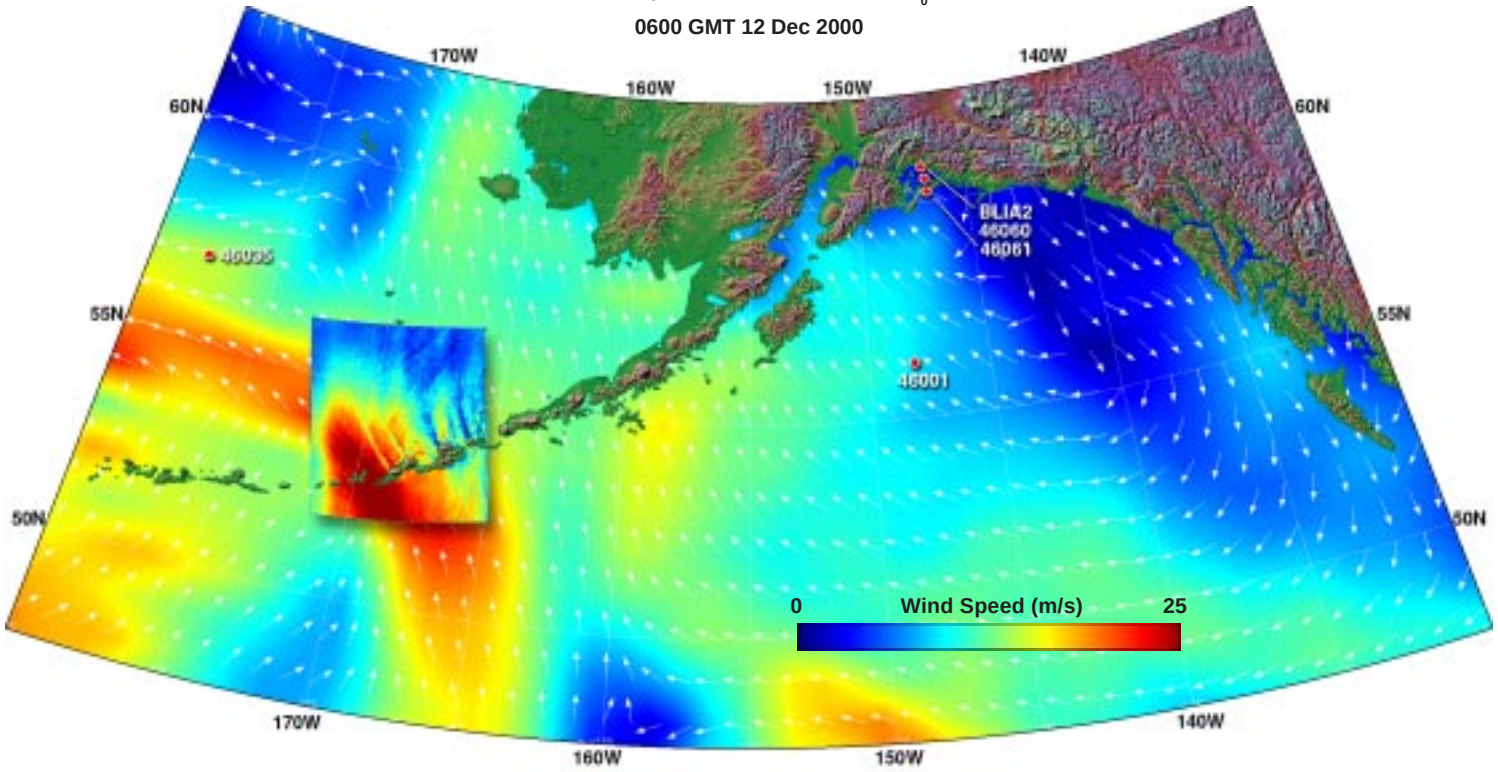

Model (this page): In the wake of a recently dissipating low pressure system, a new and more energetic one appears in the SW, crossing over the western Aleutians near overpass time (1-4), and an intense band of high winds advances over the central Aleutians (5, 9), with southerly waves highest to the south (6), but growing rapidly over the Aleutians (7) as the storm approaches. Although the MABL is highly stable to the south, it is unstable around the islands at overpass time (8).

SAR (facing page): The SAR winds show strong streaking to the NW immediately downwind of the islands, but turning to the NE further downwind, evidently indicating the earlier wind history over the islands (10, 11). Gravity waves appear transverse to the wind (10B) in the lee of the mountains. A scan nearly normal to the wind streaks (12) shows the depth of wind modulation caused by the topography. Some of the stronger variations within the streaks appear to approach the mean wind speed. Again, the mean SAR winds generally exceed the model winds by ~5 m/s. [ref. section 2.1: island and mountain wakes.]

5. Surface Wind Field (m/s) ~ t_0

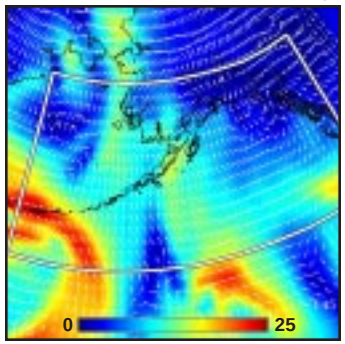

6. Surface Wave Height (m) ~ t_0

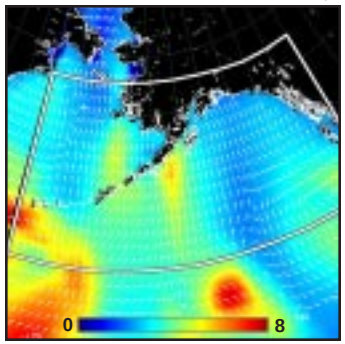

7. Inverse Wave Age (norm) ~ t_0

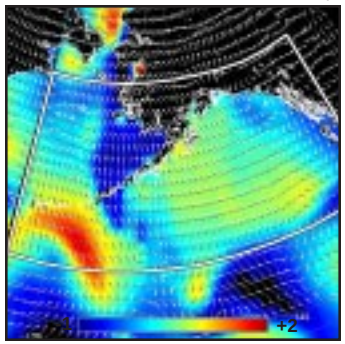

8. Air-Sea Temperature (˚C) ~ t_0

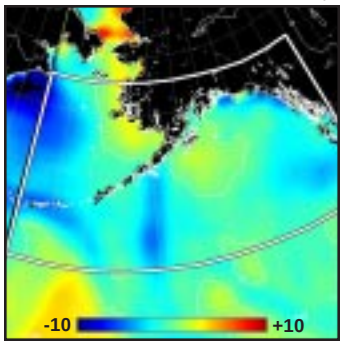

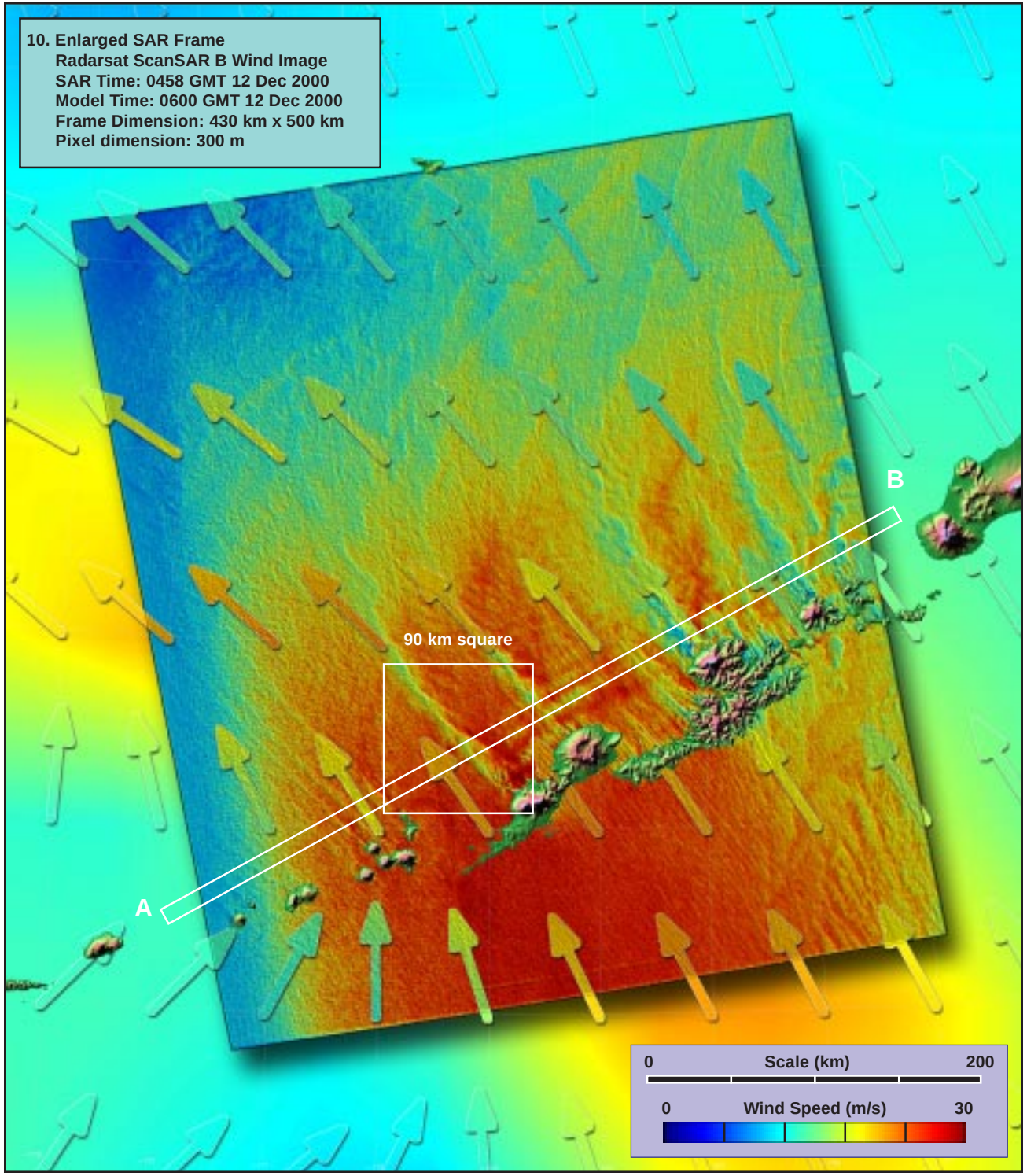

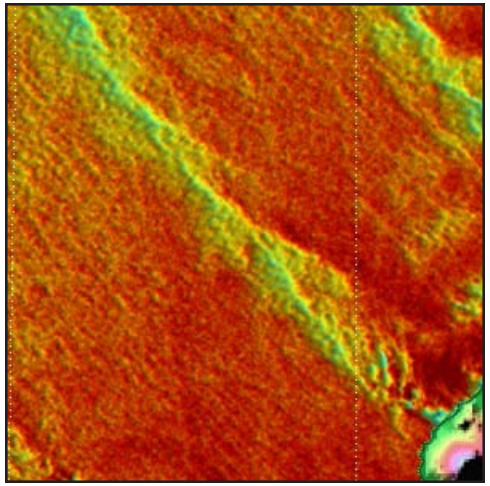

90 km square

11. Island Shadowing Detail (x 2.5)

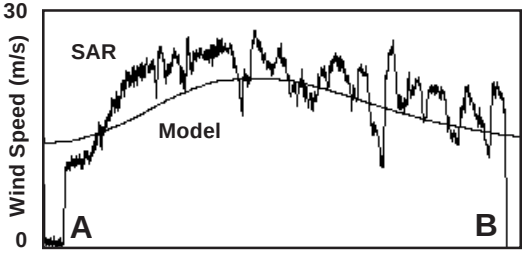

12. Model vs SAR Wind Profile along Line AB

1. Surface Pressure (mb) ~ t_0-36h

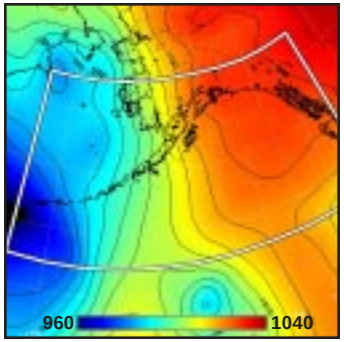

2. Surface Pressure (mb) ~ t_0-24h

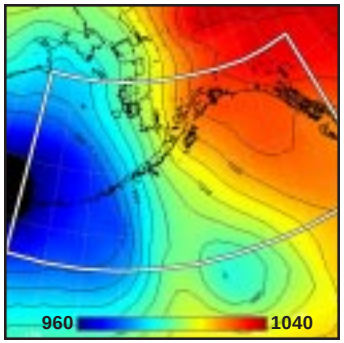

3. Surface Pressure (mb) ~ t_0-12h

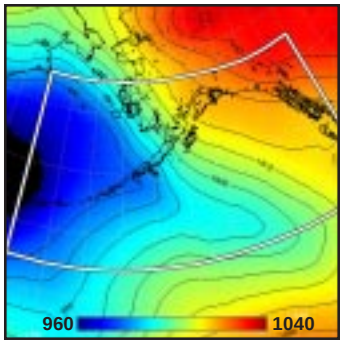

4. Surface Pressure (mb) ~ t_0

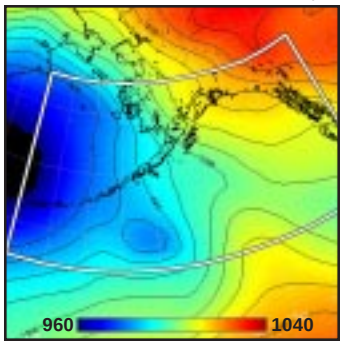

9. Enlarged Surface Wind Field ~ t_0

0600 GMT 13 Dec 2000

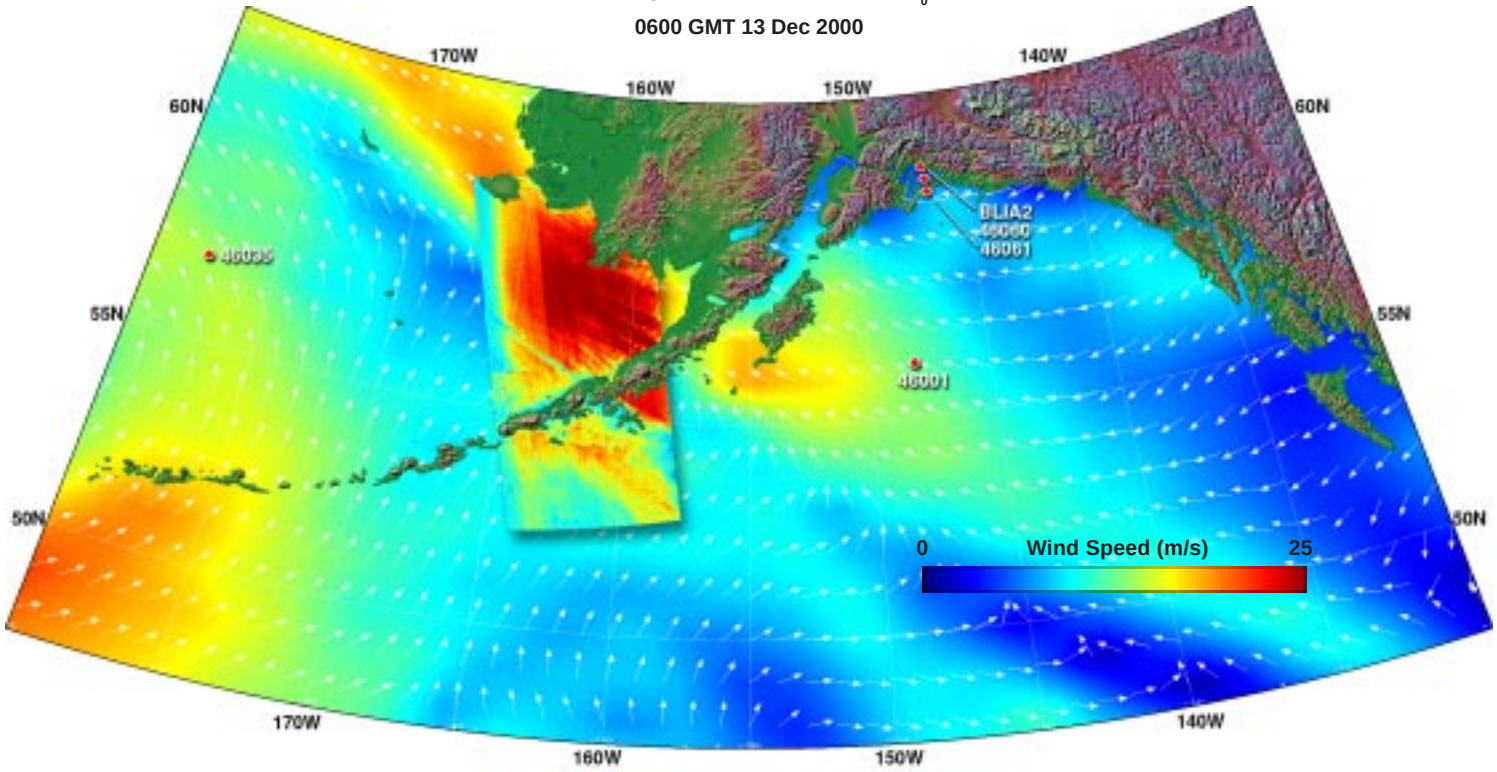

Model (this page): A day later, the same low pressure center (see 12 Dec) deepens as it moves to the north (1-4), and the intense band of high winds moves further east over the Alaskan Peninsula (5, 9), with SE waves already high (6) and well developed (7) downwind of the Peninsula, but still growing rapidly on the upwind side. The effect of limited fetch downwind of the Peninsula is evident in the model (6, 7). The MABL is stable on both sides of the Peninsula (8).

SAR (facing page): The SAR winds continue to show strong streaking to the WNW immediately downwind of the Peninsula (10), with a remarkably long (and puzzling) shadow (11) extending for at least 200 km. Mountain lee waves are superposed on the streaks. The major shadow (11) appears to be the modified extension of a front upwind of the islands to the SE. The wind speed within the shadow appears reduced from the local mean by 5-10 m/s. A scan nearly normal to the wind streaks (12) shows the SAR winds again exceeding the model by 5-10 m/s over most of the swath.

5. Surface Wind Field (m/s) ~ t_0

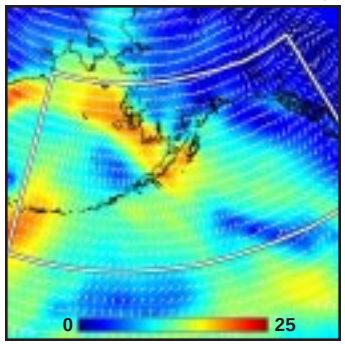

6. Surface Wave Height (m) ~ t_0

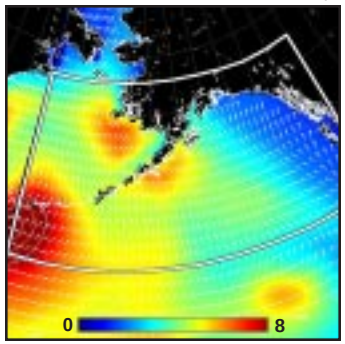

7. Inverse Wave Age (norm) ~ t_0

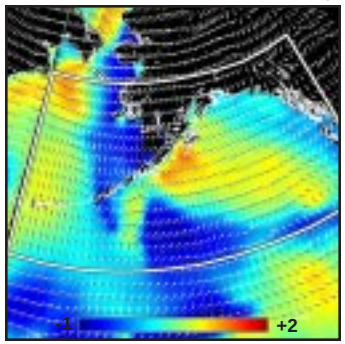

8. Air-Sea Temperature (˚C) ~ t_0

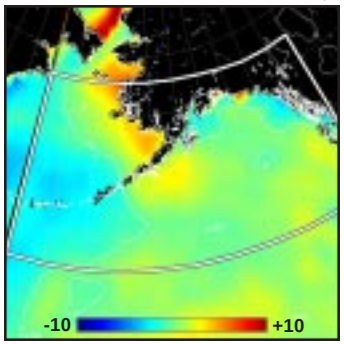

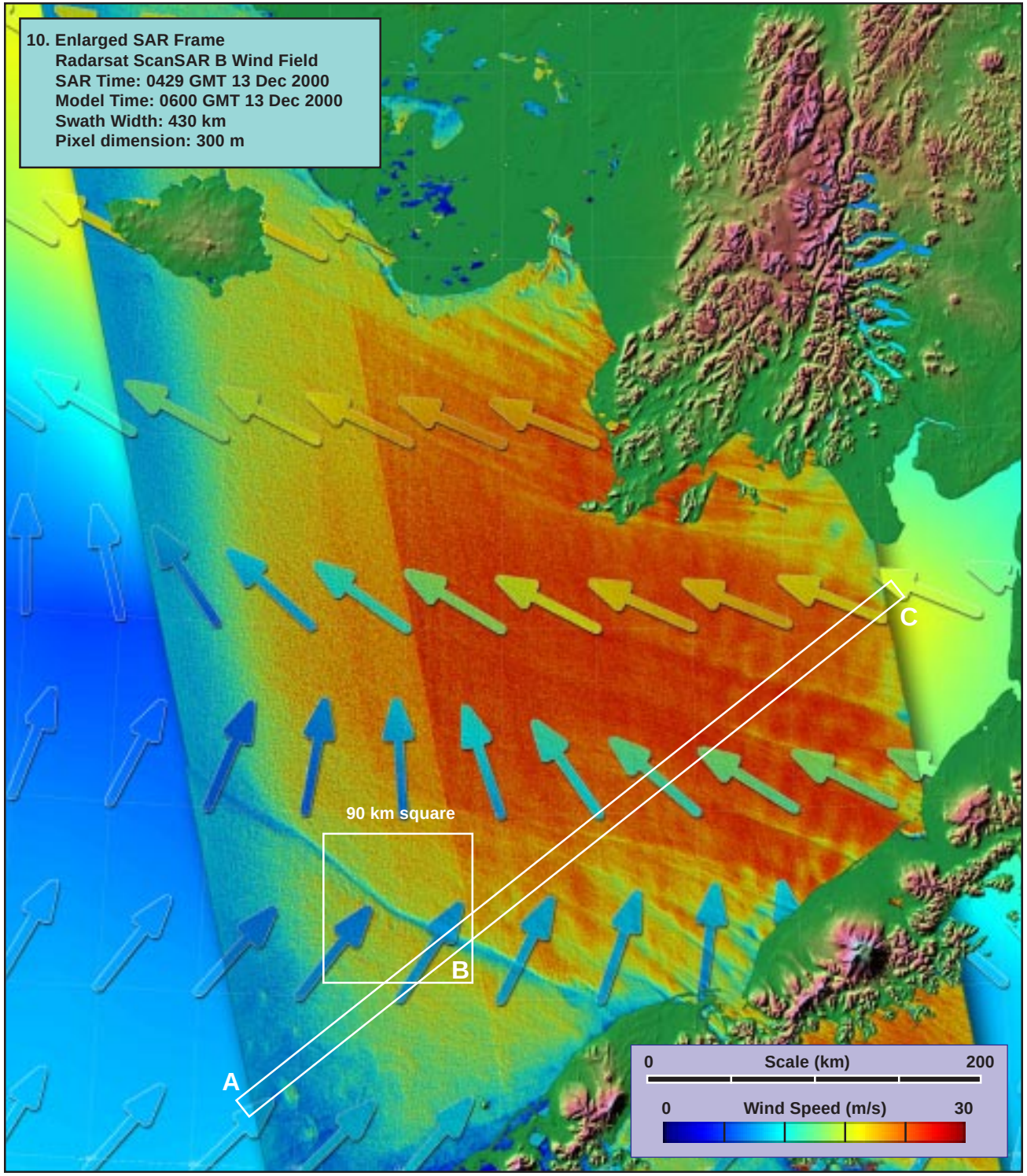

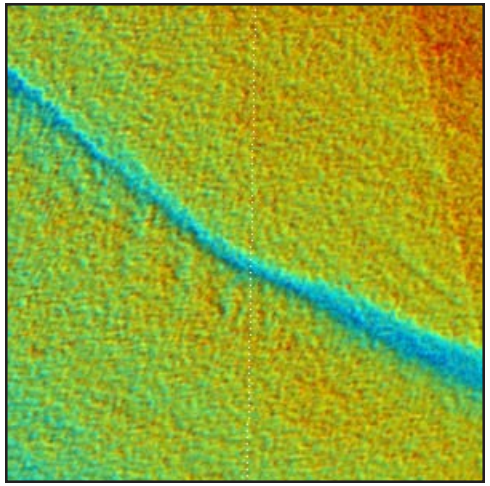

90 km square

11. Detail of Shadowing at point B

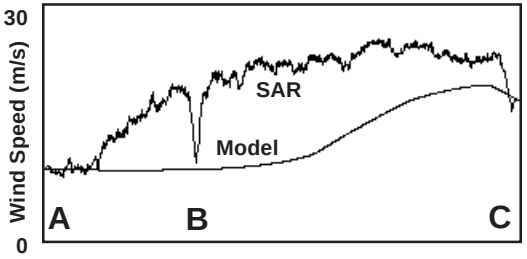

12. Model vs SAR Wind Profile along Line ABC

1. Surface Pressure (mb) ~ t_0-36h

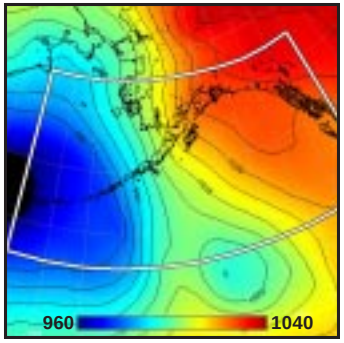

2. Surface Pressure (mb) ~ t_0-24h

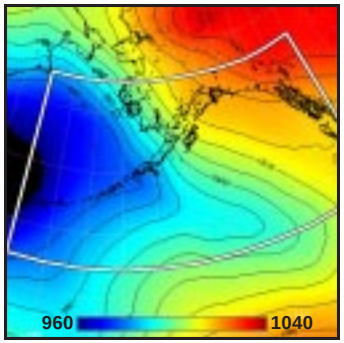

3. Surface Pressure (mb) ~ t_0-12h

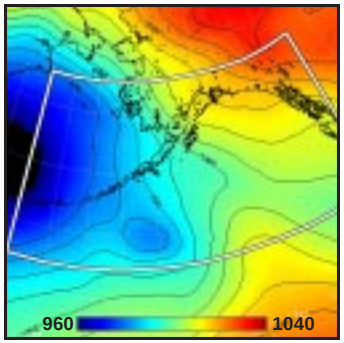

4. Surface Pressure (mb) ~ t_0

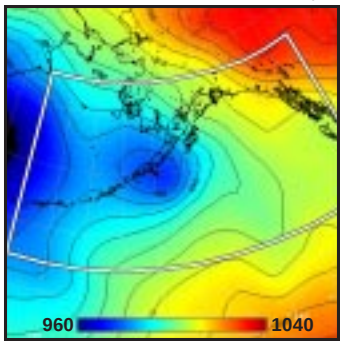

9. Enlarged Surface Wind Field ~ t_0

1800 GMT 13 Dec 2000

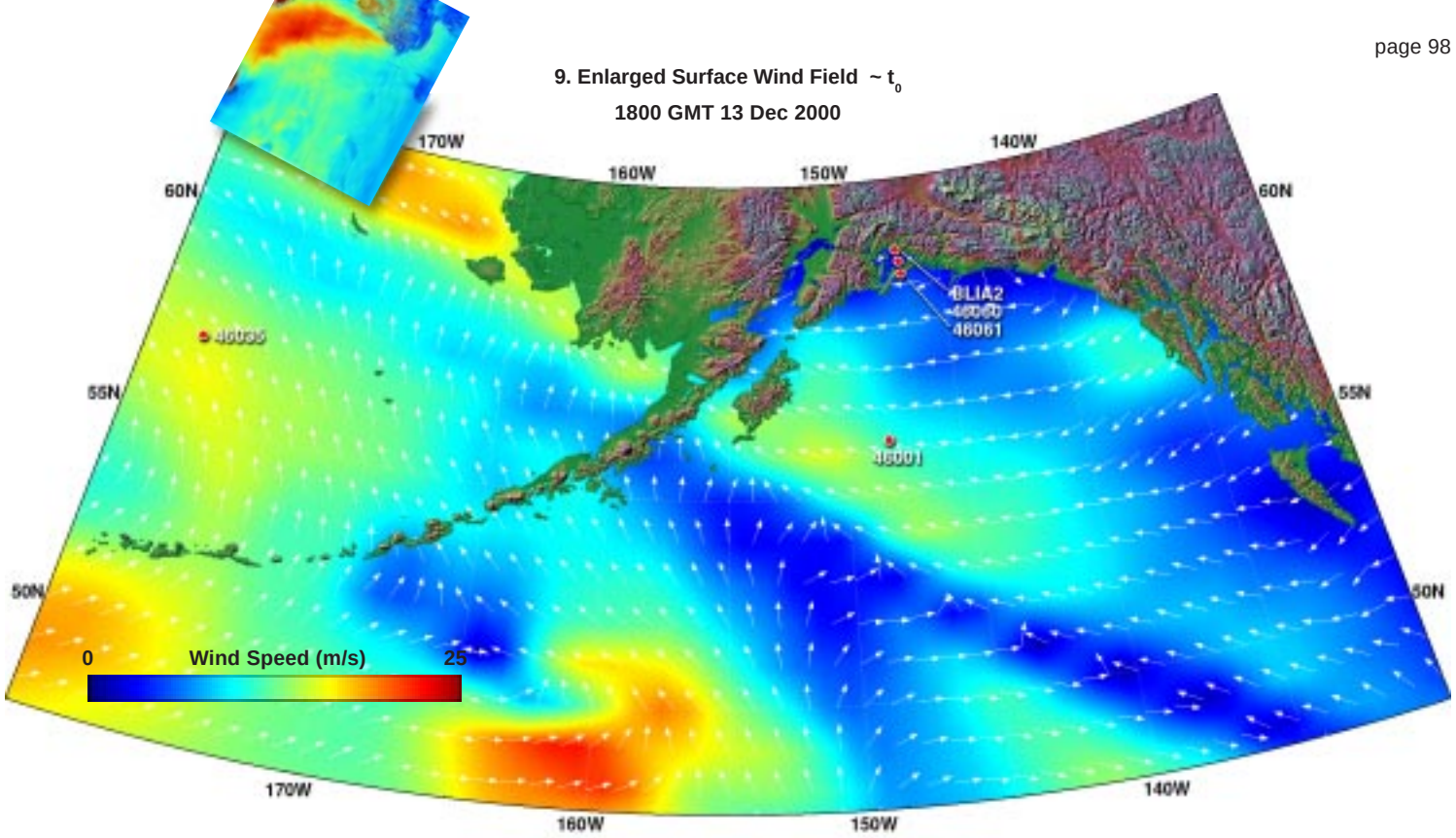

Model (this page): A deep, nearly stationary low pressure system lingers just to the west of the above delineated region (1-4), producing strong easterly winds along the southern Siberian coast . Model winds along the coast (5) show a maximum of 15 to 20 m/s . Concurrent model waves, approaching from the southeast, are 6 to 7 m, still actively growing (6, 7). The MABL is extremely unstable (8).

SAR (facing page): Instead of a broad region of 10 to 15 m/s model winds, the SAR (10, 11) clearly reveals a strong topographically generated point wake emanating from Cape Chukotskiy. An expansion fan spreads out downwind of the generating point, with maximum winds of nearly 25 m/s occurring about 200 km downwind of the source. This fan structure is completely absent in the model. [ref. section 2.2: point wakes.]

5. Surface Wind Field (m/s) ~ t_0

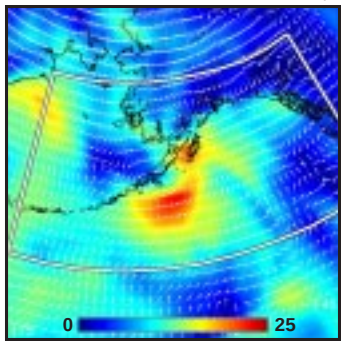

6. Surface Wave Height (m) ~ t_0

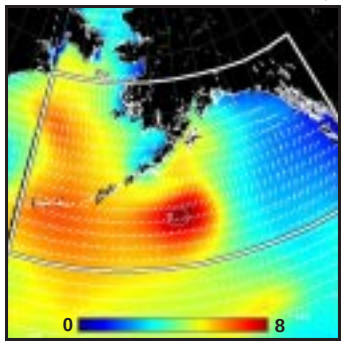

7. Inverse Wave Age (norm) ~ t_0

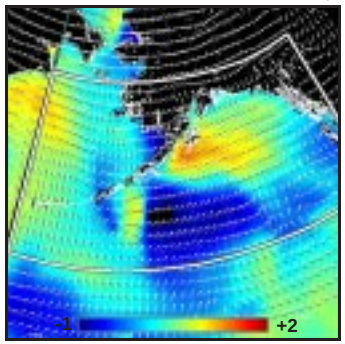

8. Air-Sea Temperature (˚C) ~ t_0

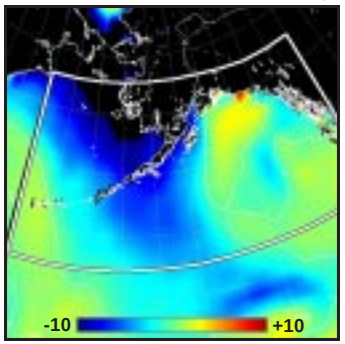

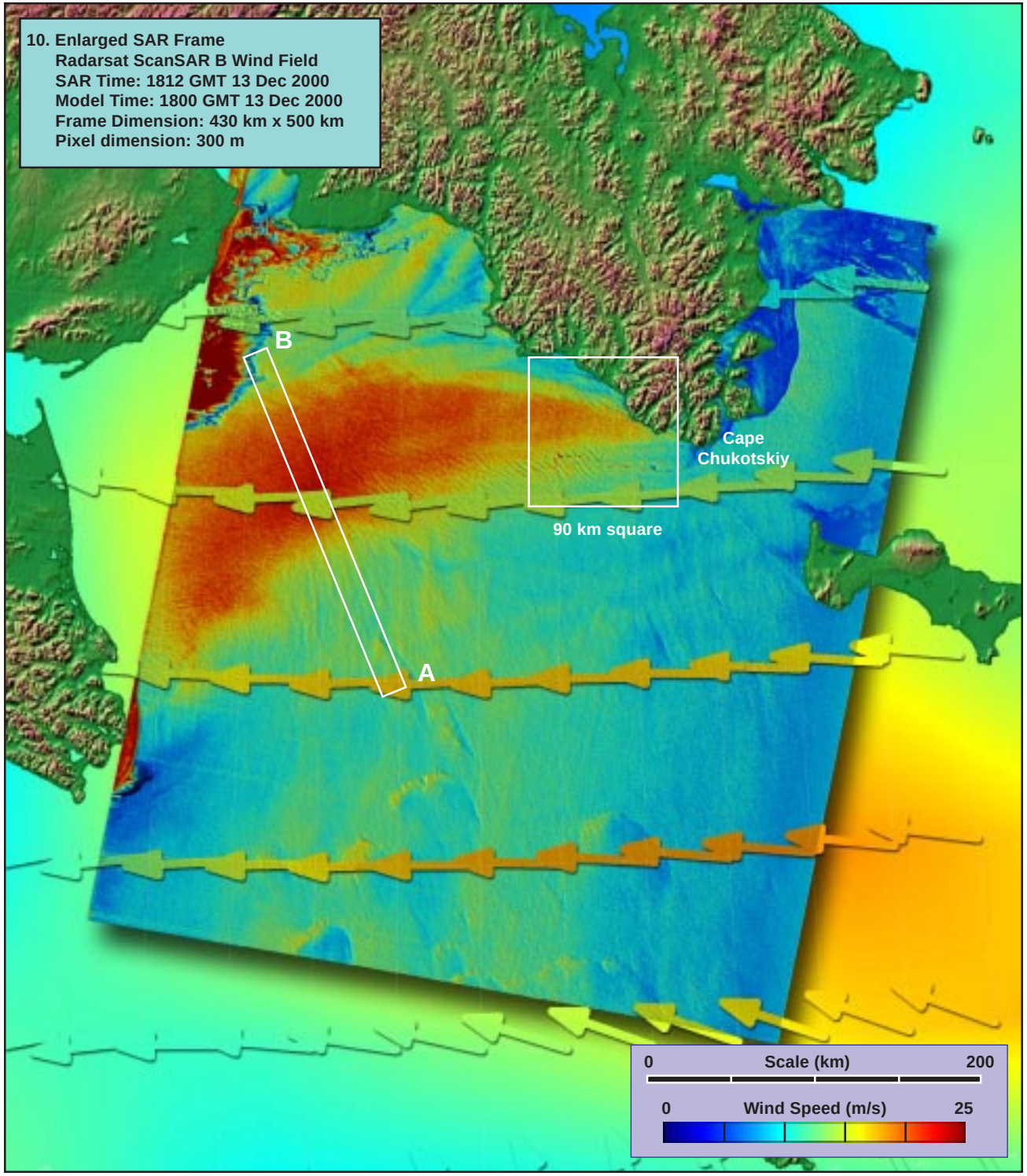

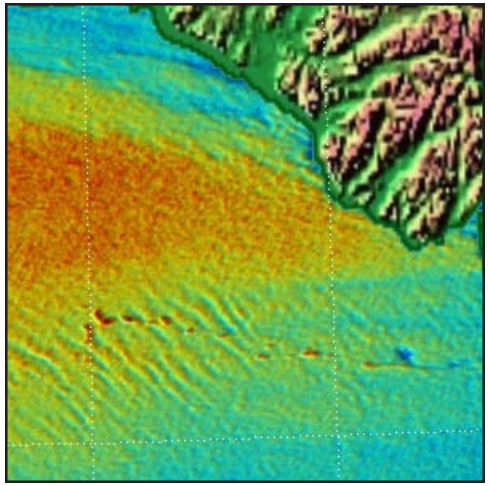

90 km square

11. Detail of Plume (x 2.5)

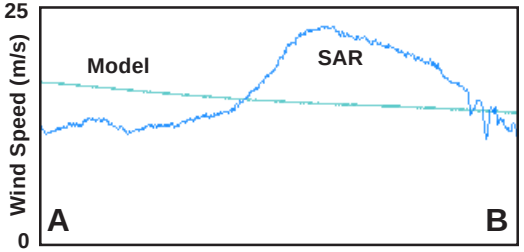

12. Model vs SAR Wind Profile along Line AB

1. Surface Pressure (mb) ~ t_0-36h

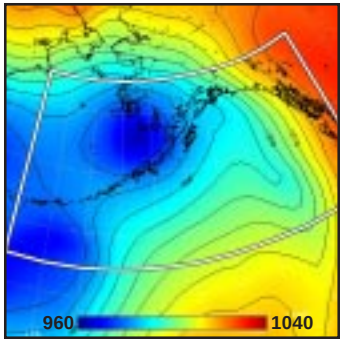

2. Surface Pressure (mb) ~ t_0-24h

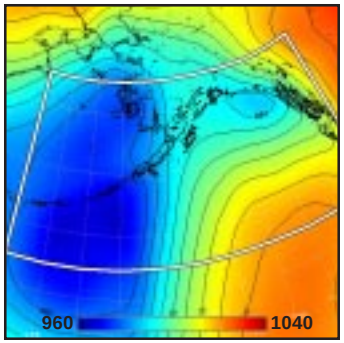

3. Surface Pressure (mb) ~ t_0-12h

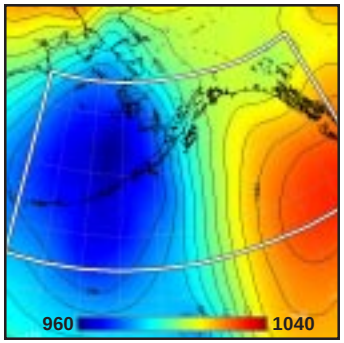

4. Surface Pressure (mb) ~ t_0

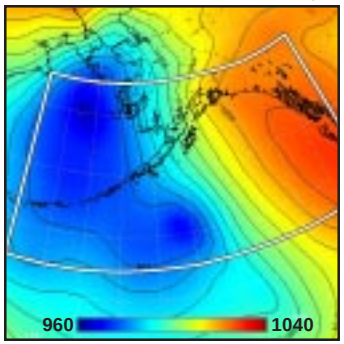

9. Enlarged Surface Wind Field ~ t_0

1800 GMT 19 Dec 2000

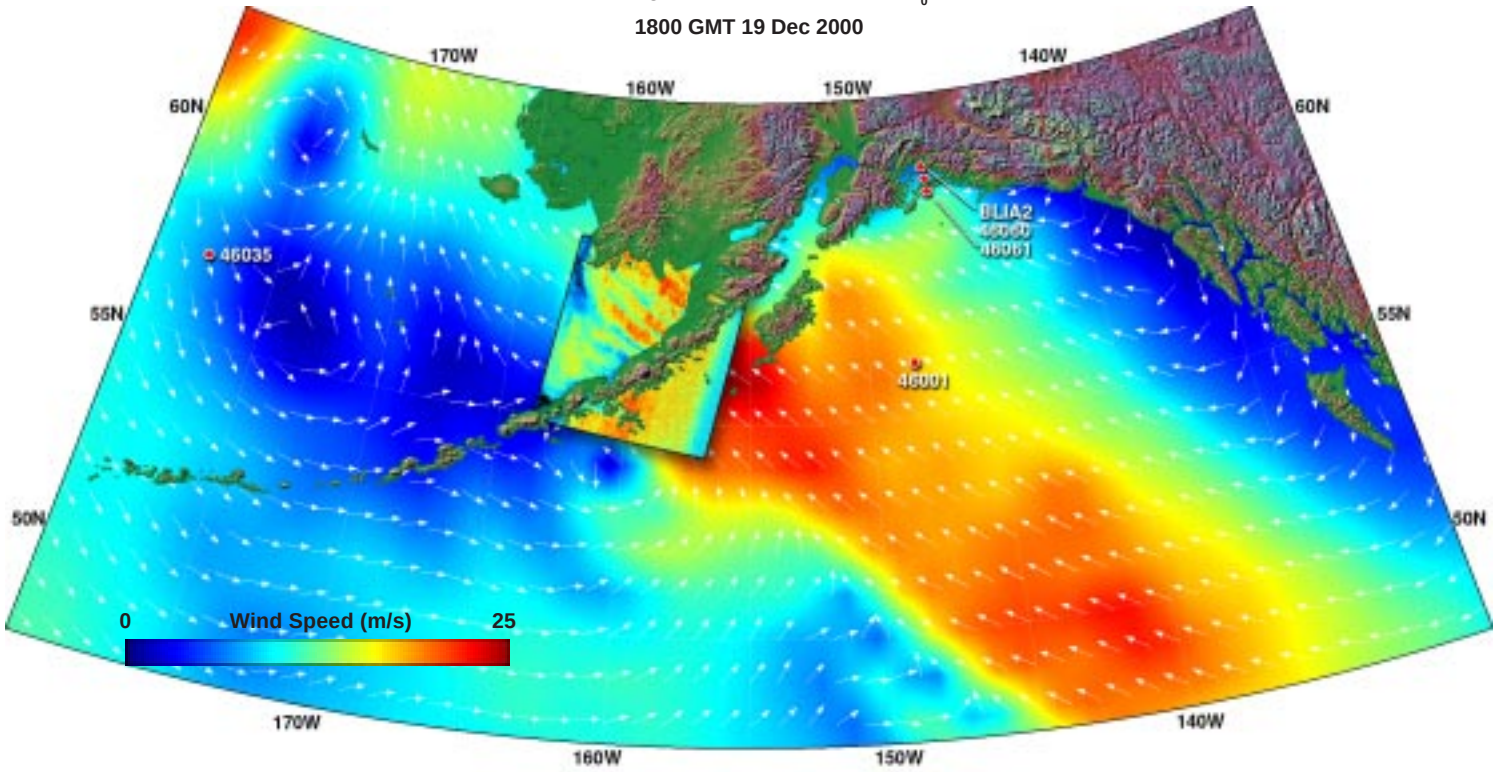

Model (this page): A large coupled pair of low pressure systems slowly gyrate about one another to the west of a blocking high, resulting in a strong pressure gradient extending from the southern Gulf of Alaska through the Aleutian peninsula to the Bering Strait (1-4). Model winds show an extensive, remarkably homogeneous region of high (20 to 25 m/s) winds extending completely through the Gulf of Alaska (5, 9) to the Aleutian mountain chain. Concurrent model waves exceed 8 m over a broad region to the southeast of the SAR pass. On the windward side of the pass, the waves are about 6 m, actively growing (6, 7); on the leeward side, the waves are less than 3 m, decaying as they are opposed by the wind. The MABL is extremely unstable everywhere within the SAR pass (8).

SAR (facing page): The SAR winds reveal a rich pattern of mountain wakes leeward of the Aleutians, with wind speed sometimes varying from 10 m/s to 20 m/s within a few 10's of km (10, 11, 12).

5. Surface Wind Field (m/s) ~ t_0

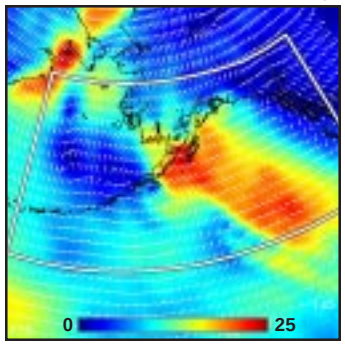

6. Surface Wave Height (m) ~ t_0

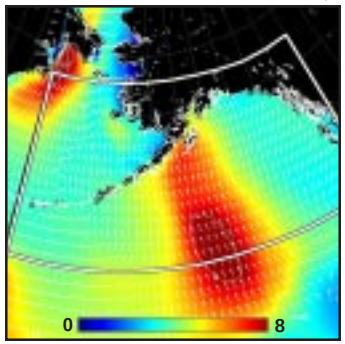

7. Inverse Wave Age (norm) ~ t_0

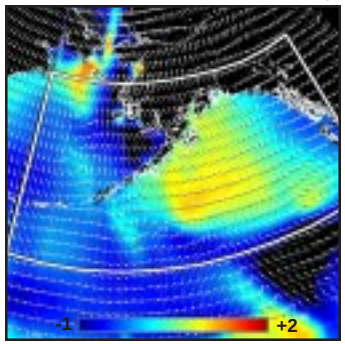

8. Air-Sea Temperature (˚C) ~ t_0

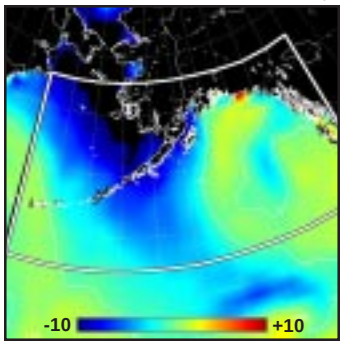

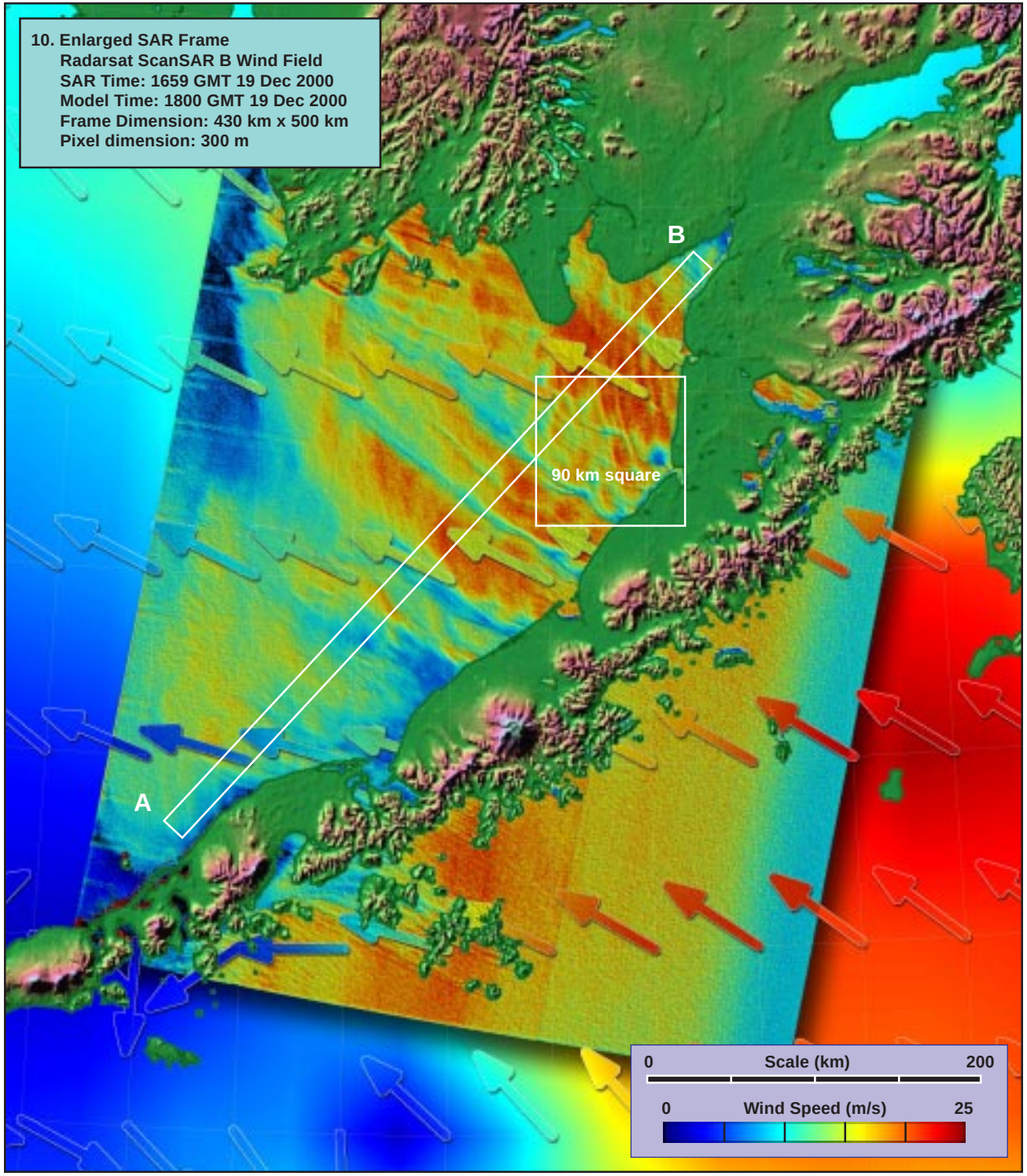

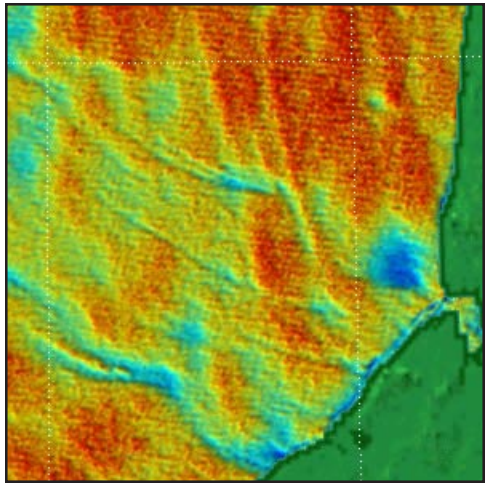

90 km square

11. Detail of Wake Patterns (x 2.5)

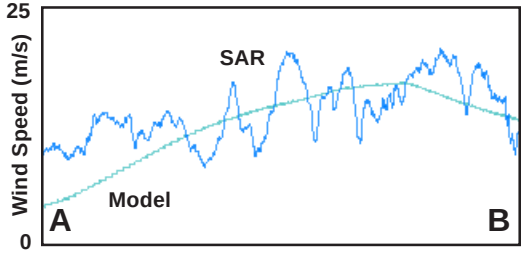

12. Model vs SAR Wind Profile along Line AB

1. Surface Pressure (mb) ~ t_0-36h

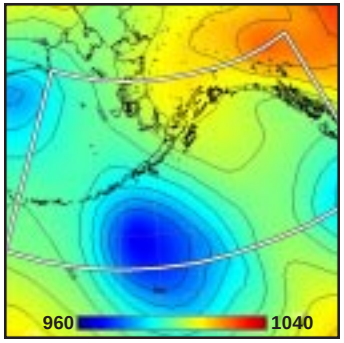

2. Surface Pressure (mb) ~ t_0-24h

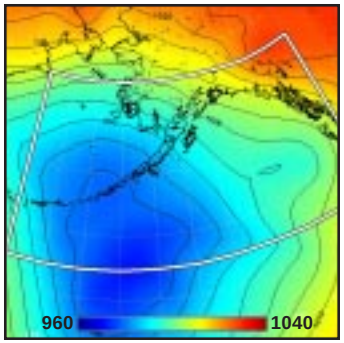

3. Surface Pressure (mb) ~ t_0-12h

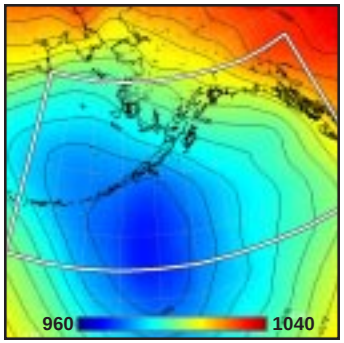

4. Surface Pressure (mb) ~ t_0

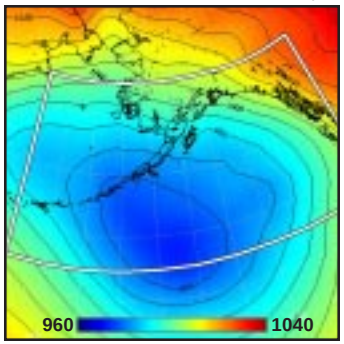

9. Enlarged Surface Wind Field ~ t_0

0600 GMT 25 Dec 2000

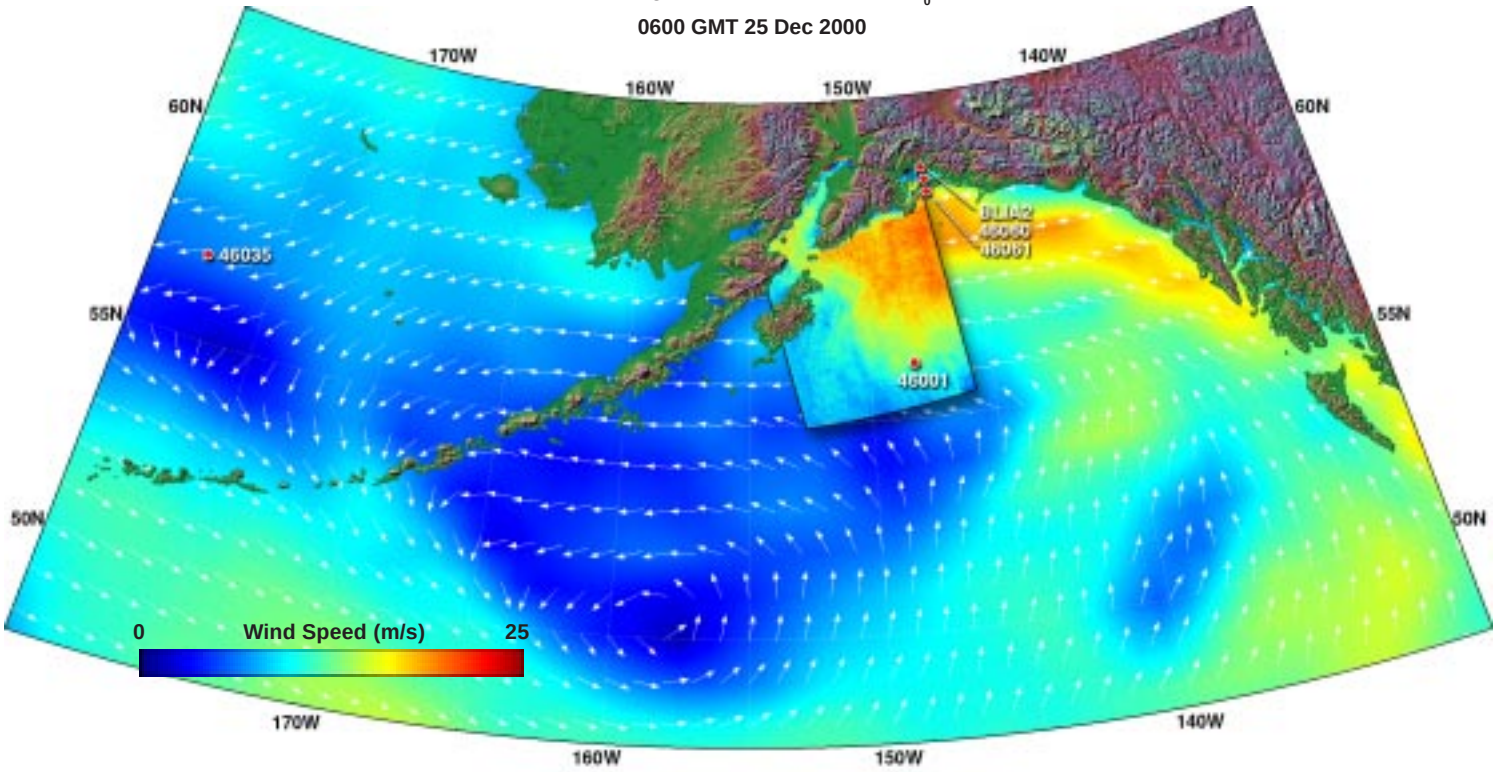

Model (this page): A broad, nearly stationary low pressure system centered in the western Gulf of Alaska generates a strong pressure gradient all along the southern Alaskan coast (1-4). Model winds peak at around 20 m/s just south of Prince William Sound (5, 9). Concurrent model waves are about 5 m, diminishing as they travel nearly normal to the local wind (6, 7). The MABL is stable to nearly neutral (8).

SAR (facing page): Except for regions of local sheltering immediately adjacent to the coast, the SAR winds exceed those of the model by 5 to 10 m/s (10, 11, 12). Sheltering from Montague Island (11) appears to extend at least 100 km downwind, producing about a 10 m/s drop in the local wind (12). Some of the wind structure within the western portion of Prince William Sound is evident on scales of 10 to 20 km.

5. Surface Wind Field (m/s) ~ t_0

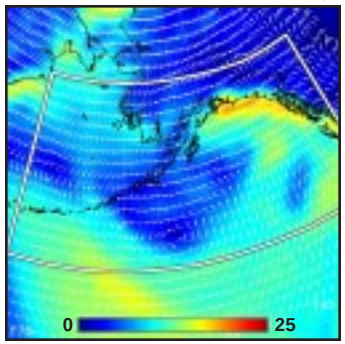

6. Surface Wave Height (m) ~ t_0

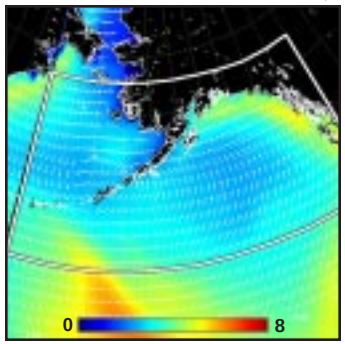

7. Inverse Wave Age (norm) ~ t_0

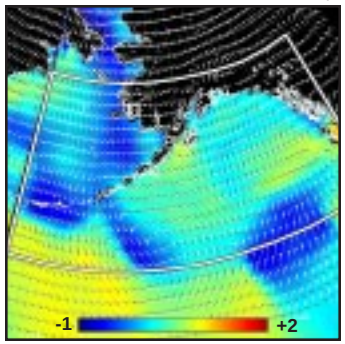

8. Air-Sea Temperature (˚C) ~ t_0

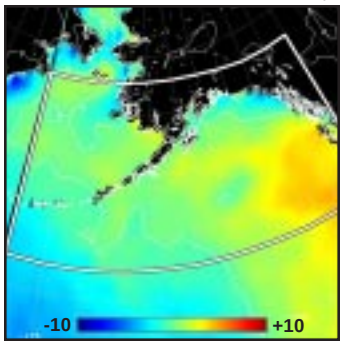

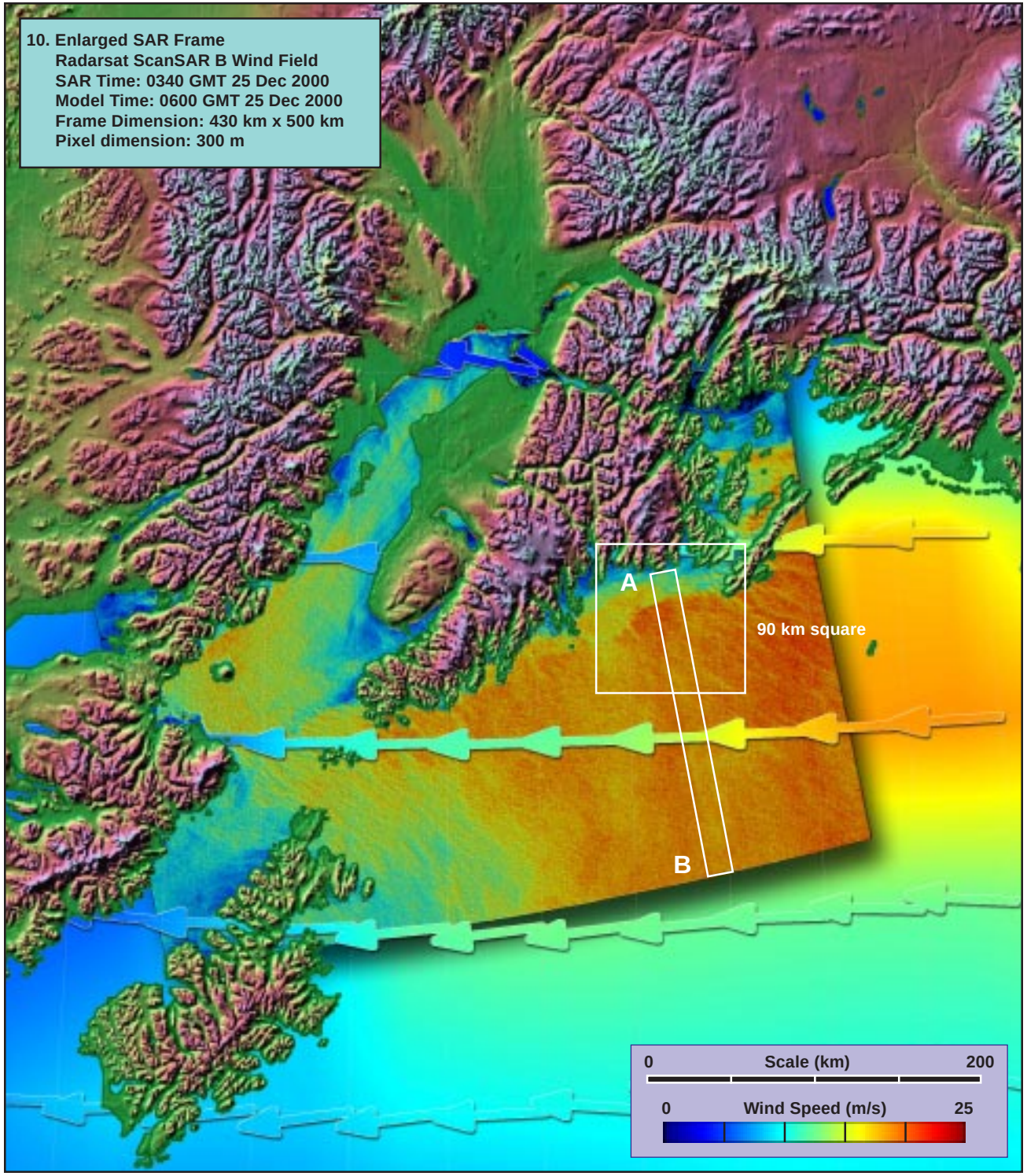

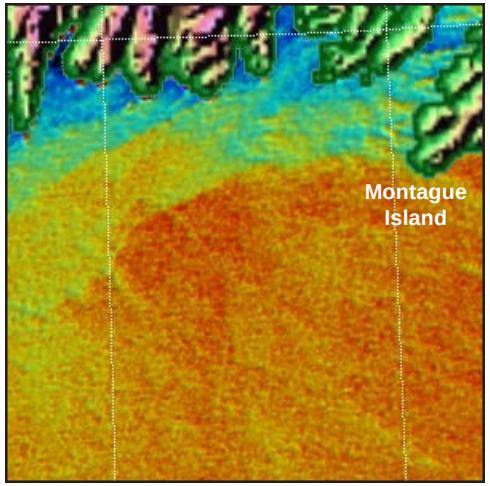

90 km square

11. Detail of Wind Front (x 2.5)

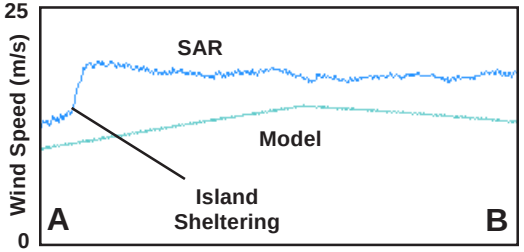

12. Model vs SAR Wind Profile along Line AB

1. Surface Pressure (mb) ~ t_0-36h

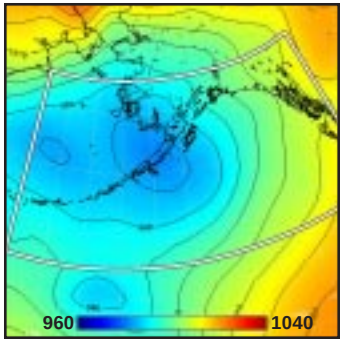

2. Surface Pressure (mb) ~ t_0-24h

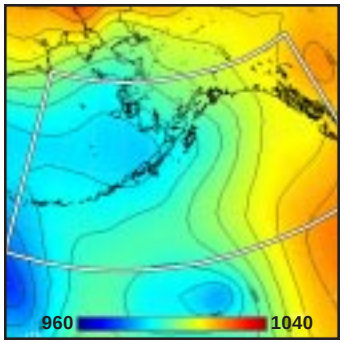

3. Surface Pressure (mb) ~ t_0-12h

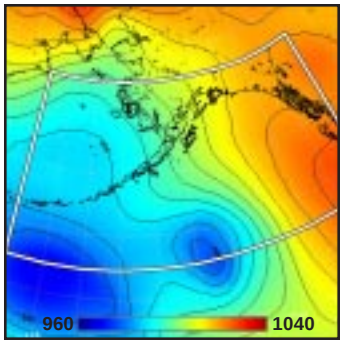

4. Surface Pressure (mb) ~ t_0

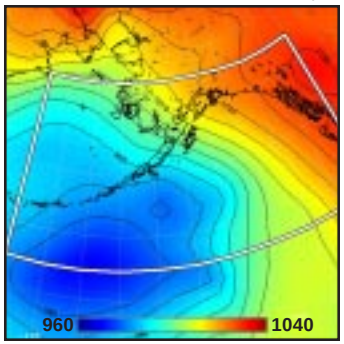

9. Enlarged Surface Wind Field ~ t_0

0600 GMT 28 Dec 2000

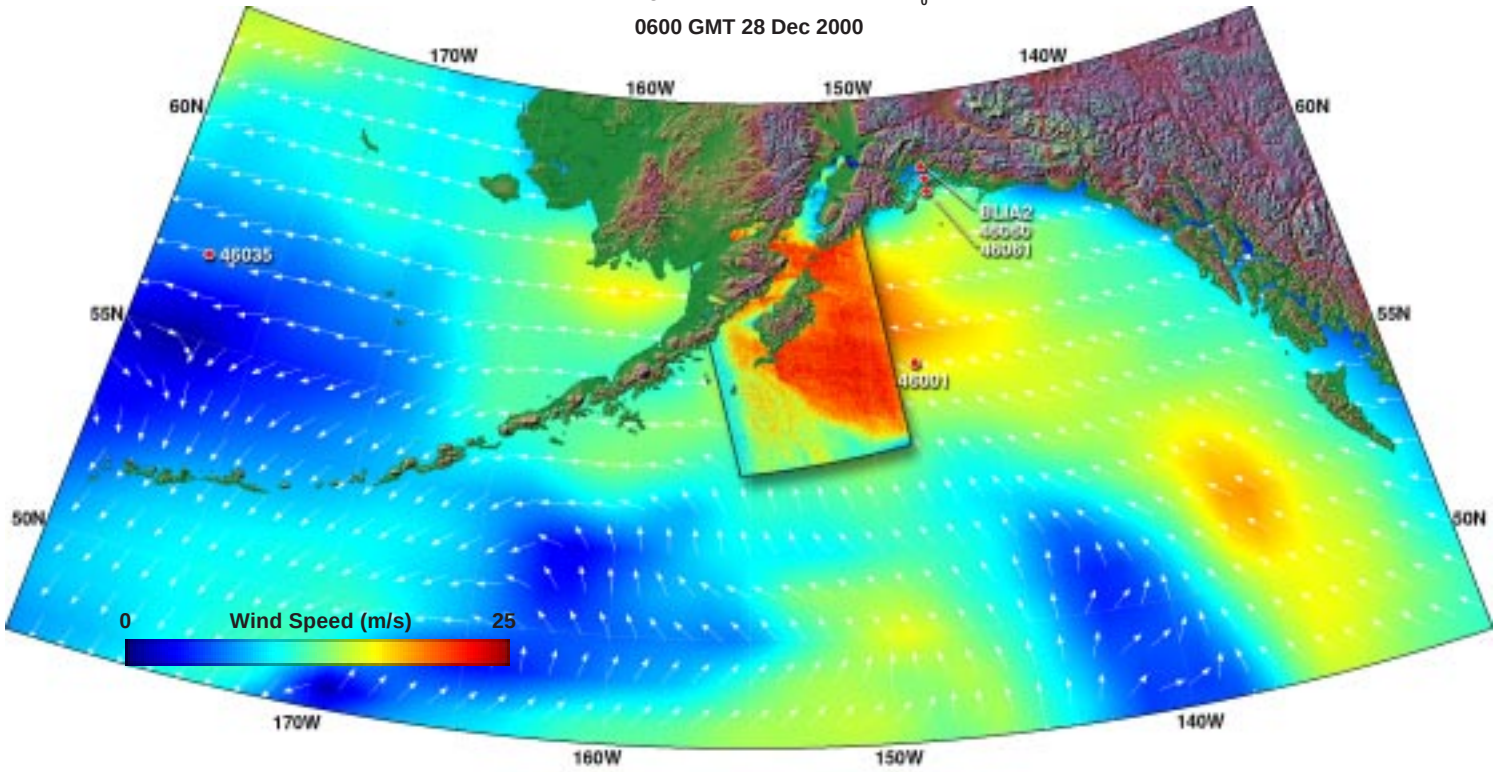

Model (this page): A strong low pressure system reforms from an earlier one in the western Gulf of Alaska, generating a strong pressure gradient cutting across Kodiak Island (1-4). Model winds peak at about 20 m/s under the SAR pass, just to the east of Kodiak Island (5, 9). Concurrent model waves are 6 to 8 m, actively growing within the high wind region (6, 7). The MABL is slightly unstable (8).

SAR (facing page): The SAR winds closely match those of the model on the eastern edge of the swath (10), but the model lacks the structure seen by the SAR to the NW of Kodiak Island (11), and fails to match the enhancement seen by the SAR along the Alaskan peninsula (12). Buoy 46001, just off the eastern edge of the pass, was not operating at the time of overpass.

5. Surface Wind Field (m/s) ~ t_0

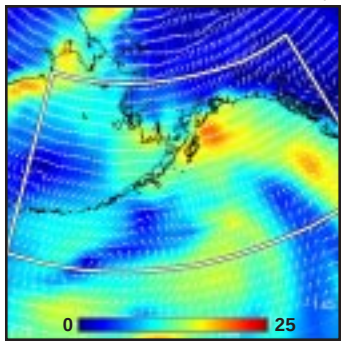

6. Surface Wave Height (m) ~ t_0

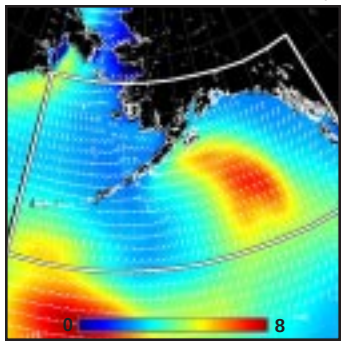

7. Inverse Wave Age (norm) ~ t_0

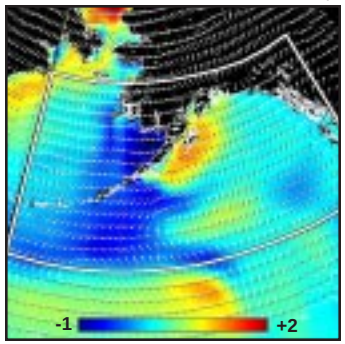

8. Air-Sea Temperature (˚C) ~ t_0

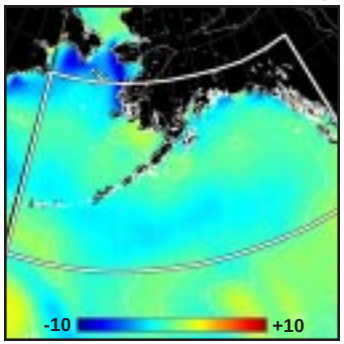

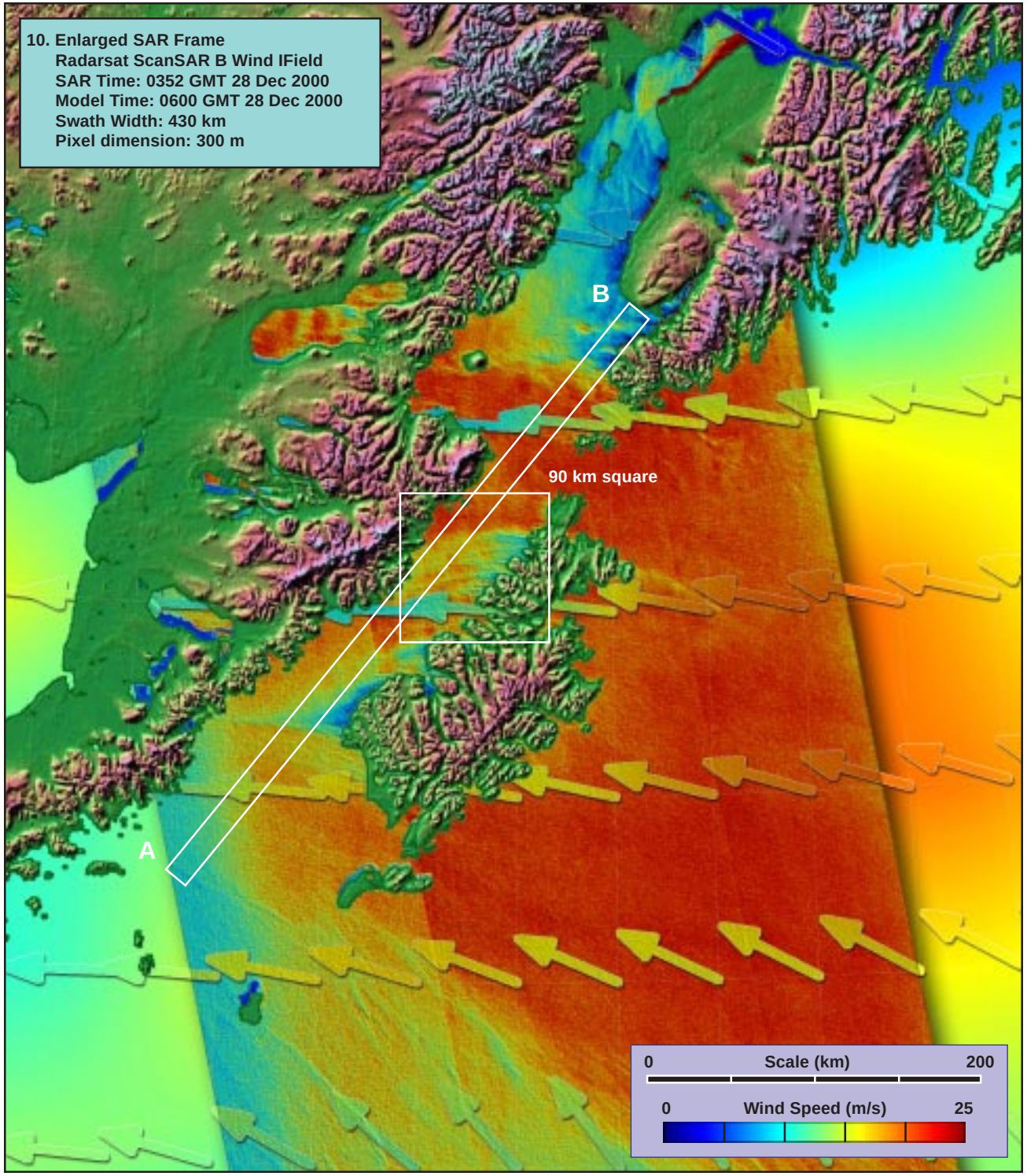

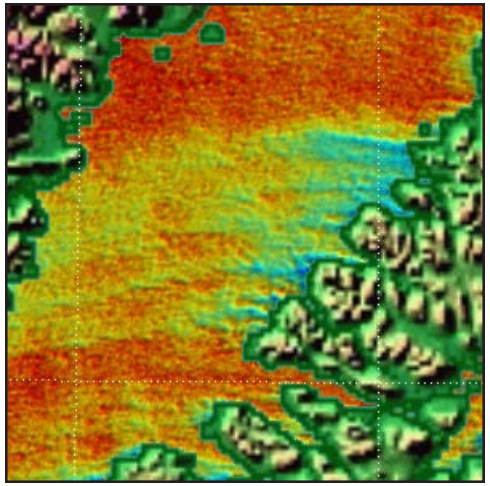

90 km square

11. Detail of Shadow Region (x 2.5)

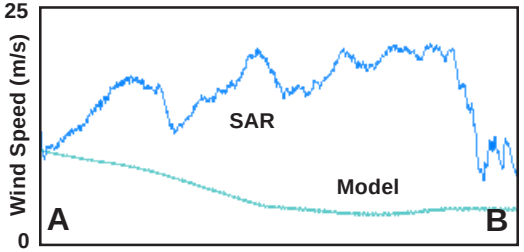

12. Model vs SAR Wind Profile along Line AB

1. Surface Pressure (mb) ~ t_0-36h

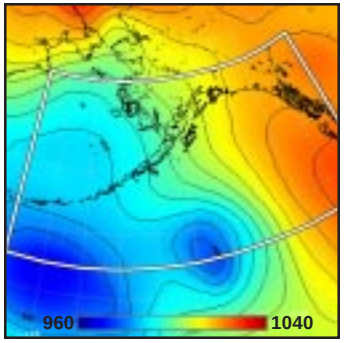

2. Surface Pressure (mb) ~ t_0-24h

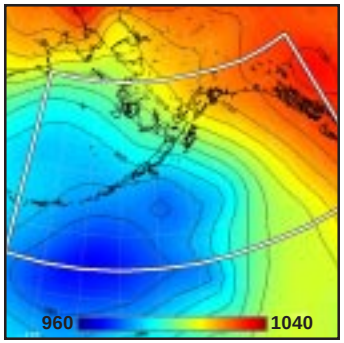

3. Surface Pressure (mb) ~ t_0-12h

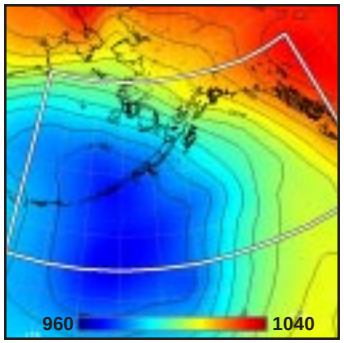

4. Surface Pressure (mb) ~ t_0

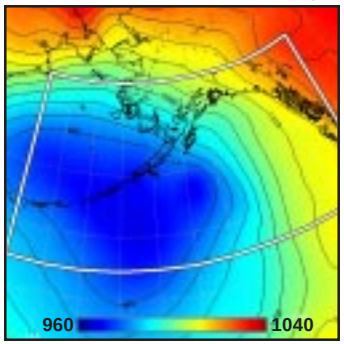

9. Enlarged Surface Wind Field ~ t_0

0600 GMT 29 Dec 2000

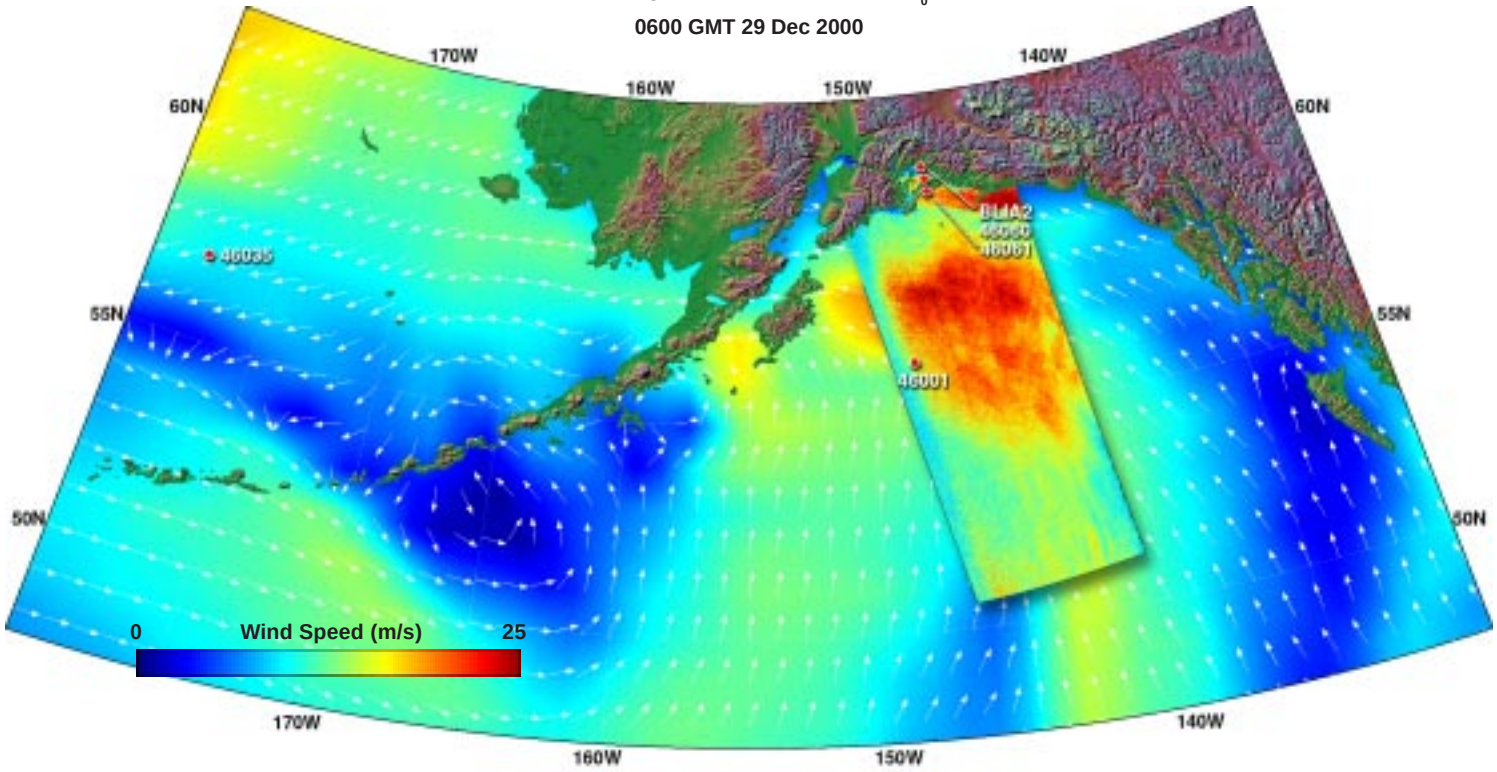

Model (this page): A growing low pressure system enters the Gulf of Alaska, pushing against a blocking high and creating a strong pressure gradient directed toward the southern Alaskan coast (1-4). Model winds peak around 15 to 20 m/s just south of Prince William Sound (5, 9). Concurrent model waves are about 6 m, and growing (6, 7). The MABL is neutral to slightly unstable (8).

SAR (facing page): The SAR winds reveal a distinct barrier jet formed along the coast, well separated from the offshore maximum corresponding to that of the model (10, 11). Within the jet, SAR winds exceed 20 m/s, about double those of the model (12). Buoy 46001 unfortunately was not operating at the time of overpass. [ref. section 2.11: coastal barrier jets.]

5. Surface Wind Field (m/s) ~ t_0

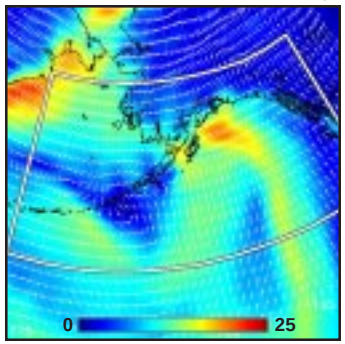

6. Surface Wave Height (m) ~ t_0

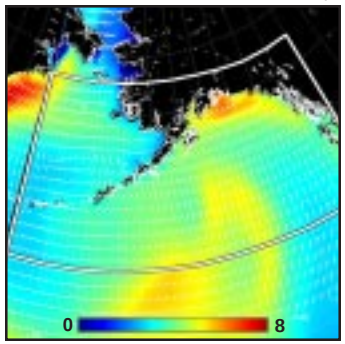

7. Inverse Wave Age (norm) ~ t_0

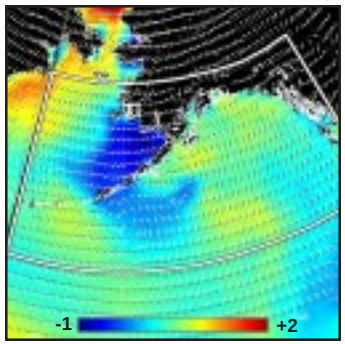

8. Air-Sea Temperature (˚C) ~ t_0

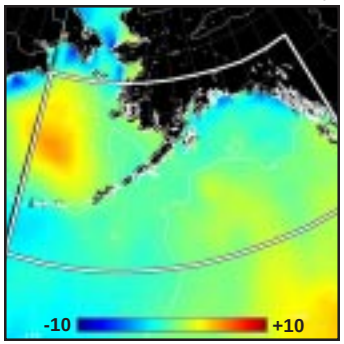

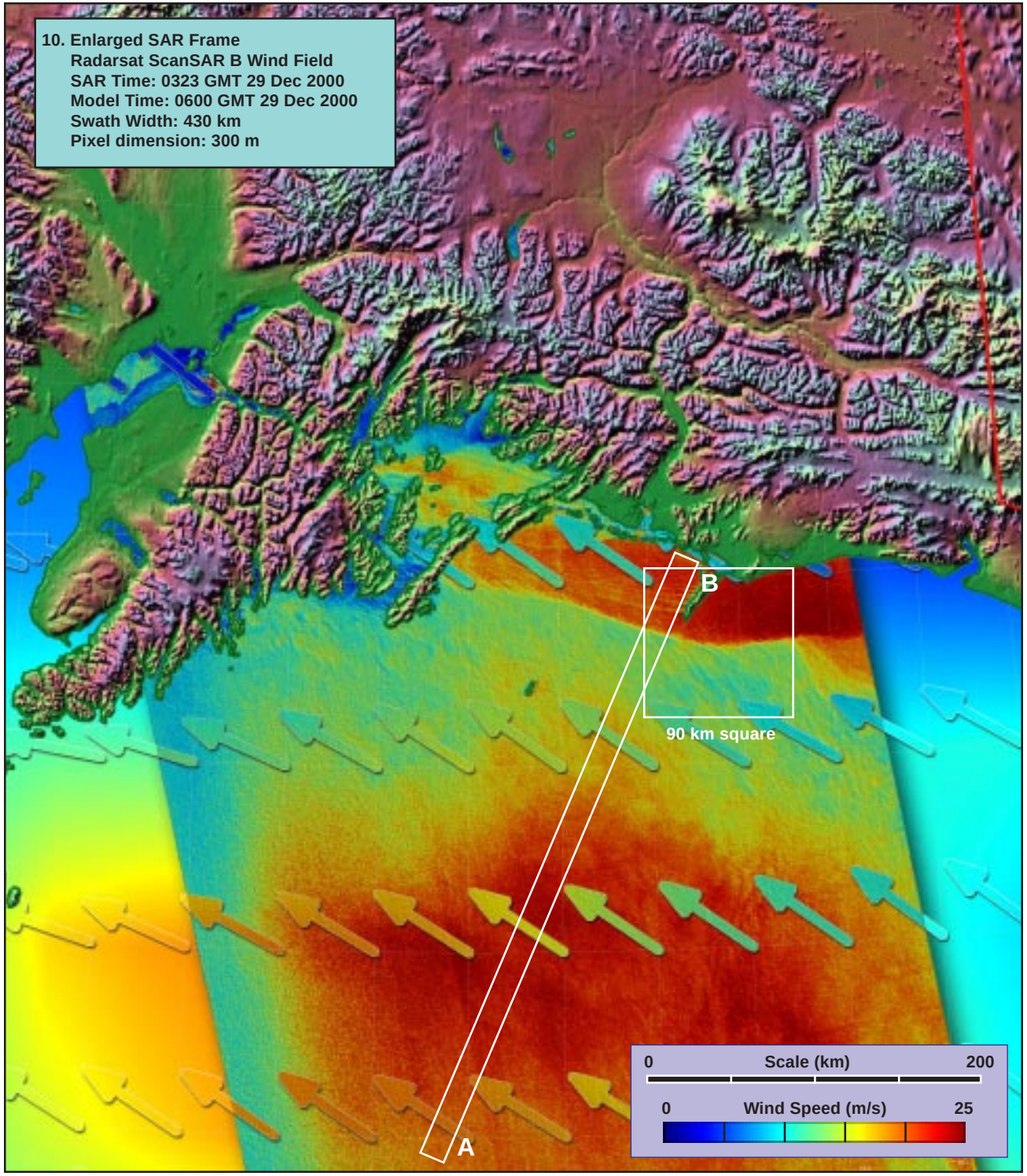

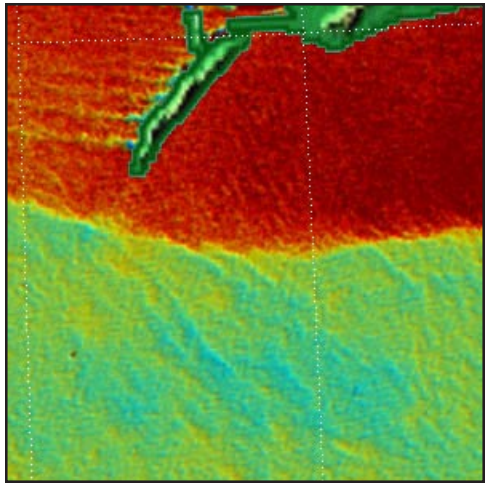

90 km square

11. Detail of Frontal Region (x 2.5)

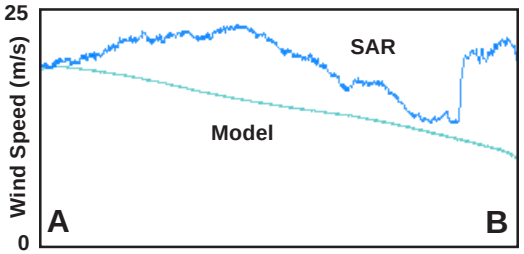

12. Model vs SAR Wind Profile along Line AB

1. Surface Pressure (mb) ~ t_0-36h

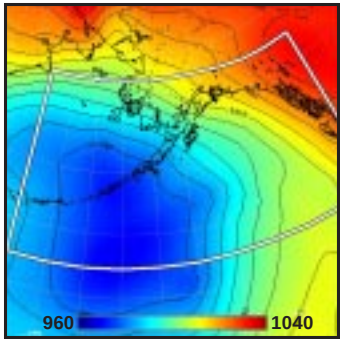

2. Surface Pressure (mb) ~ t_0-24h

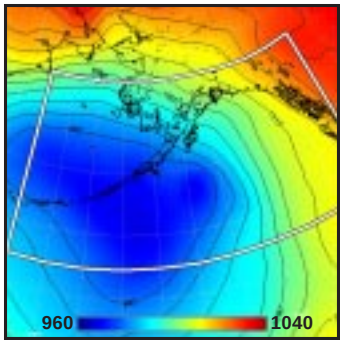

3. Surface Pressure (mb) ~ t_0-12h

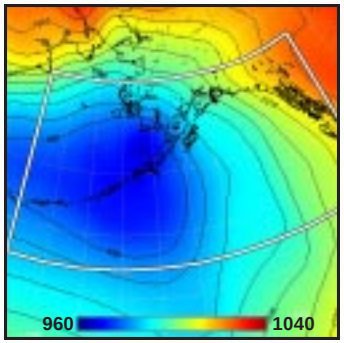

4. Surface Pressure (mb) ~ t_0

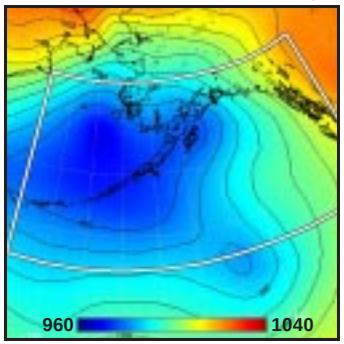

9. Enlarged Surface Wind Field ~ t_0

0600 GMT 30 Dec 2000

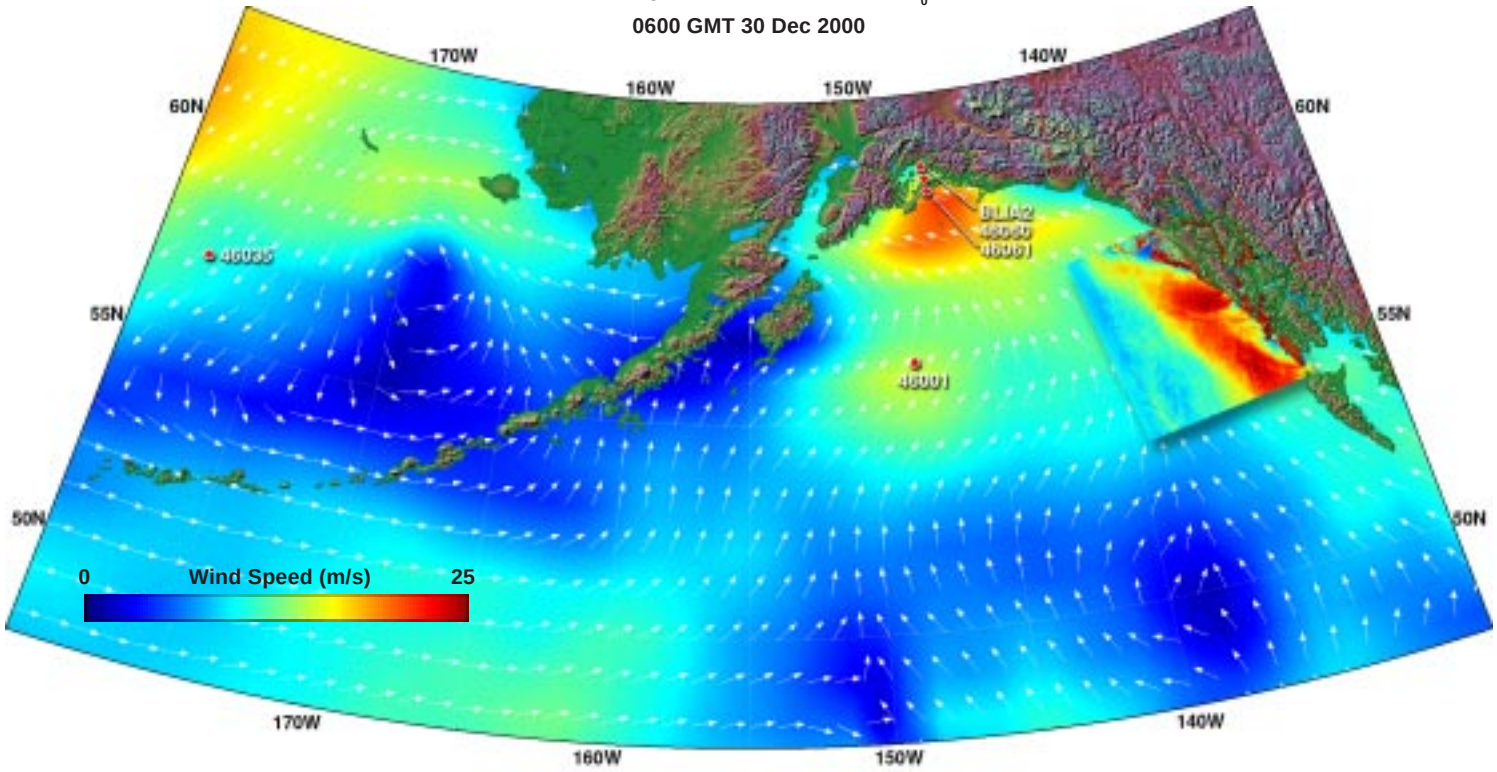

Model (this page): A huge low pressure system completely dominates the western Gulf of Alaska (1-4). Although beginning to diminish as it moves northward by SAR overpass time, a strong shoreward pressure gradient still remains all along the southern Alaskan coast. Model winds exceed 15 m/s along the coast, peaking around 20 m/s in the vicinity of Prince William Sound (5, 9). Concurrent model waves within the SAR pass are 3 to 5 m, near equilibrium (6, 7). The MABL is stable within the high wind region (8).

SAR (facing page): The SAR winds reveal a classic barrier jet along the coast, but the jet appears modified by offshore flow emanating from gaps in the topography. The gap flow interacts with the jet in a three-way balance of forces (10, 11). Very little of this action is captured by the model, which predicts a fairly uniform alongshore flow at about half the SAR wind estimates. [ref sections 2.11: coastal barrier jets, 2.5.2: gap flow/synoptic interaction.]

5. Surface Wind Field (m/s) ~ t_0

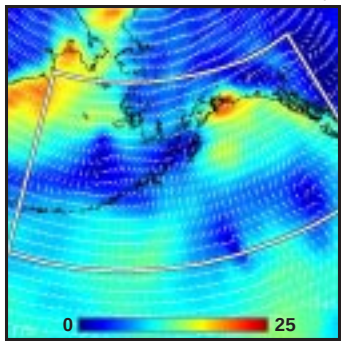

6. Surface Wave Height (m) ~ t_0

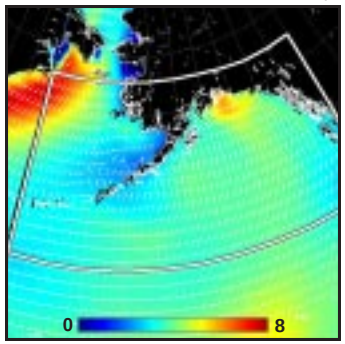

7. Inverse Wave Age (norm) ~ t_0

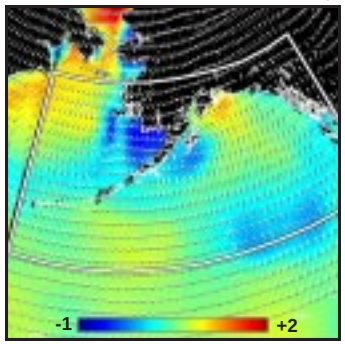

8. Air-Sea Temperature (˚C) ~ t_0

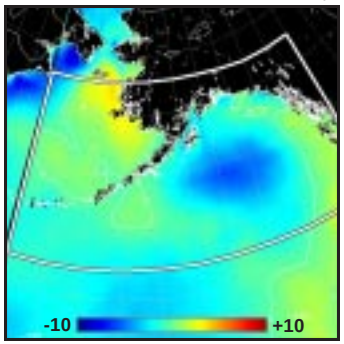

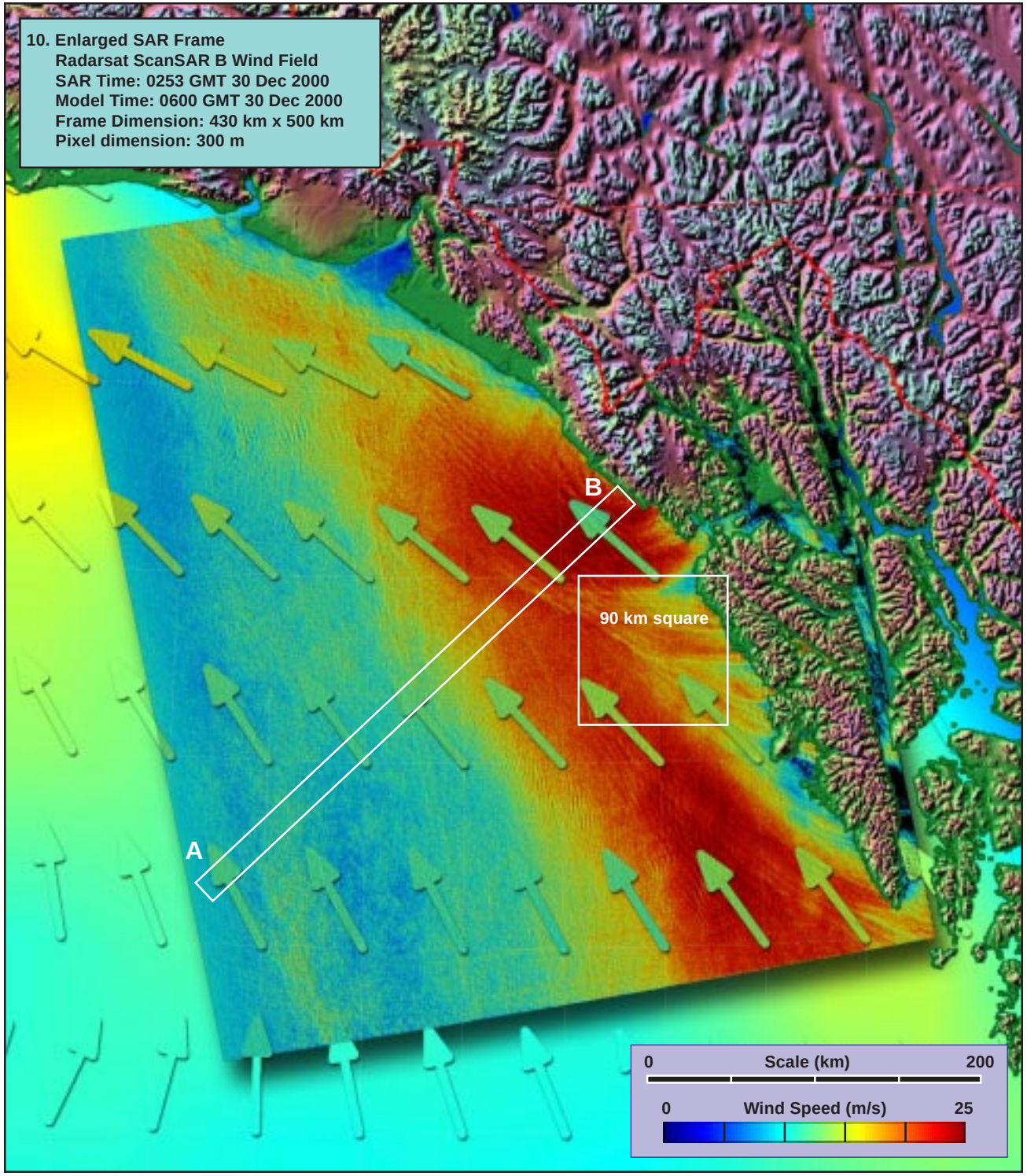

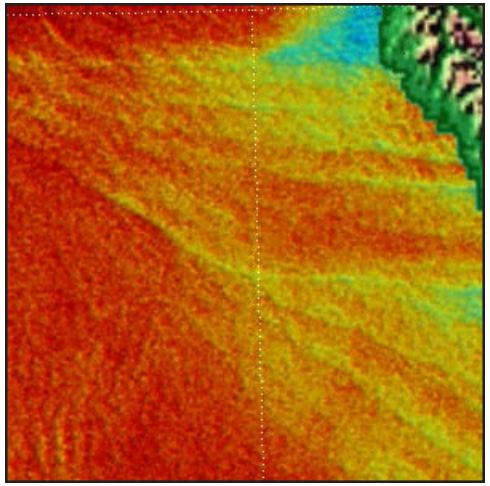

90 km square

11. Detail of Synoptic Interaction (x 2.5)

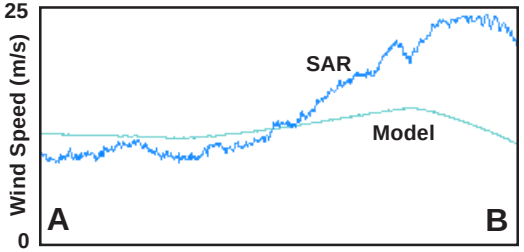

12. Model vs SAR Wind Profile along Line AB

1. Surface Pressure (mb) ~ t_0-36h

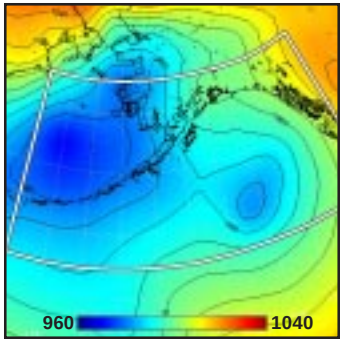

2. Surface Pressure (mb) ~ t_0-24h

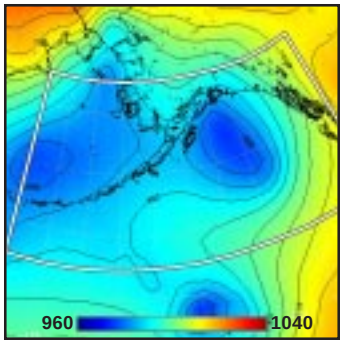

3. Surface Pressure (mb) ~ t_0-12h

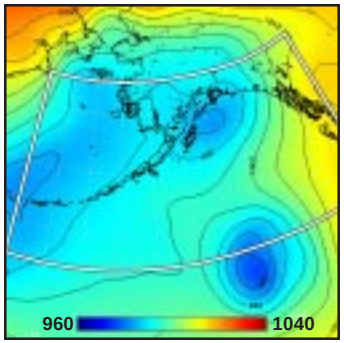

4. Surface Pressure (mb) ~ t_0

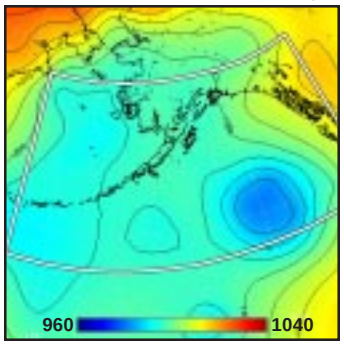

9. Enlarged Surface Wind Field ~ t_0

0600 GMT 01 Jan 2001

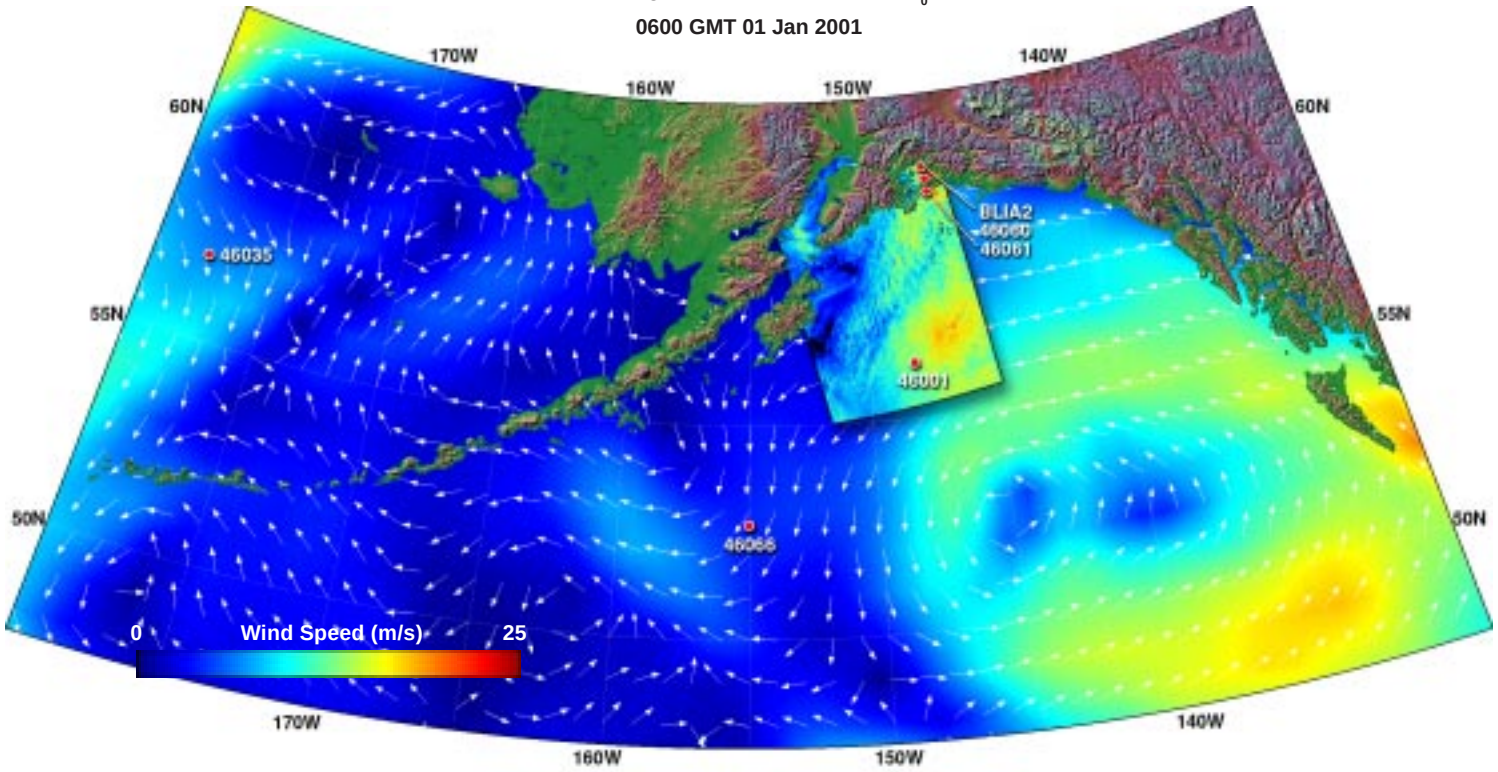

Model (this page): A diffuse triad of low pressure systems congeals by overpass time into a dominant, albeit weak, system located in the southern Gulf of Alaska (1-4). Model winds peaking at 15 to 20 m/s circulate around this low, but reach only 10 to 15 m/s in the region of the SAR overpass (5, 9). Concurrent model waves are about 3 m and growing (6, 7). The MABL is unstable in the northwest, tending to stable in the southeast (8).

SAR (facing page): The SAR winds in Prince William Sound, well north of the maximum wind annulus, show a well formed barrier jet in the northern half of the Sound, as well as some evidence of a jet passing through the southern entrance (10, 11). SAR wind speeds within the jet exceed 20 m/s, more than double the model estimates (11). In this case, because the model wind directions agree well with the three buoys located within the Sound, the SAR estimates are reasonably well validated by the buoys (12). Compare this behavior, however, with the situation on 08 January 2001, where the SAR estimates are seriously affected by the evidently sharp change in local wind direction.

5. Surface Wind Field (m/s) ~ t_0

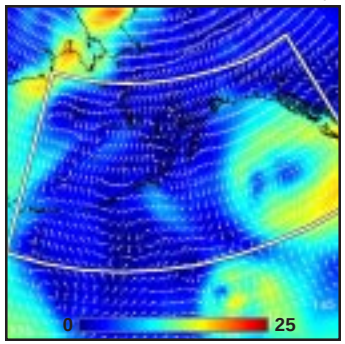

6. Surface Wave Height (m) ~ t_0

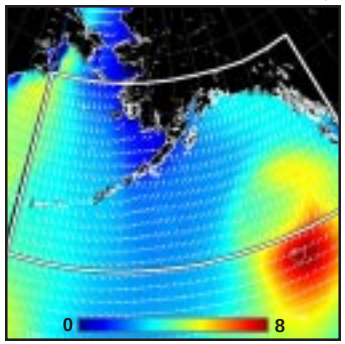

7. Inverse Wave Age (norm) ~ t_0

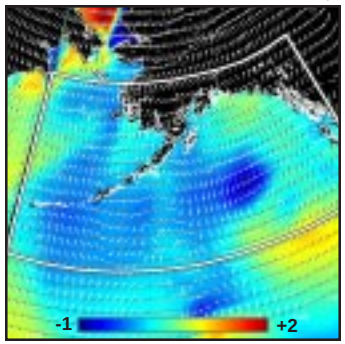

8. Air-Sea Temperature (˚C) ~ t_0

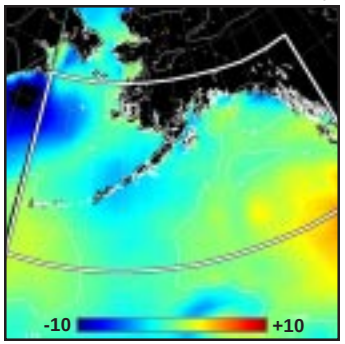

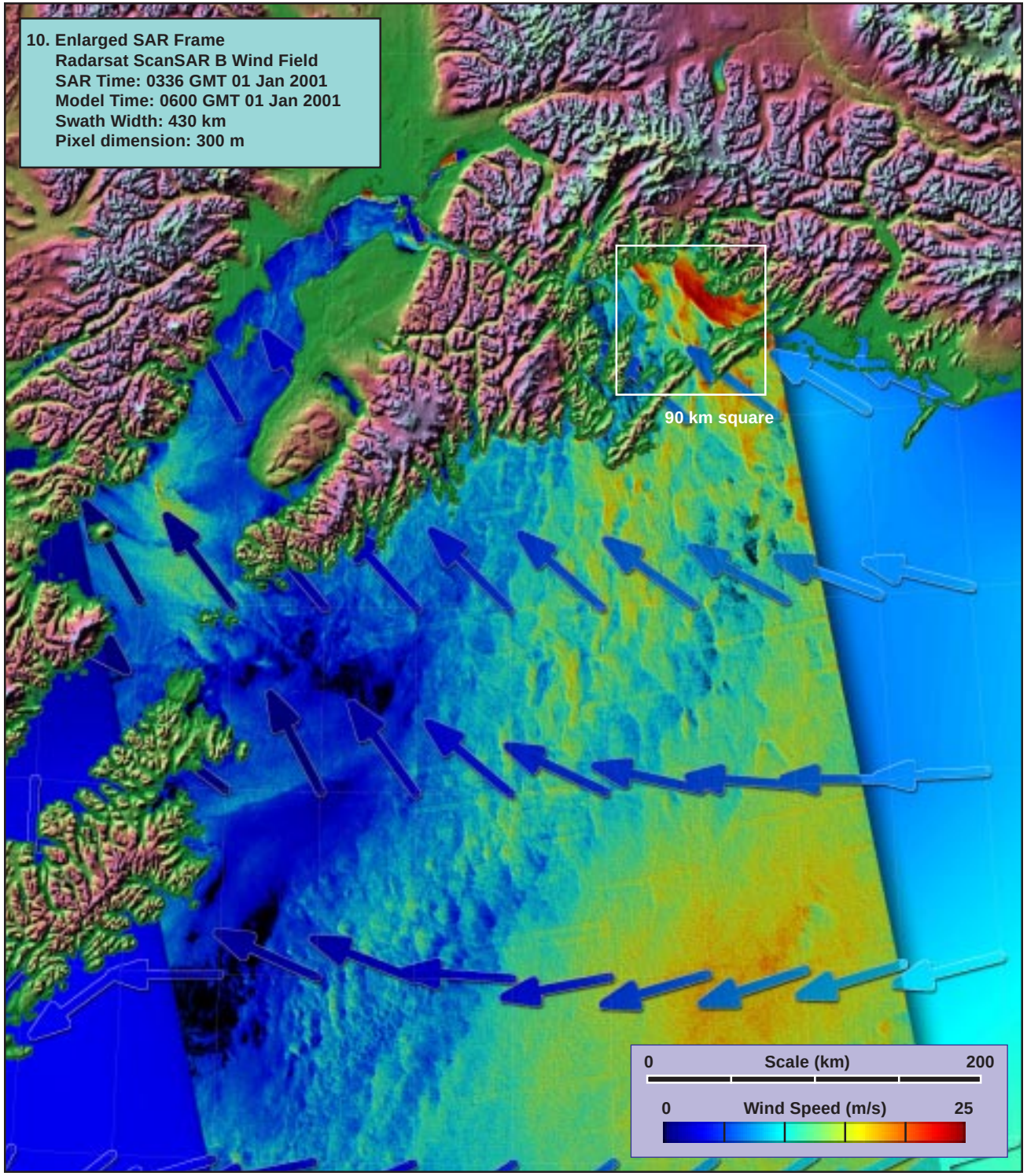

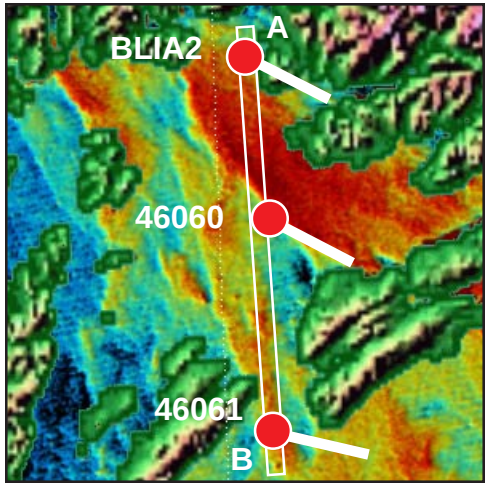

90 km square

11. Detail of Coastal Jets (x 2.5)

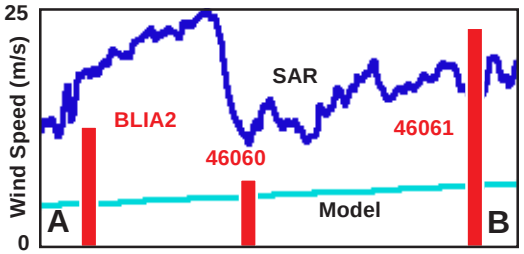

12. Model vs SAR Wind Profile along Line AB

YYYY MM DD hh WD WSPD GST

BLIA2

2001 01 01 03 129 14.7 16.8
2001 01 01 04 105 11.0 14.0

46060

2001 01 01 03 136 5.9 7.4
2001 01 01 04 119 8.7 13.8

46061

2001 01 15 03 102 23.2 27.3
2001 01 15 04 104 23.0 27.7

1. Surface Pressure (mb) ~ t_0-36h

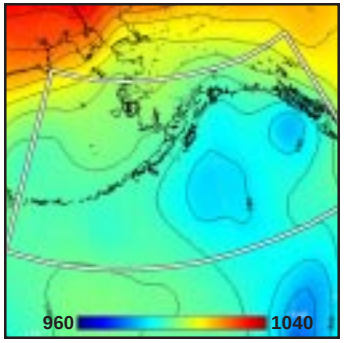

2. Surface Pressure (mb) ~ t_0-24h

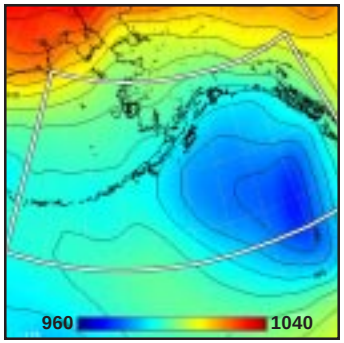

3. Surface Pressure (mb) ~ t_0-12h

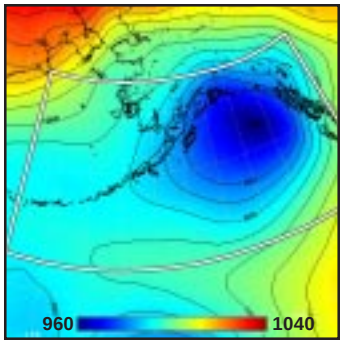

4. Surface Pressure (mb) ~ t_0

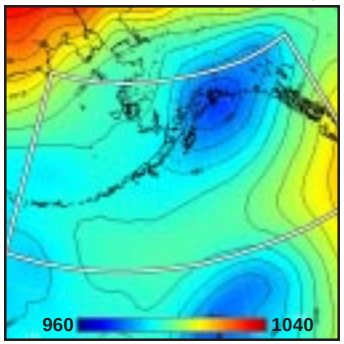

9. Enlarged Surface Wind Field ~ t_0

0600 GMT 04 Jan 2001

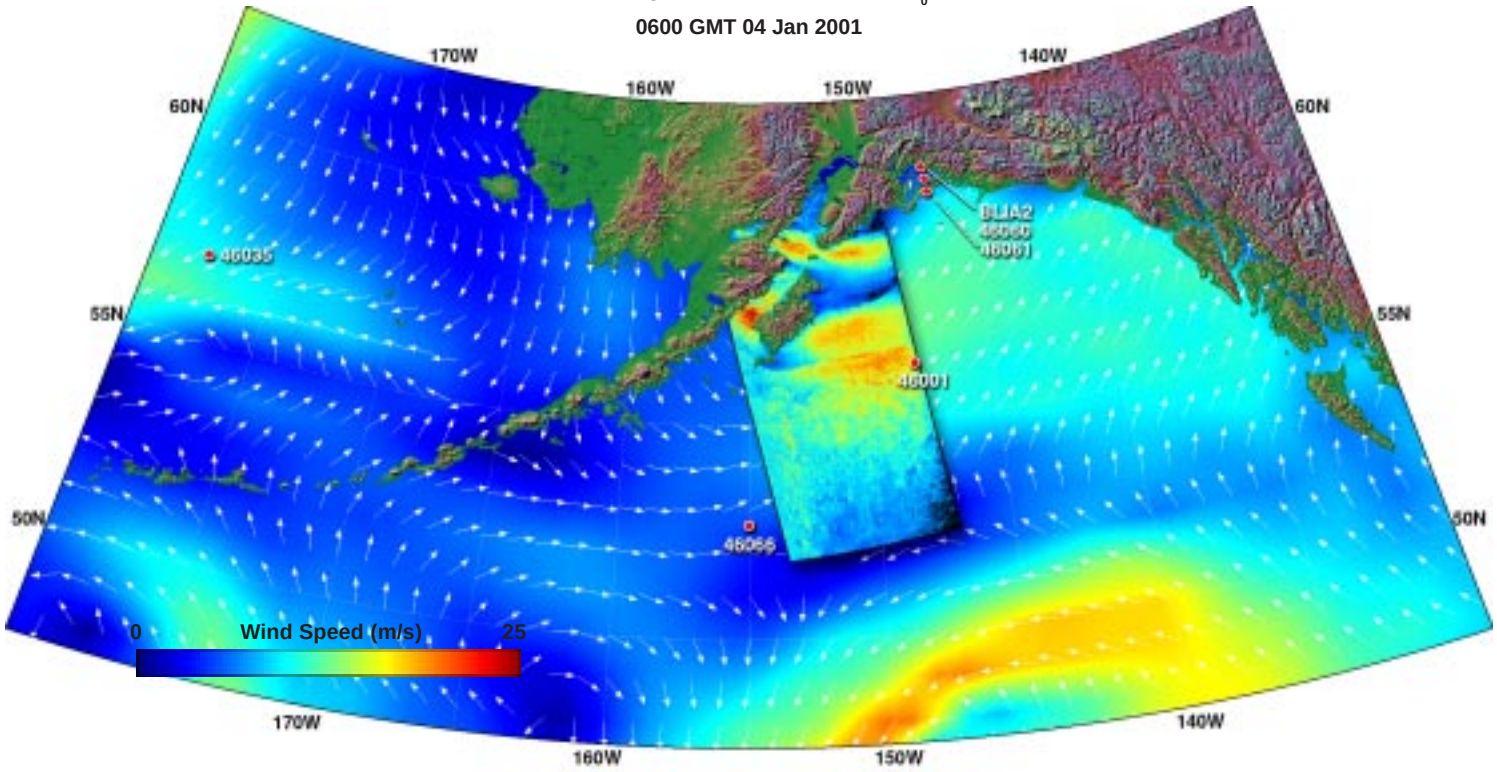

Model (this page): A deep low pressure system in the northern Gulf of Alaska begins to weaken just before overpass time as another approaches from the south (1-4). As the southernmost system approaches from south of the SAR pass, the model show a broad band of associated high (15 to 20 m/s) winds, while the northernmost system passes over the Kenai Peninsula with only residual westerly and southwesterly components of 10 to 15 m/s just to the east of Kodiak Island where the SAR pass occurs (5, 9). Concurrent model waves are less than 4 m, near equilibrium (6, 7). The MABL is unstable north and west of Kodiak Island, tending to neutral in the east (8).

SAR (facing page): The SAR winds strongly reflect both the upwind topography and, in the curved shadow of northern Kodiak Island, possibly the recent temporal history of the storm center, (10, 11). The local wind variance revealed by the SAR is quite remarkable; some regions within the shadow are only half the model estimates, while other regions to the west of Kodiak Island are more than twice the model estimates (12). Buoy 46001 was not operating at the time of overpass. [ref. section 2.5.2: gap flow/synoptic interaction.]

5. Surface Wind Field (m/s) ~ t_0

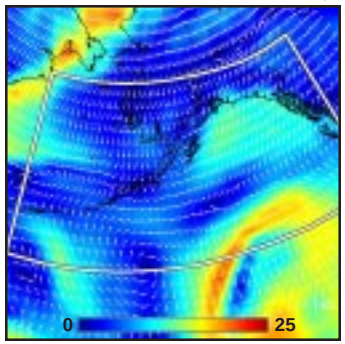

6. Surface Wave Height (m) ~ t_0

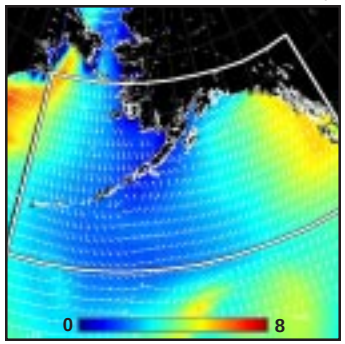

7. Inverse Wave Age (norm) ~ t_0

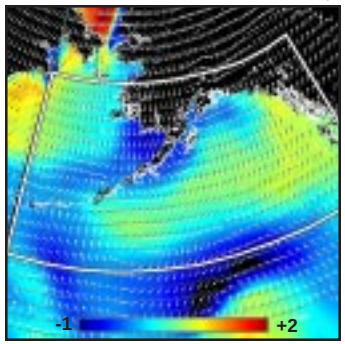

8. Air-Sea Temperature (˚C) ~ t_0

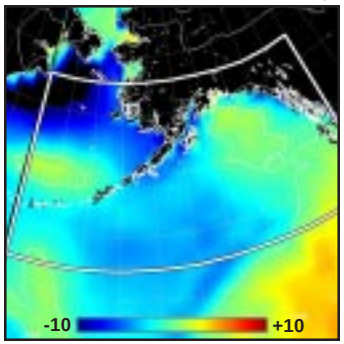

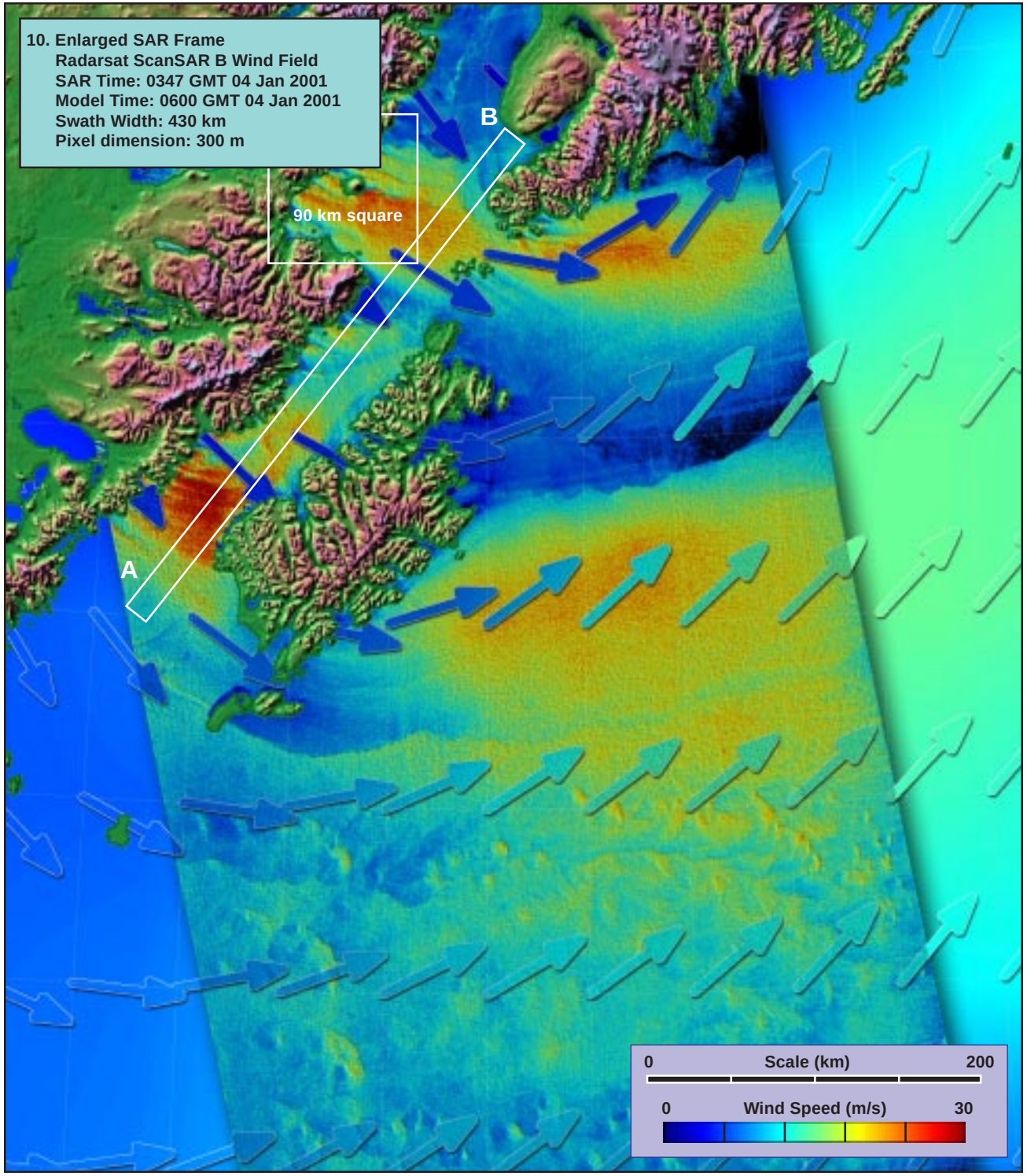

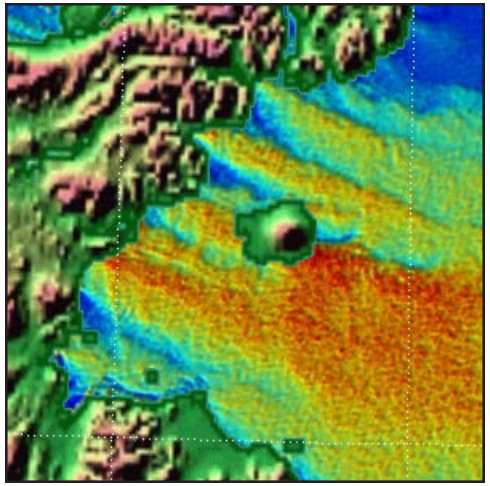

90 km square

11. Detail of Coastal Shadowing (x 2.5)

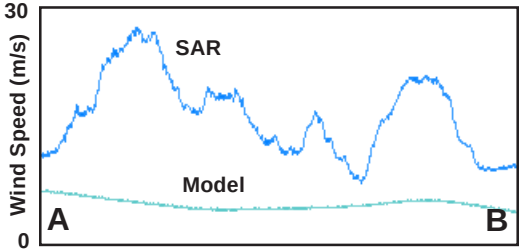

12. Model vs SAR Wind Profile along Line AB

1. Surface Pressure (mb) ~ t_0-36h

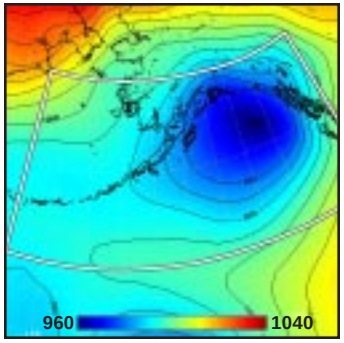

2. Surface Pressure (mb) ~ t_0-24h

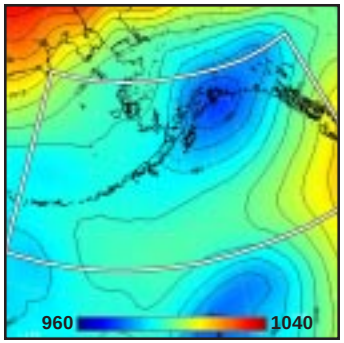

3. Surface Pressure (mb) ~ t_0-12h

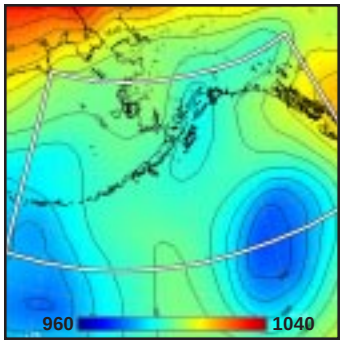

9. Enlarged Surface Wind Field ~ t_0

0600 GMT 05 Jan 2001

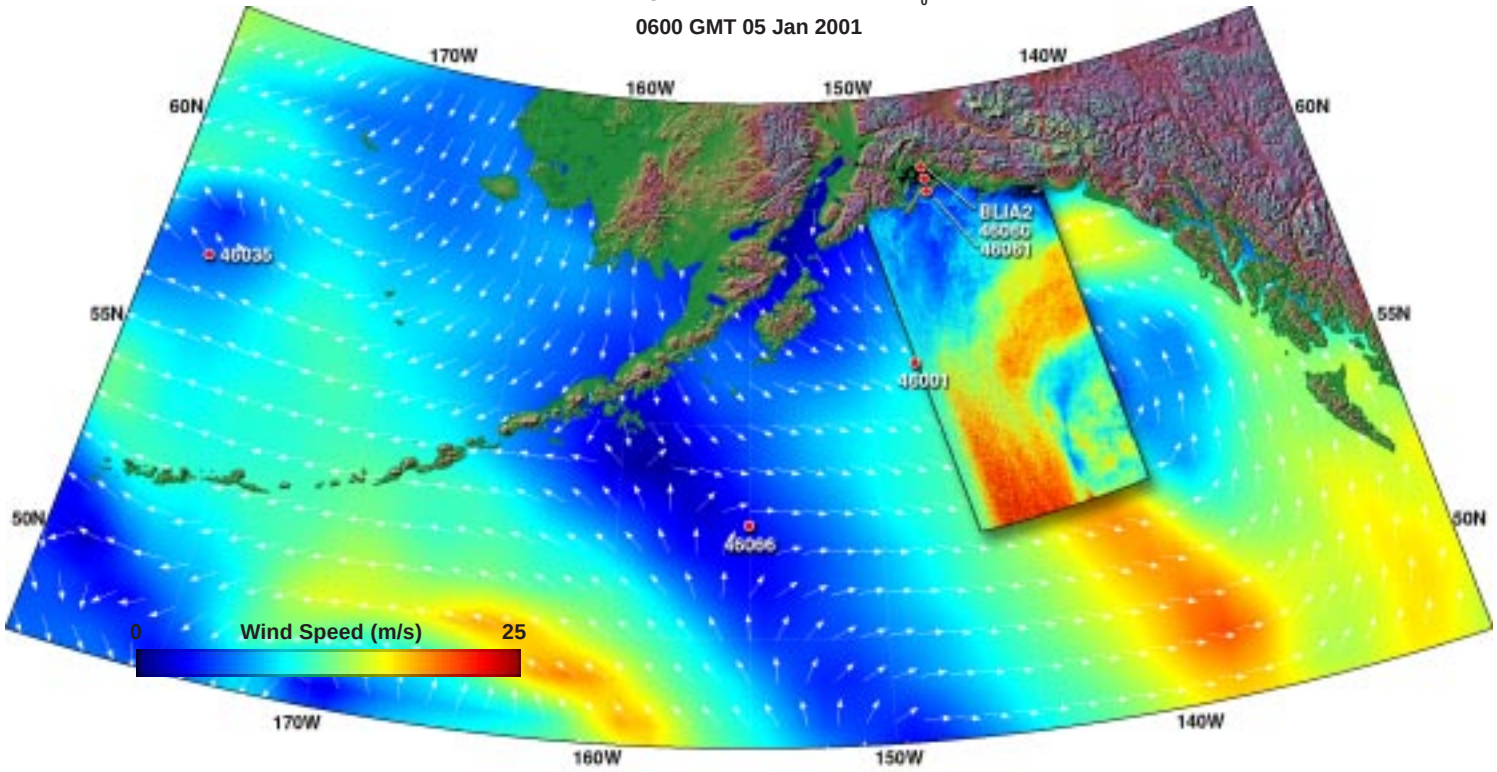

Model (this page): A deepening low pressure system in the southeastern Gulf of Alaska combines with a ridge to its southwest to form a high gradient in that direction (2-4). Model winds (5, 9) peak at about 20 m/s to the south of the SAR pass, but are only 10 to 15 m/s within the pass. Concurrent model waves peak around 6 m under the southwestern edge corner of the pass, but are decaying (6, 7). The MABL is stable in the south, unstable in the north along the coast (8).

SAR (facing page): The SAR winds [upper portion of the overlay in (9)] show the arc of high winds to the northwest of the storm center, as well as appreciable regions of variability within the high wind arc, including both gravity wave trains and long channels of low wind oriented N-S, and extending at least 50 km into the high wind region (10, 11). The SAR locates the maximum winds about 50 km to the SE from the model maximum (12). Buoy 46001 was not operating. [ref. section 2.7: synoptic lows.]

4. Surface Pressure (mb) ~ t_0

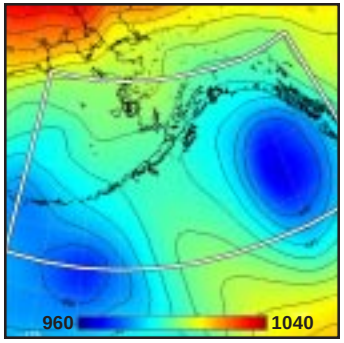

5. Surface Wind Field (m/s) ~ t_0

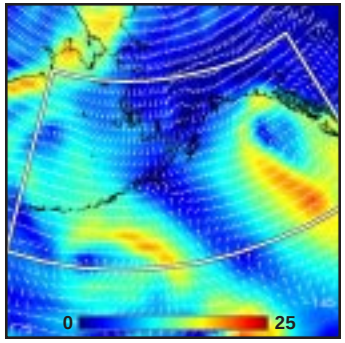

6. Surface Wave Height (m) ~ t_0

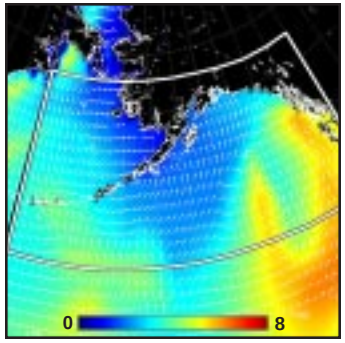

7. Inverse Wave Age (norm) ~ t_0

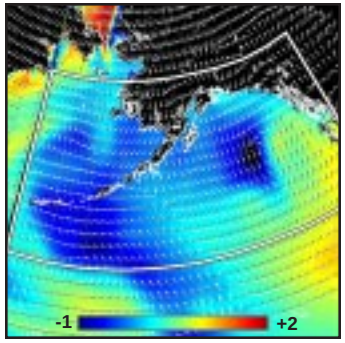

8. Air-Sea Temperature (˚C) ~ t_0

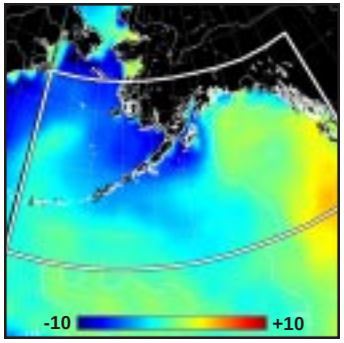

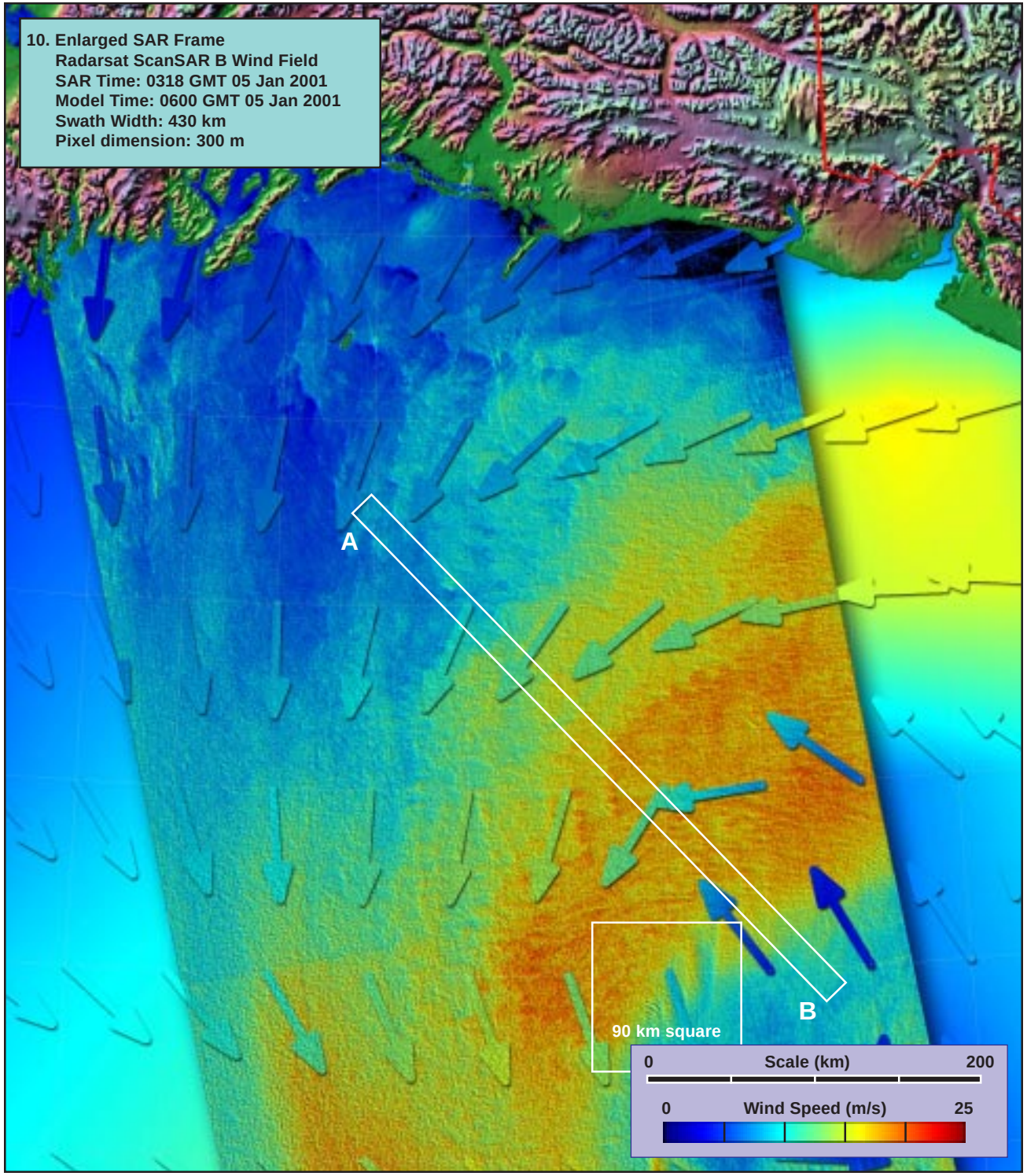

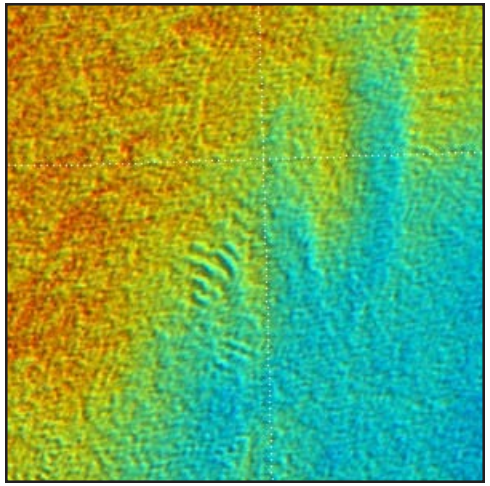

90 km square

11. Detail of Gravity Wave Region (x 2.5)

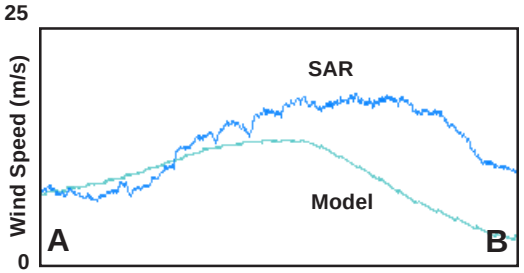

12. Model vs SAR Wind Profile along Line AB

1. Surface Pressure (mb) ~ t_0-36h

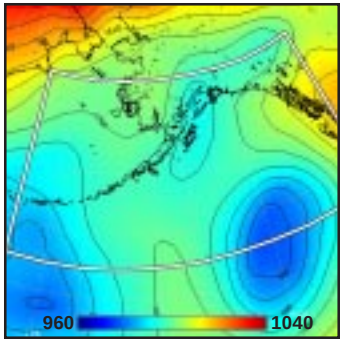

2. Surface Pressure (mb) ~ t_0-24h

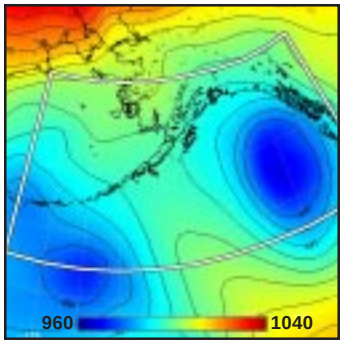

3. Surface Pressure (mb) ~ t_0-12h

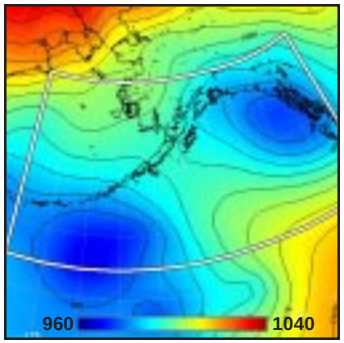

4. Surface Pressure (mb) ~ t_0

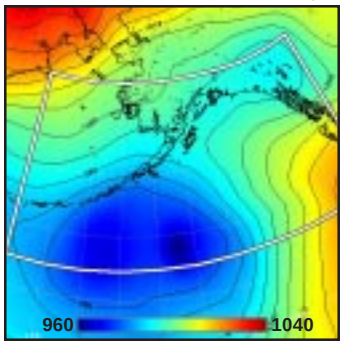

9. Enlarged Surface Wind Field ~ t_0

0600 GMT 06 Jan 2001

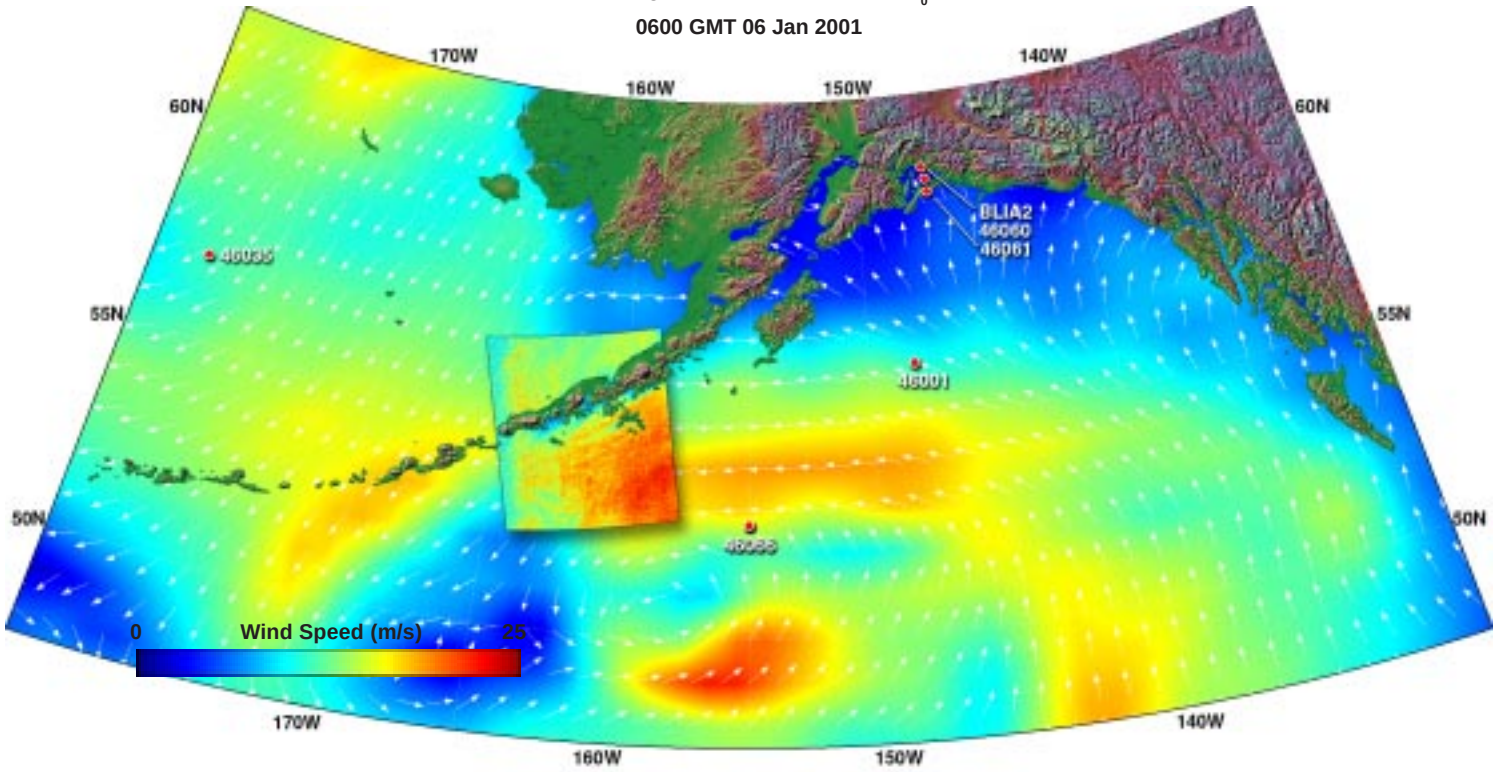

Model (this page): A broad, deepening, east-west elongated low pressure system approaches the central Gulf of Alaska from the southwest (1-4). On the northern side of the storm, model winds (5, 9) show a broad band of easterly 15 to 20 m/s winds impinging upon the northern Aleutian Chain. Concurrent model waves are 3 to 5 m, decaying (6, 7). The MABL is unstable in the north, tending to neutral in the south (8).

SAR (facing page): The SAR winds are about 5 m/s higher than the model estimates in most regions of the pass, with strong evidence of upwind sheltering from the Aleutian highlands located just to the northeast of the pass (10, 11). Some local turbulence cells can be seen along the edge of the wakes. Shadowing near shore causes about a 10 m/s drop in wind speed (12). [ref section 2.1: island and mountain wakes]

5. Surface Wind Field (m/s) ~ t_0

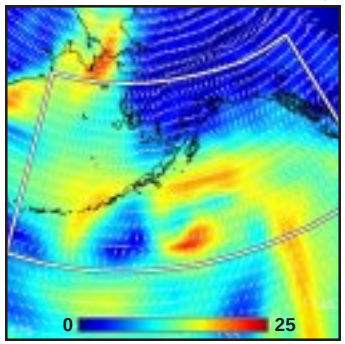

6. Surface Wave Height (m) ~ t_0

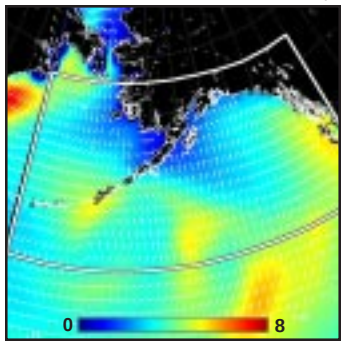

7. Inverse Wave Age (norm) ~ t_0

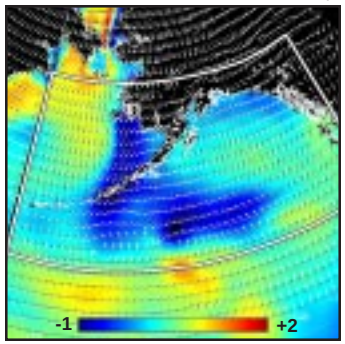

8. Air-Sea Temperature (˚C) ~ t_0

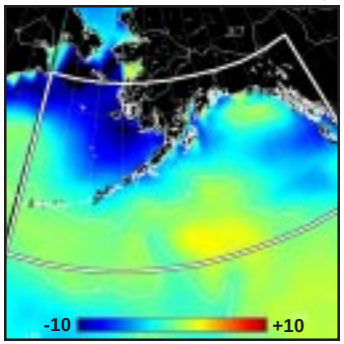

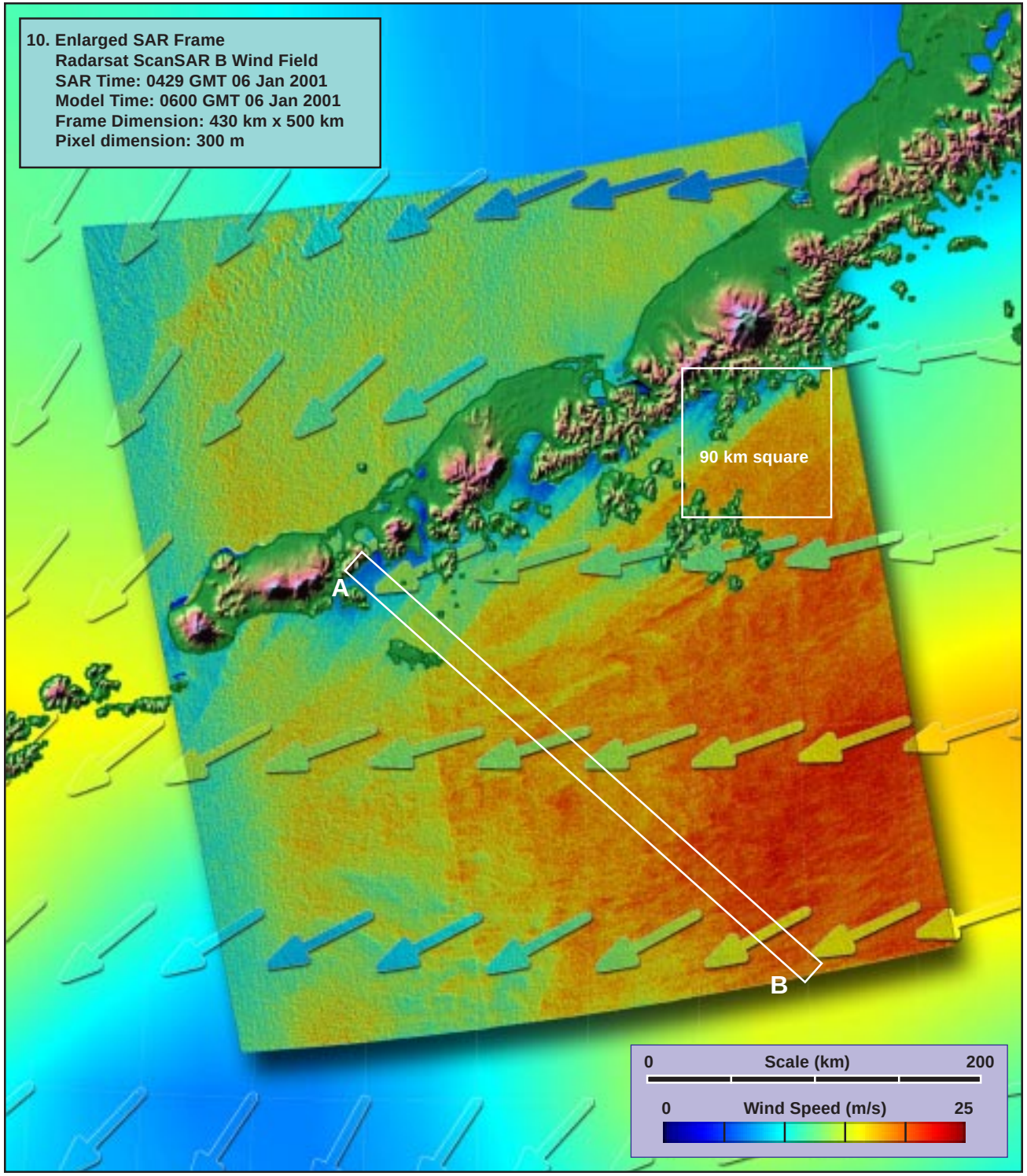

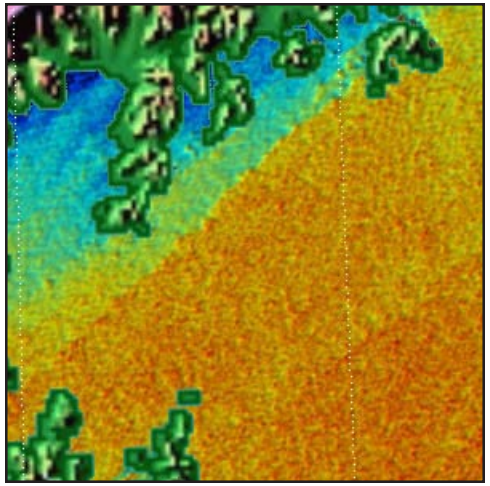

90 km square

11. Detail of Frontal Region (x 2.5)

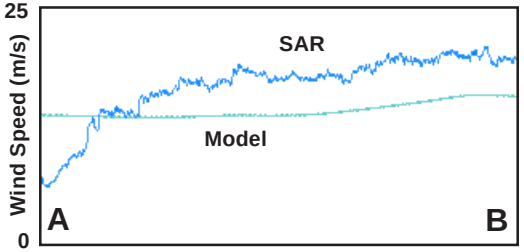

12. Model vs SAR Wind Profile along Line AB

1. Surface Pressure (mb) ~ t_0-36h

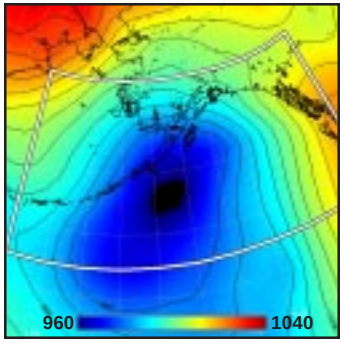

2. Surface Pressure (mb) ~ t_0-24h

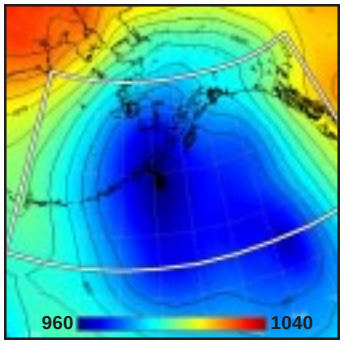

3. Surface Pressure (mb) ~ t_0-12h

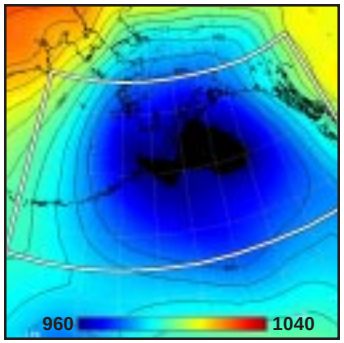

4. Surface Pressure (mb) ~ t_0

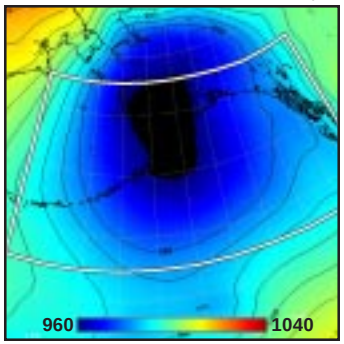

9. Enlarged Surface Wind Field ~ t_0

0600 GMT 08 Jan 2001

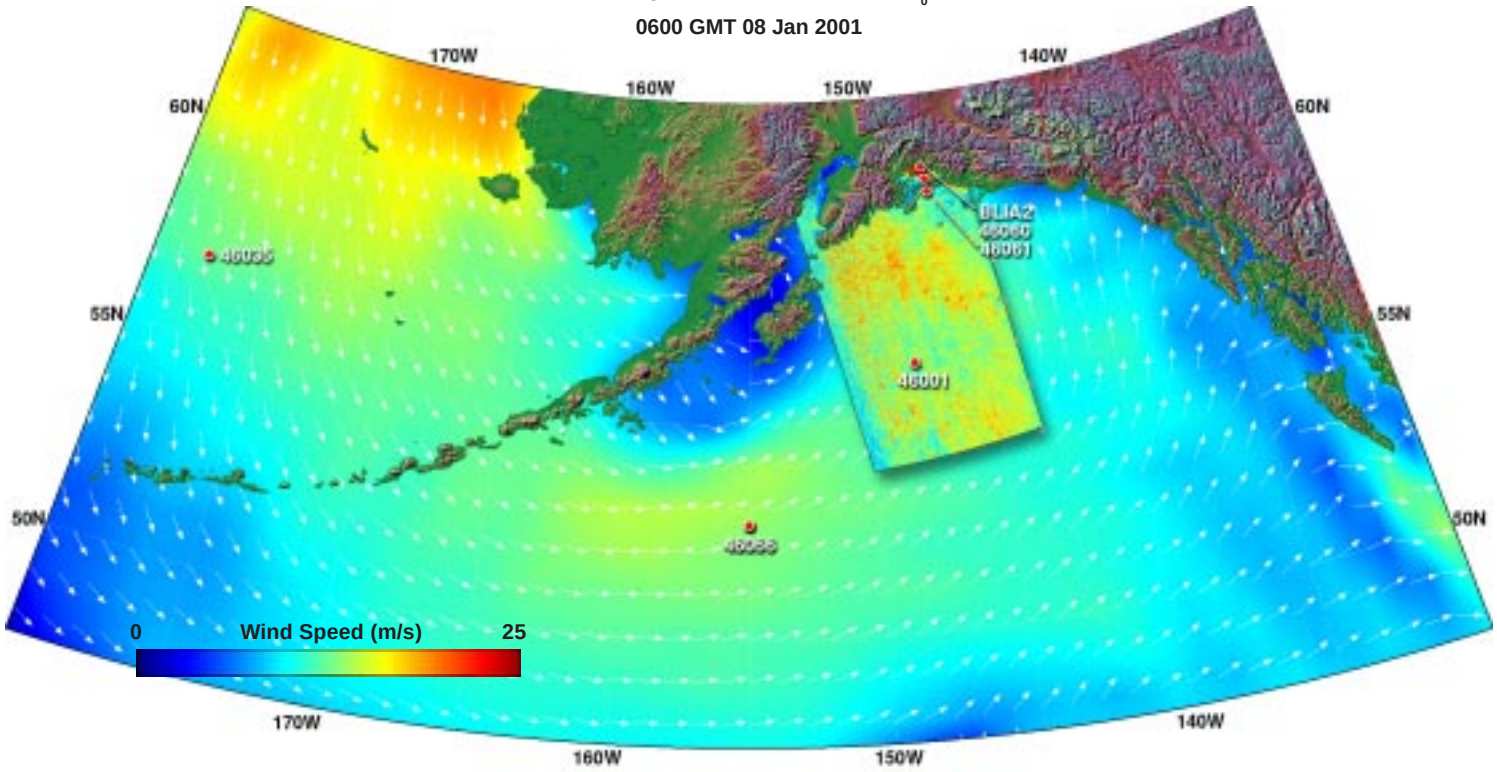

Model (this page): A broad shallow low pressure system is nearly stationary over the northern Aleutians for 36 hrs prior to overpass time, producing a moderate pressure gradient all along the eastern Gulf of Alaska (1-4). Spatially homogeneous, nearly southerly model winds of 5 to 15 m/s impinge upon the southern Alaskan coast within the SAR overpass (5, 9). Concurrent model waves to the east of Kodiak Island are 6 to 8 m, stable or slightly growing (6, 7). The MABL is nearly neutral, but more stable in the south (8).

SAR (facing page): Except for the northern half of Prince William Sound, the SAR winds show a mottled pattern, with maximum winds occasionally up to 20 m/s (10, 11, 12). Within the Sound, however, the distinct frontal boundary suggests a coastal jet (11). Signs of the jet occur upstream of the sound by as much as 100 km. The SAR-estimated wind speed change across the southern boundary of the jet is quite abrupt; however, the change is not verified by buoy 46060 (11, 12), which does, however, show a sharp change in direction not captured in the model. The SAR wind algorithm, using erroneous model directions, produces significantly excessive wind speeds within a portion of the jet.

5. Surface Wind Field (m/s) ~ t_0

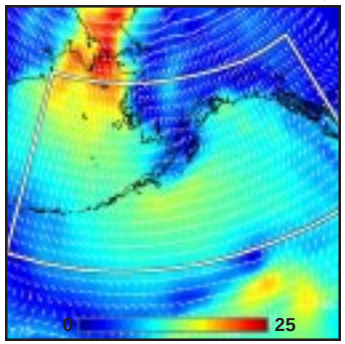

6. Surface Wave Height (m) ~ t_0

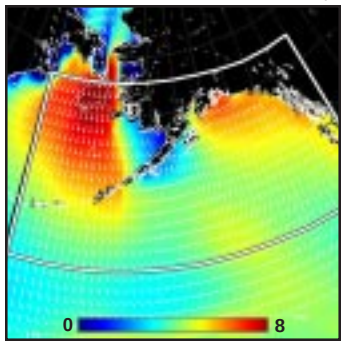

7. Inverse Wave Age (norm) ~ t_0

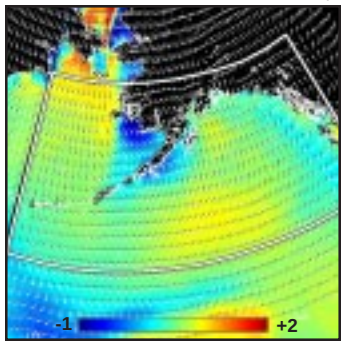

8. Air-Sea Temperature (˚C) ~ t_0

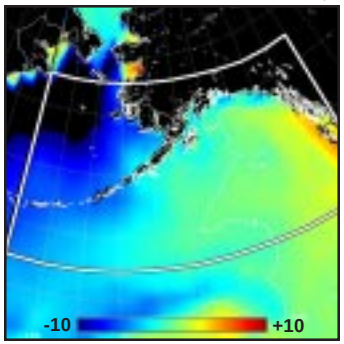

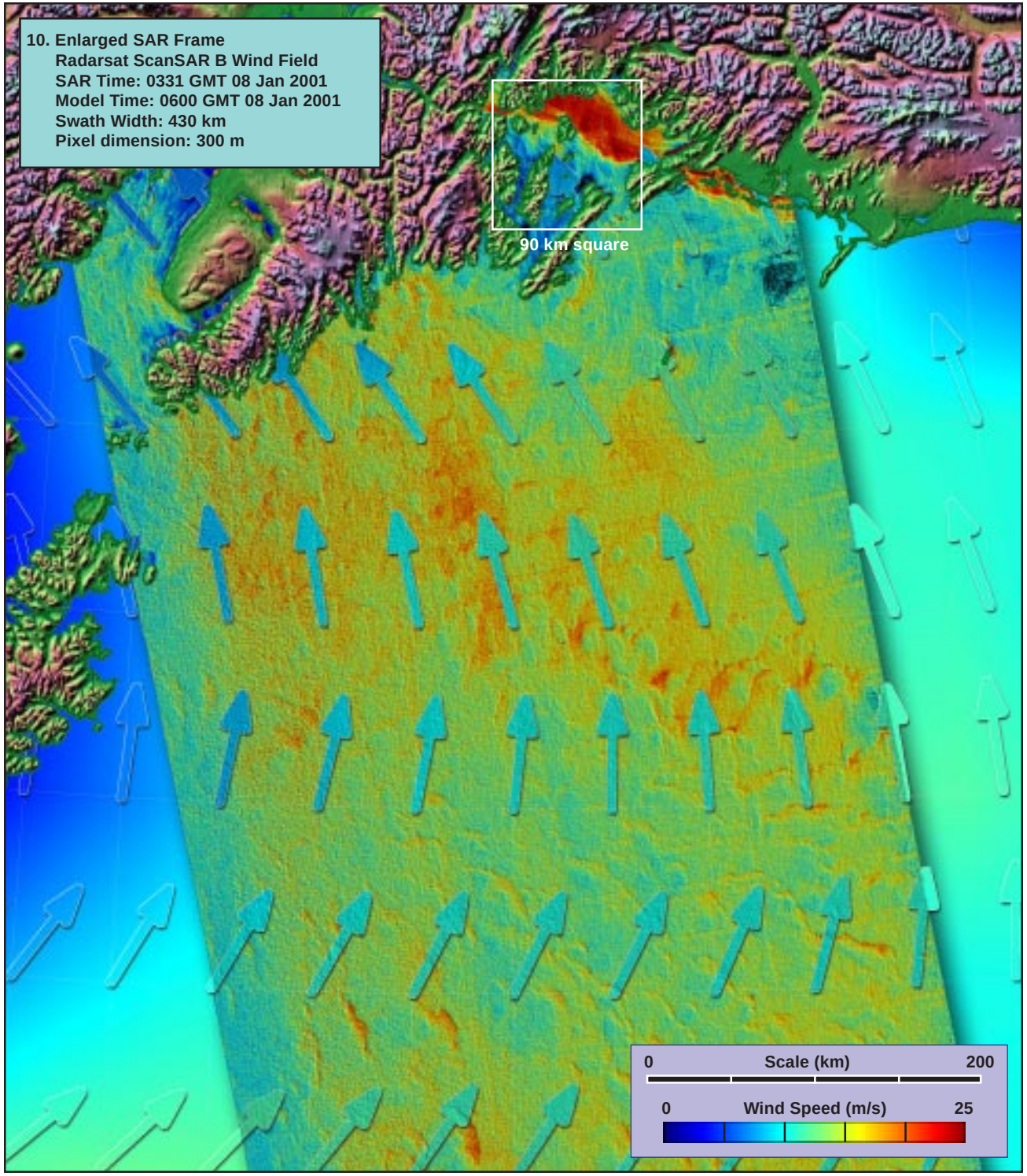

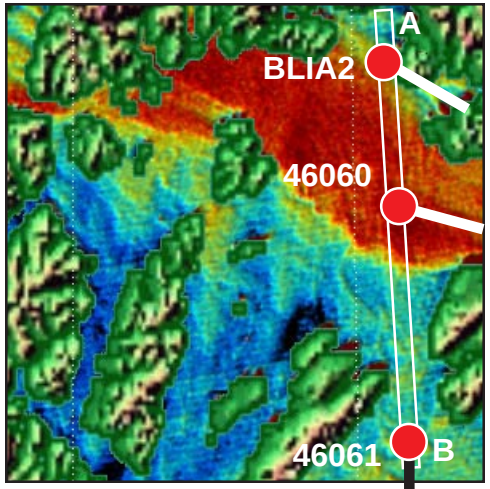

90 km square

11. Detail of Frontal Structure (x 2.5)

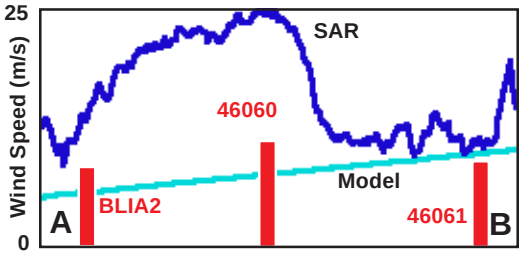

12. Model vs SAR Wind Profile along Line AB

YYYY MM DD hh WD WSPD GST

BLIA2

2001 01 08 03 121 9.9 11.7
2001 01 08 04 121 7.2 8.3

46060

2001 01 08 03 108 10.7 14.4
2001 01 08 04 103 11.9 14.5

46061

2001 01 08 03 180 9.4 12.0
2001 01 08 04 179 9.0 11.3

1. Surface Pressure (mb) ~ t_0-36h

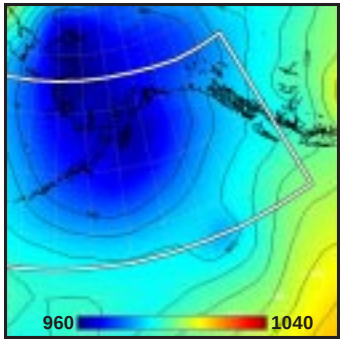

2. Surface Pressure (mb) ~ t_0-24h

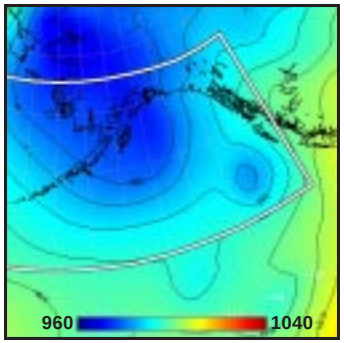

3. Surface Pressure (mb) ~ t_0-12h

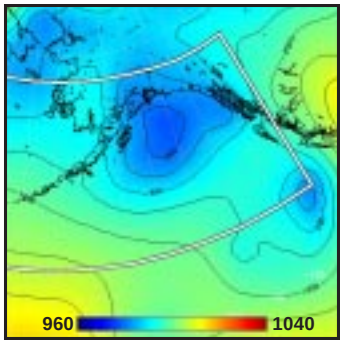

4. Surface Pressure (mb) ~ t_0

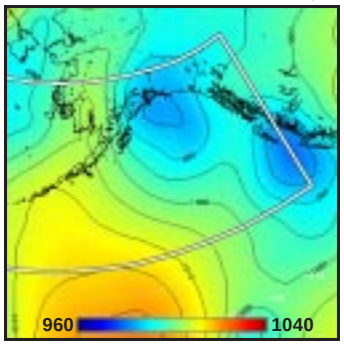

9. Enlarged Surface Wind Field ~ t_0

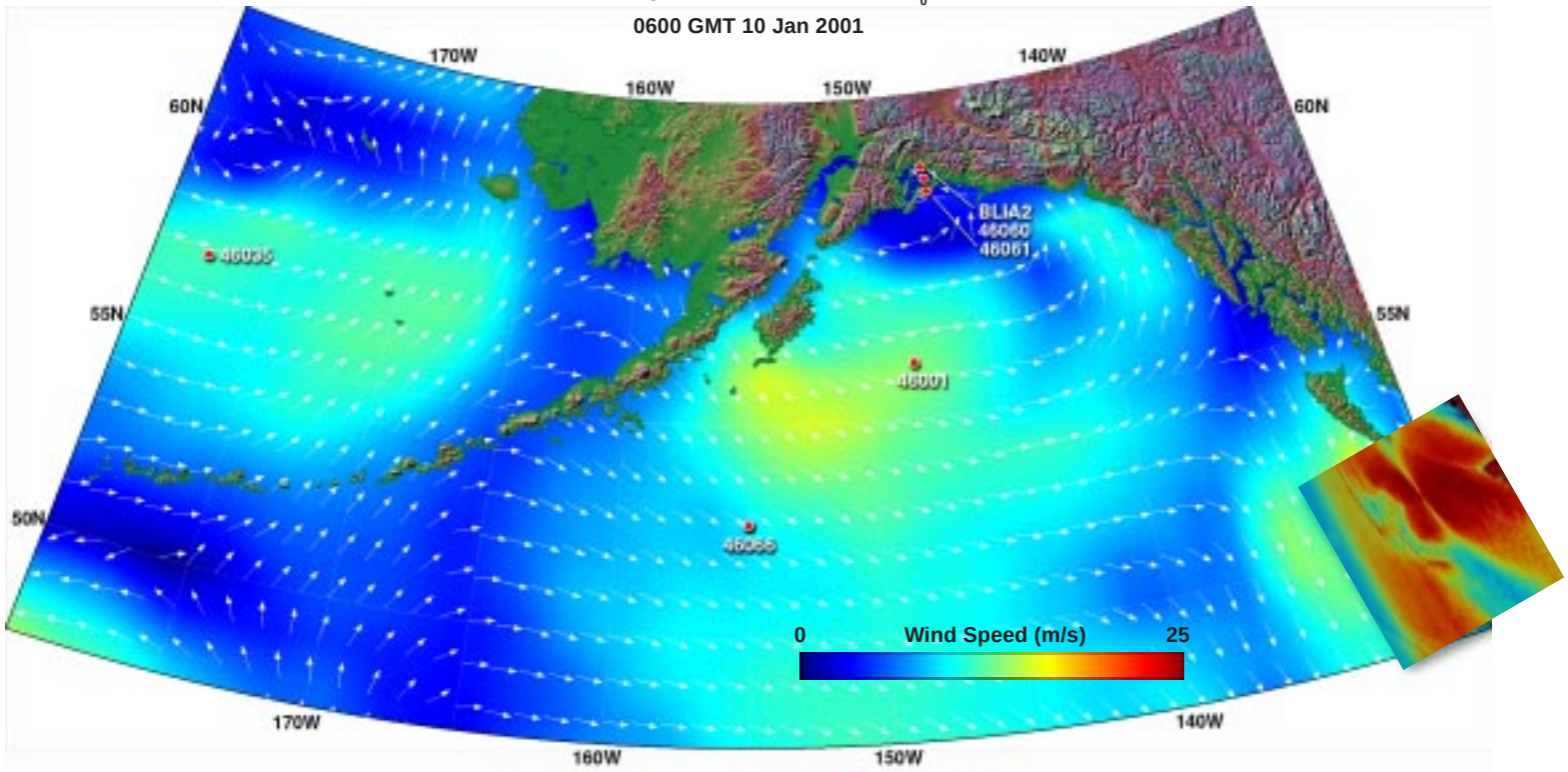

Model (this page): A large low pressure system over the northern Aleutians spins off a weaker system to its southeast (1-4). The weaker system, located just south of the Queen Charlotte Islands, evolves toward a N-S-oriented ellipse, with maximum gradients to the east and west of its center. Nearly opposing model winds in these two sectors, separated by less than 200 km, reach 15 to 20 m/s (5, 9). Concurrent model waves reach 5 to 6 m, growing in the east, but decaying in the west (6, 7). The MABL is near neutral (8).

SAR (facing page): The SAR wind estimates are much higher than those of the model, reaching nearly 30 m/s at their maxima (10, 11, 12). However, the anomalous pattern in the right center shows how a singularity in the model wind direction, especially when it is displaced from the actual storm center, can lead to substantial errors. In this case, the actual center (as suggested by the SAR minimum wind location) is probably 200 to 300 km to the south of the model estimate. This mislocation not only leads to the anomalous pattern, but probably also to a significant overestimate of the maximum winds when the correct direction is across, rather than along, the SAR flight direction.

5. Surface Wind Field (m/s) ~ t_0

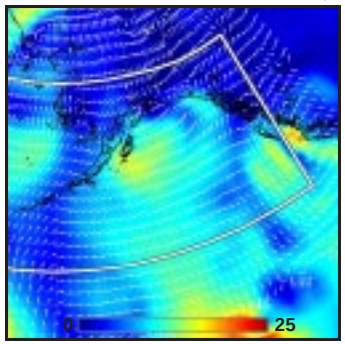

6. Surface Wave Height (m) ~ t_0

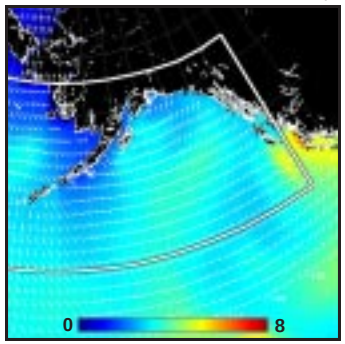

7. Inverse Wave Age (norm) ~ t_0

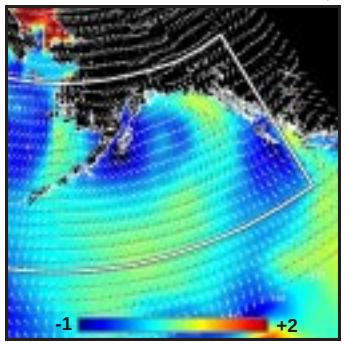

8. Air-Sea Temperature (˚C) ~ t_0

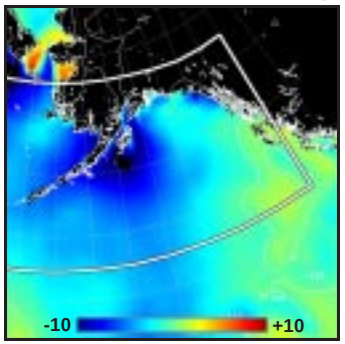

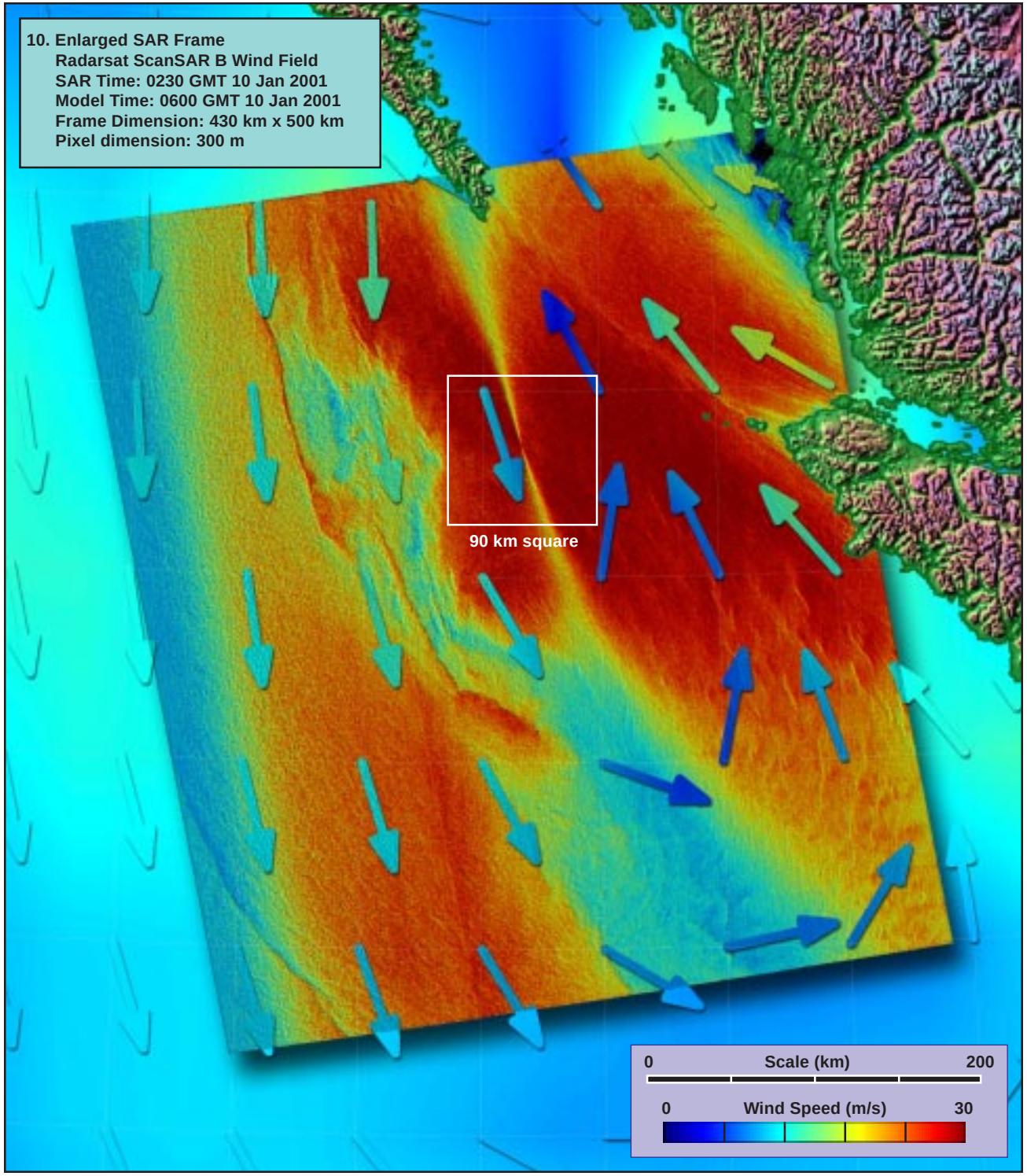

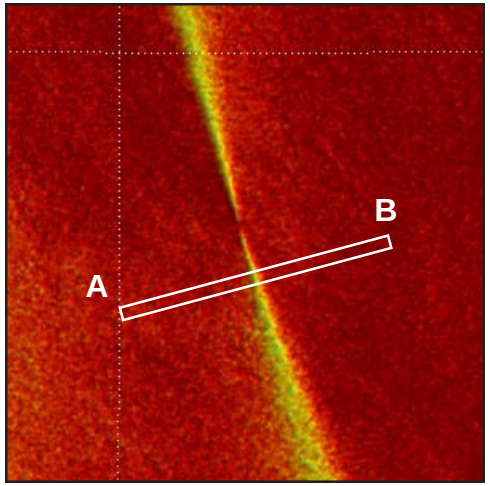

90 km square

11. Detail of Algorithm Singularity (x 2.5)

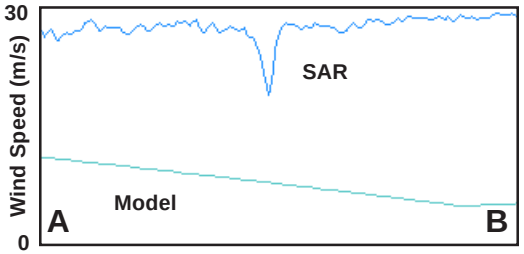

12. Model vs SAR Wind Profile along Line AB

1. Surface Pressure (mb) ~ t_0-36h

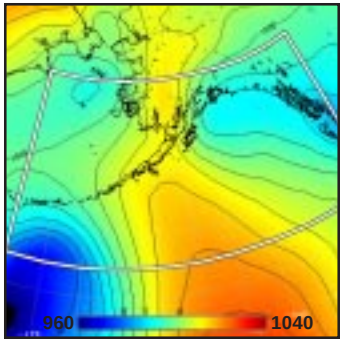

2. Surface Pressure (mb) ~ t_0-24h

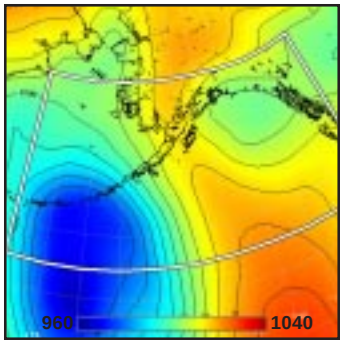

3. Surface Pressure (mb) ~ t_0-12h

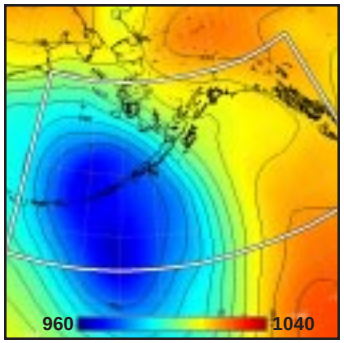

4. Surface Pressure (mb) ~ t_0

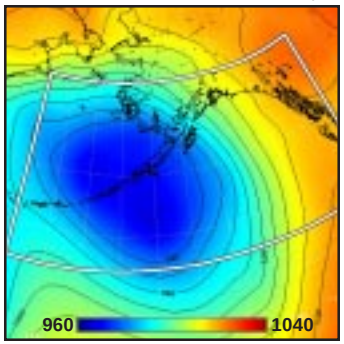

9. Enlarged Surface Wind Field ~ t_0

0600 GMT 12 Jan 2001

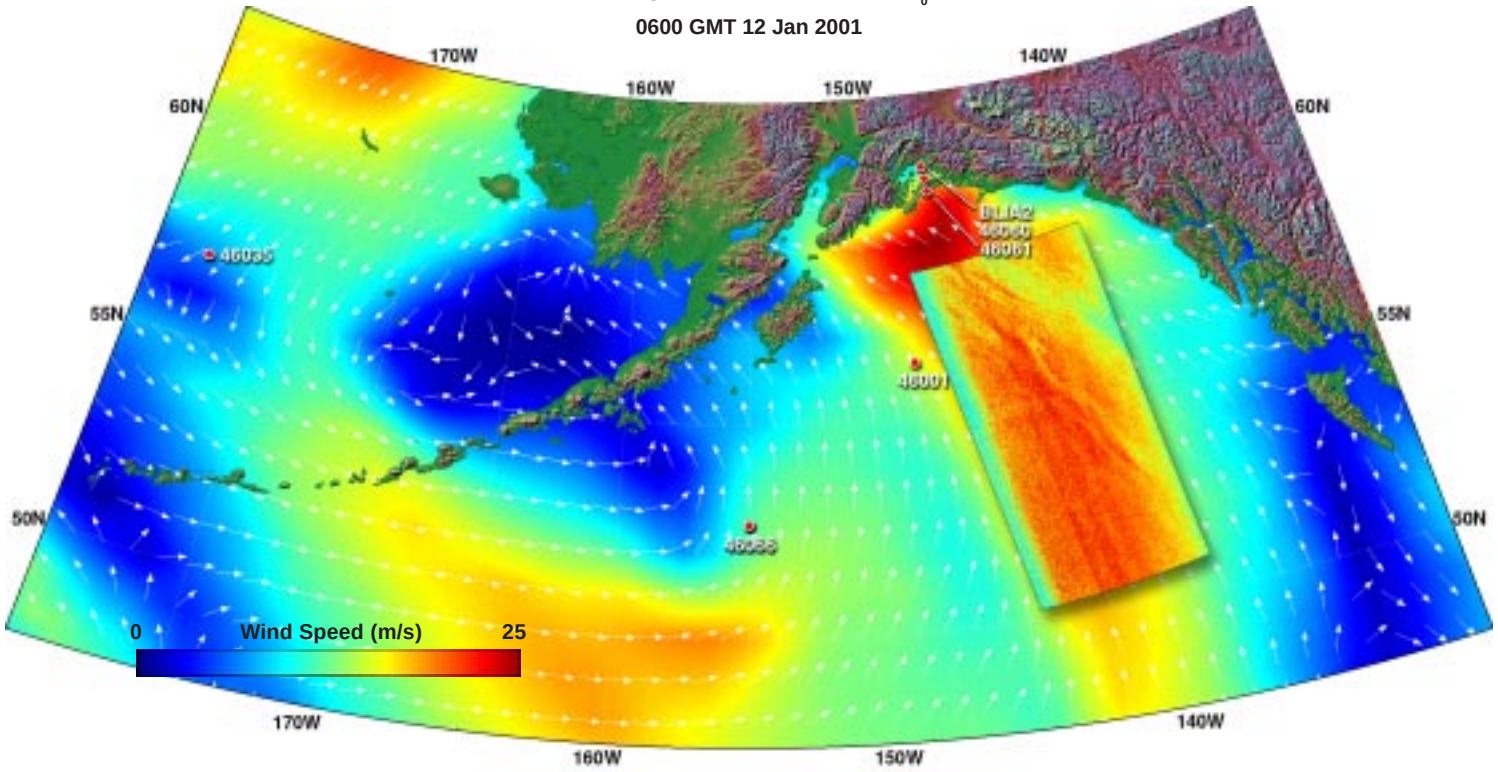

Model (this page): A deep low pressure system moves northward over the central Aleutians, creating a strong gradient to its north and east (1-4). Model winds show a band of strong (15 to 25 m/s) winds extending from the southern Gulf of Alaska all the way to the Kenai Peninsula (5, 9). Concurrent model waves are 6 to 8 m, rapidly growing at overpass time (6, 7). The MABL is extremely stable, especially under the southern half of the SAR overpass (8).

SAR (facing page): For the most part, the SAR winds agree with the model quite well, the major exception being at the northern end of the pass, where the model winds approach 25 m/s (10). Wind rows are evident over much of the northeastern portion of the pass (11), producing local surface variations in the wind field of 5 to 10 m/s (12). The band of apparently lower winds on the western edge of the pass is an artifact of the instrument.

5. Surface Wind Field (m/s) ~ t_0

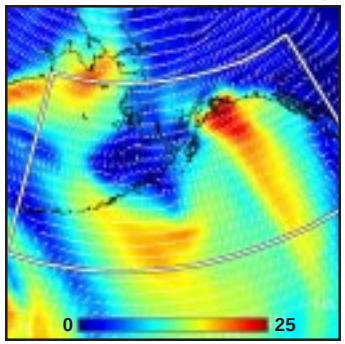

6. Surface Wave Height (m) ~ t_0

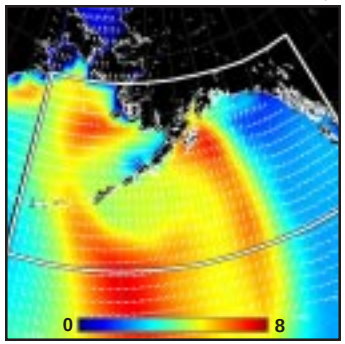

7. Inverse Wave Age (norm) ~ t_0

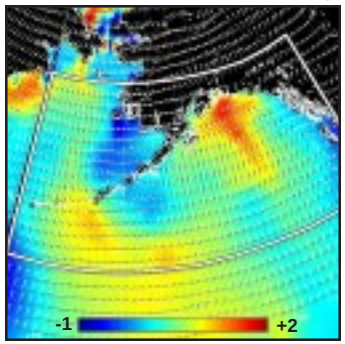

8. Air-Sea Temperature (˚C) ~ t_0

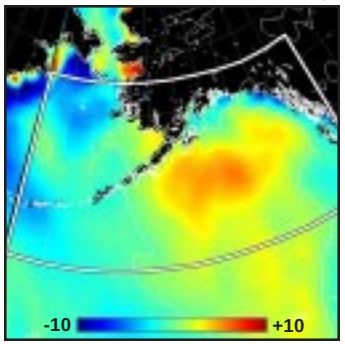

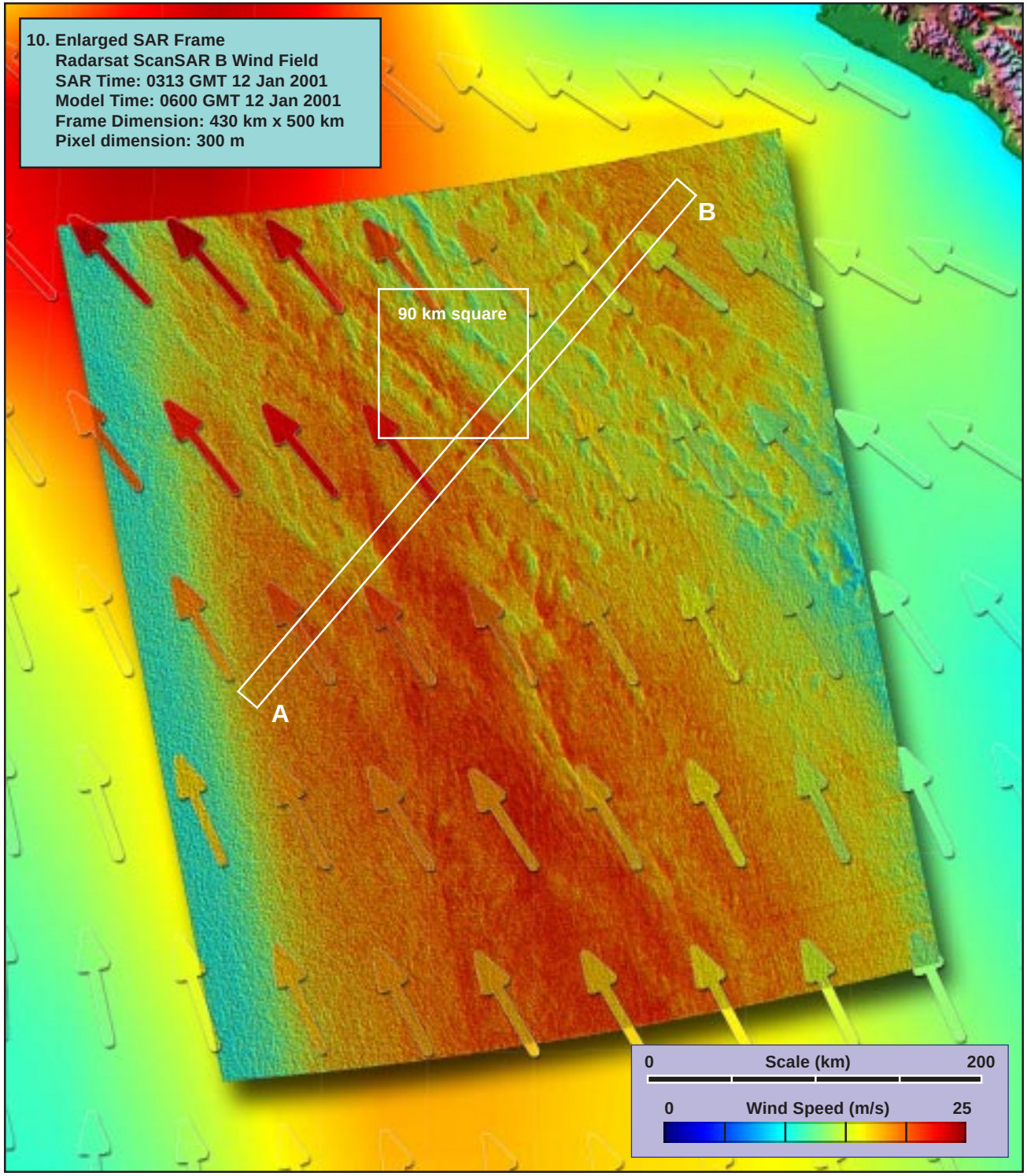

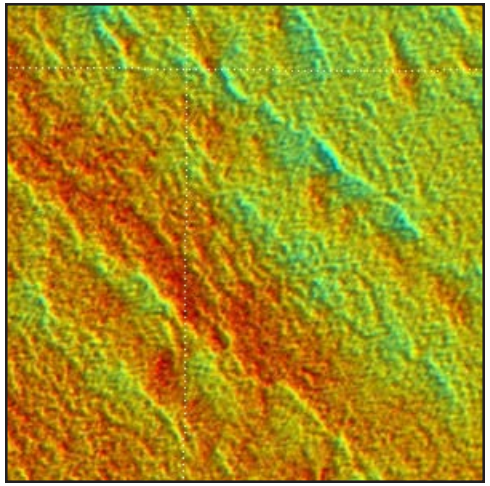

90 km square

11. Detail of Wind Rows (x 2.5)

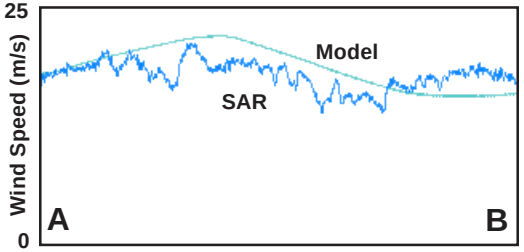

12. Model vs SAR Wind Profile along Line AB

1. Surface Pressure (mb) ~ t_0-36h

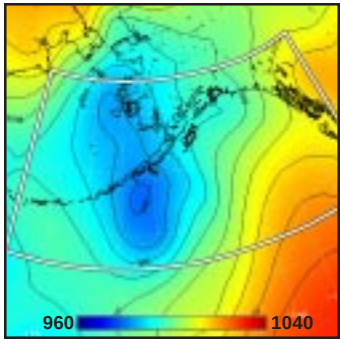

2. Surface Pressure (mb) ~ t_0-24h

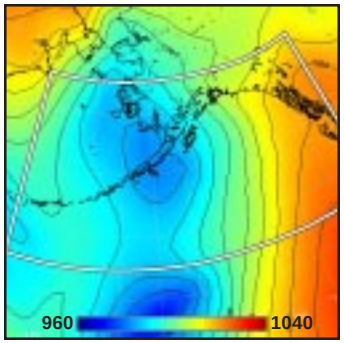

3. Surface Pressure (mb) ~ t_0-12h

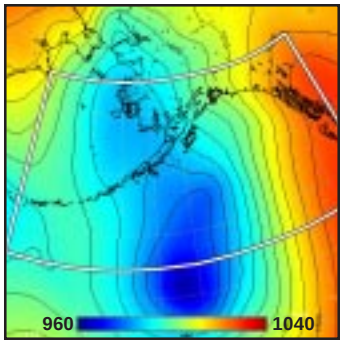

4. Surface Pressure (mb) ~ t_0

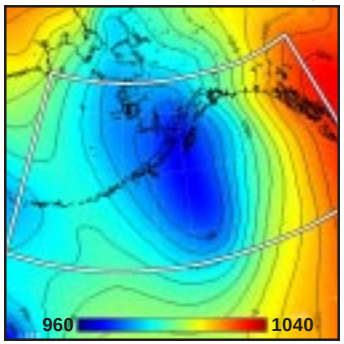

9. Enlarged Surface Wind Field ~ t_0

0600 GMT 15 Jan 2001

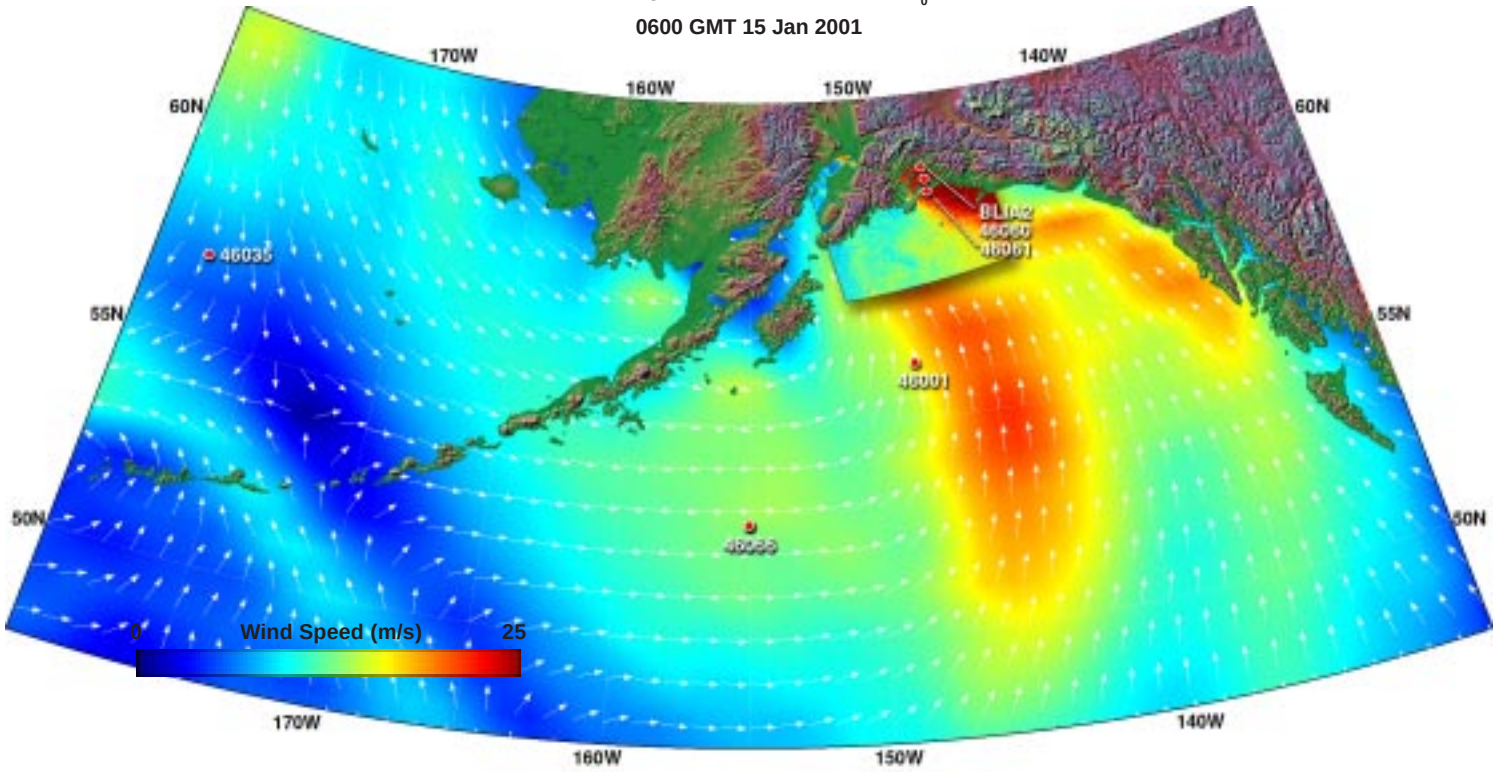

Model (this page): A relatively diffuse low pressure system congeals and deepens to the south of Kodiak Island, creating a north-south elongated region of compressed isobars in the central Gulf of Alaska (1-4). Model winds show two branches of strong (20 to 25 m/s) southerly winds converging in the vicinity of Kenai Peninsula and Prince William Sound (5, 9). Concurrent model waves are 6 to 8 m under the SAR overpass, rapidly growing (6, 7). The MABL is near neutral at the coast, tending to stable seaward (8).

SAR (facing page): The SAR winds are generally considerably lower than the model, except immediately adjacent to the coast and across Prince William Sound, where a strong coastal jet evidently dominates (10, 11). Within the jet, SAR winds reach 25 m/s, about 5-10 m/s higher than the model. In this case, the model directions agree well with the buoy directions (11), giving confidence that the resulting SAR wind estimates are faithfully capturing the high winds within the jet (12).

5. Surface Wind Field (m/s) ~ t_0

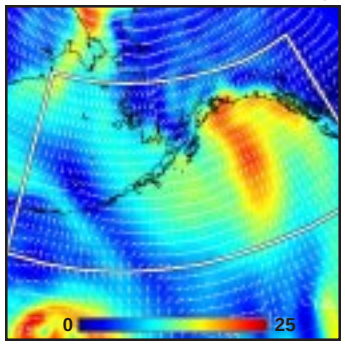

6. Surface Wave Height (m) ~ t_0

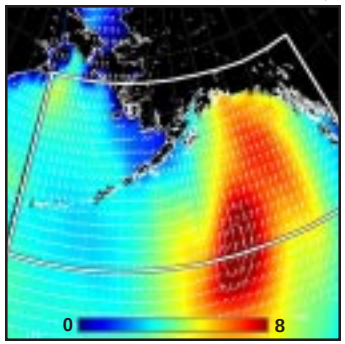

7. Inverse Wave Age (norm) ~ t_0

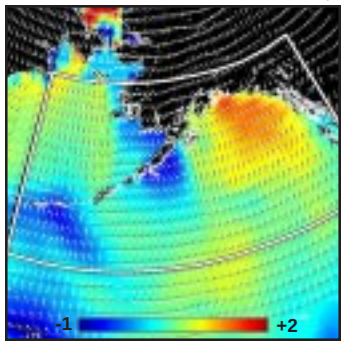

8. Air-Sea Temperature (˚C) ~ t_0

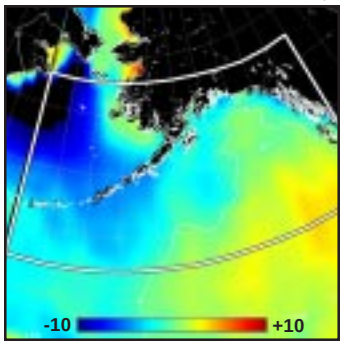

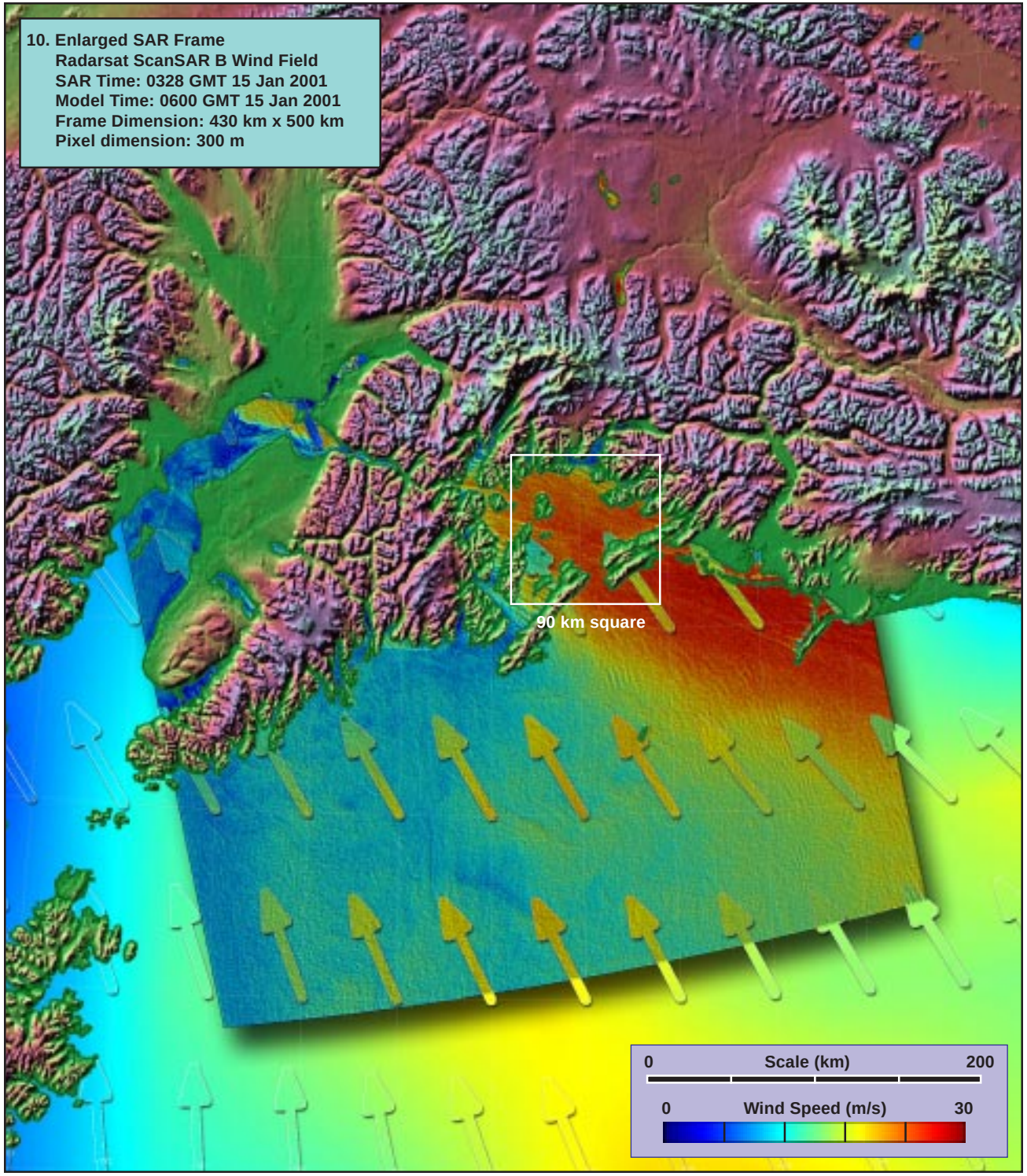

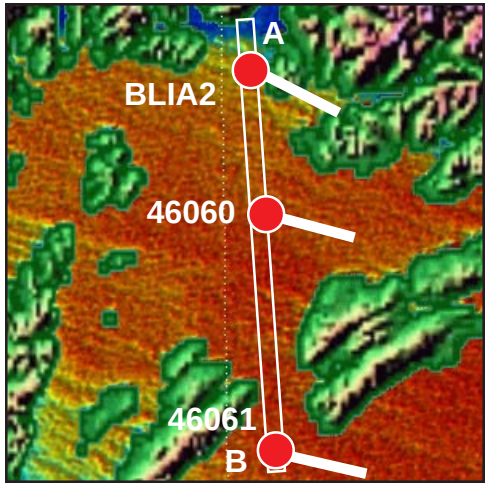

90 km square

11. Detail of High Wind Region (x 2.5)

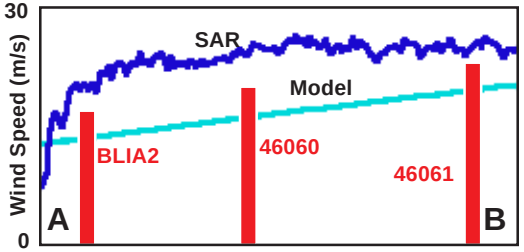

12. Model vs SAR Wind Profile along Line AB

YYYY MM DD hh WD WSPD GST

BLIA2

2001 01 15 03 112 12.6 18.4
2001 01 15 04 122 21.6 28.5

46060

2001 01 15 03 103 19.5 24.6
2001 01 15 04 106 20.7 26.2

46061

2001 01 15 03 102 23.2 27.3
2001 01 15 04 104 23.0 27.7

1. Surface Pressure (mb) ~ t_0-36h

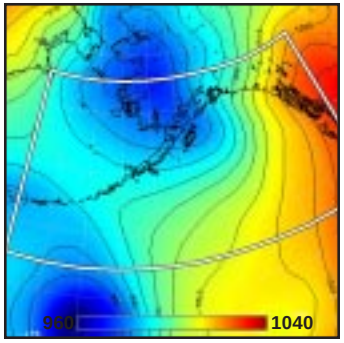

2. Surface Pressure (mb) ~ t_0-24h

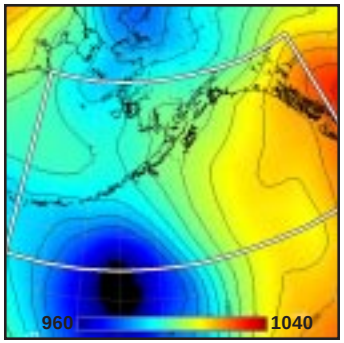

3. Surface Pressure (mb) ~ t_0-12h

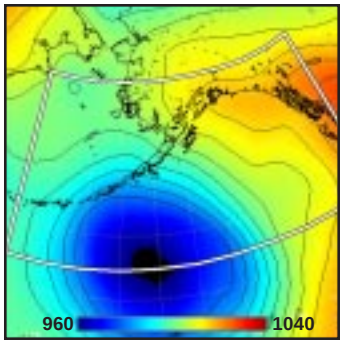

4. Surface Pressure (mb) ~ t_0

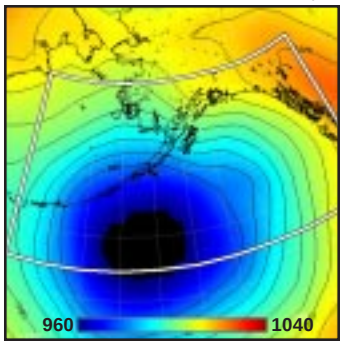

9. Enlarged Surface Wind Field ~ t_0

1800 GMT 15 Jan 2001

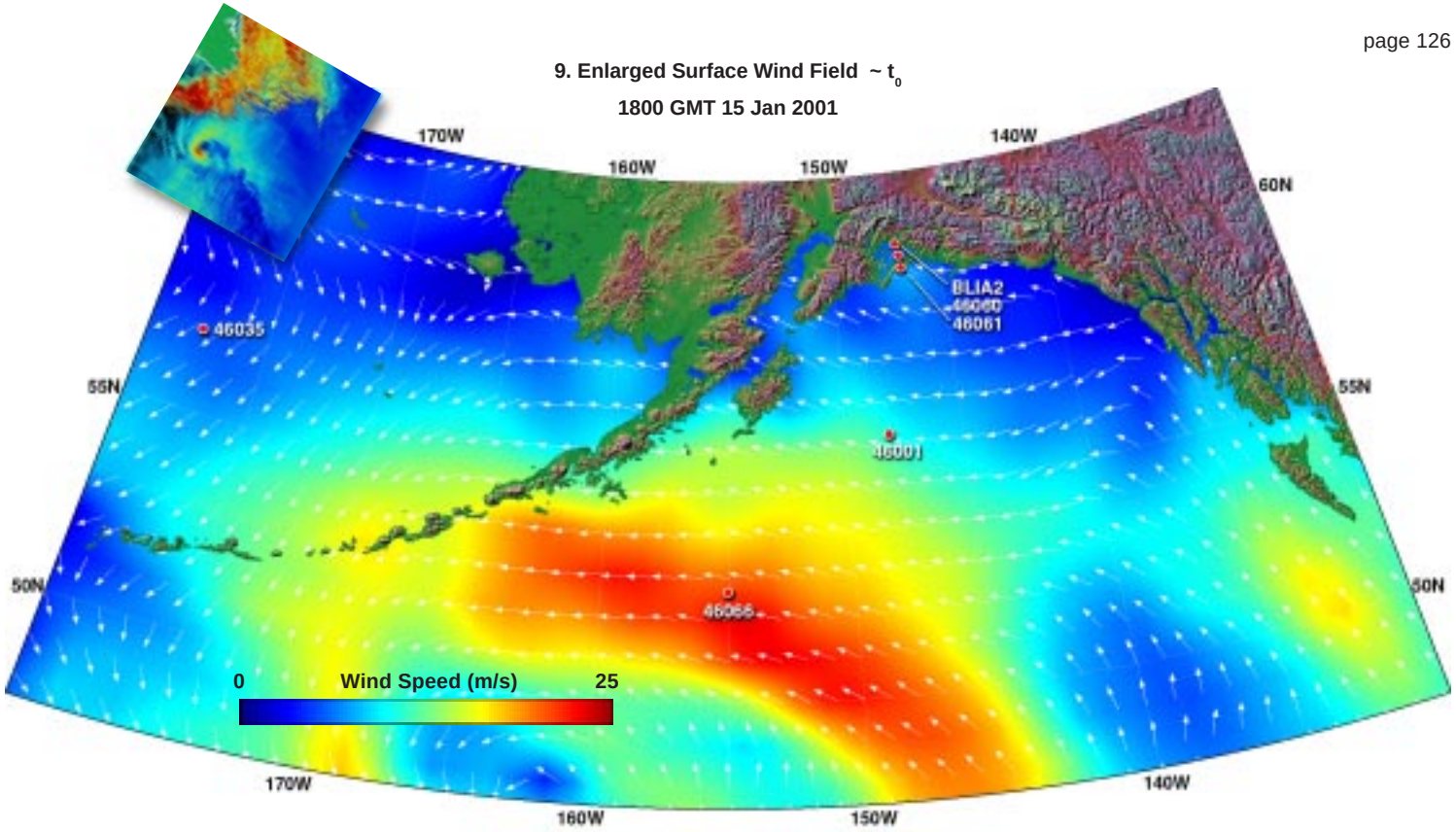

Model (this page): In the wake of a previous event, a large low pressure system moves northward toward the Aleutians (1-4), drawing cold arctic air southward across the western Bering Sea. Model winds (5, 9) reach 20 m/s in a broad band to the northeast of the low, but are relatively light (~10 m/s) from the north under the SAR overpass. Concurrent model waves are low, but growing (6, 7). The MABL is extremely unstable (8).

SAR (facing page): The SAR winds (10, 11) capture the early stages of a developing mesoscale low spawned by the cold air outbreak. Maximum SAR winds in the inner arm of the developing storm exceed 25 m/s, while the concurrent model estimates barely exceed 5 m/s (12). The SAR also shows evidence of a front extending southeast from the developing low, the shear across which is spawning submesoscale cyclonic activity. [ref. section 2.9: mesoscale lows associated with cold air outbreaks.]

5. Surface Wind Field (m/s) ~ t_0

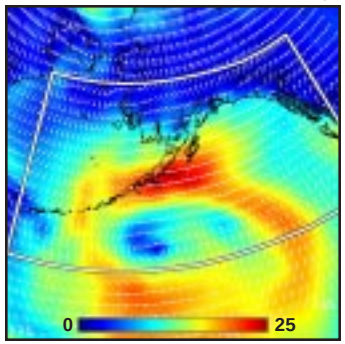

6. Surface Wave Height (m) ~ t_0

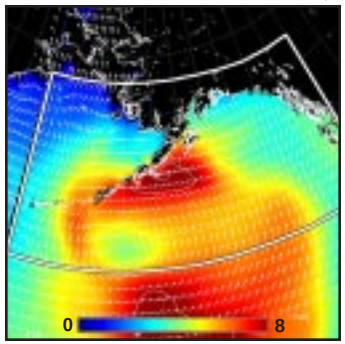

7. Inverse Wave Age (norm) ~ t_0

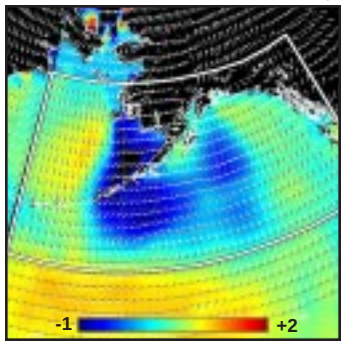

8. Air-Sea Temperature (˚C) ~ t_0

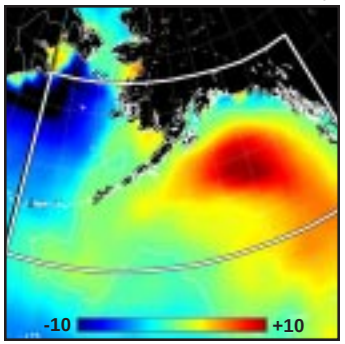

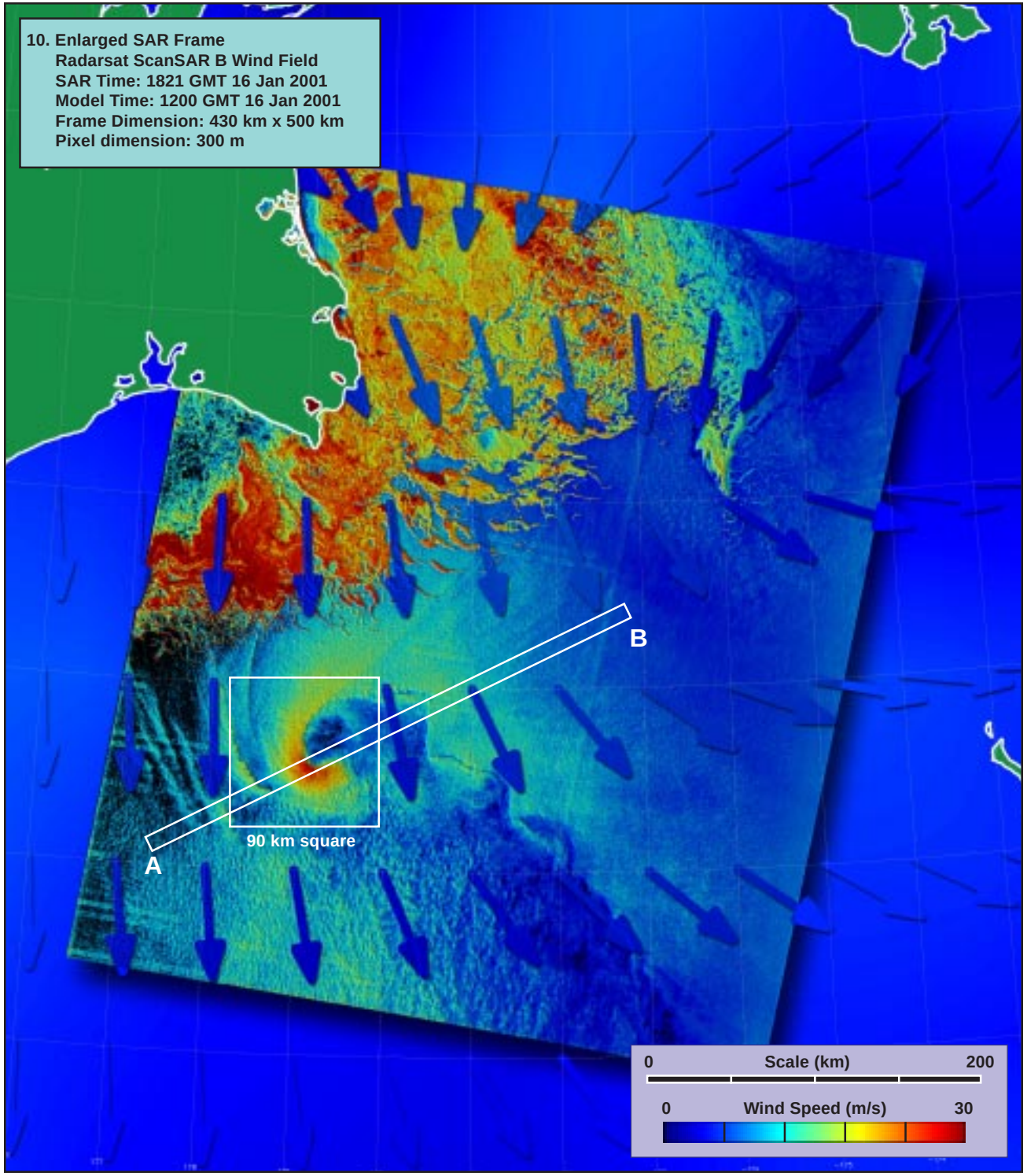

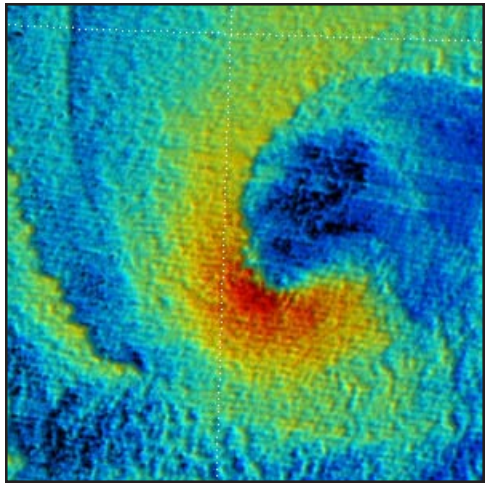

90 km square

11. Detail of Cyclonic Structure (x 2.5)

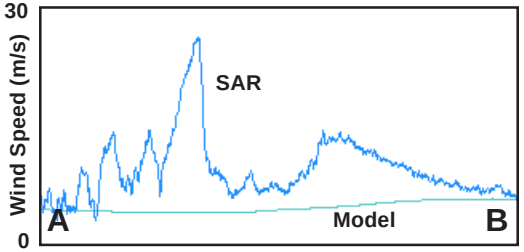

12. Model vs SAR Wind Profile along Line AB

1. Surface Pressure (mb) ~ t_0-36h

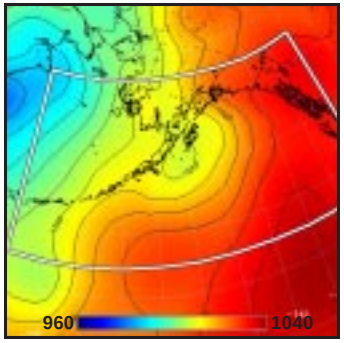

2. Surface Pressure (mb) ~ t_0-24h

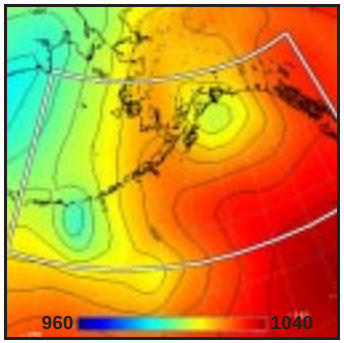

3. Surface Pressure (mb) ~ t_0-12h

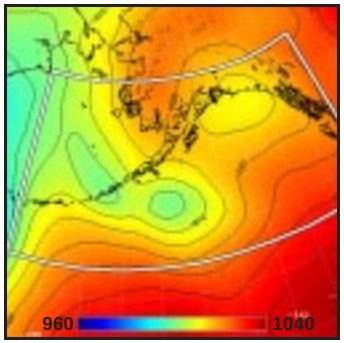

4. Surface Pressure (mb) ~ t_0

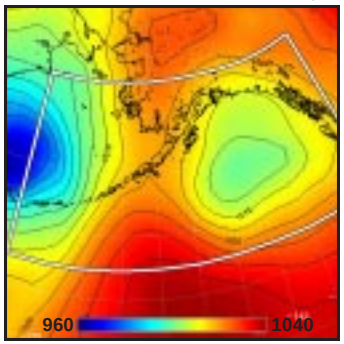

9. Enlarged Surface Wind Field ~ t_0

0600 GMT 08 Feb 2001

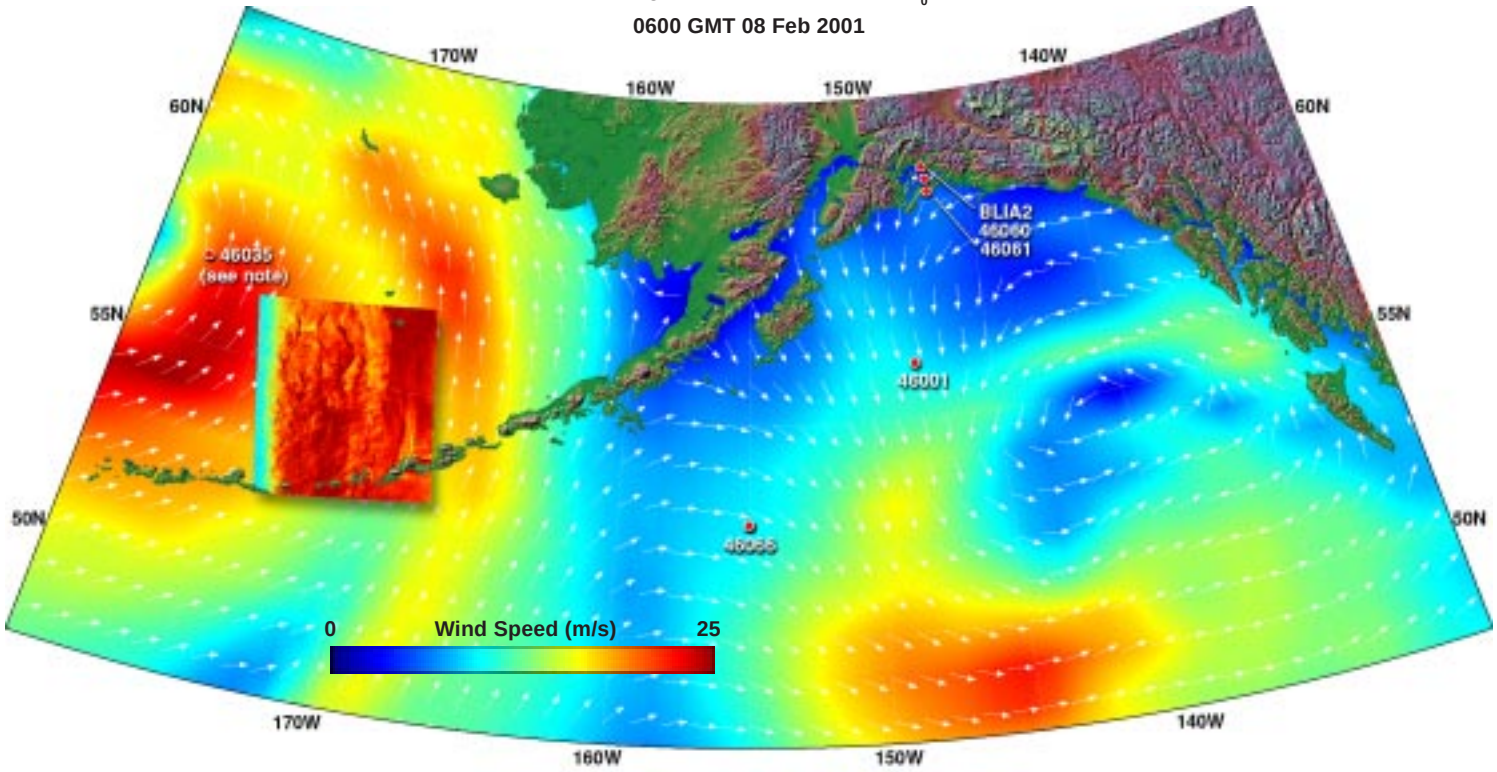

Model (this page): A deep, well formed low pressure system passes over the outer Aleutians into the Bering Sea, generating high pressure gradients to its east (1-4). The model shows two concentric bands of high (25 to 30 m/s) winds (5, 9) advancing in front of the storm center. Concurrent model waves are 6 to 8 m, growing (6, 7). The MABL is neutral to slightly stable within the high wind arcs (8).

SAR (facing page): The SAR winds clearly show a pattern of sharp gust fronts moving toward the ENE (10, 11) in the air behind a north/ south oriented cold front (12). Along this cold front, a large number of (presumably) tightly wrapped vortices are spawning. One 90 km stretch of this front (11) exhibits at least 8 such shear instabilities of dimension 1 to 2 km. Mean winds at buoy 46035 between 0800 and 1600 GMT were sustained at above 25 m/s, with gusts to 36 m/s, the highest sustained buoy wind speeds of this entire data set. Unfortunately, these high winds incapacitated buoy 46035 for the remainder of the winter. [ref. sections 2.8: mesoscale lows along fronts, 2.10: convection.]

5. Surface Wind Field (m/s) ~ t_0

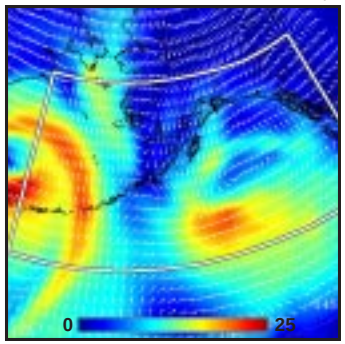

6. Surface Wave Height (m) ~ t_0

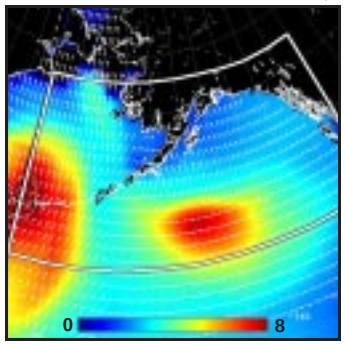

7. Inverse Wave Age (norm) ~ t_0

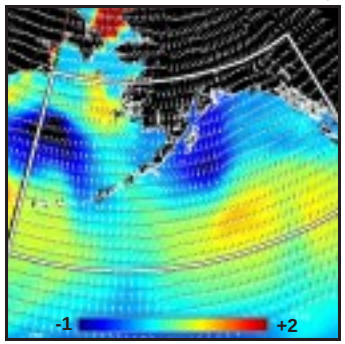

8. Air-Sea Temperature (˚C) ~ t_0

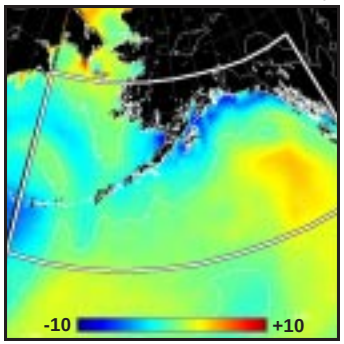

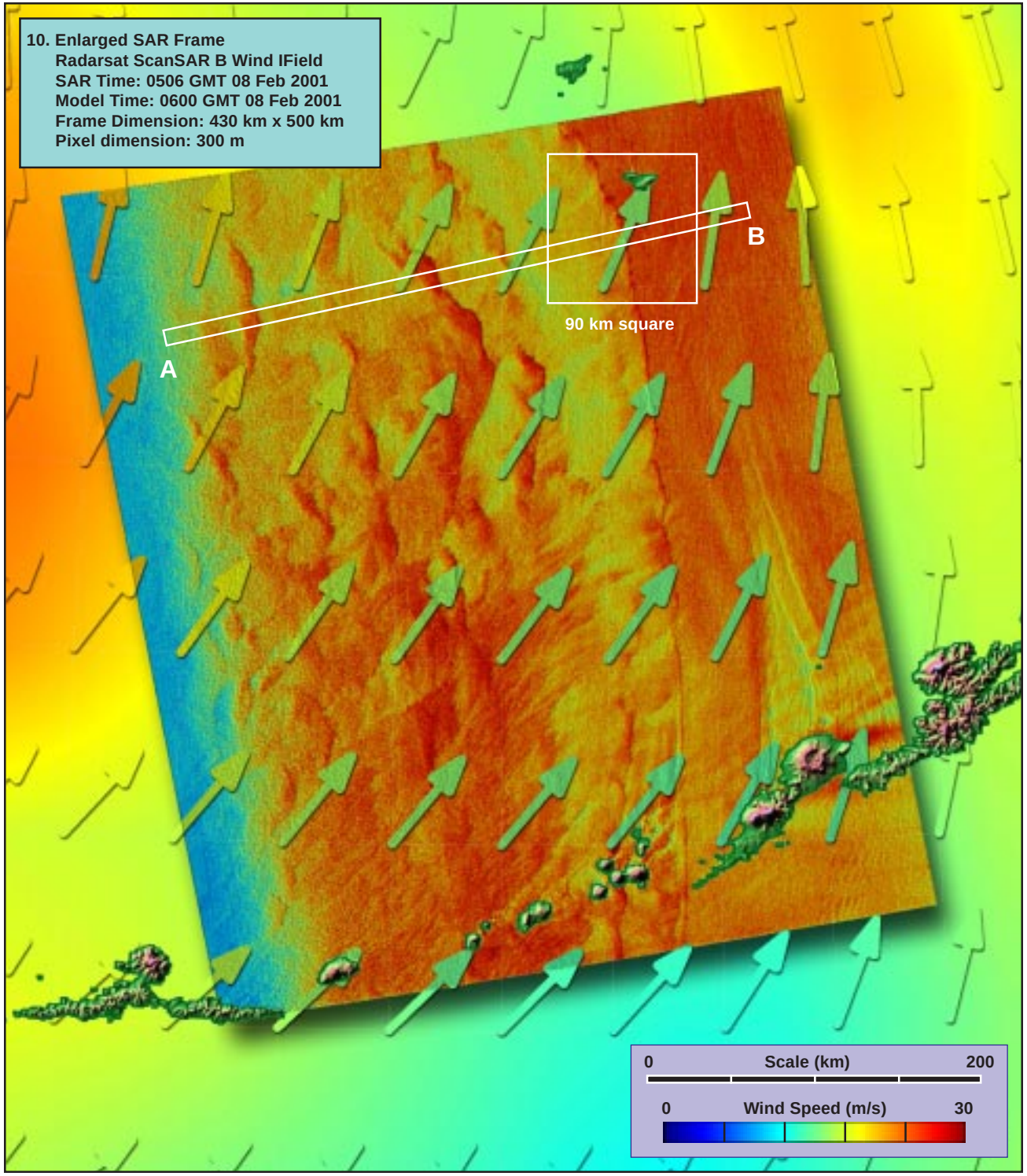

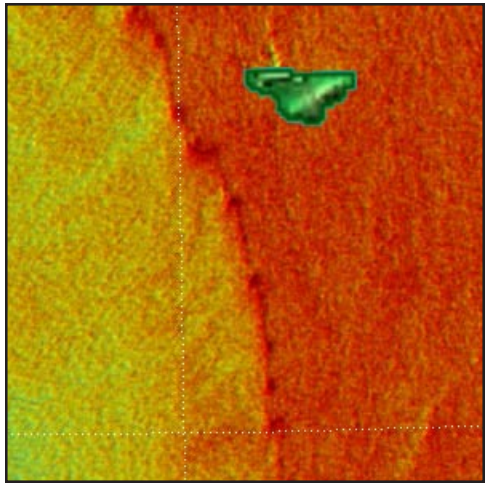

90 km square

11. Detail of Sharp Frontal Instabilities (x 2.5)

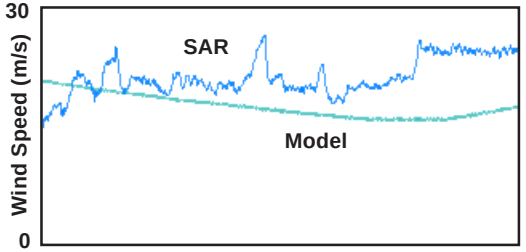

12. Model vs SAR Wind Profile along Line AB

1. Surface Pressure (mb) ~ t_0-36h

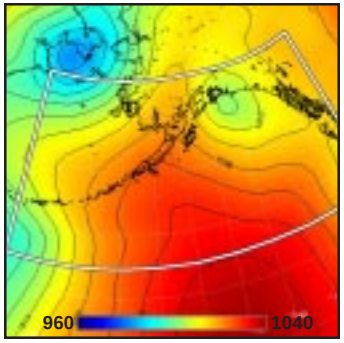

2. Surface Pressure (mb) ~ t_0-24h

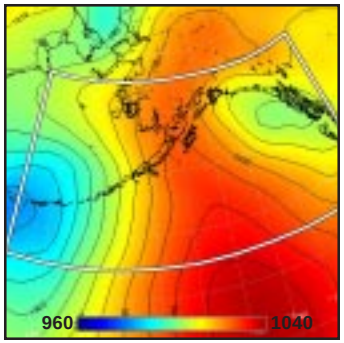

3. Surface Pressure (mb) ~ t_0-12h

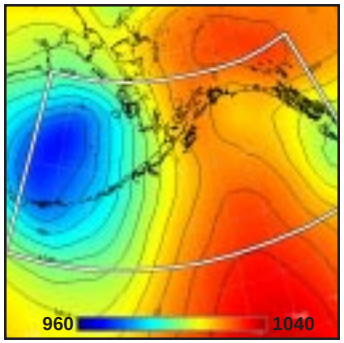

4. Surface Pressure (mb) ~ t_0

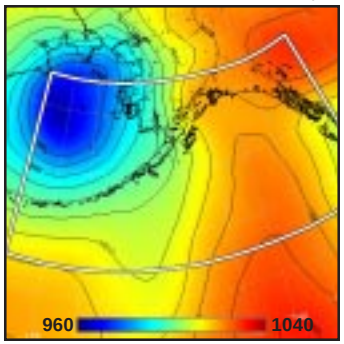

9. Enlarged Surface Wind Field ~ t_0

0600 GMT 11 Feb 2001

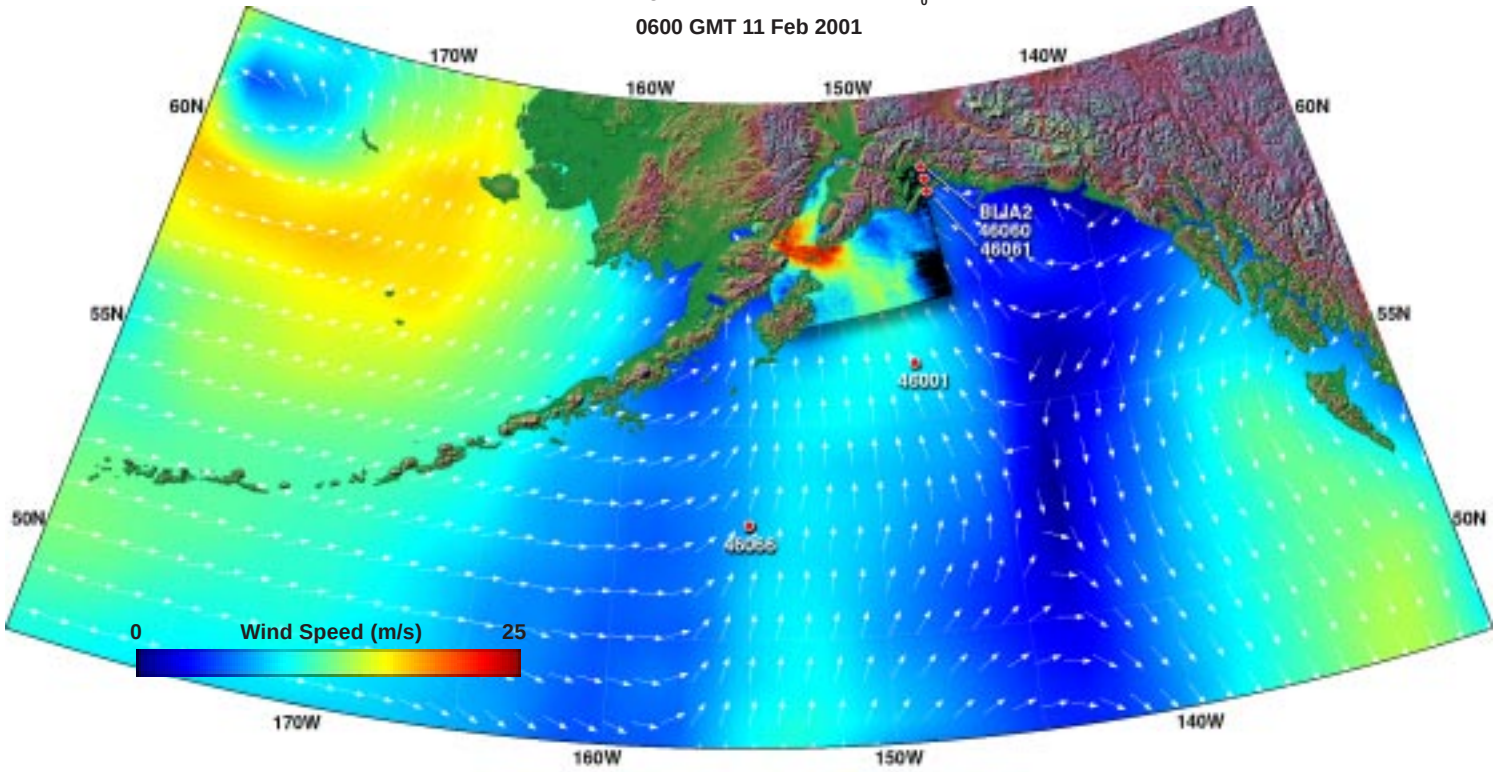

Model (this page): Blocked by a high pressure ridge in the Gulf of Alaska, a strong low pressure system moves northward over the outer Aleutians and into the Bering Sea (1-4). Model winds along the western side of the ridge are moderate (10 to 15 m/s) but steady from the south and east, with a slight gradient toward the north (5, 9). Concurrent model waves under the SAR pass are 2 m or less, growing slightly (6, 7). The MABL is unstable to near neutral under the SAR pass (8).

SAR (facing page): The SAR winds clearly show the amplifying effect of the gap between Kodiak Island and the Kenai Peninsula, in this case producing more than a doubling of the wind speed within a distance of less than 100 km (10, 11, 12). This southeasterly flow is met at right angles by a similar gap flow from the Cook Inlet, with the resulting sharp convergence line extending west from the Kenai Peninsula. [ref. section 2.5.1: reverse gap flow.]

5. Surface Wind Field (m/s) ~ t_0

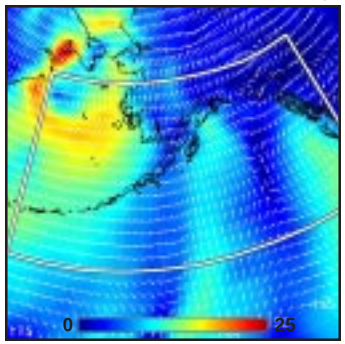

6. Surface Wave Height (m) ~ t_0

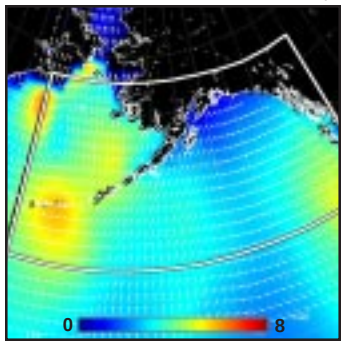

7. Inverse Wave Age (norm) ~ t_0

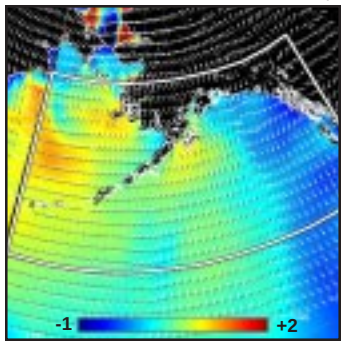

8. Air-Sea Temperature (˚C) ~ t_0

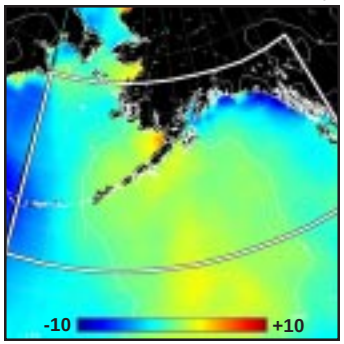

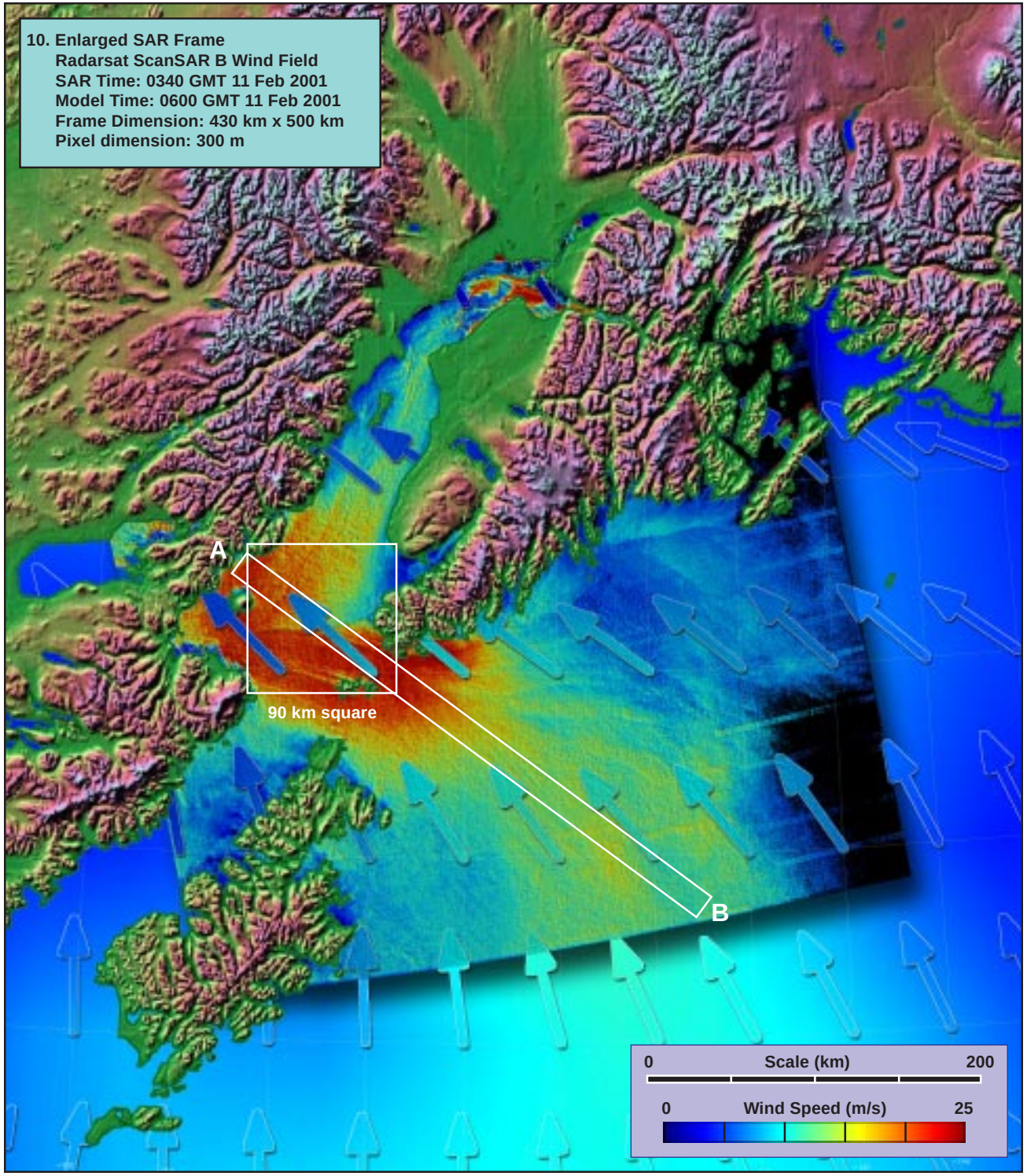

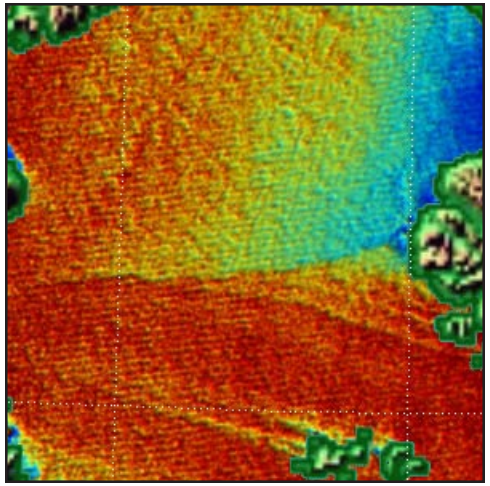

90 km square

11. Detail of Convergence Region (x 2.5)

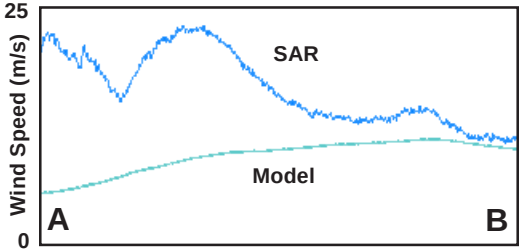

12. Model vs SAR Wind Profile along Line AB

1. Surface Pressure (mb) ~ t_0-36h

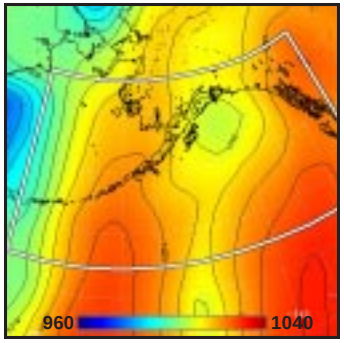

2. Surface Pressure (mb) ~ t_0-24h

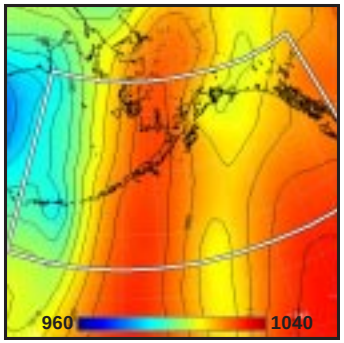

3. Surface Pressure (mb) ~ t_0-12h

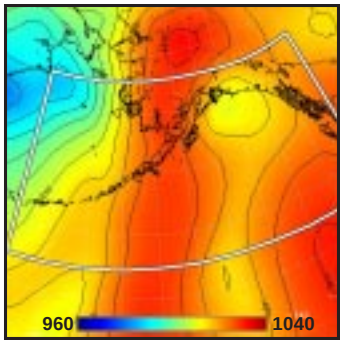

4. Surface Pressure (mb) ~ t_0

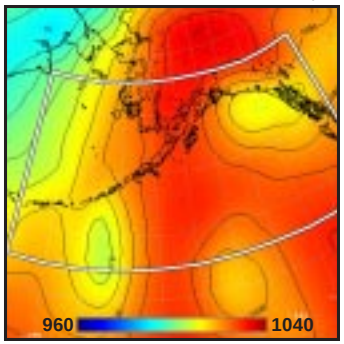

9. Enlarged Surface Wind Field ~ t_0

0600 GMT 14 Feb 2001

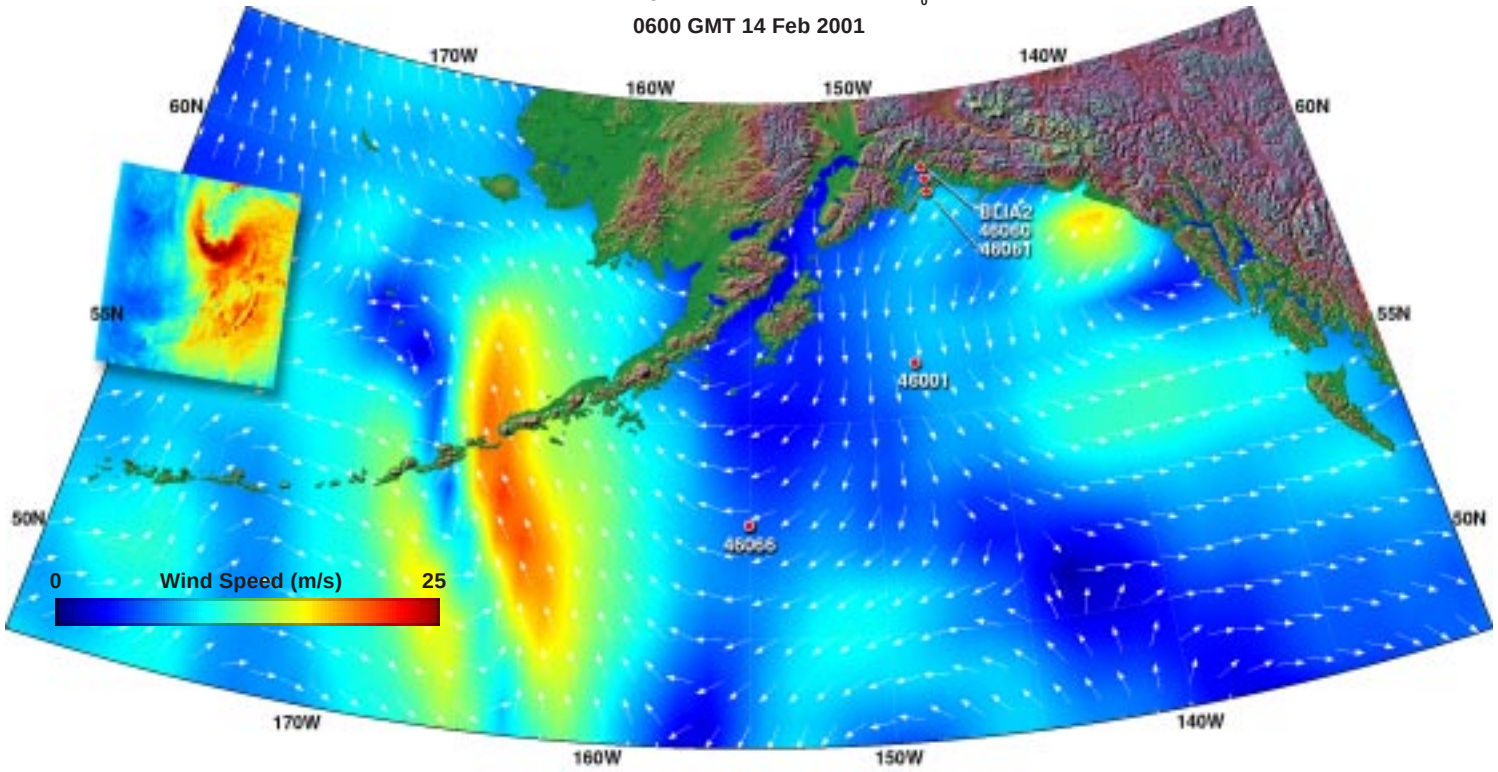

Model (this page): A weakening low pressure system moves north through the Bering Sea, blocked by a north-south oriented high pressure ridge to its east (1-4). Model winds show only a uniform southerly wind of 5 to 15 m/s over most of the Bering Sea under the SAR, with no evidence of any new storm development (5, 9). Concurrent model waves are about 4 m, from the south, and nearly in equilibrium (6, 7). The MABL is unstable within the SAR pass (8).

SAR (facing page): In clear contrast to the model, the SAR winds reveal evidence of a small developing polar low, with a characteristic arc of high (25 to 30 m/s) winds rotating around a nearly calm (0 to 5 m/s) center (10, 11, 12). The highest wind region of the storm passed directly over buoy 46035; unfortunately it had been rendered inoperative just a few days earlier by one of the strongest North Pacific storms of the winter. [ref. section 2.9 mesoscale lows associated with cold air outbreaks]

5. Surface Wind Field (m/s) ~ t_0

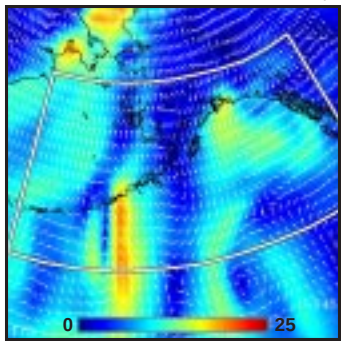

6. Surface Wave Height (m) ~ t_0

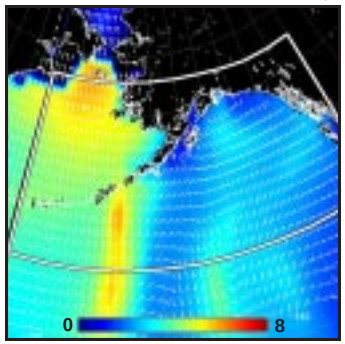

7. Inverse Wave Age (norm) ~ t_0

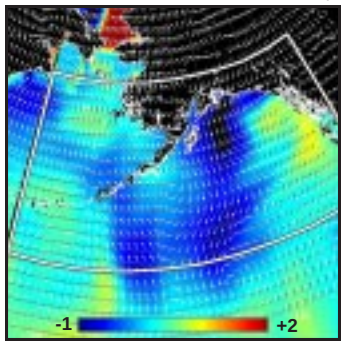

8. Air-Sea Temperature (˚C) ~ t_0

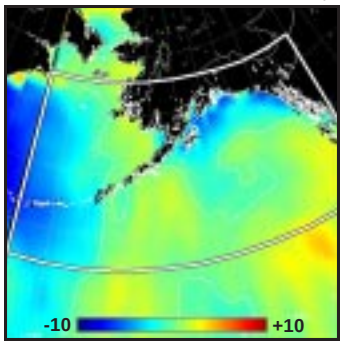

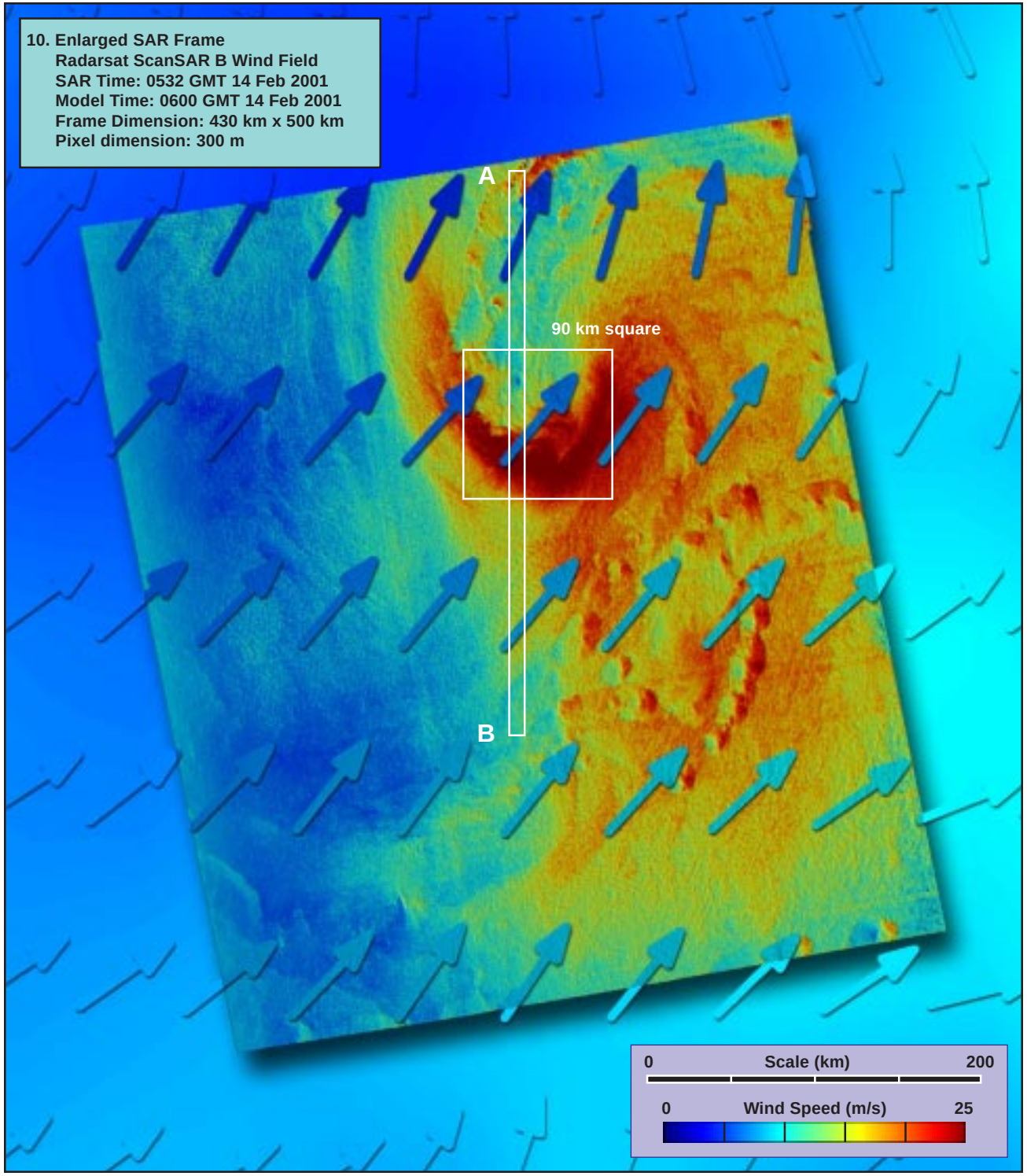

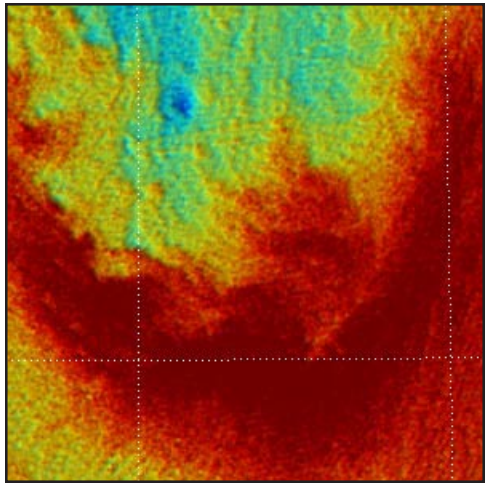

90 km square

11. Detail of Storm Center (x 2.5)

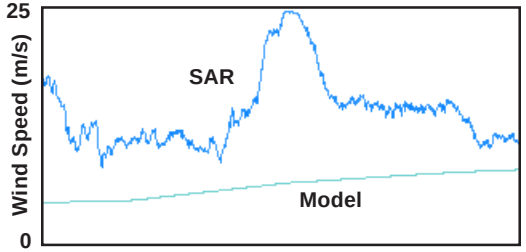

12. Model vs SAR Wind Profile along Line AB

1. Surface Pressure (mb) ~ t_0-36h

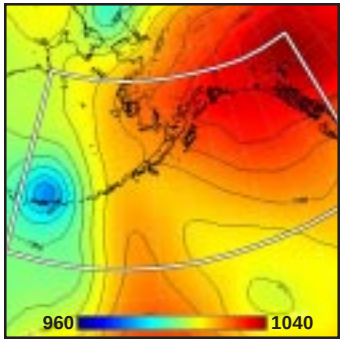

2. Surface Pressure (mb) ~ t_0-24h

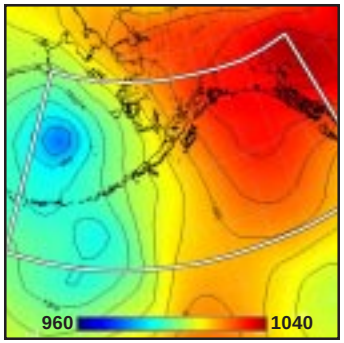

3. Surface Pressure (mb) ~ t_0-12h

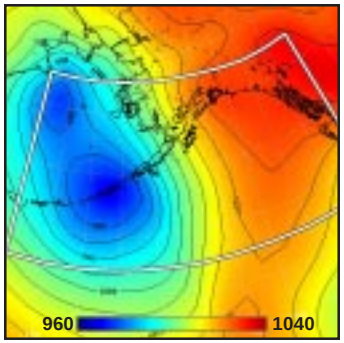

4. Surface Pressure (mb) ~ t_0

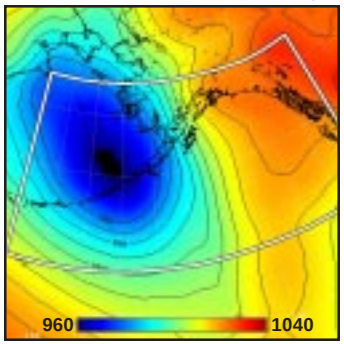

9. Enlarged Surface Wind Field ~ t_0

1800 GMT 16 Feb 2001

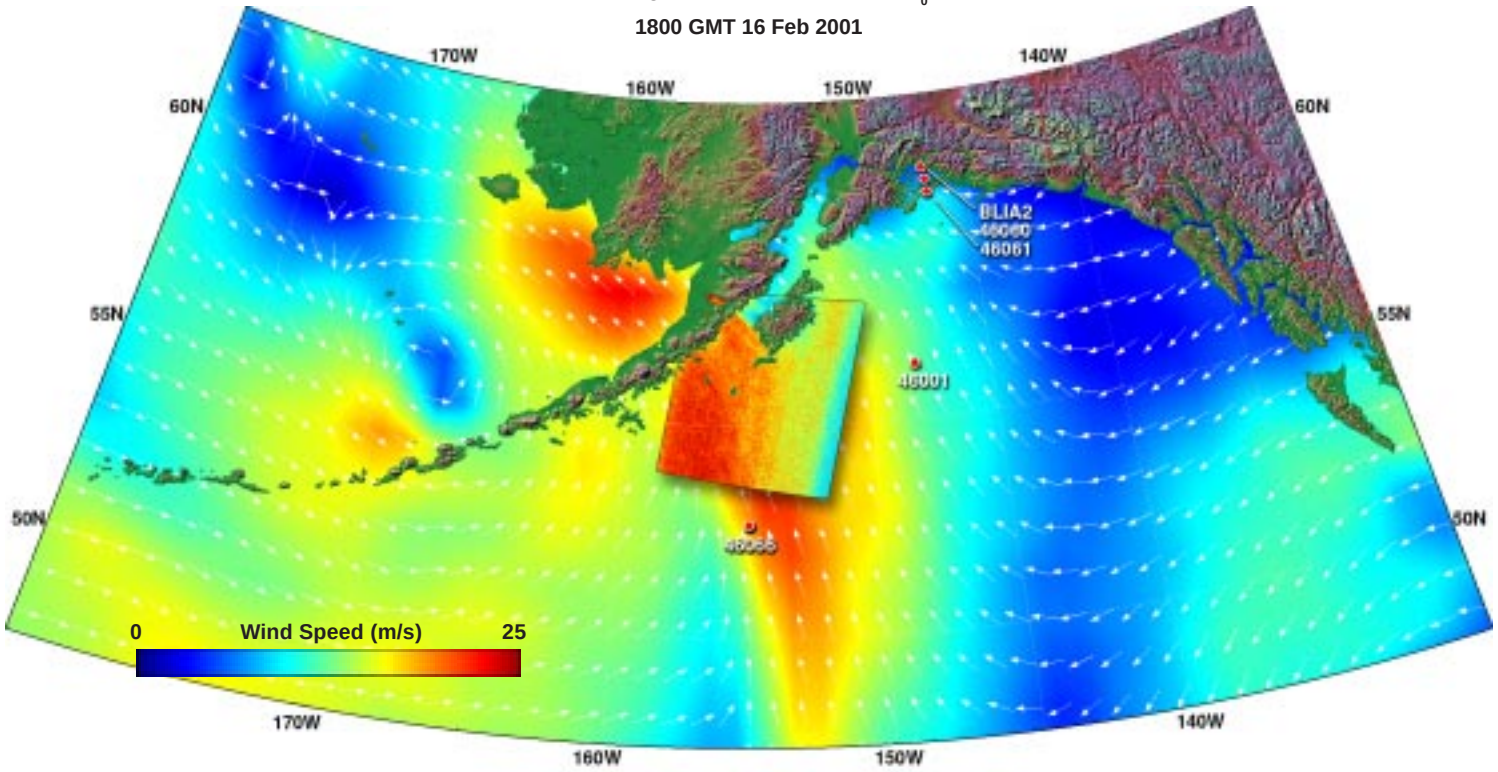

Model (this page): A deepening low pressure system over the central Aleutians creates an extended band of high winds cutting across the Alaskan Peninsula just to the south of Kodiak Island (1-4). Model winds peak at 20 to 25 m/s under the SAR pass, cutting diagonally across the pass from southeast to northwest (5, 9). Concurrent model waves are highest (about 6 m) south of the SAR pass, but are growing rapidly within the pass (6, 7). The MABL is near neutral around Kodiak Island, but increasingly stable to the south (8).

SAR (facing page): The SAR winds also peak at about 25 m/s just south of Kodiak Island, but show evidence of a much stronger northern boundary, no doubt resulting from the island sheltering (10, 11). The instrument sensitivity problem is evident on the eastern edge of the pass (12). Buoy 46066 measured mean winds of 17 m/s with gusts to 22 m/s at overpass time.

5. Surface Wind Field (m/s) ~ t_0

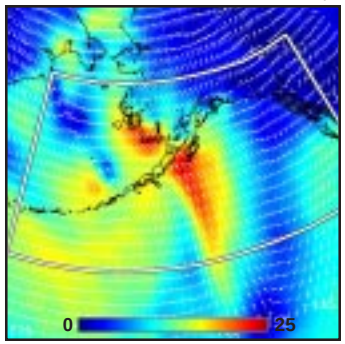

6. Surface Wave Height (m) ~ t_0

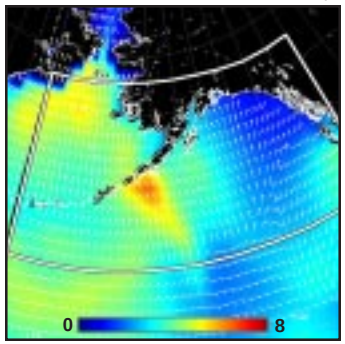

7. Inverse Wave Age (norm) ~ t_0

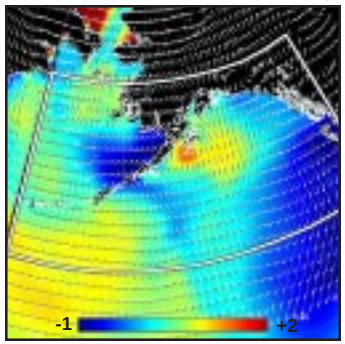

8. Air-Sea Temperature (˚C) ~ t_0

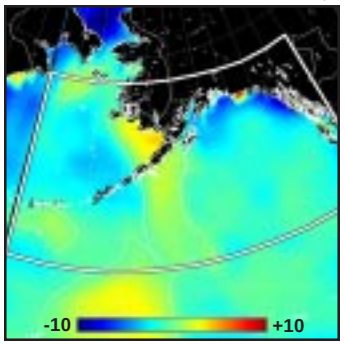

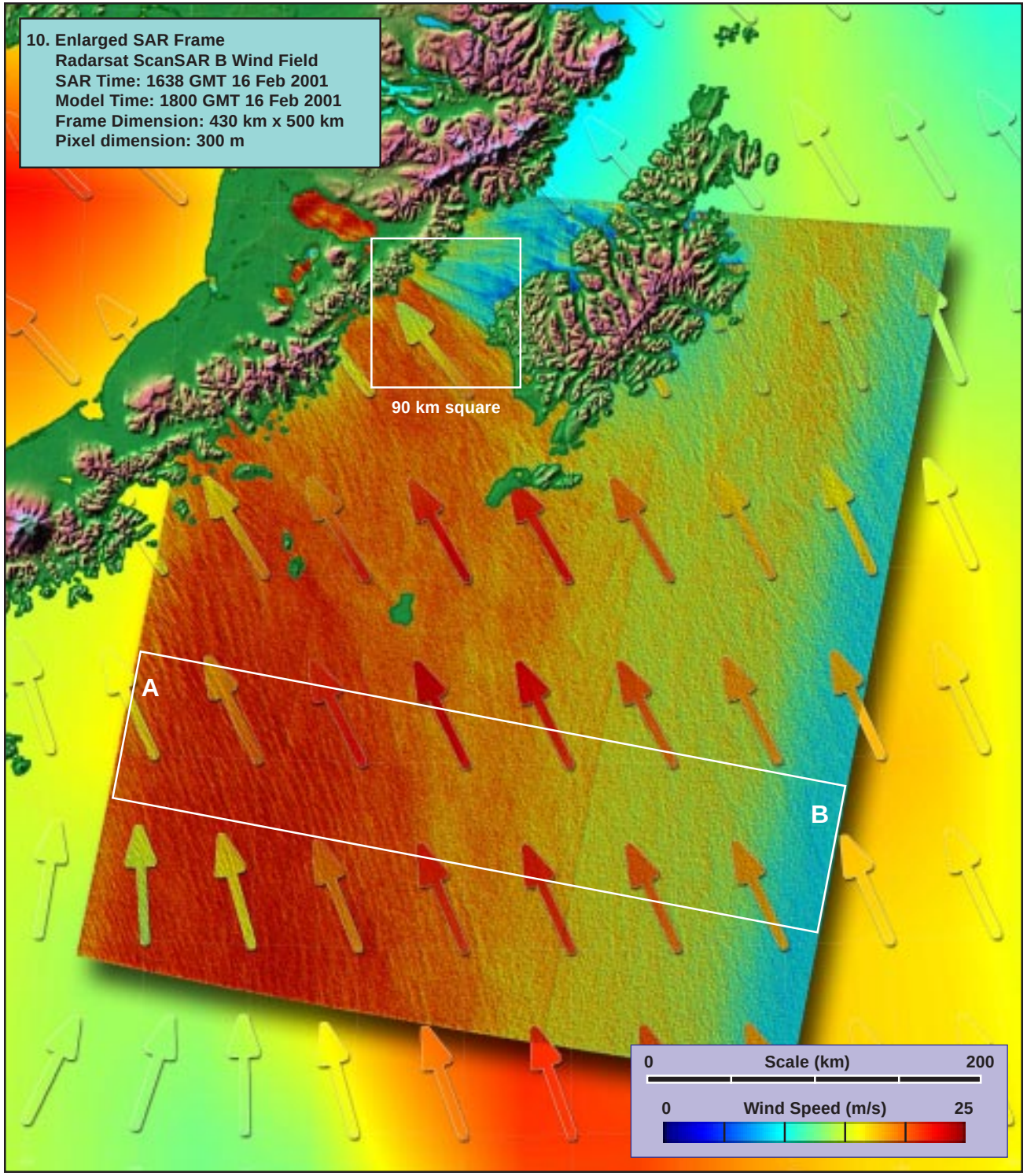

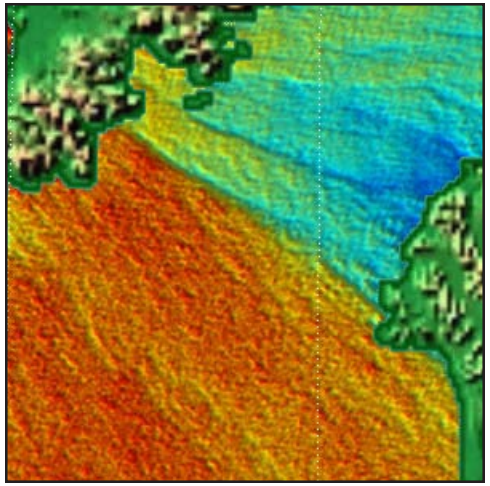

90 km square

11. Detail of Frontal Structure (x 2.5)

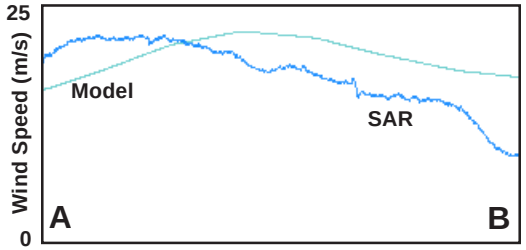

12. Model vs SAR Wind Profile along Line AB

1. Surface Pressure (mb) ~ t_0-36h

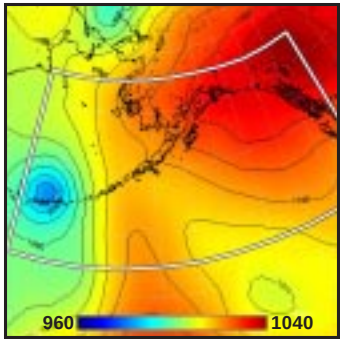

2. Surface Pressure (mb) ~ t_0-24h

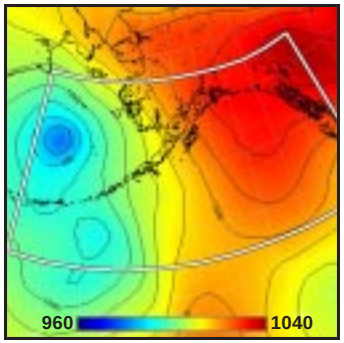

3. Surface Pressure (mb) ~ t_0-12h

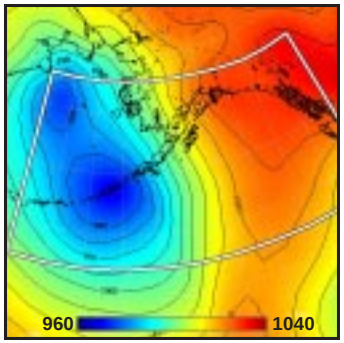

4. Surface Pressure (mb) ~ t_0

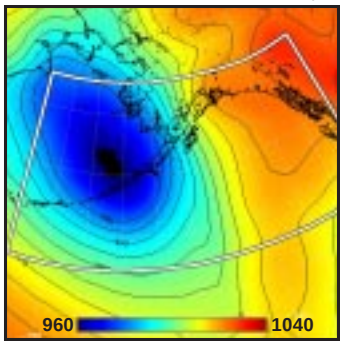

9. Enlarged Surface Wind Field ~ t_0

1800 GMT 16 Feb 2001

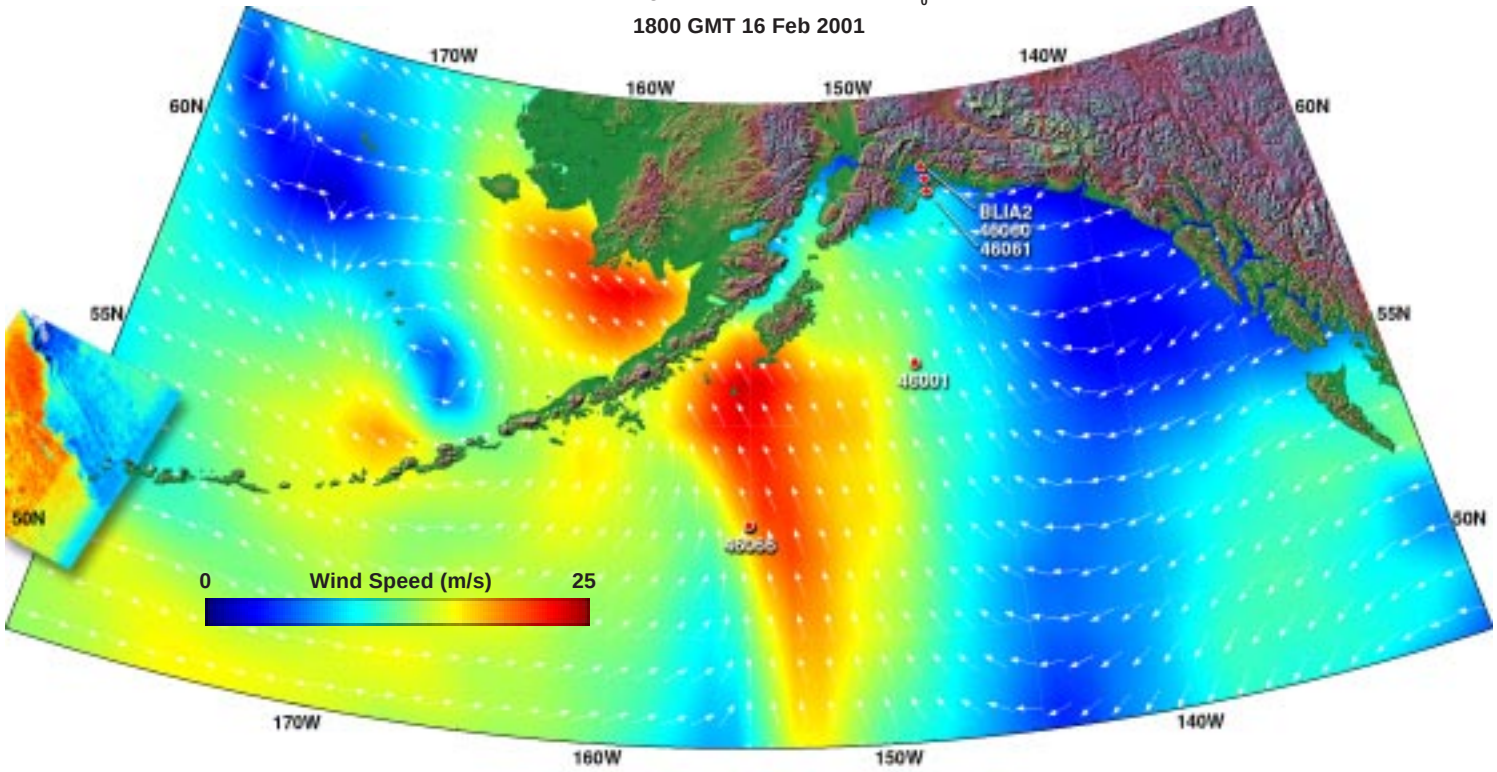

Model (this page): A rapidly intensifying low pressure system develops in the southeastern Bering Sea, just north of the central Aleutians (1-4). Model winds to the west of the developing low (under the SAR overpass) are westerly at ~15 m/s in the south, dropping to less than 5 m/s directly to the north (5, 9). Concurrent model waves are 3 to 5 m, actively growing (6, 7). The MABL is unstable over the entire region of the SAR pass (8).

SAR (facing page): The SAR wind estimate reveals a ragged front having much more structure than the model shows, but with the same general trend toward low winds in the northwest corner (10, 11). There the SAR shows an extremely sharp gradient, with the wind speed dropping from near 25 m/s on the south side of the front to less than 10 m/s on parts of the north side, just a few km away (12). [ref. section 2.6: synoptic fronts.]

5. Surface Wind Field (m/s) ~ t_0

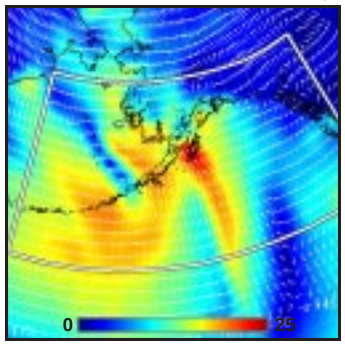

6. Surface Wave Height (m) ~ t_0

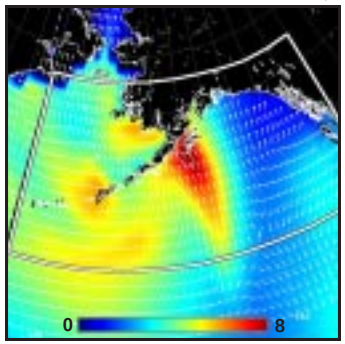

7. Inverse Wave Age (norm) ~ t_0

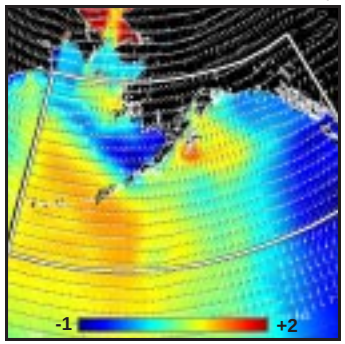

8. Air-Sea Temperature (˚C) ~ t_0

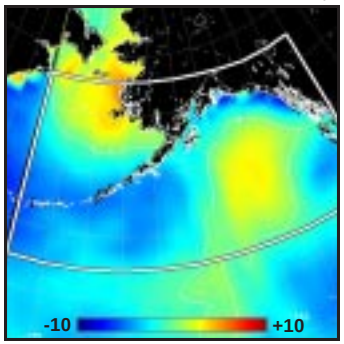

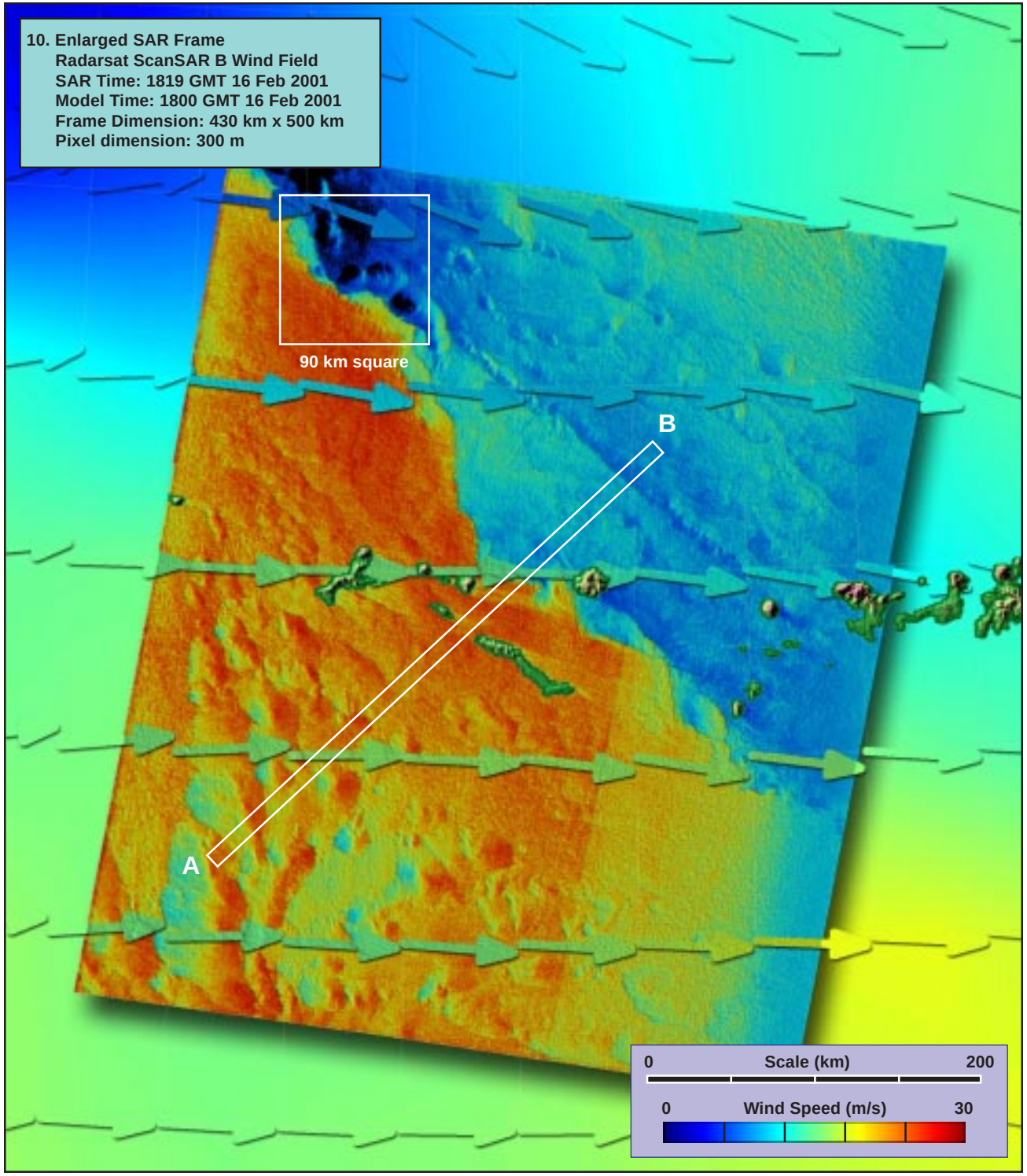

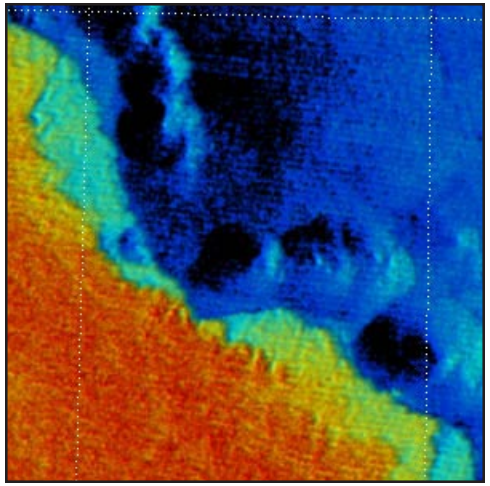

90 km square

11. Detail of Frontal Structure (x 2.5)

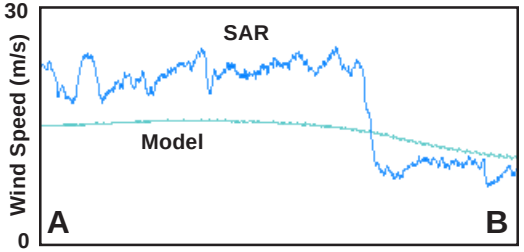

12. Model vs SAR Wind Profile along Line AB

1. Surface Pressure (mb) ~ t_0-36h

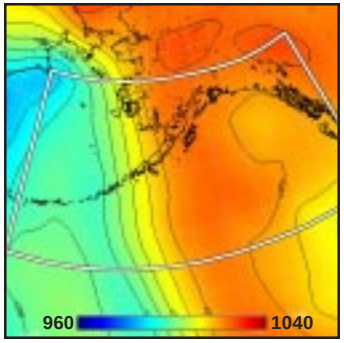

2. Surface Pressure (mb) ~ t_0-24h

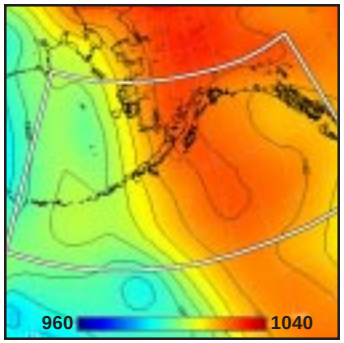

3. Surface Pressure (mb) ~ t_0-12h

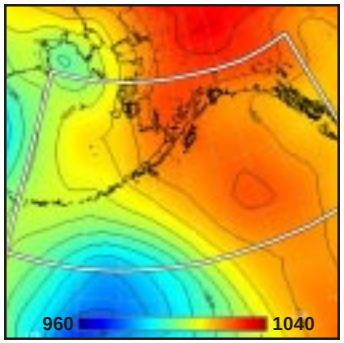

4. Surface Pressure (mb) ~ t_0

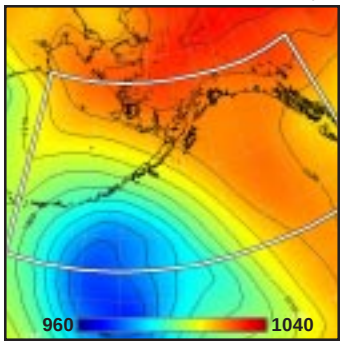

9. Enlarged Surface Wind Field ~ t_0

0600 GMT 23 Feb 2001

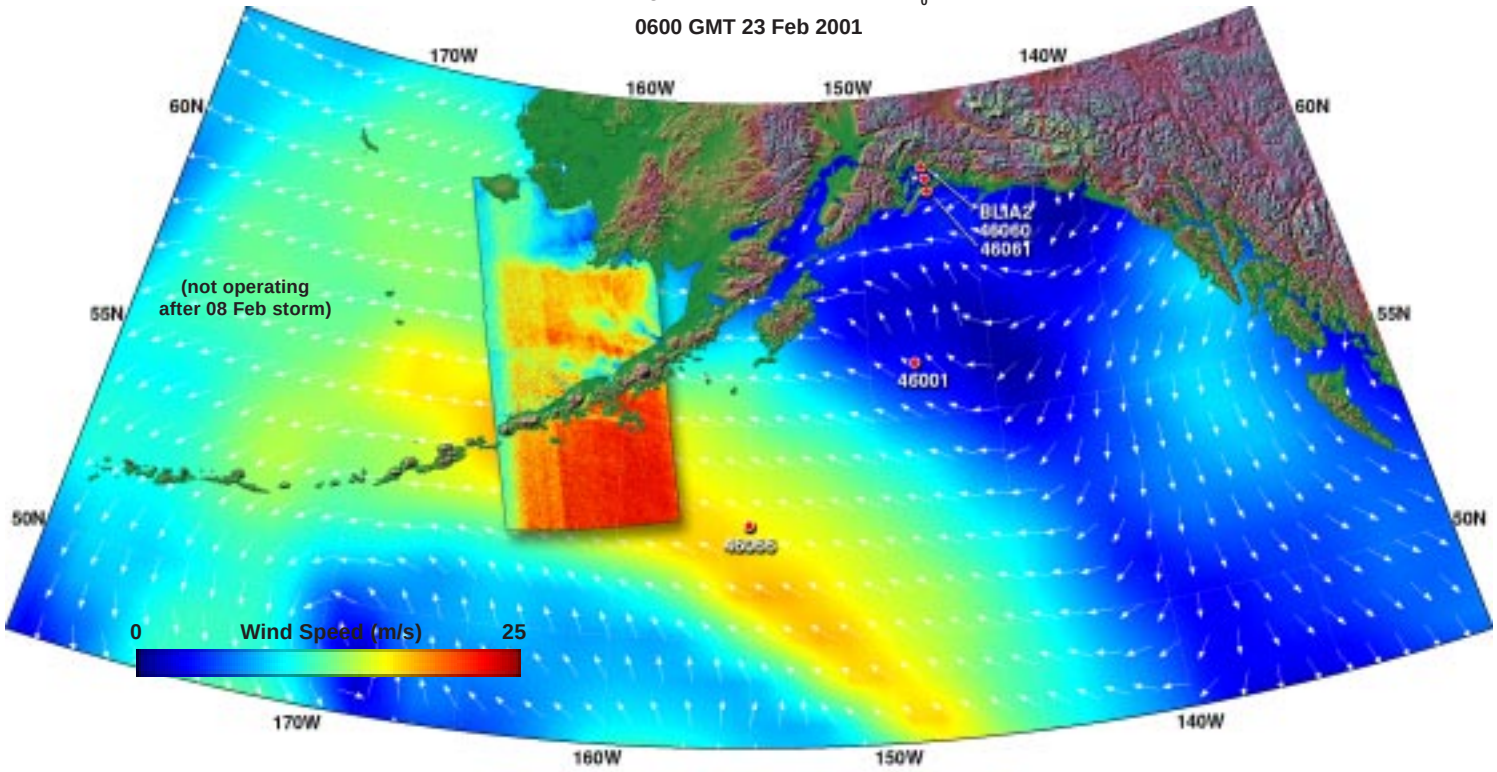

Model (this page): A deepening low pressure system advances from the south toward the outer Aleutian Chain, resulting in a strong pressure gradient to its northeast (1-4). The model shows an extended band of high (15 to 20 m/s) winds reaching from the southern Gulf of Alaska through the Aleutians to the Bering Sea (5, 9). Concurrent model waves in the high wind band peak at about 6 to 8 m on the upwind side of the Aleutians (6, 7). The MABL is generally stable under the SAR overpass (8).

SAR (facing page): The SAR winds show a broad region of high (20 to 25 m/s) winds upwind of the Aleutians, with little structure. On the downwind side, however, rich, deeply modulated patterns of topographically induced lee waves dominate the SAR image (10, 11). Some of the deeper modulations show alternating bands of 5 m/s and 25 m/s wind regions occurring over spatial scales of less than 10 km. The southern third of the SAR frame clearly illustrates the form of the crosstrack bias function (12). [ref. section 2.3: mountain lee waves.]

5. Surface Wind Field (m/s) ~ t_0

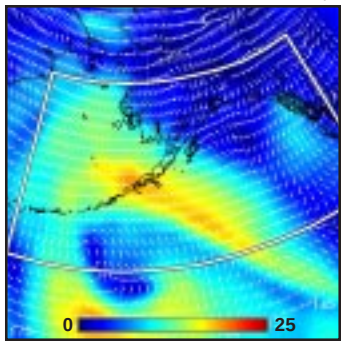

6. Surface Wave Height (m) ~ t_0

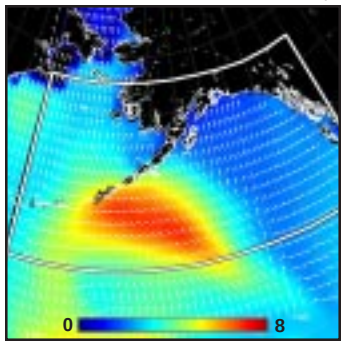

7. Inverse Wave Age (norm) ~ t_0

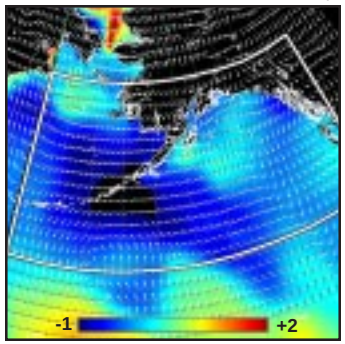

8. Air-Sea Temperature (˚C) ~ t_0

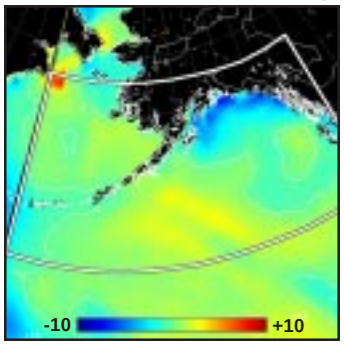

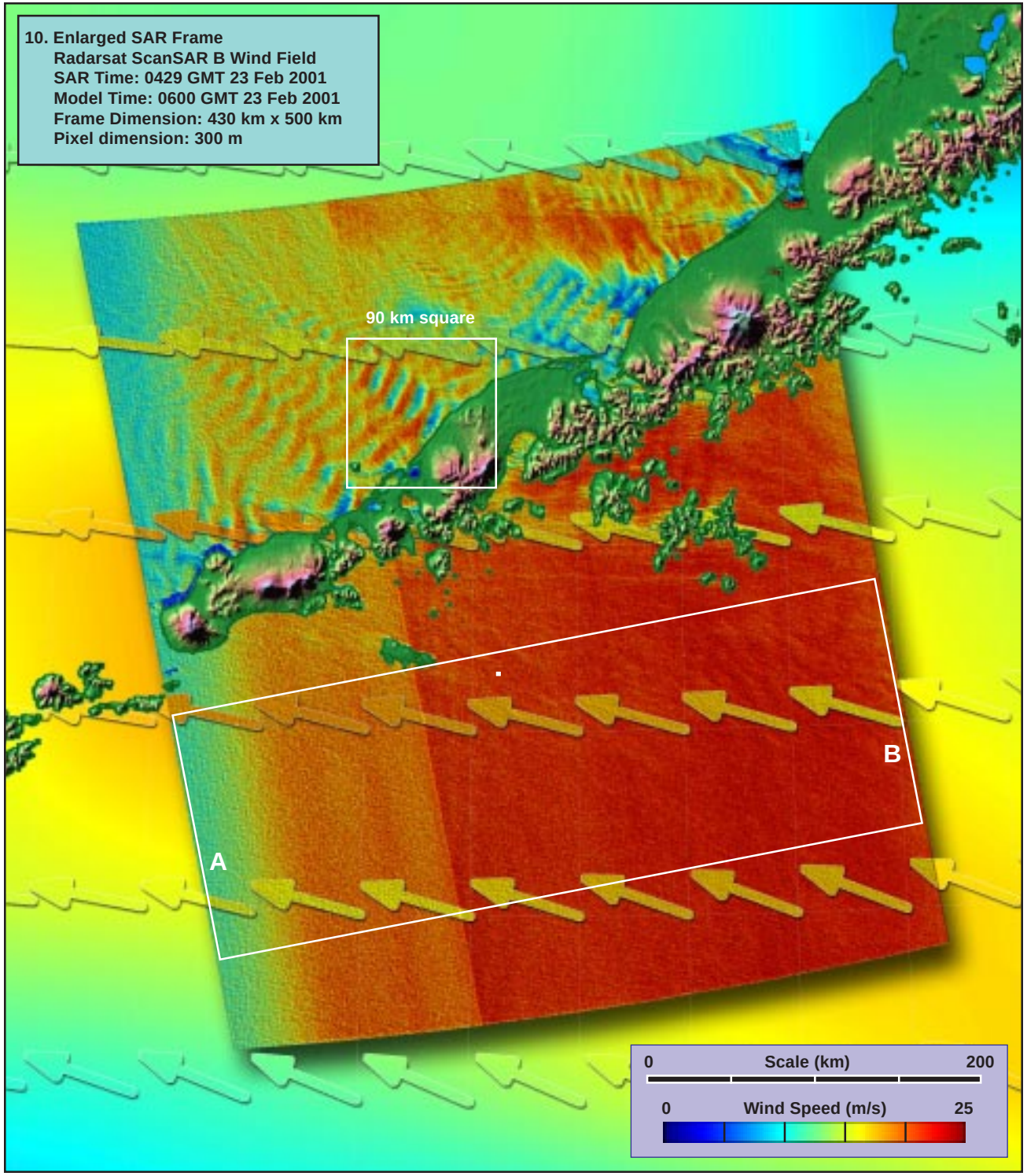

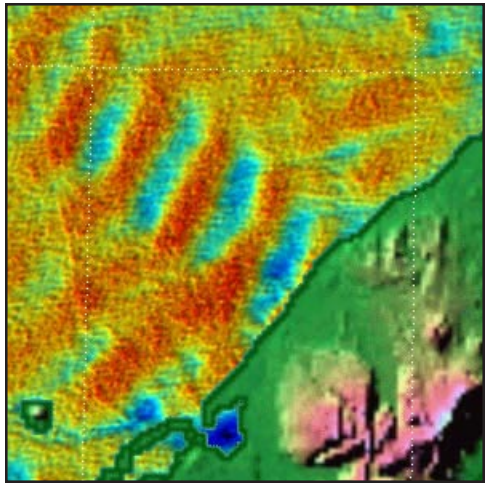

90 km square

11. Detail of Lee Waves (x 2.5)

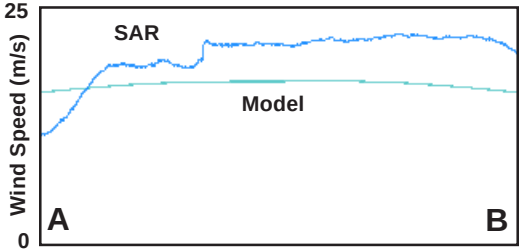

12. Model vs SAR Wind Profile along Line AB

1. Surface Pressure (mb) ~ t_0-36h

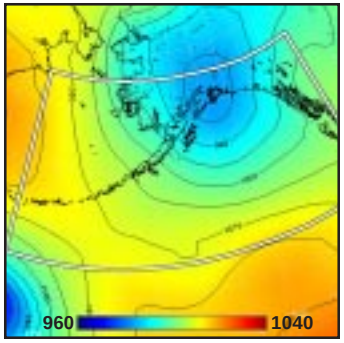

2. Surface Pressure (mb) ~ t_0-24h

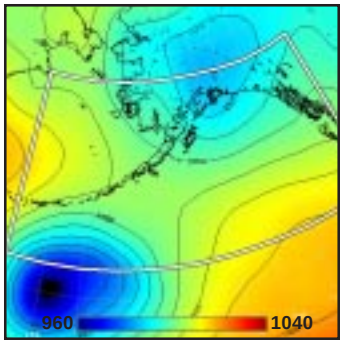

3. Surface Pressure (mb) ~ t_0-12h

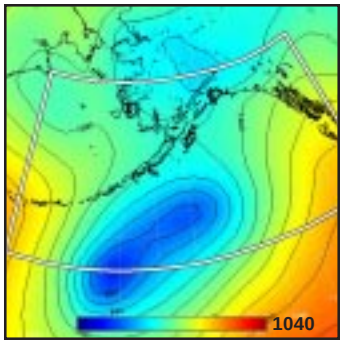

4. Surface Pressure (mb) ~ t_0

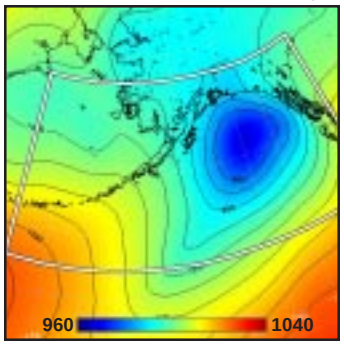

9. Enlarged Surface Wind Field ~ t_0

0000 GMT 12 Oct 2001

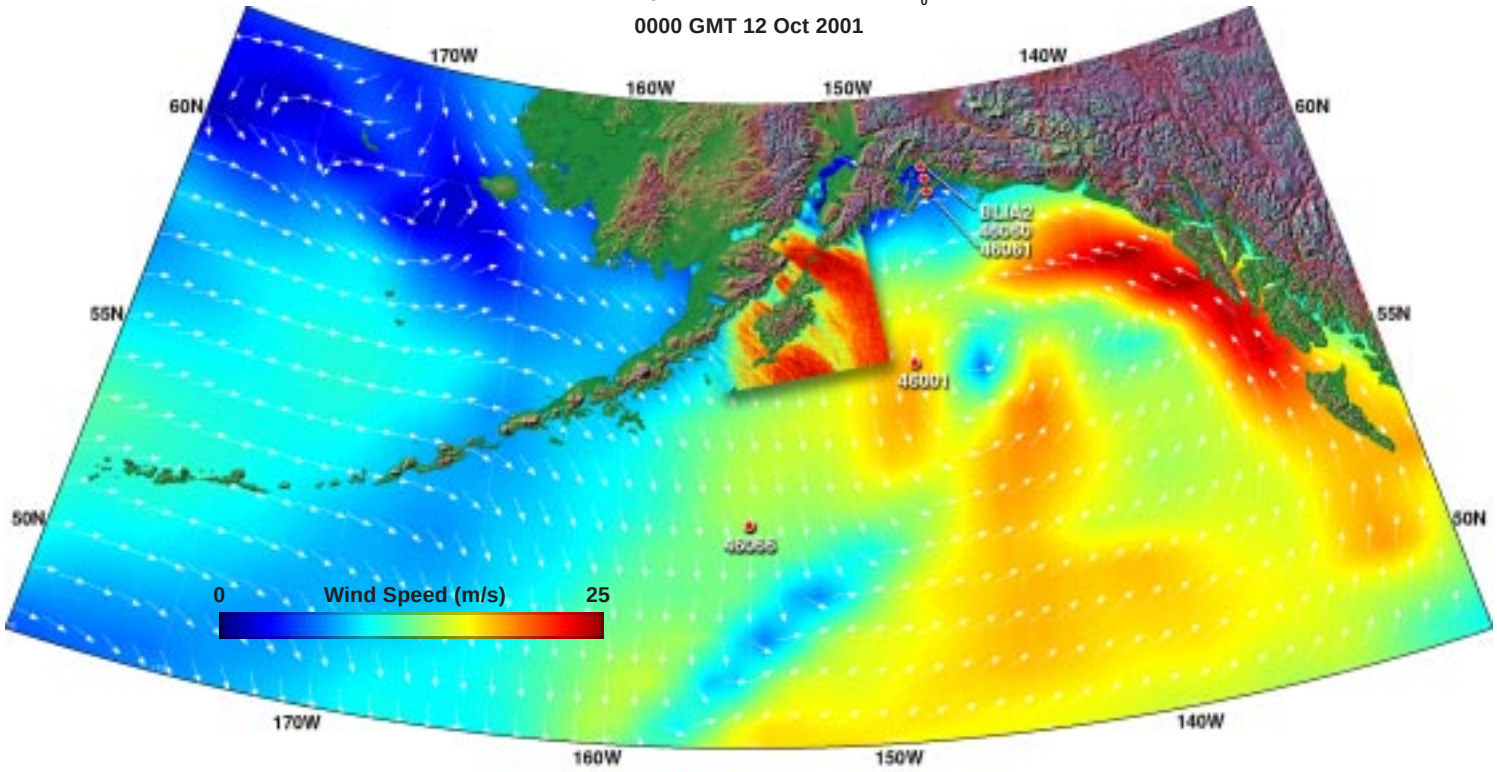

Model (this page): Two low pressure systems merge in the northern Gulf of Alaska, forming substantial gradients around the resulting rim, but especially along the northeast portion (1-4). Model winds in the northeast sector of the storm reach 25 m/s, but in the northwest sector, under the SAR overpass, only 15 to 20 m/s (5, 9). Concurrent NOGAPS model wave fields were unavailable from this date forward to the end of the data collection period. The MABL under the SAR overpass is extremely unstable (8).

SAR (facing page): The SAR winds reveal an enhanced flow inside the gap north of Kodiak Island, reaching 20 to 25 m/s within the gap, but dropping to about half those values immediately adjacent to (crosswind of) the gap (10, 11, 12). Model winds within the gap never exceed 10 m/s. [ref. section 2.4: gap flows.]

5. Surface Wind Field (m/s) ~ t_0

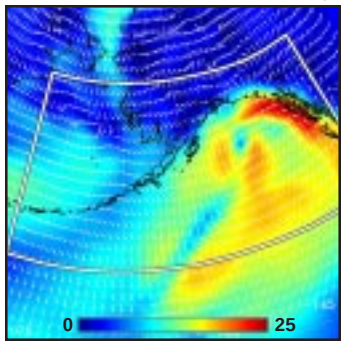

6. Surface Wave Height (m) ~ t_0

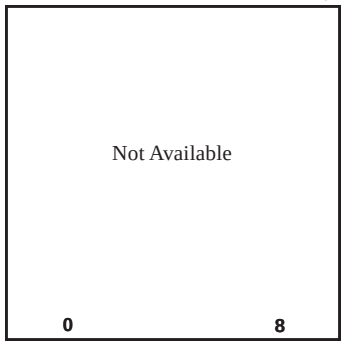

7. Inverse Wave Age (norm) ~ t_0

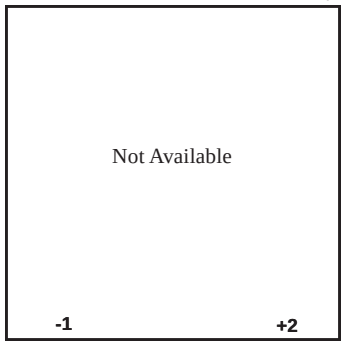

8. Air-Sea Temperature (˚C) ~ t_0

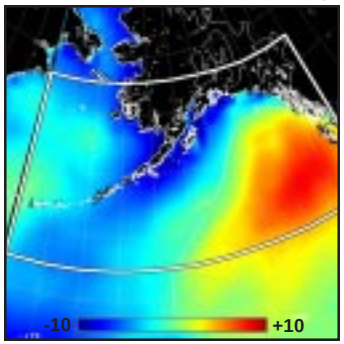

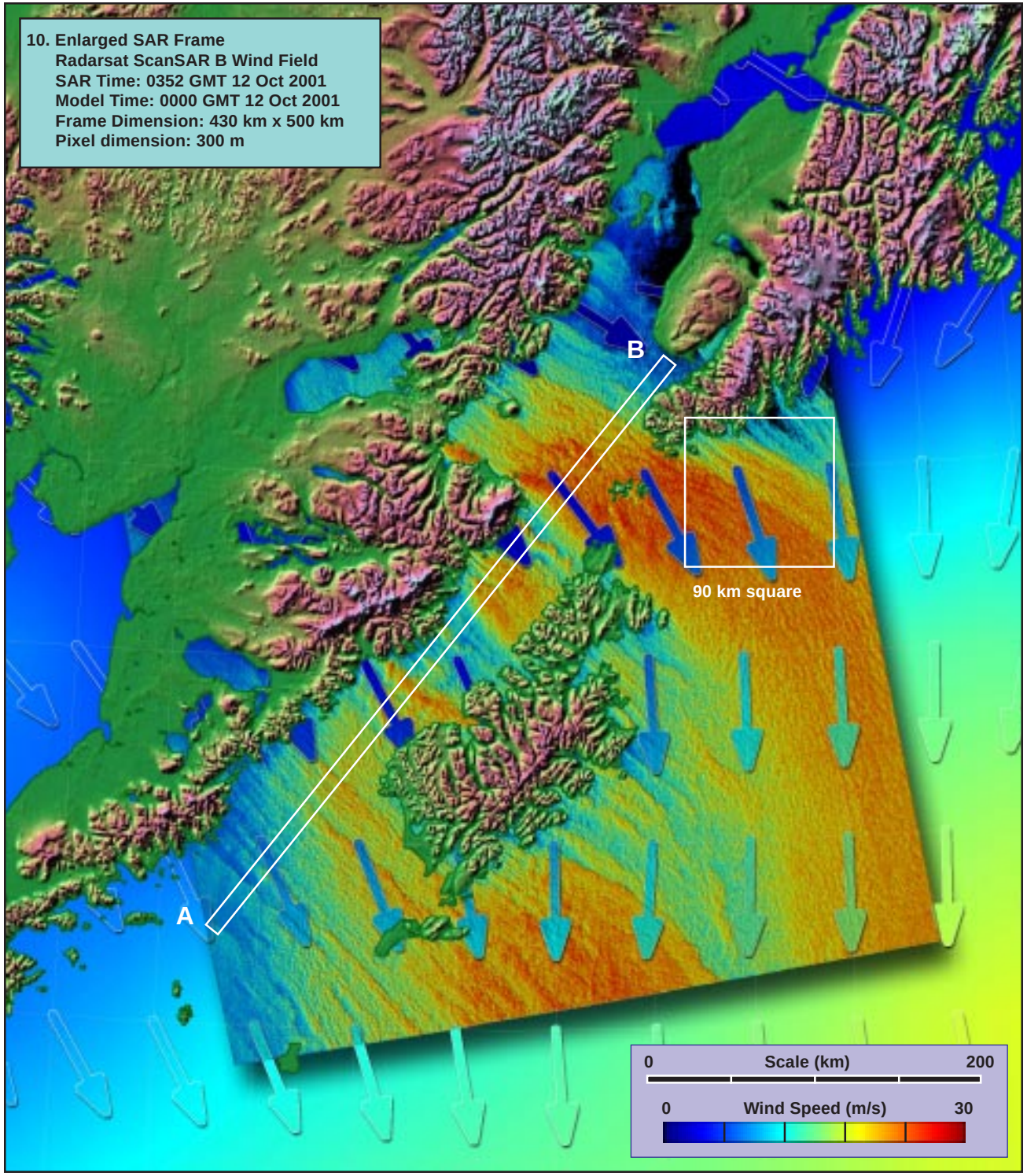

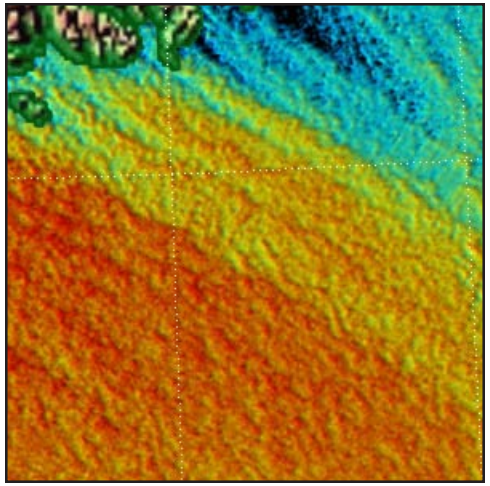

90 km square

11. Enlargement of gap flow edges (x 2.5)

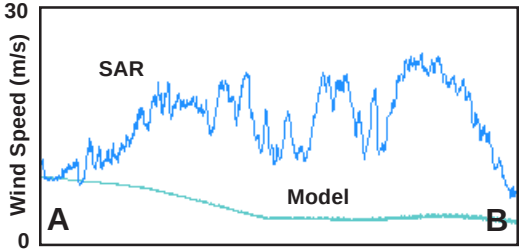

12. Model vs SAR Wind Profile along Line AB

1. Surface Pressure (mb) ~ t_0-36h

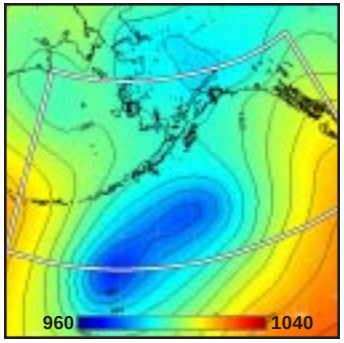

2. Surface Pressure (mb) ~ t_0-24h

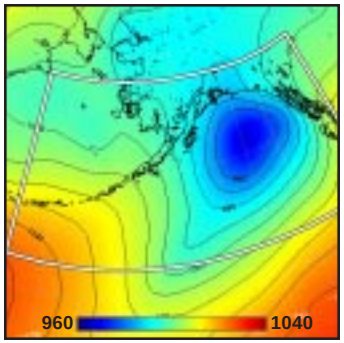

3. Surface Pressure (mb) ~ t_0-12h

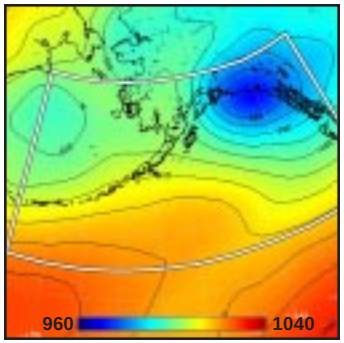

4. Surface Pressure (mb) ~ t_0

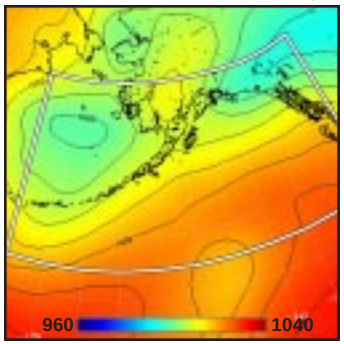

9. Enlarged Surface Wind Field ~ t_0

1800 GMT 12 Oct 2001

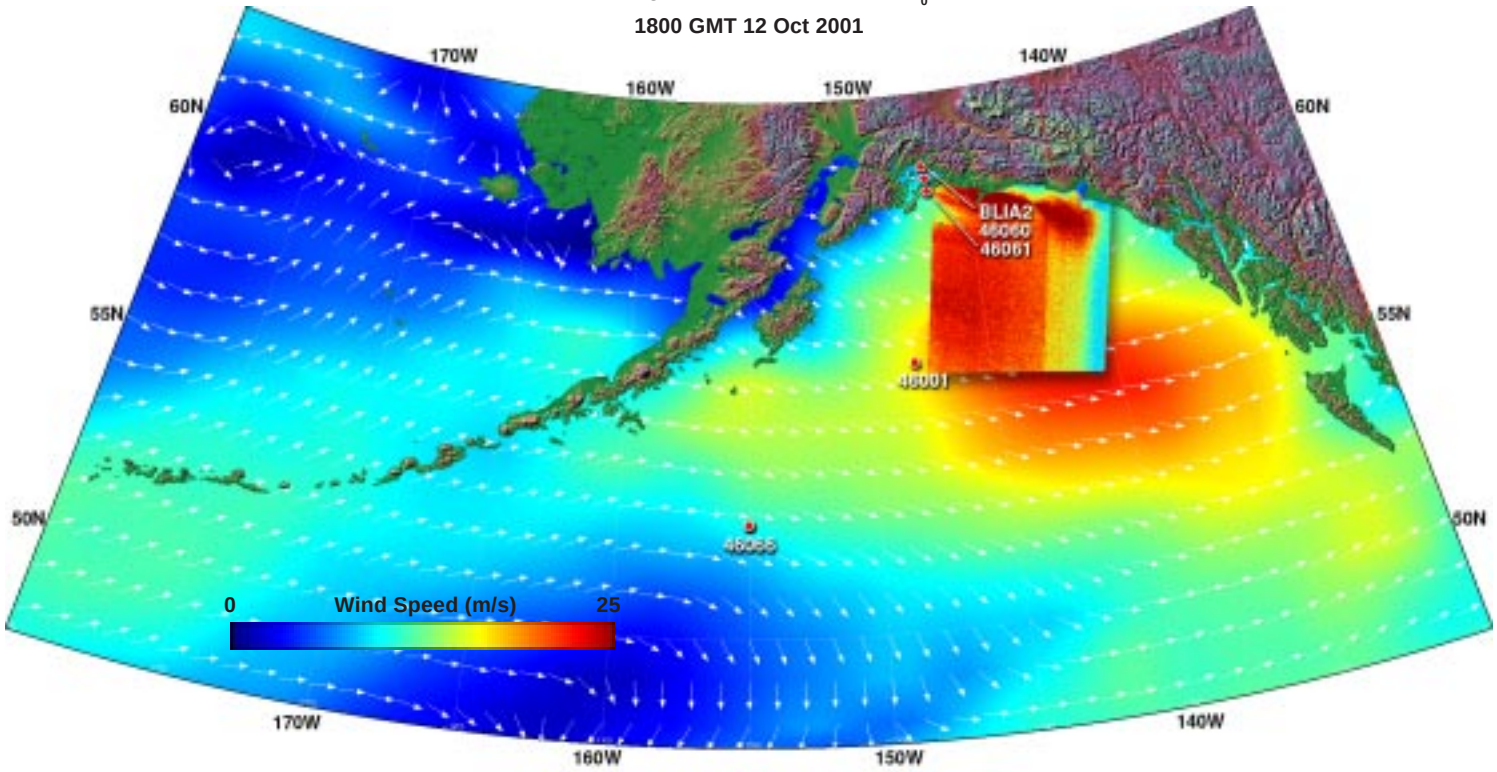

Model (this page): An elongated low pressure system in the southwestern Gulf of Alaska deepens as it moves to the northeast, approaching the coast just prior to overpass time (1-4), by which time substantial weakening is occurring. Model winds (5, 9) are still about 20 m/s in the southern sector of the storm, but diminishing toward the coast. The vortex center in the wind field is located just off the coast. Concurrent model waves are unavailable. Under the SAR pass, the MABL is increasingly unstable toward the west (8).

SAR (facing page): The SAR winds (10, 11) here exhibit two major anomalies: 1) the anomalous "butterfly-shaped" pattern at the top center, which results from a direction singularity at the estimated (but clearly misplaced) vortex center, and 2) the antenna beam pattern bias and discontinuity running down the right third of the image, and most exaggerated on the right edge (12). The first anomaly causes positive SAR wind biases of ~10 m/s along the "wing centers"; the second causes negative biases of up to 10 m/s, evidently exacerbated at true wind speeds greater than about 20 m/s. This is an excellent example of two main sources of error in the Radarsat wind algorithm.

5. Surface Wind Field (m/s) ~ t_0

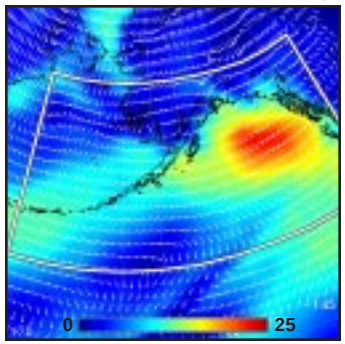

6. Surface Wave Height (m) ~ t_0

Not Available

0 8

7. Inverse Wave Age (norm) ~ t_0

Not Available

-1 +2

8. Air-Sea Temperature (˚C) ~ t_0

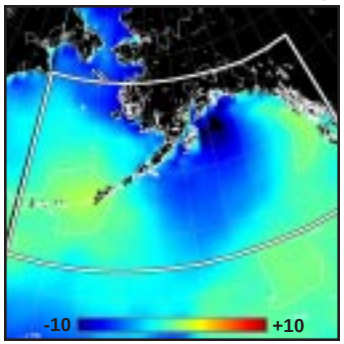

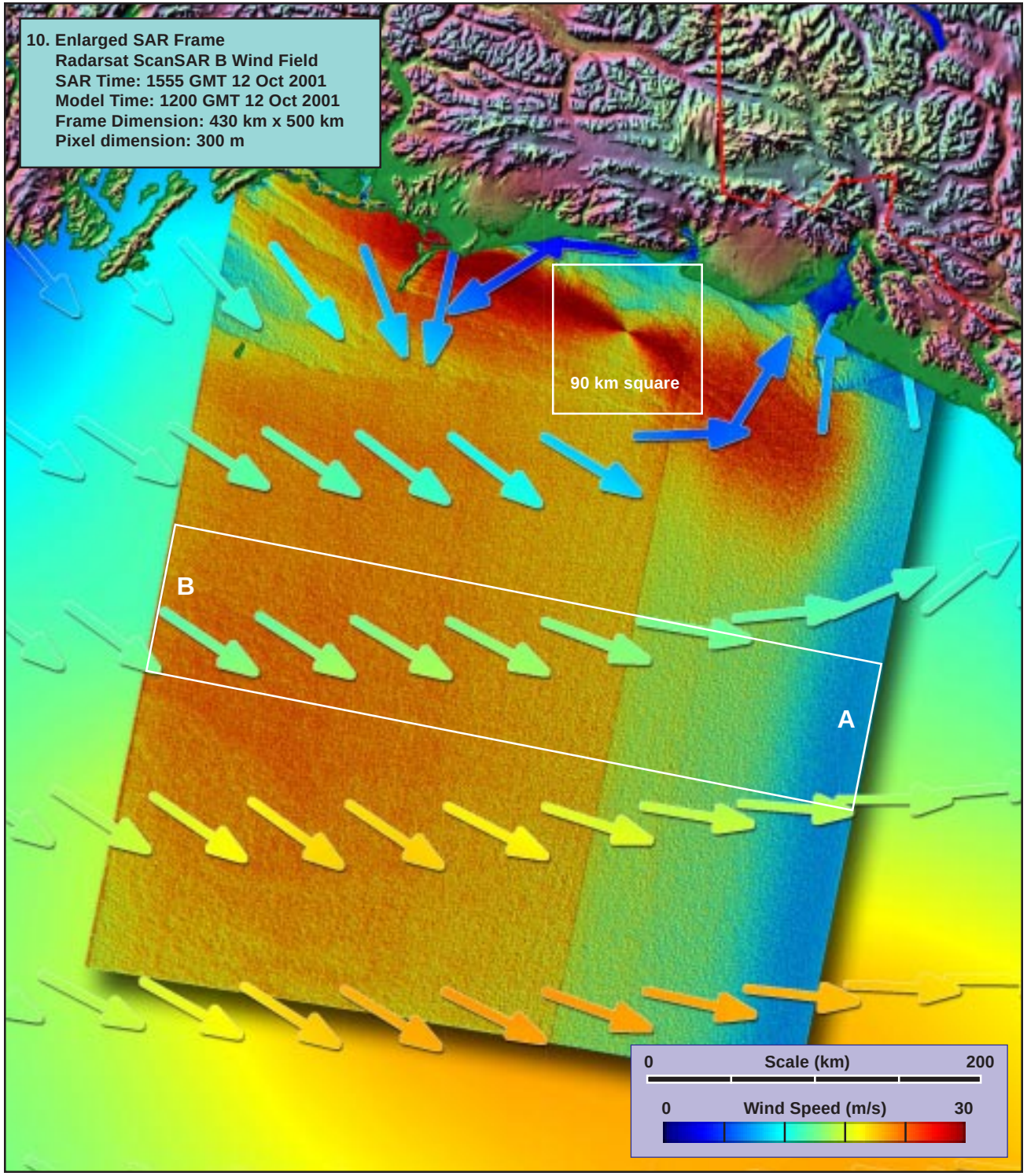

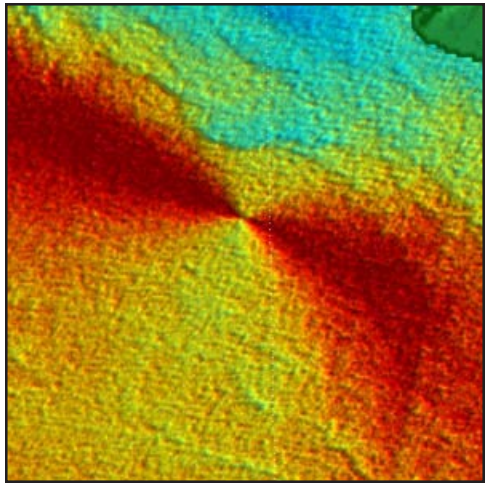

90 km square

11. Enlargement of Singularity Effect (x 2.5)

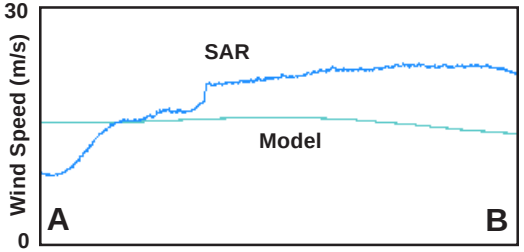

12. Model vs SAR Wind Profile along Line AB

1. Surface Pressure (mb) ~ t_0-36h

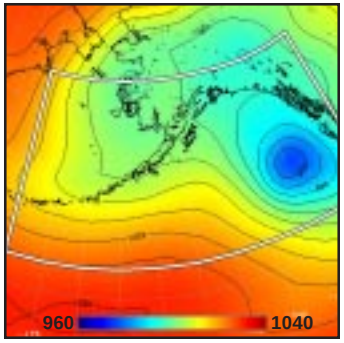

2. Surface Pressure (mb) ~ t_0-24h

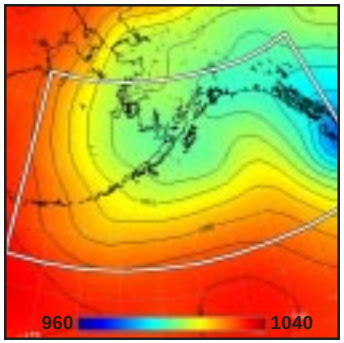

3. Surface Pressure (mb) ~ t_0-12h

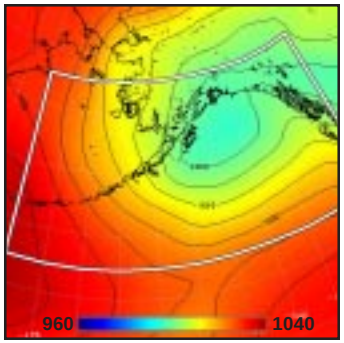

4. Surface Pressure (mb) ~ t_0

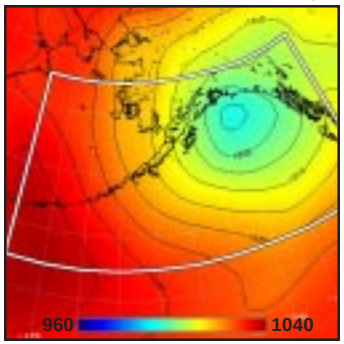

9. Enlarged Surface Wind Field ~ t_0

0000 GMT 24 Oct 2001

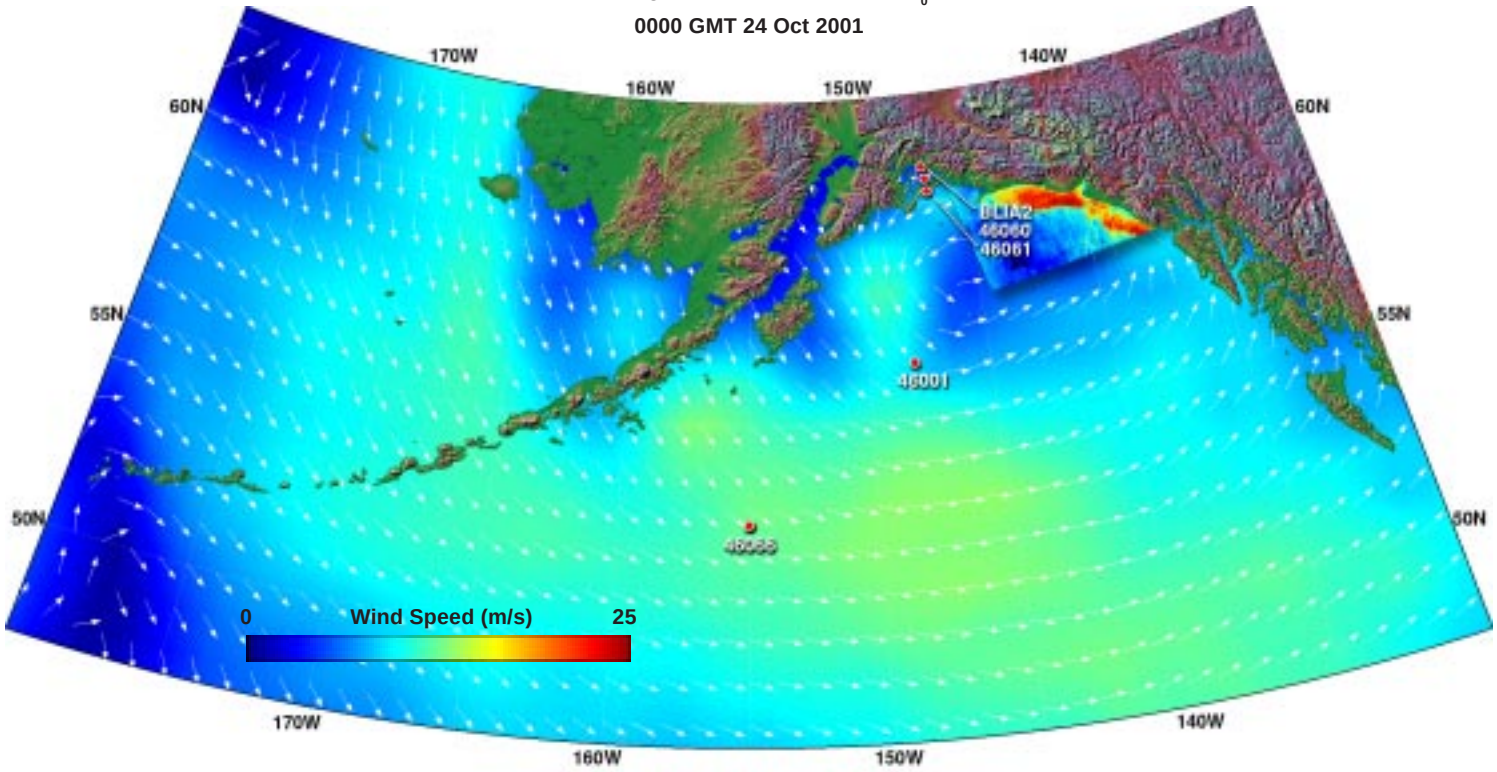

Model (this page): A weak low pressure system begins to strengthen in the northern Gulf of Alaska, just to the northeast of Kodiak Island (1-4). Model winds around its center are no more than 10 to 12 m/s, roughly parallel to the coast in the northern sector (5, 9). Concurrent model waves are unavailable. The MABL is unstable all along the coast (8).

SAR (facing page): This is another fine example of a barrier jet caused by the abrupt topographic differential along the coast. The SAR winds within the jet approach 20 m/s, about double that of the model (10, 11, 12). The jet shows a complex morphology, possibly directly connected to the similar morphology of the coastal mountain chain. Wind speed at the seaward boundary of the jet jumps abruptly (within a few km) from less than 10 m/s to more than 20 m/s (12).

5. Surface Wind Field (m/s) ~ t_0

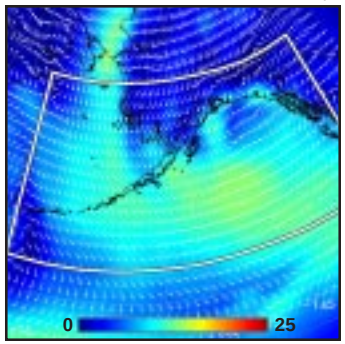

6. Surface Wave Height (m) ~ t_0

Not Available

0 8

7. Inverse Wave Age (norm) ~ t_0

Not Available

-1 +2

8. Air-Sea Temperature (˚C) ~ t_0

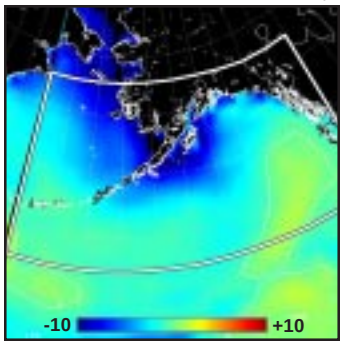

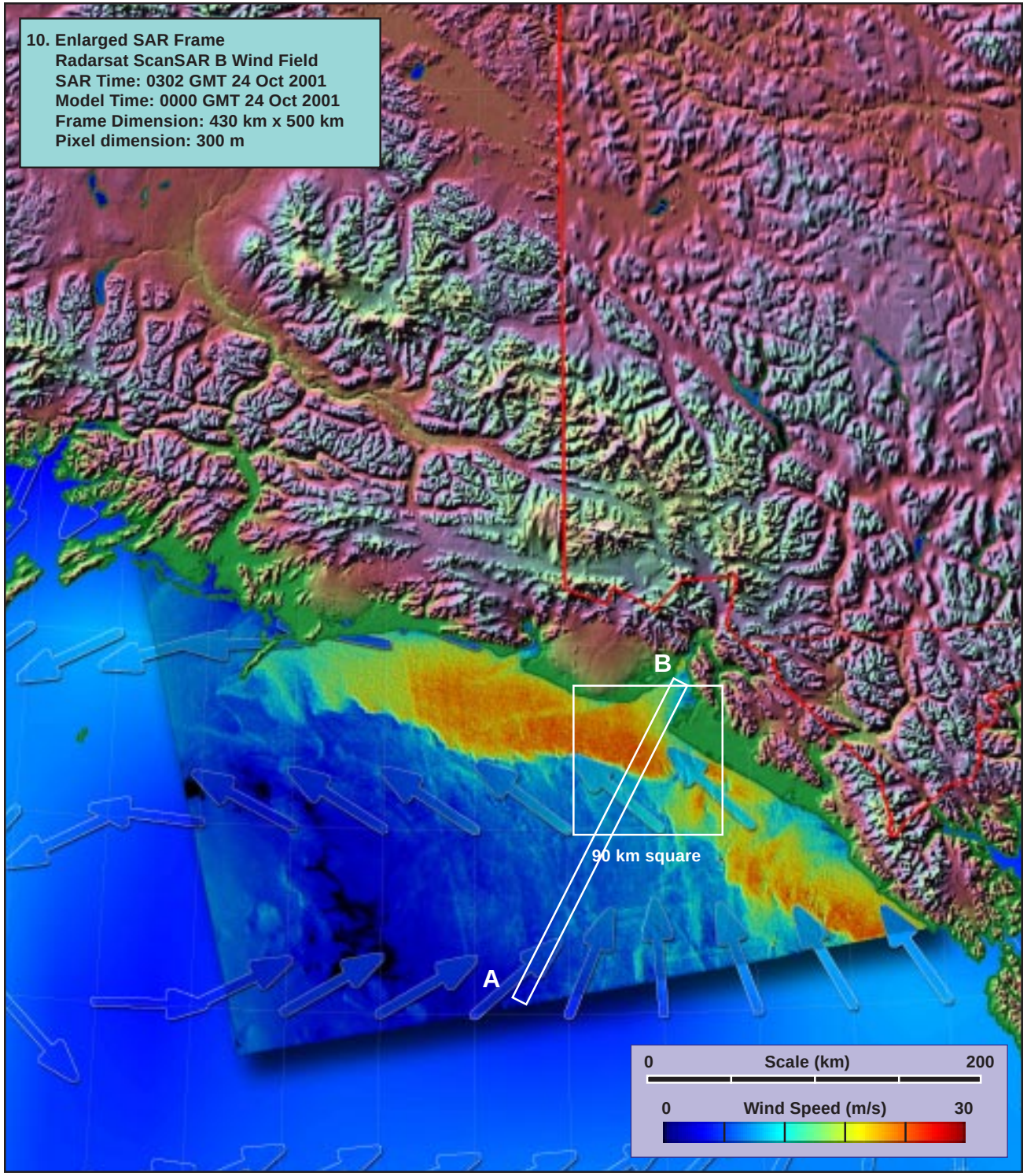

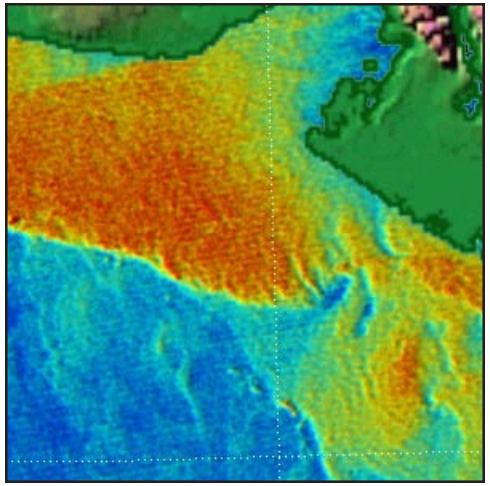

90 km square

11. Enlargement of Costal Jet Detail (x 2.5)

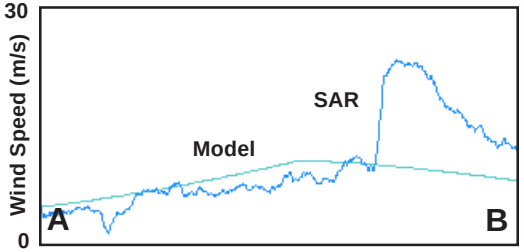

12. Model vs SAR Wind Profile along Line AB

1. Surface Pressure (mb) ~ t_0-36h

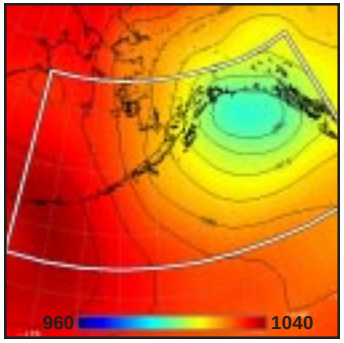

2. Surface Pressure (mb) ~ t_0-24h

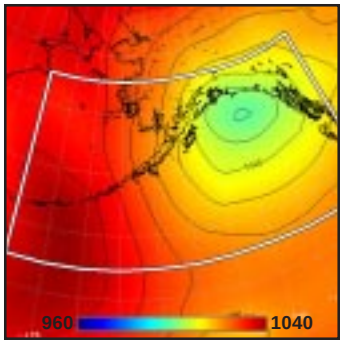

3. Surface Pressure (mb) ~ t_0-12h

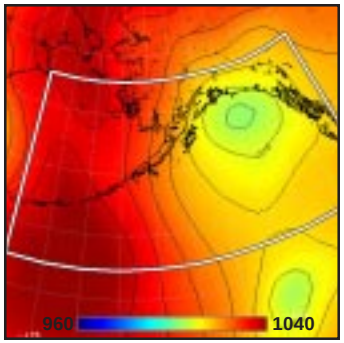

4. Surface Pressure (mb) ~ t_0

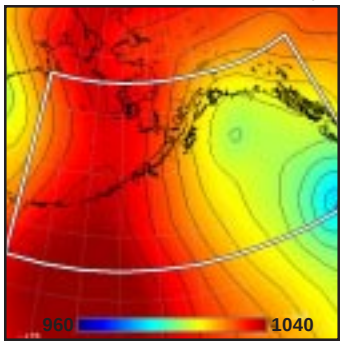

9. Enlarged Surface Wind Field ~ t_0

0000 GMT 26 Oct 2001

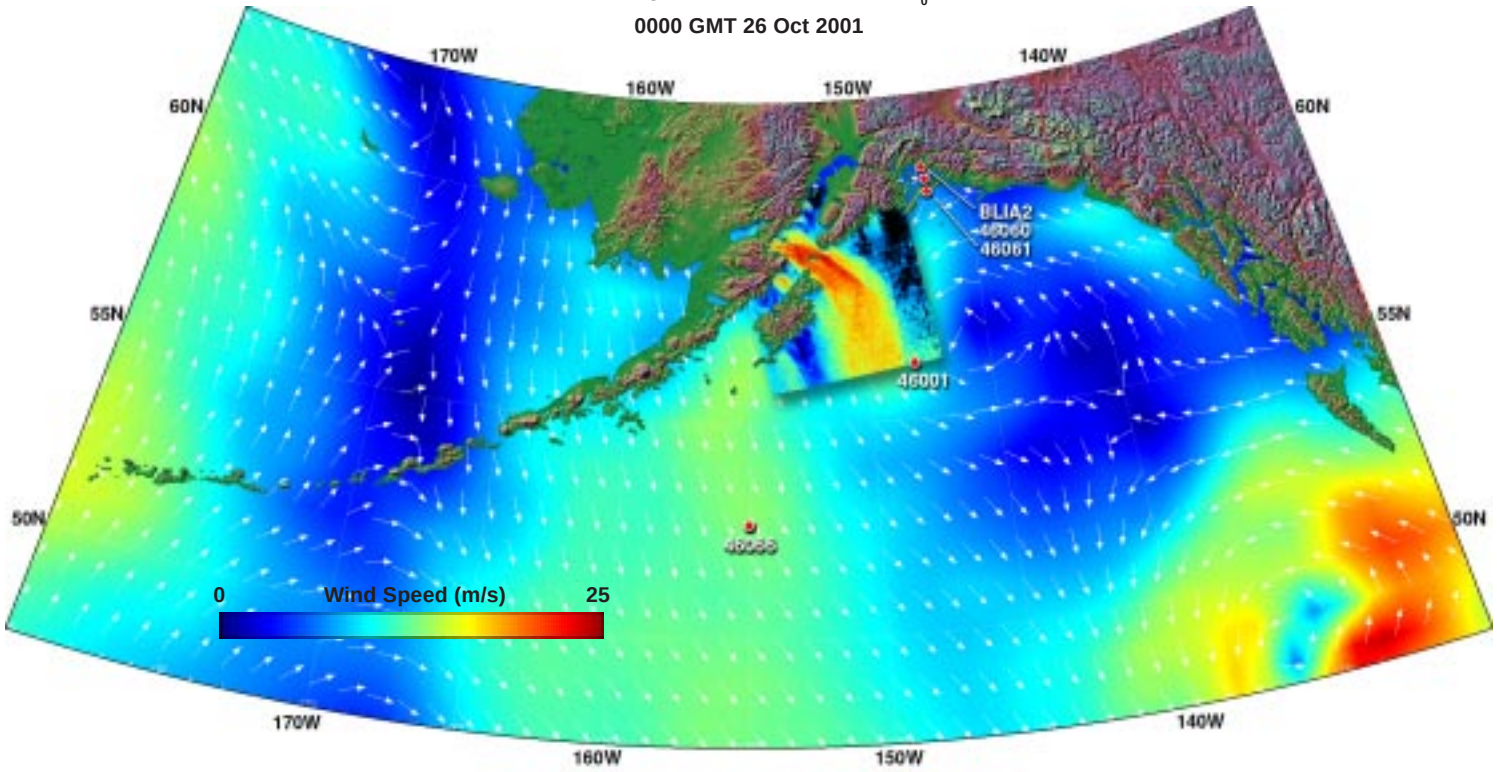

Model (this page): A pair of low pressure systems in the eastern Gulf of Alaska interact with a high pressure ridge to the west to create a persistent gradient across the Alaskan Peninsula (1-4). Model winds are consistently from the north to northwest all along the Peninsula, with speeds ranging from 5 to 15 m/s (5, 9). Concurrent model waves are unavailable . The MABL is extremely unstable everywhere along the Peninsula (8).

SAR (facing page): The SAR winds show another fine example of gap flow and island shadowing in the region just to the north of Kodiak Island (10, 11). Although the model winds never exceed 10 m/s within the gap, the SAR winds exceed 20 m/s in the center of the gap (12). Furthermore, the SAR winds show the gap flow curving southward to merge with the ambient synoptic flow. The jet appears to maintain its integrity for several hundred km south of the gap. [ref. section 2.5.2: gap flow/synoptic interaction.]

5. Surface Wind Field (m/s) ~ t_0

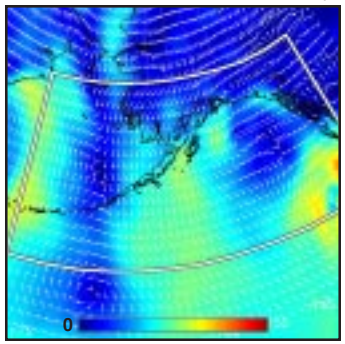

6. Surface Wave Height (m) ~ t_0

Not Available

0 8

7. Inverse Wave Age (norm) ~ t_0

Not Available

-1 +2

8. Air-Sea Temperature (˚C) ~ t_0

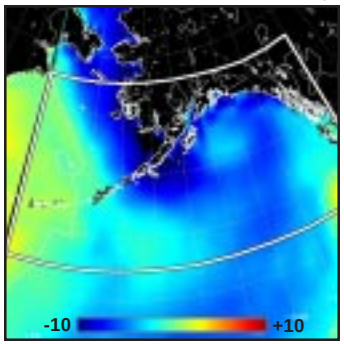

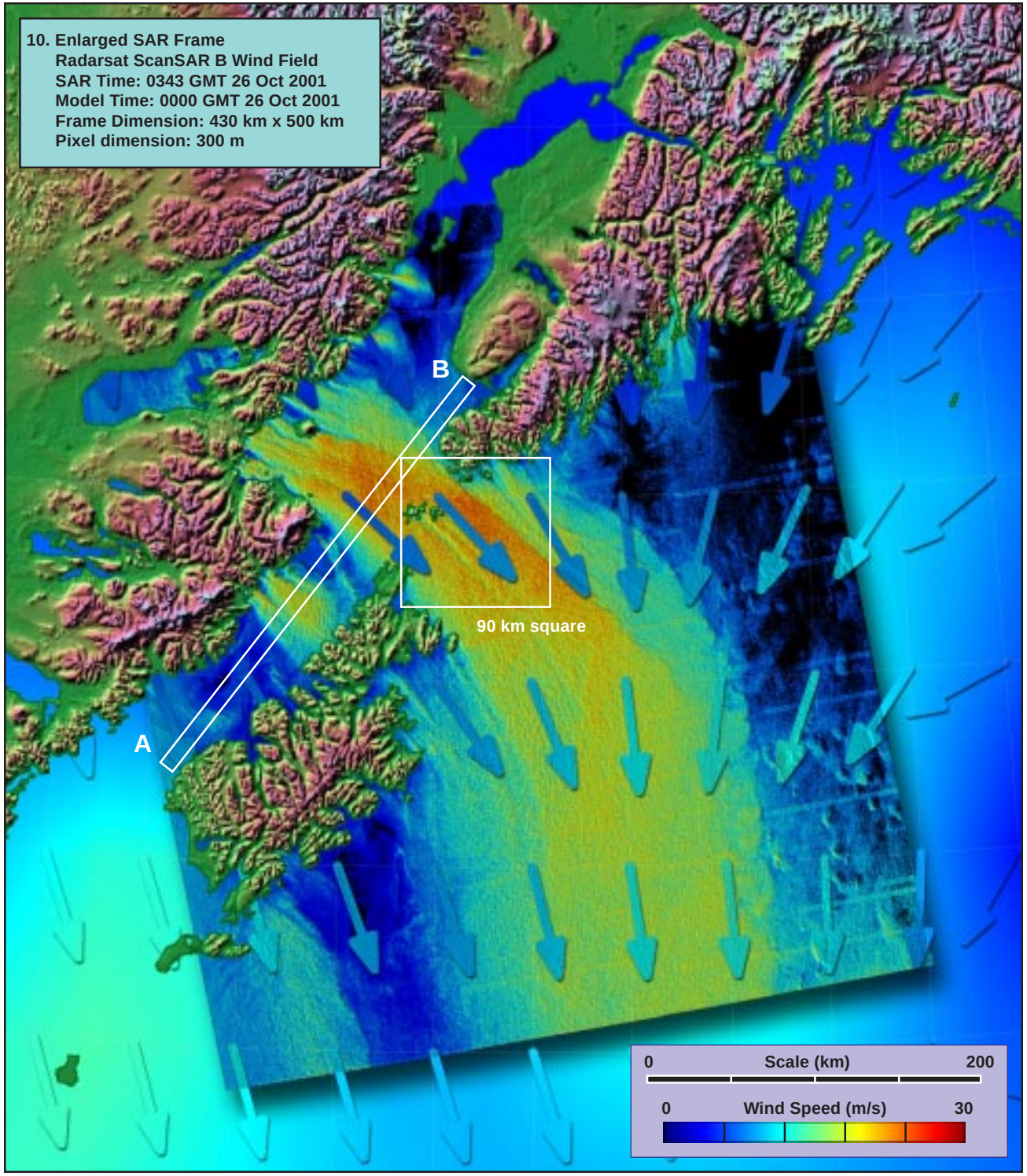

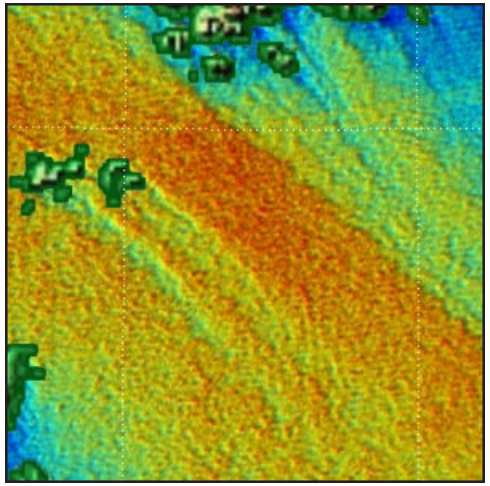

90 km square

11. Enlargement of Frontal Intersection (x 2.5)

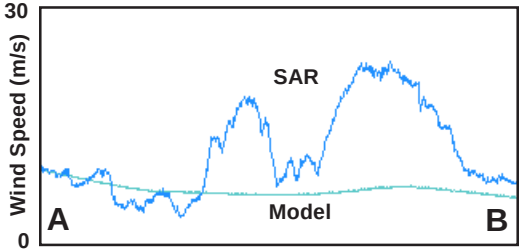

12. Model vs SAR Wind Profile along Line AB

1. Surface Pressure (mb) ~ t_0-36h

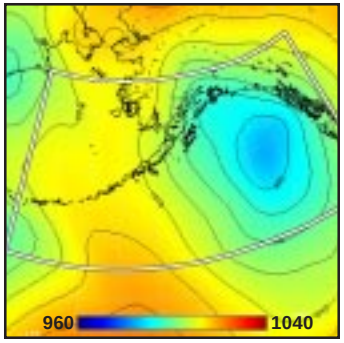

2. Surface Pressure (mb) ~ t_0-24h

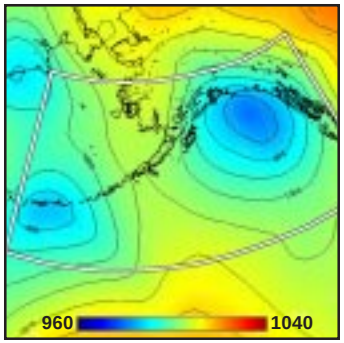

3. Surface Pressure (mb) ~ t_0-12h

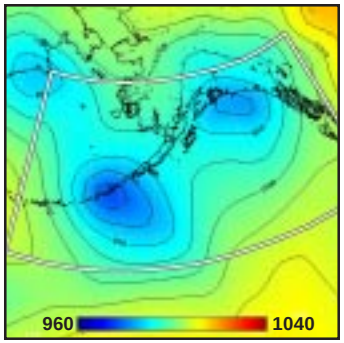

4. Surface Pressure (mb) ~ t_0

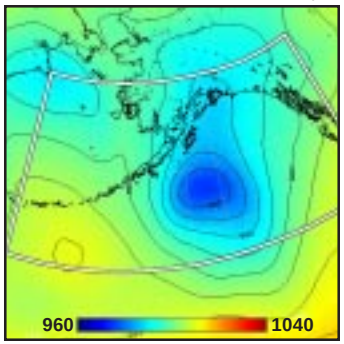

9. Enlarged Surface Wind Field ~ t_0

0000 GMT 30 Oct 2001

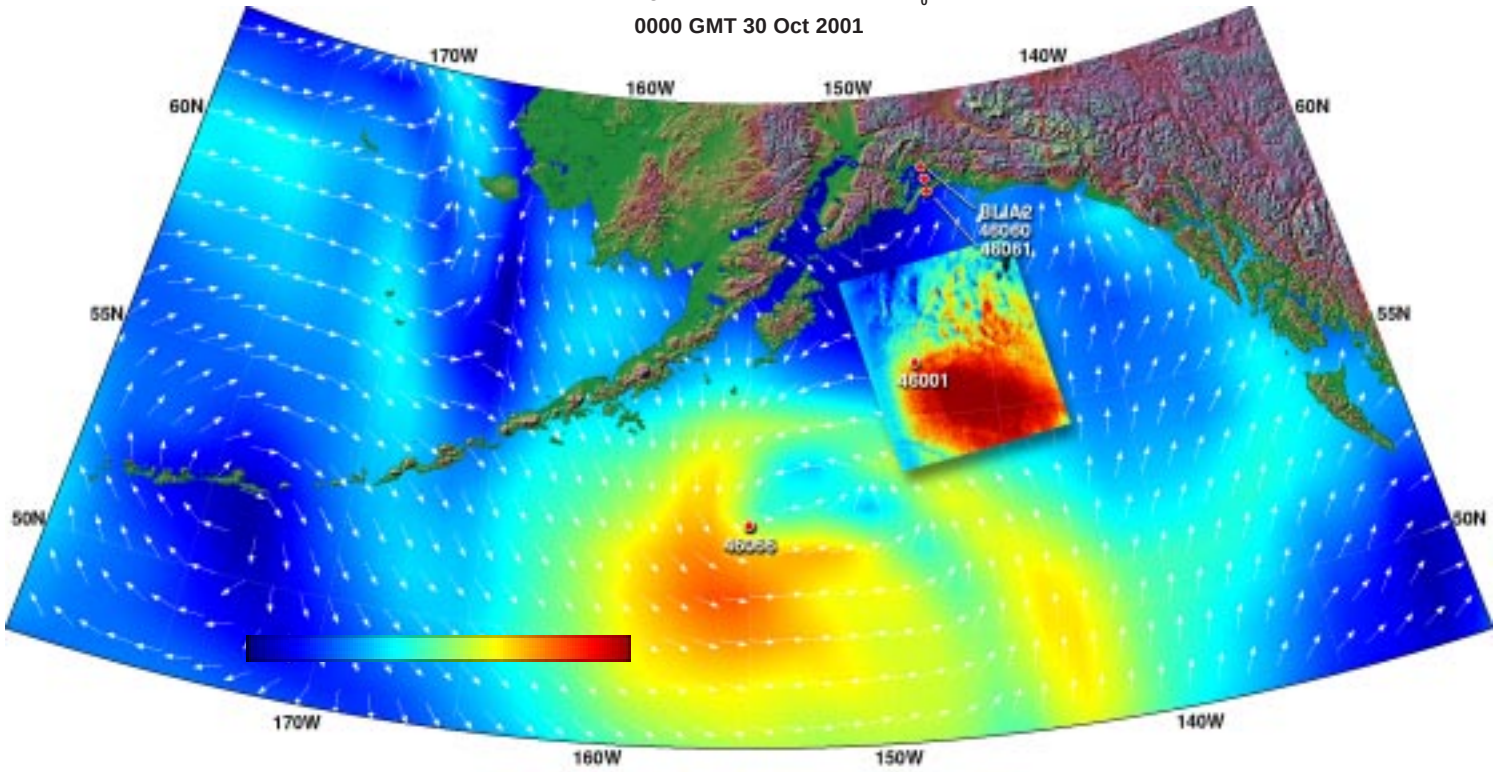

Model (this page): A pair of low pressure systems converge in the central Gulf of Alaska, producing a N-S-elongated gradient region under the SAR pass to the northeast (1-4). Model winds show a spiral of high winds, peaking in the southwest around 20 m/s, and in the northeast around 15 m/s (5, 9). Concurrent model waves are unavailable. The MABL is extremely unstable under the SAR overpass, especially toward the north (8).

SAR (facing page): Allowing for the SAR algorithm insensitivity on the western edge of the swath, the SAR winds appear to be capturing the advancing northeastern arm of the storm with peak winds within the arm between 25 and 30 m/s, accompanied by the splotchy winds of convective cells on its advancing edge (10, 11). Even allowing for the plausible displacement of the model from the SAR by 200 to 300 km, the SAR is indicating wind speeds in the forward arm of the storm at least twice those of the model (12).

5. Surface Wind Field (m/s) ~ t_0

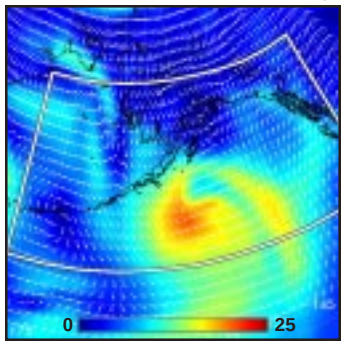

6. Surface Wave Height (m) ~ t_0

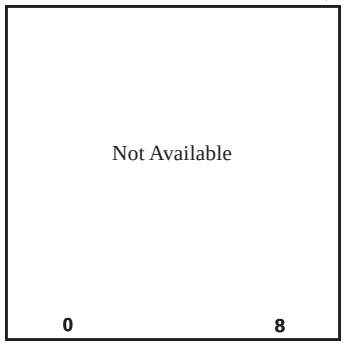

7. Inverse Wave Age (norm) ~ t_0

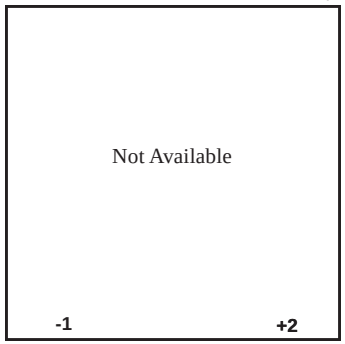

8. Air-Sea Temperature (˚C) ~ t_0

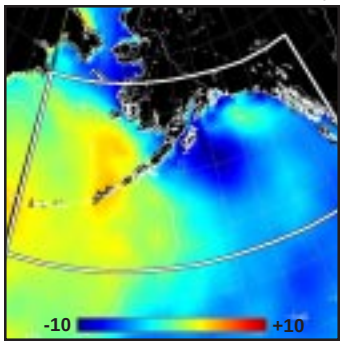

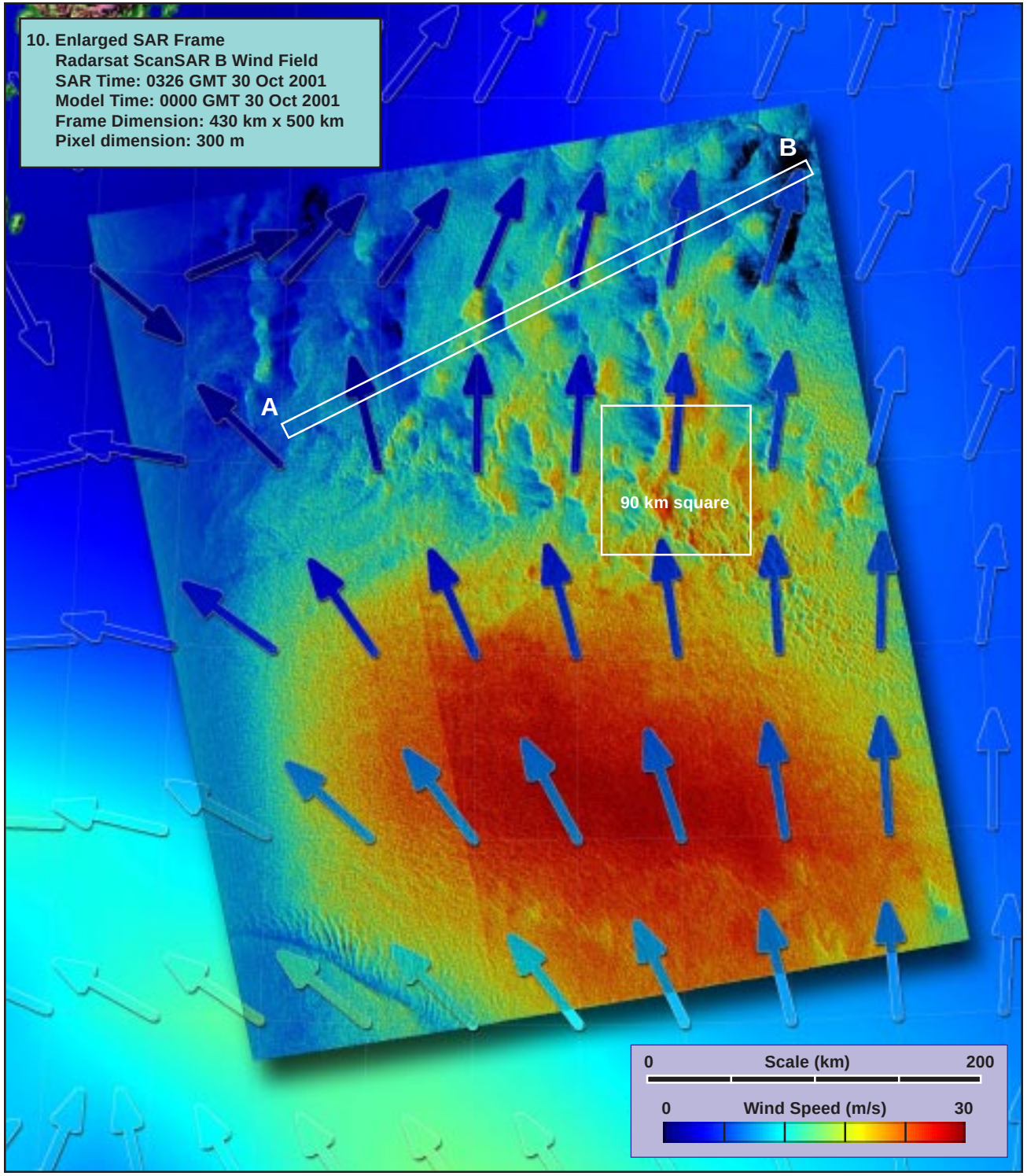

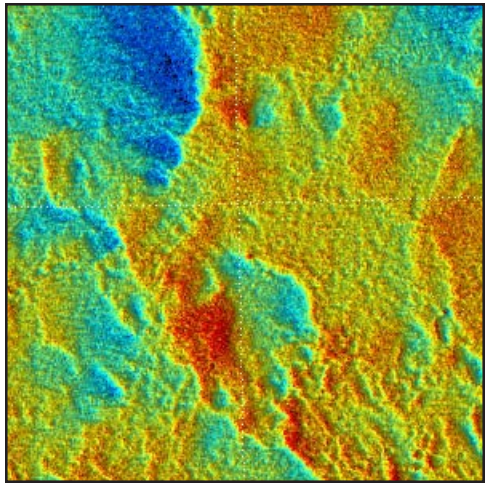

90 km square

11. Enlargement of Storm Front Edge (x 2.5)

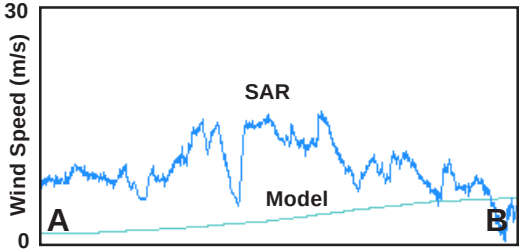

12. Model vs SAR Wind Profile along Line AB

1. Surface Pressure (mb) ~ t_0-36h

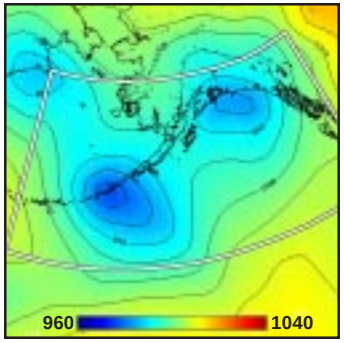

2. Surface Pressure (mb) ~ t_0-24h

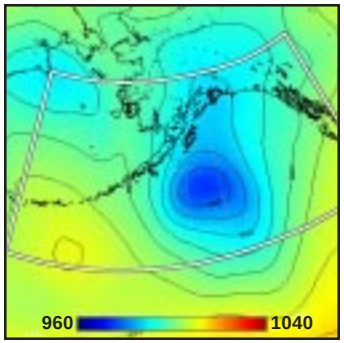

3. Surface Pressure (mb) ~ t_0-12h

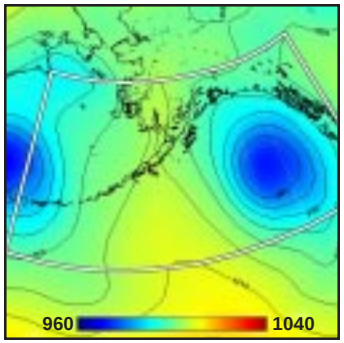

4. Surface Pressure (mb) ~ t_0

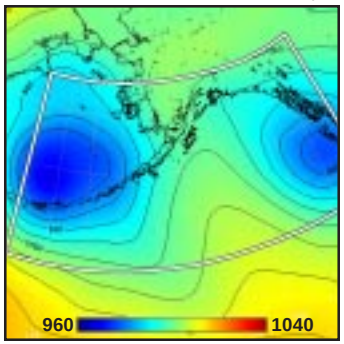

9. Enlarged Surface Wind Field ~ t_0

0000 GMT 31 Oct 2001

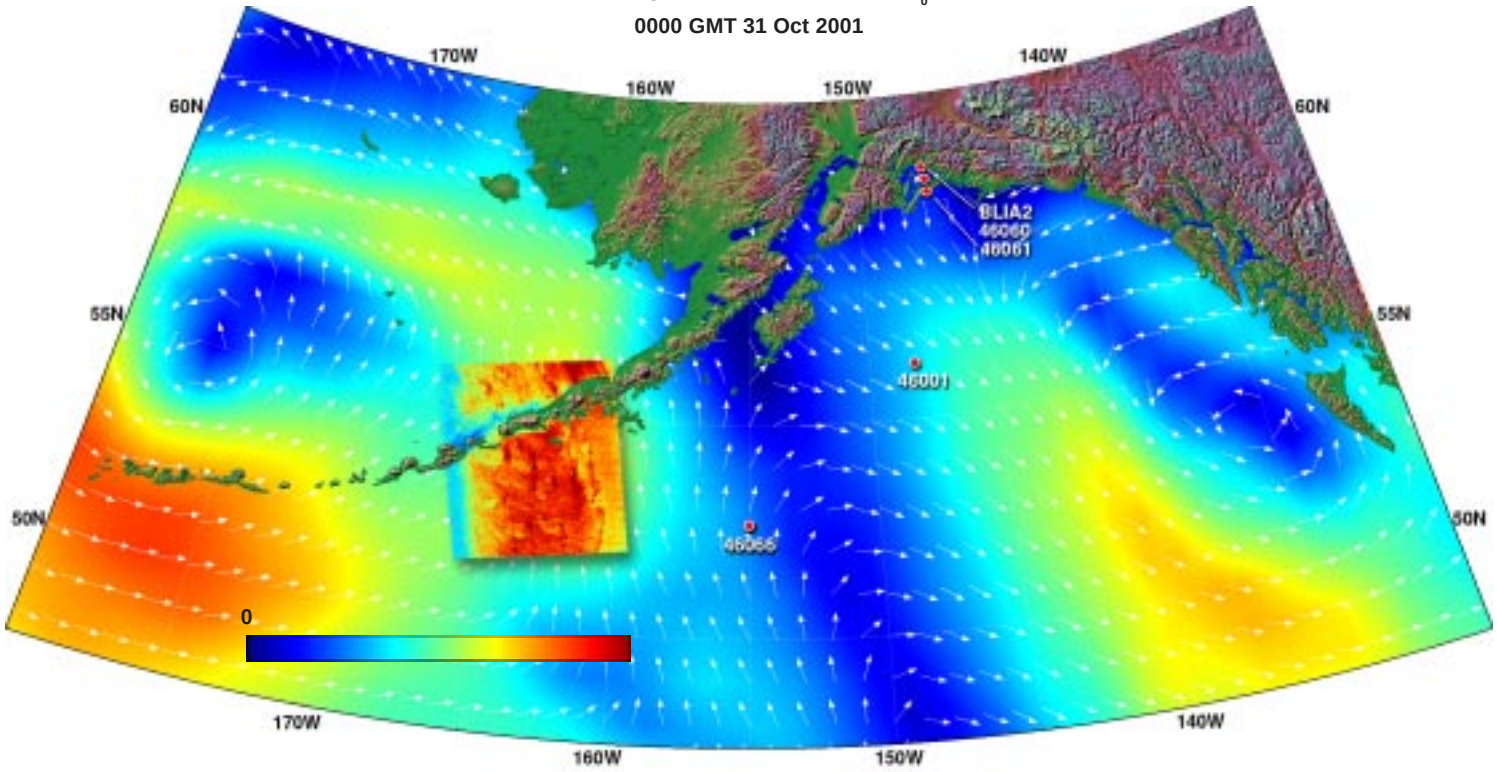

Model (this page): The third of a triad of low pressure systems advances eastward in the southern Bering Sea, producing strong gradients across the southern end of the Alaskan Peninsula (1-4). Concurrent model winds on the eastern side of the storm are southerly at ~15 m/s (5, 9). Concurrent model waves are unavailable. The MABL is stable in the southern portion of the SAR pass, unstable in the north (8).

SAR (facing page): The SAR shows a rich, nearly ubiquitous pattern of advancing gust fronts (10, 11, 12). The gust fronts are distinct and well separated from each other, with peak winds at the frontal edge nearly 30 m/s, tapering off to the rear. The leading edge of this convective field (11) is marked by a synoptic-scale frontal boundary. The kink and dot structure along the front is suggestive of horizontal shear instability and vortex wrap-up. [ref. section 2.8: mesoscale lows along fronts.] The more complex pattern of the front in the upper center of the SAR wind field results from added modulation from the upwind topography.

5. Surface Wind Field (m/s) ~ t_0

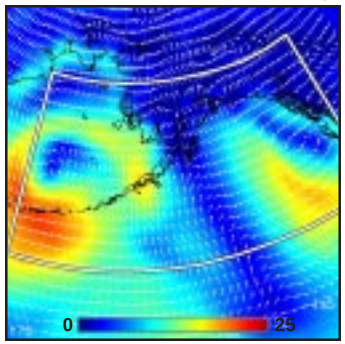

6. Surface Wave Height (m) ~ t_0

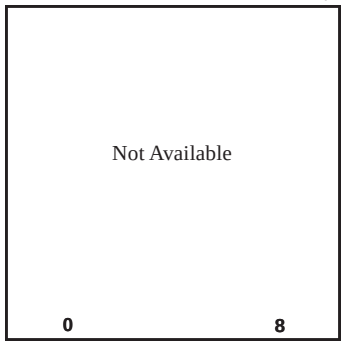

7. Inverse Wave Age (norm) ~ t_0

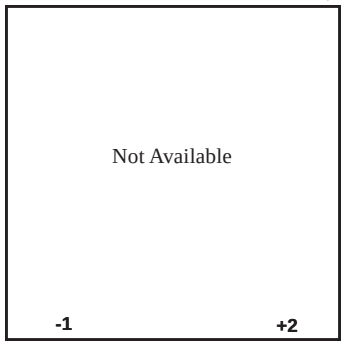

8. Air-Sea Temperature (˚C) ~ t_0

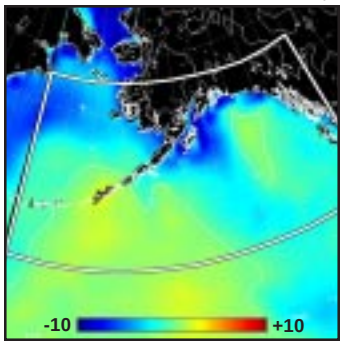

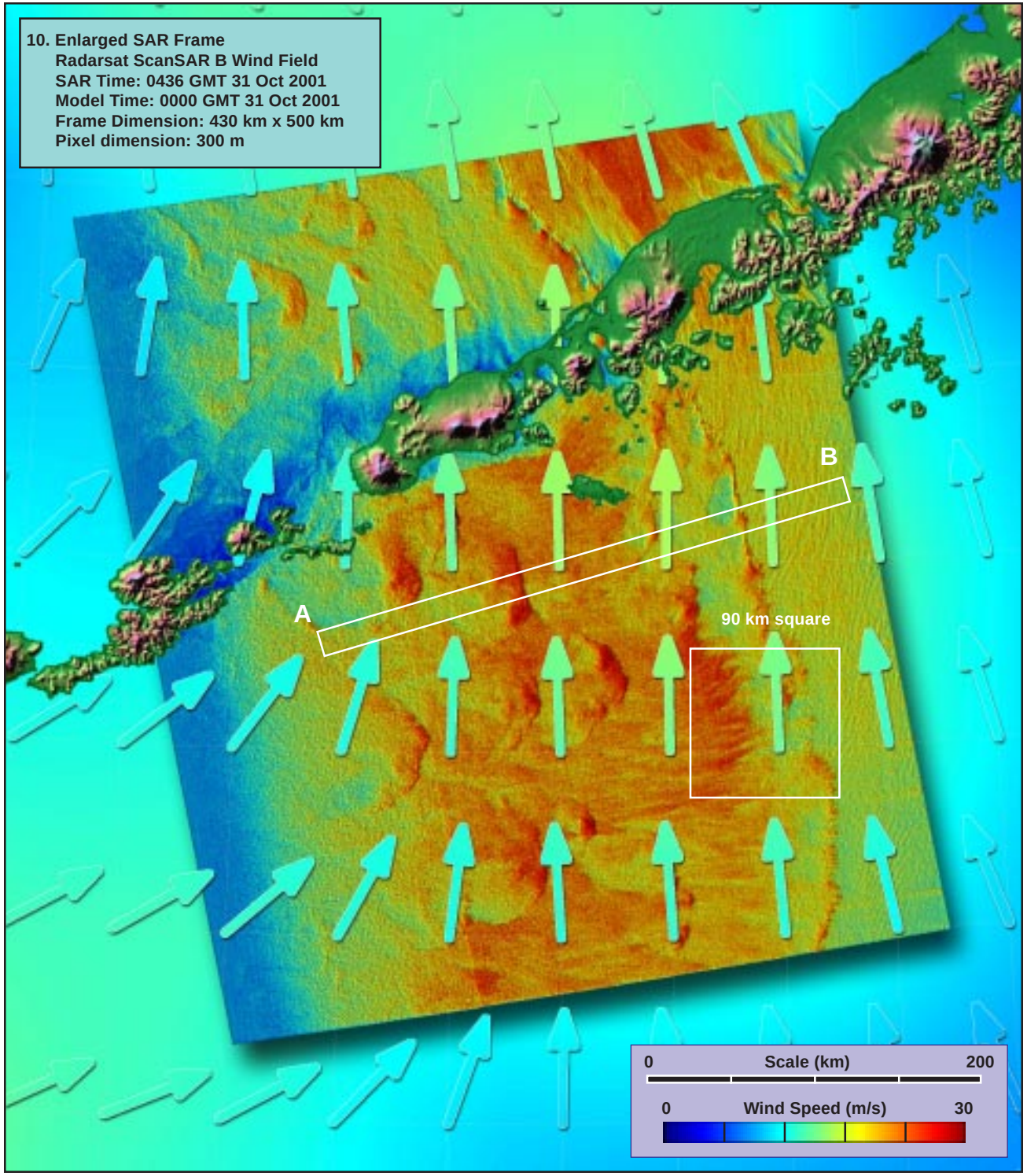

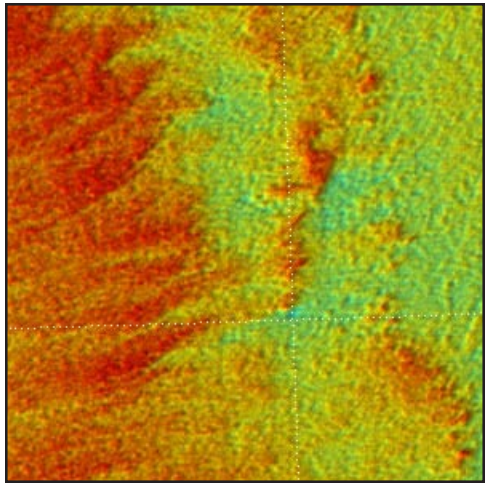

90 km square

11. Advancing Family of Gusts (x 2.5)

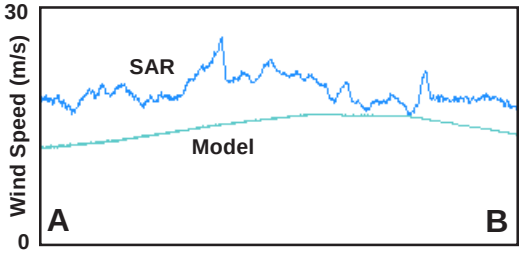

12. Model vs SAR Wind Profile along Line AB

1. Surface Pressure (mb) ~ t_0-36h

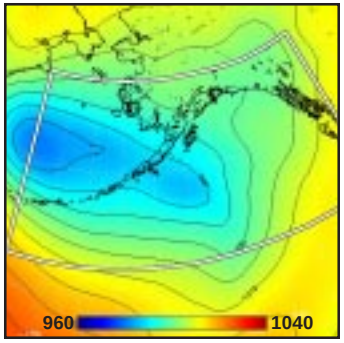

2. Surface Pressure (mb) ~ t_0-24h

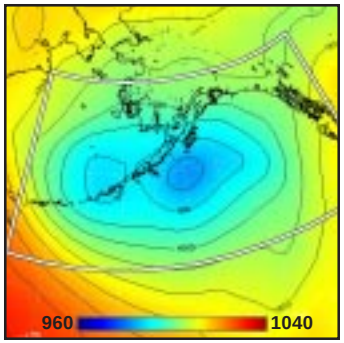

3. Surface Pressure (mb) ~ t_0-12h

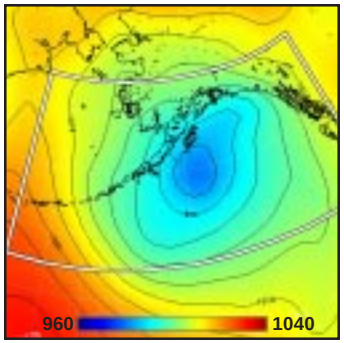

4. Surface Pressure (mb) ~ t_0

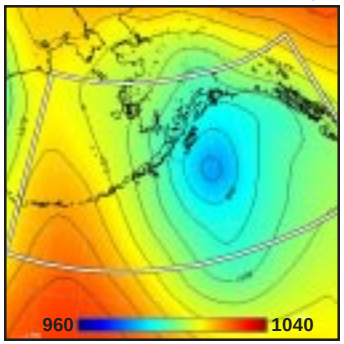

9. Enlarged Surface Wind Field ~ t_0

1200 GMT 10 Nov 2001

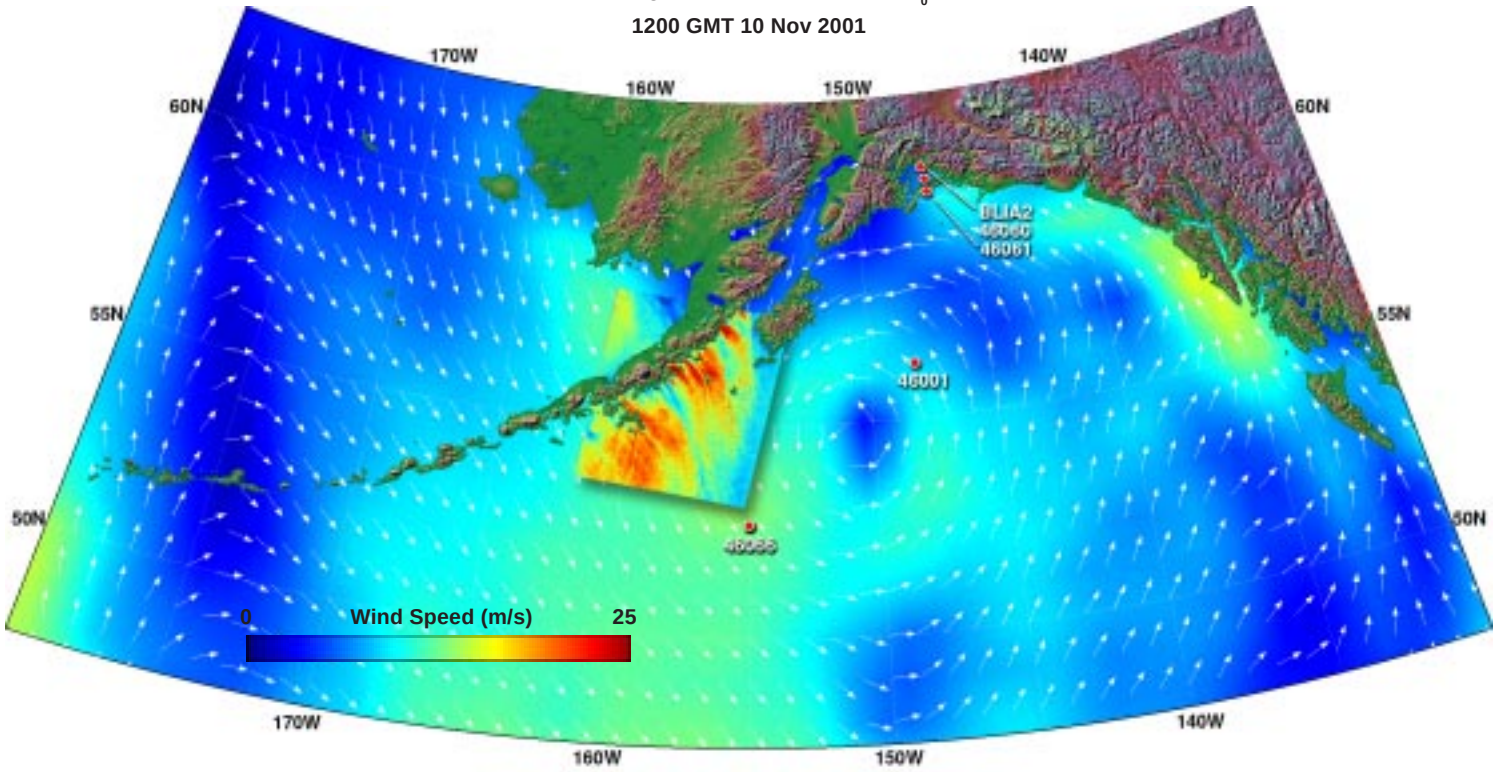

Model (this page): A low pressure system moves from the Bering Sea across the southern Alaska Peninsula to the northwestern Gulf of Alaska, remaining nearly stationary for the 24 hrs prior to the SAR overpass, and generating strong gradients all along the Peninsula (1-4). Model winds are consistently from the northwest at 10 to 15 m/s (5, 9). Concurrent model waves are unavailable. The MABL is slightly unstable northwest of the Peninsula to near neutral to the southeast (8).

SAR (facing page): The SAR winds show a rich topographical modulation with multiple jets and shadowing extending several hundred km downwind of the Peninsula (10, 11, 12). The jets curve gradually to the south, following the synoptic flow pattern. Peak SAR winds within the jets sometimes exceeding 20 m/s just downwind of their source, but then diminishing to half that value within 100 km. Concurrent model winds are nearly uniform at about 10 m/s. Cross patterns in the southwest may be lee waves from Mount Veniaminof.

5. Surface Wind Field (m/s) ~ t_0

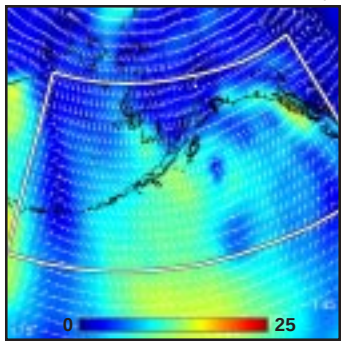

6. Surface Wave Height (m) ~ t_0

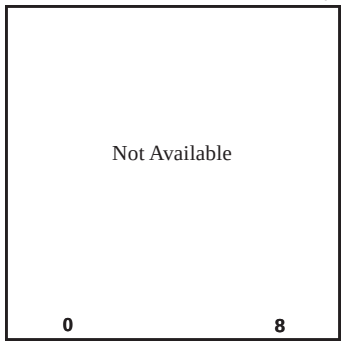

7. Inverse Wave Age (norm) ~ t_0

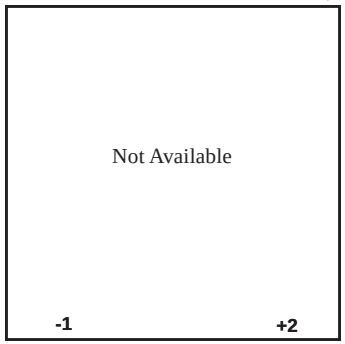

8. Air-Sea Temperature (˚C) ~ t_0

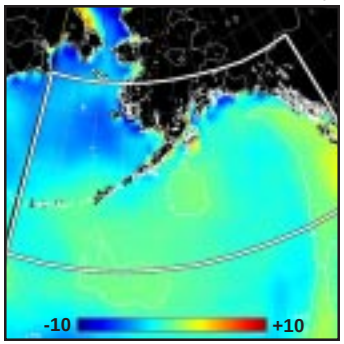

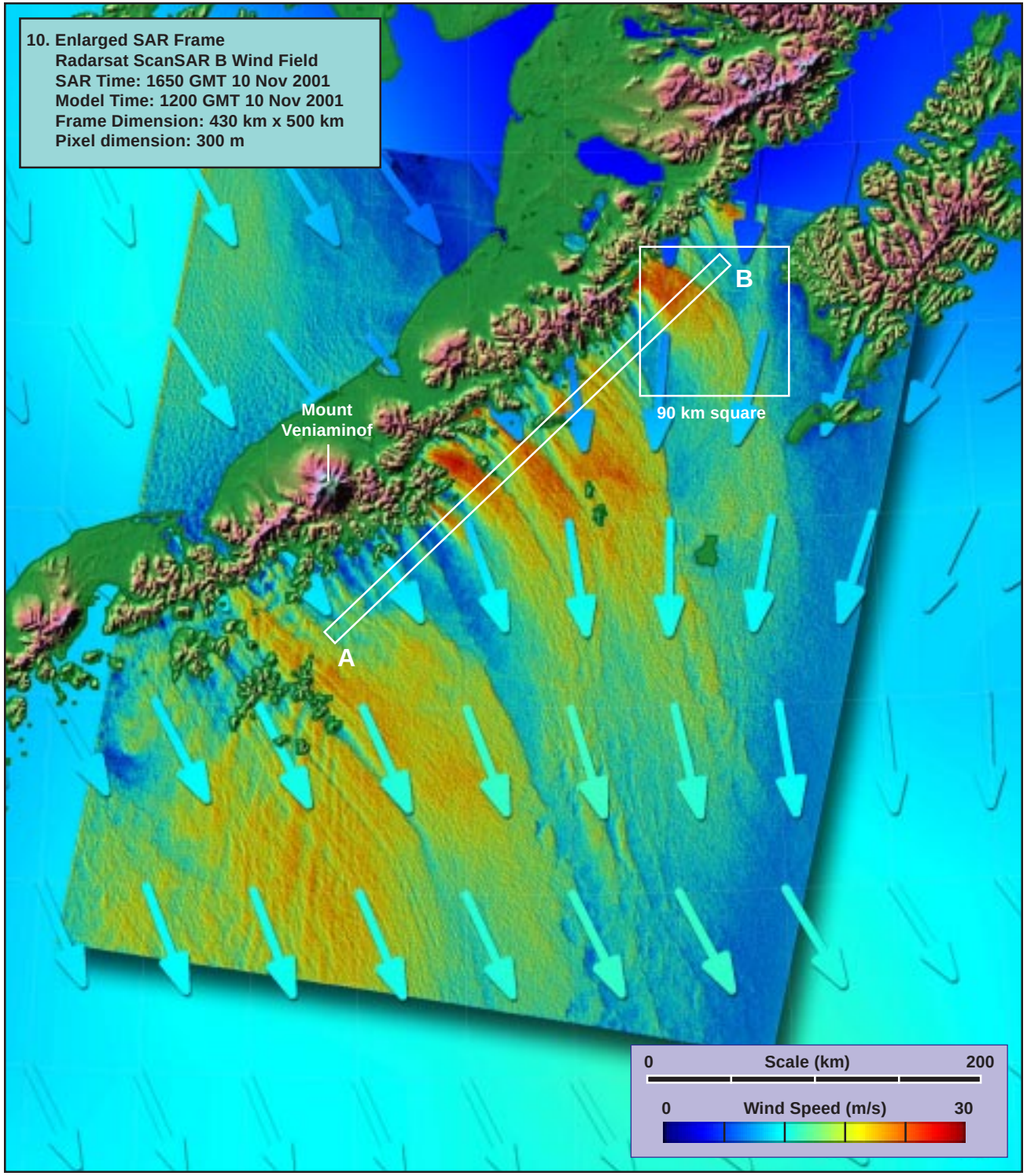

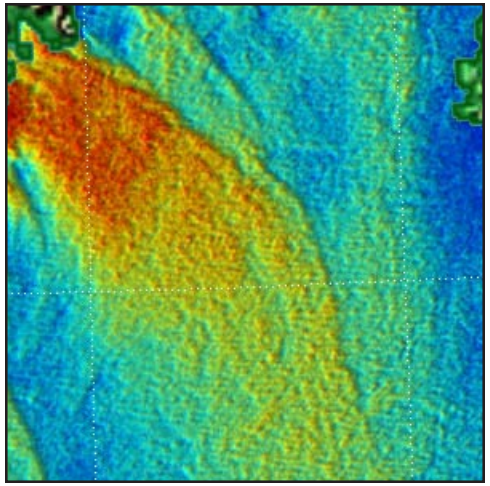

90 km square

11. Enlargement of Frontal Intersection (x 2.5)

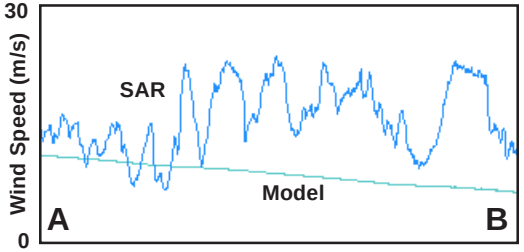

12. Model vs SAR Wind Profile along Line AB

1. Surface Pressure (mb) ~ t_0-36h

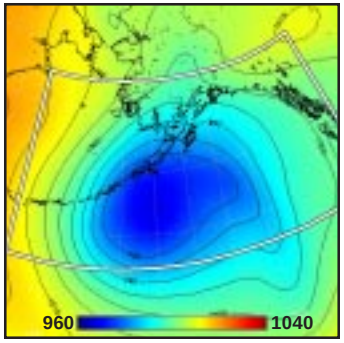

2. Surface Pressure (mb) ~ t_0-24h

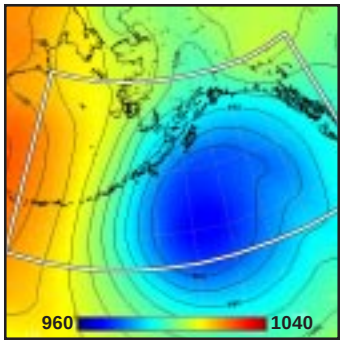

3. Surface Pressure (mb) ~ t_0-12h

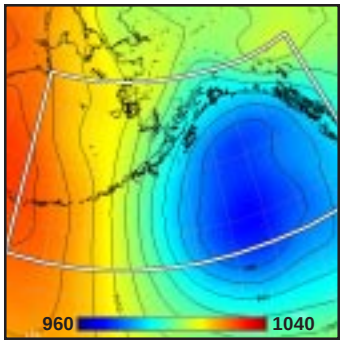

4. Surface Pressure (mb) ~ t_0

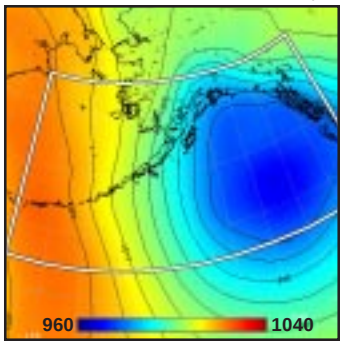

9. Enlarged Surface Wind Field ~ t_0

0600 GMT 14 Nov 2001

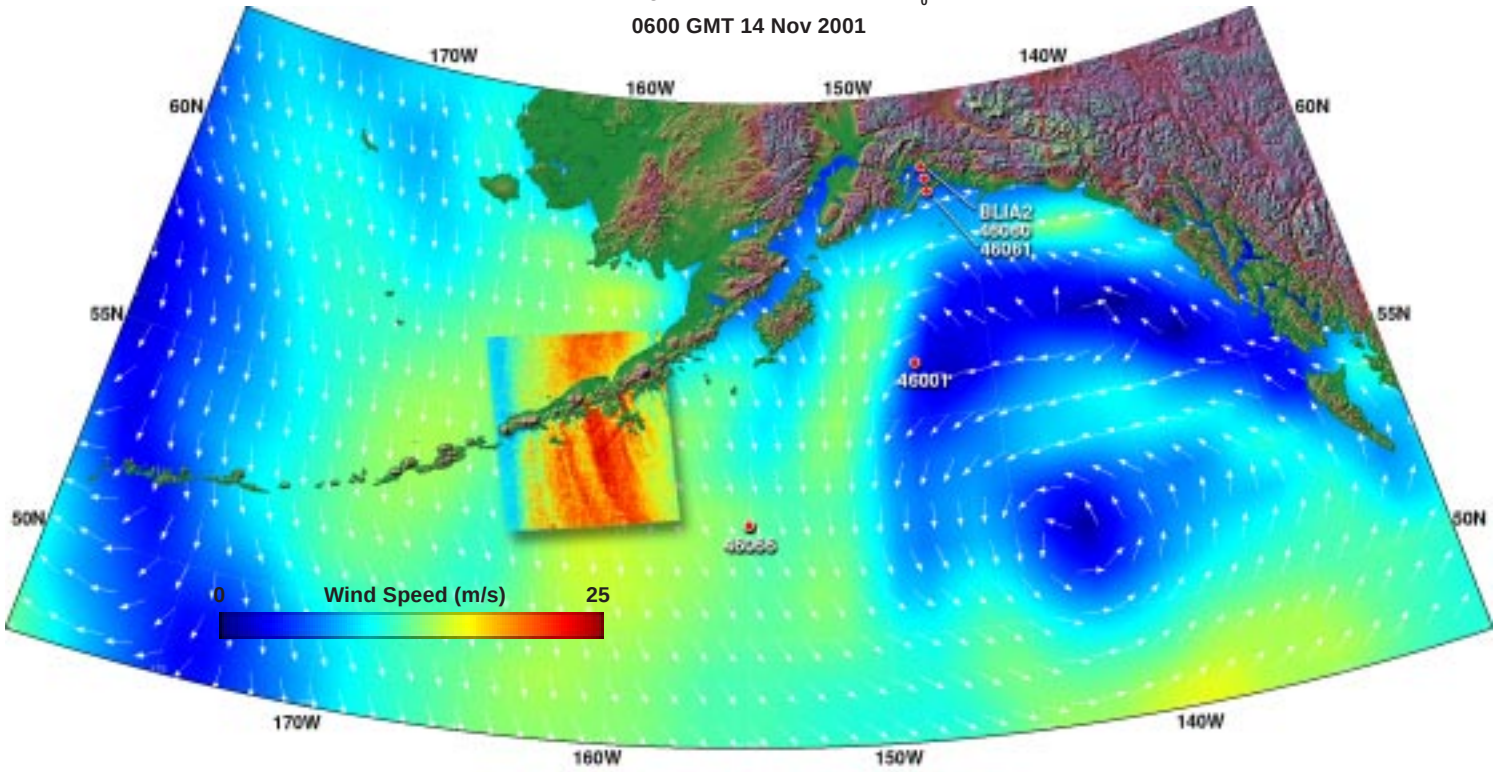

Model (this page): A large and deep low pressure system dominates the entire Gulf of Alaska for at least the 36 hrs prior to SAR overpass time (1-4). Model winds are consistently from the north to northwest at 10 to 15 m/s (5, 9). Concurrent model waves are unavailable. The MABL is extremely unstable over the entire Alaskan Peninsula (8).

SAR (facing page): The SAR winds show the usual topographically induced modulations extending hundreds of km downwind of the Peninsula (10, 11). Peak SAR winds reach 25 m/s in the topographically modulated region, compared with about 15 m/s from the model. Within the predominantly along-wind patterns, an additional family of linear patterns can be seen crossing the main along-wind patterns at an angle of about 60 degrees (11). These are probably lee waves angling downwind from the isolated Mount Veniaminof. [ref. section 2.3: mountain lee waves.]

5. Surface Wind Field (m/s) ~ t_0

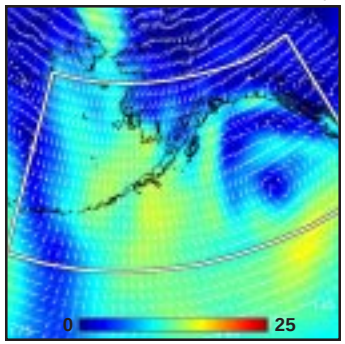

6. Surface Wave Height (m) ~ t_0

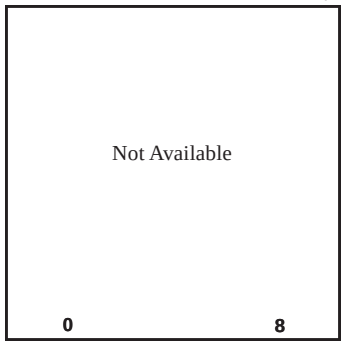

7. Inverse Wave Age (norm) ~ t_0

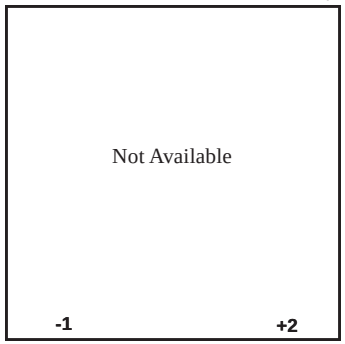

8. Air-Sea Temperature (˚C) ~ t_0

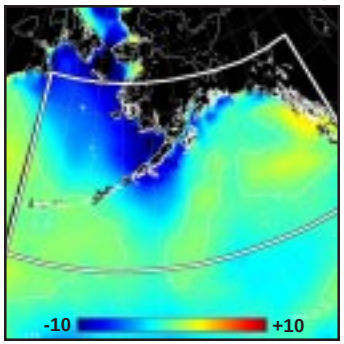

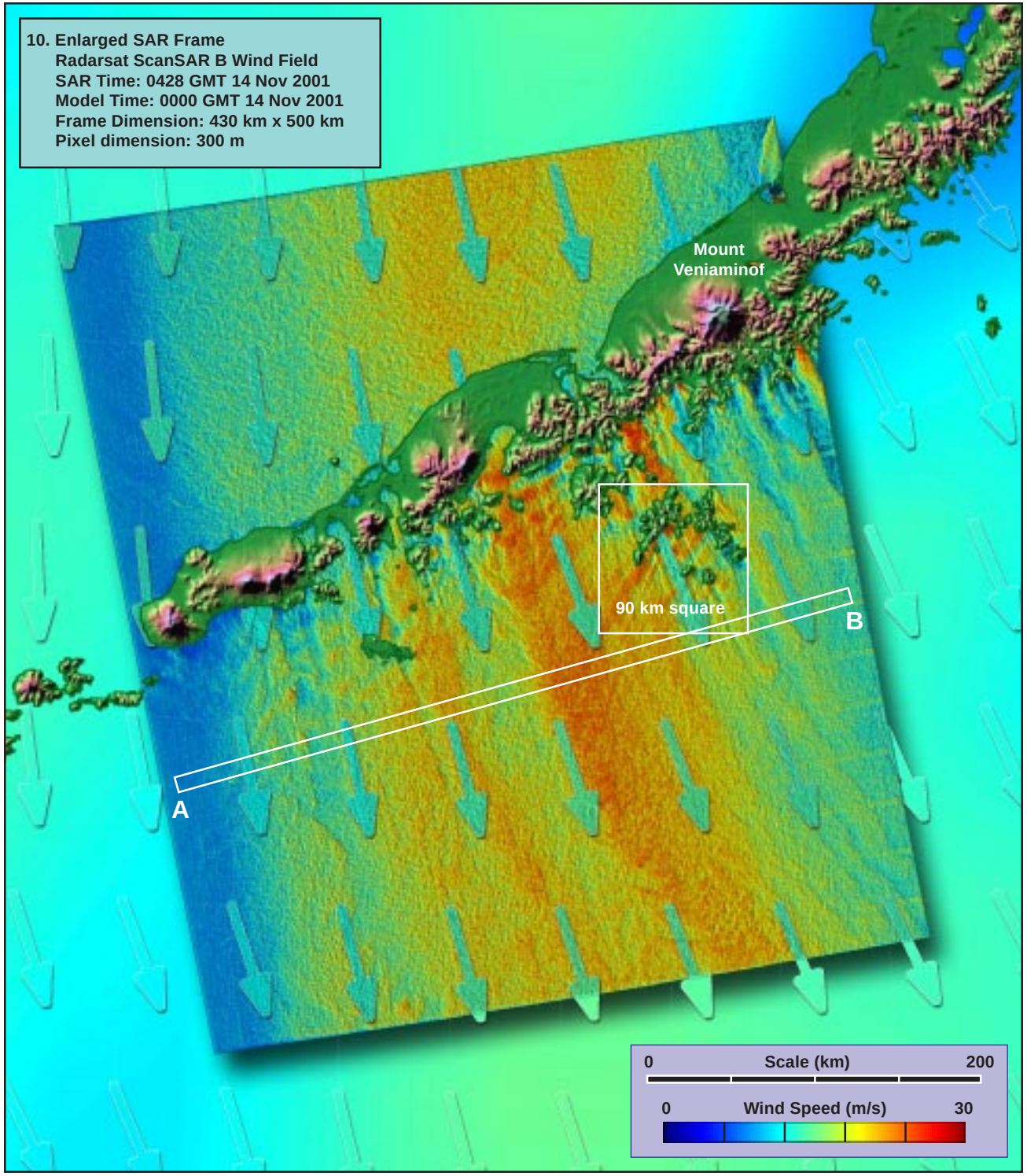

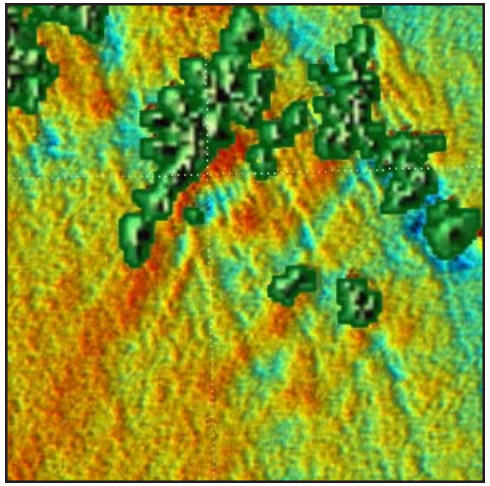

90 km square

11. Enlargement of Crossing Shadows (x 2.5)

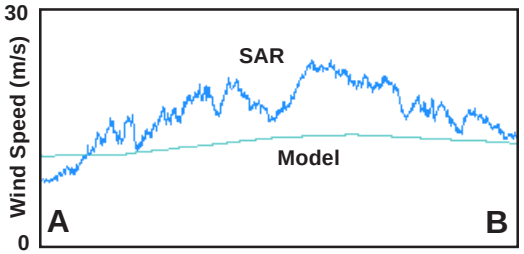

12. Model vs SAR Wind Profile along Line AB

Appendix 1

Operational Implications of SAR: A Recent Case Study

Carven Scott

A1.0 Introduction

The Weather Forecast Office (WFO) in Anchorage, Alaska, like most other NWS offices with marine responsibility, relies heavily on remote sensing tools to perform its primary mission: the protection of life and property and the enhancement of the national economy. WFO Anchorage has a marine area of responsibility that is an order of magnitude larger than those in the continental U.S. Moreover, the Bering Sea and North Pacific experience a large number of storms, significant in both strength and spatial extent. The Anchorage Area of Responsibility (AOR) can experience upwards of 20 hurricane-force storms in a single winter season. It is therefore easy to understand how important SAR imagery can be in both analysis and diagnosis of the marine environment.

A1.1 A Recent Example

As a case in point, figure A-1 shows a typical Radarsat-measured wind event that affected South Central Alaska on 02 and 03 Feb 2003. Although Radarsat was not available to the forecaster in real-time during this event, the wind field imagery was used extensively in the post-mortem analysis. The implications of the imagery are striking both to the forecast meteorologist and the operational user.

The potential for significant downslope winds was well known for both the Upper Anchorage Hillside and western Turnagain Arm. Typical of the downslope wind events experienced across South Central Alaska, a deep low pressure area at the surface in the western Gulf of Alaska moved north across the Alaska Peninsula in a strong, high amplitude flow in the mid levels.

As a major low pressure area and associated frontal systems approached the peninsula, the east-west pressure gradient increased dramatically across South

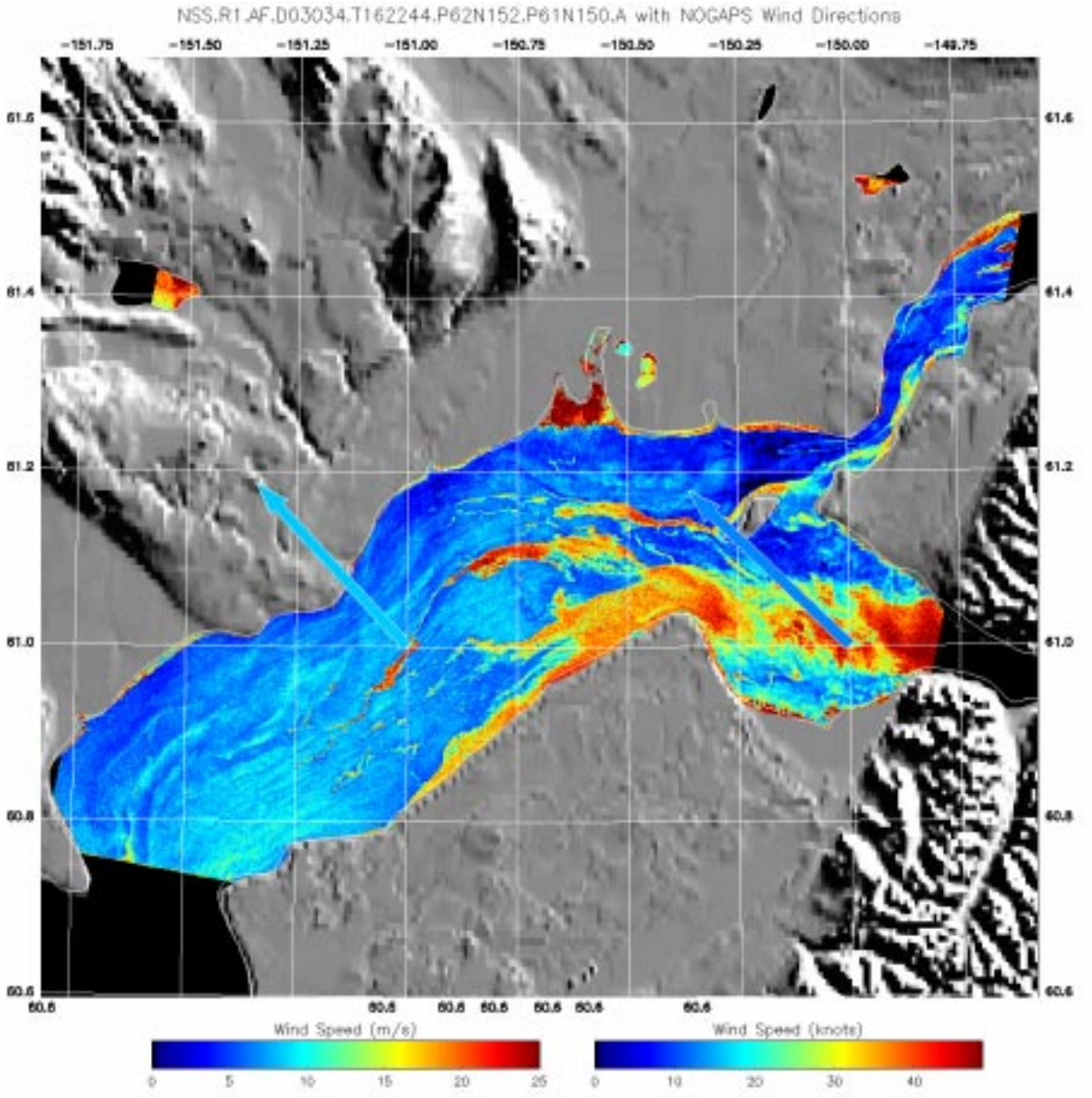

Figure A-1: Radarsat Image of Upper Cook Inlet February 3, 2003

Central Alaska. Standard (non-Radarsat) WFO indicators validated the intensity of the system. Velocity data from both the Kenai and the Middleton Island weather radars were available during both days. The Kenai radar consistently measured inbound velocities in excess of 80 kt. These wind speeds were measured in the vicinity of the gap flow in Turnagain Arm, and surprisingly also out of gaps on the Kenai Peninsula, more often during the second event. A peak inbound velocity of 109 kt was measured near the end of this second

event. The caveat on the use of the Kenai radar for estimating surface winds is that mid-beam is well above the surface of the terrain. The Middleton radar also measured excessive velocities with both events. For Middleton the maximum velocities were less, about 70 kt. However, the higher wind speeds seemed to be associated with a barrier jet that set up during the second event. The weather radars are excellent analysis and short term forecast tools for these wind events.

Figure A-2 is a Radarsat image near the end of the second wind event, around 0300 GMT 05 Feb. Strong winds (in excess of 55 kt) continue in Turnagain Arm. Surface observations in "The Arm" back this up with reported wind speeds in excess of 60 kt. Of particular interest also was the orientation of the wind plume exiting Turnagain Arm into Cook Inlet. Earlier in the day, the plume turned southwest along Cook Inlet upon exit. At overpass time, the plume appears oriented more east-west, perpendicular to the long axis of Cook Inlet. This orientation indeed was borne out in surface observations on the west side of Cook Inlet. This plume pattern also agrees well with subtle changes in the surface pressure gradient through the day, which became increasingly more east-west oriented.

Wind patterns in Prince William Sound were also very interesting. Both wind and wave spectra data were extracted from buoys in the Sound to determine if the Radarsat information was reasonable. Radarsat imagery suggests wind speeds in the 35 kt range (gale force) associated with the two major plumes. Buoy 46060 (West Orca Bay), on the eastern side of the Sound near the edge of the northern-most plume, measured sustained winds of 22 kt with gusts to 32 kt, very close to that indicated by the Radarsat wind field. As another indicator, the wave spectra for the buoy showed extremely steep (wind driven) waves, exactly what one would expect from the sort of wind forces evident in the imagery.

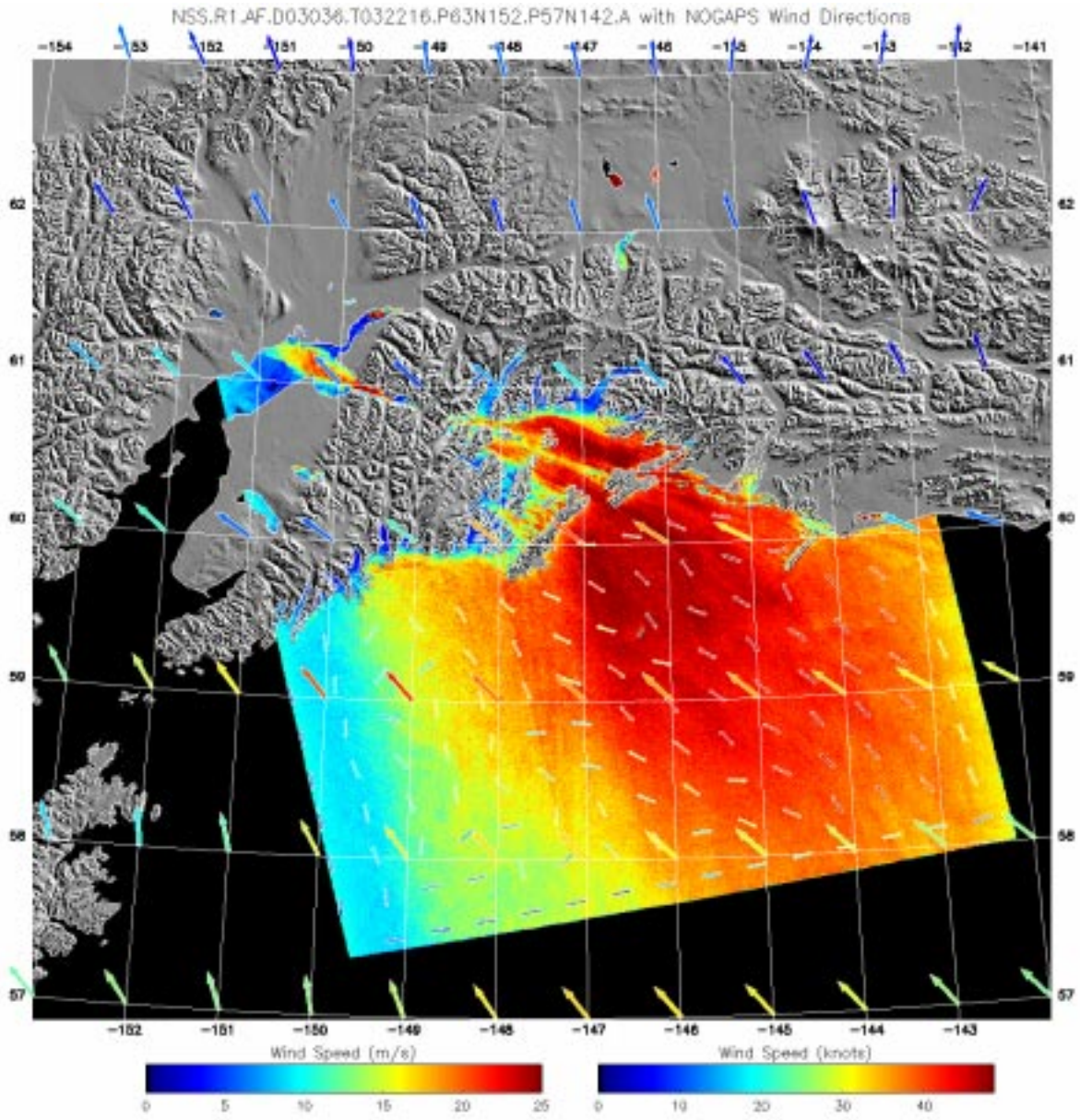

Figure A-2: Radarsat Image of South Central Alaska February 5, 2003

A1.2 Conclusion

Over land, meteorologists routinely use mesoscale network observational data combined with a variety of remote sensing tools and mesoscale models to provide high temporal and spatial resolution products for public product customers. Except in coastal waters, no such infrastructure exists for the marine forecaster. Real-time SAR images would bridge that gap for the operational meteorologist in a marine environment.